Mixed-metal amide catalysts for ammonia decomposition applications



Charlotte Kirk

New College

University of Oxford

A thesis submitted for the degree of

Doctor of Philosophy

Trinity 2019

The University of Oxford
Department of Chemistry

The work reported in this thesis was carried out at the Inorganic Chemistry Laboratory in Oxford and the ISIS Facility at the Rutherford Appleton Laboratory between October 2015 and September 2019 under the supervision of Professor Bill David FRS. All the work is my own, unless stated to the contrary, and has not been submitted, either in full or part, for any degree in this or any other university.

Charlotte Marie Kirk

Don’t fall over, don’t give up

Acknowledgments

There are a number of people who I would like to thank for helping me through the past few years that this thesis represents. My greatest thanks have to go to Josh Makepeace. I simply would not have been able to produce this thesis without him. He is kind, patient and unbelievably selfless, as well as one of the most intelligent people I know. He is an amazing role model and has been a really important part of my academic life over the course of my DPhil, as well as a friend. He truly deserves every success in the world.

I would equally like to thank Tom Wood. He always makes me smile and is one of the best people to work around. I cannot imagine having gone through this process without him. Incredibly clever and so wholesome as a person, his guidance and calming influence has been so important to me. Both of their support and advice has been invaluable, and they constantly inspire me to be a better person.

I would like to acknowledge Bill David for providing the opportunity for me to do this DPhil. Pursuing this path has opened up other avenues in my life which I would otherwise never have had the chance to experience. Whilst this thesis reflects my academic endeavours over the past four years at Oxford, it is the friendships I have formed and the opportunities that have arisen that I am most grateful for.

I hope all my friends know how special they are to me in their own individual ways. Alex and Polly deserve a special acknowledgement for their specific role in this thesis, as they were my rocks that fateful night in February. I am so thankful for the friendship, support and patience of all of my friends. I am so lucky to be surrounded by such amazing people. They believed in me long after I stopped believing in myself and I am very blessed to have such wonderful, kind and caring people in my life.

My final thanks must go to my parents and Joe and Ben for everything. My mum has always been there for me, through many a tearful phone call and I rarely get to express how much it means to me.

Abstract

Our current reliance on fossil fuels is highly unsustainable due to their limited supply and environmental impact. There is an urgent global need to revolutionise the way in which we source and store our energy. Hydrogen is undoubtedly going to play a role in re-designing the transportation sector in particular, but there are significant barriers preventing its widespread implementation. The reversible chemical storage of hydrogen as ammonia provides all the benefits of hydrogen as a fuel, whilst also having characteristics enabling some of the challenges faced by hydrogen to be overcome.

It is the catalytic cracking of NH_3 to release the intrinsic H_2, enabling the provision of hydrogen on demand for use in fuel cells or combustion engines that is arguably the most viable solution to developing a sustainable energy system. The main reason the potential of ammonia as a carbon free hydrogen vector at the point of use has yet to be realised is largely due to the unavailability of an efficient, cheap and effective means for accessing its hydrogen content at scale.

Earth abundant Group 1 and 2 metal amides are among the most highly active and effective NH_3 decomposition catalysts at modest temperatures and have matched or surpassed the performance of optimised transition metal based catalysts. A progression of different systems have been studied to investigate the ability of mixed-metal amides to tailor the active form and activity of the catalyst towards decomposing ammonia.

A wide range of mixed-metal amides can be successfully synthesised by straightforward ball-milling of the constituent single metal amides in the appropriate ratios. The structure and behaviour of these high purity samples was then investigated under inert gas at a range of temperatures through both *ex-situ* laboratory based, and *in-situ* neutron diffraction experiments. Correlating changes in the structures of these mixed-metal amides with variations in the mass of the sample as a function of temperature have enabled a complete description of the behaviour and dynamics of the systems to be obtained.

Analysis of the low temperature behaviour of $Li_3Na(NH_2)_4$ and $Li_3K(NH_2)_4$ under argon, showed initially $NaNH_2$ or KNH_2 melts and separates out of the structure via non-stoichiometric $Li_3R_{(1\text{-}x)}(NH_2)_{(4\text{-}x)}$ (R=Na or K). There is then a small temperature range for which the amides are present as separate components, before the solid $LiNH_2$ dissolves into the liquid $NaNH_2$ or KNH_2 to form an inter-mixed molten phase with a composition approaching that of the constituent amides. $LiNa_2(NH_2)_3$ and $LiK_2(NH_2)_3$ cannot support this non-stoichiometry as they are line phases so they simultaneously separate and melt in one step, but ultimately form analogous inter-mixed molten phases. $NaK_2(NH_2)_3$ does not separate on melting and instead forms molten $NaK_2(NH_2)_3$ which is stable to at least 300 °C, and only separates above this temperature into a molten phase approaching $NaNH_2 + 2KNH_2$.

At high temperatures it is the decomposition of the two amides within the inter-mixed molten phases that is observed, and there is a degree of interaction between these two concurrent processes. It is ultimately H_2 and N_2 release that is observed, in ratios dependent on those of the constituent single metal amides, rather than NH_3 which is seen for the decomposition of $LiNH_2$ alone. The decomposition temperatures of the single metal amides,

when part of this combined melt phase are also significantly lower than those seen during their individual decomposition.

A thorough analysis of the phase space between the two end members of the Li-K-N-H and Na-K-N-H systems led to the identification of two new phases, nominally "$LiK(NH_2)_2$" and "$Na_3K(NH_2)_4$". The synthesis of a novel triple mixed-metal amide with a composition of $Li_6NaK(NH_2)_8$ has been proven and all these species are close to being crystallographically characterised.

Imides generally have higher melting points than their corresponding amides, so an imide which forms at low temperatures and remains solid over a wide range of operating conditions would be an ideal candidate for a practical NH_3 decomposition catalyst. $K_2Mg(NH_2)_4$ and $Na_2Mg(NH_2)_4$ are metastable kinetic products and do not readily separate, instead displaying a single melt temperature. They are stable to much higher temperatures before they decompose to novel molten mixed amide-imide phases, $KMg(NH_2)(NH)$ or $NaMg(NH_2)(NH)$ which crystallise out of solution at 367 °C and 413 °C respectively and do not themselves decompose until over 500 °C.

It is the correlation of the behaviour of each of these mixed-metal amides under inert gas, with their catalytic activity towards NH_3 that is crucial to improving their performance and understanding how to optimise NH_3 decomposition conditions. The initial crystal structure of the mixed-metal amides does not affect the NH_3 decomposition ability of the intra Group 1 mixed-metal catalysts, as these have separated and melted into a molten phase of the constituent metal amides at the temperatures required for NH_3 decomposition.

$LiNH_2$ decomposes to the imide under NH_3 whereas $NaNH_2$ and KNH_2 decompose to the respective metals. It is therefore Li_2NH, Na, K that are the active forms of the catalysts and it is the stoichiometry to which these are present, that ultimately affects the overall NH_3 decomposition ability of the system. However, $K_2Mg(NH_2)_4$ and $Na_2Mg(NH_2)_4$ decompose to $KMg(NH_2)(NH)$ and $NaMg(NH_2)(NH)$ which are the active forms of the catalysts for these systems.

Mixed-metal amide systems can out-perform single metal amides across the entire temperature range. $LiNa_2(NH_2)_3$ and $LiK_2(NH_2)_3$ are currently the best low temperature catalysts and $Li_3Na(NH_2)_4$ and $Li_3K(NH_2)_4$ show the best conversion at high temperatures to date. It is the imide forming component which appears crucial to optimising the NH_3 decomposition ability. This provides evidence that there is added value of the mixed-metal amides as NH_3 decomposition catalysts compared to single metal amides.

The percentage recovery of the catalyst is crucially important in order to maintain efficiency and improve lifetimes. Na and K are volatile so the Li-Na-N-H and Li-K-N-H systems suffer from poor containment and reversibility of such materials is clearly limited under these conditions. The NH_3 decomposition ability of the K-Mg-N-H and Na-Mg-N-H systems is entirely different to that of the Group 1 mixed-metal amides, but significantly worse. However, $K_2Mg(NH_2)_4$ and $Na_2Mg(NH_2)_4$ show the highest catalytic mass recovery rates of close to 90 %, due to stabilisation provided by the amide-imide complexes.

Future research efforts will therefore identify elements which combine the important properties of high activity towards NH_3 decomposition with high mass recovery. This is likely to occur within a system which has an unstable amide and a stable imide or amide/imide in order to optimise the best catalysts for commercial applications.

Contents

1 Introduction **1**

1.1 The energy challenge and global warming 3

1.1.1 Issues with current fossil fuel usage 3

1.1.2 Changes to fossil fuel usage 4

1.1.3 Societal and policy changes 6

1.1.4 Increase in electrification to fuel development 8

1.1.5 Move towards a sustainable energy system 10

1.2 Decarbonising transport 11

1.2.1 Opportunities for change 12

1.2.2 Long-term cost advantages 14

1.2.3 Challenges with electric vehicles 15

1.3 Transitioning to a hydrogen based economy 18

1.3.1 Production of hydrogen 20

1.3.2 Hydrogen end-use technologies 21

1.3.3 Distribution of hydrogen 25

1.3.4 Storage of hydrogen 27

1.3.5 Limitations of hydrogen as a fuel 31

1.4 Ammonia as a hydrogen store and energy vector 31

1.4.1 Current role of ammonia 33

1.4.2 Distribution and storage of ammonia 34

1.4.3 Comparison of H_2 and NH_3 infrastructure 35

1.5 Future role of ammonia 37

1.5.1 Production of ammonia 37

1.5.2 Ammonia end-use technology 43

1.5.3 Safety considerations for NH_3 as a fuel 48
1.5.4 Current limitations for NH_3 as a fuel 49
1.6 Ammonia cracking 50
1.6.1 Traditional ammonia decomposition catalysts 52
1.6.2 "First generation" Group 1 single metal amides as catalysts 56
1.6.3 "Second generation" Group 1/2 mixed-metal imides as catalysts . . 61
1.7 Thesis aims 63

2 Experimental Methods **67**

2.1 General Sample Handling 69
2.1.1 Air and moisture-sensitive sample handling 69
2.2 Synthesis techniques 70
2.2.1 Solid-gas reactions 70
2.2.2 Overview of solid-gas reactions 74
2.2.3 Solid-solid reactions experimental setup 75
2.2.4 Overview of solid-solid synthesis reactions 77
2.3 Ammonia decomposition experiments 86
2.4 Thermal analysis 87
2.4.1 Thermogravimetric analysis (TGA) 87
2.4.2 Differential scanning calorimetry (DSC) 87
2.4.3 Simultaneous thermal analysis (STA) 88
2.5 Vibrational analysis 88
2.5.1 Raman 89
2.6 Structural Analysis 89
2.6.1 Introduction to Crystallography 90
2.6.2 Introduction to Diffraction 91
2.6.3 Neutron Powder Diffraction (NPD) 97
2.6.4 Powder X-ray Diffraction (PXRD) 106
2.6.5 Structure prediction and solution 111
2.6.6 Rietveld Refinement 114

3 Mixed Lithium-Sodium system **119**

3.1 Chapter overview . . . 120

3.2 Background . . . 120

3.2.1 Crystallography . . . 123

3.2.2 Synthesis . . . 124

3.2.3 Raman . . . 125

3.3 Thermal decomposition behaviour . . . 126

3.3.1 Constituent single metal amides . . . 126

3.3.2 Mixed-metal amides . . . 131

3.4 Inert gas summary . . . 145

3.5 Ammonia decomposition . . . 148

3.5.1 Quantitative fitting and analysis . . . 152

3.5.2 Catalyst recovery . . . 155

3.6 Decomposition under ammonia . . . 157

3.7 Summary . . . 159

4 Mixed Lithium-Potassium system **161**

4.1 Background . . . 162

4.1.1 Group 1 metal amides . . . 163

4.1.2 Crystallography . . . 167

4.1.3 Chapter overview . . . 168

4.2 Synthesis . . . 169

4.2.1 $Li_3K(NH_2)_4$ . . . 169

4.2.2 $LiK_2(NH_2)_3$ . . . 169

4.2.3 $Li_7K(NH_2)_8$ . . . 173

4.3 Phase space between $LiNH_2$ and KNH_2 . . . 177

4.3.1 I11 powder X-ray diffraction . . . 177

4.3.2 Raman . . . 179

4.4 Unknown Li-K-N-H phase . . . 182

4.4.1 Where it has been observed . . . 182

4.4.2 Raman . . . 186
4.4.3 Structure solution . . . 187
4.4.4 Summary and future work . . . 191
4.5 STA traces for the phase space between $LiNH_2$ and KNH_2 . . . 191
4.6 $Li_3K(NH_2)_4$ . . . 194
4.6.1 *Ex-situ* thermal decomposition behaviour . . . 194
4.6.2 GEM experiments . . . 202
4.6.3 Inert gas summary for $Li_3K(NH_2)_4$ . . . 220
4.7 $LiK_2(NH_2)_3$ . . . 222
4.7.1 *Ex-situ* thermal decomposition behaviour . . . 222
4.7.2 GEM experiments . . . 229
4.7.3 Inert gas summary for $LiK_2(NH_2)_3$ . . . 245
4.8 Ammonia decomposition . . . 247
4.8.1 Quantitative fitting and analysis . . . 247
4.8.2 Catalyst recovery . . . 251
4.9 Decomposition under ammonia . . . 252
4.10 Summary . . . 254

5 Mixed Sodium-Potassium system 255

5.1 Background . . . 256
5.1.1 Crystallography . . . 258
5.1.2 Chapter overview . . . 258
5.2 Phase space between $NaNH_2$ and KNH_2 . . . 259
5.2.1 Powder X-Ray Diffraction (PXRD) on I11 . . . 259
5.2.2 Raman . . . 265
5.2.3 Simultaneous Thermal Analysis (STA) . . . 268
5.3 *Ex-situ* thermal decomposition behaviour . . . 271
5.4 GEM data . . . 276
5.4.1 $NaND_2 + 2KND_2$ synthesis . . . 277
5.4.2 $NaK_2(ND_2)_3$ decomposition . . . 281

5.5 Inert Gas Summary . . . 285
5.6 Ammonia decomposition . . . 286
5.6.1 Quantitative analysis and fitting . . . 286
5.6.2 Catalyst recovery . . . 289
5.7 Decomposition under ammonia . . . 289
5.8 Summary . . . 291

6 Group 1 triple mixed-metal amides 293
6.1 Chapter overview . . . 293
6.2 Crystallography . . . 294
6.3 Simultaneous Thermal Analysis (STA) . . . 296
6.3.1 6:1:1 mixture of $LiNH_2$:$NaNH_2$:KNH_2 . . . 296
6.3.2 1:1:1 and 2:3:4 mixtures of $LiNH_2$:$NaNH_2$:KNH_2 . . . 299
6.4 Synthesis . . . 301
6.4.1 6:1:1 mixture of $LiNH_2$:$NaNH_2$:KNH_2 . . . 301
6.4.2 1:1:1 and 2:3:4 mixtures of $LiNH_2$:$NaNH_2$:KNH_2 . . . 303
6.5 Raman spectra . . . 306
6.6 Summary . . . 307

7 NH_3 decomposition summary for Group 1 mixed-metal amides 308
7.1 Chapter overview . . . 308
7.2 Analysis . . . 309
7.3 Future work . . . 317
7.4 Conclusions . . . 318

8 Mixed Potassium-Magnesium system 319
8.1 Background . . . 320
8.1.1 Chapter overview . . . 321
8.1.2 Crystallography . . . 321
8.2 Synthesis . . . 323
8.2.1 $K_2Mg(NH_2)_4$ . . . 323

8.3 *Ex-situ* thermal decomposition 325
8.3.1 $Mg(NH_2)_2$ 325
8.3.2 $K_2Mg(NH_2)_4$ 327
8.4 POLARIS experiments under inert gas 333
8.4.1 Synthesis of $K_2Mg(ND_2)_4$ 333
8.4.2 Decomposition of $K_2Mg(ND_2)_4$ 339
8.5 Inert gas summary 345
8.6 Ammonia decomposition (*ex-situ*) 347
8.6.1 Quantitative fitting and analysis 347
8.6.2 Catalyst Recovery 353
8.7 Decomposition under ammonia 353
8.8 POLARIS experiment - Ammonia decomposition (*in-situ*) 354
8.9 Summary 361

9 Mixed Sodium-Magnesium system 363

9.1 Background 364
9.1.1 Chapter overview 364
9.2 Synthesis/ Crystallography/ Phase Space/ Raman 365
9.3 *Ex-situ* thermal decomposition 372
9.4 POLARIS experiments under inert gas 377
9.4.1 Synthesis of $Na_2Mg(ND_2)_4$ 377
9.4.2 Decomposition of "$Na_2Mg(ND_2)_4$" 380
9.5 Inert gas summary 389
9.6 Ammonia decomposition 389
9.6.1 Quantitative fitting and analysis 389
9.6.2 Catalyst Recovery 391
9.7 Decomposition under ammonia 392
9.8 Summary 393

10 Conclusions and Future Work **395**

10.1 New phases 399

10.2 Ball-mill synthesis 399

10.3 Thermal behaviour 400

10.4 Implications for NH_3 decomposition 401

10.5 Future work 407

10.6 Conclusions 409

A Appendix **413**

A.1 Chapter 3 - Li-Na-N-H System 414

A.2 Chapter 4 - Li-K-N-H System 416

A.3 Chapter 5 - Na-K-N-H System 430

A.4 Chapter 6 - Group 1 triple mixed-metal amides 435

A.5 Chapter 8 - K-Mg-N-H System 436

A.6 Chapter 9 - Na-Mg-N-H System 445

Bibliography **451**

Abbreviations

AFC	Alkaline fuel cell
BEV	Battery electric vehicle
BM	Ball-mill
CFC	Chlorofluorocarbon
CSIRO	Commonwealth Scientific and Industrial Research Organisation
DSC	Differential scanning calorimetry
EV	Electric vehicle
GDP	Gross domestic product
GEM	General Materials diffractometer
GHG	Greenhouse gas
HER	Hydrogen evolution reaction
HFCV	Hydrogen fuel cell vehicle
IC	Internal combustion
IEA	International energy agency
IGA	Intelligent gravimetric analysis
IGA^n	Intelligent gravimetric analysis with neutron diffraction
IPCC	Intergovernmental Panel on Climate Change
LDV	Light duty vehicle
LOHC	Liquid organic hydrogen carrier
LPG	Liquid petroleum gas
OECD	Organisation for Economic Co-operation and Development
OPEC	Organization of the Petroleum Exporting Countries
PEMFC	Proton exchange membrane fuel cell
PHEV	Plugin hybrid
POLARIS	High intensity, medium resolution powder diffractometer
RDS	Rate determining step
SOFC	Solid oxide fuel cell
STA	Simultaneous thermal analysis

TF	Tube furnace
TGA	Thermogravimetric analysis
US DOE	US Department of Energy

Å	Ångström(s)
sccm	Standard cubic centimeters per minute
Wh	Watt-hour
wt %	Weight percent
rpm	Revolutions per minute
bar	Unit of pressure defined as 100 kilopascals
dm	Decimeter
°C	Degrees Celsius
K	Kelvin
km	Kilometres
ml	Millilitres
g	Grams
J	Joules
k	Kilo (10^3)
M	Mega (10^6)
G	Giga (10^9)
T	Tera (10^{12})

Chapter 1

Introduction

Contents

1.1 The energy challenge and global warming 3

1.1.1 Issues with current fossil fuel usage 3

1.1.2 Changes to fossil fuel usage 4

1.1.3 Societal and policy changes 6

1.1.4 Increase in electrification to fuel development 8

1.1.5 Move towards a sustainable energy system 10

1.2 Decarbonising transport 11

1.2.1 Opportunities for change 12

1.2.2 Long-term cost advantages 14

1.2.3 Challenges with electric vehicles 15

1.3 Transitioning to a hydrogen based economy 18

1.3.1 Production of hydrogen 20

1.3.2 Hydrogen end-use technologies 21

1.3.2.1 Hydrogen as a chemical fuel for the storage of energy . . 21

1.3.2.2 Hydrogen use in vehicles 22

1.3.3 Distribution of hydrogen 25

1.3.4 Storage of hydrogen 27

1.3.5 Limitations of hydrogen as a fuel 31

1.4 Ammonia as a hydrogen store and energy vector 31

1.4.1 Current role of ammonia 33

1.4.2 Distribution and storage of ammonia 34

1.4.3 Comparison of H_2 and NH_3 infrastructure 35

1.5 Future role of ammonia 37

1.5.1 Production of ammonia 37

1.5.1.1 Haber-Bosch 37
1.5.1.2 Feed-stocks and CO_2 emissions 38
1.5.1.3 Renewable H_2 39
1.5.1.4 Distributed production 41
1.5.1.5 Other Ammonia synthesis methods 41
1.5.2 Ammonia end-use technology 43
1.5.2.1 Proton exchange membrane fuel cells (PEMFC) 44
1.5.2.2 Alkaline fuel cells (AFC) 45
1.5.2.3 Alkaline membrane fuel cells (AMFC) 46
1.5.2.4 Solid oxide fuel cells (SOFC) 46
1.5.2.5 Internal combustion (IC) engine 47
1.5.3 Safety considerations for NH_3 as a fuel 48
1.5.4 Current limitations for NH_3 as a fuel 49
1.6 Ammonia cracking 50
1.6.1 Traditional ammonia decomposition catalysts 52
1.6.1.1 Volcano plots 53
1.6.1.2 Support structures and promoter species 55
1.6.1.3 Transition metals and transition metal nitrides 56
1.6.2 “First generation” Group 1 single metal amides as catalysts 56
1.6.3 “Second generation” Group 1/2 mixed-metal imides as catalysts . 61
1.7 Thesis aims 63

1.1 The energy challenge and global warming

1.1.1 Issues with current fossil fuel usage

It is widely acknowledged that an energy supply based primarily on coal, oil and natural gas is unsustainable because of the environmental impact and future limited supply of these fossil fuels.

The consumption of fossil fuels has driven global industrialisation but the current relationship between economic growth, energy demand and the rapid increase in greenhouse gas (GHG) emissions is dangerously coupled and inter-dependent. Global energy demand has nearly doubled since 1980 which has led to increasing concentrations of GHG in the atmosphere. This has resulted in substantial global warming and significant CO_2 emissions. Global energy-related CO_2 emissions have risen inexorably, reaching a historic annual high of 32.5 Gigatonnes in 2017 due to higher energy demand and the slowing of energy efficiency improvements (Figure 1.1) [11]. We need to return the Earths climate to its pre-industrial state without doing the same to the economy.

CO_2 emissions will rise another 85 % by 2050 [320] if current energy usage trends continue unabated, largely due to predicted population growth, coupled with the anticipated increase in energy demand *per capita* [87, 235]. If left unchanged, this will lead to around a 6 °C rise in the average global temperature [223].

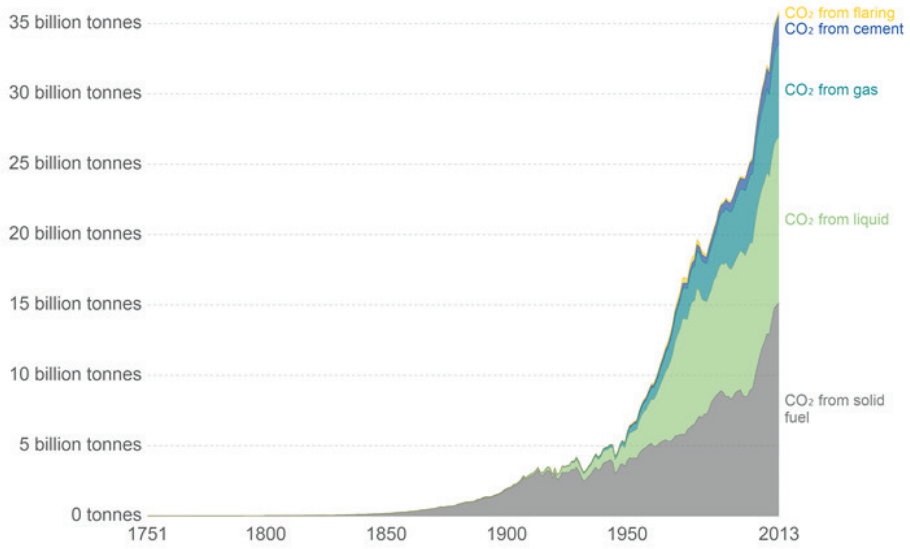


Figure 1.1: Annual global fossil fuel carbon emissions: CDIAC [175]

Climate change is the feedback of the planetary system expressing and manifesting the problem of global warming and its full impact has not yet been experienced. Consequences include rising sea levels and coastal flooding, severe decreases in crop yields and fish stocks threatening starvation and triggering mass migration, vanishing ecosystems and coral reefs, droughts, heat waves and the spread of tropical diseases such as malaria and dengue fever [202]. Man-made climate change is arguably the greatest crises currently facing the planet and a concerted global response is required to tackle it.

The Intergovernmental Panel on Climate Change (IPCC) has reported that it is still possible to limit the temperature rise to 1.5 °C, but anthropogenic CO_2 emissions must be reduced to 45 % of their 2010 levels by 2030 and to zero by 2050. Every year emissions fail to be reduced corresponds to an additional 40 Gigatonnes of CO_2 that will need to be scrubbed out of the atmosphere in the second half of the century to meet the 1.5 °C scenario. The only way to reverse global warming is to avoid emitting more GHG to the atmosphere and to "drawdown" what is already there. This will require radical changes in all aspects of society but especially in de-carbonising the energy sector [222]. Indeed, decarbonisation is the growth story of the 21^{st} century.

1.1.2 Changes to fossil fuel usage

Each of the fossil fuels has both a different historical responsibility for global warming and future lifetime. Fossil fuels currently provide 81 % of world energy requirements [42] but Figure 1.2 shows that OECD oil and coal use for electricity production is decreasing and that of natural gas and renewable sources is increasing [94]. It is unlikely that fossil fuel usage will completely cease as energy use becomes more balanced due to such high current levels of dependency but their importance and role in the overall system will have to change.

Coal is the most polluting and most carbon intensive fossil fuel and has contributed most to emissions. Health implications mean it is losing its social and economic acceptability and the fact renewables are now competitive with coal means its demise has been accelerated. For example, the cost of solar has decreased by 85 % in the past 8 years and is now, in places (Saudia Arabia and Chile), less than 3 cents/kWh which will kill the economics of coal. Reducing coal usage and improving the efficiency of coal-fired power plants are crucial

first steps. There is an accelerated retirement of coal plants in Europe and a decline in construction of new plants in China and India which are also refusing to finalise many plants near cities because of the detrimental health effects.

To halve CO_2 emissions by 2050, coal demand would need to fall by 45 % compared to 2009 levels. It is likely that natural gas usage will continue to increase for the near future (Figure 1.2) as emissions targets tighten, displacing some of the existing coal usage as natural gas can flexibly complement variable renewable energies and balance generation and demand fluctuations.

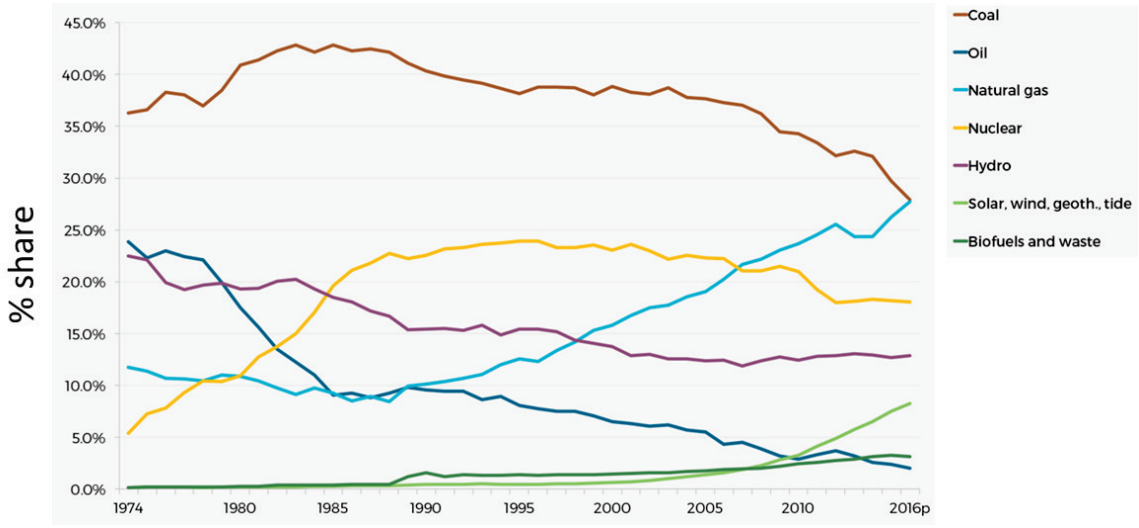


Figure 1.2: OECD gross electricity production by source. Source IEA

A sustainable and diverse low-carbon energy system will provide a better balance than that of today, but technologies will need to be more integrated and complex and will rely more heavily on distributed generation. Diversification of the energy industry away from fossil fuels is of vital political and economic importance [222]. Supply chains based on imported petroleum can be easily disrupted by natural disasters (hurricanes, earthquakes, floods), terrorism, technical failures (such as the 2010 Deepwater Horizon BP oil spill), wars, and the political whims of unstable regimes. During the 1973 OPEC oil embargo and subsequent oil price shocks, huge rises in oil prices sent the world economy into serious recession sparking double-digit inflation and large interest rate hikes in many countries. The limited ability of the USA to increase domestic energy production in the short term led to price controls, rationing, and extreme conservation measures that are inconceivable today.

Having learned from the past, the USA massively increased its domestic supply and this year is set to become the top oil and gas producing country and a net energy exporter by 2022. Ending the uncertain supply of imported petroleum for any country will improve the balance of trade, improve national security by strengthening leverage in foreign relations, decrease the potential for world conflict over petroleum supplies (it may be argued that a part of the external militarily involvement in the Middle East is related to petroleum interests) and provide the opportunity to decrease the negative impacts of petroleum on the environment.

1.1.3 Societal and policy changes

The world's mega problems are all interlinked and the solutions are similarly synergistic with cascading benefits to both human and planetary well-being. If fossil fuels are replaced by renewables and clean technology, not only will global warming be reduced but it will also help save some of the seven million people that die every year from poor health from the air pollution caused by fossil fuels. There are three viable, scalable and financially feasible solutions which in combination can feasibly reverse global warming:

1. Replace existing fossil fuel based energy generation with clean, renewable sources
2. Reduce consumption and improve resource efficiency with systemic technological and behavioural changes
3. Bio-sequester carbon in the planets biomass and soil through photosynthesis

Implementing these solutions will change the global system from one that is exploitive and extractive to being more restorative and regenerative. Global goals need to be rethought beyond sustainability towards regeneration which will implicitly reverse global warming. The scientific understanding of global warming has been established and we are in a period of exponential change driven by technological developments, price decreases, policy framework and finances, as companies are putting money where there is less risk (the green economy). When these four factors are overlaid with artificial intelligence based on digitalization, two of the most powerful accelerators, the transformation is likely to be rapid.

Carbon capture, which involves isolating CO_2 at its emission source, trapping it and transporting it to a storage location (usually deep underground) is going to have to become an industry standard. Turning CO_2 into a mineral is a permanent way to keep it out of the atmosphere and Blue Planet is a company that captures CO_2 from power plants and uses it as a raw material to make synthetic limestone for concrete. However, any realistic chance of avoiding highly dangerous levels of global heating will need to involve the removal of CO_2 already present in the atmosphere using nascent technology. One trillion tonnes of CO_2 needs to be permanently removed and stored by 2050. Climeworks is a Swiss company which captures CO_2 from the air via cyclic absorption/desorption cycles which can then be sold commercially to customers for use in the food/beverage industries, for use as a synthetic fuel/material or stored underground.

It is hoped that the Paris Agreement which was committed to in 2015 and comes into effect in 2020 on a range of measures agreed at the 2018 COP24 conference, will reinforce this positive change. Its central aim is to strengthen the global response to the threat of climate change by keeping this century's global temperature rise to well below 2 °C above pre-industrial levels and to pursue efforts to limit the temperature increase even further to 1.5 °C. Meeting this goal will require rapid reductions of carbon emissions.

Governments are beginning to see that investing in clean energy creates new jobs, and also leads to a healthier, more productive workforce as a low carbon economy is also a prosperous economy. The welfare costs of pollution have been estimated to be at $ 4.6 trillion a year, equivalent to 6% of global GDP [174]. A full-scale integration of low-carbon and sustainable technologies into the current global economic system, could lead to financial benefits of more than US $ 26 trillion through to 2030, compared to the "business-as-usual" case scenario [61]. This would lead to the creation of 65 million low-carbon jobs and avoid over 700,000 premature deaths from air pollution [3].

1.1.4 Increase in electrification to fuel development

There will be 4 billion more people on Earth by the end of the century than there are today, and 3 billion of those will have been born in Africa. Europe and North America's populations are set to shrink slowly and Asia's to shrink fast, but the population of sub-Saharan Africa is projected to nearly double in size by 2050.

It is estimated that nearly 1.3 billion people globally lack access to electricity and about half of these people live in sub-Saharan Africa [143]. In at least 37 sub-Saharan countries, less than half the population has access to electricity and extremely poor and post conflict countries (Liberia, South Sudan, and Sierra Leone) access to electricity is less than 5 %. Human development is inexorably linked to increased access to, and use of, electricity [22].

Investing to provide future opportunities for this demographic bulge will both fuel and drive electrification and is vital to reducing poverty. Energy consumption is expected to grow by around 5 % per year in non-OECD countries over the next decade where *per capita* energy is still on average only 30 % of that in OECD countries. In 2014, in the US, annual *per capita* electricity consumption was 12,984 kWh compared to 806 kWh and 70 kWh in India and Ethiopia respectively [272].

Access to electricity is a building block of human development and well-being (Figure 1.3) enabling energy consumption for lighting, cooking, refrigeration, heating, cooling and communicating which all improve quality of life and serve productive economic purposes. Living without electricity affects:

- Health - Cooking with biomass kills more people through respiratory illness worldwide than AIDS and malaria combined [143]. 60 % of refrigerators used in health clinics have unreliable electricity, compromising the effectiveness of vaccines and medicines.
- Education - Preclusion from modern learning tools like computers, or access to amenities necessary for a conducive learning environment.
- Gender disparity - Women bear the brunt of the added time and labour costs, from collecting firewood to processing agricultural products

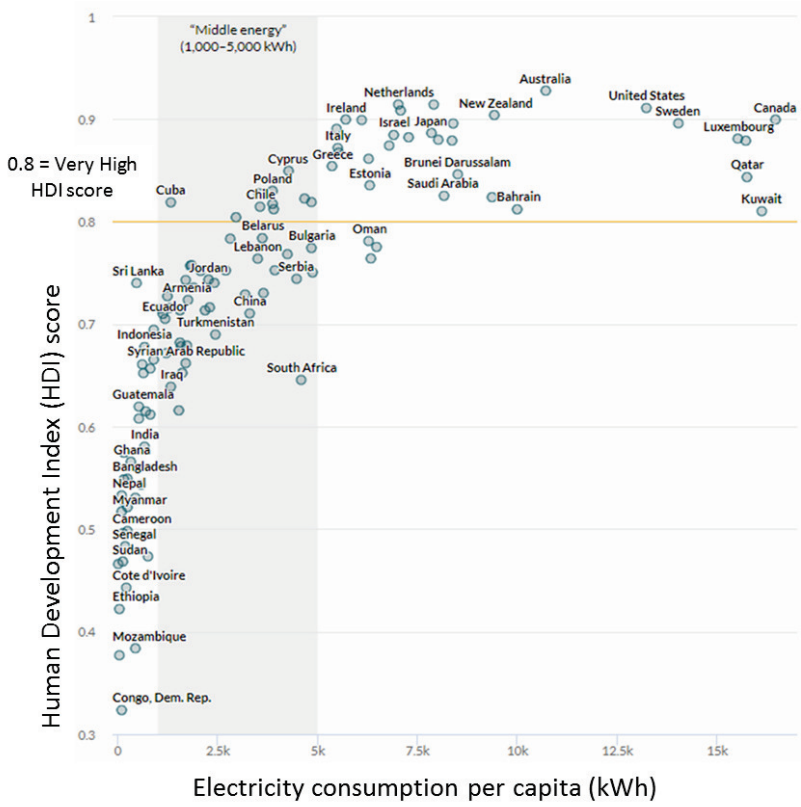


Figure 1.3: Electricity consumption is correlated with higher development and welfare. Source: UNDP Human Development Index (2013)

The World Bank and United Nations have launched a Sustainable Energy for All (SE4All) initiative, which aims to bring universal access to electricity by 2030. In June 2013 President Obama launched "Power Africa" with the goal of boosting electricity generation by 30 GW and providing first-time access to 300 million Africans, half of those currently living without electricity [47]. These are achievable targets given China extended access to more than 650 million people in only 20 years.

Clearly such a rise in global electricity use is going to require much greater energy provision, but where electricity is being introduced for the first time also provides the opportunity to bypass conventional technologies that rely on fossil fuels and implement clean energy systems straight away.

1.1.5 Move towards a sustainable energy system

To meet growing energy requirements, low-carbon electricity generation will have to be at the core of a sustainable energy system and is already competitive in many markets due to concerted international research efforts. More balanced energy systems have been developed, featuring renewable sources with greater efficiency and minimal environmental impact such as solar, wind, biomass, geothermal, wave, tidal and hydroelectric.

10 years ago, 4 % of electricity was from renewable sources but by 2016, renewable sources contributed 19.3 % to the global primary energy consumption and 24.5 % to the generation of electricity [215]. Renewable capacity is being duplicated on the grid every 4 years and it is expected that 50 % of electricity will be from renewable sources by 2030.

A high proportion of renewable sources are intermittent suppliers of energy, but consumer demand is also irregular. Energy storage is about transporting energy in space and time and it is this storage (particularly for more than a few hours) that is increasingly important for sustainably load balancing electric grids, back-up power and transportation.

A full grid requires many orders of magnitude of energy storage and power duration to secure the uninterrupted supply of energy and a diverse range of technologies currently exist (Table 1.1).

Table 1.1: Energy storage technologies. Source: SBC Energy Institute

Kinetic energy			**Potential energy**		
Thermal	**Electrical**	**Mechanical**	**Mechanical**	**Electrochemical**	**Chemical**
Hot water	Super-capacitors	Flywheels	Pumped hydro	Lithium ion	Hydrogen
Molten salt	Superconducting magnetic energy		Compressed air energy	Lead acid	Synthetic natural gas
Phase change material				Redox flow	**Ammonia**
				Sodium sulphur	

Pumped hydroelectric systems currently account for over 95 % of all bulk grid power storage globally with a minor role played by other technologies such as battery grids, compressed air and hot water tanks. However, pumped hydro and compressed air regimes are inflexible and unsuitable for all locations as well as having short discharge durations so there is a dire need for alternative approaches for storage of renewable energy at scale, and convenient ways for its transportation to its place of use [14].

1.2 Decarbonising transport

One of the biggest uses for stored renewable energy is in the transport industry, where it is needed for future on-board use. Energy demand in the transport sector has steadily increased in recent years. It currently accounts for 20 % of the world's primary energy use and 25 % of energy related CO_2 emissions [138] with a disproportionate percentage of these emissions coming from industrialised countries. These numbers are projected to be more than doubled by 2050. In 2016, the transport sector generated the largest share of both the US (28 %) and UK (26 %) GHG emissions primarily from burning fossil fuels as over 90 % of the fuels currently used are petroleum based [76]. Therefore, if energy and emissions targets are to be met, the transport industry in particular needs to undergo vast and transformative changes.

Global transport GHG emissions have increased due to greater demand for travel and a rise in personal mileage resulting from a combination of population growth, rise in the motorisation rate, urban sprawl, economic growth, changes in mobility costs and periods of low fuel prices, especially compared to rising rail transport costs [77]. Although there is an indication that transport GHG emissions are falling in the UK, economic growth in emerging economies has spurred widespread demand for personal vehicles and for moving freight by road. It is road transport from light-duty vehicles (cars and vans) and heavy-duty trucks, that consume the most (75 %) energy within the transport sector [238] and have shown the most rapid growth (20 % increase from 2000 to 2009) so provide the opportunity to make the greatest efficiency savings.

Increasing worldwide car sales have been driven by the growing affluence of Asian markets, where passenger vehicle sales have doubled over the past seven years. In China, vehicle sales quadrupled to 28.9 million vehicles in 2017 and although personal mileage in China is still a long way behind levels in Europe and the US, it is set to increase sharply in the next few years and is expected to overtake the US by 2030. In addition to the environmental consequences of GHG emissions, increasing vehicle usage (particularly diesel) has led to illegal levels of nitrogen oxide pollutants in many cities which is a public health concern. In the

UK, NO_x emissions have been linked to about 40,000 premature deaths a year, incentivising the need to adopt alternatively powered vehicles.

1.2.1 Opportunities for change

Switching away from fossil fuels, reducing CO_2 emissions, slowing climate change and massively reducing air pollution will require a combination of improved fuel efficiency, new types of vehicles and alternative fuels. Future vehicles will most likely be developed around a balance of Battery-Electric (BEV), Plugin-Hybrid (PHEVs) and Fuel-Cell technologies. PHEVs operate on electric power until their battery is depleted to a predetermined level, at which point the vehicle's internal combustion engine or fuel cell is engaged. The battery can be recharged by plugging it into an external source of electric power or by its on-board engine and generator.

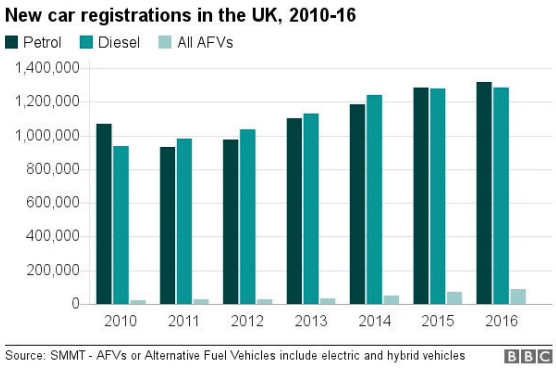
New battery technologies have moved away from traditional lead-acid systems to lithium-ion batteries which show significant promise for vehicular transport [68]. Rechargeable lithium–air batteries have far higher theoretical specific energy density than conventional batteries (5-10 times that of traditional lithium-ion units), and comparable to that of gasoline but currently have a limited cycle life owing to side reactions involving the cathode, anode and electrolyte so are not technically viable or commercially feasible [2, 23, 140].

Oil is the next most carbon intensive fuel after coal and as transport becomes increasingly electrified there is a decreasing demand for oil. Oil has to be seen as secondary to natural gas and transition pathways are being developed to curb its use. Shell has committed to becoming carbon neutral by 2070 and Exon Mobil and Chevron joined the Oil and Gas Climate Initiative (OGCI) in 2018.

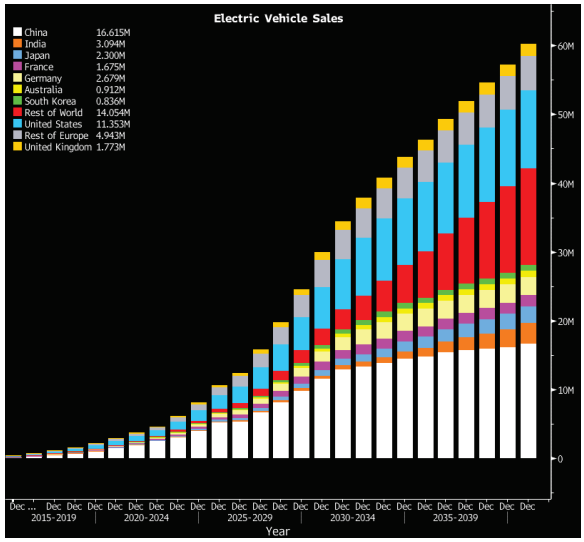
With an estimated 130 million more light-duty vehicles per year expected on the world's roads by 2030, the International Energy Agency (IEA) estimates about 2.57 million barrels of oil per day will be saved if these were to be electric. The global fleet of electric vehicles (EVs) is likely to more than triple to 13 million by 2020 (still only 1% of global car numbers) from 3.7 million in 2017 according to the IEA (Figure 1.4b) [38]. China remains the biggest market for EVs with more than half the global sales in 2017, followed by the US.

Tesla and Nissan currently produce the most well-known EVs (which run on lithium ion batteries), but now all of the major car companies have started to go electric; Volkswagen, General Motors and Audi have also announced battery-powered versions of their models and Volvo has said that it will stop designing new combustion engine-only cars by 2019.

The IEA has also predicted there will be 1.5 million electric buses in use worldwide by 2030, up from 370,000 last year and wind farms in the Netherlands produce enough energy to power its electric rail system [128].



(a) New car registrations in the UK, 2010-2016



(b) Predicted electric vehicle sales. Source: Bloomberg New Energy Finance.

Figure 1.4: Electric vehicle trends

Regulation is also moving forwards and most governments (including India and China) have said they will stop the sale of internal combustion engine only cars and vowed to ban all petrol and diesel vehicles in the next 15-20 years, although in practice this will not be possible. The UK Government released a "Road to Zero" Strategy in July 2018 with the aim for all new cars and vans to be effectively zero emission and to end the sale of any new conventional petrol and diesel cars and vans by 2040. It includes funding of £1.5 billion for ultra-low-emission vehicles by 2020 as well as an additional £100 million of funding for innovators in ultra-low-emission vehicles and hydrogen technology. Achieving this goal is requisite on increasing electric vehicle production, lowering costs, developing infrastructure and boosting consumer confidence, but the goal is technology neutral so does not speculate

on which technologies might help achieve the 2040 target. The UK government also passed an "Automated and Electric Vehicles Act" in July 2018 which will lead to the improvement of electric charging infrastructure across the country, particularly at motorway services.

1.2.2 Long-term cost advantages

Investing in clean energy makes economic sense as the cost of developing low-carbon energy systems now will be outweighed by the potential savings in the future. In the USA, it has been predicted that a sustainable energy system will require $ 140 trillion in investments to 2050 but would generate overall undiscounted net savings of more than $ 60 trillion [320]. It has been predicted that it will cost 3-5% of global GDP for 20-30 years to return the atmosphere to 300ppm CO_2. This is achievable given in 2008 USA diverted 3.5% of annual GDP to prevent the financial system collapsing.

Currently electric vehicles are more expensive than similar models with internal combustion engines, but offer significantly lower lifetime costs (Figure 1.5). EVs could be over four times more affordable to run than petrol and diesel vehicles by 2040 although a direct comparison of costs is difficult due to the artificial impact of tax (required to keep the road infrastructure going) on overall price [288]. Before tax, recharging an electric vehicle could add around £175 per year to a household's electricity bill under standard charging (at peak times) compared to around £ 800 for a petrol or diesel vehicle (including tax and based on $\approx$ 8,000 miles per year at 52.3 mpg, at 117 pence per litre). Smart charging at off-peak times (overnight or during the day) and in combination with "vehicle to grid" charging (EVs provide electricity back to the grid at peak times) could reduce the running costs by a further 42 % and 49 % respectively. Indeed the charging profile is a more important factor than the overall number of electric vehicles on the cost of integrating EVs into the electricity system [288]. This demonstrates the importance of storing energy for load-balancing in electric grids.

As EVs become more mainstream, their cost will continue to fall as economies of scale will drive down costs and as this new form of transport takes hold the benefits of further development, research and funding are likely to be reinforcing. This will bring down the cost of motoring and it has been predicted that if all cars were to remain privately self-driven

but turn electric, vehicle numbers in Britain would increase by 51 % by 2050. Therefore it is crucial autonomous and shared forms of transport develop concurrently as these would work to minimise the total number of vehicles on the roads.

BEVs are material and energy intensive to produce but as electricity is a cleaner energy source than gasoline they make up for their higher manufacturing emissions within approximately eighteen months of driving. Current BEVs have a 23 % advantage in global warming potential from greenhouse gas emissions (CO_2-equivalents) compared to an ICEV over the full vehicle lifetime [275]. EVs engines are also much simpler with only 20 moving parts compared to the 2,000 or so in an internal combustion engine.

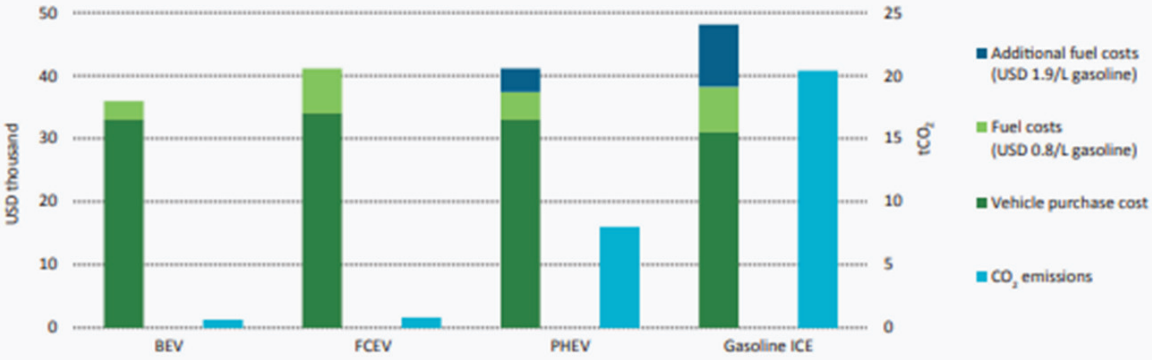


Figure 1.5: Long-term vehicle and fuel costs compared to lifetime CO_2 emissions. Source: [137]

1.2.3 Challenges with electric vehicles

However, this expansion in EV capacity is not without associated challenges. Bloomberg has predicted that by 2028 there will be 1.1 TWh of Li-ion batteries produced [1]. Taking an average of 50 kWh per EV (Tesla requires 100 kWh and the Nissan leaf 40 kWh), this allows for the production of 22 million EVs per year. However, there are currently 100 million cars produced each year and demand for EVs is predicted to rise (Figure 1.4b). Additionally, this only considers battery power for cars, not other applications such as trucks, maritime transport or grid-balancing.

This increasing demand for batteries, largely driven by LDVs meaning many more giant battery gigafactories will need to be built. Tesla's $ 5 billion, 3,200 acre battery manufacturing plant in Nevada achieved a 35 GWh annualised battery power production volume by the

end of 2018 and has since increased the planned total capacity to 105 GWh of battery cells and 150 GWh of total battery pack output by additionally using other battery suppliers for its energy storage projects [92]. Other issues for BEVs include achieving ranges over 200 km (batteries do not carry enough energy although flow batteries are better but are not suitable for use in cars and will mainly have grid-based applications), weight (600 kg), recharging times and safety. A 100 kWh lithium-ion battery could cause a significant accident as a result of all the stored energy. These safety concerns would be slightly mitigated by future development of lithium-air batteries as oxygen does not reside in the battery itself (though there will probably need to be an oxygen tank onboard and these may not be able to be built on a big enough scale).

Cobalt and lithium are key components in the cathode of current lithium-ion rechargeable batteries. Cobalt is both scarce and expensive and the cost of cobalt (currently $ 32,000 per tonne but reached an all time high of $ 95,250 in March 2018) may make the mass production of >100 kWh batteries prohibitively expensive. There are also ethical concerns, as currently 60 % of the world's cobalt is mined in the Democratic Republic of Congo where child labour still exists [280]. There are also concerns surrounding the large scale use of lithium, starting in 2015, prices for lithium almost tripled to more than $20,000 a tonne in just ten months. Large amounts of drinking water are used in lithium extraction and extraction techniques are becoming more energy intensive as lithium demand rises. The pace of advance is slowing as conventional technology approaches fundamental limits as the amount of charge that can be stored in gaps within the crystalline structures of electrode materials is nearing the theoretical maximum [280]. These factors not only provide incentives to shift away from lithium and cobalt heavy batteries and revolutionise the battery industry as a whole but to begin exploring other carbon free fuel sources.

Sodium is inexpensive and virtually limitless but is a larger ion than lithium, so it is not possible to simply "swap" it for lithium in current battery systems. In developing sodium-ion batteries the main problem is the lack of a high-capacity anode as sodium will not fit between the carbon layers of the graphite anode used in lithium ion batteries. However, there is progress being made in this field as the UK company Faradion's Na-ion battery has a similar performance to $LiFePO_4$ [29].

Battery development currently has the most momentum, but developing chemical fuels on a global scale (alongside batteries - it is not a case of one or the other) is a key element for clean energy technologies [177, 281]. 55 million tonnes of H_2 are produced each year and currently 1 kg of H_2 gives a driving range of 100 km, although Toyota have predicted this will increase to 154 km/kg H_2 by 2024. The average car (in the UK) does 13,000 km/year which means the current level of production of H_2 could fuel 400 million cars per year (there is just over 1 billion cars on the road globally, and almost 100 million new vehicles sold each year). This is significantly greater than the 22 million battery powered cars possible by 2028. Half the H_2 currently produced is used to make ammonia, so using ammonia as a chemical fuel (in which the H_2 is already stored) would currently be able to fuel 200 million cars.

The benefit of liquid chemical fuels is that they have a high volumetric energy density and there are various applications where this is advantageous. For example, the batteries commercially used in the Nissan Leaf occupy a volume 30 times greater than the amount of petrol required for the same energy output. However, the benefit of increased energy density is concomitant with decreased efficiency as the fuel has to be synthesised before it can be converted to energy. Chemical fuels are therefore not in direct competition with batteries as their different energy densities and efficiencies means they are suited for different purposes. There will be some applications where the high efficiency of batteries means they are the technology of choice.

Batteries are available on a range of scales from 1 kW to over 100 MW, but their gravimetric energy density is low (1 kg of H_2 can store 236 times more energy than 1 kg of Li-ion batteries) and electricity cannot be stored in batteries for extensive periods of time. They are very good for small scale applications - for an hour or so after the sun has gone down, batteries can be used to store that energy to be used in the next few hours, but batteries are not on a large enough scale for inter-seasonal storage (over a 6 month period), therefore a different system is required.

Although less efficient than batteries, these losses are worth it to store inter-seasonal quantities of energy as chemical fuels such as H_2 or NH_3. In the UK, the energy demand between summer and winter is a difference of 51 TWh. In summer the excess energy can be

used to generate a chemical fuel such as NH_3 that can be safely stored until winter when it can be used as an energy buffer.

1.3 Transitioning to a hydrogen based economy

Hydrogen as a fuel presents an appealing alternative to fossil fuels and has long been talked about as the sustainable fuel of the future. Developments towards transitioning to a sustainable hydrogen-based economy have been stalled for about a decade but hydrogen is likely to play a growing and important role as an energy carrier in the future energy and low-carbon road transport sectors. There is going to have to be a shift from a society of "energy gatherers" to one of "energy farmers" making use of vectors such as hydrogen which allow energy to be stored, transported and converted to electricity.

Hydrogen has many attractive properties:

- High gravimetric energy content, 120 $MJ\,kg^{-1}$ is released during the oxidation of hydrogen ($H_2 + \frac{1}{2}O_2 \longrightarrow H_2O$) [138]. By weight H_2 has an energy density 3 times that of gasoline and a much higher energy density than batteries. Liquid hydrogen could be an alternative to traditional kerosene jet fuel as it has a 3 times greater energy density per unit mass, which is important when weight is a constant consideration.
- Vastly abundant
- Clean emissions profile free from CO_2 at the point of use (H_2O is the only by-product of complete combustion) [28, 305]
- Efficient end-use applications (fuel cells)
- Possibility for decentralised generation and storage

An overview of all the elements of an idealised potential energy cycle is shown schematically in Figure 1.6. This thesis is premised on the importance of ammonia as a hydrogen store and energy vector so the role of NH_3 has been included here for completeness. Each part of the system is discussed and elaborated on in more detail.

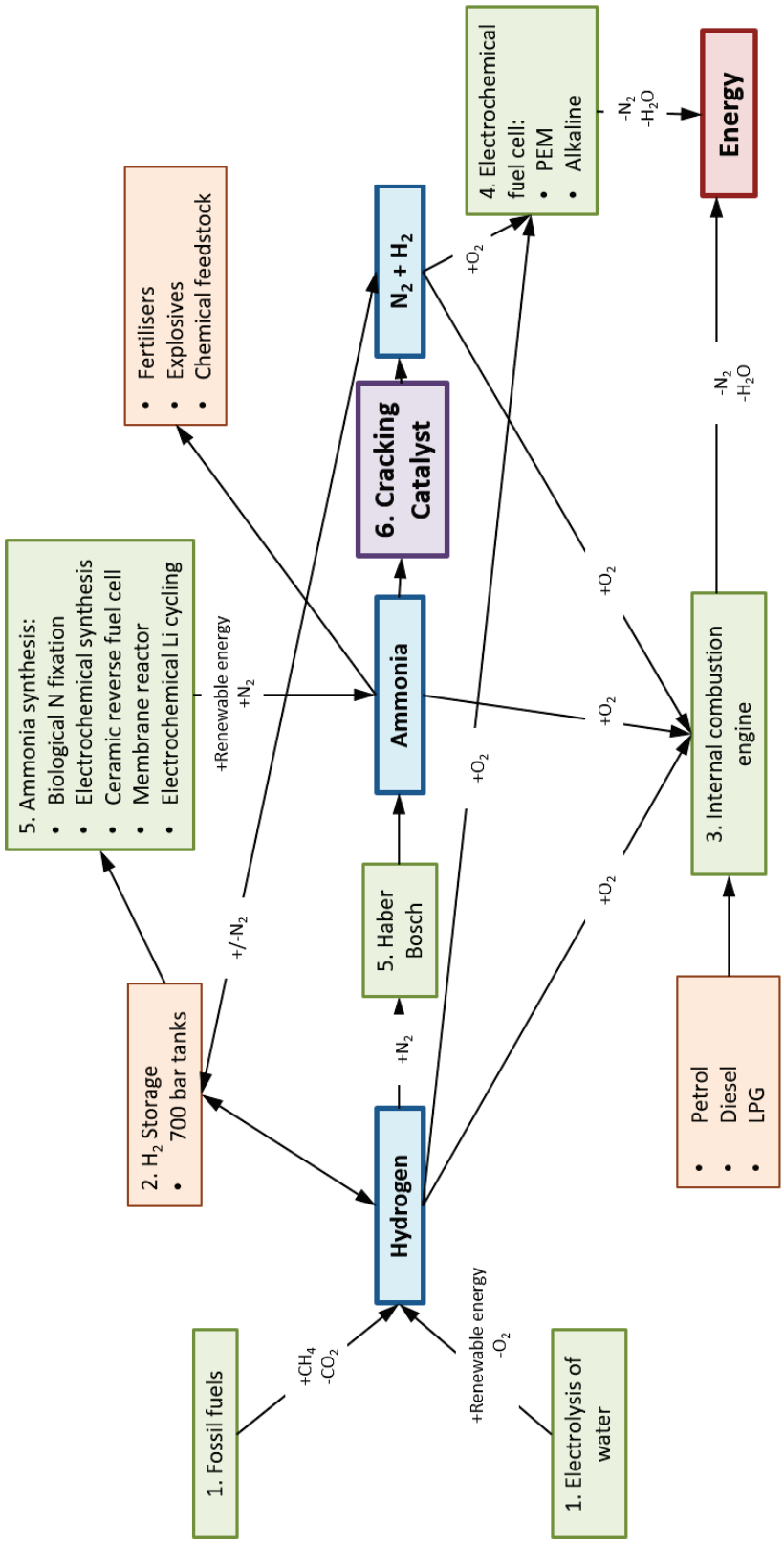


Figure 1.6: Flow chart demonstrating the role of both H_2 and NH_3 in a potential energy cycle

1.3.1 Production of hydrogen

Despite being the most abundant element on earth, hydrogen is almost entirely found in combined chemical forms. Therefore a hydrogen based energy cycle must first start with the production of hydrogen (Stage 1 in Figure 1.6).

Over 60 million tonnes of hydrogen are produced annually for industrial purposes [244], half is used for NH_3 and fertiliser production (Section 1.4.1), petroleum refining is another major use but transportation and utilities are emerging markets [31, 113, 161, 173, 205, 251, 311, 312].

Currently, 95 % of H_2 is produced from the steam reformation of hydrocarbon fossil fuels such as natural gas [89] ($CH_4 + H_2O \longrightarrow 3\,H_2 + CO$) with additional hydrogen obtained by subsequently reacting the CO with water via the water-gas shift reaction ($CO + H_2O \longrightarrow CO_2 + H_2$). Unless the CH_4 is from bio sources, the obvious drawback of these processes is concomitant CO_2 release. Although this conflicts with the aim of de-carbonising the energy sector, the steam reformation of CH_4 results in an overall CO_2 release that is only half of that produced during the combustion of petrol [182]. This method of H_2 production could therefore act as an intermediate stop-gap solution during the concurrent development of sustainable alternatives.

H_2 is preferably produced from the electrolysis of water ($H_2O \longrightarrow H_2 + \frac{1}{2}O_2$) [51], also known as the Hydrogen Evolution Reaction (HER) using a Proton Exchange Membrane (PEM) or alkaline electrolyser and either electricity from diverse regionally-prevalent renewable energy sources, or via a thermochemical cycle. A key benefit of this production method is that the only by-product is O_2 making it a zero-emissions fuel at the point of production.

Additional methods of hydrogen production exist on a smaller scale such as biomass derived liquid reforming or gasification. Direct water splitting using high-temperatures (generated by solar concentrators or nuclear reactors), photo-biology (algae and microbes) or photo-electrochemical systems (using semiconductors) are also in development [34].

It is the cost of electricity that is the main hurdle for the widespread implementation of water electrolysis. Despite the electrolysis processes being relatively efficient (56-73 %

system efficiency [131]) hydrogen produced from grid electricity is costly unless more affordable electricity produced from renewable sources can be used. For cost-effective renewable hydrogen, the availability of low-cost, surplus renewable electricity is a prerequisite. At a national level for UK energy security, on-shore wind is slightly cheaper than PV and much cheaper than steam reformation of methane. However, for the UK the cheapest renewable energy would be wind from Chile or solar energy from Morocco. Minnesota alone has enough wind energy to supply electricity to the whole of the US, and Australia has renewable energy potential from abundant sunshine and off-shore wind (25,000 GW) which is four times the global installed electricity production capacity [254].

There has been a fourfold increase in solar electricity generation over the last five years and the rapid global deployment of solar energy is catalysing the decentralisation of installed power generation. The price and accessibility of cheap silicon based panels means millions of people across the world can now generate their own electricity and access power off-grid. Working with only ubiquitous resources, the global commons of sun, air and water are important for independent sustainable energy production, particularly for the democratisation of energy storage. Therefore, the ability to store and export renewable energy is of vital and growing importance.

The primary challenge for hydrogen generation is reducing the cost of production technologies to make the resulting hydrogen cost competitive with conventional fossil fuels [89].

1.3.2 Hydrogen end-use technologies

1.3.2.1 Hydrogen as a chemical fuel for the storage of energy

With continuous improvements to renewable energy based electricity generation technologies and a subsequent reduction in prices [13] it is logical to explore methods of transporting renewable energy in the form of a transportable and commercially viable commodity [108].

One solution to this problem would be for electricity produced during periods of excess renewable energy availability to be used to create hydrogen via electrolysis of water (HER) and the hydrogen can then be converted back later to electricity in fuel cells. Hydrogen is an energy carrier not a primary energy source and therefore provides an option for large-

scale and long-term energy storage of excess electricity for hours, days, weeks or months. It provides a means to temporally decouple the electricity supply and demand on a variety of time scales which could provide the flexibility needed to maximise the integration of variable renewable sources of energy.

Conversion of renewable electricity to a chemical fuel (such as H_2 or NH_3) is only more efficient than the immediate use of electricity (distribution losses in most grids being less than 10 % [144]) if there are constraints that preclude the direct use of the generated electricity. The use of electricity to directly charge electric vehicles would also result in significantly better efficiency as the losses during charging of most modern electric vehicles are typically significantly less than 20 % [253].

However, as many renewable energy sources occur in geographically remote locations, not necessarily near major cities the storage of energy for extended periods of time and for safe transportation (potentially over long distances) is becoming increasingly important as renewable electricity generation increases. Conversely, chemical fuels such as H_2 or NH_3 are also a good way to transport energy to remote locations that do not have a grid connection [27, 244].

1.3.2.2 Hydrogen use in vehicles

Hydrogen fuel cell vehicles (HFCVs) offer many advantages over both conventional petrol or diesel vehicles and more recent BEVs and PHEVs [115]. Road-transport is one of the most demanding sectors due to the dynamic hydrogen need in transient driving conditions. Hydrogen could power vehicles in two ways, in an internal combustion (IC) engine, burning the fuel and converting the heat into electricity (Stage 3 in Figure 1.6) or as a source of electrons for electricity generation using different types of fuel cells (Stage 4 in Figure 1.6). Conventional combustion ($H_2 + \frac{1}{2}O_2 \longrightarrow H_2O$) as with fossil fuels is not being developed in practical terms due to low efficiency (≈25 % compared to 50-60 % hydrogen utilisation for a PEMFC and up to 70 % for an alkaline fuel cell [224]).

It is the electrochemical application in hydrogen fuel-cell electric vehicles (HFCV) which has attracted the most research and application. Hydrogen fuel cell vehicles are just electric cars that store their energy as hydrogen instead of in a battery. In a rechargeable battery

an electric power source drives the regeneration of the fuel whereas in a fuel cell the spent fuel has to be extracted and new fuel added to the system. In a HFCV, to access the energy, it must first be converted from hydrogen to electricity (hence the lower efficiency of HCFVs compared to BEVs).

Globally there were 8,000 HFCVs in April 2018, with the United States and Japan accounting for nearly 90 % of the vehicles [20]. In the US, battery powered vehicles are still generally favoured over HFCVs but Japan has spent more than $ 12 billion on H_2 technology and expects the number of HFCVs on the road to increase from 2500 in 2018 to 800,000 by 2030 with the aim of this H_2 coming from NH_3 [254].

The world's first hydrogen-powered trains have begun running in Germany. A single tank of hydrogen gives them a range of around 1,000 km, on par with a diesel train [4, 9]. The area's many wind turbines will produce part of the energy to create the hydrogen to power the trains. The UK Department for Transport has announced plans to eradicate all diesel trains from the UK network by 2040 (currently about 30% of the fleet). Hydrogen fuel cells represent a much cheaper option than electricity as no expensive overhead power lines need to be installed and electric trains can be easily converted to hydrogen power by having gas storage tanks.

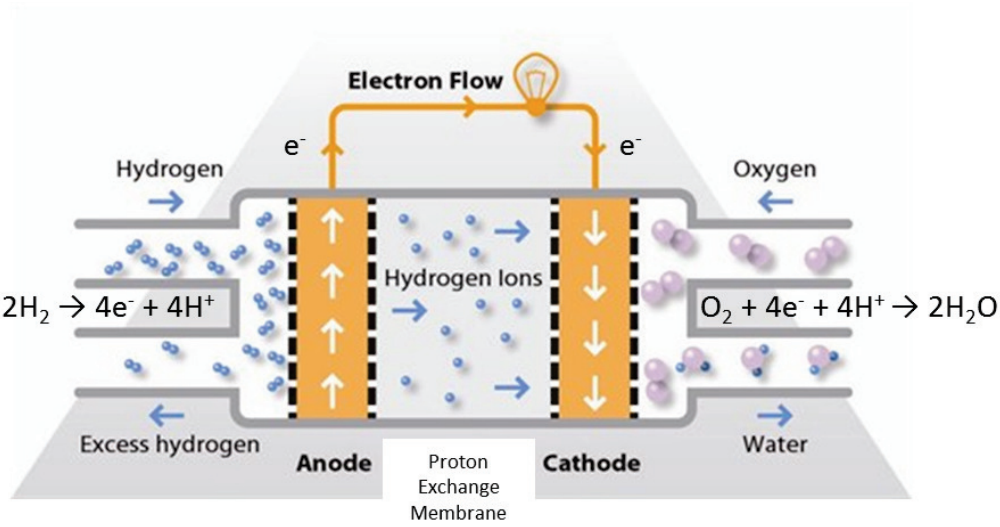


Figure 1.7: Basic structure of a PEM fuel cell [66]

Several types of fuel cells exist in terms of power (sub kW to multi MW), usage, systems and efficiencies for both stationary and transport applications [93, 105, 141]. Currently, more than 80% of all fuel cells sold are used in stationary applications [20]. They can be categorised by the type of electrolyte they use and include alkaline fuel cells (AFC), proton exchange membrane fuel cells (PEMFC), phosphoric acid fuel cells (PAFC), solid oxide fuel cells (SOFC), molten carbonate fuel cells (MCFC), direct methanol fuel cells (DMFCs) and reversible fuel cells. Individual hydrogen fuel cells do not produce a large amount of electricity (typically $<1\,\mathrm{V}$ [224]) which is not enough voltage to power a car so cells are typically coupled together to form a "stack" [224].

Although alkaline fuel cells are a mature and affordable technology, PEMFC and SOFCs show a greater potential to increase efficiency and to reduce capital costs. PEMFCs are the most common and extensively researched type of fuel cell for transportation applications due to their compactness, favourable power-to-weight ratio (high power density) and low operating temperature ($80\,^{\circ}\mathrm{C}$) allowing them to start quickly (less warm-up time) and results in less wear on system components, resulting in better durability [227]. They are a leading candidate to replace the alkaline fuel-cell.

In a PEMFC (Figure 1.7), hydrogen is in constant supply at the anode where it is catalytically split ($\mathrm{H_2(g)} \longrightarrow 2\,\mathrm{H^+} + 2\,\mathrm{e^-}$). Protons pass through the proton exchange membrane conducting electrolyte to the cathode while the electrons pass through an external circuit, generating the electrical output of the cell. At the cathode the protons and electrons recombine with oxygen (provided in a purified form, or extracted at the electrode directly from the air) to produce water (the only waste product) $\mathrm{O_2(g)} + 4\,\mathrm{H^+} + 4\,\mathrm{e^-} \longrightarrow 2\,\mathrm{H_2O(l)}$. Currently PEMFCs have two significant issues:

1. They are sensitive to even low parts per million of contaminants (crucially $<0.1\,\mathrm{ppm}$ $\mathrm{NH_3}$ [284]) due to the electrolytes used, so high purity hydrogen must be used

2. The high cost from the use of platinum electrodes catalysts on the porous carbon electrodes [157]

1.3.3 Distribution of hydrogen

Liquid or gaseous fuels can be transported over long distances (unlike some electrical energy storage options) and then converted to usable energy at end-use sites [25, 112, 124].

H_2 is produced as a gas, and the distribution of it in this form would require significantly different infrastructure to that which is currently in place for liquid fuels such as petrol. If hydrogen is centrally produced, three options for the transport of pure hydrogen are available in the near term [20, 34, 278]:

1. Transport of high pressure hydrogen gas in tube-trailers by lorry at pressures of 180 bar (limited to pressures of 250 bar by U.S. Department of Transportation regulations). However, these have a low load capacity (one lorry of H_2(g) can only carry 180-540 kg H_2 which would only fill 50-150 cars), are expensive and are only practical for distances of 200-300 km from a centralised production site

2. Transport of liquefied hydrogen using truck-trailer combinations with capacities up to 4,000 kg. Liquefied hydrogen significantly increases trailer capacity so would hypothetically enable hydrogen to be transported more efficiently and over longer distances than as a gas. The truck capital cost and operating costs are much smaller, so liquid trucking is less dependent upon the transport distance and would be more economical than gaseous trucking for long distances (400-10,000 km) and for medium amounts of hydrogen. Kawasaki aims to develop the world's first cargo ship to transport liquid hydrogen by 2020, from where it is produced in Australia to power-generation companies and others in Japan [6]. The ship will accommodate two cargo containment systems of 1,250 m^3. Hydrogen will not to be used for propulsion which will instead come from electric motors which will receive power from generators driven by diesel engines. However, whilst liquefaction of $H_2(g) \longrightarrow H_2(l)$ at 20 K is easily reversible, it is a very expensive and energy intensive process requiring more than 30 % of the energy content of hydrogen, in addition to boil off losses during transportation. On balance, the disadvantages outweigh the benefits and liquid hydrogen has largely been side-lined in favour of compressed hydrogen gas for both distribution and storage.

3. Transport of hydrogen gas via pipelines is the least expensive option method to deliver large volumes of hydrogen. At pressures below 100 bar, pipelines require about 3 % of the transported energy per 100 km. In the US there is only about 1,600 miles of pipeline currently available so building the necessary point-to-point transmission and inner-city distribution networks would require considerable investment.

An additional complication to the distribution of hydrogen is embrittlement for hydride-forming metals and hydrogen-assisted cracking for steels which will affect pipeline and trucking materials and compressor designs. Any effective hydrogen infrastructure would therefore require significant capital investment to develop, build and maintain, although this is only a small percentage of the expected total transport spending. On a global scale, hydrogen generation, transmission, distribution and refuelling infrastructure could be developed for around $ 2 trillion with the aim to serve a global fleet of 500 million hydrogen vehicles by 2050. This represents about 1 % of total projected road transport vehicle and fuel costs between 2010 and 2050 [238]. The costs associated with HFCV infrastructure (including retail outlets, production and distribution) are significantly lower than those for a similar roll-out of BEVs.

Due to the lack of suitable distribution technologies and infrastructure, currently most hydrogen is produced at or close to where it is required. Producing hydrogen at the end point of use, for example at fuelling stations could cut distribution costs, although this is balanced against increased production costs for on-site production in comparison to large plants which benefit from economies of scale [34]. Electrolysers are available at small capacities of $<50\,\mathrm{kg\,H_2}$/day. At current electricity costs, on-site electrolysis, compression and storage for a station dispensing $1{,}500\,\mathrm{kg\,H_2}$/day, would cost $ 4.90-5.70/$\mathrm{kg\,H_2}$ [120] which could supply about 300 cars per day. Individual compressed hydrogen refuelling stations have been estimated to cost of the order of $ 3-5 million [203]. ITM Power, the energy storage and clean fuel company, has opened five public hydrogen refuelling stations in the UK at which hydrogen is generated from the electrolysis of water. Investment in water electrolysis to produce H_2 for clean energy applications is on the rise and if all the current UK projects come online, cumulative capacity will rise from 55 MW in 2017 to over 150 MW by 2020.

1.3.4 Storage of hydrogen

Although H_2 presents an attractive solution to the storage of energy, the storage of H_2 itself still remains a challenge. For stationary uses, hydrogen can be stored in ground storages (old salt mines, gas fields, caves), in pressure vessels, or as a liquid in Dewar systems. Storing hydrogen on a small scale and for long time periods is limited due to hydrogen losses.

The greatest issue facing the transportation industry is the inadequacies of current methods of storing hydrogen on-board vehicles at a sufficient density to allow for practical driving ranges (Stage 2 in Figure 1.6) [248]. Although by mass the oxidation of H_2 releases more energy than any other hydrocarbon fuel, in its gaseous form, H_2(g) is 3000 times less energy dense than petrol on a volumetric basis. It is volumetric energy density that is the most practical measure for the comparison of energy storage methods. In 2015, the US Department of Energy (DOE) released targets for the physical storage of hydrogen: high storage capacity (2 kWh/kg gravimetric, 1.5 kWh/dm^3 volumetric), low cost (<$ 4/kWh), operational temperatures between 60-120 °C, reversible thermal absorption and desorption cycle, rapid system filling and non-toxic materials [217, 247]. These standards therefore need to be achieved by research objectives.

Many hydrogen storage options exist and the feasibility of different strategies depend on the demands of their target sectors. For example, in the transport sector and residential use, the energy density, hydrogen release rate and safety are of primary importance, while different criteria apply when hydrogen is used as a seasonal storage or to buffer power fluctuations [14].

Three hydrogen powered cars are currently commercially available: the Toyota Mirai, the Hyundai ix35 and the Honda Clarity. All rely on on-board 700 bar tanks as the storage technology of choice with a total capacity of 5 kg of hydrogen which allows for a 500 km driving range. However, as a storage method, creating the high gas pressures required in these tanks is expensive and energy intense (compression, dispensing and cooling costs 10-20 % of the energy content of the dispensed hydrogen) and carry the risk of explosion [105, 125]. The tanks are also very heavy, affecting the car's fuel economy and often made of carbon fibre, an expensive material.

Three methods of compression exist, mechanical (the most common, involving pistons, 40-50 % efficient [187]), electrochemical (using a voltage to force protons through a membrane [12], 70-80 % efficient but lower flow rates) and chemical (reversible bonds are created between hydrogen and solid state materials, less than 30 % efficient but can use waste heat for compression) [267].

Chemical storage has been increasingly researched in order to discover new ways to store H_2 with higher volumetric energy density, more moderate storage conditions and fewer real and perceived safety issues than high pressure tanks. Good hydrogen storage materials must have high volumetric and gravimetric hydrogen densities in addition to good reversibility, low cost, and ease of practical usage. Three types of solid hydrogen storage material currently exist:

1. H_2 can be stored by physical adsorption into porous materials such as zeolites [257, 304], microporous polymers, activated carbons [256], carbon nanotubes [79, 234] and metal organic frameworks [88, 184, 252, 274]. During physisorption the electronic structure of the H_2 molecule remains unchanged and weak van der Waals forces (10-100 meV) form between the H_2 molecule and the host framework. The nature of these interactions means although the H_2 uptake is highly reversible, the adsorption capacity is too low (<1 wt %) at room temperature and substantial adsorption is restricted to cryogenic temperatures ($<$-150 °C) and 10-100 bar H_2 pressure. These materials are mainly useful for reducing the pressure of high pressure hydrogen tanks [249].

2. H_2 can be stored by chemisorption via a topotactic reaction with metals to form binary or ternary simple metal hydrides (AH_x and $A_mB_nH_x$ respectively) [114]. This involves dissociation at the surface followed by diffusion into bulk interstitial sites. Transition metal hydrides display high volumetric densities and have facile reaction kinetics but their gravimetric hydrogen densities are too low for practical applications. Group 1-3 binary metal hydrides have better gravimetric hydrogen densities but are generally too stable and slow kinetics of hydrogen storage and release mean they only release H_2 at temperatures above the targets outlined by the US DOE. The only metal hydride with a commercial application related to hydrogen storage is MgH_2 which is used in

industrial processes which require low pressure hydrogen where it removes the need for expensive compression equipment [8].

3. Complex metal hydrides are hydrogen-containing compounds consisting of at least one metal or metalloid (mainly Group 1 or 2 metal) ionically bonded to a molecular anion containing hydrogen. Containing two or more chemically distinct non-hydrogen atoms they can often store more hydrogen than simple metal hydrides [69]. Some key examples of these materials include:

   - Metal alanates. $NaAlH_4$ doped with $TiCl_3$ is the best performing alanate (doping reduces the operating temperature by increasing reaction kinetics) [36, 37, 39, 40, 65, 160, 176, 200, 233, 282]. It produces a pure H_2 stream and is stable to reversibly store 4 wt % hydrogen over many cycles [265] (although this is still well below US DOE targets). It has been scaled up to prototype fuel tanks [33, 158].
   - Metal borohydrides have some of the highest gravimetric hydrogen densities observed for complex hydrides [180], the most notable of which is $Mg(BH_4)_2$ [53, 67]. It decomposes at 330 °C to polyborane species during which it releases up to 14 % hydrogen but it suffers from poor re-hydrogenation despite favourable thermodynamics of decomposition [54, 220, 255].
   - Metal amides (NH_2^-) are usually mixed with metal hydrides of which the Li-N-H system (with $TiCl_3$ or halide doping additives) shows facile reversibility for hydrogen storage [50]. In the Li-N-H system Li_3N takes up H_2(g) to form the imide which is itself hydrogenated to form the amide (Equation 1.1) [134, 135].

$$Li_3N + H_2 \longrightarrow Li_2NH + LiH \tag{1.1}$$

$$Li_2NH + H_2 \longrightarrow LiNH_2 + LiH \tag{1.2}$$

   Overall this system has a hydrogen storage capacity of 10.4 wt % and a volumetric hydrogen density of 100.3 kgm^{-3} but the dehydrogenation requires temperatures in excess of 350 °C. However, Equation 1.2 alone has a hydrogen storage capacity

of 6.5 wt %, a volumetric hydrogen density of 67.3 kgm^{-3}, a dehydrogenation temperature of 150-200 °C, hydrogenation requires only a few bar H_2 pressure to proceed with reasonable kinetics and can be cycled with a relatively stable capacity [221]. Therefore the Li-N-H system could provide a viable option for transport applications, especially if the low temperature kinetics of the reactions can be improved.

- Solid ammonia borane $H_3N{-}BH_3$ contains up to 19.5 wt % of hydrogen (exceeding gasoline) [156, 231]. Half of the hydrogen atoms are protic $H^{\delta+}$ and the other half hydridic $H^{\delta-}$ and the resulting dihydrogen bonds explain why ammonia borane is a solid at room temperature [75]. Ammonia borane releases a large amount of hydrogen at comparatively low temperatures (starting from around 100 °C), close to US DOE targets. However, despite promise, small amounts of ammonia and borazine irreparably damage PEMFCs and it does not exhibit facile reversibility.

There are two key problems associated with complex anion hydrogen storage materials. Firstly, too high decomposition temperatures for hydrogen release due to the strength of the covalent bonds within the molecular anion complex. Secondly, they suffer from poor reversibility so most of the high-capacity hydrogen stores show very little potential for on-board regeneration [161]. Additionally they have the potential to form gaseous by-products which contaminate the hydrogen gas stream.

None of the solid-state options for H_2 storage are approaching a commercially viable solution and they are not regarded as mature technologies. Solid hydrogen storage would require a new infrastructure as the present system is designed for liquid fuels [14] and in order for them to be used in vehicles the spent fuel would have to be removed and regenerated in designated separate laboratories which is unlikely to be cost effective. There are also other challenges related to the high pressures and elevated temperatures needed in the hydrogenation and dehydrogenation cycles.

Hydrogen can also be stored in Liquid Organic Hydrogen Carriers (LOHCs) which are systems made up of pairs of hydrogen-lean and hydrogen-rich organic compounds (mainly

aromatic and cyclic aliphatic molecules) that store hydrogen by repeated hydrogenation and dehydrogenation cycles catalysed by platinum group metals and their metal carbides [5] by cycling between saturated and unsaturated double bonds. Operating conditions are usually in the range of 150–250 °C at 1 bar. The advantage of the liquid state is that LOHCs can be readily transported by pipelines, trucks and ships over long distances and easily integrated into existing infrastructure. Challenges with LOHC systems are related to the limited experience with this relatively new technology; system durability, hydrogen release rate and catalyst performance for long-term use needs to be proven [195].

1.3.5 Limitations of hydrogen as a fuel

In recent years, the decreasing cost of electricity from renewable sources for producing hydrogen from the electrolysis of water means this is now becoming cost competitive with steam reformation of methane. There has also been more than a 50 % cost reduction in fuel cells since 2006 due to technological innovations such as a five-fold reduction in the platinum content of the catalysts. Despite hydrogen's promise as a clean fuel, there are two significant limitations which are currently hindering the widespread implementation of the potential "hydrogen economy" and the widespread implementation of HFCV.

The biggest hurdle is the need for better and more efficient infrastructure for distributing and transporting hydrogen to the end user. Although these will evolve over time, fuelling stations are not currently widespread, so car makers are not likely to pursue hydrogen unless they see more investments in infrastructure. The second drawback is the insufficiencies of current methods for safely and effectively storing large quantities of high density H_2 to enable portable applications [248]. Identifying and developing suitable reversible H_2 storage materials is of growing and significant importance.

1.4 Ammonia as a hydrogen store and energy vector

Ammonia as a hydrogen-rich molecule is the ideal solution to overcoming the challenges of temporarily and reversibly storing and transporting H_2. NH_3 as a conduit for hydrogen has the potential to solve the problem of an inadequate H_2 only distribution infrastructure.

Indeed green ammonia has the potential to play a significant role in the solution to two of the greatest challenges currently facing humanity, the growing needs for CO_2-free energy and food production.

Previously ammonia has been considered as a vector for nitrogen (Section 1.4.1), but as a liquid fuel its use would be as a hydrogen vector (Figure 1.8). This would mean ammonia could be a key enabler for exporting renewable energy as 1 tonne of NH_3 has a net hydrogen energy content of 5.88 MWh. As an energy store, ammonia would allow countries with rich renewable energy sources to provide cheap renewable energy to less resource rich countries striving to de-carbonise their economies, while improving energy security and reducing dependence on fossil fuels [10]. The "ammonia economy" is an appealing and realistic extension to the "hydrogen economy" [125, 169]; indeed, the application of ammonia to sustainable energy storage applications could have a similarly transformative impact as the Haber-Bosch process has had on the food and ammunitions industries (Section 1.4.1) [24, 56, 113, 161].

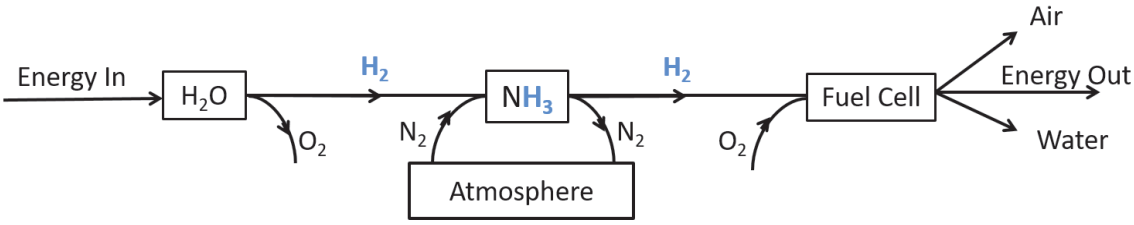


Figure 1.8: Ammonia as a hydrogen vector

Ammonia has both highly attractive chemical and physical properties as well as logistical advantages. Figure 1.9 is a Ragone plot that maps the gravimetric and volumetric H_2 density of a range of potential hydrogen storage materials and NH_3 can be seen to be comparatively favourable. Unlike H_2, NH_3 is easily liquefied at 33 °C and 10 bar pressure. Liquid ammonia has a very high hydrogen content: 17.8 % H_2 gravimetric and 121 kg H_2/m^3 volumetric (40 % that of petrol [114] and 50 % greater than liquid hydrogen in its elemental form when it is either liquefied below 33 K or at gas pressures above 700 bar on both a gravimetric and volumetric base [197, 251]. Similarly to hydrogen, ammonia has no carbon emissions at the point of use (although it may lead to a small amount of nitrous oxide emissions which

can be controlled). Liquid NH_3 can be easily transported before being converted back into hydrogen gas to power fuel cells or burned in a combustion engine.

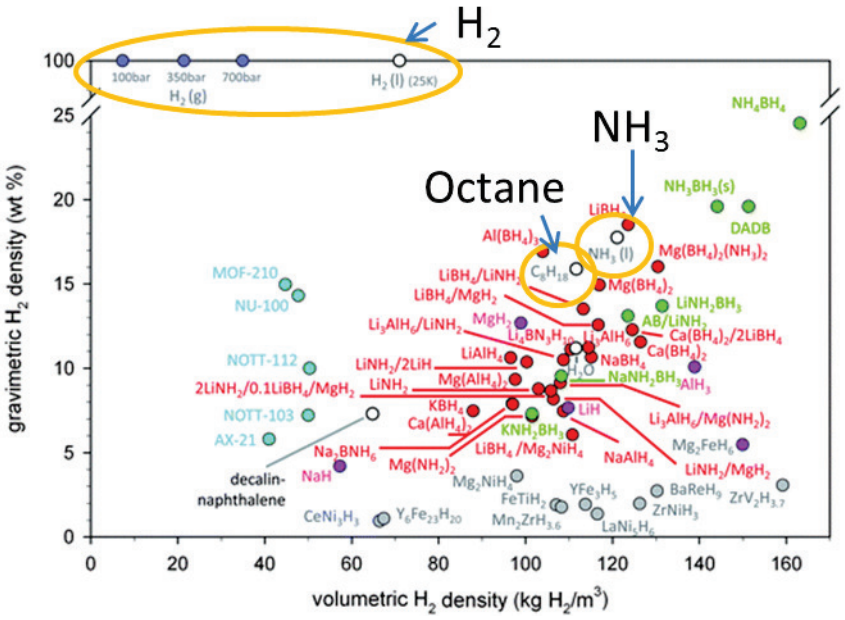


Figure 1.9: Gravimetric H_2 density (wt %) against Volumetric H_2 density (kg H_2/m^3) for selected potential hydrogen storage materials [69]

Methanol (87 kgm^{-3} volumetric H_2 content), methane and formic acid (HCOOH) are alternative energy vectors and fuels which have the potential to store hydrogen and offer similar benefits to NH_3 in its ability to transport energy [16, 136]. However, they do not offer any significant efficiency gains over NH_3 and as carbonaceous substances are CO_2 emitting fuels at the point of use so are less attractive.

1.4.1 Current role of ammonia

Ammonia is a chemically reactive, highly usable form of nitrogen and the industrial synthesis of ammonia through the Haber-Bosch process (Section 1.5.1.1) has had a globally transformative effect.

The initial and main motivation for NH_3 synthesis was for its use in fertilisers (currently 80 % of NH_3 global usage) where it is either applied directly or converted to urea or ammonia nitrate [7]. Nitrogen is needed by plants to synthesise proteins and the yield of intensive agriculture is limited by its availability due to losses from the soil due to the harvesting of

crops [262]. Production of fertilisers on an industrial scale has led to massive global agricultural growth as 62 % of total nitrogen required for crop production comes from fertiliser and manure [262]. It has been predicted that fertilisers have supported 42 % of all births since 1908, by 2008 they had been responsible for feeding 48 % of the global population and around half the nitrogen in the human body (through amino acids in proteins) today originates from a synthetic ammonia plant [95].

The world population is projected to be 9.8 billion by 2050 [283] and the growing demand for food is the main driver behind the increasing production of NH_3 (Figure 1.12). Demand for ammonia for fertiliser alone is predicted to increase by almost 100 % by 2050 compared to 2000 levels to meet hunger alleviation targets as global living standards improve [183]. In much of sub-Saharan Africa, the under-use of fertilisers is leading to land degradation and declining yields and so these countries have huge potential to increase their agricultural production with increased fertiliser use [244]. This will be necessary in order to feed their growing population which is projected to at least double by 2030 [183]. Developed countries have gradually reduced their fertiliser consumption over time through regulations and improved agricultural production technologies and are also set to reduce their food and animal product consumption but not by enough to offset the increasing NH_3 demand [209].

Production of ammonia accounts for 80-90 % of the energy used in the manufacture of fertilisers. Given the need to feed a growing world population whilst simultaneously reducing global carbon emissions, it is necessary to break the link between industrial production of ammonia and fossil fuels. 5-10 % of global NH_3 production is used in synthetic chemical compounds particularly cleaning products [261]. Ammonia is also a common refrigerant of choice with many advantages over CFCs; its thermodynamically 3-10 % more efficient, it does not deplete the ozone layer, its substantially cheaper and leaks can be easily identified by its odour.

1.4.2 Distribution and storage of ammonia

Due to the extent of its current demand (Section 1.4.1), there are already well established infrastructure, handling and usage procedures for NH_3 as well as dedicated international markets [95]. There are also safe, extensive, and mature existing distribution channels and

transportation networks for NH_3 similar to that of liquefied petroleum gas (LPG), particularly useful if NH_3 is to be used as a fuel [312]. NH_3 can be liquefied at 33 °C and low pressure (10 bar) enabling easy transportation and (on-board) storage in cheap, lightweight plastic tanks and it is more easily transported through pipes than hydrogen. Existing natural gas (almost two million miles) and petroleum pipelines can be cost-effectively converted to carry ammonia, making it available to nearly every community in the US. However, additional infrastructure would be need for densely-populated urban areas on the East and West coasts.

The largest NH_3 storage tanks are in Qatar where the fertiliser company QAFCO has built two 50,000 tonne double cement walled tanks to store NH_3 at -35 °C synthesised with H_2 produced by the steam reformation of methane [46]. In the UK just one of these tanks could store enough energy inter-seasonally for 250,000 people, but in reality multiple tanks would be used on a variety of scales.

Metal halides are a good method of storing NH_3 as ammines in a compact solid salt material to aid in transportation. These systems were initially investigated to pick up large amounts of ammonia with the objective of the safety of home refrigerators but research stopped when freons were introduced. $MgCl_2$ is the traditional absorber of choice forming $MgCl_2(NH_3)_6$ which has a high volumetric ammonia density of up to 93 % that of liquid ammonia. 1 tablespoon will hold 74 litres of NH_3(g) at room temperature and pressure [57, 161, 169], it is both easy to handle and safe and almost 99 % of the ammonia contained in the salt can be desorped. Metal bromides are better than metal chlorides as NH_3 absorbers, but they are not stable. Other cations are possible, calcium and magnesium are interchangeable but Mg forms tighter bonds. Strontium is also known to work well (Section 1.5.2.5).

1.4.3 Comparison of H_2 and NH_3 infrastructure

Hydrogen can be stored in a variety ways which each incur different costs prior to its use or export. Figure 1.10 shows ammonia production and storage is the cheapest way to store H_2 for mobile applications.

At the end of 2017, globally there were 323 dedicated hydrogen refuelling stations and less than 7000 H_2 powered cars on the road (with about half of these found in California),

Method of storage	2018 (Base case)			2025 (Best case)		
	35 bar	150 bar	350 bar	35 bar	150 bar	350 bar
Compression and storage in tanks	0.43–0.53	0.30–0.37	0.34–0.42	0.37–0.45	0.23–0.28	0.24–0.29
Compression and storage in salt caverns		0.22–0.26			0.16–0.20	
Ammonia production and storage		0.24–0.29			0.19–0.23	
Liquefied hydrogen production and storage		2.57–3.14			1.30	

Figure 1.10: Storage costs of hydrogen ($/kg H_2) Source: CSIRO [15]

exemplifying the lack of a H_2 infrastructure. However, looking at the existing NH_3 distribution infrastructure, in Iowa alone there are 1089 different NH_3 storage outlets - currently mostly for use in agricultural settings. Using NH_3 as a fuel within an agricultural environment makes a lot of sense due to its dual use as a fertiliser. Very few places in Iowa are more than 30 km away from where NH_3 is stored which could help enable its widespread deployment to the rest of the civilian population. Iowa currently has enough NH_3 to power all its cars for 4 months of the year, so would just have to replenish its NH_3 stores 3 times a year using the available renewable wind energy.

South Australia has awarded AU $ 12 million in grants and loans to a renewable ammonia project [254] and the Australian Renewable Energy Agency has just announced AU $20 million to support renewable export technologies including shipping green ammonia. 90 % of the NH_3 produced globally is used as a feedstock at production sites. The remaining 10% (around 20 million tons per year) is traded and transported often covering large distances [142]. Australia therefore has the potential to become a renewable energy superpower to export NH_3 as a vector for H_2 around the world. Japan is the world's third largest economy by GDP and currently imports 94 % of its energy as fossil fuels; Australia is geographically well positioned to establish itself as the renewable energy supplier of choice to Japan and the rest of Asia in a cost-effective route to reducing emissions. Separated by the Pacific Ocean, this means establishing transportation methods compatible with shipping which is where liquid NH_3 has a key benefit. The energy penalty of converting hydrogen to ammonia and back is roughly the same as liquefying H_2, but liquid NH_3 is much less costly than liquid H_2 to store for half a year ($ 0.5 /kg NH_3 compared to $ 15 /kg H_2) [244] and at least three times less costly to ship on sea or on land (Figure 1.11). Of all the costs for transporting H_2, NH_3 comes out the cheapest to facilitate the distribution of H_2 (Figure 1.11).

Transport method	Compression 350 bar	Compression 430 bar	Liquefaction	Ammonia
Truck	2.98	2.33	0.92	0.33
Rail	0.62	0.55	0.28	0.04
Shipping	0.59	0.52	0.09 (loading cost included)	0.03

Figure 1.11: Transport costs of hydrogen ($/Kg H_2) Source: CSIRO [15]

1.5 Future role of ammonia

The following sections will cover topics that are important for ammonia to be a green energy store; green ammonia production, efficient technologies to extract energy from ammonia and ammonia cracking.

1.5.1 Production of ammonia

NH_3 is currently produced on an industrial scale (186 Mt/year) with an estimated $\$60$ billion annual market value [90, 254]. It is the second most produced chemical globally (after H_2SO_4) and is widely-distributed around the world for a variety of agricultural and industrial applications [21].

Current levels of NH_3 production would need to increase dramatically were it to become a dominant fuel in the global transportation system. For a full replacement of fossil fuels it has been estimated that production would have to increase by over five times to cover US and UK consumption alone, based on the relative energy densities of ammonia and gasoline and assuming average fuel efficiency [110, 285]. Considering ammonia as a hydrogen carrier also increases its economic value, whereas ammonia itself sells for $\$300$-750 a tonne as a fertiliser [78], hydrogen for HFCV can sell for more than 10 times that amount.

1.5.1.1 Haber-Bosch

The Haber-Bosch process "for the synthesis of ammonia from its elements" (Equation 1.3) was developed by Fritz Haber and translated into a large-scale process using high pressures by Carl Bosch, for which they won Nobel Prizes in 1918 and 1931 respectively.

$$N_2 + 3\,H_2 \longrightarrow 2\,NH_3 \tag{1.3}$$

It is the main industrial method for ammonia production and typically utilises pressures of 100-300 bar, temperatures of 400-500 °C and an iron catalyst. The N≡N bond is particularly strong (225 kcal mol^{-1}) so the synthesis of ammonia under mild conditions is a significant challenge. Each pass in the synthesis reactor converts only ≈15 % of the reactants to NH_3 so multiple passes are required to achieve near 100 % conversion. 60 % of the energy input ends up in NH_3 bonds but the Haber-Bosch process is resource demanding and if NH_3 production is to increase exponentially, this will be unsustainable if it is solely achieved using H_2 and input energy for the Haber-Bosch process derived from fossil fuels.

NH_3 synthesis is exothermic (ΔH = -46 kJ/mol) and involves a decrease in entropy so thermodynamically the reaction favours low temperatures and high pressures. However, due to the slow kinetics of the reaction, the synthesis is performed at high temperatures and pressure. Ideally a catalyst could be found that enables the synthesis reactor to run at 300 °C, the same temperature as the absorber used to remove ammonia from the synthesis loop, removing the need for a heat exchanger.

1.5.1.2 Feed-stocks and CO_2 emissions

Nitrogen is extracted from air by cryogenic distillation or pressure swing adsorption. Currently H_2 for NH_3 synthesis is mainly produced from fossil fuel feed-stocks:

- Globally, 72 % of ammonia is produced using H_2 from the steam reformation of methane [137].
- The partial oxidation process of heavy oils or coal produces a mixture of H_2, CO and CO_2. This process has the highest energy consumption and CO_2 emissions and is only used in China where it accounted for 75 % of production in 2010. Over the past 15 years, China has seen the largest absolute growth in NH_3 production (65 % increase) and is the largest NH_3 producing country (31 % of global production in 2011) but NH_3 production is also 35 % less efficient than in Western Europe.

Ammonia synthesis requires energy for the high temperatures and pressures needed, which currently mainly comes from fossil fuels. Together with the fossil fuel generated

hydrogen feedstock, current ammonia production (Stage 5 in Figure 1.6) is responsible for 420 million tonnes of CO_2 emissions (1.8 % of global energy-related CO_2 emissions [244]) and 2.0 % of the world's fossil fuel energy [90]). If CO_2 emissions were ranked by country, CO_2 emissions from NH_3 production would place eleventh as it is such a globally prevalent commodity (25 % more than the total emissions coming out of the UK).

In some NH_3 plants, up to 40 % of the CO_2 produced is captured and used in combination with NH_3 to manufacture urea, the simplest fertiliser [244]. However, few ammonia plants are equipped with carbon sequestration capabilities and efforts to add these are not currently being pursued as they are not economically beneficial.

Most of the energy intensity and cost which goes into making ammonia is from synthesising the precursive H_2 not the NH_3 itself, so one of the key challenges to decarbonising the energy sector is the need to decarbonise the H_2 synthesis process. Switching from coal and oil based H_2 feed-stock production to natural gas based production for NH_3 synthesis and increasing efficiency will result in major energy and CO_2 emission savings.

Table 1.2: Ammonia synthesis from different H_2 feedstocks

Feedstock	**NG**	**Coal**	**Oil**	**Electrolysis of H_2O**
Share of global NH_3 production (%) [287]	72	22	4	2
Energy consumption (MWh/tonNH_3) [27]	7.8	10.6	11.7	10-12
CO_2 emissions (/tonNH_3) [139]	1.6	3	3.8	0.1

1.5.1.3 Renewable H_2

Ultimately, the aim is to make green ammonia in a sustainable synthesis process using H_2 produced from the electrolysis of water using a variety of renewable energy sources.

Until the 1960s, most fertilisers sold in Europe came from hydro-power based electrolysis and NH_3 production in Norway [244]. However, these have since been closed due to falling natural gas prices and the emergence of steam reformation of methane, or converted into natural gas feedstock based plants for NH_3 synthesis [130, 244]. Hydro-power currently produces more than 75 % of the world's renewable energy output each year and 84 % per

cent of Africa's non-fossil fuel energy use. In a continent rich in lakes and rivers, the opportunities for expanding hydro-power are therefore huge. Forthcoming hydro-power plants in Africa may provide a large output in excess of regional needs, providing new opportunities for manufacturing NH_3 and fertilisers in sub-Saharan Africa where they are likely to be in growing demand.

Recent and drastic cost reductions from renewable energy sources such as solar and wind offer new possibilities for competitive NH_3 production in large-scale plants based on electrolysis of water using surplus renewable electricity. This latter route means ammonia production can be made completely carbon free and can compete with ammonia production based on natural gas (the interim best case alternative [104, 142]). By switching to renewable electricity to make ammonia, over 40 million tonnes of CO_2 could be saved each year in Europe and over 360 million tonnes worldwide. Enabling the synthesis of green ammonia gives way to an expanded role for ammonia as an energy store.

Dramatic growth in NH_3 production has been predicted after 2019 (Figure 1.12) when The Yara facility in Western Australia is set to open a pilot plant producing NH_3 using hydrogen produced from the solar powered electrolysis of water [254]. If successful they then aim to replace all natural gas feed-stocks with renewable solar energy which would halve overall CO_2 emissions.

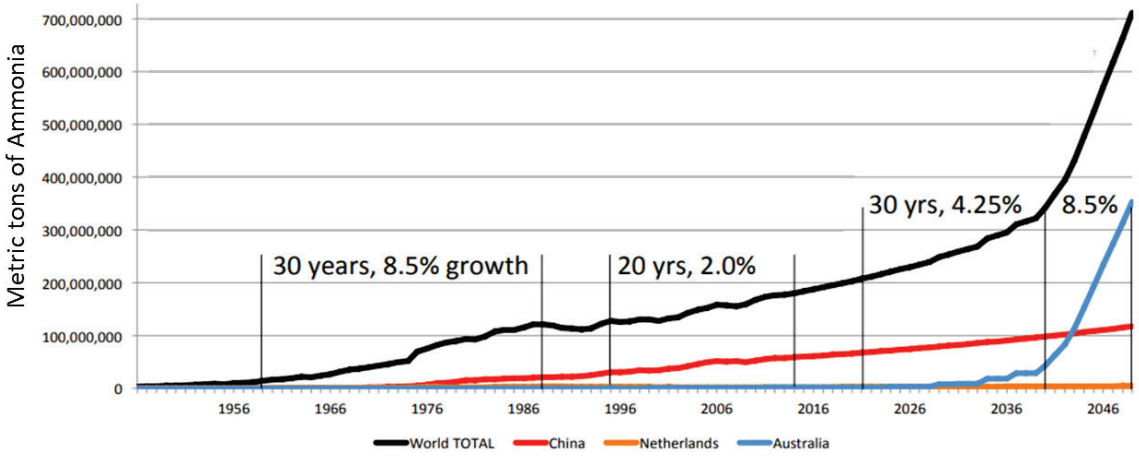


Figure 1.12: Global ammonia production forecast to 2050 at export strength. Source: US Geological Survey 2017

1.5.1.4 Distributed production

Opportunities for distributed production may favour alternative production routes over Haber-Bosch. Electrolysers are modular so exhibit economies of scale. Small individual electrolysers would be ideal for farmers to be self-sufficient in producing fertiliser for their fields and fuel for their machinery, and individuals could each produce ammonia for personal vehicles.

Renewable energy, such as sun and wind, is often most prevalent in the regions where ammonia for fertiliser for farming is needed most. De-centralised production of ammonia fertiliser could be beneficial in a number of ways, particularly in locations where there is minimal infrastructure for the distribution of centralised fertiliser. Distribution costs would be substantially reduced and nitrogen utilisation efficiencies could be significantly improved by enabling continuous application, possibly coupled to irrigation systems during crop growth rather than bulk application with wasteful run-off.

1.5.1.5 Other Ammonia synthesis methods

Biological fixation - bio-mimicry

Until 1909, biological nitrogen fixation from bacteria using the nitrogenase enzyme with air and water at ambient temperatures and pressures made most of the ammonia on the planet which is normally used directly by the plants as fertiliser. Nitrogenase reduces N_2 molecules using high energy electrons released though the hydrolysis of 16 ATP molecules ($N_2 + 16\,\mathrm{ATP} + 8\,e^- \longrightarrow 2\,NH_3 + H_2 + 16\,\mathrm{ADP}$). Bio-mimicry attempts have been made to copy the enzymatic process with molecular complexes, achieving high selectivity under strongly reducing conditions, however the stability of these catalysts is a challenge [242, 250].

Electro/Photo-chemical synthesis

Water and air are the most abundant sources for hydrogen and nitrogen respectively so the preferred choice for ammonia synthesis would bypass the hydrogen production and nitrogen separation stages, significantly reducing electricity consumption [19, 104, 170]. The ability to use H_2O rather than H_2 could also help decouple ammonia production from fossil fuels, which would reduce susceptibility to regional and temporal fluctuations in cost

and supply and reduce CO_2 emissions. The reaction between H_2O and N_2 to form ammonia is thermodynamically non-spontaneous under normal pressure but can be achieved through an electrochemical process in a single reactor because an applied voltage (from supplied renewable electricity) provides the extra driving force.

Many photochemical and electrochemical routes to ammonia from water (the H_2 source) and air (the N_2 source) using heterogeneous catalysts have been explored with a range of temperatures from 25-800 °C depending on the type of electrolyte used [164, 207, 319]. Water reacts at the anode to make H^+ ions which migrate through a proton permeable membrane to the cathode where they combine with electrons and split N_2 molecules to form NH_3. Both aqueous (alkaline, ionic liquids, molten salts) and solid state (polymer and ceramic electrolyte membranes) electrolytes with different electrodes and catalysts are being investigated to achieve the required H_2 conversion and synthesis rates. NH_3 production and current efficiencies are usually below 1 % due to the exceptional stability of the N≡N triple bond and due to competition with the "Hydrogen Evolution Reaction" (HER). These methods need to be improved to allow for commercial use and have currently only been developed on a fundamental scale. Experimentally, some progress has been made by moving to molten salt systems, which have allowed for higher selectivity towards ammonia production [181, 212]. Fundamentally however, it remains a challenge to provide protons and electrons at high enough chemical potential to reduce nitrogen without producing substantial amounts of H_2.

The most successful method uses Pt/C electrodes under mild conditions (room temperature, one atmosphere) with a mixed NH_4^+/H^+ conducting Nafion 211 solid separating electrolyte membrane [171]. Currently at room temperature and pressure it is slow, but efficiencies can be up to 70 % with an ionic liquid electrolyte. The rate though still needs to be massively improved in order to meet US DOE targets and challenge Haber-Bosch.

Other options for NH_3 synthesis include reverse fuel cells with an ionic liquid electrolyte and a membrane reactor (currently low efficiency) which works at 450 °C [254]. In this, H_2 is piped into the small gap between a pair of concentric long metal tubes where catalysts produce hydrogen atoms which are forced by modest pressure (lower than Haber Bosch)

through the inner tube wall to its hollow core to N_2 molecules which are themselves split by catalysts lining the inner surface leading to NH_3 production.

Thermo/Electro-chemical cycles

A novel lithium-mediated cycling synthesis method is being developed which circumvents the otherwise competing and dominant HER by using a stepwise approach to separate the reduction of N_2 from subsequent protonation to NH_3, so is selective for ammonia production [132].

Molten salt electrolysis, in which LiOH is reduced to Li, is followed by direct nitridation as Li is exposed to flowing N_2 and held at 22-100 °C to form Li_3N. H_2O is then added to rapidly hydrolyse the nitride to form NH_3 in an exothermic release which reproduces LiOH, completing the cycle. Advantages of this technique include operation at ambient pressure and moderate temperatures, the use of H_2O instead of H_2, and the possibility of direct coupling to renewable electricity sources promoting local on-site production.

1.5.2 Ammonia end-use technology

NH_3 is a flexible fuel, it can be cracked to produce hydrogen for subsequent use in fuel cells [52] or utilised as a direct fuel in solid oxide fuel cells or internal combustion engines and gas turbines. Figure 1.13 shows that the energy pathways for these two processes have the same end products and therefore have the same overall thermodynamic change. Theoretically, the thermodynamic efficiencies of fuel cells and (Carnot) heat engines are equivalent and limited by the same maximum efficiency [191].

In practice, fuel cells are more efficient (50 %) than combustion engines (25 %), but 55-60 % efficiencies can be reached in combined cycle ammonia gas turbines [142] (batteries are up to 80 % efficient). This is because fuel cells are not limited by having to deal with the high temperature of combustion engines, so water is produced as a liquid not a gas. However, it is not unreasonable to assume that next-generation combustion engines will approach the overall efficiency of a fuel cell. As ammonia has an energy density 40 % that of petrol, the fuel mileage of ammonia is about half of that of petrol.

There are merits to both FCEVs, IC engines (and BEVs) and a combination of the available technology, required efficiency, cost and robustness of each route will be the determining

factors for which is adopted.

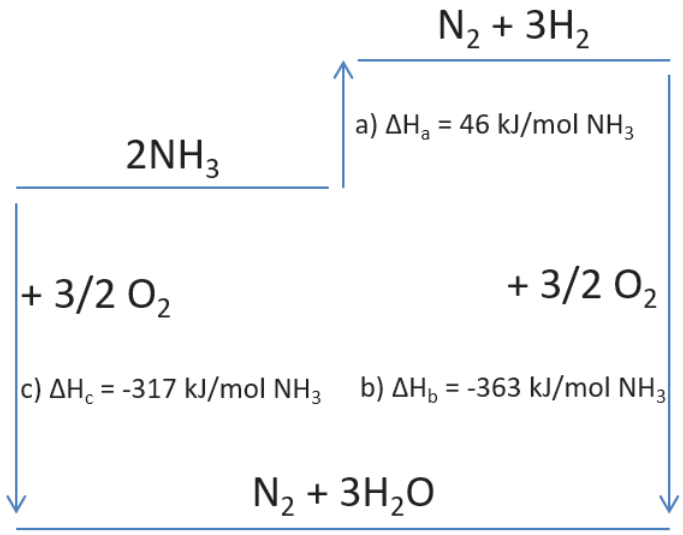


Figure 1.13: Enthalpy diagram for a) Decomposition of NH_3, b) Reaction in a fuel cell, c) Direct combustion

1.5.2.1 Proton exchange membrane fuel cells (PEMFC)

PEMFCs are the best performing fuel cells and the H_2 produced from the catalytic cracking of NH_3 can be used in PEMFCs as described in Section 1.3.2.2. However, PEMFC are irreparably degraded by even low ppm concentrations of NH_3 due to the acidic membrane used so high purity H_2 (>99.999 %) must be achieved from near-complete conversion of NH_3 and through downstream post cracking purification [284, 303]. From Figure 1.14, it can be seen even at 1173 K and 10 bar there is 0.15 % (1500 ppm) un-reacted ammonia, far in excess of the ammonia concentration required for safe PEMFC usage [269].

For stationary PEMFC chemical scrubbing of un-reacted NH_3 by bubbling the post reaction gas mixture through water or a mild acidic solution is sufficient due to the high solubility of ammonia. Metal halides, as described in Section 1.5.3, can be used to absorb NH_3 and reduce its vapour pressure in the outlet gas stream of the cracker to millibar levels which would otherwise poison the PEMFC. 1.2 kg of adsorbent material can remove 500 ppm of NH_3 which gives a 1800 mile driving range before it needs replacing [286]. However, both of these approaches require periodic replacement of the absorbing medium.

In fuel cell applications, unconverted ammonia can also be adsorbed using resin or zeolite and onboard regeneration of the zeolite adsorbent would be possible at temperatures around 327 °C which would be close to the temperature of ammonia decomposition [251].

A more recent approach is to integrate NH_3 cracking with hydrogen selective permeable membranes based on Pd [146], Pd-Ag alloys or micro-porous ceramics such as silica. These lower the NH_3 cracking temperature to 400-500 °C and enhance the efficiency due to the continuous removal of H_2 through the membrane leaving N_2 and NH_3 behind [179, 190, 243]. The fragility of these membranes, which must be free of defects to achieve the purity thresholds required and their poor tolerance to thermal cycling means their role is likely to be centralised in H_2 generation prior to compression and dispensing H_2 into HFCVs rather than on-board applications.

For on-board PEMFC, there is the additional requirement for unreacted N_2 to be removed from the post synthesis gas stream using a pressure swing adsorption process or a membrane process as only the high purity H_2 is stored on-board in the high pressure tanks.

In 2018, CSIRO fuelled Toyota Mirai and Hyundai Nexo HFCVs using ultra-high purity hydrogen produced from ammonia in a two-stage process. Firstly, a ruthenium catalyst was used to crack the ammonia into into N_2 and H_2 and then a vanadium metal membrane was used to separate the hydrogen from the other gas species before it was compressed and transferred to the vehicles.

The potential end use application of ammonia in the transport sector can be assessed by comparing the amount of energy required to produce the ammonia, to the amount of energy available to power the car. This is done by considering the efficiency of the on-board ammonia cracker and hydrogen compressor and shows that PEMFC and IC engines produce the best life-cycle efficiencies of 19 % and 21 % respectively [106]. PEMFCs themselves are generally considered to be 60% efficient in terms of the energy stored in the H_2 in the tank compared to the power that goes out to the fuel cell.

1.5.2.2 Alkaline fuel cells (AFC)

Alkaline fuel cells were one of the first fuel cell technologies to be developed. NASA has used alkaline fuel cells since the mid-1960s in Apollo-series missions and on the Space Shuttle.

Ammonia can be directly used without the need for shift converters, selective oxidisers or co-reactants such as water. AFCs operate at 10–66 °C and are among the most efficient fuel cells having the potential to reach 70 % efficiency, which is higher than PEMFCs and yield the highest voltage at comparable current densities [224].

The electrolyte is an aqueous alkaline solution, such as potassium hydroxide (KOH) [165]. At the anode, hydrogen is oxidised ($H_2 + 2\,OH^- \longrightarrow 2\,H_2O + 2\,e^-$) to produce water and electrons which flow round an external circuit to the cathode where hydroxide ions are produced ($O_2 + 2\,H_2O + 4\,e^- \longrightarrow 4\,OH^-$). AFCs are the cheapest fuel cells to manufacture as inexpensive catalysts can be used such as iron and the electrodes are normally nickel.

AFCs are not sensitive to up to 10 % NH_3 [123, 172]. The company GenCell currently has an alkaline fuel cell which can utilise hydrogen produced from cracking liquid ammonia as the fuel. They are not without associated challenges though mainly from their sensitivity to poisoning by CO_2 in the air supply due to carbonate formation with KOH.

1.5.2.3 Alkaline membrane fuel cells (AMFC)

Recently, AMFCs have been reported (but not yet developed) in which NH_3 can be used directly as a fuel [172, 173]. They use a solid anion exchange polymer membrane instead of a liquid electrolyte which aids with the problem of NH_3 poisoning. These closely resemble PEMFCs, except that OH^- ions travel through an alkaline membrane instead of an acid membrane but CO_2 still affects their performance and durability which lags behind PEMFCs.

1.5.2.4 Solid oxide fuel cells (SOFC)

Solid oxide fuel cells produce electricity directly from oxidising a fuel and the cells are characterised by a solid oxide or ceramic electrolyte and involve conducting O^{2-} from the cathode to the anode [102, 192, 204, 266]. Due to the high operating temperatures of the SOFC (600-1000 °C) ammonia can be directly input into the SOFC as a fuel without any pre-treatment so the cracking process necessary to free the hydrogen from the NH_3, and the generation of electricity in the fuel cell can be combined ($4\,NH_3(g) + 3\,O_2(g) \longrightarrow$

$2\,N_2(g) + 6\,H_2O(g)$) [173]. SOFCs are not poisoned by NH_3 so complete conversion is not required.

SOFCs have many advantages; high efficiency, long-term stability, fuel flexibility, low emissions, and relatively low cost (high temperatures do not require platinum catalysts). Their higher operating temperature means SOFCs are useful for applications with heat engine energy recovery devices or combined heat and power (which increases overall fuel efficiency). However, these temperatures of operation are much too high for on-board transport applications.

1.5.2.5 Internal combustion (IC) engine

Cheaper and more robust than PEMFCs, conventional petrol, diesel or LPG internal combustion (IC) engines and gas turbines can be converted to run on ammonia with only small modifications [17, 111, 239]. In Belgium in 1942, crippling diesel shortages from World War II stopped the public bus system from working. In under 6 months all the buses had been converted to hybrid ammonia and coal gas engines which ran over 100,000 km without a single chemical accident or major spill and several private vehicles were also converted to use the ammonia pumps built for the bus fleet. More recently, developed in 2013 the Marangoni Toyota GT-86 Eco-Explorer has an ammonia and gasoline compressed gas hybrid combustion engine which has a range of 180 km on one tank of ammonia with zero-emissions.

NH_3 has a high octane rating (about 120 vs. 86-93 for petrol) so does not compression ignite except at very high pressures, does not need an octane enhancer and can be used in high compression engines [129]. Therefore NH_3 is normally used in conjunction with other fuels or a small amount of cetane (5 %) is added to the NH_3 to start the combustion process. Alternatively partial decomposition (15-20 %) of the ammonia can provide sufficient hydrogen to enable optimal combustion to occur [208].

During combustion in an IC engine, nitrogen and oxygen present in the air combine to form NO_x so internal combustion engines inherently produce NO_x when they burn any fuel [271]. Emitted NO_x contributes to the formation of fine particles and ground level ozone. This fine particulate matter is reckoned to have led to 4.2 million premature deaths

worldwide in 2015 as a result of respiratory diseases. The ozone formed adversely affects ecosystems and agricultural crops.

Fuel cells and BEVs are likely to dominate the transport industry of the future but the internal combustion engine is going to remain prevalent in many developing countries such as in sub-Saharan Africa. Therefore, there remains the need to improve this technology and decouple the internal combustion engine from NO_x emissions from the exhaust. Fast chemistry in after-treatment devices apply selective catalytic reduction (SCR) to reduce NO_x to nitrogen and water using ammonia as the catalytic reductant.

Metal halides as described in Section 1.4.2 are good temporary ammonia stores. The chemical company Amminex have developed a solid compound "AdAmmine" which is based on $SrCl_2$. It is carried on-board vehicles in a cartridge and was designed so the stored ammonia can be released on-demand by gentle heating to convert any NO_x present in the engine exhausts to N_2 and H_2O by selective catalytic reduction (SCR). Further down the exhaust process metal halides can be used to re-absorb any un-reacted NH_3 in the gas stream to levels which adhere to both environmental and health regulations. Therefore one benefit of ammonia as a fuel is that it can be used to clean up after itself through "scrubbing" any nitrogen oxides left after combustion.

Converting conventional fuel IC engines to run on NH_3 and combining them with SCR devices and metal halides in the exhaust, it is possible to run the vehicles with no CO_2, soot, NO_x, particulate or NH_3 emissions.

1.5.3 Safety considerations for NH_3 as a fuel

There are both real and perceived safety risks with the use of ammonia but these are comparable to those for petrol and diesel and indeed lower than LPG so should not be an obstacle to the funding, development, or implementation of ammonia fuel technologies [99]. Ammonia has high toxicity (causes irritation to humans at low concentrations and is life threatening at high concentrations) and has a high vapour pressure under standard conditions, so may be hazardous in densely populated areas [269]. However, the widespread use of ammonia for over 100 years comes with an accumulation of safety experience, a mature

international set of laws and regulations, and a sophisticated support sector providing ammonia users and first responders with safety equipment, training, and education. Ammonia is already widely used in industrial refrigeration and is commonplace in factories which often lie within residential areas. NH_3 can be quickly and easily detected by human smell due to its strong odour (even in low ppm quantities far below concentrations hazardous to health) so leaks can be quickly stopped. It is lighter than air and therefore will quickly dissipate from the scene of a spillage (unlike petrol). Ammonia is toxic to aquatic life which must be taken into consideration. When ammonia is present in water at high enough levels, it is difficult for aquatic organisms (particularly invertebrates and fish) to sufficiently excrete the toxicant, leading to toxic buildup in internal tissues and blood, and potentially death.

Ammonia refuelling stations would be compatible with the current set-up of user-operated fuel pumps, so safety concerns should not be more technically challenging or much different to those for LPG delivery. Fuelling stations would be much easier to safely convert to dispensing ammonia than elemental hydrogen as the complex and high pressure gas delivery technologies necessary for 700 bar H_2 storage are not required. Ammonia refuelling stations are likely to require a safety distance to residential or highly populated areas greater than those for LPG or normal gasoline stations. The NH_3 storage tanks at refuelling stations need to be located underground as to avoid any possible impact (physical or from fires) and isolated from the ground to avoid leakages to the soil.

There are also positive safety aspects of ammonia compared to petrol. Ammonia is not carcinogenic, does not burn readily or sustain combustion (low ignition energy and burning velocity) except under narrow fuel-to-air mixtures of 15-25 % air [17] (compared with 4–75 % for H_2) so explosions and fires are less likely with a ruptured ammonia tank than with petrol [312]. Combustion of petrol can produce hazardous carbon soot particles but because ammonia contains no carbon, it does not produce soot or CO_2.

1.5.4 Current limitations for NH_3 as a fuel

The potential of ammonia as a clean, safe, efficient and secure energy storage material has yet to be realised due some challenges yet to be overcome:

- Green NH_3 production
- NH_3 is less energy-efficient than competitors in life-cycle terms which is especially relevant for cyclical processes such as energy storage
- Ammonia can have significant environmental consequences, it causes acidification and encourages particulate matter formation if emitted directly to air, either via spillage or through exhaust systems if incompletely consumed
- PEM fuel cells are irreparably degraded by even low part-per-million concentrations of NH_3. The dominance of PEMFC in the market has been one of the main drawbacks to the widespread roll out of NH_3 as fuel [284, 303]

However, the main reason ammonia's potential as a carbon free hydrogen vector at the point of use has yet to be realised is largely because of the unavailability of an efficient, cheap and effective means for accessing its hydrogen content at scale [273].

1.6 Ammonia cracking

It is the catalytic cracking of NH_3 to release the intrinsic H_2 (Equation 1.4) enabling the provision of on-site hydrogen production (fed straight into a fuel cell) that is arguably the most viable solution to finding a clean, safe, efficient and secure low carbon energy vector (Stage 6 in Figure 1.6) [24]. The need to optimise the efficiency of the ammonia cracking reaction will drive the search for more active catalysts for the decomposition reaction in order to develop ammonia as an alternative to fossil fuels.

$$2\,NH_3 \rightleftharpoons N_2 + 3\,H_2 \tag{1.4}$$

For thermodynamically favourable, effective ammonia cracking, high temperatures (400-500 °C) and modest pressures are required which leads to a low pressure (< 2 bar) stream of hydrogen. This can be directly used in a fuel cell but if it is to be distributed, stored or used to refuel HFCV it must be compressed, which is only 88 % efficient. Therefore, it would be ideal to be able to produce the hydrogen on-demand within the car and store H_2 as NH_3 until such a time.

Thermodynamically, NH_3 cracking will be favourable above 466 K (Figure 1.14). Using thermodynamic data at standard pressure the equilibrium constants for the conversion of NH_3 during decomposition can be calculated, to establish the amount of conversion that should happen at different temperatures if the reaction reached equilibrium [305]. At 673 K, the equilibrium conversion is 99.1 % so from a thermodynamic viewpoint it is possible to develop active catalysts for complete NH_3 decomposition from around this temperature. This is a useful measure for assessing catalysts to ascertain how close the catalyst has come to equilibrium.

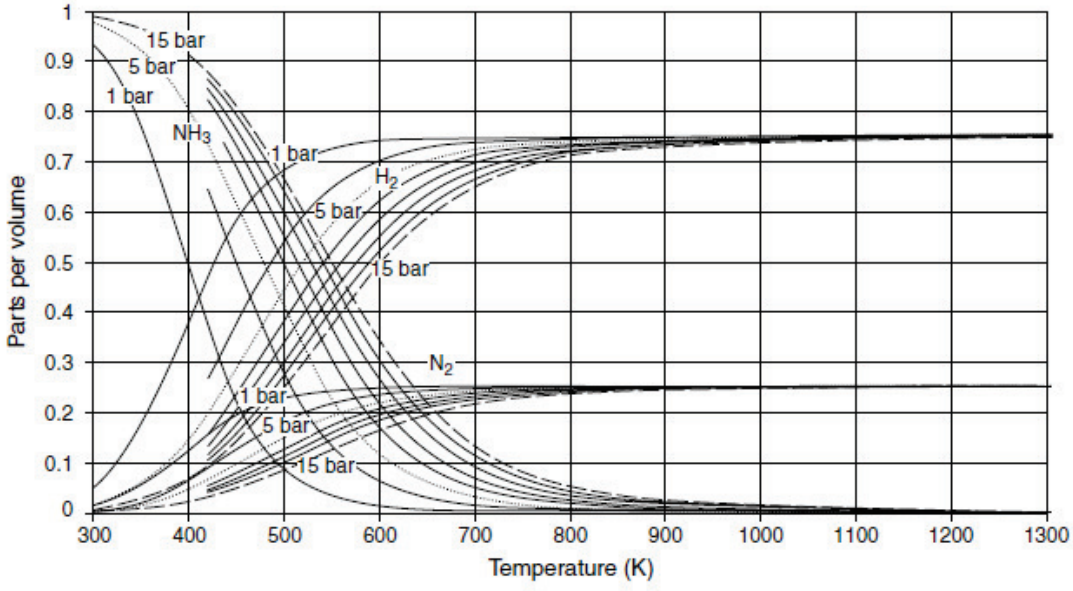


Figure 1.14: Equilibrium position for $2\,NH_3 \longrightarrow N_2 + 3\,H_2$ at various temperatures and pressure [225]

Of course, thermodynamic conversion is not obtained in kinetically-limited situations, such as the high flow rates used in a vehicle, and the decomposition reaction must be catalysed.

Using current low-cost catalyst technology, hydrogen release kinetics require very high operating temperatures ($> 600\,°C$) which compromise the efficiency of the ammonia-based energy cycle. The US DOE has indicated that the feasibility of NH_3 as a hydrogen storage molecule relies on its decomposition at temperatures aligned with those of the proton exchange membrane (PEM) fuel cell [247]; in the range of 150–180 °C. Therefore, it is crucial

to develop a new generation of affordable catalysts capable of releasing H_2 at adequate rates under acceptable conditions.

It is unlikely that full ammonia decomposition will be achieved using only the waste heat from a fuel cell or combustion engine; some power will be required for heating the cracking reactor. Given the very high hydrogen density of ammonia, this can be accommodated up to a point, but the very high temperatures used with some catalysts (873 K or above) [258] will decrease the system efficiency to an unacceptable level. Therefore, for transport applications, the search for more active catalyst materials is paramount.

1.6.1 Traditional ammonia decomposition catalysts

Traditional and well-studied catalysts for low-temperature NH_3 cracking mirror those used for its synthesis via the Haber Bosch process, and are predominantly based on transition metals. Cracking catalysts have been investigated primarily as an indirect method for examining the kinetics of the ammonia synthesis reaction as the conditions of ammonia decomposition are more straightforward to achieve in the average laboratory. However, it has been observed and calculated using Density Functional Theory (DFT) that the optimal ammonia synthesis catalyst is not the optimal ammonia decomposition catalyst [43]. This does not mean the principle of microscopic reversibility does not apply, but due to the different reaction conditions in ammonia synthesis compared to decomposition, the optimal binding energies for the two reactions are very different.

The mechanism for the decomposition of NH_3 on transition metal catalysts follows a first order heterogeneous catalytic pathway with NH_3 adsorbed onto the catalyst surface, with sequential breaking of N−H bonds (dehydrogenation) to give adsorbed nitrogen and hydrogen atomic species which then recombine and desorb as molecular N_2 and H_2. It occurs via the following steps where $*$ is an adsorbed surface species [103]:

Adsorption: $$NH_3 + * \rightleftharpoons NH_3^* \quad (1.5a)$$

Dehydrogenation: $$NH_3^* + * \rightleftharpoons NH_2^* + H^* \quad (1.5b)$$

$$NH_2^* + * \rightleftharpoons NH^* + H^* \quad (1.5c)$$

$$NH^* + * \rightleftharpoons N^* + H^* \quad (1.5d)$$

Desorption: $$N^* + N^* \rightleftharpoons N_2 + 2* \quad (1.5e)$$

$$H^* + H^* \rightleftharpoons H_2 + 2* \quad (1.5f)$$

1.6.1.1 Volcano plots

Volcano plots (Figure 1.15b) can be used to demonstrate the effect of the Sabatier principle on the activity of a metal catalyst [210]. The rate determining step (RDS) for ammonia decomposition varies and is a trade-off in the relationship between ammonia decomposition activity (dehydrogenation of the NH_n species) and nitrogen binding energy (desorption from the surface). The activity of transition metals in heterogeneous catalysis is usually rationalised in terms of the ability of the metal centres to accept electron density from the gas molecules via their vacant or partially vacant *d*-orbitals. The peak in the volcano plot is therefore correlated with an ideal intermediate value of nitrogen absorption enthalpy, the energy level of the *d*-band centre and ammonia adsorption enthalpy.

Figure 1.15b shows two volcano plots demonstrating the variation in metal activity as a function of dissociative nitrogen adsorption enthalpy (the key step and the RDS for ammonia synthesis). For NH_3 decomposition, Ru is at the peak and for NH_3 synthesis Fe is at the peak [251]. These volcano plots have also been rationalised by invoking a change in rate determining step.

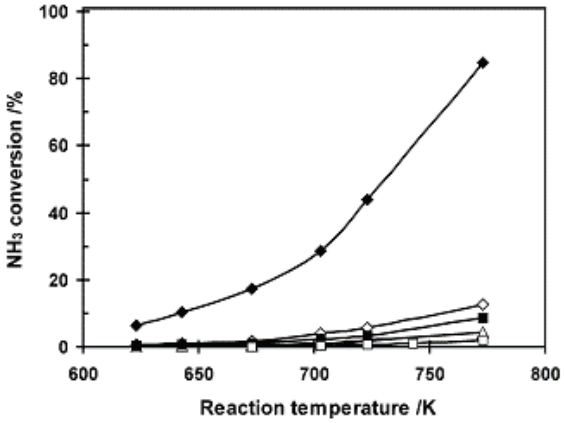
For NH_3 decomposition, an initial rise in activity to the peak of the volcano plot is due to increasing M−N bond enthalpies which weakens the N−H bond making NH_3 decomposition easier. Recombination and desorption of N_2 (the formation of the N≡N triple bond) is the RDS due to increasing nitrogen absorption enthalpy for non-precious metals like Fe, Co and Ni [21, 43, 152].

The subsequent decrease in activity is due to the weakening M−N bond enthalpy and therefore increasing N−H scission enthalpy so the cleavage of this bond now becomes the RDS for precious metals like Ru, Rh, Ir, Pt, or Pd [43, 103, 152].

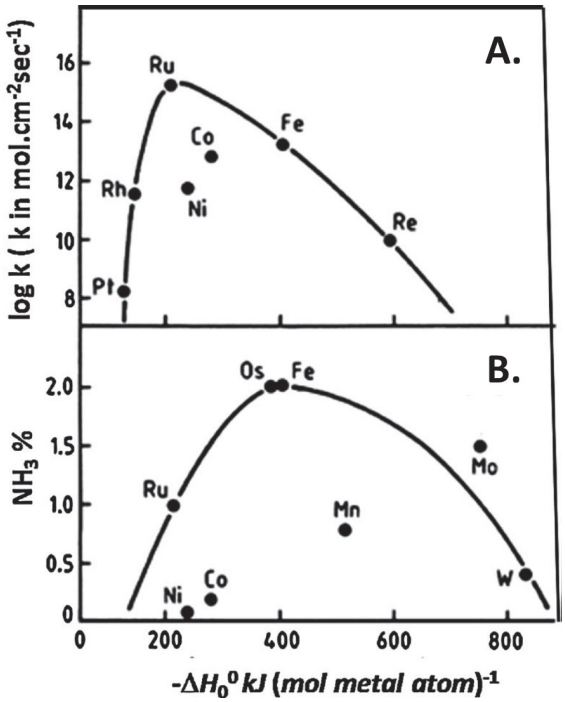
As well as the catalytic metal used, the kinetics of the reaction are dependent on the reaction conditions such as temperature, nature of the catalyst, geometry of active sites [91], presence of support and promoters [251]. With ruthenium, at low pressure and temperatures ($< 650\,\mathrm{K}$) the RDS is the recombination and desorption of N_2; however, at high temperatures ($> 650\,\mathrm{K}$) the RDS is the cleavage of the first N−H bond. It has been found that increasing the temperature of the reaction decreases the activation energy of the decomposition which could also explain the change in RDS as less energy is required to desorb N_2 from the surface of the catalyst [279].

Ruthenium has been widely shown to be the most active single transition metal for NH_3 decomposition (Figure 1.15a) [43, 55, 279, 307].

A ruthenium-based catalyst supported on graphite-containing carbon and co-promoted with Cs (Rb) and Ba is used in the Kellogg advanced ammonia process (KAAP). Ru can produce ammonia with a higher yield at lower pressure and lower temperature conditions than a conventional Fe-based catalyst (used in the Haber–Bosch reaction). Although it shows the highest catalytic activity per mole, it still operates at high temperatures and is both rare and expensive and so iron [292, 297] (used in the vast majority of commercial ammonia synthesis reactors) and nickel based catalysts [218] are often favoured per unit mass as their cost advantage allows for higher metal loadings [32]. Ganley et al. [103] expanded the number of metals studied for their catalytic activity for NH_3 decomposition and reported them to be in decreasing order $\mathrm{Ru} > \mathrm{Ni} > \mathrm{Rh} > \mathrm{Co} > \mathrm{Ir} > \mathrm{Fe} > \mathrm{Pt} > \mathrm{Cr} > \mathrm{Pd} > \mathrm{Cu} > \mathrm{Te} > \mathrm{Se} > \mathrm{Pb}$. Some modified iron catalysts do show catalytic activities similar to supported ruthenium for an equivalent total mass basis [85, 314] but when considering as a whole the catalyst and the support, Ru is more active than Fe per mole of metal. Although ruthenium is the optimal single metal catalyst for NH_3 decomposition, tri-metrical compounds such as a Ni-Pt-Pd (111) surface may have a conversion percentage closer to the peak of the volcano [118, 216].



(a) Ammonia decomposition conversion percentage for different metals and temperatures (♦) Ru, (◇) Rh, (■) Ni, (△) Pd, (□) Fe [307]



(b) Volcano plots showing variation of rate constant for NH_3 decomposition (A) and NH_3 synthesis (B) over metals as a function of dissociative nitrogen adsorption enthalpy [251]

Figure 1.15: Transition metal catalyst activity for NH_3 synthesis and decomposition

1.6.1.2 Support structures and promoter species

The activity of the metal catalyst is enhanced when the metal is deposited onto complex support structures alongside promoter species [121, 162, 264].

Support structures need to remain stable under operating conditions and their main purpose is to increase the surface area of the catalyst and ensure its effective dispersion into nano-sized domains reducing the amount of the (often expensive) catalyst required, by increasing the number of active sites. They may influence various properties of the catalyst such as having an electronic effect which in turn affects its NH_3 decomposition ability [306, 315]. Novel supports based on carbon nano-tubes [49, 86, 259], or blends of metal oxides and carbon nanotubes have been shown to be more active than traditional supports based on alumina, silica, zirconia and titania [307].

If N_2 desorption is the RDS, effective promoters would donate electrons to the anti-bonding electronic states of the metal, weakening the nitrogen-metal interaction so nitrogen

desorption becomes more facile [210]. Therefore, basic promoters are favoured and promoted Ru catalysts are found to decrease in the order of K-Ru > Na-Ru > Li-Ru > Ce-Ru > Ba-Ru > La-Ru > Ca-Ru > Ru indicating that within the same group, the higher the electronegativity of the promoter, the lower the conversion of ammonia.

Increasing the basicity of the support with promoter species such as alkali and alkaline earth-metal salts also improves the effectiveness of the catalyst due to decreased activation energy leading to increased turnover frequency. K^+ is the most effective (over Ba^{2+} and Cs^+) at increasing NH_3 conversion rate [153, 166, 167, 236, 237, 293, 309] (most effectively introduced as KOH) due to electron donation to the transition metal centre influencing the electronic interaction with NH_3 and the desorption of nitrogen from the catalyst surface.

1.6.1.3 Transition metals and transition metal nitrides

Transition metal nitrides form from the metal under ammonia decomposition conditions [297, 298]. There is some evidence that the presence of first row transition metals or metal nitrides (Fe or Mn) enhance the catalytic decomposition of ammonia by light metal amide and imide catalysts, of which manganese nitride is the best performing co-catalyst [116].

Although ternary transition metal nitrides are known to form at elevated temperatures under inert gas, they are only present as intermediates under ammonia decomposition conditions and are not a complete explanation for the reported enhancements in catalytic activity for imide-nitride composites [116, 199]. Rather than forming ternary transition metal nitrides, under NH_3 the transition metal nitride and Li_2NH have been shown to form [199]. The presence of the transition metal nitrides makes it easier to contain the catalyst but it is Li_2NH that is the active catalytic species and the bulk formation of a ternary nitride is not necessary for ammonia decomposition.

1.6.2 "First generation" Group 1 single metal amides as catalysts

Recently, earth abundant Group 1/2 light metal amides and imides have been discovered as a new class of inexpensive and effective NH_3 decomposition catalysts.

The $LiNH_2$ – LiH system has been extensively studied due to the facile nature of its reversible hydrogen storage (6.5 wt;%) (Equation 1.2). The inter conversion of $LiNH_2$ and

Li_2NH is reversible at around 200 °C and requires only a few bar of hydrogen to achieve appreciable hydrogenation kinetics at these temperatures. However, fundamentally the kinetics of its hydrogenation and dehydrogenation are too slow, which inhibit its applicability for use in transportation. $NaNH_2$ was initially studied as an extension to this system but had previously gathered little interest as a hydrogen store due to its low melting-point and high chemical reactivity, meaning conventional thermal analysis methods are challenging and it has a high decomposition enthalpy ($\Delta H = 123.8\,kJ\,mol^{-1}$). However, sodium amide is known to decompose on heating into its constituent elements (Equation 1.6a) [276].

$$NaNH_2(s) \longrightarrow Na(s) + \frac{1}{2}N_2(g) + H_2(g) \tag{1.6a}$$

$$Na(s) + NH_3(g) \longrightarrow NaNH_2(s) + \frac{1}{2}H_2(g) \tag{1.6b}$$

The true potential of this system comes from looking at the net reaction of Equations 1.6a and 1.6b. Run concurrently, these two reactions show the chemical decomposition of ammonia by cycling between sodium amide and sodium metal, in essence the $NaNH_2$ is acting as a catalyst for ammonia decomposition.

Although the $NaNH_2$ system has a combined hydrogen storage capacity of 7.5 wt % (which is in excess of the Li-N-H system), considered in this way, the hydrogen storage content of the amide is irrelevant as it is ammonia that is the hydrogen vector. The hydrogen density of liquid ammonia (17.8 wt %, 121 kg H_2 m^{-3}) is significantly higher than any of the light metal amides. This led to a revolutionary way of thinking about light metal amides in the context of hydrogen storage, not as hydrogen stores themselves, but as catalysts for the decomposition of ammonia – the true hydrogen store.

Earth abundant Group 1/2 light metal amides and imides are not only inexpensive and effective NH_3 decomposition catalysts but all show similar or superior activities to optimised transition metal based catalysts (Figure 1.16).

Inexpensive, bulk sodium amide ($NaNH_2$) [71] was the first light metal amide to show the catalytic chemical decomposition of NH_3 into its constituent elements by cycling between $NaNH_2$ and sodium metal (Equation 1.6) [299]. Conversely to $NaNH_2$, $LiNH_2$ is known

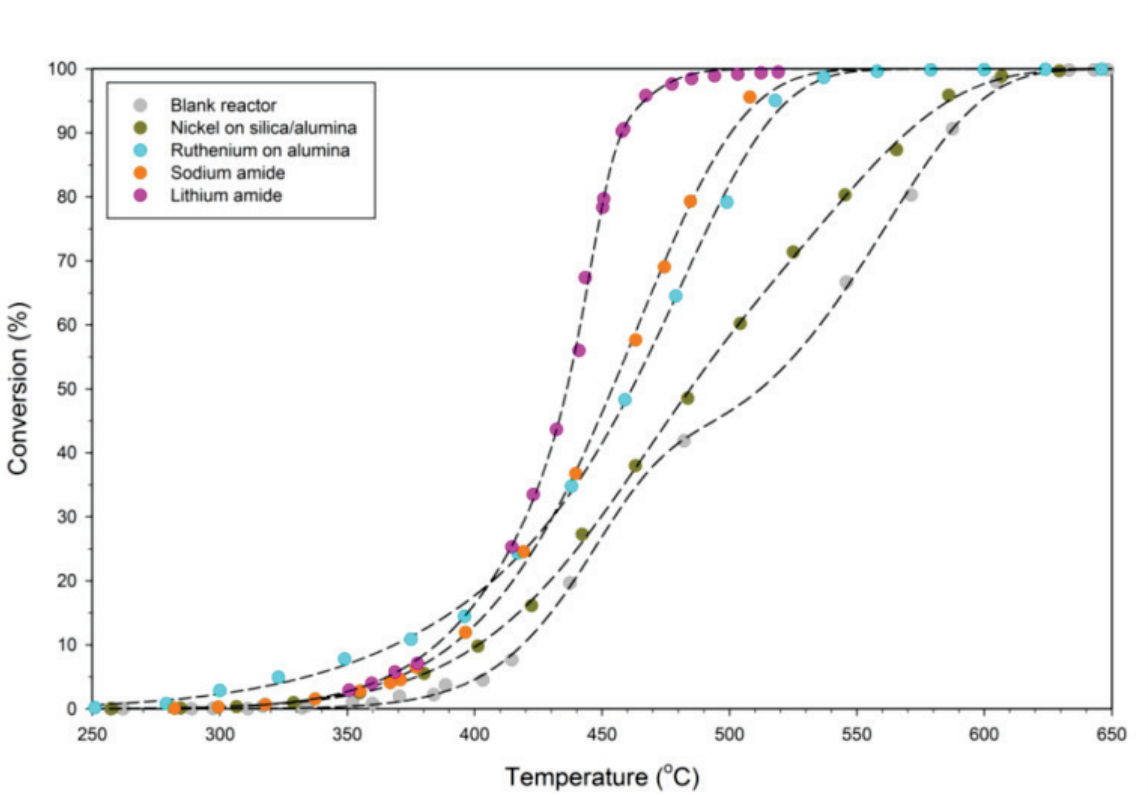


Figure 1.16: First generation Group 1/2 amide catalysts [198]

to decompose to the imide on heating, not the metal, so it would not be expected to show appreciable ammonia decomposition according to the mechanism described for $NaNH_2$ (Equation 1.6). Therefore, $LiNH_2$ was re-visited, but this time in the context as an NH_3 decomposition catalyst (not as a hydrogen store) and was initially tested as a negative control.

However, startlingly, lithium amide shows superior catalytic activity per unit mass and higher NH_3 decomposition than $NaNH_2$. However, the active form of the lithium amide catalyst (and its stoichiometry) is dependent on the precise NH_3 decomposition conditions of NH_3 flow rate and temperature. It only becomes highly active at temperatures at which it is no longer stable and has undergone partial, reversible, NH_3-mediated thermal decomposition to non-stoichiometric lithium imide (Equation 1.7) [198]. Previous *in-situ* neutron experiments have shown isothermal variations in the lattice parameter which indicate that the active form of the catalyst is indeed $Li_{(2-x)}NH_{(1+x)}$ $0< x <1$ unlike stoichiometric $NaNH_2$. The formation of $Li_{(2-x)}NH_{(1+x)}$ is topotactic and driven by bulk ionic conductiv-

ity as the lithium ions and protons can diffuse through the crystal structures to inter-convert between Li_2NH ($Fm\overline{3}m$) and $LiNH_2$ ($I\overline{4}$) [194, 296]. $LiNH_2$ can be considered to be an ordered (a×a×2a) supercell of Li_2NH with half the Li^+ sites vacant. These previous *in-situ* neutron powder X-ray diffraction experiments have shown that a stoichiometry value close to $Li_{1.5}ND_{1.5}$ was the approximate limit of maintaining a solid phase at 500 °C under very low NH_3 flows. Therefore, reaction conditions for the NH_3 decomposition with $LiNH_2$ must be maintained within specific limits (at a temperature at which only the imide is stable) if the catalyst is to be kept in the solid state during the reaction.

$$LiNH_2 \longrightarrow Li_2NH + NH_3 \tag{1.7a}$$

$$x\,LiNH_2 + Li_2NH \longrightarrow 2\,Li_{(2-x)}NH_{(1+x)} \tag{1.7b}$$

$LiNH_2$ does not follow the stoichiometric NH_3 decomposition of $NaNH_2$ and shows that imide-forming amides can be active NH_3 decomposition catalysts in addition to metal-forming amides. This leads to the possibility that a broader range of metal amide-based materials might be expected to show appreciable NH_3 decomposition activity and that a range of reaction mechanisms may operate within this catalytic family.

Another key advantage of $LiNH_2$ over $NaNH_2$ is much improved containment, 80 % and 5–20 % mass recovery respectively when heated under NH_3 to 500 °C. Imide-forming amide catalysts can be contained more effectively than amides through their greater propensity to remain solid, so are more practical choices than amides which will be molten or aerosol-like at the temperature of operation. In the $NaNH_2$ system, both components are liquid and volatile above 450 °C at the temperatures of operation (Na has a vapour pressure in the order of 25 mbar at 600 °C and $NaNH_2$ has a melting point of 210 °C) [107] leading to material loss over extended reaction periods, especially at high NH_3 flow rates. By contrast, Li_2NH (the active form of the $LiNH_2$ catalyst) is solid across the temperature range at which NH_3 decomposition occurs and remains so until its own decomposition at around 600 °C [316, 317]. However, at lower temperatures Li_2NH will react back to form $LiNH_2$ which melts at 370 °C and becomes volatile meaning difficulties are still encountered

with the effective containment of the catalyst. The lithium imide catalyst must be heated under argon in order to avoid amide formation, before switching to ammonia to effect the decomposition (at temperatures at which the imide is the stable form). While heating under inert gas is not a practical solution for a transportation application, it does demonstrate the principle that an imide catalyst can be contained more effectively than the amide.

The lithium amide-imide catalyst system has been integrated in an ammonia cracking unit with a post-reactor gas purification system and a small-scale PEMFC to create a successful bench-top demonstrator for the production of hydrogen and nitrogen [133].

From the perspective of practicality, the ability to keep the catalyst solid at high temperatures has important implications as it allows for the traditional catalysis routes to higher turnover frequency, such as nano-sizing and complex support structures, to be explored. Solids are simpler to contain in a practical catalytic system, and, academically, are easier to probe.

One problem experienced with these amide and imide based catalysts is their high reactivity due to the fact they are strong bases which makes the application of traditional heterogeneous catalyst methods challenging. Ideally catalysts are fixed on a porous scaffold to enhance the surface area of the catalyst for better kinetics and catalytic activity. $LiNH_2$ has been investigated with a range of classic catalyst supports [295]. Activated carbon, silicon dioxide, aluminium oxide have been found to have a negative impact on catalytic activity and are unsuitable because of their reactivity with the catalyst, especially under flowing ammonia at decomposition conditions (>400 °C and 1 bar). However, MgO is unreactive as a support system and gave the best performance, perhaps unsurprising as it is a basic support whereas the others are amphoteric or acidic. The challenge is therefore how to integrate these catalysts into traditional support systems because of their strong reactivity.

Anion promoters such as Cl^- have been shown to aid the decomposition of $LiNH_2$ and Li_2NH. The decomposition temperature of Li_2NH has been shown to have been decreased by about 110 °C due to the inclusion of Cl^- anions [316].

1.6.3 "Second generation" Group 1/2 mixed-metal imides as catalysts

Imides have much higher melting points than their corresponding amides, so an imide which forms at low temperatures and therefore remains solid over a more favourable range of operating conditions would seem to be an ideal candidate for a practical NH_3 decomposition catalyst.

A logical extension of doping catalysts with electropositive atoms to destabilise the N−H bond, is to chemically vary the Metal-N-H system by combining Group 1 metals with other alkali and alkaline earth metals (these have been supported by DFT calculations [219, 313]).

Calculations suggested that K-doped $LiNH_2$ would also display a lower decomposition temperature than pure $LiNH_2$ due to destabilisation of the N−H bond, although the effect would be less pronounced than that observed in the Mg-Li-N-H system [313]. Because of charge balancing, including elements with a higher oxidation state than +1 may cause an increase in the number of vacancies, which would potentially increase the cationic mobility within the material.

Systems including Li-Na-N-H (Chapter 3), Li-K-N-H (Chapter 4), Li-Ca-N-H [58, 196, 277], K-Mg-N-H (Chapter 8) [214, 245, 291], Na-Mg-N-H (Chapter 9) [81, 232, 260, 301], Li-Mg-N-H [213, 219], Rb-Mg-N-H [148], Rb-Li-N-H [151] and Cs-Li-N-H [149] have, to date, been investigated mainly as H_2 storage materials.

Mixed-metal systems are a promising route to tailoring the active form of the catalyst and so it is possible that ternary imide structures, with two integrated metal ions, may provide a route to a low temperature NH_3 decomposition catalyst.

Lithium-calcium imide ($Li_2Ca(NH)_2$) is not known to form an amide under the reaction conditions, nor decompose to its constituent metals. It shows the best variable temperature conversion yet and specifically the highest low-temperature activity towards NH_3 decomposition reported for any metal amide/imide system studied to date (Figure 1.17) [196]. Importantly, it also shows substantially improved containment of the catalyst mass within the reactor hot-zone with almost complete mass recovery (98 % when heated to 500 °C). Combined high activity and ease of containment makes $Li_2Ca(NH)_2$ the most promising amide/imide-based catalyst for the production of H_2 from NH_3 identified so far. Lithium-

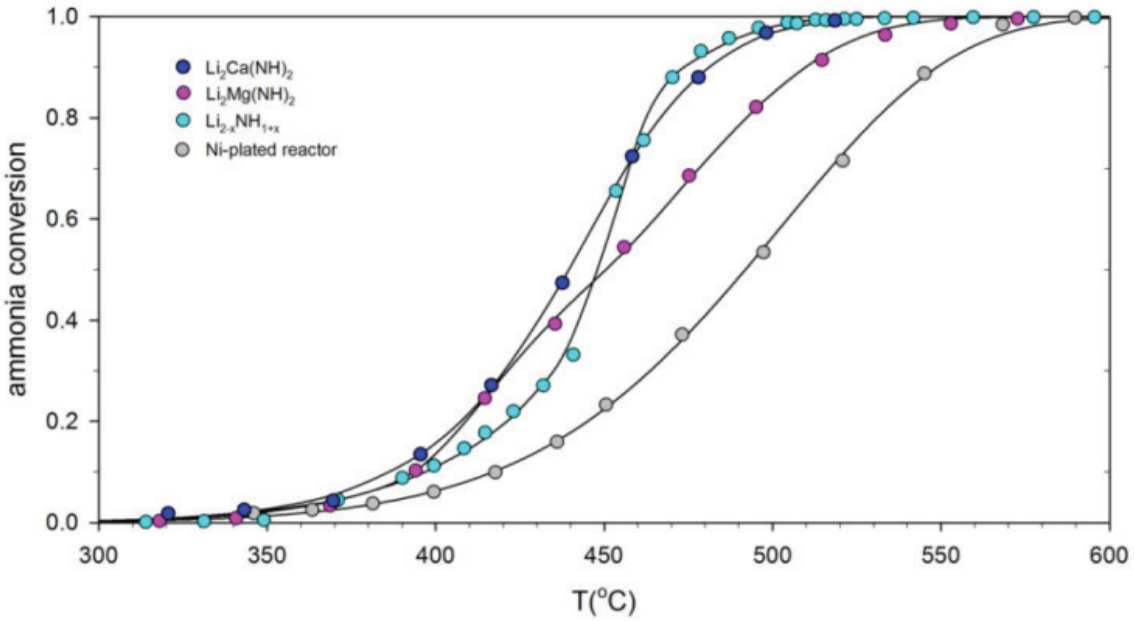


Figure 1.17: Second generation Group 1/2 amide catalysts [196]

calcium imide does not readily form an amide so it does not require heating under argon to achieve good recovery values, as is required for lithium amide-imide samples. Therefore the lithium-calcium imide could be more readily applied to a practical device, and would be compatible with support architecture to improve its activity.

Despite being stable in the temperature range used for NH_3 decomposition under inert gas, one of the challenges presented by $Li_2Ca(NH)_2$ is the difficulty in keeping it solid at intermediate temperatures in part due to the formation of $LiNH_2$. The $Li_2Ca(NH)_2$ crystal structure consists of alternating layers of lithium imide and calcium imide (CaNH), which between 200-460 °C is susceptible to attack by NH_3 causing it to decompose to CaNH and Li_2NH which readily reacts with NH_3 to form the observed $LiNH_2$. However, the ternary structure does appear to stabilise the Li_2NH layer to attack by NH_3 until higher temperatures than those seen for Li_2NH alone. This may be due to a degree of non-stoichiometry (identified by Rietveld analysis) which can be accommodated in the $Li_2Ca(NH)_2$ structure without causing decomposition of the phase. It is thought that Li_2NH is the most active component in decomposing the NH_3 but CaNH plays a role in stabilising the material, making it much easier to handle and less likely to escape from the reactor.

Isotopic exchange reactions and *in-situ* neutron powder diffraction results indicate that all three catalysts; $NaNH_2$, Li_2NH and $Li_2Ca(NH)_2$ operate via a combination of surface and bulk reaction mechanisms in contrast to traditional surface based catalysts. Li, Na and K do not have access to *d*-orbitals, and so cannot accept electron density from the gas molecules via vacant or partially vacant *d*-orbitals as transition metal centres in heterogeneous catalysis are known to. For these amides/imides, total interaction and exchange of both the N and H from the bulk with the NH_3 being decomposed is seen rather than NH_3 just decomposing on the surface. Although the decomposition occurs at the surface of the catalyst, it is the composition of the bulk of the catalyst which affects the concentration of active surface sites. DFT studies have suggested that the energy barrier for the migration of protons between lithium imide and amide groups is low [122, 206] so it is possible that hydrogen formed from surface decomposition of NH_3 could diffuse into the amide-imide structure. This can be considered both as a Grotthuss type mechanism in terms of the protons hopping, and as a Frenkel defect, as the protons are moving through the structure [70, 197].

From looking at the Mg-N-H system [80, 126], magnesium amide releases ammonia at a lower temperature than lithium amide and therefore lithium-magnesium imide ($Li_2Mg(NH)_2$) has also been studied to a degree as a potential NH_3 decomposition catalyst. However, despite showing good low temperature conversion, it showed poor high temperature conversion (Figure 1.17) and containment (material recovery was less than 5 %) so it was not investigated further.

1.7 Thesis aims

This thesis is focused around synthesising, characterising and optimising new highly active and effective ammonia cracking catalysts. It aims to further explore the potential and function of mixed-metal amides as effective catalysts towards the decomposition of ammonia through optimising turnover frequency at the lowest costs and temperatures. Inexpensive metal amides/imides are clearly among the most highly active NH_3 decomposition catalysts at modest temperatures and have surpassed the performance of optimised transition metal

based catalysts, facilitating the widespread use of ammonia in sustainable energy applications. Further improvement of their performance is predicated on the development of a detailed understanding of the catalytic reaction mechanisms involved in NH_3 decomposition. Even within the small number of systems examined to date there is significant variation in the NH_3 decomposition behaviour of the various amide/imide catalysts. Exploring a range of materials is important in order to get a wider understanding of the systems and periodic trends as it is hard to directly compare systems which have different decomposition pathways.

There are three key goals for the development of more effective metal amide-imide catalysts:

1. To design new systems which display higher NH_3 decomposition activity at low operating temperatures (ideally 300-400 °C just operating on waste heat)

2. To develop materials which are easier to maintain as a solid and remain stable across the range of NH_3 decomposition reaction conditions and up to maximum operating temperature

3. To identify materials that are tolerant to small amounts of water and limited exposure to air

These can be embodied by two challenges which need to be overcome:

- Chemistry challenge: To discover and characterise an amide/imide system where the amide decomposes at room temperature or below and the imide is stable and solid up to maximum operating temperature

- Chemical engineering challenge: To develop a solid catalyst and support which is maintained within the catalyst reactor.

Mixed-metal catalysts are attractive systems for developing "design rules" for achieving these goals, as they allow for an exploration of the role of different metal cations and different amide decomposition pathways. A number of Group 1/2 mixed-metal amide families have been identified for these investigations.

1. "Third generation" intra Group 1 mixed-metal amides:

    - Mixing metals with different decomposition pathways:
        - Lithium-sodium amides - These were chosen based on their close crystallographic similarity to $LiNH_2$
        - Lithium-potassium amides - KNH_2 thermally decomposes via the same route as $NaNH_2$ but has a higher melting point so these may suffer from less significant catalyst loss
    - Mixing metals with the same decomposition pathway:
        - Sodium-potassium amides - Some members of the Li-K-N-H and Na-K-N-H systems are isostructural but there is a cost advantage of using $NaNH_2$ over $LiNH_2$

    Whilst the crystallography of the Li-Na-N-H system has been well documented, it has not been studied for the other Group 1 mixed-metal systems under investigation; Li-K-N-H (Chapter 4) and Na-K-N-H (Chapter 5). The Li-Na-N-H system is therefore a good starting point for studying mixed-metal systems as a whole, as in this system the structures are already known. This knowledge can therefore be used as a basis for understanding how the catalysts work through analysis of the thermal data collected. Structure is important in terms of the thermal behaviour of a sample and is important in dictating and understanding its properties. For the other Li-K-N-H and Na-K-N-H systems, there is the added component of understanding the less well studied crystallography and their structures in addition to their behaviour as NH_3 decomposition catalysts.

2. "Fourth generation" inter Group 1 and Group 2 mixed-metal amides:

    - Potassium-magnesium amides
    - Sodium-magnesium amides

    Mixed amide-imide phases have been reported for the K-Mg-N-H system [214, 245, 291] and suggested for the Na-Mg-N-H system [81, 232, 260, 301], meaning they are a

new class of mixed-metal NH_3 decomposition catalyst. They bridge the intra Group 1 "third generation" amide systems for which no mixed-metal imide exists and the Li-Ca-N-H and Li-Mg-N-H systems for which only an imide is known.

The chemical intuition involved in the development of the initial amide/imide systems for NH_3 decomposition has achieved impressive results. However, the further advances that are necessary for future application of mixed-metal amide systems are likely to come from a deeper understanding of the mechanisms by which unstable amides exothermically decompose to a stable imide. Understanding how the decomposition mechanisms of these novel ternary amides are correlated with their NH_3 decomposition activity will be crucial to improving their performance. Comparing these mechanisms to those already known for $LiNH_2$, $NaNH_2$ and $Li_2Ca(NH)_2$ will enable a better understanding of how tailoring the catalyst can lead to different decomposition routes through comparison of how closely these systems behave compared to the known imide and metal forming pathways.

The need for a renewable based H_2 carrier has been highlighted and it is hoped this work may help facilitate a transition to a future sustainable energy economy where the potential of ammonia is exploited to play a dominant role in transporting and storing clean and carbon free energy.

Chapter 2

Experimental Methods

Contents

2.1 General Sample Handling 69

2.1.1 Air and moisture-sensitive sample handling 69

2.2 Synthesis techniques 70

2.2.1 Solid-gas reactions 70

2.2.1.1 Gas flow panel 70

2.2.1.2 Cambridge reactor 72

2.2.1.3 Sealed cylindrical reactor 73

2.2.2 Overview of solid-gas reactions 74

2.2.2.1 KNH_2 74

2.2.2.2 $Mg(NH_2)_2$ and $Mg(ND_2)_2$ 75

2.2.3 Solid-solid reactions experimental setup 75

2.2.3.1 Ball-mill (BM) 76

2.2.3.2 Gas flow panel 76

2.2.3.3 Tube furnace (TF) 76

2.2.4 Overview of solid-solid synthesis reactions 77

2.2.4.1 Lithium-sodium system 78

2.2.4.2 Lithium-potassium system 79

2.2.4.3 Sodium-potassium system 83

2.2.4.4 Potassium-magnesium system 84

2.2.4.5 Sodium-magnesium system 85

2.3 Ammonia decomposition experiments 86

2.4 Thermal analysis 87

2.4.1 Thermogravimetric analysis (TGA) 87

2.4.2 Differential scanning calorimetry (DSC) 87

2.4.3 Simultaneous thermal analysis (STA) 88

2.5 Vibrational analysis 88

2.5.1 Raman 89

2.6 Structural Analysis 89

2.6.1 Introduction to Crystallography 90

2.6.2 Introduction to Diffraction 91

2.6.2.1 Bragg's law 91

2.6.2.2 Structure Factors 92

2.6.2.3 Powder Diffraction 95

2.6.3 Neutron Powder Diffraction (NPD) 97

2.6.3.1 ISIS neutron and muon facility 99

2.6.3.2 GEM and POLARIS 101

2.6.3.3 Intelligent Gravimetric Analysis with Neutron Diffraction (IGA^n) 103

2.6.3.4 *In-situ* sample stick 105

2.6.4 Powder X-ray Diffraction (PXRD) 106

2.6.4.1 Advantages of X-ray diffraction 107

2.6.4.2 Laboratory X-ray diffraction equipment 107

2.6.4.3 X-ray synchrotrons 109

2.6.4.4 Diamond/I11 110

2.6.5 Structure prediction and solution 111

2.6.5.1 Charge Flipping 113

2.6.5.2 Simulated annealing 113

2.6.5.3 Structure prediction software 114

2.6.6 Rietveld Refinement 114

2.6.6.1 Refinement Software 117

2.6.6.2 Batch Refinements 118

2.1 General Sample Handling

Details of the reagents used in the work in this thesis are shown in Table 4.1.

Reagent name	Chemical formula	Form	Supplier	Purity (%)
Lithium amide	$LiNH_2$	Powder	Sigma Aldrich	95
Sodium amide	$NaNH_2$	Powder	Sigma Aldrich	95
Lithium nitride	Li_3N	Powder	Sigma Aldrich	95
Potassium hydride	KH	Powder	Sigma Aldrich	95
Magnesium hydride	MgH_2	Powder	Sigma Aldrich	95
Ammonia	NH_3	Liquefied gas	Sigma Aldrich	99
Ammonia – D_3	ND_3	Liquefied gas	Sigma Aldrich	99

Table 2.1: Reagents used in the work presented in this thesis

2.1.1 Air and moisture-sensitive sample handling

The majority of materials presented in this thesis are sensitive to oxygen and water so samples were stored and manipulations were performed in an air and moisture free inert atmosphere. This was achieved by using an argon filled glove box (MBraun Unilab) equipped with a gas recirculation system which passes the argon through a copper-based catalyst bed in order to remove trace amounts of oxygen and water (O_2 and $H_2O < 0.1$ ppm). All glassware and equipment that entered the glove box had been previously dried in an oven and thorough pump-purging of the ports before use ensured the glove box atmosphere did not become contaminated.

Polypropylene glove bags (Sigma Aldrich) had to be used on occasions when size restrictions meant that glove box use was impossible. The bags must be sequentially purged and refilled with argon gas at least 5 times before sample manipulation can begin as they do not possess the active purification system of the glove box. Instruments were housed within these inert environments, or loaded using inert atmosphere techniques such as a dry loader.

2.2 Synthesis techniques

2.2.1 Solid-gas reactions

Solid-gas reactions were required to synthesise the single metal amides which could not be bought pre-formed. These reactions were also utilised to produce deuterated versions of the single metal amides which are a pre-requisite for neutron diffraction experiments (Section 2.6.3). Three different reactor set-ups were used to perform solid-gas reactions; the gas flow panel, the Cambridge reactor and a sealed cylindrical reactor which are discussed in more detail below. Table 2.2 lists the different reactions performed, as well as the experimental conditions and set-up utilised for each.

Solid reactant	Reactive gas	Desired product	Temp (°C)	Pressure (bar)	Method
KH	NH_3/ND_3	KNH_2/KND_2	200	1	Gas flow panel
$NaNH_2$	ND_3	$NaND_2$	200	1	Gas flow panel
Li_3N	ND_3	$LiND_2$	300	3	Sealed cylindrical reactor
MgH_2	NH_3/ND_3	$Mg(NH_2)_2/Mg(ND_2)_2$	375	5	Cambridge Reactor

Table 2.2: Summary of solid-gas reactions used in this thesis

KNH_2 was prepared by first washing KH with hexane (which had been pre-dried using calcium hydride) to remove the mineral oil it was stored in. This was then dried for 10 hours under argon at 120 °C to remove all residual solvent before being heated to 210 °C for 10 hours under flowing NH_3 to form KNH_2.

2.2.1.1 Gas flow panel

The gas flow panel is a custom-designed through-flow gas reactor as shown in Figure 2.1. Reactions are performed in cylindrical 316 stainless steel flow reactors with an internal volume of 46.9 cm^3 and 24.0 mm in diameter. The reactors are fitted with an inlet gas pipe running from the reactor lid to about 1cm from the base of the reactor, an outlet gas pipe from the lid and a thermocouple to monitor the internal temperature. The solid reactant

is loaded into the reactor in an argon filled glove box, sealed and transferred to a vertical tube furnace (Severn Thermal Solutions) connected to a gas control panel.

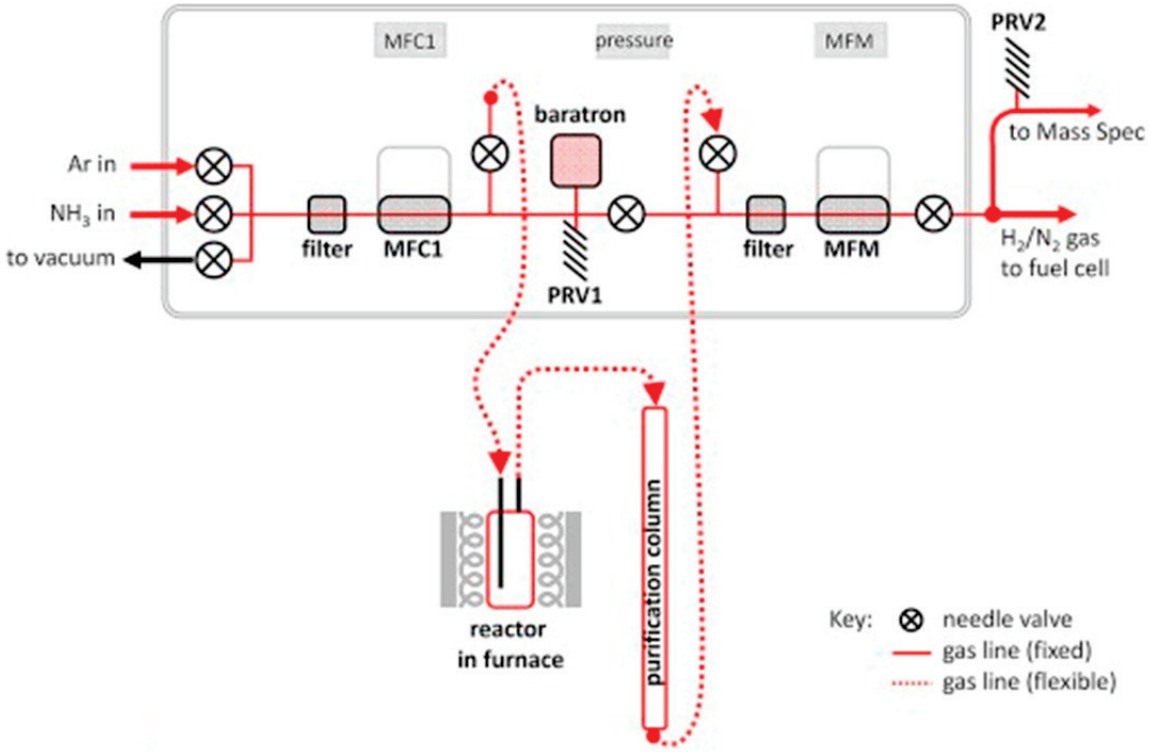


Figure 2.1: Schematic diagram of the gas flow panel set-up for reactions under flowing gas [133]

The panel is first evacuated up to the reactor, before both the panel and reactor are flushed with either $NH_3/ND_3/Ar$ (as required) prior to heating. Input gas is controlled using a mass flow controller (HFC-302, Teledyne Hastings Instruments) and the outlet gas flow is measured using a mass flow meter (HFM-300, Teledyne Hastings Instruments). This set-up also enables automatically switching between two gas species during an experiment, in which case these must be connected to different MFCs. The gas species flowing out of the reactor are quantitatively analysed and characterised using a Hiden Analytical HPR-20 QIC R&D mass spectrometer (equipped with MASsoft v7 software) in histogram mode, monitoring peaks with a mass-to-charge ratio (m/z) of 1-40 inclusive.

The experiments are performed at atmospheric pressure with the system operated at constant flow up to 60 sccm while varying the reaction temperature. The gas flow rates into and out of the reactor, the reactor temperature and system pressure are concurrently

recorded.

The sensitivity factors of the gas species measured were calibrated using a certified gas mixture consisting of 2% ammonia, 2% hydrogen, 2% nitrogen and 94% argon. The sensitivity factors account for the difference in the ease of ionisation of each species, and for the fragmentation of those species in the mass spectrometer, which has the effect of artificially lowering their signals. The mass spectrometer was set to auto-range for the gas values. The quadrupole mass spectrometer works by taking a portion of exhaust gas into a vacuum chamber where electrons generated from a filament are accelerated into the gas flow, ionising the gas molecules. The ionised molecules then pass into the quadrupole mass analyser which consists of 4 parallel metal rods made up of 2 pairs of opposite electric polarity. A variable radiofrequency (RF) voltage is applied to the rods which together with a DC voltage, stabilise the trajectory of ions of a selected mass-to-charge ratio (m/z) as they travel through the quadrupole to a Faraday cup where they are neutralised. Ions with an m/z not selected for analysis won't have a stable trajectory, and will hit one of the metal rods and be neutralised. The current generated at the Faraday cup is proportional to the number of ions hitting it enabling the amount of ions of particular m/z in the gas stream to be quantified. The experiments presented here were run in Multi-Ion Detection (MID) mode, monitoring a pre-selected set of m/z values.

2.2.1.2 Cambridge reactor

This is a modified set-up of the gas flow panel described in Section 2.2.1.1. The panel is designed to deliver flowing gas to a reactor system and to facilitate analysis of the composition of the gas flow with mass spectrometry. The advantage of this system is that is enables high pressure synthesis (5 bar) under flowing gas by maintaining a significant back pressure on the system.

A flow-through reactor system is loaded with the sample in an argon filled glove box, sealed connected to the gas control panel as shown in Figure 2.2. The desired gas supply is also connected to the panel and set to the required pressure. The panel is first evacuated up to the reactor, before both the panel and reactor are flushed with either NH_3/ND_3/Ar (as required) prior to heating. The back-pressure regulator can be used to increase the pressure

in the panel. The furnace temperature, panel pressure are recorded and the gas composition at the panel outlet can be analysed using the mass spectrometer with the Massoft software package.



Figure 2.2: Gas panel with flow-through reactor setup

2.2.1.3 Sealed cylindrical reactor

The advantage of this system is that it enables high pressure synthesis due to the evacuated sealed environment. Samples were loaded into the cylindrical reactor in an argon filled glove box and sealed by closing the valve. This was then connected to the gas loading panel shown in Figure 2.3 which was evacuated up to the valve on the reactor, before which the cell was loaded with the required pressure of gas (up to 20 bar). The valve on the reactor was then closed before it was disconnected from the panel and heated to the desired temperature at the specified heating rate whilst supported by a retort stand and surrounded by a heat shield. The pressure and temperature of the reactor were monitored throughout. Once the reaction was complete, the reactor was allowed to cool and then reconnected to the gas loading panel and evacuated to below 10^{-6} bar. The valve on the reactor was then closed and it was transferred to the glovebox to unload the sample.

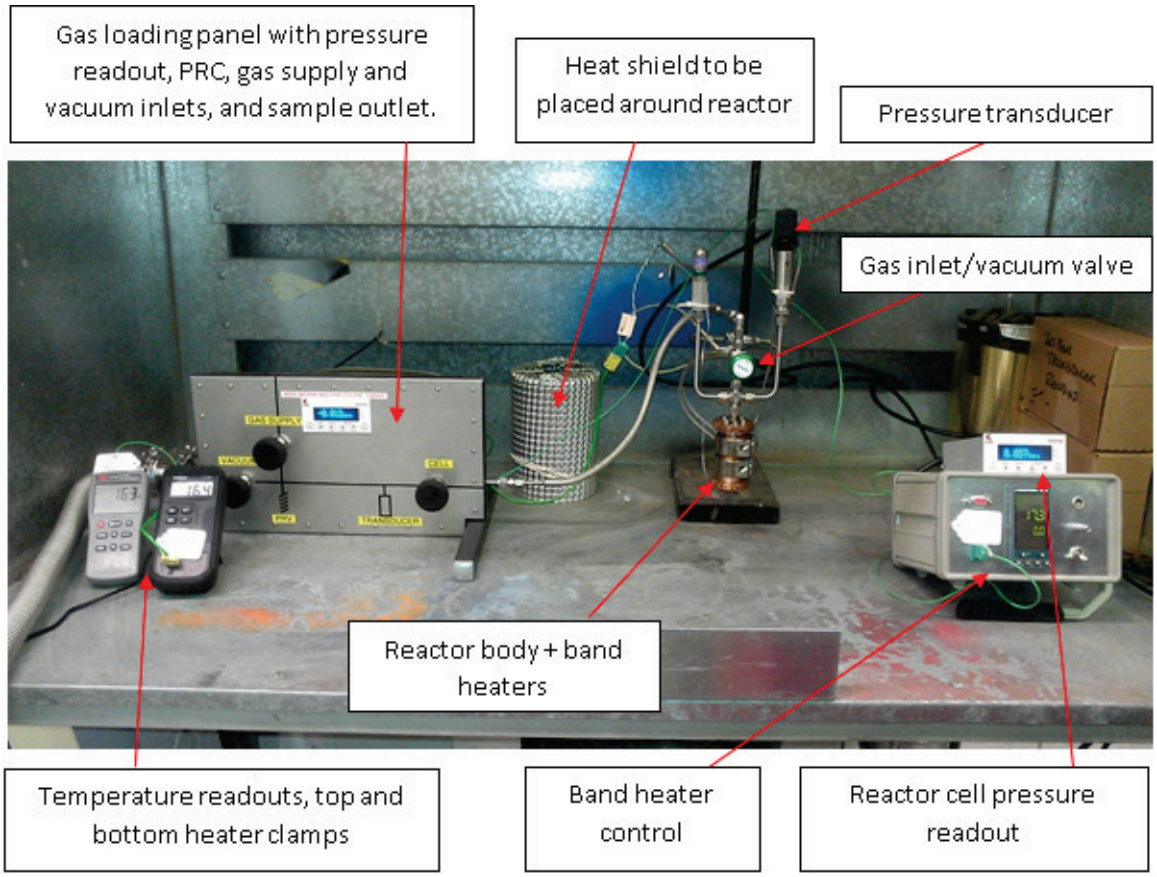


Figure 2.3: Configuration of the sealed cylindrical reactor and its ancillary systems

2.2.2 Overview of solid-gas reactions

2.2.2.1 KNH_2

Unlike $LiNH_2$ and $NaNH_2$ which can be bought, KNH_2 must first be synthesised by reaction of ammonia with potassium hydride (which itself has to first washed with hexane to remove the oil and then dried under vacuum). This was initially attempted in the sealed cylindrical reactor (Section 2.2.1.3) however this produced very impure KNH_2, containing a large amount of KH and KOH. However, reaction of dried KH with flowing ammonia for 12 hours at 200 °C on the gas flow panel resulted in pure monoclinic KNH_2 which could then be used for further synthesis and analysis.

2.2.2.2 $Mg(NH_2)_2$ and $Mg(ND_2)_2$

$Mg(NH_2)_2$ must first be synthesised as it cannot be purchased. MgH_2 was ball-milled for 1 hour before being loaded into the through flow reactor and attached to the gas flow panel (Section 2.2.1.2) and heated to 200 °C under 5 bar flowing ammonia for 12 hours. The advantage of this system is that it enables high pressure synthesis under flowing gas by maintaining a significant back pressure on the system.

$$MgH_2 + 2\,NH_3 \longrightarrow Mg(NH_2)_2 + 2\,H_2 \tag{2.1}$$

Analysis of the MS data from the gas flow panel enabled the identification of the point at which this reaction (Equation 2.1) had reached completion, as H_2 was no longer given off and NH_3 was detected again. Powder X-ray diffraction data was collected of the recovered sample and analysed to determine the percentage composition using TOPAS, which showed that 98.4 % $Mg(NH_2)_2$ was synthesised with only 1.6 % MgNH (a reaction intermediate) present. This sample could therefore be used for further synthesis and analysis.

$Mg(ND_2)_2$ was synthesised using the same method and experimental set-up as that for $Mg(NH_2)_2$, however ND_3 was used instead of NH_3. Whereas the reaction of MgH_2 and NH_3 required only one heating cycle to synthesise $Mg(NH_2)_2$, MgH_2 and ND_3 required two heating cycles to form high purity $Mg(ND_2)_2$. MgH_2 was initially heated to 200 °C under 5 bar flowing ND_3 for 12 hours before it was cooled, removed from the reactor and hand-ground with a pestle and mortar for 10 minutes. Powder X-ray diffraction data collected at this stage showed that the sample contained a significant impurity of magnesium imide. The sample was therefore loaded back into the reactor and heated to 200 °C under 5 bar of flowing ND_3 for a second period of 12 hours. This produced a sample that was over 98 % pure $Mg(ND_2)_2$ and could therefore be used for further synthesis and analysis.

2.2.3 Solid-solid reactions experimental setup

Solid-solid reactions under flowing gas are required for the synthesis of the mixed-metal amides discussed in this thesis. Three main experimental setups were utilised; the ball-mill, the tube furnace and the gas flow panel. All of these techniques started by weighing out

the appropriate quantity of each starting material followed by the thorough grinding of the reaction mixtures using an agate pestle and mortar. This is important to create an intimate mixture of the reactants prior to solid-state reaction. Samples were hand ground for a minimum of 5 minutes, or 5 minutes per gram of sample if larger quantities were used.

2.2.3.1 Ball-mill (BM)

The mixed powder was loaded into a tungsten carbide milling jar (Retsch 80 ml) with 3 mm diameter stainless steel balls in a ball:powder mass ratio of 60:1 which was sealed and placed into a Retsch PM100 planetary ball-mill. When the mill is operational, the main "sun wheel" of the mill rotates in the opposite direction to the grinding jar with equal rotational velocity causing the grinding balls to repeatedly crush and grind the powder sample. Samples were milled at 400 rpm for 90 minutes unless stated otherwise with the milling time split into 12 minute sections with 2 minute rest periods between each section to dissipate the heat generated by the friction of the milling process. The direction of milling rotation was reversed after each section in order to minimise the formation of "dead zones", where powder accumulates without being subject to continuous milling.

2.2.3.2 Gas flow panel

The experimental set-up used is the same as described in Section 2.2.1.1. The mixed powder was loaded into the stainless steel flow reactor and heated at 5 °C/min to 200 °C where it was held for a further 8 hours. Synthesis experiments using this set-up were performed under both argon and NH_3 to determine the effect of the gaseous atmosphere on sample synthesis.

2.2.3.3 Tube furnace (TF)

The mixed powder was loaded into a cylindrical alumina crucible (chosen based on its relative inertness) and placed into a glass tube which was sealed at one end. The open end of the tube was then sealed with a Swagelok fitting and a rubber O-ring, and connected to a glass T-piece fitted with three Young's taps forming an air-tight seal. This tube was then placed into a horizontal Carbolite MTF 12/38/400 tube furnace as shown in Figure 2.4.

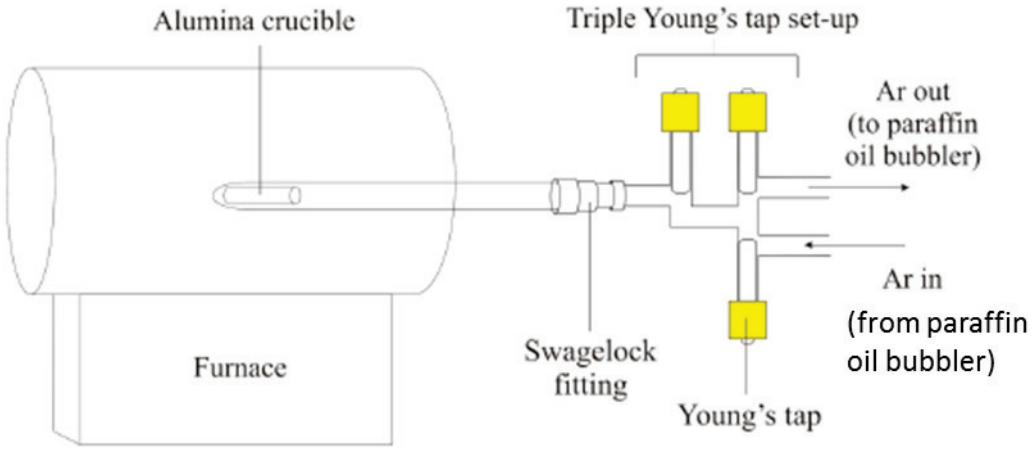


Figure 2.4: Schematic diagram of the tube furnace set-up for solid-solid reactions under flowing gas

The incoming and exhaust gases were connected to the T-piece via paraffin oil bubblers which act as one-way valves and are used to exclude air from the system. Gas was flowed through the upper section of the glass T-piece for 5 minutes before the tap to the sample was opened.

The sample was heated at 1 °C/min to 200 °C where it was held for 12 hours. The product was allowed to cool, evacuated to below 10^{-6} bar on a vacuum line, collected in the glove box and hand ground prior to analysis.

2.2.4 Overview of solid-solid synthesis reactions

Table 2.3 lists the different reactions performed. All three experimental setups described in Section 2.2.3 were attempted to synthesise each desired product.

Reactants		Desired Product	Successful Methods
$LiNH_2$	$NaNH_2$	$Li_3Na(NH_2)_4$	BM, TF, Gas flow panel
		$LiNa_2(NH_2)_3$	BM, TF, Gas flow panel
$LiNH_2$	KNH_2	$Li_3K(NH_2)_4$	BM, TF
		$LiK_2(NH_2)_3$	BM
$NaNH_2$	KNH_2	$NaK_2(NH_2)_3$	BM, TF, Gas flow panel
$NaNH_2$	$Mg(NH_2)_2$	$Na_2Mg(NH_2)_4$	BM, TF, Gas flow panel
KNH_2	$Mg(NH_2)_2$	$K_2Mg(NH_2)_4$	BM, TF, Gas flow panel

Table 2.3: Summary of solid-solid reactions used in this thesis

2.2.4.1 Lithium-sodium system

The solid state reaction of $LiNH_2$ with $NaNH_2$ has been shown to form two mixed-metal amides of formula $Li_3Na(NH_2)_4$ and $LiNa_2(NH_2)_3$ [189]. Mixed sodium-lithium amide species were first reported to have been formed from the condensation of supercritical ammonia over a mixture of Li and Na metals [147]. Solid state syntheses have since been reported from the reaction of $LiNH_2$ and $NaNH_2$ [154, 189] which results in the formation of $Li_3Na(NH_2)_4$ for lithium-rich compositions and $LiNa_2(NH_2)_3$ for sodium-rich compositions and avoids the direct use of ammonia. A variety of methods for the synthesis of $Li_3Na(NH_2)_4$ and $LiNa_2(NH_2)_3$ were explored (Table A.1 in the Appendix) in order to find the optimum conditions.

For each sample, $LiNH_2$ and $NaNH_2$ were weighed out in a stoichiometric ratio under an argon atmosphere and intimately ground together with a mortar and pestle for 10 minutes followed by synthesis via the sets of conditions outlined in Table A.1. For each ratio, a reaction temperature of 200 °C was chosen as this was low enough to ensure minimal $LiNH_2$ decomposition but high enough to encourage cation migration, especially as it is close to the melting point of $NaNH_2$ (210 °C [107]) so high Na^+ mobility is expected. Rietveld analysis of the data was performed using TOPAS Academic fitting software which led to the phase

compositions presented in Table A.1. It can be seen that the most important experimental parameter to obtain mixed lithium-sodium samples of the highest purity was the total mass of the sample. The smaller the sample size, the purer the product, so only samples $< 0.5\,g$ were synthesised for experiments presented in this thesis.

The sealed environment of the cylindrical reactor produced non-stoichiometric $Li_{4-y}Na_y(NH_2)_4$ $(0 < y < 1)$ indicated by 2θ dependent asymmetry in the Bragg diffraction peaks, but samples synthesised under flowing argon (in the tube furnace and gas flow panel) and in the ball-mill, produced highly stoichiometric phases. Therefore the sealed cylindrical reactor was not considered further as a synthetic route for mixed-metal amides. All the Bragg reflections corresponding to $LiNa_2(NH_2)_3$ were sharp and symmetrical, indicating the presence of a highly crystalline, stoichiometric phase as expected. Although the ball-mill presented the quickest and easiest method to synthesise high purity $Li_3Na(NH_2)_4$ and $LiNa_2(NH_2)_3$, this method was only discovered retrospectively after the Li-K-N-H system had been investigated (Section 4.2.2). $Li_3Na(NH_2)_4$ and $LiNa_2(NH_2)_3$ synthesised for analysis in Chapter 3 by a variety of techniques in order to increase understanding of their behaviour and decomposition properties, were therefore made in the tube furnace. Analogous synthesis experiments under NH_3 were also performed on the gas flow panel to ensure the mixed-metal amides could still formed (Table A.1).

2.2.4.2 Lithium-potassium system

$Li_3K(NH_2)_4$

In a similar manner to the mixed lithium-sodium amides, the solid state reaction of $LiNH_2$ and KNH_2 in the tube furnace, ball-mill and on the gas flow panel under argon resulted in the successful synthesis of $Li_3K(NH_2)_4$ as shown in Table 2.4. However, on the gas flow panel under ammonia, very different powder X-ray diffraction data was collected in which $Li_3K(NH_2)_4$ was only a minor component. This is discussed in more detail in Section 4.4.

For each sample, $LiNH_2$ and KNH_2 were weighed out in a stoichiometric ratio under an argon atmosphere and ground together with a mortar and pestle for 10 minutes followed by synthesis via the sets of conditions outlined in Table 2.4. For all the heating methods described, starting materials of the same purity were used and a total sample mass of 0.5 g

was used. After each synthesis attempt, powder X-ray diffraction data was collected and analysed using TOPAS to determine the percentage composition of the sample.

Heating Method	Ramp rate (°C/min)	Composition (mol%) $Li_3K(NH_2)_4$	$LiNH_2$
Tube furnace	1	100.0	0.0
Ball-mill	-	86.3	13.7
Gas flow panel - argon	1	99.2	0.8
Gas flow panel - ammonia	1	See Section 4.4	

Table 2.4: Synthesis attempts for $Li_3K(NH_2)_4$

$LiK_2(NH_2)_3$

$LiK_2(NH_2)_3$ was first synthesised via two methods by Franklin et al. [101]; firstly from lithium iodide (from a liquid ammonia solution of ammonium iodide on metallic lithium) added to potassium amide, and secondly from metallic lithium and metallic potassium in solution with liquid ammonia in the presence of platinum black. More recently it has been formed in a Schlenk tube with distilled potassium, $Li_2B_{10}H_{10}$ and dried ammonia at -78 °C, which was then stored at -38 °C for two weeks [168].

$LiNa_2(NH_2)_3$ and $LiK_2(NH_2)_3$ have analogous crystal structures and based on the success of the tube furnace as a method for the synthesis of $LiNa_2(NH_2)_3$ (and $Li_3K(NH_2)_4$ and $Li_3Na(NH_2)_4$) this method was initially attempted for the synthesis of $LiK_2(NH_2)_3$ from a hand ground mixture of its constituent metal amides, $LiNH_2 + 2KNH_2$.

Initial attempts to synthesise $LiK_2(NH_2)_3$ in the tube furnace for 12 hours at 200 °C produced a sample that was only partially pure (42.0% $LiK_2(NH_2)_3$ and 58.0% monoclinic KNH_2 (Figure A.2 in the Appendix)) which, while indicating the potential for this phase to form under these conditions, was less successful as a synthesis method for high purity samples than for $Li_3Na(NH_2)_4$, $Li_3K(NH_2)_4$ and $LiNa_2(NH_2)_3$.

Further attempts to synthesis $LiK_2(NH_2)_3$ on the gas flow panel for 12 hours at 200 °C under argon produced a sample that was equally impure (39.0 % $LiK_2(NH_2)_3$ and 61.0 % monoclinic KNH_2 (Figure A.3 in the Appendix)).

Synthesis attempts at 200 °C under ammonia on the gas flow panel were also not successful and instead of forming $LiK_2(NH_2)_3$ as expected, 25.0 % $Li_3K(NH_2)_4$, 59.9 % $LiNH_2$ and 15.1 % Li_2O was produced (Figure A.4 in the Appendix). This is discussed further in Section 4.8. Recent theoretical studies of high-pressure polymorphs of $NaNH_2$ suggest that the octahedral coordination of Na^+ atoms is less stable and has higher energies compared to tetrahedral coordination [318]. In $Li_3K(NH_2)_4$ the K^+ ions have 8-coordinate body centred coordination but in $LiK_2(NH_2)_3$ $\frac{1}{4}$ are tetrahedral and $\frac{3}{4}$ are octahedral which may explain why $Li_3K(NH_2)_4$ is more thermodynamically favourable than $LiK_2(NH_2)_3$.

The composition of all these residues as determined by powder X-ray diffraction are detailed in Table A.2.

An STA experiment (both DSC and TGA) was therefore performed on a sample of $LiNH_2 + 2KNH_2$ with the aim of determining the temperature of the synthetic step for $LiK_2(NH_2)_3$ formation (Section 4.2.2).

Analysis of the post-reaction powder X-ray diffraction data shows that on heating the mixed single metal amides to a variety of temperatures in the tube furnace, $LiNH_2$ appears to be lost at a faster rate than KNH_2. This is unexpected as $LiNH_2$ would not be expected to melt or react at these temperatures (below 200 °C) so it is unclear why it is not detectable in some of the powder X-ray diffraction data. If KNH_2 were present, it is known to be easily detectable by powder X-ray diffraction as it can be seen to be present in some of the other samples and there is no evidence that it forms non-stoichiometric materials. An experiment was therefore run in which $LiNH_2$ and KNH_2 were hand-ground in a 1:1 ratio (less KNH_2 than would be expected for $LiK_2(NH_2)_3$, to account for some $LiNH_2$ being lost) and heated to 225 °C in the tube furnace for 12 hours. However, when powder X-ray diffraction data was collected from the residual sample remaining at the end of this experiment, rather than any $LiK_2(NH_2)_3$ being formed as was expected, powder X-ray diffraction data relating to an unknown phase was obtained which is discussed further in Section 4.4.

As a result of the inability to form high purity $LiK_2(NH_2)_3$ in the tube furnace or on the gas flow panel, use of the ball-mill was investigated as a preparation method. Multiple different experiments using the ball-mill were performed (Table A.2) to ascertain the best experimental conditions for the synthesis of $LiK_2(NH_2)_3$. Various factors were adjusted

including the ball size, number of balls, pot size, rotation speed, number of milling intervals and total time. They all had an interval length of 12 minutes followed by a break time of 1 minute and all used a sample size of 0.5 g.

Table A.2 and Figure 4.4 (Samples F-P) detail the weight percent composition of the samples synthesised by each set of conditions. These data show that the conditions that led to the highest proportion of $LiK_2(NH_2)_3$ being synthesised were conditions "M" which used a reactor volume of 80 ml, 30 g of 2mm diameter balls, 0.5 g sample size, 400 rpm, 12 minute interval length with a 1 minute break for a total time of 60 minutes and did not involve heating in the tube furnace. These conditions consistently produced $LiK_2(NH_2)_3$ close to 100 % purity so were used for the synthesis of the $LiK_2(NH_2)_3$ used for further analysis throughout this thesis. Ball-milling $LiNH_2$ and KNH_2 in a 1:2 ratio clearly presents a novel method for the simple, quick and reliable synthesis of $LiK_2(NH_2)_3$ in much milder conditions than previously reported methods.

$Li_7K(NH_2)_8$

The direct synthesis of $Li_7K(NH_2)_8$ has only been reported once before by the reaction of ammonia with the metals in high-pressure autoclaves [148]. Samples with a 7:1 ratio of $LiNH_2$:KNH_2 were heated in the tube furnace to both 200 °C and 220 °C in separate experiments where they were held for 12 hours. Post-reaction powder X-ray diffraction on both the residual products obtained, showed that no $Li_7K(NH_2)_8$ had been produced in either experiment. Instead, the major phases of the residual products were $Li_3K(NH_2)_4$ ($\sim$ 55.0 %) with a minor phase of $LiNH_2$ ($\sim$ 45.0 %) to satisfy the stoichiometry (Figure A.5 in the Appendix for the experiment heated to 200 °C).

Synthesis was then attempted in the ball-mill with a 7:1 ratio of $LiNH_2$:KNH_2 with conditions "M" from Table A.2 in Section 2.2.4.2 (80 ml reactor volume, 30 g of 2mm diameter balls, 0.5 g sample size, 400 rpm with 12 minute intervals and 1 minute breaks for a total time of 60 minutes). However, powder X-ray diffraction showed that this experiment also produced $\sim$ 55% $Li_3K(NH_2)_4$ and $\sim$ 45% $LiNH_2$ and no $Li_7K(NH_2)_8$. These results are discussed with additional STA data and Raman spectra in Section 4.2.3. Li et al. also found that 7:1 $LiNH_2$:KNH_2 ball-milled for 12 hours produced $Li_3K(NH_2)_4$ and residual

$LiNH_2$ rather than any $Li_7K(NH_2)_8$ [178]. As no $Li_7K(NH_2)_8$ could be formed, no further analysis on this reported member of the Li-K-N-H system was performed.

2.2.4.3 Sodium-potassium system

Only one synthetic method for the preparation of $NaK_2(NH_2)_3$ has been previously reported in the literature which uses a Schlenk tube and requires distilled potassium metal and $Na_2B_{10}H_{10}$ in condensed liquid ammonia left at -78 °C for 8 weeks [168].

Analogous synthetic methods for $NaK_2(NH_2)_3$ were attempted as for $LiK_2(NH_2)_3$ and $LiNa_2(NH_2)_3$ by the solid state reaction of $NaNH_2$ and KNH_2 in the tube furnace, ball-mill and on the gas flow panel under argon and ammonia as shown in Table 2.5.

For each sample, $NaNH_2$ and KNH_2 were weighed out in a a 1:2 molar ratio under an argon atmosphere and ground together with a mortar and pestle for 10 minutes followed by synthesis via the sets of conditions outlined in Table 2.5. For all the heating methods described, starting materials of the same purity were used and a total sample mass of 0.5 g was used. After each synthesis attempt, powder X-ray diffraction data was collected and analysed to determine the percentage composition of the sample using TOPAS. The difficulties observed in forming high purity $LiK_2(NH_2)_3$ in the tube furnace did not arise for the Na-K-N-H system. Rietveld refinements in TOPAS on the powder X-ray diffraction data for all four of these novel synthesis methods, show $NaK_2(NH_2)_3$ can be routinely made to over 90% purity. Therefore all of the synthetic methods demonstrated here offer much simpler, quicker and less energy intensive methods to form $NaK_2(NH_2)_3$ than that previously reported in the literature. Mild synthesis in the ball-mill is the best method to routinely form $NaK_2(NH_2)_3$ so this was used to prepare the samples analysed in Chapter 5.

Heating Method	Ramp Rate °C/min	Temperature held at (°C)	Composition (as weight %)		Unfitted peaks (*d*-spacing (Å))
			$NaK_2(NH_2)_3$	KNH_2	
Tube furnace	1	200	88.8	11.2	2.74, 2.17
Ball-mill	-	-	90.6	9.4	
Gas flow panel - argon	1	200	94.6	5.4	2.78, 2.55
Gas flow panel - ammonia	1	200	98.0	2.0	2.78, 2.73, 2.55

Table 2.5: Synthesis methods for $NaK_2(NH_2)_3$

2.2.4.4 Potassium-magnesium system

Novel synthetic methods for the formation of $K_2Mg(NH_2)_4$ directly from KNH_2 and $Mg(NH_2)_2$ have been developed using both tube furnace (to 200 °C) and ball-mill preparations. For each sample, KNH_2 and $Mg(NH_2)_2$ were initially weighed out in a 2:1 ratio under an argon atmosphere and intimately ground together with a mortar and pestle for 10 minutes.

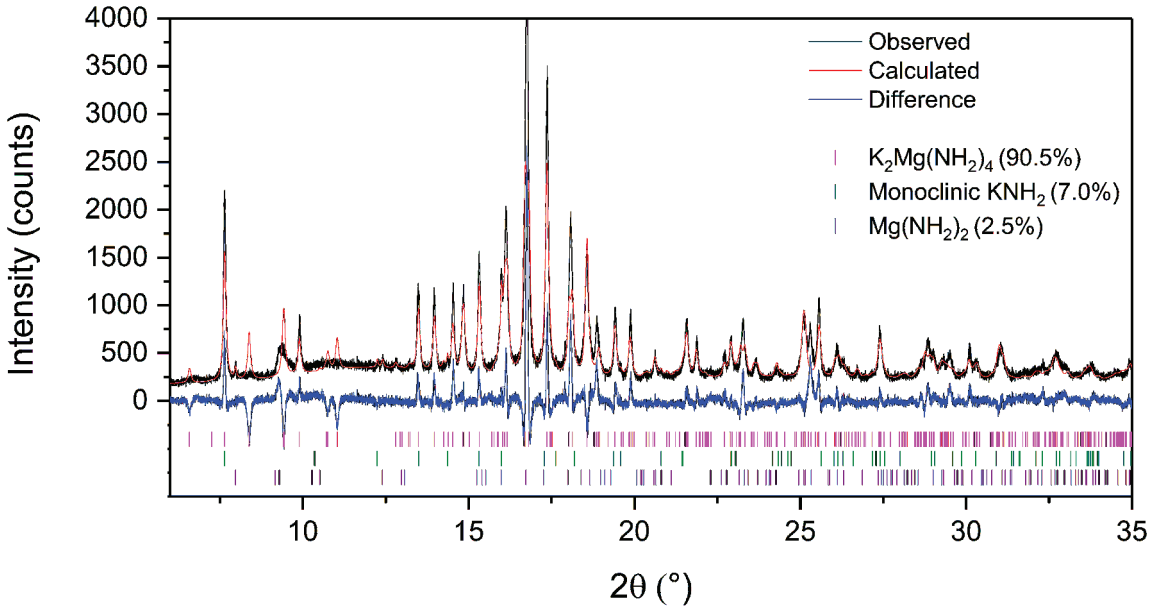


Figure 2.5: Powder X-ray diffraction data from a sample of $K_2Mg(NH_2)_4$ collected on the I11 beam-line at Diamond (Wavelength = 0.8248901 Å)

Figure 2.5 shows the powder X-ray diffraction data collected from the sample of $K_2Mg(NH_2)_4$ synthesised in the tube furnace which was collected on I11 at Diamond. Rietveld analysis of the data was performed using TOPAS Academic fitting software and three phases were identified. The pattern fits to 90.5 % $K_2Mg(NH_2)_4$, 7.0 % monoclinic KNH_2 and 2.5 % $Mg(NH_2)_2$. The sample made in the ball-mill was too amorphous for Rietveld analysis. However, analysis of Figure 2.5, particularly at low 2θ values, shows that the simulated peaks at 7.18 ° (100), 5.64 ° (10-2), 4.42 ° (111), 4.40 ° (11-2) and 4.29 ° (102) are absent from the collected powder X-ray diffraction data. Whilst these unfitted peaks do not seem to correspond to a particular set of indices, it may be that the reported space group is incorrect.

2.2.4.5 Sodium-magnesium system

Novel synthetic methods for the formation of "$Na_2Mg(NH_2)_4$" directly from $NaNH_2$ and $Mg(NH_2)_2$ have been developed using both tube furnace and ball-mill procedures. For each sample, $NaNH_2$ and $Mg(NH_2)_2$ were weighed out in a stoichiometric ratio (2:1) under an argon atmosphere and intimately ground together with a mortar and pestle for 10 minutes. Synthesis was then performed either by heating at 1 °C/min to 200 °C where it was held for 12 hours in the tube furnace, or placed in the ball-mill for 1 hour (30 g small balls, 80 ml reactor volume, 400 rpm).

Figure 2.6 shows the *ex-situ* powder X-ray diffraction data collected for the sample of "$Na_2Mg(NH_2)_4$" synthesised in the tube furnace plotted in terms of *d*-spacing (Å) for a wavelength of 1.5418 Å. Neither $NaNH_2$ or $Mg(NH_2)_2$ fits to the powder X-ray diffraction data collected from this sample. Attempts have been made to index this pattern and solve the structure but this has proved as yet unsuccessful.

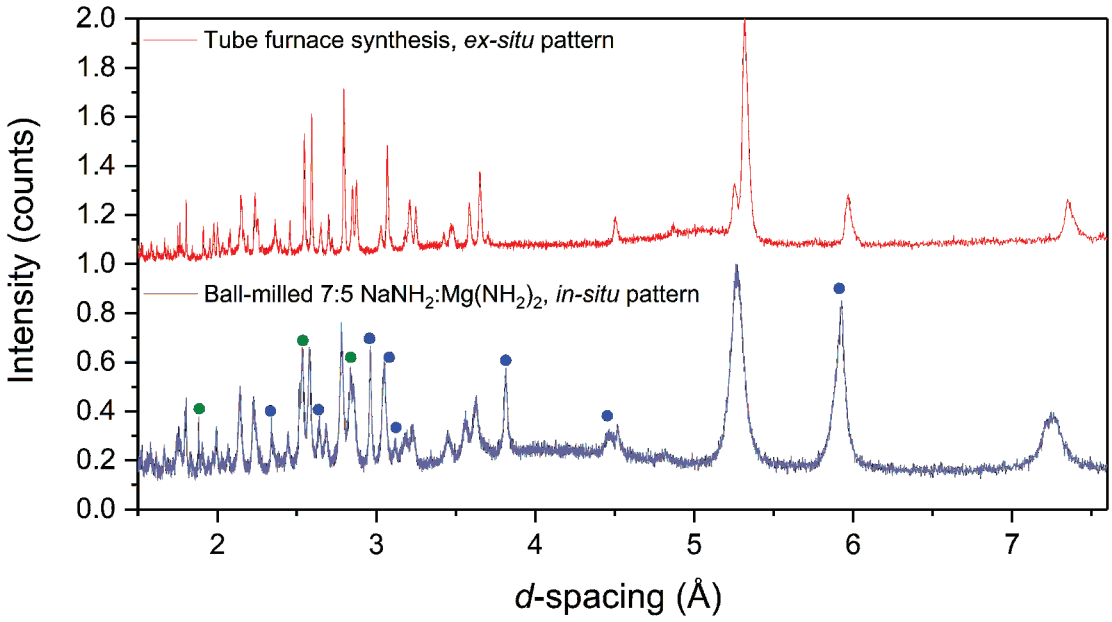


Figure 2.6: Observed powder X-ray diffraction data for the sample of "$Na_2Mg(NH_2)_4$" synthesised from $2NaNH_2 + Mg(NH_2)_2$ in the tube furnace (*ex-situ*), and the ball-milled 7:5 $NaNH_2$:$Mg(NH_2)_2$ sample (*in-situ*) plotted in terms of *d*-spacing (Å). Blue and green circles denote peaks assigned to $Mg(NH_2)_2$ and WC respectively

2.3 Ammonia decomposition experiments

The experimental set-up used is the same as described in Section 2.2.1.1 but with NH_3 supplied to the reactor via the gas control panel. Mass spectrometry data were recorded at the same time as the flow into and out of the reactor, the reactor temperature and system pressure.

Conversion efficiencies were calculated using a custom-written program written by Dr Thomas Wood using Python code. This program removes the background signals of the ammonia, nitrogen and hydrogen traces (the signals observed during argon flow, and the hydrogen and nitrogen signals seen when ammonia is flowing through the reactor at room temperature), and accounts for the discontinuities in the signals when the detector switches which range it is using (seen as a vertical discontinuity in the mass spectrometry plot). Once these signals are corrected, the conversion efficiency is calculated by expressing the ammonia signal as a percentage of the total signal, and thus the conversion efficiency is 100% minus the percentage of ammonia in the gas stream.

2.4 Thermal analysis

Thermal analysis is particularly important as this research aims to characterise and optimise novel ammonia cracking catalysts which:

1. Operate at low temperatures in order for commercial use in line with the targets outlined by the US Department of Energy

2. Remain solid up to maximum operating temperatures

2.4.1 Thermogravimetric analysis (TGA)

TGA monitors how the mass of a sample changes over time, under a controlled temperature regime consisting of linear ramps in temperature under flowing inert gas. This enables any step-wise losses in gas release to be observed and identified.

2.4.2 Differential scanning calorimetry (DSC)

DSC looks at how a materials heat capacity is changed by temperature, enabling the determination of thermal events. A DSC experiment involves placing the sample in an alumina or aluminium pan (both of which have well-defined heat capacities over the required temperature range) which is then placed on a heater. A reference pan made of the same material as the sample pan is located on a second heater and both pans are simultaneously heated or cooled according to a defined temperature regime. Both pans have sensors which measure the heat flow to each pan. During an enthalpic event, more or less heat will be required to maintain the sample pan at the same temperature as the reference pan. By measuring this difference in heat flow, the amount of heat absorbed or released by the sample during these thermal events can be calculated.

During an endothermic transition such as melting, more heat will be required to keep heating the sample at the same rate as the reference pan, leading to a peak being observed in the DSC heat flow trace. For exothermic events such as crystallisation, less heat is required to raise the sample temperature and a trough will be seen in the heat flow trace. Integrating the peak associated with each transition enables the enthalpy of the transition to be calculated.

2.4.3 Simultaneous thermal analysis (STA)

STA combines the concurrent application of TGA and DSC in one experiment. In this thesis, STA analysis was performed on a Netzsch STA 449 F3 Jupiter machine which was additionally coupled to a QMS 403 Aëolos Quadro-Quadrupole Mass Spectrometer. This has a heated capillary inlet system for analysis of the exhaust gas enabling the quantitative detection of volatile decomposition products of thermal analysis and all identified gas components. During the experiment, approx 3 mg of sample was sealed inside 20 μL alumina or aluminium pans in an argon filled glove box. The lid of each pan was pierced as it was loaded into the instrument. A purge flow of nitrogen gas was used during sample loading to protect the sample from moisture in the atmosphere. Once loaded, the sample was then heated under a linear regime to the desired temperature (specified for each individual experiment) at 5 °C/min under 20 sccm nitrogen. Correlating changes in the mass of the sample with the composition of the outlet gas stream and the occurrence of thermal events, STA is a powerful tool to probe reaction mechanisms by enabling the identification of the gaseous species responsible for mass loss.

2.5 Vibrational analysis

These techniques correlate features in the instrumental output with the local environment in the material. Vibrational spectroscopy such as Raman or Infra-red enables valuable data to be collected describing the dynamics of a molecule which is a useful additional tool in structure determination. It is particularly useful as these measurements can be performed rapidly on laboratory scale apparatus.

A molecule can be approximately considered as a simple harmonic oscillator (SHO) obeying Newtons laws of motion and Hookes law, but due to the atomic scale, the quantisation of energy must be taken into account. This leads to a system consisting of equally spaced non-degenerate energy levels and selection rules for allowed transitions (the dipole must change during the vibration). However, molecular bonds are not harmonic oscillators, as a bond is stretched it gets weaker and will eventually break and a finite dissociation energy can be identified for this. To account for this anharmonicity the Morse Oscillator

model is used, to which the SHO is a good approximation at small distances. This means that overtones as well as fundamental transition can be observed in the spectrum as the energy levels are no longer equally spaced and the selection rules have been relaxed.

2.5.1 Raman

When photons of monochromatic light from a laser are shone on a sample, most will be scattered elastically; however a small amount will be scattered inelastically. During inelastic scattering, a photon excites the sample to a higher virtual energy state after which it relaxes into an excited vibrational state. This causes a change in frequency of the inelastically scattered light in relation to the incoming and elastically scattered light which is related to the specific vibrational energy levels of that molecule or structure.

In this work, Raman spectra were recorded using a Bruker Senterra Raman microscope system. Samples for analysis were loaded into 0.7 mm internal diameter (i.d.) borosilicate capillaries and sealed with vacuum grease. The sample was then placed on the microscope stage, aligned and brought into focus using the motorised X-Y stage. Once a grain of the sample was in focus in the correct position, the system doors were locked and the light that had been used for focussing was extinguished. Raman analysis was normally performed using a 532 nm laser, chosen depending on the quality of the signal obtained, and whether any fluorescence was observed. After checking the quality of the signal, the Raman spectrum was recorded using 5 co-additions of 8 second data collections.

2.6 Structural Analysis

Structural analysis through neutron and X-ray diffraction is a key component of the experimental work in this thesis and combined with thermal and vibrational analysis enables a comprehensive understanding of how these materials behave. Diffraction enables the determination and representation of a crystal structure and has many potential uses such as identification and characterisation of materials (e.g. to confirm synthesis), details of bonding and conformation, intermolecular interactions, relative stereo-chemistry, thermal motion and disorder and electron density distributions which can reveal bonding electrons

and lone pairs. It also enables the study of physical phenomena within a sample such as magnetic structure, structural disorder and charge density studies.

2.6.1 Introduction to Crystallography

A crystal is a solid in which the arrangement of atoms exhibits translational periodicity in three dimensions. Lattice points correspond to positions of identical environments up to translations only. The asymmetric unit is the recurring structural motif associated with each lattice point, and is the part of the unit cell volume that defines the contents, as the crystal structure can be considered as a convolution of the lattice and the asymmetric unit. A unit cell is the smallest parallelepiped with lattice points at its vertices that reflects the crystal symmetry. On application of the symmetry operations of the relevant space group, the complete unit cell will be generated from the asymmetric unit. Metric symmetry is the symmetry of the unit cell alone and it does not necessarily follow that the cell contents will have the same apparent symmetry as the unit cell.

There are 32 crystallographic point groups, each of which is a set of symmetry operations (rotations, reflections, inversions) which leaves a central point fixed while moving other directions and faces of the crystal to the positions of features of the same kind. The combined action of 2 symmetry operations must result in a transformation that corresponds to an existing symmetry element of that object but since all rotation axes must pass through the centre of the object there is always at least one point which remains invariant.

There are 7 lattice systems which can be used to tile 3D space (due to restrictions imposed by translational symmetry) and these describe the relationship between the lengths of the unit cell axes (a, b, c) and the angles between them (α, β, γ). These expand to 14 Bravais Lattices as a result of imposing the different types of centring (primitive-, base-, body- or face-centred).

The combination of the symmetry operations of the 32 point groups and the 14 Bravais Lattices leads to 73 different symmorphic space groups (there are points in the cell that have the full symmetry of the point group). The inclusion of translational symmetry elements (screw axes and glide planes) generates a further 157 non-symmorphic space groups, leading to a total of 230 different crystallographic space groups which encompasses all possible

crystal structures. Therefore the number of equivalent points in the unit cell is equal to the number of independent symmetry operations of the space group. Whilst centring, screw axes and glide planes do not directly affect the symmetry of a diffraction pattern, they do affect which reflections are observed as they lead to absences of any diffraction intensity at specific sets of reciprocal lattice points. In a diffraction pattern, all those systematic extinctions/absences can be traced back to the translational symmetry elements that have caused them, providing a very useful method for space group determination.

2.6.2 Introduction to Diffraction

2.6.2.1 Bragg's law

Wave-particle duality means that a beam of moving particles such as neutrons or electrons will have an associated de Broglie wavelength. Crystalline materials act as a diffraction grating for this radiation if it is of appropriate energy. When the wavelength is comparable to the interatomic separations in a crystalline material, the wavefronts will be scattered from parallel planes of atoms.

The scattering by adjacent planes gives interference effects. Figure 2.7 shows for the scattered waves to remain in phase and constructive interference to occur, the path length difference between waves reflected from successive layers of atoms must be an integer number of wavelengths. In this case, the elastically scattered radiation will be coherent, producing Bragg reflections in well-defined directions for which Bragg's law is satisfied by a set of Bragg planes $(h\,k\,l)$.

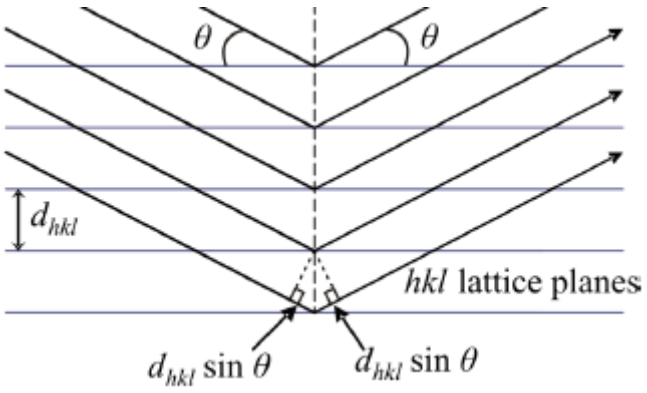


Figure 2.7: Schematic diagram showing the Bragg conditions for diffraction

Bragg's law (Equation 2.2) provides a simplistic model to understand the geometrical conditions that are required for a diffracted beam to be observed. Bragg showed that every diffracted beam produced by an appropriate orientation of a crystal in a radiation beam can be regarded geometrically as if it were a reflection from sets of parallel planes passing through lattice points.

A family of lattice planes is determined by three integers h, k, and l, which are collectively known as the Miller indices and written (hkl). These denote the family of planes orthogonal to $h\mathbf{b}_1 + k\mathbf{b}_2 + l\mathbf{b}_3$, where $\mathbf{b}_i$ are the basis of the reciprocal lattice vectors.

The Bragg condition relates the angle between the incoming beam of radiation with the constructive interference (θ) to the wavelength of the radiation (λ), to give d, the spacing between the planes of atoms in the sample which gives rise to that interference.

In reality, this is a simplified description of what is actually happening as it is 3D scattering not reflection that is occurring; the Bragg description is, however, a useful way of describing the diffraction relationship:

$$\lambda = 2d \sin \theta_{hkl} \tag{2.2}$$

Radiation scattered from each atom in the unit cell contributes to the overall scattering pattern. Since each atom acts a source of scattered radiation, the waves will add constructively or destructively depending on the direction of the diffracted beam and the atomic positions (the amplitude and phase vary continuously).

2.6.2.2 Structure Factors

There are two ways of thinking about structure:

1. Density of matter at a given point in real space $\sigma(\mathbf{r})$ where $\mathbf{r}$ is a position vector xyz
2. Amplitude of a wave of given periodicity $F(\mathbf{Q})$ in reciprocal space where the orientation of the wave vector $\mathbf{Q}$ corresponds to the direction of propagation of the wave.

A diffraction experiment produces a pattern in reciprocal space with a structure factor value $F(\mathbf{Q})$ at each reciprocal point $\mathbf{Q}$, from an object with a real-space density function

$\sigma(\mathbf{r})$. This relationship is described by a Fourier transform as shown in Equation 2.3. A diffraction pattern is the Fourier transform of electron density. The structure factor F_{hkl} sums the result of scattering from all of the atoms in the unit cell to form a diffraction peak from the hkl planes of atoms so every structure factor has contributions from every atom.

$$F(\mathbf{Q}) = \int \sigma(\mathbf{r}) e^{(i\mathbf{Q}.\mathbf{r})} d\mathbf{r} \tag{2.3}$$

The term $e^{(i\mathbf{Q}.\mathbf{r})}$ is a complex number of magnitude 1 whose phase is given by the vector dot product $\mathbf{Q}.\mathbf{r}$ so $\mathbf{Q}.\mathbf{r}$ can be thought of as an angle. Structure factors $F(\mathbf{Q})$ are complex numbers with both a magnitude $|F(\mathbf{Q})|$and a phase $\sigma(\mathbf{r})$. However $|F(\mathbf{Q})|^2$ is a real number with magnitude only.

$$F(\mathbf{Q}) = |F(\mathbf{Q})| \times e^{i\phi} \tag{2.4}$$

During a diffraction experiment, it is the raw intensity $I(\mathbf{Q})$ that is measured which is proportional to the square of the modulus of the structure factor: $I(\mathbf{Q}) \propto |F(\mathbf{Q})|^2$ due to geometrical and instrumental effects. This leads to Friedel's rule which states that $h\,k\,l$ and $\overline{h}\,\overline{k}\,\overline{l}$ reflections are equal i.e $|F(h\,k\,l)|$ is the complex conjugate of $\left|F(\overline{h}\,\overline{k}\,\overline{l})\right|$ making the magnitudes equal and relating the phases as $\phi(h\,k\,l) = -\phi(\overline{h}\,\overline{k}\,\overline{l})$. In the absence of resonant scattering, the diffraction pattern of a crystal is necessarily centrosymmetric irrespective of whether or not the crystal itself has a centre of symmetry. The observed point group of a diffraction pattern is always the centrosymmetric parent of the point group of the crystal and is known as the Laue class, of which there are 11. The Laue class is related to the relevant crystallographic space group through loss of any translational symmetry and addition of inversion symmetry.

Bragg's law is concerned with the geometry of the diffraction pattern, which only contains information about the geometry of the unit cell and its metric symmetry from the positions of the Bragg reflections. The intensity of each reflection is determined by the atomic arrangement within the unit cell and contains information about the continuous electron density throughout the cell. The relative atomic positions affects the electron distribution within the unit cell which through the combination of their individual interactions

with the radiation, generate different amplitudes for different directions of scattering. The intensity of a reflection hkl can be represented as the result of an integration over the continuous periodic electron density in the crystal.

The intensity of the scattering is determined by a number of factors aside from the precise location of the atoms in the structure. Several of these factors are wavelength dependent and are also different for neutron scattering and X-ray diffraction.

- Atomic scattering factor/form factor f_j (quantifies the interaction of the radiation as a function of Bragg angle)
- Character of the powder sample (preferred orientation may be important)
- Primary and secondary extinction (attenuation) $g(F)$
- Absorption
- Atomic displacement parameter (ADP) U_j (probable mean displacement of atoms from their equilibrium positions)
- Multiplicity of the reflection (some reflections or their symmetry equivalent reflections can occur at the same angular value and are useful to reduce both random and systematic errors).

For most materials in this study, the analysis of diffraction patterns was simplified in that the crystal structures for the main species were already known and stored in crystallographic databases, removing the need to solve the crystal structure *ab initio* (which can be both difficult and time consuming for novel materials). The known structures summarised in Table 2.6 were used as starting points for analysis of the experimental data, with the structures then refined against the experimental data using refinement techniques described in Section 2.6.6. However, there were some materials synthesised in this thesis for which no known crystal structure has been reported so attempts to solve these were made with techniques described in Section 2.6.5.

Compound		Space Group	a, b, c (A)	a, b, c ()
Lithium amide	$LiNH_2$	I $\overline{4}$	5.043, 5.043, 10.226	90, 90, 90
Sodium amide	$NaNH_2$	F d d d	8.964, 10.456, 8.073	90, 90, 90
Potassium amide	Monoclinic KNH_2	P 1 2_1/m 1	4.586, 3.904, 6.223	90, 95.8, 90
	Tetragonal KNH_2	P 4/n m m	4.282, 4.282, 6.182	90, 90, 90
	Cubic KNH_2	F m $\overline{3}$ m	6.129, 6.129, 6.129	90, 90, 90
Magnesium amide	$Mg(NH_2)_2$	I 4_1/a c d	10.37, 10.37, 20.15	90, 90, 90
Lithium sodium amide	$Li_3Na(NH_2)_4$	I $\overline{4}$	5.072, 5.072, 11.478	90, 90, 90
	$LiNa_2(NH_2)_3$	P 4_2/m	6.284, 6.284, 11.149	90, 90, 90
Lithium potassium amide	$Li_3K(NH_2)_4$	I 4_1/a m d	7.238, 7.238, 23.956	90, 90, 90
	$LiK_2(NH_2)_3$	P 4_2/m	6.872, 6.872, 11.706	90, 90, 90
Sodium potassium amide	$NaK_2(NH_2)_3$	P 4_2/m	7.004, 7.004, 12.362	90, 90, 90
Potassium magnesium amide	$K_2Mg(NH_2)_4$	P 1 2_1/c 1	7.455, 7.024, 13.545	90, 105.6, 90
Potassium magnesium amide-imide	$KMg(NH_2)(NH)$	P n m a	9.35, 3.66, 9.89	90, 90, 90

Table 2.6: Selected data from the crystal structures of the most commonly studied materials in this thesis

2.6.2.3 Powder Diffraction

In most diffraction experiments (lab/synchrotron, X-ray/neutron) a monochromatic beam of known wavelength is incident on the sample and the scattered radiation is measured as a function of scattering angle (2θ). Single crystal experiments require collection of a full 3D diffraction pattern. Polycrystalline materials (powders) can be considered as millions of small single crystals in random orientations so for any hkl reflection, there will always be a finite number of planes inclined at the correct Bragg angle - all possible diffraction peaks should be observed. The random orientation of these crystallites means the constructive interference emerges as "Debye cones" of intensity from the sample about the axis of the incident beam as shown in Figure 2.8. Each cone corresponds to a single Bragg 2θ angle and will be simultaneously produced for all hkl reflections. A linear 1D diffraction pattern is formed as the detector step-scans through an arc that intersects each Debye cone at a single point, giving the appearance of a discrete diffraction peak. A plot is produced of scat-

tered intensity versus angle with Bragg peaks corresponding to the regions of constructive interference. 2D area detectors cover a range of scattering angles allowing the entire ring of diffraction intensity to be sampled giving higher intensity and providing more information. The intensity of these rings can be integrated to generate the standard powder diffraction pattern.

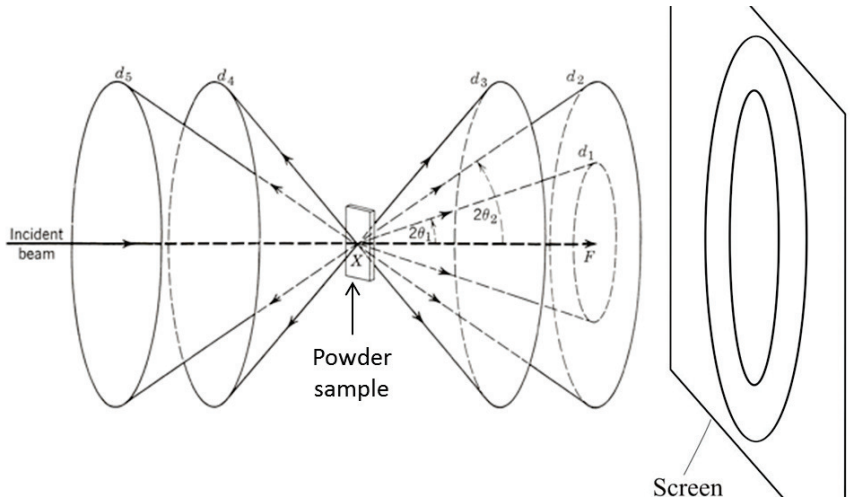


Figure 2.8: Diffraction of Debye X-ray cones from a polycrystalline sample

Often for powder diffraction, ambiguity due to loss of directional information and overlap of individual Bragg reflections (especially for low symmetry cells) makes indexing difficult. Overlap of reflections reduces the number of independent observations and may hide systematic absences, making it difficult to determine the space group. The peak shape, width and hence overlap, is often limited by the quality of the micro-crystalline sample.

The peak positions and intensities from a powder diffraction pattern enable the interplanar d-spacings of the planes of atoms that give rise to this interference to be calculated. In turn, this enables the symmetry of the atoms in the crystal structure to be determined. X-rays are scattered by the electrons surrounding the nuclei so a diffraction experiment produces an electron density map from which the positions of the nuclei can be deduced. Neutrons, however, are scattered by the nuclei themselves so a neutron diffraction experiment gives a direct measurement of nuclear positions.

2.6.3 Neutron Powder Diffraction (NPD)

Most of the diffraction studies reported in this study focus on neutron scattering, which has complementary advantages over X-ray diffraction for the materials examined in this thesis.

1. In X-ray diffraction, radiation is scattered by electrons in orbitals surrounding the nucleus due to their electrostatic interaction with the incident X-rays. The X-ray scattering power of an atom is strongly related to its number of electrons. However in neutron diffraction, the scattering process involves an interaction between the neutron beam and the atomic nucleus and the scattering power is dependent on properties of the nucleus itself. The scattering cross section/length is a measure of how strongly neutrons will be scattered from a given nucleus. There is an almost random variation in the neutron scattering length b with atomic number Z. Neighbouring elements and even different isotopes of the same element can have vastly different neutron scattering lengths and can therefore be easily distinguished by neutron diffraction but not by X-ray diffraction. Figure 2.9 shows both the X-ray and coherent neutron scattering cross-sections. Relative sizes are only accurate within each group; the X-ray and neutron values for a single element are not directly comparable. It should be noted that the neutron scattering lengths for ^{1}H and Li are, in fact, negative which means neutrons are subjected to an attractive Fermi pseudo-potential as they approach the nucleus rather than the repulsive potential experienced for the other elements with a positive neutron scattering length.

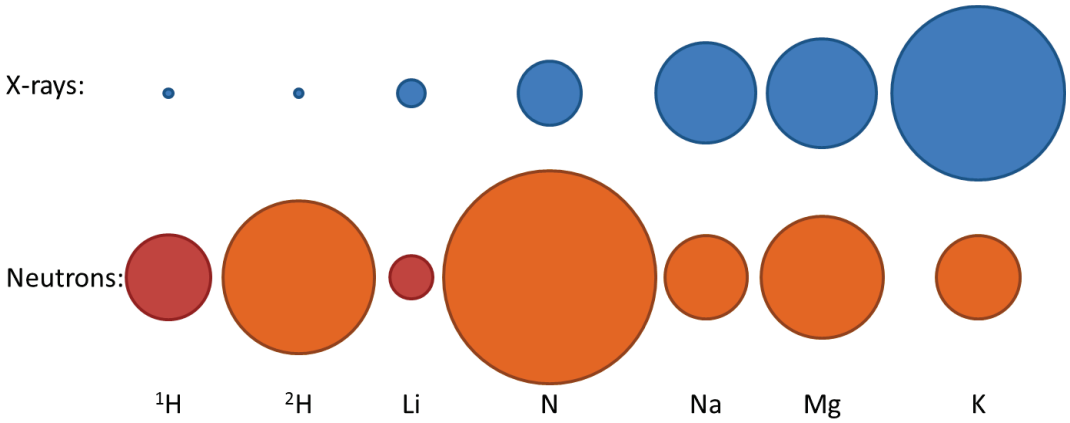


Figure 2.9: X-ray and coherent neutron scattering cross-sections. (The size of the circles are only proportional within a group)

2. NPD is good for locating light elements, particularly deuterium. Whilst it is difficult to observe light elements and almost impossible to see hydrogen using X-rays, hydrogen has a large coherent neutron scattering cross-section so should be easier to observe with neutrons. However, every element has both a coherent (scattered waves from different nuclei of the same atom-type interfere constructively) and an incoherent scattering cross-section (the isotopic order of the sample destroys local order reducing interference between the scattered waves). This latter property has the effect of increasing the background signal of the measurement by causing uniform scattering in all directions meaning incoherent scatterers have to be avoided in neutron diffraction. With neutrons, hydrogen produces significant incoherent scattering so getting usable signal-to-noise ratios for diffraction experiments in its presence can be difficult. However, deuterium has both a smaller incoherent and larger coherent scattering cross section than hydrogen so deuterated analogues have been used for all NPD work presented in this thesis. The effect of this isotopic substitution needs to be considered during the analysis of the results collected. Neutron diffraction therefore enables the ability to accurately locate light elements, especially hydrogen atoms and refine their positions and thermal parameters.

3. The atomic scattering factor shows no angular dependence (NPD does not have a form factor) so useful NPD data and high angle reflections can be collected up to

180 ° as intensity does not drop off as with X-rays (where data can realistically only be collected up to $2\theta < 70$ ° for Cu K_α radiation). The wavelength of the incident neutron beam is several orders of magnitude greater than the size of the nucleus with which it interacts, meaning that radiation scattered from different parts of a nucleus does not have any significant difference in path length. The Debye Waller factor reduces the scattering intensity of the diffraction pattern by the same amount for both X-rays and neutrons but X-rays have the additional form factor fall off to consider aswell.

4. Unlike X-rays, neutrons are weakly interacting uncharged particles and this weak interaction means that neutrons penetrate the sample well, providing a probe of the bulk sample behaviour and allowing more complex sample environments such as cryostats, furnaces and pressure cells to be used.

5. Because of their weak interaction neutrons are a non-destructive probe even for complex and delicate biological or polymeric samples.

2.6.3.1 ISIS neutron and muon facility

All of the neutron scattering experiments reported in this thesis were performed at the ISIS neutron and muon facility at the STFC Rutherford Appleton Laboratory near Oxford in the UK. ISIS is a spallation source and neutron beam production begins with the ion source producing a beam of H^- ions. This is extracted and passed into the Radio Frequency (RF) Quadrupole accelerator which also focuses it. Discrete bunches of H^- ions are then passed into the linear accelerator which uses high intensity RF fields to accelerate them to 70 MeV. The beam passes through a thin sheet of Al_2O_3 foil on entry to the synchrotron which strips the electrons away as the H^- ions pass through it leaving a beam of protons. This is then accelerated by RF electric fields to high energy (≈800 MeV) and the RF system traps the beam into two bunches. 4 in 5 pulse pairs are sent to Target Station 1 (TS1) by kicker and septum magnets and the rest are diverted to Target Station 2 (TS2). When it reaches the target stations the proton beam is travelling at 84% speed of light and is collided with a cylinder of tungsten metal (the target) and neutrons are produced by the spallation process.

The high energy protons violently strike the nuclei of tungsten atoms, destabilising them and causing primary neutrons to be ejected from the nucleus. Each proton collision releases about 15 neutrons from the target so about 2×10^{13} neutrons are produced every second. In Target Station 1, four moderators are used to slow down the high-energy primary neutrons so they have suitable wavelengths for neutron diffraction experiments by dissipating almost all the energy of the neutrons through intermolecular collisions. Two of the moderators use room temperature water, one uses 100 K liquid methane and one uses 20 K liquid hydrogen so that different energy neutron beams can be produced for different applications on each individual beam line.

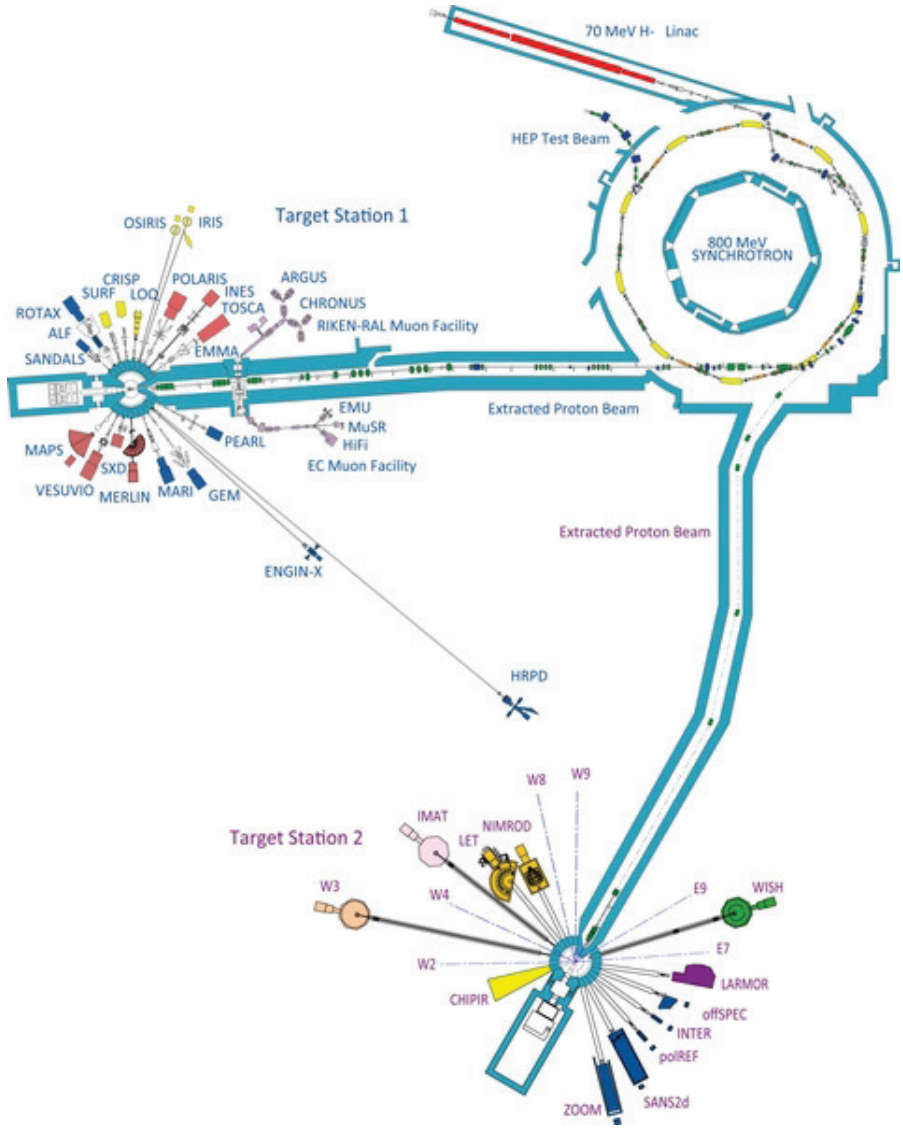


Figure 2.10: Schematic of the ISIS neutron facility. Image credit: STFC

The pulsed neutron flux produced is ideally suited to time-of-flight (t-o-f) diffraction, as the time the neutrons are produced can be known precisely. This technique measures the time-of-flight, t, for a neutron to travel the distance from the moderator, via the sample to the detector, known as the total flight path, L. Because of their different velocities, neutrons with wavelength, λ, arrive at the detector with a time-of-flight, t, given by Equation 2.5a where m is the mass of the neutron and h is Plank's constant. Combining this with the de-Broglie relationship and Bragg's law gives Equation 2.5b which relates the t-o-f to the interplanar d-spacing between lattice planes.

$$t = \frac{mL\lambda}{h} \tag{2.5a}$$

$$t = 505.56\, L\, m\, d\, sin(2\theta) \tag{2.5b}$$

Elastic scattering is assumed, enabling the neutron wavelength to be calculated. The beam therefore does not need to be monochromated and all neutron wavelengths present in the neutron pulse (a white beam) can be used, so the final flux available to scattering experiments is comparable to that produced by a reactor source (such as the ILL in France). Experiments must therefore be conducted at a series of fixed angles and each static detector will collect a different range of neutron energies depending on the angle of the detector. Detectors are arranged in a series of different banks, each with its own characteristic resolution, d-spacing and count rate. Each bank collects all wavelengths and it is the time the neutrons arrive at the stationary detector that is measured. Higher energy neutrons (higher velocity) with a shorter wavelength will arrive at the detectors first.

2.6.3.2 GEM and POLARIS

Two ISIS instruments were used to collect the elastic neutron scattering data presented in this thesis, GEM [117] and POLARIS [263] which have similar setups. GEM was used to investigate the Li-K-N-D and Na-K-N-D systems and POLARIS was used to investigate the K-Mg-N-D and Na-Mg-N-D systems. Figure 2.11 shows the respective sample tanks which are 2-3 m tall and consist of a series of detector banks covering most angles surrounding the sample position in order to detect the highest possible proportion of scattered neutrons.

There is a range of detector banks from very low to very high angles as well as high resolution back-scattering banks. The resolution of the diffraction pattern varies with $\cot\theta$ so improves with increasing angle.

For standard measurements in both instruments, samples were loaded into 8 mm i.d. cylindrical vanadium cans which were sealed with indium wire in the glove box. These were then screwed into a centre stick which was inserted into a Tompkinson flange (the standard flange used for ISIS instrument tanks) which is bolted onto the sample port which can be seen in Figure 2.11. This set-up ensures the sample is held in the path of the beam, 30 cm below the top of the flange. Once this is bolted in place, the sample tank is evacuated so that air scattering does not interfere with the measurements. Each sample measurement taken in a vanadium can lasted $\approx$ 1 hour.

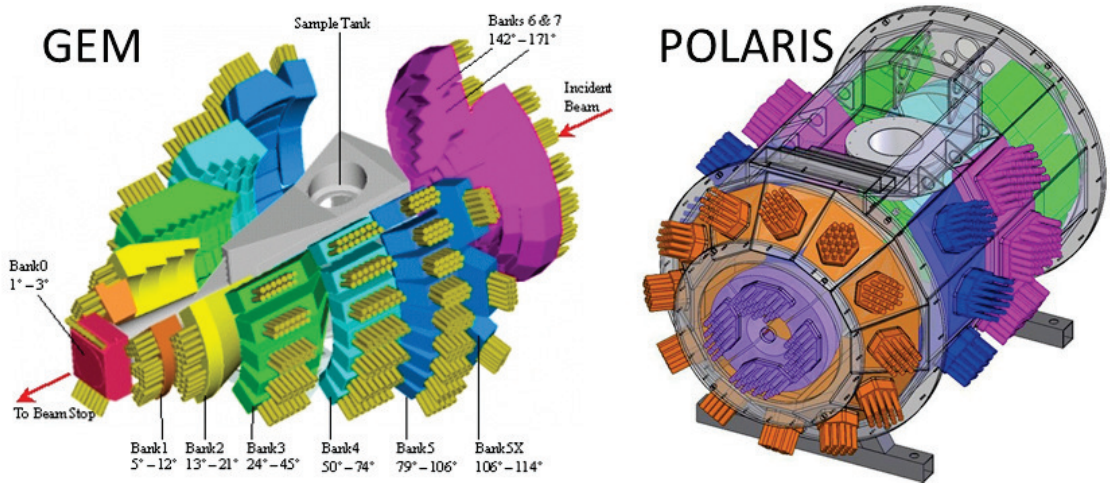


Figure 2.11: GEM [117] and POLARIS diffractometer sample tanks showing the positions of the different banks of neutron detectors. POLARIS image: Credit STFC

Two pieces of specialist equipment, the IGA^n and the *in-situ* sample stick (discussed below) were used on these beamlines in order to collect relevant data. *In-situ* experiments are beneficial as high quality neutron diffraction data showing the structure of the forming and decomposing mixed-metal amides can be correlated with either mass changes as a function of temperature (IGA^n instrument) or ND_3 conversion efficiency under ammonia decomposition conditions (*in-situ* sample stick). *In-situ* measurements are taken in real time and can be interpreted immediately enabling the determination of each structural

transformation during these multi-step processes which in turn helps in the identification of the microstructure, phase composition, and active form of the catalysts under investigation.

2.6.3.3 Intelligent Gravimetric Analysis with Neutron Diffraction (IGA^n)

The IGA^n (Hiden Isochema) is a unique instrument that has been designed specifically for use in neutron scattering experiments at the ISIS facility and can be seen in Figure 2.12. It allows the simultaneous collection of thermogravimetric (variation of the sample mass in response to changes in the pressure and temperature) and neutron diffraction data. This combination enables the connection of crystallographic and mass changes that occur during the experiment, assisting in the characterisation of reaction intermediates.

The balance and reactor components of the IGA^n are fixed to a standard Tomkinson flange which allows for flexible use across the neutron scattering instruments available at ISIS. For sample loading and for experiments not involving the use of neutrons (the IGA^n can also be used off-line as a standard IGA), the flange is bolted onto a custom-designed argon filled glove box as depicted in Figure 2.12. The glove box relies on a constant flow of argon to keep the atmosphere free of water and oxygen, rather than the recirculating purification system used in more advanced glove boxes. The glove box was purged for ≈1 hour prior to sample loading.

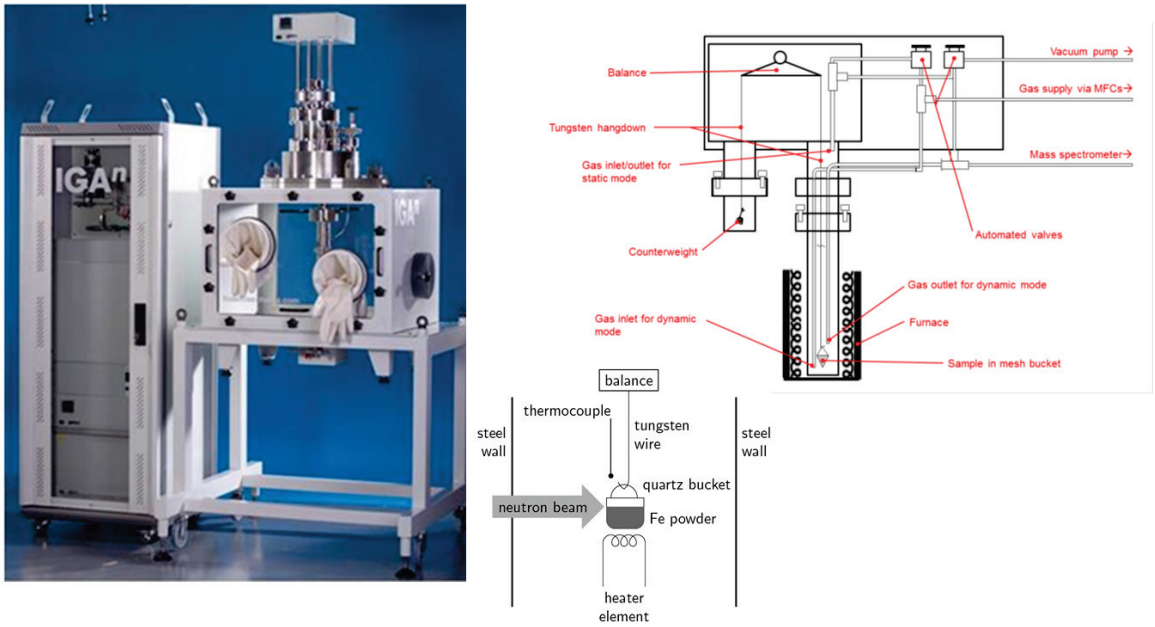


Figure 2.12: The IGA^n apparatus [298] Source: STFC.

Two types of experiment were run on this equipment; synthesis and decomposition. Synthesis experiments were only heated to 200 °C and no gases were expected to be given off, so vanadium buckets (essentially transparent to neutrons) could be used. These were hung on a fine tungsten wire under inert atmosphere and connected to the IGA^n balance by a gold chain which was then zeroed. The sample ($\approx$ 0.5 g) was then loaded into the bucket and re-hung on the tungsten wire. For the synthesis experiments, a quartz tail (which produces no Bragg peaks but cannot be used at high temperatures) could be used to surrounded the sample. The entire set-up was sealed and evacuated of gas (100 mbar/min) and refilled with argon. Two resistive heating elements were located above and below the bucket (positioned to ensure minimum interaction with the neutron beam) and a thermocouple was also positioned above. Constant pressure was maintained by inlet and outlet valves which could open to mitigate changes in local pressure from, for example, release of gas from the sample. The IGA^n was then unbolted from the glove box and craned into the neutron instrument before the neutron beam was switched on and the *in-situ* experiment could begin. An initial 1 hour long scan of the evacuated sample was taken to give a sample diffraction baseline. The sample was then heated at a ramp rate of 1 °C/min to 200 °C where it was held for 3 hours whilst the pressure, temperature, mass and the gases released by mass spectrometry

were recorded simultaneously. It was then cooled at 10 °C/min.

For the decomposition experiments, hydrogen was expected to be produced which causes the decrepitation of vanadium. Therefore the samples were loaded into stainless steel buckets which are unreactive towards alkali metal amides, and sealed with a stainless steel tails (which can operate up to the higher temperatures required but give steel peaks in the diffraction data). These were heated to 400 °C by an otherwise analogous experimental set-up and procedure to that used for the synthesis experiments. During the experiments, diffraction data were collected every 100 seconds (this is the electronic limit) by all the detector banks under a static gas setup.

2.6.3.4 In-situ sample stick

On POLARIS, the *in-situ* sample stick was used to look at ND_3 decomposition ability and is shown in Figure 2.13. A cylindrical stainless steel through-flow cell with an 11 mm internal diameter and 0.35 mm thick walls was filled with 3 g of sample in an argon filled glove box. This set-up enabled maximum exposure of the sample to flowing NH_3 gas. NH_3 flows into the cell via a pipe which extends 14.5 mm down from the top of the cell into the cell volume, and out through a hole in the top of the cell. This minimises the potential for a blockage of the cell. This cell was assembled into the rest of the POLARIS *in-situ* sample stick in an argon filled glove bag as it was too large to fit into the glove box.

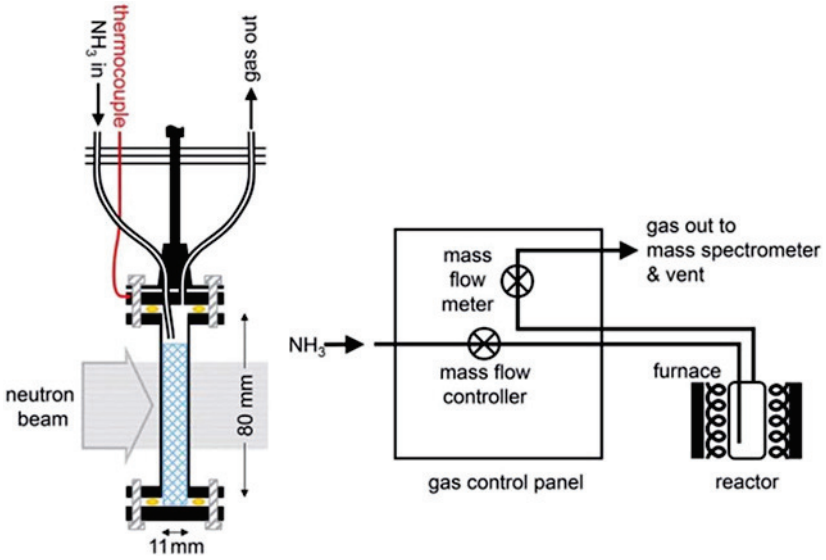


Figure 2.13: *In-situ* sample stick experimental setup [196, 198]

The cell was then encased in a boron-nitride collimation shell, with gadolinium shielding, to remove the diffraction signal of the stainless steel sample cell from the collected diffraction data. Finally the sample cell was attached to the same gas delivery panel used in the *ex-situ* ammonia decomposition experiments described in Section 2.2.1.1 which was equipped with argon and ND_3. The *in-situ* sample stick was placed within the standard furnace housed in the POLARIS sample tank and an initial 1 hour diffraction dataset were collected at room temperature under flowing Ar (20 sccm). Neutron diffraction data was collected in 100 second intervals as the sample was heated under flowing argon before being exposed to ND_3. Outgas composition and ammonia decomposition percentages were calculated as described for the *ex-situ* ammonia decomposition experiments in Section 2.3. Additionally, reference neutron powder diffraction datasets were collected of the as prepared sample (pre-experiment) and the recovered post-experiment sample in 8 mm i.d. vanadium cans over 3 hours each at room temperature.

2.6.4 Powder X-ray Diffraction (PXRD)

X-ray diffraction gives complementary information to neutron diffraction. Neutron parameters fix the nuclear positions and the X-ray data determine the electron density involved in bonding and non-bonding interactions as X-rays are scattered from the electron clouds

around atoms.

2.6.4.1 Advantages of X-ray diffraction

Neutrons are more difficult to produce than X-rays so generally NPD experiments are restricted to central facilities such as ISIS. By contrast, there is a high availability of X-ray diffraction equipment in terms of laboratory based instruments.

The high intensity of X-ray sources can be sacrificed in favour of high resolution so X-ray diffraction is capable of measuring very small structural distortions. This is not possible with medium resolution neutron diffractometers, but can be done on specific specialist machines such as HRPD and WISH at ISIS.

It is difficult to produce a high flux of neutrons, which combined with the fact that neutrons are weakly interacting particles, means that for equivalent signal:noise using neutrons, larger sample sizes need to be used in addition to longer collection times compared to with X-rays.

2.6.4.2 Laboratory X-ray diffraction equipment

Powder X-ray diffraction for the purposes of pre- and post-reaction phase identification and quantification was performed using three laboratory X-ray diffractometers shown in Figure 2.15.

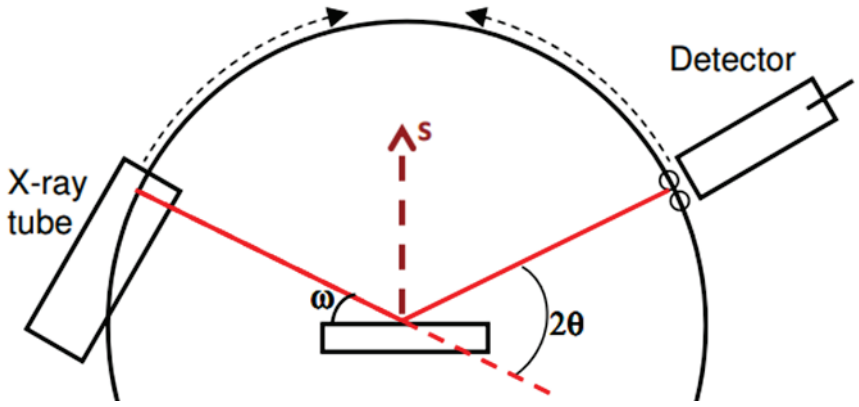


Figure 2.14: X-ray diffractometer geometry

These diffractometers each contain a 45 kV potential difference high voltage tube which is used to accelerate electrons which have been generated by passing a current through a

filament. A copper anode is positioned at the end of the tube and when the electrons impact it, they have sufficient energy to remove core shell electrons from the copper atoms. Electrons from higher energy levels will drop down energy levels to replace them and radiation will be emitted with a wavelength corresponding to the difference in energy levels. The specific Cu $K_{\alpha 1}$ transition with a λ=1.54051 Å is selected using a germanium (111) crystal which acts as a monochromator.



Figure 2.15: Laboratory X-ray diffractometers. Top left: Rigaku SmartLab. Bottom left: PANalytical X'Pert diffractometer. Right: Xenocs Nano-InXider. Image Credits: STFC

Some diffraction patterns were collected on a PANalytical X'Pert diffractometer using Cu K_{α} radiation, produced using a 40 mÅ filament tube. Samples were prepared for measurement by hand-grinding using an agate mortar and pestle. A thin layer of the powder was mounted onto a glass microscope slide using vacuum grease taking care to ensure the powder sample was as flat as possible, and placed inside an airtight sample holder with a polyvinyl acetate window for X-ray transmission. Diffraction patterns were measured in the range of 10-90 ° 2θ, with a step size of 0.008 °, with total measurement times of 1-3 hours.

To use the Rigaku SmartLab, samples were hand-ground in the glove box and loaded

into 0.7mm i.d. borosilicate capillaries which were sealed at the end using vacuum grease. A 2-bounce monochromator and Anton Paar capillary extension stage was used to collect measurements in the 2θ range 4-90°.

The third laboratory X-ray machine used was the Xenocs Nano-InXider (SAXS). Samples were hand-ground in the glove box and loaded into 0.7 mm i.d. borosilicate capillaries which were sealed at the end using vacuum grease. Diffraction data were generally collected using Dectris Pilatus3 hybrid pixel detectors allowing 2θ measurements up to 60 °. This machine features a vertical architecture and a motorised X-Z sample stage allowing 6 preloaded capillaries to be analysed consecutively. It has a low resolution but each scan only takes 1 minute and the machine is readily available and thus it is a very good method for a quick cursory check for pre- and post-reaction phase identification and quantification.

2.6.4.3 X-ray synchrotrons

Synchrotrons, such as the Diamond Light Source, are very powerful tools for X-ray diffraction as the light produced is at least five orders of magnitude more intense than that of the best laboratory instruments. This allows diffraction patterns to be collected much faster and at better resolution. Synchrotron light is electromagnetic radiation covering the whole spectrum that is emitted when a high energy beam of electrons is deflected by a magnetic field.

Bunches of electrons are generated in an electron gun and these are accelerated in a 100 MeV linear accelerator and further accelerated in a 3 GeV booster synchrotron. Variable magnetic fields are used to guide the electrons around a pseudo-circular path so they repeatedly pass through electric field regions until they attain their target energy. The "ring" consists of straight sections joined together by strong magnetic fields which bend the bunch of electrons around the ring. They are then accumulated in a 3 GeV storage ring. These electrons are stored under ultra-high vacuum ($<$1.33 x10^{-13} bar) on a closed loop to minimise collisions between electrons and other particles and electron-electron events which occur in the ring which reduces the flux. Here, their energy is kept constant but acceleration sections are still present as a means to replace energy lost through generation of synchrotron radiation during the bending process. The specific wavelength required for

a given experiment can be selected and tuned to the requirements of the experiment. This minimises the potential for beam damage and excessive absorption of X-rays. The X-rays are emitted tangentially to the electron's circular orbit and are polarised in the direction perpendicular to the magnetic field as it is guided into an experimental hutch (beamline) for e.g. powder X-ray diffraction analysis. The radiation received at an experimental station consists of a series of pulses but with a duration of ≈1 ns so the time averaged intensity of the beam can be considered to be constant.

The beam is extremely intense and well collimated and can be focused to sub-micron spot sizes allowing rapid experiments on small and dilute samples. This leads to more reliable phase quantification with lower detection limits for minor phase components. Whereas from lab X-ray sources the intensity is spread over a relatively divergent beam, synchrotron X-ray beams are nearly parallel giving excellent signal to noise ratios. The beam is plane polarised in the beam orbit and has a pulsed time structure allowing dynamic and kinetic studies of fast chemical and biological processes where diffraction data can be collected in seconds to monitor the course of fairly rapid reactions.

2.6.4.4 Diamond/I11

The I11 beamline at the Diamond Light Source was used to collect data presented in this thesis. I11 has five multi-analyser crystal (MAC) detector banks for high-resolution studies which each consist of nine detectors, preceded by silicon (111) crystals to ensure that only X-rays scattered at precisely the specified angle reach the detector. Diffraction data were collected by scanning the MAC detectors through the 2θ arc around the sample in steps of 0.002 ° in the 2θ range of 0.002-150 °, with a wavelength of 0.81861 Å.

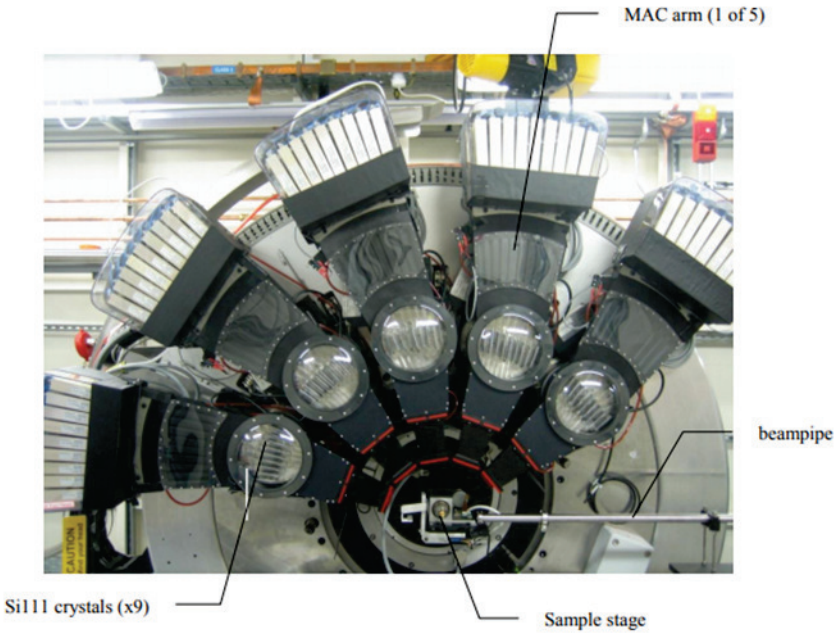


Figure 2.16: Close-up of MAC detector array on I11. Image credit: Diamond

Samples were loaded into 0.7 mm i.d. borosilicate capillaries and flame sealed using a propane torch. This was then mounted onto a brass sample holder and attached to a magnetic base for use with the I11 robot to enable automated measurements. The robot arm sequentially picks up each sample holder and places it on the magnetic mount on the diffractometer. The samples are spun whilst the diffraction data were collected in order to minimise any preferred orientation effects.

2.6.5 Structure prediction and solution

There are a number of materials discussed in this thesis for which structures have not been reported in the literature so efforts were made to predict solutions to these. There are two problems to be overcome in structure determination from powder diffraction data:

1. Experimental and theoretical diffraction can be compared to check if a model is correct but it is not possible to directly transform a diffraction pattern back into electron density or atomic positions. On taking the inverse Fourier transform of $|F(\mathbf{Q})|^2$, the phase of the diffracted X-rays are lost and cannot be measured from the experimental data; they can only be computed from the theoretical model. This "phase problem"

makes it very difficult to reconstruct a real space image. However, there are ways of overcoming the phase problem and understanding the symmetry of the crystalline material can help.

2. With many materials, the degree of reflection overlap in a powder diffraction pattern arises from the fact that the pattern has been essentially collapsed from 3D to 1D and is known as the "reflection overlap problem".

The task of structure solution programs is to determine good estimates of the unobservable phases to give physically reasonable structural models.

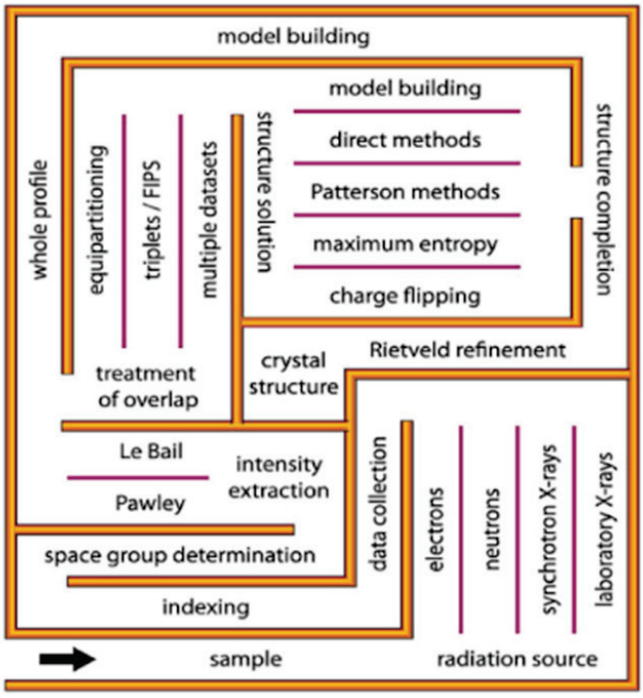


Figure 2.17: Structure determination maze. Image credit: [163]

Figure 2.17 schematically shows the sequence of steps that is required to obtain a crystal structure. The art of structure determination from powder diffraction data lies in selecting the best path through the maze of possibilities [163] from the sample through to the crystal structure. Each step depends on the previous one having been done correctly.

A well crystallised sample must be selected to be analysed with the most appropriate radiation. The collected data pattern is then indexed (with a program such as TOPAS [228])

and systematic absences are examined to determine the most probable space group (DASH was used in this work [73]) and the profile parameters were estimated. The intensities are refined by the Pawley method and the structure solution algorithm most appropriate for the material and the data is chosen and applied. Finally, the partial structural model must be completed and refined.

Pawley analysis is a process in which observed peaks in a powder pattern are fitted without a structural model but at 2θ values constrained by the size and symmetry from the lattice parameters and space group (or at least crystal class) of the inputted unit cell. It is a useful precursor to Rietveld refinement and gives an indication of the best fit possible from an eventual structural refinement. Individual peak intensities are free parameters.

Two structure solution models, charge flipping and simulated annealing which were used in this thesis are described in more detail below.

2.6.5.1 Charge Flipping

Charge flipping uses real-space constraints to iteratively push a random solution towards the correct model. It relies on the fact that electron density is both continuous and never negative. It works by assigning random phases to every reflection and computing the resulting electron density. It flips any charge below a given threshold and computes new phases from the modified density. In this way, it iterates towards a stable solution. Although a relatively new method for determining phases, it relies on a simple algorithm that does not even require identification of "atoms" in the density maps. It is carried out in the $P1$ space group and only once the structure is solved are the unit cell contents scanned for symmetry related features and potential space groups assigned. Therefore it is a good method to use when the determination of symmetry is hard.

2.6.5.2 Simulated annealing

Powder diffraction patterns are often degenerate through peak overlap so it is sometimes difficult to determine the unit cell and the space group. If the connectivity is known, trial structures can be proposed which can be optimised with respect to the observed profile by simulated annealing of the model. This uses a known molecular connectivity and optimises

a set of parameters (translation, rotation and twisting) to find the best fit to the data. If the space group is ambiguous, the alternatives also have to be tried. Simulated annealing works by generating a model and computing an associated cost function. Cost functions can be anything which gets lower as the model improves; packing energy, internal energy, agreement with the measured data, pair distribution function. A random perturbation (placement, orientation, torsion angle) is generated, a new cost function is then computed and the most acceptable model is selected. One of its main features is some "uphill" moves are allowed to avoid local minima and find the global minimum so it is a useful method if the starting model is poor. The "temperature" decreases as the experiment is run so the model is less likely to move uphill and more likely to "lock in" to one minimum. The problems associated with this method can be designing the cost function, generating the perturbations to the model and matching them to the cooling regime.

2.6.5.3 Structure prediction software

Attempts to index peaks were made in:

1. TOPAS [228] (with both charge flipping, simulated annealing and fourier maps)
2. DASH [73] (with a variety of rigid body z-matrices)
3. FOX [97, 98] (which uses parallel tempering)
4. DICVOL [44] (more accurate if there are multiple phases present)

2.6.6 Rietveld Refinement

Once diffraction data have been collected from either neutron or X-ray experiments, it must be analysed in order for useful structural information to be extracted. Finding the best parameter values in crystallographic models is an iterative process and refinement techniques seek to obtain values that are both precise (a good representation of the data) and accurate (an estimate of correctness).

The structural refinements presented throughout this thesis were performed using the Rietveld method [240]. This is one of the most effective methods for refining crystalline

structures and uses a weighted least-squares (LSQ) approach to refine a calculated theoretical line profile y_c until it matches the measured observed profile y_o. It is particularly useful for powder diffraction data as rather than assigning each diffraction peak to several Bragg reflections, the LSQ treatment considers each point in the pattern as an individually observed intensity, allowing for the treatment of overlapping reflections.

The method starts by taking a hypothesised model of either the molecular CIF file from the ICSD database if the structure has previously been reported, or the structure predicted from the charge flipping/simulated annealing process if the structure is as yet unreported. The starting model will include the space group, unit cell, atomic coordinates, thermal and crystallite size and strain parameters. Combined with instrumental parameters such as source, wavelength and peak shapes, this generates a calculated model of the experimental data. Each calculated data point y_c is compared to the observed data y_o and their squared residual is calculated and weighted to reflect the quality of the observation (w_i). This enables a chi-squared function (χ_0^2) to be summed for all observations as shown in Equation 2.6.

$$\chi_0^2 = \sum_i w_i (y_{oi}^2 - y_{ci}^2)^2 \tag{2.6}$$

Parameters are then adjusted to get the best agreement between y_o and y_c and changes which minimise the residual are accepted. LSQ refinements need a good starting model with any positional errors to be less than 0.5 Å. One issue with LSQ refinement is that if the model is inadequate it can still be used to fit the data because the Rietveld method only optimizes parameters rather than alerting problems; it is a structure refinement method not a structure solution method. An additional issue is that LSQ will converge to local minima and will not find the global minima which can lead to false solutions.

Chemical knowledge must be used to ensure molecular connectivity and bond lengths/angles make sense from the suggested parameter values. The covariance matrix should also be checked to see how strongly the uncertainties are correlated. The uncertainties in one parameter might be correlated with the uncertainties in others, leading to a large square weight matrix. Some parameters are more sensitive to uncertainties than others so care

must be taken in the choice of which and how many parameters to vary in each cycle; for example displacement parameters are very sensitive to errors in atomic position. It is therefore necessary to exercise caution in the refinement of atomic thermal parameters (which model a smearing of the scattering density) and lattice site occupancies (which assume that the electron density is concentrated at the atomic site), in order to ensure that correlation does not influence the refined values of these parameters. The form factor, f_j, occupancy, occ_j, and thermal parameters, U_j, are often strongly dependent on each other. f_j is fixed so reducing occ_j lowers the scattering density at the site of atom j, but increasing U_j lowers the scattering density at the site of atom j (more smeared out). For a given $F(h\,k\,l)$, there can be a wide range of occ_j and U_j which give similar values in the structure factor equation so a spread of reflections are required to distinguish the effects. The correlation becomes more resolvable with high quality, high-angle reflections.

Normally, the lattice parameters of the proposed structure, the background (modelled by a high-order polynomial expression), the zero error correction and scale factor (determines the magnitude of the diffraction peaks) are allowed to vary first. Then sequentially, the size and strain, thermal parameters and, if need be, atomic positions are varied until a suitable structural model is obtained. For X-ray diffraction, heavy atoms can be refined first and then lighter elements such as hydrogen only added in at the end which may help in some cases, but it is different for neutron diffraction. LSQ cannot indicate missing parameters but may reveal surplus parameters.

To aid a Rietveld refinement, supplementary information can be included that is either constrained and totally enforced, or restrained and only tentatively introduced. The most commonly used restraints relate the atomic coordinates to some geometric parameter (distances, angles, planarity) or to satisfy some physical law (Hirshfeld Rigid Bond Condition on ADPs [127]). The equations of restraints are set up in the same way as the structure factor equations and are added on to the minimisation function with suitable weights.

χ_0^2 enables statistical R value parameters to be calculated. A weighted profile R value (R_{wp}) calculated from the data is compared to an expected R value (R_{exp}) calculated from the model. The refinement continues in an iterative manner until the R_{wp} converges, ideally on a value close to R_{exp}. The deviation between these R values is expressed in

terms of their ratio R_{wp}/R_{exp} and is referred to as the "goodness of fit". A difference plot showing the absolute intensity difference between the observed and calculated patterns is often included when analysing diffraction data as a visual aid, as the final difference map should be featureless. For multiphase mixtures, the various scale factors can be converted into a percentage composition, which is useful for watching phase changes as the reaction progress and determining sample purity.

For diffraction data collected on GEM, banks 3, 4 and 5 were generally used and for diffraction data on POLARIS banks 3 and 4 were used for refinements. For relevant neutron diffraction datasets steel peaks were fitted by Pawley analysis [226] using two $Fm\bar{3}m$ phases, with slightly different lattice constants, corresponding to the reactor walls at neutron beam entry and exit points. Small peaks pertaining to the thermocouple were fitted to an $Im\bar{3}m$ NiCr alloy phase. A previously collected silicon pattern was used as a scalable background to fit the scattering from the quartz bucket in conjunction with a Chebyschev polynomial function.

2.6.6.1 Refinement Software

Rietveld refinements carried out in this thesis were done using the TOPAS program [63]. The program uses a LSQ approach with additional minimisation methods included [62, 201]. The theoretical diffraction pattern is generated in the TOPAS program, which then performs the optimisation routine. The program is very flexible and the user is free to define their own peak shape functions and variables as required. This allows physical models for peak shapes to be generated based on the particular experimental setup. For example, the neutron diffraction data are modelled using a custom-defined peak shape for the ISIS neutron source, developed by David [30] and based upon the peak shapes proposed by Ikeda and Carpenter [289]. Multiple refinements can be undertaken sequentially in a batch refinement, where data from multiple different detector banks can all be used to refine a structural model.

2.6.6.2 Batch Refinements

A particularly useful feature of TOPAS is the ability to run batch refinements. A refinement is carried out on an initial, carefully manually refined n^{th} data set and a script is generated which uses this refinement as the starting point for the refinement of the next $(n+1)^{th}$ data set as they are likely to closely resemble each other. This process is automatically repeated sequentially for all the data sets of interest. All of the allowed parameters for all of the phases included in the seed file are refined simultaneously, which means that the refined parameters obtained from batch analysis may not be as reliable as those obtained from the refinement of individual data sets. The initial seed dataset is normally collected over a much longer time period than subsequent runs in order for an accurate and precise model to be obtained as a good starting point for the batch process. The batch process can be run in both the forward and reverse directions.

Parameters of interest are output at the end of each individual refinement allowing for easy extraction of refined physical parameters such as weight percent or cell parameters in order to monitor crystallographic changes occurring within the sample throughout the data collection. The batch approach works best when only small changes occur between the data sets. In order to prevent unrealistic features being incorporated into the batch refinement process, the physical parameters of each phase are carefully constrained. For a reaction at constant temperature, the lattice parameters, crystallite size and strain parameters and isotropic thermal parameters for each phase are generally held constant, while the scale factors are allowed to vary.

Chapter 3

Mixed Lithium-Sodium system

Contents

3.1 Chapter overview 120

3.2 Background 120

3.2.1 Crystallography 123

3.2.2 Synthesis 124

3.2.3 Raman 125

3.3 Thermal decomposition behaviour 126

3.3.1 Constituent single metal amides 126

3.3.1.1 $LiNH_2$ 127

3.3.1.2 $NaNH_2$ 129

3.3.2 Mixed-metal amides 131

3.3.2.1 $Li_3Na(NH_2)_4$ and $3LiNH_2 + NaNH_2$ 131

3.3.2.2 $LiNa_2(NH_2)_3$ and $LiNH_2 + 2NaNH_2$ 139

3.4 Inert gas summary 145

3.5 Ammonia decomposition 148

3.5.1 Quantitative fitting and analysis 152

3.5.2 Catalyst recovery 155

3.6 Decomposition under ammonia 157

3.7 Summary 159

3.1 Chapter overview

This chapter presents a synthetic, thermogravimetric and catalytic study of $Li_3Na(NH_2)_4$ and $LiNa_2(NH_2)_3$. Presented first is an in-depth study of the decomposition behaviour of high-purity samples of $Li_3Na(NH_2)_4$ and $LiNa_2(NH_2)_3$. An analysis of their decomposition under inert gas is used as a basis for understanding what the systems may go on to do as NH_3 decomposition catalysts. Potential mechanisms are discussed and the catalytic activity of these materials for NH_3 decomposition is investigated.

3.2 Background

Mixed-metal systems are a promising route to tailoring the activity and active form of catalysts for NH_3 decomposition. The Li-Na-N-H system was investigated, building on the successes of $LiNH_2$ and $Li_2Ca(NH)_2$ as the best amide/imide NH_3 decomposition catalysts to date. Three mixed lithium sodium amides have been reported, $Li_3Na(NH_2)_4$, $LiNa_2(NH_2)_3$ and $Li_5Na(NH_2)_6$ [147].

The Li-Na-N-H system was chosen based on the close crystallographic similarity of $Li_3Na(NH_2)_4$ to $LiNH_2$, where one quarter of the Li^+ ions have been replaced by Na^+ ions (Figure 3.1). The similarity in the ionic radii of Ca^{2+} and Na^+ (6-coordinate radii of 1.00 Å and 1.02 Å respectively) means that $Li_3Na(NH_2)_4$ has a similar layered structure to that seen for $Li_2Ca(NH)_2$. Although the Li-Ca-N-H system forms a mixed-metal imide ($Li_2Ca(NH)_2$), the Li-Na-N-H system displays interesting thermogravimetric behaviour, as it appears unable to form a mixed-metal imide and only amides are known.

$Li_3Na(NH_2)_4$ and $LiNa_2(NH_2)_3$ have been previously studied in the context of solid-state H_2 storage due to their H_2 gravimetric densities of 7.5 and 6.0 weight percent respectively [189] but little is known about their behaviour during thermal decomposition and their potential activity as NH_3 decomposition catalysts. The Li–Na–N–H system has been disregarded for hydrogen storage applications as a bi-metallic lithium-sodium nitride or imide is not observed during the thermal decomposition, and the formation of nitrides or imides is required in order to obtain a reversible hydrogen storage system based on metal amides. The Li–Na–N–H system is therefore considered non-reversible in this regard.

Table 3.1 details the key thermodynamic properties of $LiNH_2$, $NaNH_2$, $Li_3Na(NH_2)_4$ and $LiNa_2(NH_2)_3$ which are the components of the Li-Na-N-H system. The significance of these are discussed throughout the chapter but they are collated here as a reference guide.

			Melting	**Onset of decomposition**
$LiNH_2$			375 °C	347 °C
$NaNH_2$			210 °C	420 °C
	Synthesis	**Separation**	**Full sample melt**	**Onset of decomposition**
$Li_3Na(NH_2)_4$	185 °C	199 °C	234 °C	296 °C
$LiNa_2(NH_2)_3$	187 °C	201 °C	204 °C	285 °C

Table 3.1: Key thermodynamic temperatures (± 1 °C) of the single metal amides and mixed-metal amide components of the Li-Na-N-H system

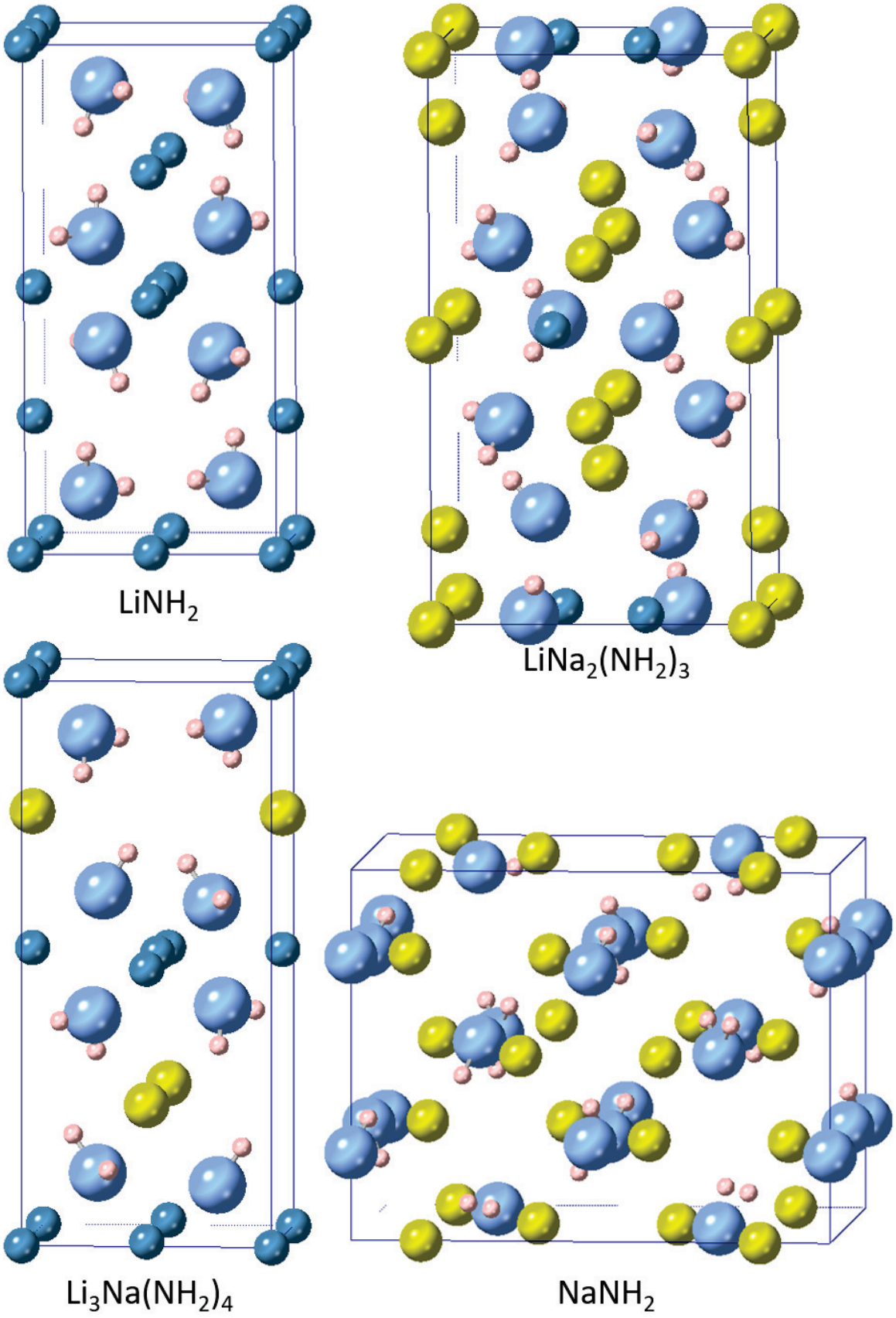


Figure 3.1: Crystallographic unit cells for $LiNH_2$, $Li_3Na(NH_2)_4$, $LiNa_2(NH_2)_3$ and $NaNH_2$, roughly proportional in size. Teal = Lithium, Yellow = Sodium, Blue = Nitrogen, Pink = Hydrogen

3.2.1 Crystallography

A small amount of Na is soluble in $LiNH_2$, forming non-stoichiometric amides of general formula $Li_{4-y}Na_y(NH_2)_4$ $(0<y<1)$ via Li-Na exchange at a quarter of the lattice sites which leads to unit cell expansion along the c axis (and small concomitant a and b axis expansion). Three tetrahedral coordination environments exist for the Li^+ ions in $LiNH_2$, and substitution of a large Na^+ ion for a smaller Li^+ ion will be most favourable (and only occurs) at the largest 2c (0, $\frac{1}{2}$, $\frac{1}{4}$) lattice site of $LiNH_2$ to form $Li_3Na(NH_2)_4$. Sodium is not observed at any of the other lattice sites, indicating that materials of composition $Li_{3-x}Na_{1+x}(NH_2)_4$ (with $x>0$) cannot be formed. $Li_3Na(NH_2)_4$ is therefore the end member of the $Li_{4-y}Na_y(NH_2)_4$ series and can be considered an ordered variant of $LiNH_2$ (both tetragonal in the $I\bar{4}$ space group) as seen in Figure 3.1.

Both $LiNH_2$ and $Li_3Na(NH_2)_4$ are layered materials based on an almost ideal cubic close packed (ccp) anti-fluorite structure and can be considered as a series of $LiNH_2$ blocks separated by layers of Na^+ cations. High 2D mobility of Li^+ and Na^+ (both tetrahedrally coordinated) between the ccp NH_2^- leads to considerable non-stoichiometry in $Li_{4-y}Na_y(NH_2)_4$ due to facile Li^+/Na^+ ion interchange at the large 2c lattice sites, similar to that seen in $LiNH_2$ [194]. This is evident from 2θ dependent asymmetry observed in the Bragg reflections of the diffraction profiles, characteristic of compositional non-stoichiometry [189]. Such mobility for Li^+ cations has been observed before in amides and imides [70] and is a common phenomenon for lithium-containing fluorite and anti-fluorite structures at temperatures approaching 80% of their melting point [18, 268].

By contrast, in $LiNa_2(NH_2)_3$ ($P4_2/m$ space group) $\frac{3}{4}$ of the Na^+ cations display octahedral coordination which is less stable and higher energy compared to the tetrahedral coordination (shown by recent theoretical studies of high-pressure polymorphs of $NaNH_2$ [318]). $\frac{1}{4}$ of the Na^+ cations display tetrahedral coordination and are all situated in environments too large for Li^+ cations. The Li^+ cations are tetrahedrally coordinated by NH_2^- ions in environments too small for Na^+ cations. This distinct difference between cation coordination environments combined with the presence of a screw axis (indicating the anion array in $LiNa_2(NH_2)_3$ is substantially distorted from an ideal cubic close packed structure)

prevents a clear cation migration pathway and means cross occupation of the metal sites in $LiNa_2(NH_2)_3$ is not possible. Ionic mobility is therefore suppressed and would lead to decomposition rather than non-stoichiometry, meaning $LiNa_2(NH_2)_3$ only exists as a pure, single and fully stoichiometric line phase. No asymmetry was observed in the Bragg reflections of $LiNa_2(NH_2)_3$ or $NaNH_2$.

$Li_5Na(NH_2)_6$ is the next member of the hypothetical family of phases of general formula $Li_nNa(NH_2)_{n+1}$ for n = 3–15 (and beyond) where the Na^+ layers are separated by ever larger lithium-containing blocks ($I\overline{4}$ space group). In the literature $Li_5Na(NH_2)_6$ has been reportedly formed during the reaction of lithium and sodium metals with supercritical ammonia but its structure has not yet been confirmed by single-crystal diffraction so the atomic arrangement remains hypothetical [147]. However, no $Li_5Na(NH_2)_6$ was observed to have been synthesised by the methods detailed in Table A.1 in the Appendix despite multiple attempts, implying that this material is unlikely to be formed from solid-state synthesis reaction conditions.

3.2.2 Synthesis

A variety of solid state methods for the synthesis of $Li_3Na(NH_2)_4$ and $LiNa_2(NH_2)_3$ were explored in order to find the optimum conditions. These are explained more fully in Section 2.2.4.1 and the experimental parameters and the phase compositions from Rietveld analysis of the data are presented in Table A.1.

The ball-mill presented the quickest and easiest method to synthesise high purity $Li_3Na(NH_2)_4$ and $LiNa_2(NH_2)_3$, but this method was only discovered retrospectively after the Li-K-N-H system had been investigated (Section 4.2.2). The samples of $Li_3Na(NH_2)_4$ and $LiNa_2(NH_2)_3$ used for the analysis of their behaviour and decomposition properties as presented in this chapter, were therefore synthesised in the tube furnace.

3.2.3 Raman

In addition to structural studies, the bonding in $Li_3Na(NH_2)_4$ and $LiNa_2(NH_2)_3$ was probed by Raman spectroscopy collected as outlined in Section 2.5.1. The N−H stretching region for each of the phases is shown in Figure 3.2 along with those of $LiNH_2$ and $NaNH_2$ for reference. The only well resolved vibrational modes in the spectra of all four compounds were the symmetric and anti-symmetric stretching modes of the NH_2^- anion.

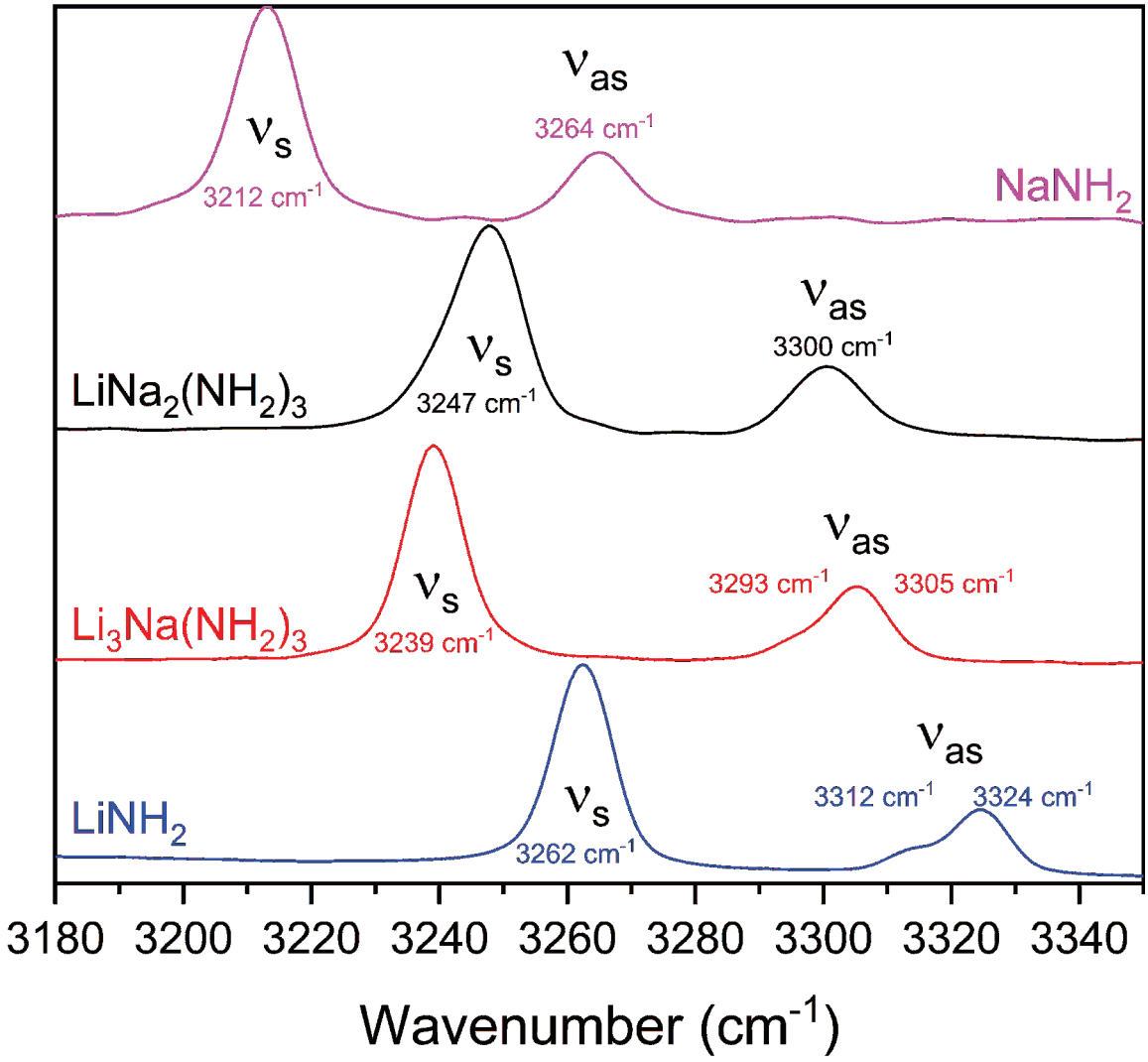


Figure 3.2: Raman stretches for the Li-Na-N-H system

Lithium amide shows characteristic vibrations for an NH_2^- unit where the large peak at 3262 cm^{-1} is the symmetric N−H stretch band, while the two smaller peaks at 3312 and 3324 cm^{-1} are the asymmetric N−H stretches [194]. The NH_2^- stretching modes of $LiNH_2$

are located at a higher energy than those of $NaNH_2$ reflecting a stronger N−H bond, due to inductive effects arising from the different electronegativities of Li^+ and Na^+ (Pauling electronegativities of 0.98 and 0.93 respectively) [41]. The experimental values collected for $NaNH_2$ of 3212 cm^{-1} and 3264 cm^{-1} are in good agreement with the literature values of 3218 cm^{-1} and 3267 cm^{-1} [64].

There was also a small shoulder observed on the asymmetric stretch of $LiNH_2$ (which is absent from that of $NaNH_2$) which is due to slight variations in the chemical environments of identical atoms. This shoulder is also visible in the anti-symmetric stretch of $Li_3Na(NH_2)_4$. In $LiNH_2$ and $Li_3Na(NH_2)_4$, the environments of the two H atoms of the NH_2^- units are slightly different, due to the orientation of the two N−H bonds with respect with respect to the Li^+ and/or Na^+ ions in the cationic sub-lattice.

Given that the amide units in both $Li_3Na(NH_2)_4$ and $LiNa_2(NH_2)_3$ coordinate both Li^+ and Na^+ ions, it is anticipated, as is observed, that the energies of the Raman modes for these materials lie in-between those of the two parent compounds. There are two N−H stretches observed for $Li_3Na(NH_2)_4$ at 3293/3305 cm^{-1} and 3239 cm^{-1} which are in agreement with the literature [59]. There is no shoulder observed on the asymmetric stretch of $LiNa_2(NH_2)_3$ at 3300 cm^{-1} suggesting that the orientation of the N−H bonds in $LiNa_2(NH_2)_3$ is such that their chemical environments in the structure are identical.

3.3 Thermal decomposition behaviour

3.3.1 Constituent single metal amides

In order to evaluate the decomposition properties of the mixed-metal amides, it was first necessary to study the behaviour of $NaNH_2$ and $LiNH_2$ alone (Figure 3.3 and Figure 3.4).

Low temperature thermal decomposition behaviour was studied by Simultaneous Thermal Analysis (STA) as this equipment is limited in its experimental temperature range and could only collect up to 400 °C because these materials have low melting points.

Complementary high temperature thermal decomposition behaviour was investigated on the gas flow panel under argon in order to obtain a comprehensive understanding of the whole decomposition process.

3.3.1.1 $LiNH_2$

$LiNH_2$ was heated to 400 °C as STA data (DSC and TGA data) were collected. MS analysis of the outlet gas flow was also collected when a sample of $LiNH_2$ was heated to 700 °C on the gas flow panel. The data from these two experiments have been aligned and presented in Figure 3.3.

The TGA data show a total mass loss of 32.02 %, compared with an expected mass loss of 37.07 % (for amide to imide decomposition with loss of NH_3). The difference is most likely attributable to the oxidation of a small portion of the sample to Li_2O.

The DSC data show a sharp endotherm at 373 °C which corresponds to $LiNH_2$ melting and is in good agreement with the reported melting point of 375 °C. The underlying broad endothermic peak from 315 °C to 400 °C corresponds to the decomposition of $LiNH_2$ to Li_2NH. This is supported by the MS data which shows that ammonia was released during decomposition (peak at 347 °C), as would be expected. The nitrogen and hydrogen emitted between 350 °C and 500 °C are in a 3:1 ratio and peak at 436 °C showing that ammonia has been decomposed into its constituent gases.

It can be seen that the decomposition of lithium amide starts before its melting point, implying that the solid-state behaviour of lithium amide is important. The fact that $LiNH_2$ melts at an early stage in the decomposition process makes analysis more difficult.

The MS data from the gas flow panel shows a second decomposition step from 600 °C with equal amounts of N_2 and H_2 observed and no NH_3 recorded. This is likely to correspond to the decomposition of the previously-formed Li_2NH to form lithium nitride hydride (rather than lithium nitride) (Equations 3.1) [316].

$$LiNH_2 \longrightarrow Li_2NH + NH_3 \tag{3.1a}$$

$$Li_2NH \longrightarrow \frac{1}{2}Li_4NH + \frac{1}{2}N_2 + \frac{1}{2}H_2 \tag{3.1b}$$

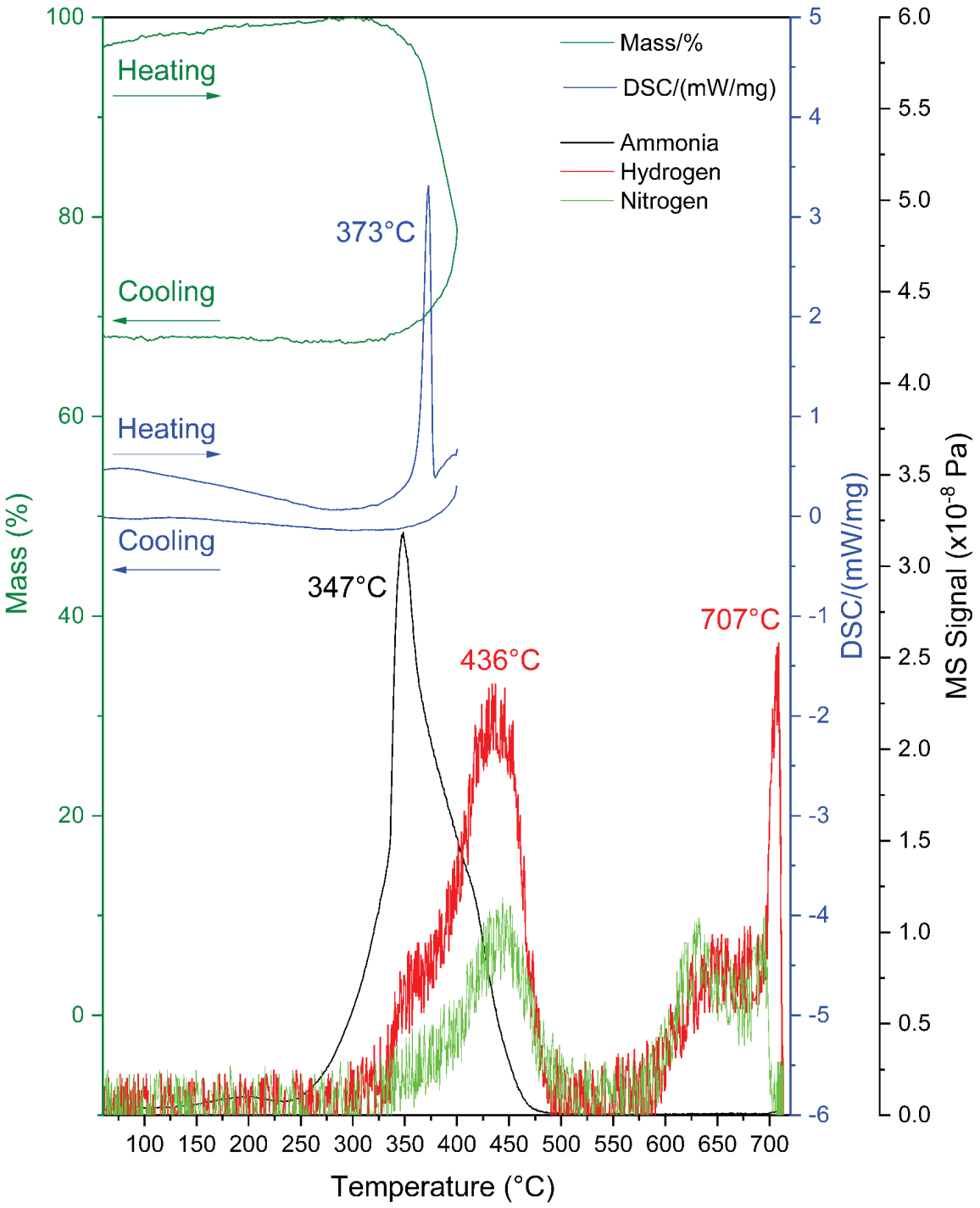


Figure 3.3: DSC trace and mass loss (TGA) alongside MS analysis (gas flow panel) collected during the decomposition of $LiNH_2$ under argon

3.3.1.2 $NaNH_2$

As an individual amide, $NaNH_2$ decomposes via a different mechanism to $LiNH_2$ in that no stable sodium imide can form (so no variable stoichiometry is detected) and no ammonia is released (Equation 3.2). Sodium amide decomposes on heating into its constituent elements: sodium, nitrogen gas and hydrogen gas [276]. The fact that two gases are formed during decomposition results in an unusually large entropy change, $\Delta S = 200.9\,J\,K^{-1}\,mol^{-1}$ which leads to a modest theoretical decomposition temperature of 343 °C to satisfy the Gibbs free energy [71].

$$NaNH_2 \longrightarrow Na + \frac{1}{2}N_2 + H_2 \tag{3.2}$$

Figure 3.4 shows the DSC data collected when $NaNH_2$ was heated to 400 °C during an STA experiment and the MS data collected when a sample of $NaNH_2$ was heated to 550 °C on the gas flow panel. The DSC trace shows that $NaNH_2$ melts at 195 °C which is in good agreement with the reported melting point value 210 °C [107]. This is accompanied by the complementary exotherm at 170 °C on cooling which shows $NaNH_2$ re-crystallising. There was no mass loss shown in the associated TGA for this experiment because $NaNH_2$ is stable above its melting point and is known to decompose between 400 °C and 500 °C, above the peak temperature of 400 °C reached in this STA experiment. Whilst $NaNH_2$ is volatile and often suffers from poor mass recovery, the experimental pan set-up of the TGA means that material loss is limited during this experiment.

The MS gas outlet trace from the gas flow panel shown in Figure 3.4 shows a low temperature N_2 release centred at 161 °C which correlates with the thermal event in the DSC trace with an onset temperature of 145 °C. Since the total decomposition of the amide is observed at higher temperatures, there is no obvious process which would result in the loss of N_2 from $NaNH_2$. Therefore it is proposed that the nitrogen evolution observed at lower temperatures is the release of occluded nitrogen remnant from the commercial synthesis of the sodium amide. This analysis is supported by the fact that when sodium amide is decomposed, reformed *in-situ* under ammonia with no nitrogen gas present, and

then heated again, it does not show this nitrogen release feature. Sodium metal is the only product observed at the end of this reaction.

It can be seen that the decomposition of sodium amide to nitrogen and hydrogen occurs from 440 °C and there is both H_2 and N_2 release in a 2:1 ratio peaking at 539 °C. This ratio is consistent with that expected for $NaNH_2$ decomposition to Na (Equation 3.2).

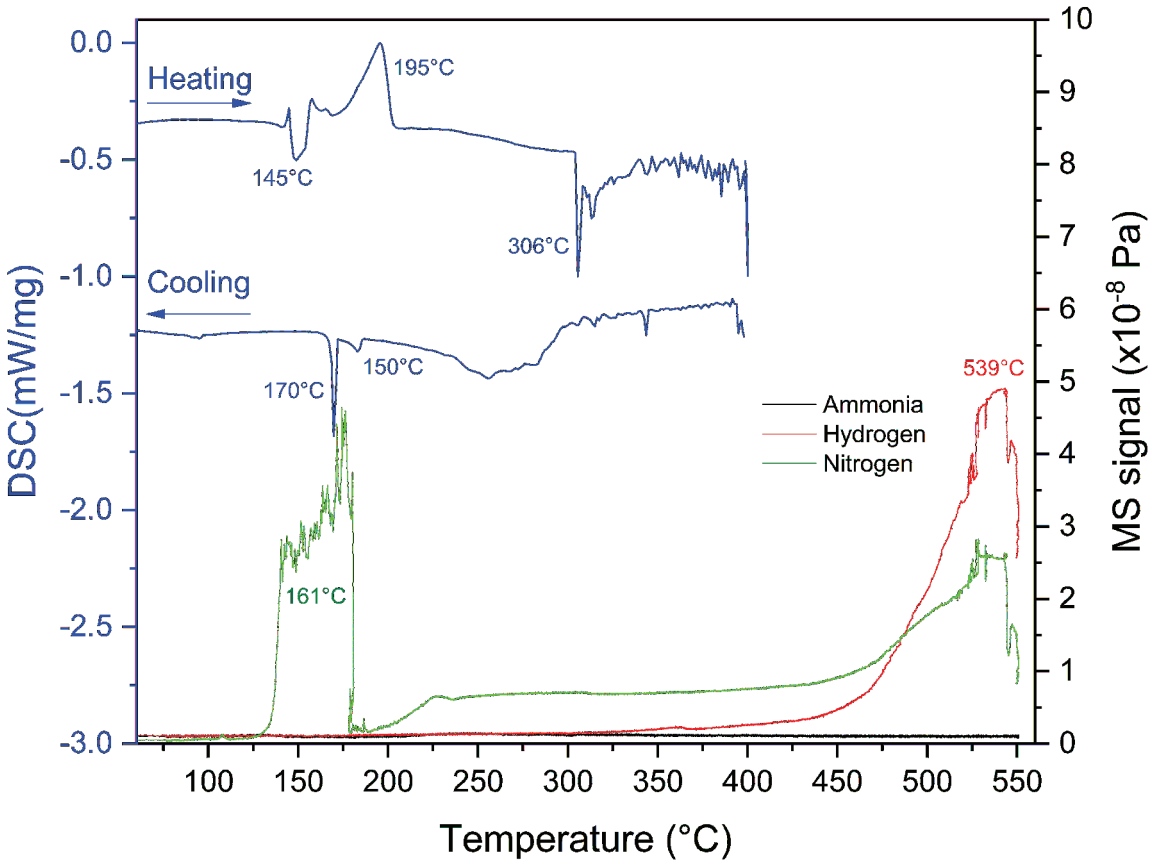


Figure 3.4: DSC trace (STA) and MS analysis (gas flow panel) collected during the decomposition of $NaNH_2$ under argon

3.3.2 Mixed-metal amides

Having found a successful method for the high purity synthesis of $Li_3Na(NH_2)_4$ and $LiNa_2(NH_2)_3$, the first step to further understanding their decomposition reactions and understanding how they behave was to analyse their activity under inert gas. Whereas $LiNH_2$ alone decomposes to the imide under inert gas, $NaNH_2$ decomposes to Na metal. It will therefore be important to ascertain the decomposition pathways for the mixed-metal amides when both these amides present.

In order to probe the inert gas synthesis and decomposition of the mixed-metal amides, the low temperature behaviour was investigated by STA which is particularly important for understanding the behaviour of these systems in relation to the melt phase. Complementary high temperature behaviour was investigated on the gas flow panel under argon in order to obtain a detailed understanding of the whole decomposition process.

3.3.2.1 $Li_3Na(NH_2)_4$ and $3LiNH_2 + NaNH_2$

DSC traces were observed for both pre-made $Li_3Na(NH_2)_4$ (black) and a hand-ground mixture of $3LiNH_2 + NaNH_2$ (blue) and are shown in Figure 3.5. The mass trace (green) comes from an analogous IGA experiment looking at the decomposition of pre-made $Li_3Na(NH_2)_4$.

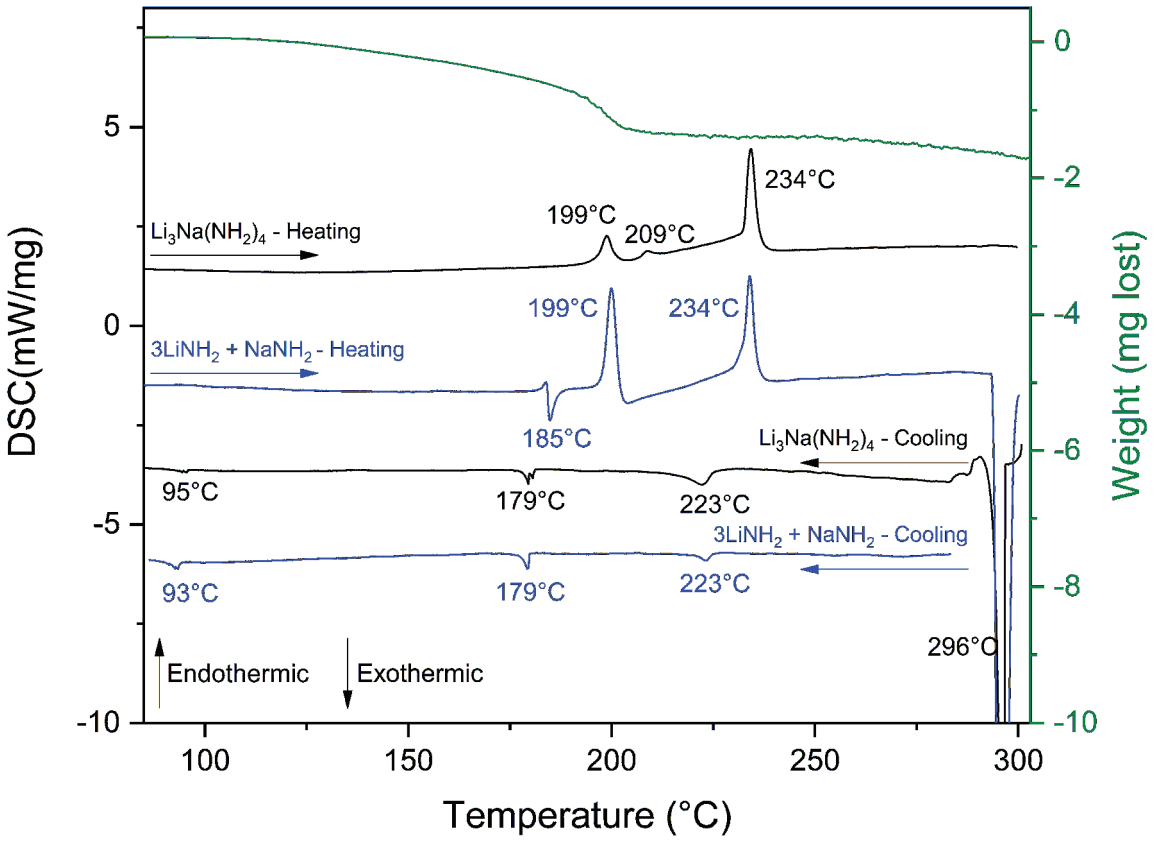


Figure 3.5: STA traces for $Li_3Na(NH_2)_4$ and $3LiNH_2 + NaNH_2$ (black and blue) and mass trace (green) from the IGA.

Comparison of the differences between these two traces suggests the synthesis of $Li_3Na(NH_2)_4$ corresponds to the exothermic event at 185 °C as from this point onwards the two traces should be, and are, identical.

It has been suggested that prior to the melting of $Li_3Na(NH_2)_4$, $NaNH_2$ is released forming non-stoichiometric $Li_3Na_{(1-x)}(NH_2)_{(4-x)}$ before partial separation into its constituent single amide components $LiNH_2$ and $NaNH_2$, as bi-metallic lithium-sodium imide is not observed after decomposition [154].

Both traces show two endothermic events at 199 °C and 234 °C on heating. It is likely that the first event at 199 °C is a separation endotherm and corresponds to the melting of the $NaNH_2$ component forming non-stoichiometric $Li_3Na_{(1-x)}(NH_2)_{(4-x)}$. This correlates well with the melting point of $NaNH_2$ seen in Figure 3.4 of 195 °C. The peaks at 199 °C occur alongside a small mass loss (0.5 mg) so it is likely that a small amount of physisorbed gases are desorbed from the powdered sample as the structure falls apart.

The second endotherm at 234 °C is the melting of the whole sample as the $LiNH_2$ dissolves into the liquid $NaNH_2$ and the mixed-metal amide fully separates to form a molten phase approaching $3LiNH_2 + NaNH_2$. The melting point of $Li_3Na(NH_2)_4$ has been reported to be 234 °C [154]. This demonstrates that the mixed-metal solid structure is stable up to 199 °C, then there is a small window for which the material is present as separate components (molten $NaNH_2$ and solid $LiNH_2$) and then beyond 234 °C there is a combined melt phase and a liquid of mixed $LiNH_2$ and $NaNH_2$ is present.

234 °C is neither the melting point of $NaNH_2$ or $LiNH_2$ but is somewhere between them both, which demonstrates that the formation of a mixed-metal amide has led to a eutectic style melting point suppression of the mixed material, compared to the individual single metal amides.

The large exothermic events at 296 °C are likely to correspond to the decomposition of either the molten $LiNH_2$ or molten $NaNH_2$. This is particularly interesting as decomposition is normally, but not exclusively, an endothermic event. The main peaks in Figure 3.3 and Figure 3.4 show that on the gas flow panel under argon, decomposition of $NaNH_2$ occurs at a higher temperature than $LiNH_2$. Therefore the thermodynamic event at 296 °C is possibly the decomposition of $LiNH_2$ as this temperature is at the lower end of the initial gas release seen in Figure 3.3.

The exothermic peaks on cooling at 223 °C are likely due to re-crystallisation of a small amount of $Li_3Na(NH_2)_4$ as it is a similar (but slightly lower) temperature to the melting of $Li_3Na(NH_2)_4$ on heating. The even smaller exotherms at 179 °C are likely to correspond to re-crystallisation of $NaNH_2$ as they match up well with the thermal events seen in the STA trace on cooling for pure $NaNH_2$ (Figure 3.4). Diffraction data collected from the products of the thermal decomposition under argon showed that $Li_3Na(NH_2)_4$ decomposes to form Li_2NH. Li_2NH is known to undergo a phase transition between a high temperature disordered structure and a low temperature ordered structure which has been reported to be at temperatures of 80 °C to 87 °C [26, 100], and it is likely that the small exotherms observed at $\sim$95 °C in Figure 3.5 correspond to this Li_2NH structural phase transition.

Comparing the STA traces for $LiNH_2$ and $Li_3Na(NH_2)_4$ (Figure 3.3 and Figure 3.5) it can be seen that $Li_3Na(NH_2)_4$ is less stable and shows a faster rate of decomposition

than $LiNH_2$ which can be explained by the lower melting point for $Li_3Na(NH_2)_4$ (234 °C) compared to $LiNH_2$ (370 °C) [45].

The high temperature decomposition of pre-synthesised $Li_3Na(NH_2)_4$ was compared to that of a hand ground mixtures of the starting materials in a 3:1 ratio under argon on the gas flow panel. This experiment was performed to determine whether the initial form of the materials was affected the high temperature decomposition. The synthesis of $Li_3Na(NH_2)_4$ occurs at 185 °C so above this temperature the same material is present in both cases, so the decomposition traces should look the same. Figure 3.6 shows the outlet gas flow mass spectrometry traces for the decomposition of $Li_3Na(NH_2)_4$ and that of a hand-ground mixture of $3LiNH_2 + NaNH_2$ under argon.

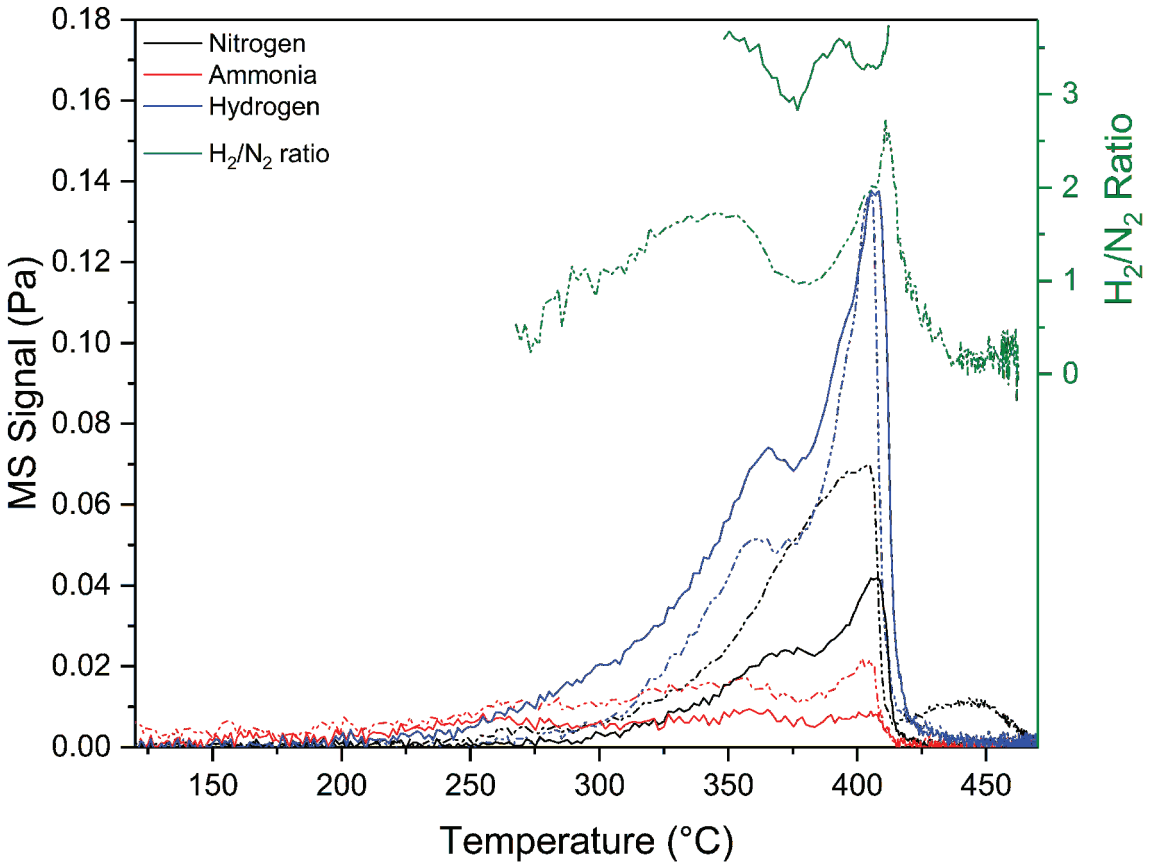


Figure 3.6: Decomposition of $Li_3Na(NH_2)_4$ (solid lines) and $3LiNH_2 + NaNH_2$ (dashed lines) on the gas flow panel under argon

Qualitatively it can be seen that the gases observed during the decomposition of $Li_3Na(NH_2)_4$ are very different to those seen during the decomposition of either single metal amide. This is a system which is mostly $LiNH_2$ but there is very little NH_3 gas release seen, whereas for $LiNH_2$ alone (Figure 3.3) NH_3 is the primary gas released. Additionally, the peak gas release at a temperature of $\sim$405 °C is significantly lower than those observed for either $LiNH_2$ or $NaNH_2$ which have been shown to occur at 347 °C and 539 °C respectively. Therefore it can be seen that mixed-metal amide systems are worth exploring as the gases given off, and the temperatures at which they are observed, are totally different to the single phase end members. The behaviour of the mixed-metal system is not simply a superposition of their individual amide components post separation.

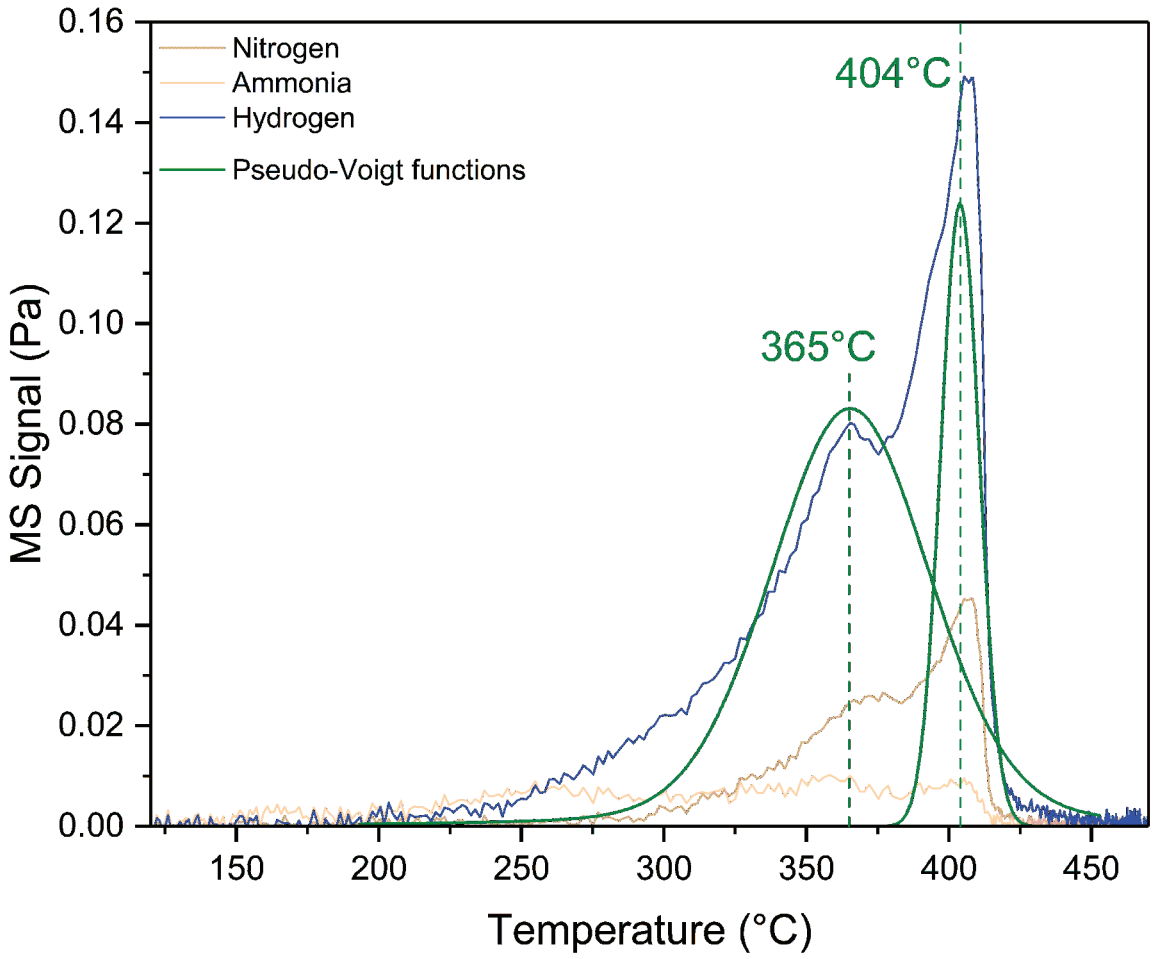


Figure 3.7: Two pseudo-Voigt functions have been used to determine the peak positions in the H_2 curve from Figure 3.6 during the decomposition of $Li_3Na(NH_2)_4$

In Figure 3.6 two peaks are observed in the traces of all three gases (H_2, N_2 and NH_3) in both experiments for which two pseudo-Voigt functions in TOPAS have been used to determine the "peak positions" of 365 °C and 404 °C (Figure 3.7). These are the temperatures at which the decomposition reactions are mainly occurring. The purpose of the pseudo-Voigt functions is not to fit or model the gas traces, but to identify the reaction temperatures. If $Li_3Na(NH_2)_4$ separates (or partially separates) on heating to form a material of composition approaching $3LiNH_2 + NaNH_2$, the two peaks observed for each gas could arise from the subsequent and separate decomposition of $LiNH_2$ and $NaNH_2$ at different temperatures, or the combined decomposition of one intermixed phase of molten $LiNH_2$ and $NaNH_2$.

A mechanism for the decomposition of $Li_3Na(NH_2)_4$ has been proposed in the literature [188]:

$Li_3Na(NH_2)_4$	$\longrightarrow Li_3Na_{(1-x)}(NH_2)_{(4-x)} + xNaNH_2$	Partial separation
	$\longrightarrow 3\,LiNH_2 + NaNH_2$	Full separation
	$\longrightarrow 3\,LiNH_2 + Na + \frac{1}{2}N_2\uparrow + H_2\uparrow$	$NaNH_2$ decomposes
	$\longrightarrow LiNH_2 + Li_2NH + NH_3 + Na$	$LiNH_2$ partially decomposes
	$\longrightarrow LiNH_2 + Li_2NH + NaNH_2 + \frac{1}{2}H_2\uparrow$	$NaNH_2$ is recycled
	$\longrightarrow LiNH_2 + Li_2NH + Na + \frac{1}{2}N_2\uparrow + H_2\uparrow$	$NaNH_2$ decomposes again
	$\longrightarrow \frac{3}{2}Li_2NH + \frac{1}{2}NH_3 + Na$	$LiNH_2$ fully decomposes
	$\longrightarrow \frac{3}{2}Li_2NH + NaNH_2 + \frac{1}{2}H_2\uparrow$	$NaNH_2$ reforms for last time
	$\longrightarrow \frac{3}{2}Li_2NH + Na\uparrow + \frac{1}{2}N_2\uparrow + H_2\uparrow$	$NaNH_2$ decomposes for last time
	$\longrightarrow \frac{3}{2}Li_2NH$	All gases lost and Na volatilised

This suggests that after separation, $NaNH_2$ decomposes first and so would be associated with the peak at 365 °C. $NaNH_2$ is known to undergo a pressure-dependent decomposition process forming Na and releasing H_2 and N_2 (and possibly some NH_3) (Equation 3.2). It has been proposed that $LiNH_2$ would then decompose (leading to the peak at 404 °C), producing Li_2NH and releasing NH_3. When solid Li_2NH begins to crystallise out of the molten phase, the remaining melt will naturally become more sodium rich. The NH_3 released would then be captured by Na under ambient pressures reforming $NaNH_2$ and H_2 would be released (ultimately it is H_2 that is released from the system not NH_3). $NaNH_2$ would then decompose

again, and capture ammonia once more. $NaNH_2$ would therefore be recycled, decomposing and reforming a number of times throughout the decomposition, until all of the $LiNH_2$ present in the sample had been converted to Li_2NH, at which point the remaining $NaNH_2$ would decompose for the final time. It is clear from the mass spectrometry data that some NH_3 was released during the decomposition reaction of $Li_3Na(NH_2)_4$, which suggests that if this mechanism is occurring, ammonia capture by Na was not 100 % effective.

Figure 3.6 shows the H_2/N_2 ratio for the released gases. To accurately calculate a H_2/N_2 ratio, an appreciable amount of each gas is required in order for the ratio to be statistically reliable. Therefore this ratio has only been plotted from 270 °C as below this temperature it is not easy to quantify, as there is only trace amounts of the gases present in the mass spectrometry trace. Decomposition of $LiNH_2$ to Li_2NH would lead to an observed H_2/N_2 ratio of 3 (Equation 3.1) but the decomposition of $NaNH_2$ to Na would lead to a H_2/N_2 ratio of 2 (Equation 3.2). It is more instructive to analyse the qualitative trends in the H_2/N_2 ration rather than the absolute values and the gas release at 365 °C shows a lower H_2/N_2 ratio than the gas release at 404 °C. This could support the idea that at least some $NaNH_2$ decomposes before $LiNH_2$.

The proposed mechanism relies on considering $LiNH_2$ and $NaNH_2$ as distinct from each other, whereas the STA trace in Figure 3.5 shows that there is a very narrow temperature window (199 °C-234 °C) where they are indeed separate from each other. This temperature range is well below the temperatures observed for decomposition. Beyond 234 °C, both components are molten and so although there may be regions which are locally more lithium or sodium rich, it will mostly be an inter-mixed molten phase so is more likely to decompose as one melt, not as $NaNH_2$ and $LiNH_2$ separately. It is therefore unlikely for it to be reasonable to consider the decomposition of $LiNH_2$ and $NaNH_2$ as completely separate from each other when they are present in a melt together, and it is the decomposition of this intermixed molten phase which must be considered. It is unreasonable to assume that $NaNH_2$ will decompose first, as the main peaks in Figure 3.3 and Figure 3.4 show that alone, on the gas flow panel under argon, decomposition of $NaNH_2$ occurs at a higher temperature than $LiNH_2$. The exothermic event at 296 °C in Figure 3.5 is therefore likely to result from the decomposition of $LiNH_2$ rather than $NaNH_2$.

The final products of $Li_3Na(NH_2)_4$ decomposition under flowing argon were determined by powder X-ray diffraction from the post decomposition residue remaining after the gas flow panel experiment. The products were principally Li_2NH (which would be expected as the product of $LiNH_2$ decomposition under argon) with a small amount of Li_2O also present.

No Bragg peaks were observed for any sodium containing material (data not presented), suggesting that the Na phase formed during the decomposition of $Li_3Na(NH_2)_4$ was either liquid or amorphous, or that Na was volatilised during the experiment. This is possible due to the appreciable vapour pressure of sodium (3.3 x 10^{-1} mbar at 400 °C). The volatilisation of Na was not confirmed by mass spectrometry, as the partial pressure recorded for Na was zero throughout the experiment, but condensed Na metal was visible on the lid of the reactor itself as shiny metallic blobs. Therefore it is likely that Na cooled and condensed inside the gas flow panel apparatus prior to reaching the mass spectrometer.

Decomposition of $Li_3Na(NH_2)_4$ (molar mass = 107.89) to $\frac{3}{2}Li_2NH$ (molar mass = 28.90), (assuming all other species were lost as gases and Na volatilised), would result in a mass loss of 59.79 % which is in good agreement with the IGA data which showed a 54.00 % mass loss before the end of the experiment (Figure 3.11). This thermogravimetric data also indicated that Na was volatilised from the sample.

3.3.2.2 $LiNa_2(NH_2)_3$ and $LiNH_2 + 2NaNH_2$

DSC traces were obtained for both pre-made $LiNa_2(NH_2)_3$ (black) and a hand-ground mixture of $LiNH_2 + 2NaNH_2$ (blue) and are shown in Figure 3.8. The mass trace in green is the percentage mass loss from the TGA part of the STA experiment, and the mass trace in red is the weight loss in mg from an IGA experiment of the decomposition of pre-made $LiNa_2(NH_2)_3$.

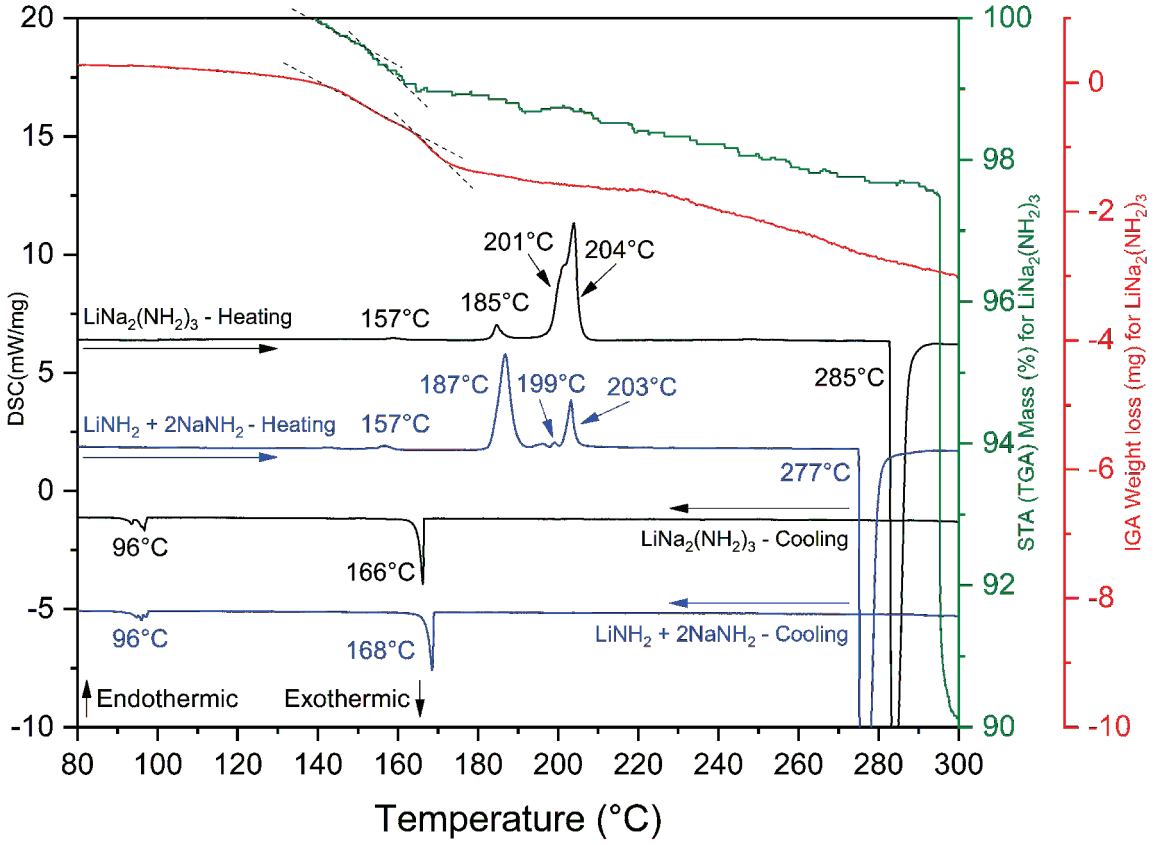


Figure 3.8: STA traces for $LiNa_2(NH_2)_3$ and $LiNH_2 + 2NaNH_2$

On heating, there is a very small endothermic event visible at 157 °C which is correlated with the main observed mass loss step (0.6 weight % at 155 °C). This is likely due to desorption of physisorbed gases from the powder grains.

The traces shown in Figure 3.8 are almost identical so the synthesis temperature of $LiNa_2(NH_2)_3$ is not obvious and unlike $Li_3Na(NH_2)_4$ there is not a strong exothermic synthesis event. The key difference between the two traces on heating is that the endotherm at 187 °C in the $LiNH_2 + 2NaNH_2$ trace is much larger than that in the trace for $LiNa_2(NH_2)_3$.

It is possible that the synthesis of $LiNa_2(NH_2)_3$ occurs at 187 °C and there is a small peak visible in the trace of pre-formed $LiNa_2(NH_2)_3$ due to incomplete synthesis of the initial $LiNa_2(NH_2)_3$ sample from the initial reaction in the tube furnace. The synthesis of $Li_3Na(NH_2)_4$ is net exothermic as expanding the layers in $LiNH_2$ and inserting Na^+ cations is a low energy process, whereas the synthesis of $LiNa_2(NH_2)_3$ is endothermic as the total rearrangement of Li^+, Na^+ and NH_2^- ions to form $LiNa_2(NH_2)_3$ is a high energy process.

The largest endotherm for $LiNa_2(NH_2)_3$ in the DSC trace has been modelled to two pseudo-Voigt peaks in TOPAS and fits well to two peaks at 201 °C and 204 °C. The analogous thermal event for $LiNH_2 + 2NaNH_2$ shows two more clearly distinct endotherms at 199 °C and 203 °C.

For $Li_3Na(NH_2)_4$, at 199 °C, $NaNH_2$ was seen to melt out of the structure via non-stoichiometric $Li_3Na_{(1-x)}(NH_2)_{(4-x)}$. There was then a small window for which the material is present as separate components and at 234 °C the solid $LiNH_2$ dissolves into the liquid $NaNH_2$ to form an inter-mixed molten phase approaching $3LiNH_2 + NaNH_2$.

Due to the different sized cation sites in $LiNa_2(NH_2)_3$, ionic mobility and therefore potential non-stoichiometry is suppressed and any ionic motion will result in decomposition instead. $NaNH_2$ cannot melt out of $LiNa_2(NH_2)_3$ via a solid non-stoichiometric intermediate in the same way as is seen for $Li_3Na(NH_2)_4$. $LiNH_2$ and $NaNH_2$ can therefore be considered to both melt congruently from the $LiNa_2(NH_2)_3$ phase. The endotherms at 199/201 °C and 203/204 °C are likely to correspond to the separation and full sample melt respectively.

The endothermic events at 203 °C/204 °C are due to the melting of the whole sample of $LiNa_2(NH_2)_3$. By comparison, $Li_3Na(NH_2)_4$ was seen to melt at 234 °C which suggests that $LiNa_2(NH_2)_3$ is less stable than $Li_3Na(NH_2)_4$. This is supported by recent theoretical studies of high-pressure polymorphs of $NaNH_2$ which suggest that the octahedral coordination of Na^+ atoms (as $\frac{3}{4}$ are in $LiNa_2(NH_2)_3$) are less stable and have higher energies compared to the tetrahedral coordination of all the Na^+ in $Li_3Na(NH_2)_4$ [318].

Independent to the nature of the initial reactants, beyond 204 °C both samples will be in the melt phase. The strong exotherms at 277 °C/285 °C correspond to the decomposition of at least some part this mixed amide molten phase. This is supported by the large mass loss observed in the TGA part of the STA trace (green Figure 3.8) (7.5 weight % at 295 °C)

due to the release of gas. The melt phase of $Li_3Na(NH_2)_4$ was seen to decompose in the STA trace at 296 °C. Although in both cases it is decomposition of a molten phase of mixed $LiNH_2$ and $NaNH_2$ that is being observed, the different ratios to which these amides are present will affect the overall decomposition temperature as they will be interacting. The decompositon of each single metal amide is being seen to affect the decomposition of the other, and it is the decomposition of the intermixed molten phase as a whole which must be considered. Similarly to $Li_3Na(NH_2)_4$ it is predicted that the exothermic event at 277 °C/285 °C in Figure 3.8 is likely to relate to the decomposition of $LiNH_2$.

On cooling, both traces in Figure 3.8 show exothermic events at 166 °C and 96 °C. The exotherms at 166 °C are likely to correspond to re-crystallisation of $NaNH_2$ as they match up well with the thermal events seen in the STA trace on cooling for pure $NaNH_2$ at 170 °C (Figure 3.4). The exotherms at 96 °C correspond to the Li_2NH transition from the high temperature disordered structure to the low temperature ordered structure (reported to be at temperatures of 80 °C to 87 °C [26, 100]).

The high temperature decomposition behaviour of $LiNa_2(NH_2)_3$ and that of a hand-ground mixture of $LiNH_2 + 2NaNH_2$ was investigated on the gas flow panel and Figure 3.9 shows the outlet gas flow MS traces under argon. As for $Li_3Na(NH_2)_4$, the NH_3 release is suppressed compared to that seen during the decomposition of $LiNH_2$ alone, and the decomposition is happening at a lower temperature than that seen for $NaNH_2$ alone. Again this highlights the differences of a mixed-metal system compared to the single metal amides alone.

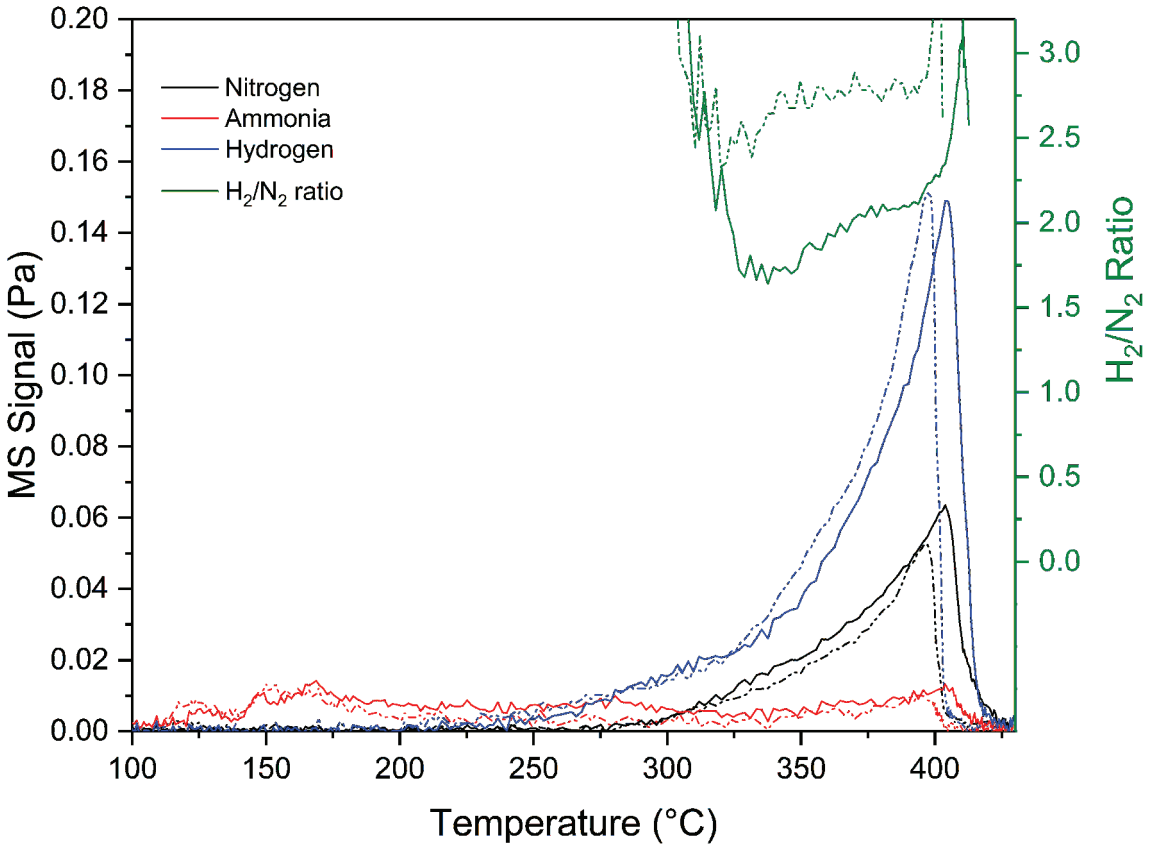


Figure 3.9: Decomposition of $LiNa_2(NH_2)_3$ (solid lines) and $LiNH_2 + 2NaNH_2$ (dashed lines) on the gas flow panel under argon

During the decomposition of $Li_3Na(NH_2)_4$, two peaks were observed in the mass spectrometry traces of all three gases as shown in Figure 3.6, but in the same range for $LiNa_2(NH_2)_3$ there is only one obvious peak in the NH_3, H_2 and N_2 traces. As in Figure 3.7, two pseudo-Voigt functions in TOPAS have been used to determine "peak positions" of the decomposition reactions and Figure 3.10 shows that it may be more accurate to consider the MS signal of the hydrogen trace during the decomposition $LiNa_2(NH_2)_3$ as two overlapping peaks centred at 376 °C and 403 °C. This would mean that the molten phase of $LiNH_2 + 2NaNH_2$ is decomposing in an analogous manner to the molten phase of $3LiNH_2 + NaNH_2$. The two peaks would therefore represent the decomposition temperatures of $LiNH_2$ and $NaNH_2$ respectively.

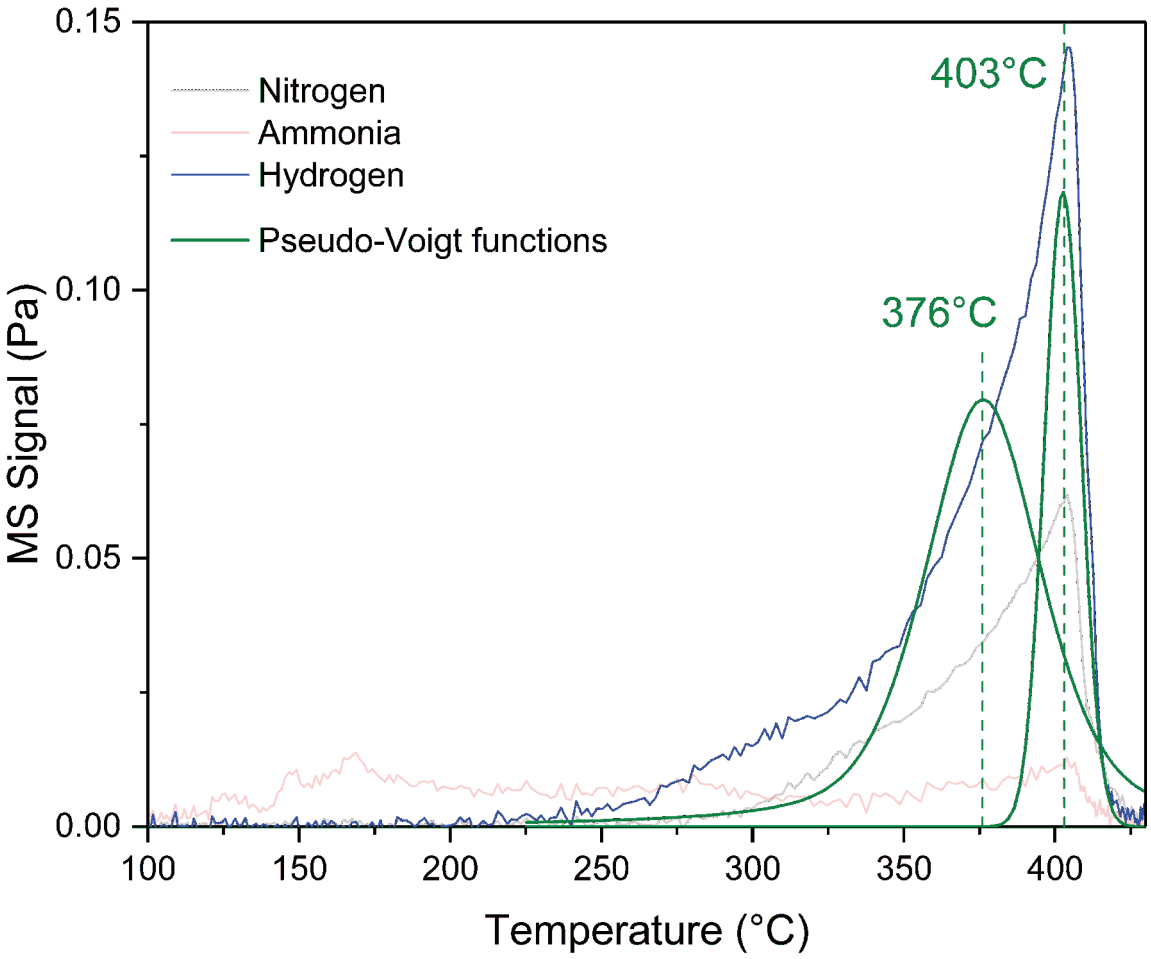


Figure 3.10: Two pseudo-Voigt functions have been used to determine the peak positions in the H_2 curve from Figure 3.9 during the decomposition of $LiNa_2(NH_2)_3$

The pseudo-Voigt functions for both $Li_3Na(NH_2)_4$ (Figure 3.7) and $LiNa_2(NH_2)_3$ (Figure 3.10) are centred about similar temperatures which would be consistent with the decomposition of $LiNH_2$ at $\sim 370\,^{\circ}C$ and $NaNH_2$ at $403\,^{\circ}C$. This is also supported by the fact the area of the pseudo-Voigt functions at each temperature has inverted between $Li_3Na(NH_2)_4$ and $LiNa_2(NH_2)_3$. There is a greater proportion of $LiNH_2$ in the molten phase of "$Li_3Na(NH_2)_4$" so the peak at $365\,^{\circ}C$ is large enough to appear as a separate peak, whereas $NaNH_2$ is the majority phase in molten "$LiNa_2(NH_2)_3$" so the peak at $403\,^{\circ}C$ has a greater area. This leads to different overall shapes of the MS signals of H_2 and N_2 so during the decomposition of $LiNa_2(NH_2)_3$ the two peaks appear to overlap. The relative ratio of $LiNH_2$:$NaNH_2$ in the molten phase will affect both the degree of mixing and the decomposition processes of $LiNH_2$ and $NaNH_2$. Whereas the molten phase of $Li_3Na(NH_2)_4$ may best be considered as

a small amount of $NaNH_2$ dissolved in molten $LiNH_2$, the molten phase of $LiNa_2(NH_2)_3$ behaves more like $LiNH_2$ dissolved in majority phase $NaNH_2$.

Figure 3.9 shows that a small amount of ammonia is released at 150 °C which correlates well with the small mass loss observed in both the TGA and IGA traces (Figure 3.8).

The STA traces in Figure 3.8 showed a large exothermic event at 277 °C/285 °C which had been attributed to the decomposition of the $LiNH_2$ component of the molten phase. Whilst the main peaks in the decomposition temperatures seen on the gas flow panel at 376 °C and 404 °C are significantly higher, it can be seen that the gas releases and therefore decomposition do indeed start at around 280 °C.

A mechanism could be proposed for the decomposition of $LiNa_2(NH_2)_3$ envisaging the combined separation and melt of $LiNa_2(NH_2)_3$ into a molten phase of $LiNH_2 + 2NaNH_2$. $LiNH_2$ would then decompose first into Li_2NH followed by the decomposition of $NaNH_2$ into Na.

$LiNa_2(NH_2)_3$	$\longrightarrow LiNH_2 + 2\,NaNH_2$	Combined separation and melt
	$\longrightarrow \frac{1}{2}Li_2NH + \frac{1}{2}NH_3\uparrow + 2\,NaNH_2$	$LiNH_2$ decomposes
	$\longrightarrow \frac{1}{2}Li_2NH + 2\,Na + N_2\uparrow + 2\,H_2\uparrow$	$NaNH_2$ decomposes
	$\longrightarrow \frac{1}{2}Li_2NH + 2\,Na\uparrow$	All gases lost
	$\longrightarrow \frac{1}{2}Li_2NH$	Na volatalised

Decomposition of $LiNa_2(NH_2)_3$ (molar mass = 100.98) to $\frac{1}{2}Li_2NH$ (molar mass = 28.90) and 2Na (molar mass = 22.99) would correspond to a mass loss of 40.12 %. The 68.58 % mass loss seen during this decomposition (Figure 3.12) is too great to be accounted for purely by the release of gases from the sample and so the decomposition of $LiNa_2(NH_2)_3$ must proceed with the volatilisation of some Na from the sample as evidenced by the presence of shiny metallic blobs on the lid of the gas flow panel reaction vessel. Na was also volatilised under such conditions during the decomposition of $Li_3Na(NH_2)_4$. If all the Na was volatilised and only $\frac{1}{2}Li_2NH$ was left in the reaction vessel, there would be a mass loss of 85.7 %. As a mass loss of 68.58 % was observed, this suggests Li_2NH was not the only product of decomposition here, so it is likely some Na is also present.

The final products of $LiNa_2(NH_2)_3$ decomposition under flowing argon were determined by powder X-ray diffraction from the post decomposition residue remaining after the gas flow panel experiment. Similarly to $Li_3Na(NH_2)_4$, this was majority phase Li_2NH (which would be expected as the product of $LiNH_2$ decomposition under argon) with a small amount of Li_2O also present. Again no Na containing products were identified by powder X-ray diffraction.

3.4 Inert gas summary

In depth analysis of the thermal decomposition of these materials under inert gas is used as a basis for understanding how these systems may perform as NH_3 decomposition catalysts. Figures 3.11 and Figure 3.12 show the superposition of key results from the three experiments performed under inert gas for $Li_3Na(NH_2)_4$ and $LiNa_2(NH_2)_3$ which have already been discussed.

The low temperature behaviour of the samples was probed by DSC recorded through STA as the samples were heated to 300 °C. The high temperature thermal decomposition behaviour was analysed through the percentage mass loss recorded during IGA experiments and the MS signal of the outlet gas flow was recorded on the gas flow panel as the samples were heated to 475 °C. The onset and peak temperatures of these decomposition events may differ slightly for the three traces due to the different conditions (sample size, heating rate and reaction pressure) used during the studies, but correlations can be clearly observed.

Analysis of the diffraction, thermogravimetric and calorimetric data collected during IGA, STA and gas flow panel experiments indicate that the decomposition of $Li_3Na(NH_2)_4$ and $LiNa_2(NH_2)_3$ proceed via multi-step processes. The similarities between the data collected for $Li_3Na(NH_2)_4$ and $LiNa_2(NH_2)_3$ suggest that both mixed-metal amides decompose via similar pathways.

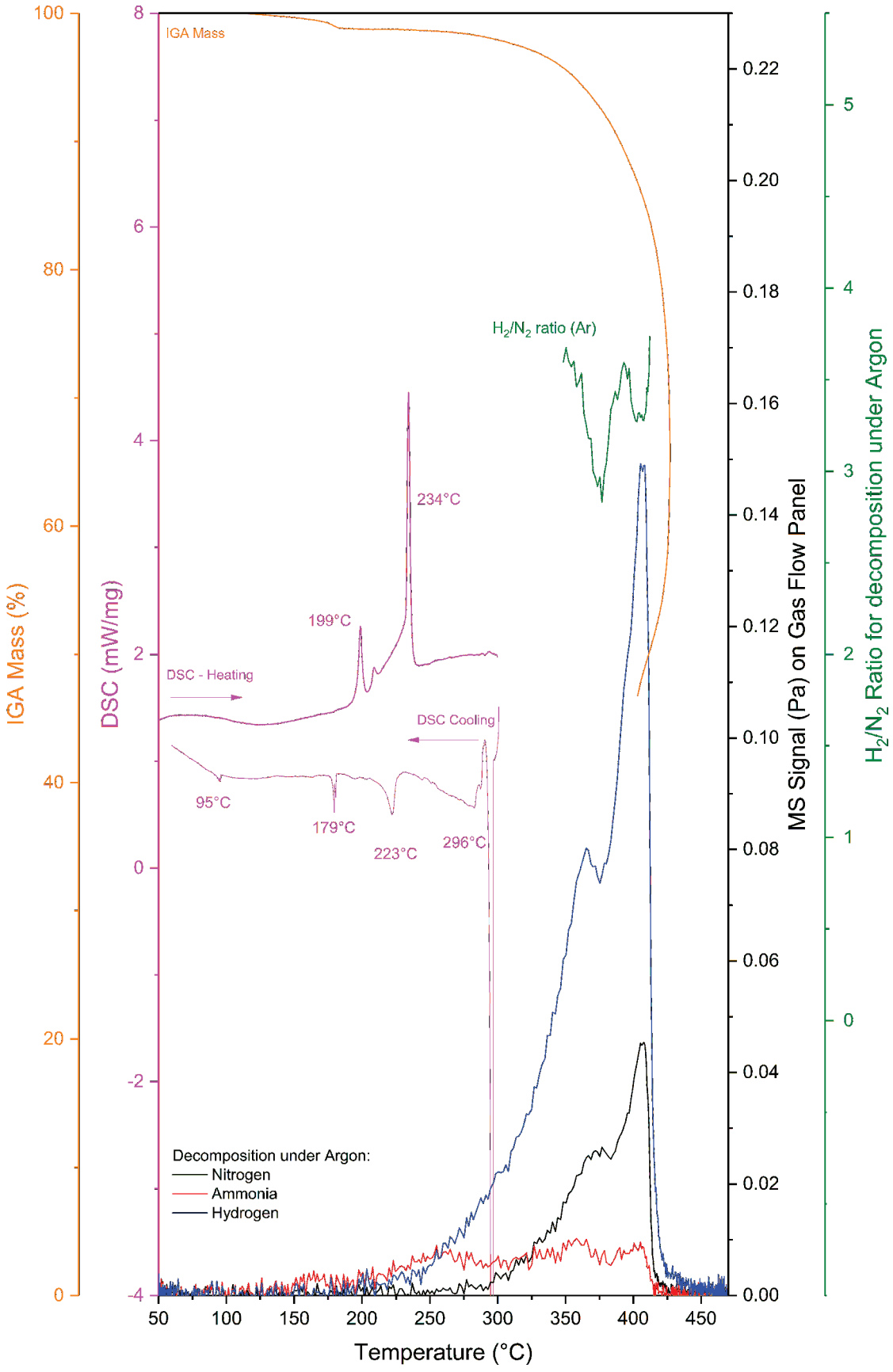


Figure 3.11: Thermodynamic properties measured during the decomposition of $Li_3Na(NH_2)_4$ under inert gas

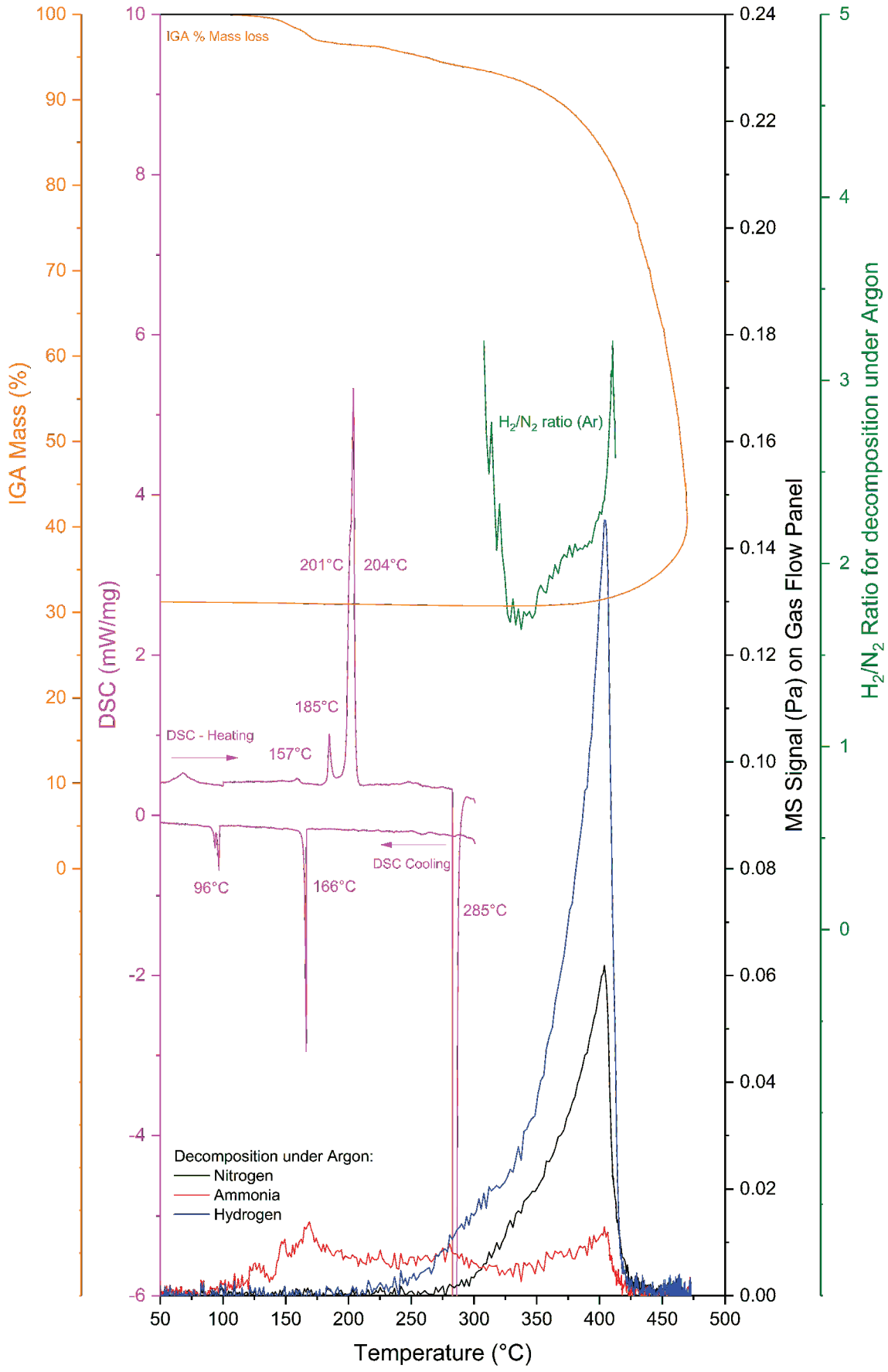


Figure 3.12: Thermodynamic properties measured during the decomposition of $LiNa_2(NH_2)_3$ under inert gas

3.5 Ammonia decomposition

Group 1/2 light metal amides and imides have been discovered as a new class of inexpensive and effective catalyst for the decomposition of ammonia into nitrogen and hydrogen for energy applications (Equation 3.3).

$$2\,NH_3 \underset{k_{-1}}{\overset{k_1}{\rightleftharpoons}} N_2 + 3\,H_2 \tag{3.3}$$

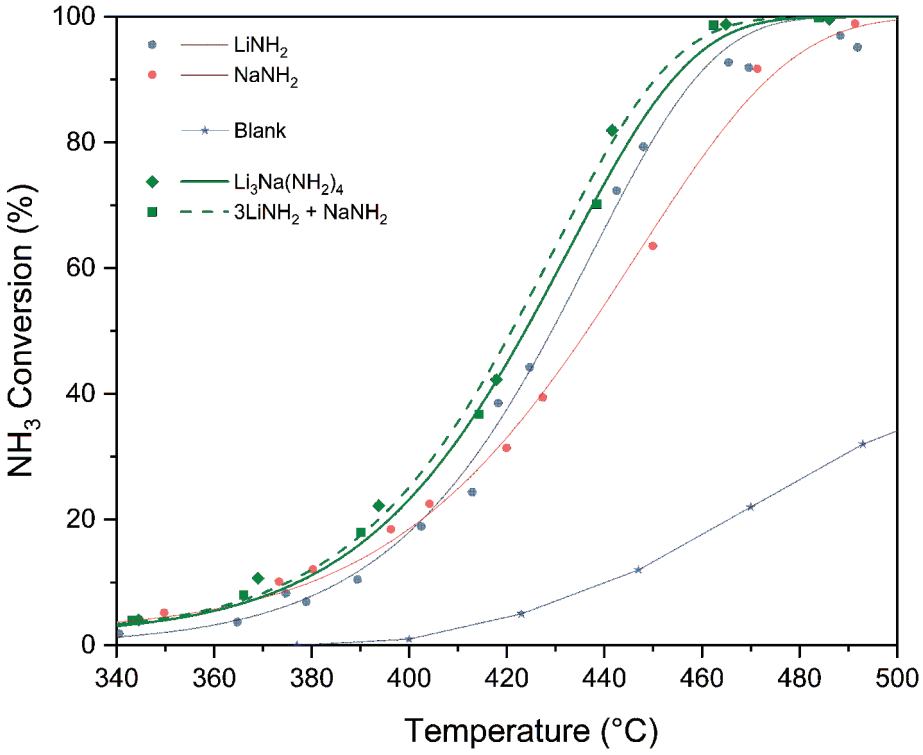
The range of amide and imide materials previously studied (Sections 1.6.2 and 1.6.3) all show appreciable ammonia decomposition activity, with similar or superior activities to optimised transition metal based catalysts. They also show significant potential for that activity to be optimised, as identifying the active form of the catalyst is only part of the effort to understand their action. Mixed-metal systems are a promising route to tailoring the active form of the catalyst and so it is possible that mixed-metal amide structures such as $Li_3Na(NH_2)_4$ and $LiNa_2(NH_2)_3$, with two integrated metal ions, may provide a route to a low temperature NH_3 decomposition catalyst.

Ammonia conversion efficiencies of these materials were analysed by loading 0.5 g of the catalyst powder into a 46.9 cm^3 stainless steel reactor, attached to the gas flow panel as described in Section 2.2.1.1 and Section 2.3. The reactor was sealed and transferred to a vertical tube furnace before being connected to the gas flow panel. The panel was first flushed with argon, then evacuated up to the reactor, before flushing the panel and reactor with ammonia prior to heating. The temperature was then varied for a given ammonia inlet flow (60 sccm) whilst the out gas from the sample cell was monitored by mass spectrometry. Conversion efficiencies were calculated using a customised computer program, which removes background signals and accounts for the signal discontinuities which occur when the detector range switches [310]. The ammonia conversion efficiency was calculated by determining the ammonia signal as a percentage of the total signal and are reported are based on average conversion values from a 2–3 hour dwell period at each temperature.

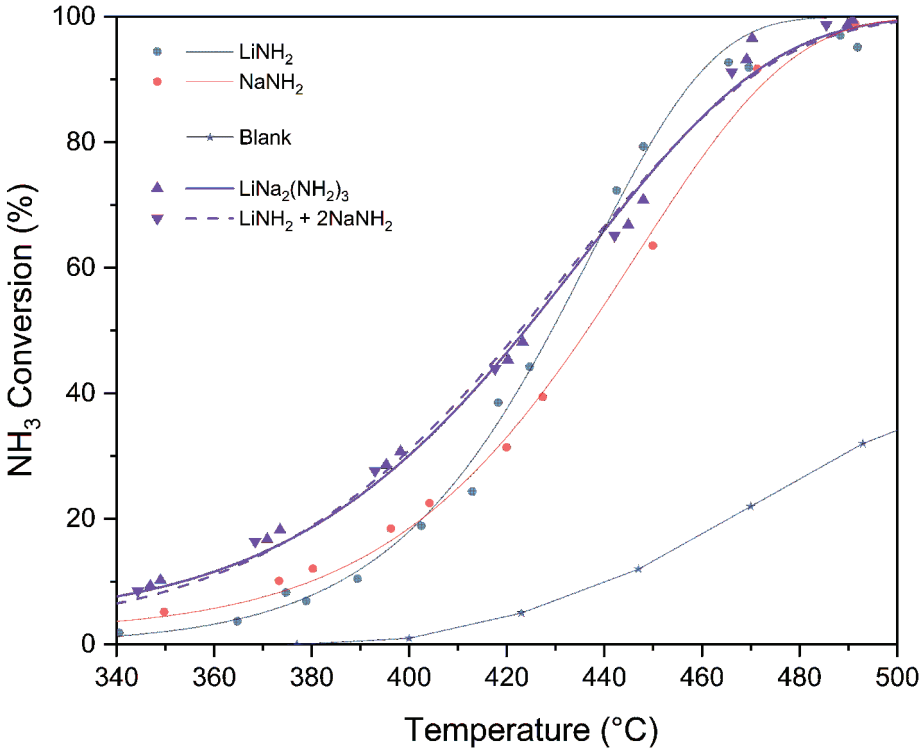
Figure 3.13 shows the ammonia conversion percentage calculated from the MS data shown in Figure 3.14a and Figure 3.14b. It compares the NH_3 decomposition ability of

the pre-formed mixed-metal amides with the analogous behaviour of ground-up mixtures of their constituent single metal amides in the relevant ratios. Sigmoids for equivalent masses of pure $LiNH_2$ and $NaNH_2$ and the empty (blank) reactor have been included for comparison.

These data show that the extent of decomposition increases with increasing temperature and the level of ammonia decomposition for all the experiments is significantly in excess of that observed for the blank reactor. This is strong evidence for the catalytic effect of mixed-metal amides on the decomposition of ammonia.



(a) $Li_3Na(NH_2)_4$ and $3LiNH_2 + NaNH_2$



(b) $LiNa_2(NH_2)_3$ and $LiNH_2 + 2NaNH_2$

Figure 3.13: Ammonia decomposition sigmoids for the Li-Na-N-H system as potential catalysts on the gas flow panel

Initially looking at the single metal amides, (as discussed in Section 1.6.2) it can be seen that $LiNH_2$ is higher performing and has a steeper curve than $NaNH_2$. A steeper sigmoidal function is indicative of higher activation energy for the ammonia decomposition reaction. $LiNH_2$ reaches high conversion at moderate temperatures, attaining 90.7 % conversion at 458 °C, compared with 54.9 % for sodium amide at the same temperature [198]. $LiNH_2$ is also significantly easier to maintain in the reactor and shows much higher post-reaction recovery than $NaNH_2$ (85 % and 6 % respectively). Whereas $LiNH_2$ decomposes to Li_2NH which is solid until its own decomposition at around 600 °C, $NaNH_2$ melts at 210 °C and decomposes to Na which is difficult to effectively contain due to its high volatility.

Qualitatively it can be seen that both mixed-metal amides out-perform $LiNH_2$ and $NaNH_2$ across the entire temperature range and particularly at high temperatures. This provides evidence that there is added value of the mixed-metal phases as ammonia decomposition catalysts compared to their individual starting materials. It can be seen that $LiNa_2(NH_2)_3$ outperforms $Li_3Na(NH_2)_4$ until 448 °C, from which point onwards $Li_3Na(NH_2)_4$ demonstrates the best NH_3 decomposition ability. Unsurprisingly the more Li rich system ($Li_3Na(NH_2)_4$ and $3LiNH_2 + NaNH_2$) have sigmoids that are shaped much more like $LiNH_2$ and the more Na rich systems ($LiNa_2(NH_2)_3$ and $LiNH_2 + 2NaNH_2$) have sigmoids much more similar to that of $NaNH_2$. This is reinforced quantitatively in Section 3.5.1.

There is very little difference between the two traces for each respective ratio, with the two sigmoids almost overlapping. This close correlation suggests there is no benefit to pre-forming the mixed-metal amides. The synthesis temperatures for $Li_3Na(NH_2)_4$ and $LiNa_2(NH_2)_3$ determined by STA are 185 °C and 187 °C respectively (Figures 3.5 and 3.8) which are well below the start of the ammonia decomposition activity. Synthesis of both the mixed-metal amides under ammonia on the gas flow panel has been confirmed (Section 3.2.2). In both cases the same material will be present at the temperatures required for NH_3 decomposition, most likely as an intermixed molten phase of $LiNH_2$ and $NaNH_2$ in the relevant ratios which is the active form of the NH_3 decomposition catalyst.

3.5.1 Quantitative fitting and analysis

Quantitatively, the ammonia decomposition data shown in Figure 3.13 can be analysed from fitting by a least-squares Levenberg-Marquardt algorithm. This optimises the parameters of single or bi-sigmoidal functions, corresponding to single- and dual-processes respectively (Equation 3.4) and producing a Gompertz curve [296]. This way of obtaining the activation energy fits the conversion data directly, rather than using traditional Arrhenius process, which plots the natural logarithm of the rate constant against the inverse of the temperature.

The Gompertz curve includes the assumptions that the reverse reaction for Equation 3.3 (k_{-1}) is so small it can be ignored, that the rate of reaction for Equation 3.3 is first order with respect to $p(NH_3)$ and that it follows Arrhenius-type behaviour. The sigmoids relate the ammonia conversion efficiency, c, ($f(NH_3)$ is the fraction of NH_3 in the MS signal) to the temperature in Kelvin, T, using a pre-exponential factor, A, (where $A = \frac{E_A}{T_e}$), an activation energy, E_A, and the gas constant, R. A and E_A are fitted parameters. When $T = T_e$ in Equation 3.4a, $c(NH_3) = 1 - \exp(-1)$ so T_e is the temperature at which $\sim 63\%$ of NH_3 is decomposed.

1 process:
$$c(NH_3) = 1 - f(NH_3) = 1 - exp\left[-exp\left(\frac{A}{R} - \frac{E_A}{RT}\right)\right] \text{ where } A = \frac{E_A}{T_e} \tag{3.4a}$$

2 processes:
$$c_{A\&B} = (c_A + c_B - 2c_A c_B)/(1 - c_A c_B) \tag{3.4b}$$
$$c(NH_3) = 1 - \alpha exp\left[-exp\left(\frac{A_1}{R} - \frac{E_{A1}}{RT}\right)\right] - (1-\alpha) exp\left[-exp\left(\frac{A_2}{R} - \frac{E_{A2}}{RT}\right)\right] \tag{3.4c}$$

T_e is a useful number for comparing the activity of different catalysts as it indicates where the sigmoid is increasing most rapidly. It is difficult to know what is meant when one catalyst is described as "more active" than another, because it depends on the reaction temperature, so T_e is useful because it takes one temperature and compares the point at which each catalyst reaches the same conversion value. For a given value of T_e, the steepness of the sigmoid function is indicative of higher activation energy for NH_3 decomposition but both the activation energy and the pre-exponential factor within the empirical Arrhenius relationship must be considered as the determinants of reaction kinetics. For example $LiNH_2$

has a larger pre-exponential factor which compensates for its high activation energy E_A.

If two processes are occurring, but under the assumption that they are independent and first order with respect to NH_3 then this function is fitted as a sum of two equations (Equation 3.4c) with different refined E_A values, and a single parameter, α, is used to modify the magnitude of each of the processes. The outputs of the fitting process in terms of the values obtained for each of the curves are summarised in Table 3.2. There is a degree of uncertainty in the numbers because the function is highly sensitive as the exponential of an exponential is a rapidly varying function. Uncertainties for T_e and E_A are estimated to be on the order of $\pm 2\,°C$ and $\pm 3\,kJ/mol$ respectively. The activation energies obtained from this fitting process are not dissimilar to those reported for similar catalysts in the literature, although there is a significant spread in the reported values [48].

The plotted points in Figure 3.13 are the recorded experimental results and the line of best fit has been drawn using the two process sigmoidal Gompertz function (Equation 3.4) with the parameters listed in Table 3.2, which were themselves generated using the sigmoid fit calculated in TOPAS (Section 3.5.1). This produces a smooth, fitted function.

A qualitative description of the shape of the curves in Figure 3.13 is important for understanding what the fitted values show and how this maps onto the quantitative parameters. A process with a high activation energy has a steeper sigmoid shape and will be more $LiNH_2$ like (such as $Li_3Na(NH_2)_4$) and a process with a lower activation energy (E_A) will have a shallower rise and be more $NaNH_2$ like (such as $LiNa_2(NH_2)_3$). However, if a high activation energy occurs at low temperature, then the function would be steep. The sigmoid for $LiNH_2$ is the steepest (highest E_A) followed by $Li_3Na(NH_2)_4/3LiNH_2 + NaNH_2$. Interestingly, $LiNa_2(NH_2)_3/(LiNH_2 + 2NaNH_2)$ has a lower E_A than either $NaNH_2$ or $LiNH_2$ individually. The presence of two amides is retarding the ammonia decomposition compared to either single metal process independently, which is discussed further in Chapter 7.

	Constant	T_e (°C)	E_A (kJ/mol)	Recovery by mass (%)
Blank	0.000(1)	547	102	n/a
$LiNH_2$	0.000(5)	439	184	88
$NaNH_2$	0.021(7)	450	154	6
$Li_3Na(NH_2)_4$	0.015(6)	434	177	73
$3LiNH_2 + NaNH_2$	0.017(8)	431	180	65
$LiNa_2(NH_2)_3$	0.039(2)	440	123	56
$LiNH_2 + 2NaNH_2$	0.019(4)	439	116	48

Table 3.2: Li-Na-N-H system Gompertz curve output values. Uncertainties for T_e and E_A are estimated to be on the order of ± 2 °C and ± 3 kJ/mol respectively and have been calculated from the TOPAS fitting process

While the blank reactor, nickel on a silica-alumina support and ruthenium on an alumina support are best fit by a two process function, all the single metal amides, and combinations of them, whether hand-ground or as pre-formed mixed-metal amides, fit to a single decomposition process [196]. This indicates there is not an obvious change in rate determining step across the temperature range. For the generation of the fitted lines shown in Figure 3.13, a two process function (Equation 3.4) has been used by considering the blank reactor and catalyst as two separate entities. However, once the catalyst is present, its activity is so much higher than that of the blank reactor that the reaction can be considered a single process as the blank reactor effectively does not contribute to the NH_3 decomposition. That these catalysts fit to a single process may relate to the fact that these are thought to be successive stoichiometric reactions within the bulk, rather than surface-mediated mechanisms, so the kinetics are less likely to be affected by occupation of surface sites by N_2 or H_2 as described for transition metals which are known to decompose NH_3 by conventional surface catalysis.

The mechanism for the reaction of NH_3 with transition metals follows a standard heterogenous catalytic pathway with ammonia adsorbed onto the catalyst surface, followed by breaking of the N−H bonds to give adsorbed nitrogen and hydrogen atomic species which then desorb as N_2 and H_2 [96, 186]. The RDS is normally desorption of nitrogen from the

metal surface due to the formation of the strong N≡N triple bond but it could also be the NH_3 N−H scission enthalpy (Section 1.6.1.1). There is some variation observed depending on the conditions and transition metal used. For transition metals that show a change in RDS, the NH_3 conversion would be fit with more than one process in this kind of analysis.

Observation of H-D exchange during previous *in-situ* neutron powder diffraction studies for the Li-N-H and Na-N-H systems have shown that the bulk of the material is active in the decomposition reaction [198]. With $LiNH_2$ and $NaNH_2$ as catalysts, the ammonia decomposition is effected on the surface of the material, but it is the composition of the bulk that affects the concentration of active surface sites [299].

This explains why there are not different mechanisms observed at high or low conversion, because at high conversion there is a high concentration of H_2 present which will saturate the surface and at low conversion NH_3 is dominant and will saturate the surface. Although these two gases may have differing impacts on the surface, it is the bulk material as well as the surface that is important for these amide catalysts, so only one process is observed at all temperatures. This contrast of the single reaction process observed for light metal amides compared with two processes observed for transition metal catalysts is indicative of significantly different reaction mechanisms.

3.5.2 Catalyst recovery

The catalyst recovery is the percentage of the starting mass of the catalyst recovered from the reactor at the end of the experiment, and is a guide to the volatility of the catalyst. A high percentage recovery is an important characteristic for potential practical applications and is crucially important in order to maintain efficiency and improve lifetimes. Poor containment of the catalyst as a whole, would not be acceptable for on-board applications in a vehicle which would be expected to run for thousands of kilometres.

The recovery results shown in Table 3.2 indicate that the pre-formed mixed-metal amides have better recovery than the mixed starting materials, again emphasising the potential benefits of mixed-metal amides. This indicates that there may be some practical value in pre-forming mixed-metal amides, even though there was not a significant difference in their

observed activity compared to starting with a mixture of the single metal amides in the relevant ratios.

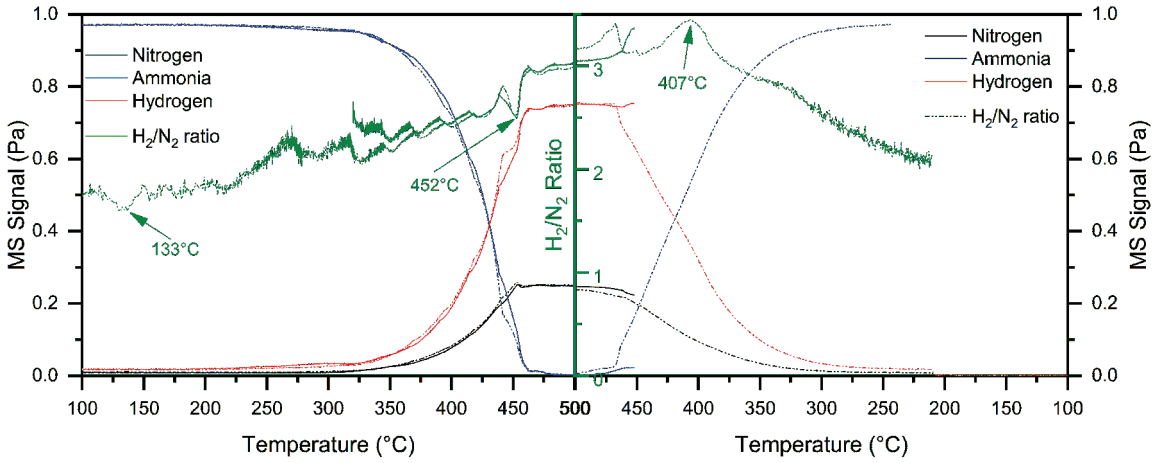
Powder X-ray diffraction analysis of the residues remaining in the reactors at the end of the ammonia decomposition reactions was performed in order to identify the decomposition products. This is an important step to help determine the mechanism by which each catalyst decomposes ammonia and these can then be compared to those already known for $LiNH_2$, $NaNH_2$ and $Li_2Ca(NH)_2$.

Decomposition of both mixed-metal amides under argon suggested the separation and subsequent decomposition of each constituent single metal amide; $LiNH_2$ and $NaNH_2$. If the same occurs under NH_3, $NaNH_2$ would remain as $NaNH_2$ after the ammonia decomposition reaction. However, lithium amide is known to decompose under ammonia to form non-stoichiometric lithium imide (the real ammonia decomposition catalyst) which reforms the amide at low temperatures under ammonia. Therefore if the reactor is cooled under ammonia, $LiNH_2$ and $NaNH_2$ would be expected. Powder X-ray diffraction analysis has shown that $LiNH_2$ is present in all the post-reaction products, however no sodium containing components were detected suggesting it had likely been volatilised and therefore lost from the reactor.

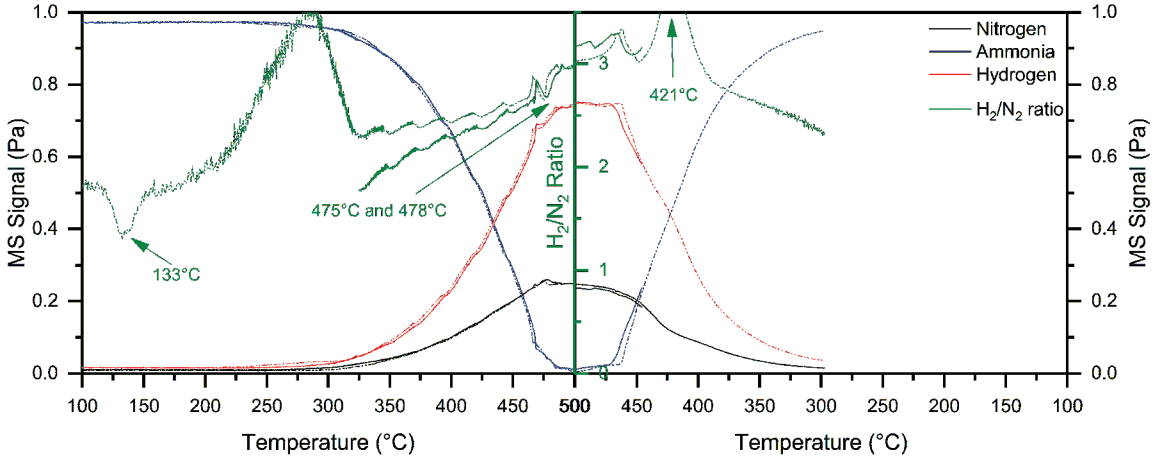
Although it is clear the molten phase of the mixed-metal melt does affect the overall properties and does have an impact on NH_3 decomposition ability, it does not prevent the downside of having Na in the system in terms of poor recovery. The solid structures of $Li_3Na(NH_2)_4$ and $LiNa_2(NH_2)_3$ are unstable and melt at lower temperatures than those required for the onset of NH_3 decomposition, so forming the mixed-metal amide does not help avoid the problems of containment. $NaNH_2$ has a melting point of 210 °C so at the temperatures required for high ammonia conversion ($\sim$450 °C) any $NaNH_2$ present will be in the form of an aerosol. This leads to poor recovery post reaction and indeed powder is often found inside the outlet tube and associated pipework. The combined melt is not able to contain sodium in the solid phase so does not avoid the issues of containment particularly associated with $NaNH_2$. Despite this, it is clear that during the reaction, the sample (or at least a fraction of it) is present in the hot zone of the reaction. The drawbacks of these systems as NH_3 decomposition catalysts are the same as for the individual amides.

3.6 Decomposition under ammonia

Figure 3.14 shows the outlet gas flow MS traces for the decomposition of $Li_3Na(NH_2)_4$ and $LiNa_2(NH_2)_3$ as well as hand-ground mixtures of the constituent single metal amides in the relevant ratios under ammonia during the experiments described in Section 3.5. Analysis of these MS traces is important to help determine the active form of the catalyst at the temperatures of interest for NH_3 decomposition and understand how they are likely to perform as catalysts.



(a) $Li_3Na(NH_2)_4$ (solid lines) and $3LiNH_2 + NaNH_2$ (dashed lines)



(b) $LiNa_2(NH_2)_3$ (solid lines) and $LiNH_2 + 2NaNH_2$ (dashed lines)

Figure 3.14: MS data collected during the decomposition of components of the Li-Na-N-H system on the gas flow panel under ammonia

The decomposition of $LiNH_2$ to Li_2NH leads to the release of NH_3 (Equation 3.1a) which will itself decompose to H_2 and N_2 in a 3:1 ratio, and so will not change the observed H_2/N_2 ratio to that seen for NH_3 decomposing alone. However, $NaNH_2$ decomposes to H_2 and N_2 in a 2:1 ratio (Equation 3.2) as it does not decompose via the production of NH_3. The decomposition of $NaNH_2$ will therefore change the overall ratio of observed H_2/N_2 from that observed solely for the catalytic decomposition of NH_3 as there is effectively less H_2 and more N_2 (relatively). The suppression observed in the H_2/N_2 ratios on heating under NH_3 in Figure 3.14 is therefore indicative of the production of Na metal and overall decomposition of at least the $NaNH_2$ component of the "melt phase".

The decomposition temperatures under NH_3 for $Li_3Na(NH_2)_4$ and $3LiNH_2 + NaNH_2$ of 452 °C is higher than those seen under argon of 360 °C and 405 °C respectively. The decomposition temperatures under NH_3 for $LiNa_2(NH_2)_3$ and $LiNH_2 + 2NaNH_2$ of 475 °C and 478 °C are also higher than those seen under argon 400 °C. Under argon there were two peaks in the gas traces of the mass spectrometry data, under NH_3, $Li_3Na(NH_2)_4$ and $LiNa_2(NH_2)_3$ appear to decompose in a single step.

The peaks in the H_2/N_2 ratio on cooling at 407 °C and 421 °C for the 3:1 and 1:2 systems respectively, correspond to extra H_2 (relatively less N_2) due to the reformation of some $NaNH_2$ from Na (the reverse of Equation 3.2).

There is a suppression in the H_2/N_2 ratio for both the $3LiNH_2 + NaNH_2$ and $LiNH_2 + 2NaNH_2$ experiments at 133 °C on heating, which is not present in the traces for pre-formed $Li_3Na(NH_2)_4$ and $LiNa_2(NH_2)_3$. Both the H_2 and N_2 signals are very low at this temperature so it is difficult to be authoritative about the exact nature of these suppressions since there is a significant amount of background ammonia signal, but these suppressions appear to be more significant than just noise. The reproducible temperature of the suppressions, and the degree to which they correlate with the temperature for the low temperature N_2 release centred at 161 °C in the MS gas outlet trace and the thermal event in the DSC trace with an onset temperature of 145 °C (Figure 3.4) suggest they are due to potential nitrogen release from $NaNH_2$. This is also evidenced by the fact it is clearer in the $LiNH_2 + 2NaNH_2$ trace (a more $NaNH_2$ rich system) than the $3LiNH_2 + NaNH_2$ trace, and it is not observed during the decomposition of $Li_3K(NH_2)_4$ or $LiK_2(NH_2)_3$ under NH_3 (Figure

4.41 and Figure 4.41b). It makes sense that this peak is observed for $3LiNH_2 + NaNH_2$ and $LiNH_2 + 2NaNH_2$ but not for $Li_3Na(NH_2)_4$ and $LiNa_2(NH_2)_3$ because, as proposed in Section 3.3.1.2, the N_2 evolution observed at lower temperatures is likely due to the release of occluded N_2 remnant from the commercial synthesis of $NaNH_2$. The pre formation of $Li_3Na(NH_2)_4$ and $LiNa_2(NH_2)_3$ will have meant the initial $NaNH_2$ has already been heated during the mixed-metal synthesis, so any N_2 release will have already occurred.

3.7 Summary

$Li_3Na(NH_2)_4$ and $LiNa_2(NH_2)_3$ can be routinely made in high purity by tube furnace and ball-mill preparations. Analysis of the low temperature decomposition of $Li_3Na(NH_2)_4$ under argon showed that at 199 °C, $NaNH_2$ melts out of the structure via non-stoichiometric $Li_3Na_{(1-x)}(NH_2)_{(4-x)}$. There is then a small temperature range for which the material is present as separate components and at 234 °C the solid $LiNH_2$ dissolves into the liquid $NaNH_2$ to form an inter-mixed molten phase approaching $3LiNH_2 + NaNH_2$. $LiNa_2(NH_2)_3$ cannot support this non-stoichiometry as it is as line phase so it simultaneously separates and melts at 204 °C forming an inter-mixed molten phase approaching $LiNH_2 + 2NaNH_2$.

At high temperatures these inter-mixed molten phases decompose with two gas releases from the decomposition of $LiNH_2$ at ∼370 °C and $NaNH_2$ at 404 °C. There is a degree of interaction between these two concurrent processes as the presence of Na in the otherwise Li–N–H system strongly encourages the production of H_2 and N_2 over that of NH_3 (seen for $LiNH_2$ decomposing alone). The presence of two amides in the reaction vessel as opposed to a single metal amide also appears to significantly reduce the decomposition temperatures observed, as $LiNH_2$ and $NaNH_2$ alone were seen to decompose at 437 °C and 539 °C.

$Li_3Na(NH_2)_4$ shows improved NH_3 decomposition over $LiNH_2$, particularly at high temperatures and $LiNa_2(NH_2)_3$ shows the best NH_3 decomposition below 430 °C. However the issues of containment with regard to the loss of Na from the reaction vessels is likely to prevent their commercial adoption as catalysts for the decomposition of NH_3 as the reversibility of such materials is clearly limited under these conditions.

Chapter 4

Mixed Lithium-Potassium system

Contents

4.1 Background 162

4.1.1 Group 1 metal amides 163

4.1.1.1 Thermal analysis comparison 164

4.1.2 Crystallography 167

4.1.3 Chapter overview 168

4.2 Synthesis 169

4.2.1 $Li_3K(NH_2)_4$ 169

4.2.2 $LiK_2(NH_2)_3$ 169

4.2.3 $Li_7K(NH_2)_8$ 173

4.3 Phase space between $LiNH_2$ and KNH_2 177

4.3.1 I11 powder X-ray diffraction 177

4.3.2 Raman 179

4.4 Unknown Li-K-N-H phase 182

4.4.1 Where it has been observed 182

4.4.2 Raman 186

4.4.3 Structure solution 187

4.4.4 Summary and future work 191

4.5 STA traces for the phase space between $LiNH_2$ and KNH_2 . . 191

4.6 $Li_3K(NH_2)_4$ 194

4.6.1 *Ex-situ* thermal decomposition behaviour 194

4.6.2 GEM experiments 202

4.6.2.1 Synthesis of $Li_3K(ND_2)_4$ 203

4.6.2.2 Decomposition of $Li_3K(ND_2)_4$ 209

4.6.3 Inert gas summary for $Li_3K(NH_2)_4$ 220

4.7 $LiK_2(NH_2)_3$ 222

4.7.1 *Ex-situ* thermal decomposition behaviour 222

4.7.2 GEM experiments 229

4.7.2.1 Synthesis of $LiK_2(ND_2)_3$ 229

4.7.2.2 Decomposition 234

4.7.3 Inert gas summary for $LiK_2(NH_2)_3$ 245

4.8 Ammonia decomposition 247

4.8.1 Quantitative fitting and analysis 247

4.8.2 Catalyst recovery 251

4.9 Decomposition under ammonia 252

4.10 Summary 254

4.1 Background

A logical progression to the analysis of mixed-metal amides in the Li-Na-N-H system is substitution for other Group 1 elements. Within the Li-K-N-H system three Li-K-N-H mixed-metal amides with different metal ratios have been reported, $Li_3K(NH_2)_4$ [83], $LiK_2(NH_2)_3$ [168] and $Li_7K(NH_2)_8$ [148]. Very little literature exists on these systems, and the majority of this literature is focused on $Li_3K(NH_2)_4$ as an intermediate formed when potassium-compounds are used as doping additives to improve the H_2 desorption kinetics of the Li-N-H [84, 270] or Mg-Li-N-H [185, 290] systems, and as its possible role in the process of H_2 storage. As with the Li-Na-N-H system, no investigations into the use of lithium-potassium amides as NH_3 decomposition catalysts have been reported. It will be interesting to ascertain whether potassium is the most active of the Group 1 amides, since it has been found to be the most effective promoter for traditional ammonia decomposition catalysts (Section 1.6.1.2). Analogous benefits may therefore be seen from formal integration to form Li-K mixed-metal amides which could be highly active to NH_3 decomposition.

4.1.1 Group 1 metal amides

The alkali metal amides $NaNH_2$, KNH_2, $RbNH_2$ and $CsNH_2$ all thermally decompose by the same method (Equations 4.1) to the metal, nitrogen and hydrogen so may display NH_3 decomposition through a similar mechanism. None of these reactions have been studied in any significant detail due to their high chemical reactivity (similar to that for $NaNH_2$) and the particularly significant hazards associated with working with rubidium and caesium. Each of these metals is less attractive than sodium in terms of cost and abundance. However, their performance may be informative in terms of understanding the parameters which might affect the ammonia decomposition efficiency.

$$\begin{aligned} KNH_2(s) &\longrightarrow K(s) + \frac{1}{2}N_2(g) + H_2(g) \\ K(s) + NH_3(g) &\longrightarrow KNH_2(s) + \frac{1}{2}H_2(g) \end{aligned} \tag{4.1}$$

The melting point of amides would be expected to decrease down the group as ionic radius increases and charge density decreases, therefore weakening the strength of the metallic bonding [159]. However, $NaNH_2$ has an anomalously low melting point despite its higher charge density and therefore has a larger lattice enthalpy than KNH_2. KNH_2 has a higher melting point than $NaNH_2$ and is more comparable to that of $LiNH_2$ (Table 4.1). This difference in melting points may mean that molten KNH_2 is less mobile than $NaNH_2$, resulting in a greater proportion of the sample remaining in the reactor hot zone where it can decompose NH_3. The drawbacks of poor recovery observed for $NaNH_2$ as an ammonia decomposition catalyst may therefore be ameliorated by replacing $NaNH_2$ with KNH_2 to form an analogous system and set of mixed-metal amides. Mixed lithium-potassium amides may therefore suffer from less significant catalyst loss than lithium-sodium amides and KNH_2 may be therefore be expected to have a higher catalytic activity than $NaNH_2$ towards NH_3.

However, potassium metal has a higher vapour pressure than sodium metal (9.3×10^{-3} mbar and 2.6×10^{-4} mbar at 200 °C respectively). This therefore leads to competing effects as KNH_2 is less volatile than $NaNH_2$, but K metal is more volatile than Na metal (the products of amide decomposition). It will therefore be important to investigate which effect is dominant and has the greatest impact on containment and this should lead

to an understanding of whether is is the amide or the metal escaping the reactor that is the problem.

	Melting	Onset of decomposition	M^+ radius (pm) [60]
$LiNH_2$	375 °C	347 °C	76
$NaNH_2$	210 °C	420 °C	102
KNH_2	338 °C	400 °C	138
$RbNH_2$	309 °C	-	152
$CsNH_2$	-	-	167

	Synthesis	Separation	Full sample melt	Onset of decomposition
$Li_3K(NH_2)_4$	161 °C	199 °C	212 °C	300 °C
$LiK_2(NH_2)_3$	-	163 °C	167 °C	350 °C

Table 4.1: Group 1 amide melting points, decomposition temperatures and ionic radii. The melting points and decomposition temperatures have uncertainties of ± 1 °C. Also key thermodynamic temperatures of the main mixed-metal amide components of the Li-K-N-H system

4.1.1.1 Thermal analysis comparison

In order to evaluate the decomposition properties of the mixed-metal amides, understanding the behaviour of the constituent single metal amides is an important first step. $LiNH_2$ alone has already been analysed in Section 3.3.1.1 as part of the Li-Na-N-H system. It has been proposed that the higher melting point of KNH_2 (338 °C) compared to $NaNH_2$ (210 °C) will mean that molten KNH_2 is less mobile than $NaNH_2$ so there will be less material loss. There is some evidence to support this from experiments investigating potassium amide alone. DSC data were obtained for both KNH_2 (green) and $NaNH_2$ (red) and are shown (alongside $LiNH_2$ for comparison) in Figure 4.1. This shows that $NaNH_2$ melts at 195 °C and recrystallises on cooling at 170 °C. By contrast KNH_2 melts at 324 °C and recrystallises on cooling at 319 °C. During the TGA part of the STA experiment, neither $NaNH_2$ or KNH_2 show material mass loss, which is as expected given the experiments were only heated to 380 °C and both $NaNH_2$ and KNH_2 are expected to decompose at temperatures above this

limit. It is also likely that the enclosed pan set-up of the STA equipment will prevent any material escaping.

KNH_2 is known to undergo phase changes from monoclinic to tetragonal to cubic at 53 °C [150] and 75 °C [211] respectively on heating. The increased symmetry observed at higher temperatures is due to the increasing orientational disorder of the amide anions and these two phase transitions and the associated rotational dynamics are reversible on cooling if the maximum temperature on heating is kept below the 340 °C, the decomposition temperature of KNH_2.

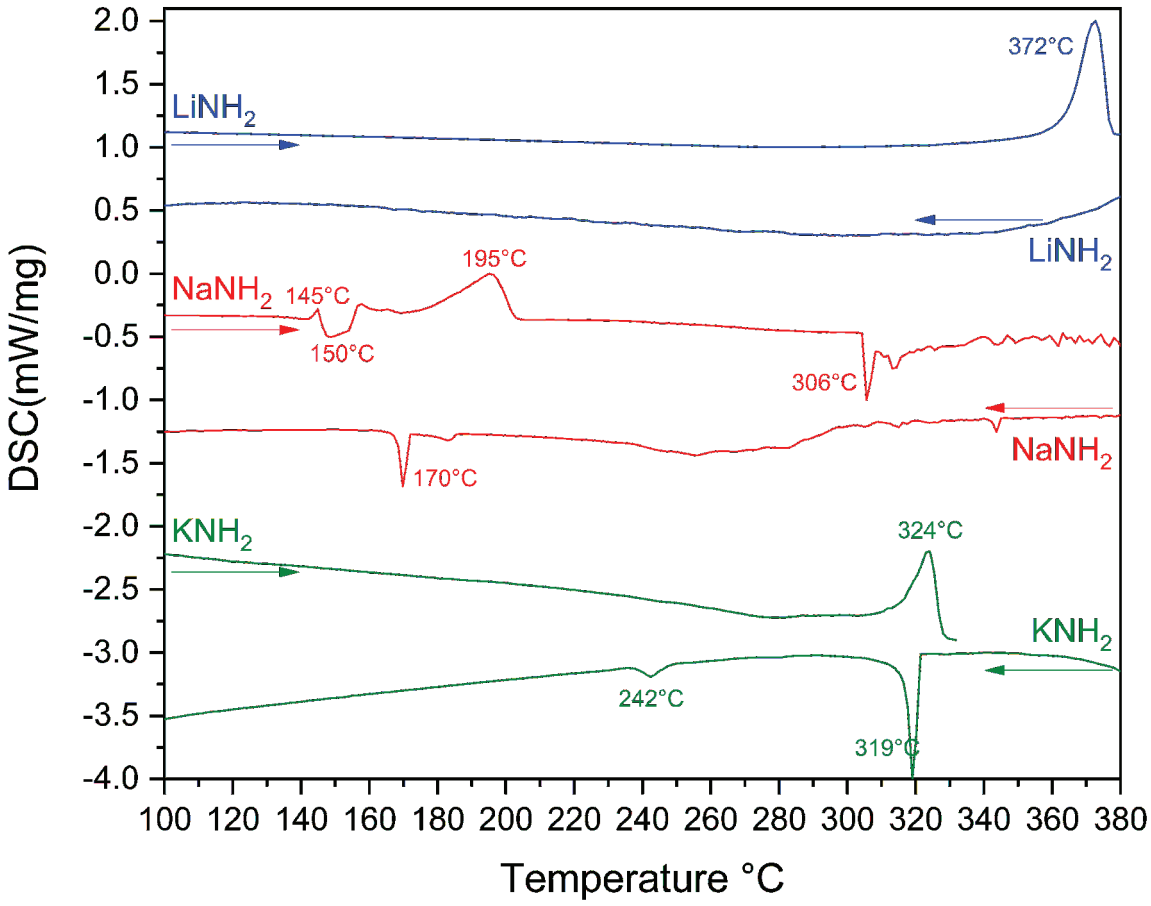


Figure 4.1: STA traces for $LiNH_2$, $NaNH_2$ and KNH_2

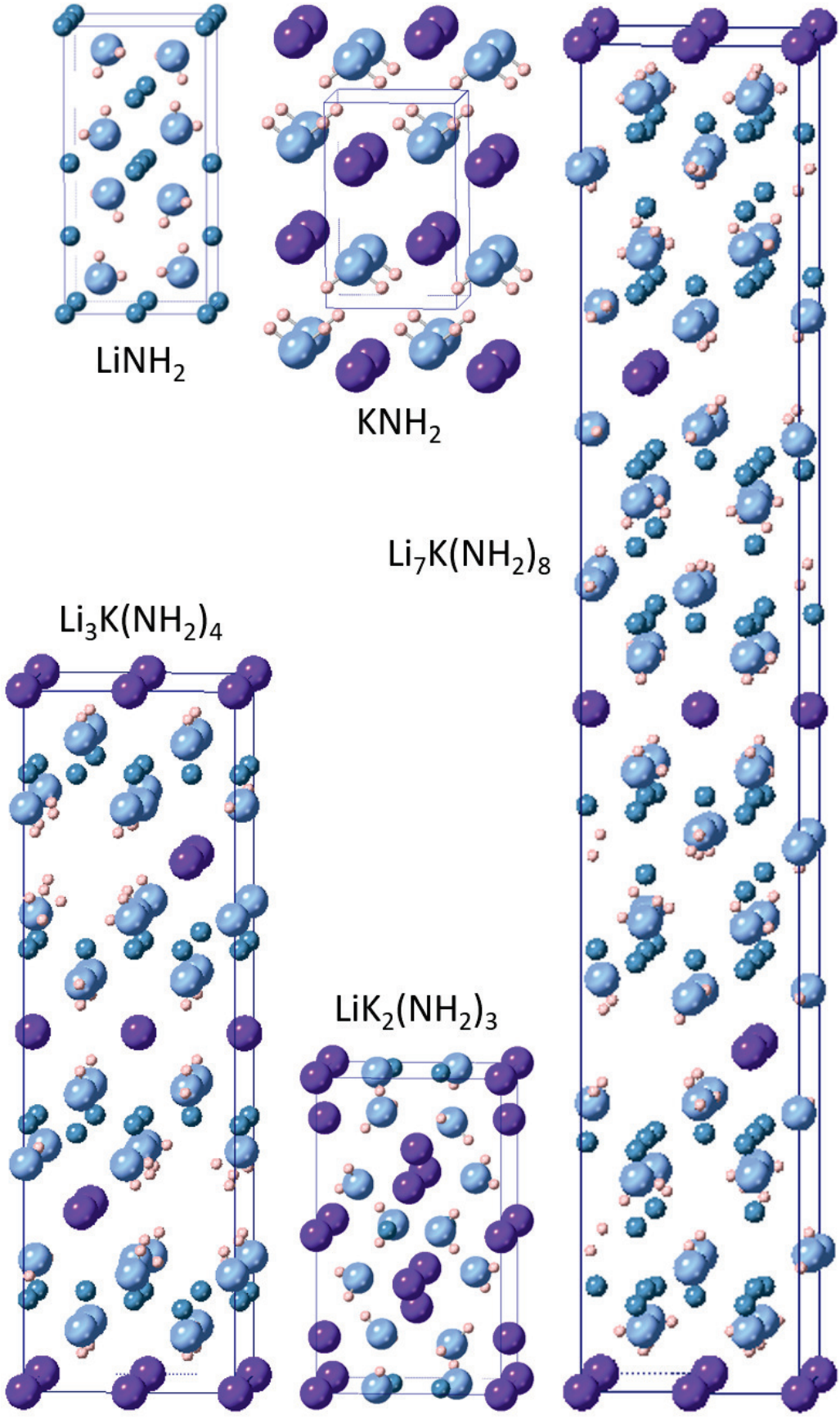


Figure 4.2: Crystallographic unit cells for $LiNH_2$, KNH_2 monoclinic, $Li_3K(NH_2)_4$, $LiK_2(NH_2)_3$ and $Li_7K(NH_2)_8$, roughly proportional in size. Teal = Lithium, Purple = Potassium, Blue = Nitrogen, Pink = Hydrogen

4.1.2 Crystallography

Figure 4.2 shows the crystallographic unit cells for $LiNH_2$, KNH_2 monoclinic, $Li_3K(NH_2)_4$, $LiK_2(NH_2)_3$ and $Li_7K(NH_2)_8$ at approximately similar scales.

As with $Li_3Na(NH_2)_4$, $Li_3K(NH_2)_4$ is based on an expanded version of $LiNH_2$ (elongated along the c axis) where $\frac{1}{4}$ of the Li^+ have been replaced by K^+ cations. $Li_3K(NH_2)_4$ is made up of alternating layers of edge sharing tetrahedra $[Li_3(NH_2)_4]^-$ ($\frac{3}{4}$ filled with Li^+) and with K^+ in an eight-fold quadratic prismatic (body centred) arrangement. The K^+ in $Li_3K(NH_2)_4$ have a greater coordination environment than the Na^+ in $Li_3Na(NH_2)_4$ due to their larger ionic radii. The K^+ ions form layers of perpendicular face-sharing body-centred chains. The ordered distribution of the cations is controlled by the orientation of the amide ions because the hydrogens of the amide ions point into the equivalent (vacant) sites where K^+ ions would otherwise be. $Li_3K(NH_2)_4$ crystallises in the $I4_1/amd$ space group but $Li_3Na(NH_2)_4$ and $LiNH_2$ crystallise in the $I\bar{4}$ space group.

$Li_3K(NH_2)_4$ can be considered as an example of an ordered defect structure of the $ThCr_2Si_2$ type. The high 2D mobility in $Li_3Na(NH_2)_4$ arises from the fact both Li^+ and Na^+ exist in tetrahedral holes, which leads to non-stoichiometry arising from ion interchange. However, Li^+ and K^+ have a much greater difference in ionic radii (Table 4.1) so in $Li_3K(NH_2)_4$ they are in different coordination environments. The Li^+ exist in tetrahedral holes too small for K^+, and K^+ exist in 8-coordinate body-centred holes too large for Li^+. It is therefore likely that $Li_3K(NH_2)_4$ does not show the non-stoichiometry observed for $Li_3K(NH_2)_4$ and $LiNH_2$.

$LiNa_2(NH_2)_3$ and $LiK_2(NH_2)_3$ (and $NaK_2(NH_2)_3$) are isostructural with the same $P4_2/m$ structure. In $LiK_2(NH_2)_3$, $\frac{3}{4}$ of the K^+ cations display octahedral (less stable and higher energy) coordination and $\frac{1}{4}$ show tetrahedral coordination, and are all situated in environments too large for Li^+ cations. The Li^+ cations are tetrahedrally coordinated by NH_2^- ions in environments too small for K^+ cations. This distinct difference between cation coordination environments combined with the presence of a screw axis indicating the anion array in $LiK_2(NH_2)_3$ is substantially distorted from an ideal cubic close packed structure, prevents a clear cation migration pathway. Cross occupation of the metal sites in $LiK_2(NH_2)_3$ is not

possible, ionic mobility is suppressed and so $LiK_2(NH_2)_3$ only exists as a pure, single and fully stoichiometric line phase. In $LiK_2(NH_2)_3$, there are pairs of edge sharing $[Li_2(NH_2)_6]^{4-}$ tetrahedra which are interconnected by three octahedrally coordinated and symmetry inequivalent potassium ions. Each octahedron is connected to another symmetry equivalent one, forming a pair of edge-sharing octahedra. These octahedron pairs share edges and corners with the edge-sharing tetrahedra of $[Li_2(NH_2)_6]^{4-}$ and generate infinite 3D networks [168].

$Li_7K(NH_2)_8$ ($I4_1/a$) is based on an expanded version of $Li_3K(NH_2)_4$ ($I4_1/amd$) and is a member of the hypothetical family of phases of general formula $Li_nK(NH_2)_{n+1}$ for n = 3–15 (and beyond) where the K^+ layers are separated by ever larger lithium containing blocks. In $Li_3K(NH_2)_4$ the K^+ face-sharing body centered layers are separated by one $\frac{3}{4}$ filled layer of $[Li_3(NH_2)_4]^-$ edge sharing tetrahedra. In $Li_7K(NH_2)_8$ the the K^+ layers are separated by one $\frac{3}{4}$ filled $[Li_3(NH_2)_4]^-$ layer, one $\frac{1}{4}$ filled $[Li_3(NH_2)_4]^-$ layer followed by another $\frac{3}{4}$ filled $[Li_3(NH_2)_4]^-$ layer (to account for the different stoichiometry).

4.1.3 Chapter overview

Whereas $Li_3K(NH_2)_4$ formed easily from existing solid-state synthesis methods, the synthesis of $LiK_2(NH_2)_3$ required the development of a novel low temperature method involving ball-milling the constituent amides together in the relevant ratio. The development of this mild technique is particularly valuable, as previous synthesis methods have required the use of autoclaves which is experimentally very challenging and energy intensive.

Given the success of the ball-mill preparation method for the synthesis of $LiK_2(NH_2)_3$, a survey of the whole phase space between $LiNH_2$ and KNH_2 was performed which led to the discovery of a previously undiscovered phase of the Li-K-N-H system of approximately 1:1 $LiNH_2$:KNH_2 stoichiometry.

Despite the discovery of this phase, it could not be unequivocally crystallographically characterised, and it is only $Li_3K(NH_2)_4$ and $LiK_2(NH_2)_3$ that could be made in routinely high purity. It is therefore these two mixed-metal amides which were investigated further and in depth.

A thorough investigation of the thermogravimetric and decomposition behaviour of high-purity samples of $Li_3K(NH_2)_4$ and $LiK_2(NH_2)_3$ under inert gas was performed. This was done both *ex-situ* by a number of techniques and also *in-situ* on the GEM beamline at ISIS. Finally the catalytic activities of $Li_3K(NH_2)_4$ and $LiK_2(NH_2)_3$ towards NH_3 decomposition were investigated.

4.2 Synthesis

4.2.1 $Li_3K(NH_2)_4$

In a similar manner to the mixed lithium-sodium amides, the solid state reaction of $3LiNH_2 + KNH_2$ in the tube furnace, ball-mill and on the gas flow panel under argon resulted in the successful synthesis of $Li_3K(NH_2)_4$ (Table 2.4 in Section 2.2.4.2). However on the gas flow panel under ammonia, very different powder X-ray diffraction data was collected in which $Li_3K(NH_2)_4$ was only a minor component. This is discussed in more detail in Section 4.4.

4.2.2 $LiK_2(NH_2)_3$

Initial attempts to synthesise $LiK_2(NH_2)_3$ in the tube furnace and on the gas flow panel under argon produced samples that were only partially pure ($\approx 42.0\%$ $LiK_2(NH_2)_3$) and are discussed more fully in Section 2.2.4.2.

An STA experiment (both DSC and TGA) was therefore performed on a sample of $LiNH_2 + 2KNH_2$ (Figure 4.3) with the aim of determining the synthetic step for $LiK_2(NH_2)_3$ formation and to ascertain to which temperature the hand-ground mixture of constituent single metal amides needed to be heated to form $LiK_2(NH_2)_3$.

Figure 4.3 shows the known KNH_2 phase changes from monoclinic to tetragonal to cubic at 65 °C and 89 °C respectively, which are slightly higher than the reported values of 53 °C [150] and 75 °C [211] for these two phase changes.

The heating part of the DSC data in Figure 4.3 shows many exothermic peaks centred at 166 °C, 202 °C, 257 °C and 292 °C. Figure 4.1 shows that in the DSC data for $LiNH_2$ and KNH_2, there are no features below 324 °C when KNH_2 melts, which then recrystallises on cooling at 319 °C. This could account for the features seen here at 312 °C on heating and

309 °C on cooling, suggesting that if some $LiK_2(NH_2)_3$ did form in this experiment, (as in the tube furnace) the reaction was incomplete. Further evidence of some unreacted KNH_2 on cooling is the exotherm at 242 °C which is visible in both Figure 4.3 and Figure 4.1 and the exotherms at 65 °C and 82 °C for the cubic to tetragonal to monoclinic KNH_2 phase changes on cooling.

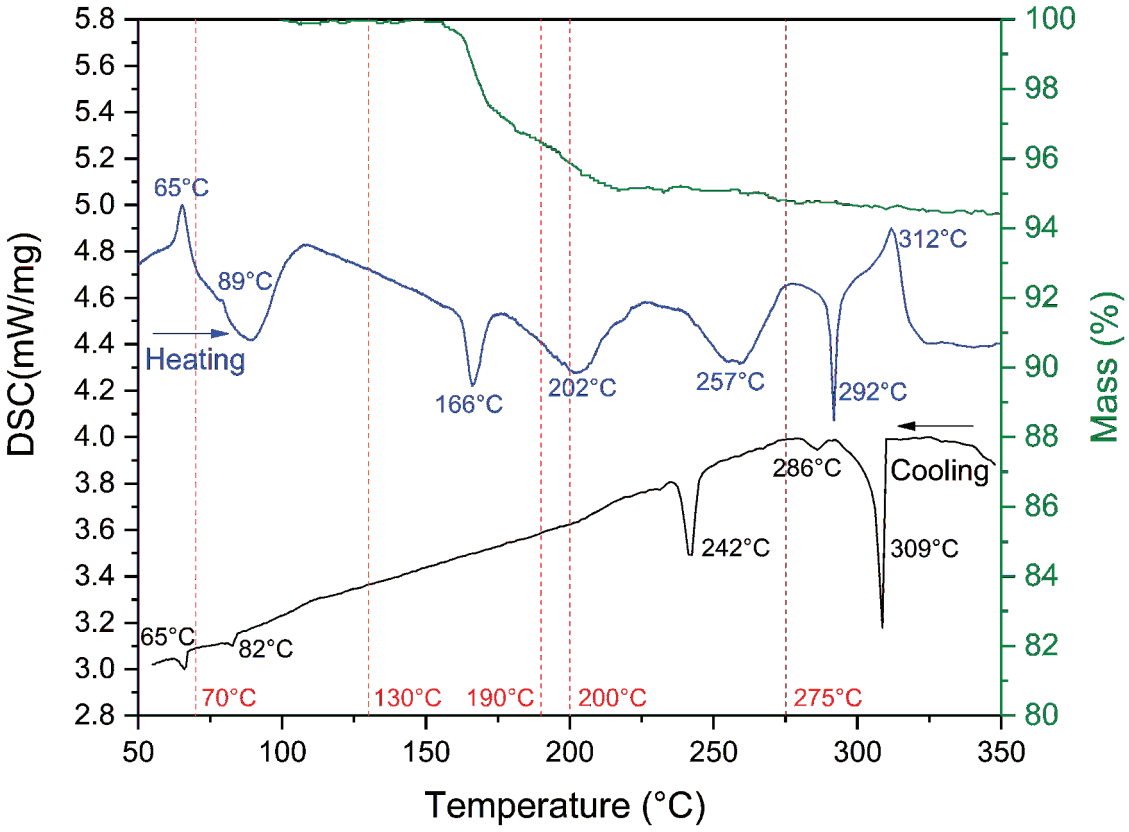


Figure 4.3: STA for $LiNH_2 + 2KNH_2$

The percentage mass curve in Figure 4.3 shows that the thermal events at 166 °C and 202 °C both have associated mass losses. The sharp thermal event at 166 °C also has a steeper mass loss (3 % total) than the broader thermal event at 202 °C which has a shallower mass loss (2.5 % total). One of these events could be desorption of physisorbed gases from the powder grains and the other could correspond to $LiK_2(NH_2)_3$ formation, as the powder X-ray diffraction data collected at 200 °C does contain 41.0 % $LiK_2(NH_2)_3$. However, it would perhaps be expected that the synthesis of $LiK_2(NH_2)_3$ would be endothermic (as it was for $LiNa_2(NH_2)_3$) as formation of this crystal structure would require total rear-

rangement of Li^+, K^+ and NH_2^- ions which would be a high energy process.

Based on the DSC data shown in Figure 4.3, in order to obtain a better understanding of what each individual thermal event refers to, the reaction of $LiNH_2 + 2KNH_2$ in the tube furnace was repeated and held at a range of temperatures (70 °C, 130 °C, 190 °C and 275 °C) indicated by dotted red lines in Figure 4.3. Powder X-ray diffraction data was collected for each sample once it had been cooled back down to room temperature, and the percentage composition of each is shown in Figure 4.4 (Samples A-E) and detailed in Table A.2.

Analysis of the samples prepared in the tube furnace in Figure 4.4 shows the onset of $LiK_2(NH_2)_3$ formation occurs at 125 °C and increases to a maximum purity of 42-44 % at 200 °C. The percentage composition of $LiK_2(NH_2)_3$ does not increase much between 200 °C and 275 °C. This indicates that the thermal event most likely to relate to $LiK_2(NH_2)_3$ synthesis is the 166 °C exotherm. It is clear that using the tube furnace for the synthesis of $LiK_2(NH_2)_3$ does not cause the reaction to go to completion.

Due to the inability to form high purity $LiK_2(NH_2)_3$ in the tube furnace or on the gas flow panel, the ball-mill was investigated for the synthesis of $LiK_2(NH_2)_3$, the first time this method had been used for the preparation of mixed-metal amides. Multiple different experiments using the ball-mill were performed as explained in Section 2.2.4.2, and a set of conditions were found for the routine synthesis of $LiK_2(NH_2)_3$ at close to 100 % purity.

The closed environment of the ball-mill prevents the loss of any reactants. Additionally, obtaining a good degree of mixing for hand-ground samples can be difficult, but when the ball-mill is used it is much more reliable to achieve a consistent level of mixing and so is a much more successful technique to use for upscaling the synthesis to commercial quantities.

It is clear from Figure 4.4 that using the ball-mill is a much more successful method for synthesising $LiK_2(NH_2)_3$ than heat treatment in the tube furnace. The unit cell volume of $Li_3K(NH_2)_4$ (1255.02 Å^3) is 2 % larger than the sum of the volumes of $3LiNH_2 + KNH_2$ (1224.93 Å^3), while the unit cell volume of $LiK_2(NH_2)_3$ (552.81 Å^3) is 4 % smaller than the sum of the volumes of $LiNH_2 + 2KNH_2$ (575.54 Å^3). This may explain why $LiK_2(NH_2)_3$ is readily formed by mechanochemical treatment (compression), and $Li_3K(NH_2)_4$ is easily produced by heat treatment (thermal expansion).

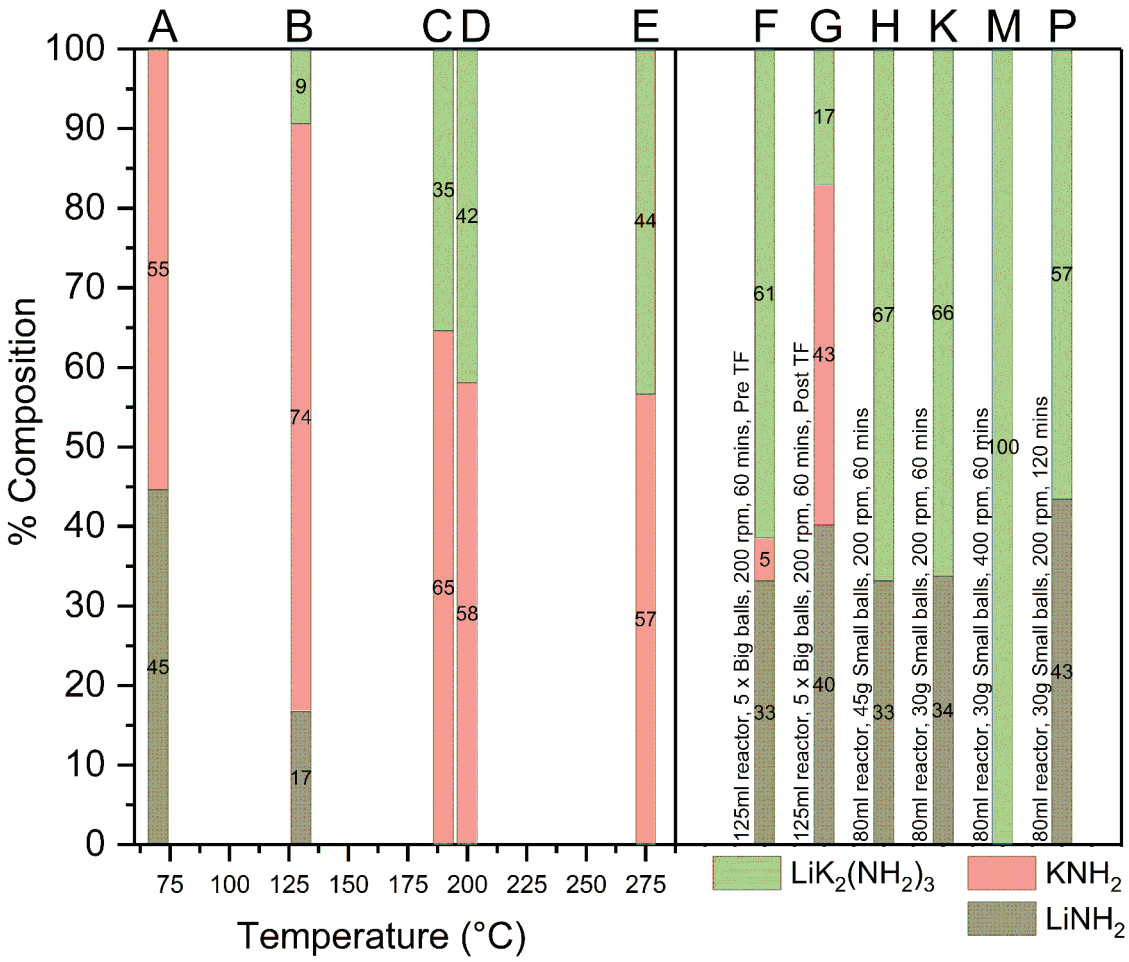


Figure 4.4: Percentage composition of $LiNH_2 + 2KNH_2$ heated to different temperatures in the tube furnace and under different conditions in the ball-mill as detailed in Table A.2

Ball-milling $LiNH_2$ and KNH_2 in a 1:2 ratio clearly presents a novel method for the simple, quick and reliable synthesis of $LiK_2(NH_2)_3$ in much milder conditions than previously reported methods. Samples of $LiK_2(NH_2)_3$ synthesised in the ball-mill were therefore used for further analysis throughout this thesis.

4.2.3 $Li_7K(NH_2)_8$

Samples with a 7:1 ratio of $LiNH_2$:KNH_2 heated in the tube furnace or placed in the ball-mill produced $Li_3K(NH_2)_4$ ($\sim$55.0 %) with a minor phase of $LiNH_2$ ($\sim$45.0 %) instead of $Li_7K(NH_2)_8$ (Section 2.2.4.2).

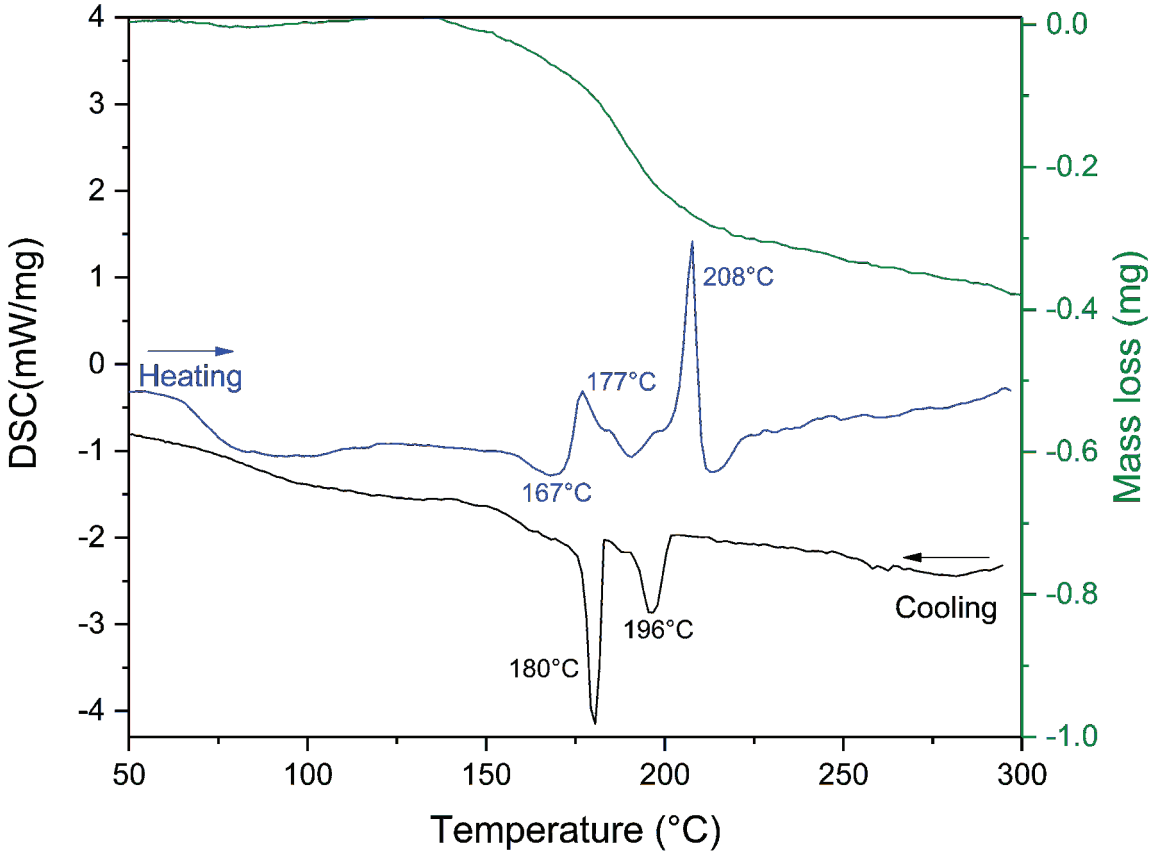


Figure 4.5: STA trace for $7LiNH_2 + KNH_2$

An STA experiment was therefore performed on a sample of $7LiNH_2 + KNH_2$ (Figure 4.5) to try and identify thermal events which could correspond to the synthesis of $Li_7K(NH_2)_8$. From Figure 4.1 it can be seen that alone, $LiNH_2$ and KNH_2 only show thermal events at 373 °C and 324 °C respectively when they melt. Therefore in Figure 4.5 a mixed-metal amide is being made, as this trace shows additional thermal events compared to the single metal amides alone. In Figure 4.5 the phase changes for KNH_2 monoclinic to tetragonal to cubic reported at 53 °C [150] and 75 °C [211] respectively are not seen, likely due to the fact that because of the 7:1 ratio of $LiNH_2$:KNH_2, the lithium amide dom-

inates the STA signal. From the STA experiments shown in Figure 4.15 and Figure 4.28 it can be seen that on heating $Li_3K(NH_2)_4$ and $LiK_2(NH_2)_3$ each show two endotherms at 199 °C/212 °C and 148 °C/≈165 °C respectively. The endotherms seen in Figure 4.5 for this 7:1 ratio at 177 °C/208 °C align much more closely with those of $Li_3K(NH_2)_4$, as expected from the powder X-ray diffraction data (Figure A.5). This therefore confirms that instead of $Li_7K(NH_2)_8$, it is $Li_3K(NH_2)_4$ that is being synthesised as the more thermodynamically stable product. Figure 4.5 shows an exotherm at 167 °C which also aligns well with that seen in Figure 4.15 at 161 °C which corresponds to the synthesis of $Li_3K(NH_2)_4$.

It is likely that the mass loss observed in the TGA part of the trace (green) is due to desorption of physisorbed gases within the powder grains on melting. The exotherms in Figure 4.5 on cooling at 196 °C/180 °C are the reverse steps of the endotherms at 208 °C/177 °C respectively and also correlate well with the exotherms observed on cooling in Figure 4.15 at 188 °C/182 °C.

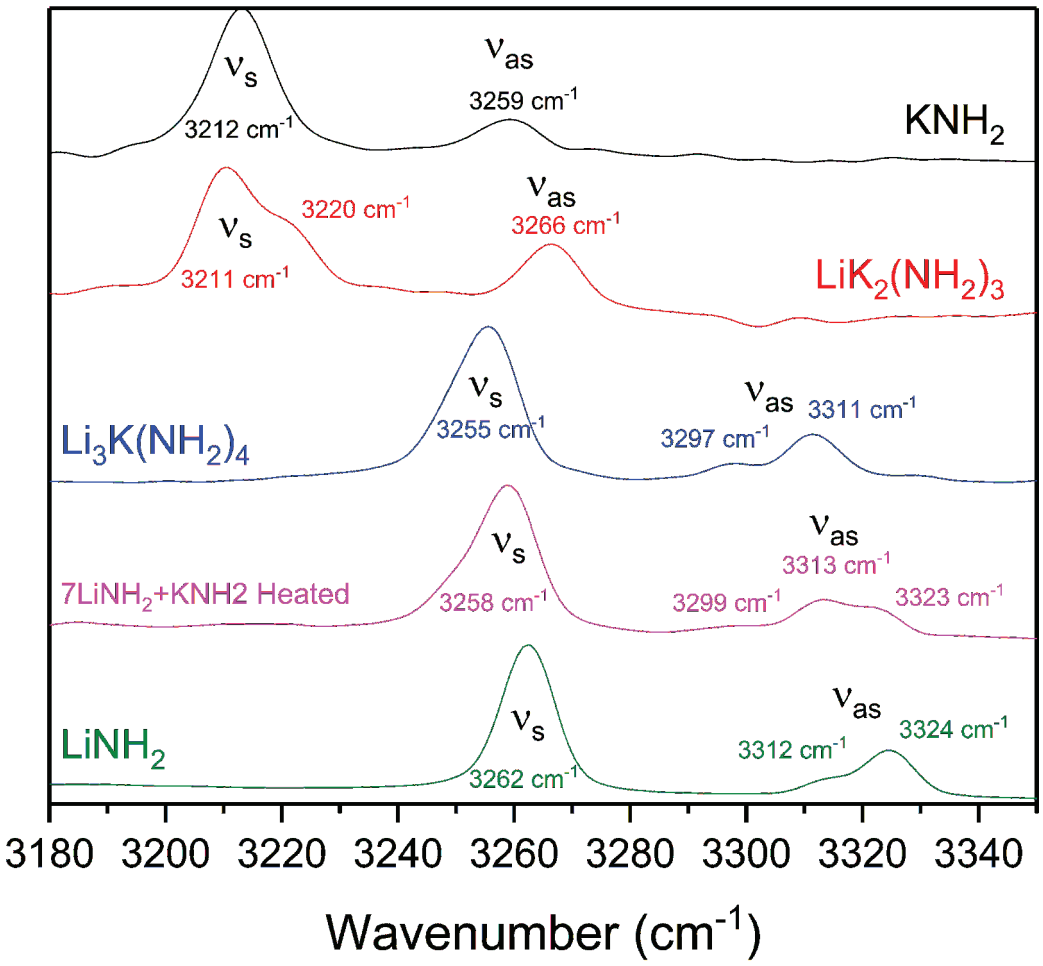


Figure 4.6: Raman traces for the known phases of the Li-K-N-H system

Figure 4.6 exemplifies how the structural relationship between the members of the Li-K-N-H system plays out in the Raman spectra. The $LiK_2(NH_2)_3$ Raman stretches are most similar to those of KNH_2 due to the similar local coordination geometry. In $LiK_2(NH_2)_3$ the amide ions are more strongly coordinated by potassium than in $Li_3K(NH_2)_4$, so the stretching frequencies observed are most similar to those of KNH_2. $Li_3K(NH_2)_4$ is essentially a layered version of $LiNH_2$ so it is unsurprising that the Raman stretches are most similar to $LiNH_2$, but are shifted to a lower wavenumber as a result of coordination to some potassium in addition to lithium (which has a different Pauling electronegativity).

Figure 4.6 shows that the sample of $7LiNH_2 + KNH_2$ heated in the tube furnace produced a Raman pattern which is a superposition of those of $Li_3K(NH_2)_4$ and $LiNH_2$ which was expected given this was the composition of the sample determined by powder X-ray diffraction.

It was concluded that the harsh conditions provided by the high-pressure autoclaves [148] were essential for the successful direct synthesis of $Li_7K(NH_2)_8$. As no $Li_7K(NH_2)_8$ could be formed here, no further analysis on this reported member of the Li-K-N-H system could be performed.

4.3 Phase space between $LiNH_2$ and KNH_2

Having developed the novel ball-milling technique to synthesise $LiK_2(NH_2)_3$, a survey of the whole phase space between $LiNH_2$:KNH_2 was investigated via this technique to determine if any other phases could be formed. This was performed by ball-milling together nine molar ratios between the two end members ($LiNH_2$:KNH_2 of 11:1, 9:3, 8:4, 7:5, 6:6, 5:7, 4:8, 3:9, 1:11).

3 mg of a hand-ground mixture of each sample was analysed by STA (heated from 20 °C to 400 °C at 5 °C /min) in order to identify the temperatures corresponding to any synthesis, phase change or decomposition events of possible mixed-metal amides for each ratio. The remainder of each hand-ground mixture was ball-milled for 1 hour. For each resulting sample, powder X-ray diffraction data was collected on I11 at Diamond and a Raman spectrum obtained. In addition to the two known phases $Li_3K(NH_2)_4$ and $LiK_2(NH_2)_3$, a third, unknown phase has been identified in the samples with $LiNH_2$:KNH_2 ratios of 9:3, 8:4, 7:5, 6:6 and 5:7.

4.3.1 I11 powder X-ray diffraction

Figure 4.7 shows the powder X-ray diffraction data collected on I11 for each of the ratios investigated between the $LiNH_2$ and KNH_2 end members alongside the percentage composition of each sample determined using TOPAS.

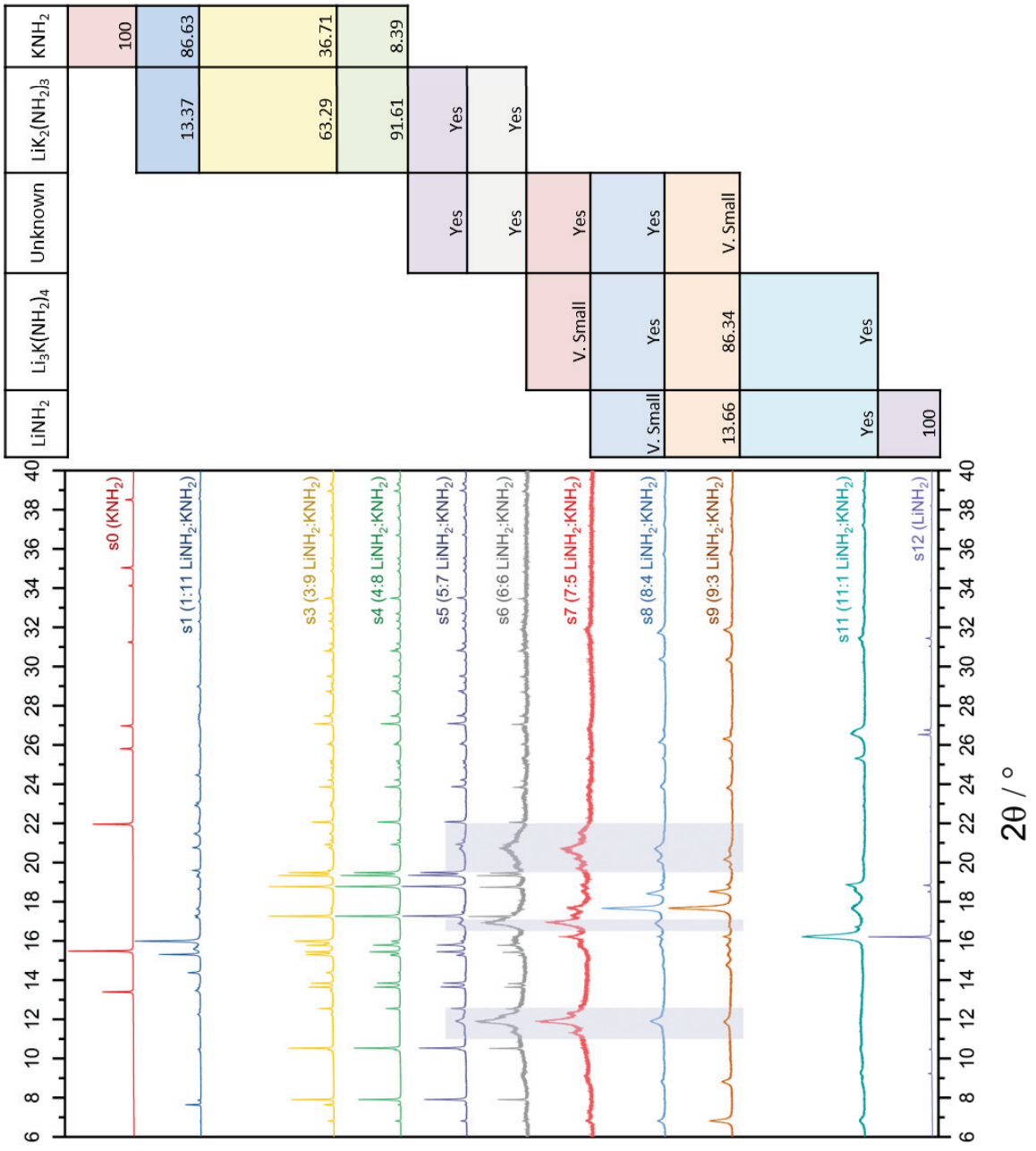


Figure 4.7: I11 powder X-ray diffraction data for the phase space between $LiNH_2$ and KNH_2 and percentage composition of each pattern

As would be expected, the 4:8 $LiNH_2$:KNH_2 ratio contains the greatest proportion of $LiK_2(NH_2)_3$ and the 9:3 $LiNH_2$:KNH_2 ratio contains the greatest proportion of $Li_3K(NH_2)_4$. Qualitatively it can be seen that there is an unknown phase present in the 5:7, 6:6, 7:5, 8:4 and to a very small extent, the 9:3 ratio. The peaks of this unknown phase are particularly broad and can be seen most clearly by the large features at 2θ values of 11.87°, 16.94°, 20.67° (highlighted by shaded purple boxes) but peaks are also observed at 2θ values of 11.29°, 12.31°, 12.63°, 17.27°, 17.65°, 19.68°, 20.21° and 21.49°. The unknown phase is present in the greatest proportion (visually) in the 6:6 and 7:5 ratios but is discussed further in Section 4.4.1.

In the 11:1 $LiNH_2$:KNH_2 sample, there are unfitted peaks in the powder X-ray diffraction data that clearly have features of the $Li_3K(NH_2)_4$ structure but are very broad and get progressively sharper between the 11:1 and 9:3 ratios. Additionally, not all of the known $Li_3K(NH_2)_4$ peaks appear in the pattern collected for the 11:1 ratio. The fact the 11:1 $LiNH_2$:KNH_2 sample does not fit well to a crystalline structure may result from the ball-milling preparation of the sample which has led to a disordered and slightly non-stoichiometric version of $Li_3K(NH_2)_4$ in which there is only partial substitution of K^+ for Li^+. Therefore it may be more accurate to think of it as $Li_{4-y}K_y(NH_2)_4$ ($0 < y < 1$) that is present in the 11:1 $LiNH_2$:KNH_2 ratio than fully stoichiometric $Li_3K(NH_2)_4$.

4.3.2 Raman

The Raman spectra of the phase space between $LiNH_2$ and KNH_2 were collected as outlined in Section 2.5.1 with the N−H stretching region for each of the phases shown in Figure 4.8. The only well resolved vibrational modes in the spectra were the symmetric and anti-symmetric stretching modes of the NH_2^- anion. The peaks were fitted to pseudo-Voigt functions in TOPAS and the positions of these have been overlain with the Raman spectra.

Given the differences in the intensity of the absolute signals given by the various samples, it is difficult to compare the peak heights or areas directly, so the discussion of these data is limited to a comparison of relative peak areas and the position of the peaks. Fitting of the data provides a degree of insight into the composition of the spectra, with the best fit obtained by the inclusion of some additional N-H stretches.

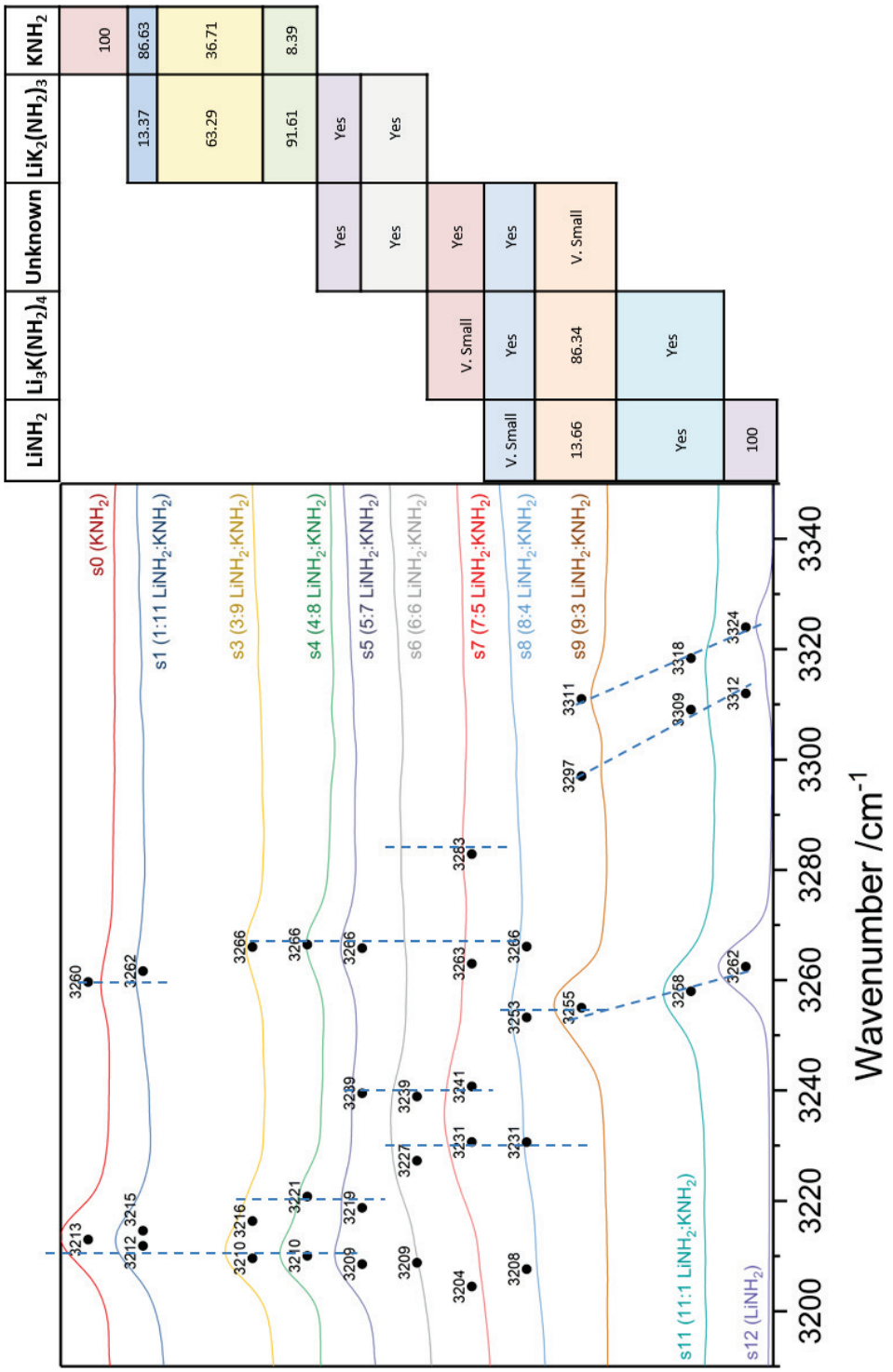


Figure 4.8: Raman spectra of the phase space between $LiNH_2$ and KNH_2 alongside the percentage composition of each sample

Lithium amide shows the characteristic vibrations for an NH_2 unit with the symmetric N−H stretch at 3262 cm^{-1} and the asymmetric N−H stretches at 3314 cm^{-1} and 3325 cm^{-1}. Potassium amide shows a symmetric N−H stretch at 3212 cm^{-1} and the asymmetric N−H stretch at 3260 cm^{-1} as would be expected [82, 83].

The NH_2^- stretching modes of $LiNH_2$ are located at a higher energy than those of KNH_2 reflecting a stronger N−H bond, due to inductive effects arising from the different electronegativities of Li^+ and K^+ which have Pauling electronegativities of 0.98 and 0.82 respectively [41].

A small shoulder is observed on the asymmetric stretch of $LiNH_2$ (which is absent from that of KNH_2) due to slight variations in the chemical environments of the NH_2 group and potential non-stoichiometry of the $LiNH_2$ system. A shoulder is also visible in the symmetric stretch of $LiK_2(NH_2)_3$ and asymmetric stretch of $Li_3K(NH_2)_4$ (it was also visible in the asymmetric $Li_3Na(NH_2)_4$). The shoulder arises because the environments of the two H atoms of the NH_2^- units are slightly different, due to the orientation of the two N−H bonds with respect to the Li^+ and/or K^+ ions in the cationic sub-lattice.

Examination of Figure 4.8 shows that the transition through the range of stoichiometry values does not result in a simple linear decrease in the $LiNH_2$ peaks, and a concomitant increase in the KNH_2 peaks. Additional peaks are observed in the spectra, which are most pronounced in the intermediate stoichiometry range. The intermediate stoichiometries have Raman stretches that are not equivalent to either $LiNH_2$ or KNH_2 indicating that one or more double-cation amides have formed.

Given that the amide units in $Li_3K(NH_2)_4$, $LiK_2(NH_2)_3$ and presumably the unknown phase coordinate both Li^+ and K^+ ions, it is not surprising that the energies of the Raman modes for these materials lie between those of the two parent compounds.

From Figure 4.8 it can be seen there are three N−H stretches observed for $Li_3K(NH_2)_4$ (s9) identified at 3255 cm^{-1}, 3297 cm^{-1} and 3311 cm^{-1}, and a shoulder is observed on the asymmetric stretch of $Li_3K(NH_2)_4$ which is in line with the literature [82, 83, 178].

From $LiNH_2$ (s12) to $Li_3K(NH_2)_4$ (s9), there is a gradual progression of the Raman peaks which is consistent with the powder X-ray diffraction data shown in Figure 4.7 where it was deduced that the 11:1 $LiNH_2$:KNH_2 sample possibly contained a disordered or variable

stoichiometry $Li_{4-y}K_y(NH_2)_4$ ($0 < y < 1$) type phase (due to the broad peaks) which did not fit a fully crystalline $Li_3K(NH_2)_4$ phase. This conclusion is supported by these Raman data which show that the 11:1 ratio has peaks which are shifted to higher wavenumbers than the $Li_3K(NH_2)_4$ sample, but are still at lower wavenumbers than the stretches seen for $LiNH_2$ alone.

From Figure 4.8, it can be seen there are three N−H stretches observed for $LiK_2(NH_2)_3$ (s4) at $3210\,cm^{-1}$, $3221\,cm^{-1}$ and $3266\,cm^{-1}$ which is in line with the literature [178]. Comparison between KNH_2 and $LiK_2(NH_2)_3$ and the various ratios between (s1 and s3) supports the idea that $LiK_2(NH_2)_3$ is present only as a line-phase and does not accommodate variable stoichiometry. The Raman spectra in Figure 4.8 show this, as the wavenumbers of the peaks do not vary gradually as would be expected for a steady stoichiometry change, but instead appear at set points as linear combinations, which is more consistent with separate line phases.

Examination of the region between $Li_3K(NH_2)_4$ and $LiK_2(NH_2)_3$ for the Raman spectra in Figure 4.8, shows there is something else going on entirely, (consistent with the diffraction data in Figure 4.7). This supports the presence of an unknown phase, as additional and different Raman peaks to any of those corresponding to the known phases can be seen at $3231\,cm^{-1}$, $3241\,cm^{-1}$, and $3283\,cm^{-1}$ (for the 7:5 ratio). Locally the Raman stretches of this unknown phase look like they are between those of $LiNH_2$ and KNH_2 which makes sense as the unknown phase is most prevalent in the 6:6 ratio, so the local coordination geometry of the amide ions will be influenced by both lithium and potassium.

4.4 Unknown Li-K-N-H phase

4.4.1 Where it has been observed

Analysis of the powder X-ray diffraction data in Figure 4.7 and the Raman spectra in Figure 4.8 indicates that there is an unknown phase present in the s5-s9 samples, arising from particularly complex powder X-ray diffraction data.

The three unknown large features at 2θ values of 11.87°, 16.94°, 20.67° (highlighted by shaded purple boxes in Figure 4.7) have been fitted to pseudo-Voigt functions in TOPAS.

Figure 4.9 shows the areas of these pseudo-Voigt peaks for the 5:7, 6:6, 7:5, 8:4 and 9:3 ratios. Because the peaks are so big and broad (most likely as a result of the ball-milling synthesis which leads to a low degree of crystallisation) a quantitative principal component analysis is difficult. This would compare the area of the unknown peaks to the area of peaks corresponding to known phases present in each pattern. Instead, it is more instructive to compare the area of each these four broad peaks between each ratio to see where the unknown phase is most prominent, which Figure 4.9 suggests is in the 6:6 $LiNH_2$:KNH_2 ratio.

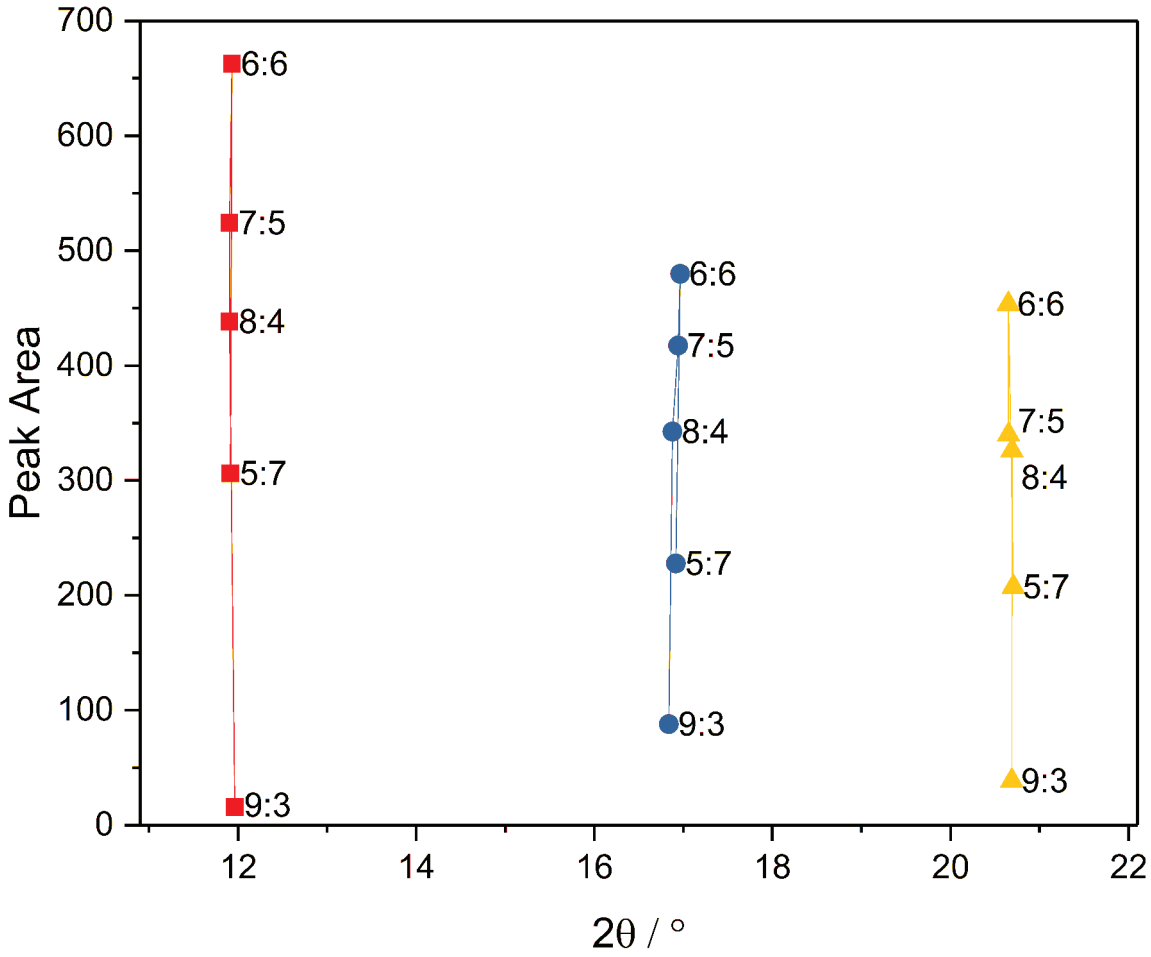


Figure 4.9: Areas of the pseudo-Voigt peaks at 2θ values of 11.87°, 16.94°, 20.67° for the 5:7, 6:6, 7:5, 8:4 and 9:3 ratios (highlighted by shaded purple boxes in Figure 4.7)

Similar powder X-ray diffraction data to that observed for the s5-s9 samples in Figure 4.7 have been collected for other "$Li_3K(NH_2)_4$" synthesis attempts under alternative conditions (Figure 4.10). These include when $LiNH_2$ and KNH_2 are mixed in a 3:1 ratio and heated under NH_3 on the gas flow panel (Section 2.2.4.2), in offline *ex-situ* synthesis attempts on the IGA^n under argon (Section 4.6.2.1), and when $LiNH_2$ and KNH_2 were hand-ground in a 1:1 (analogous to 6:6) ratio and heated to 225 °C in the tube furnace for 12 hours (Section 2.2.4.2).

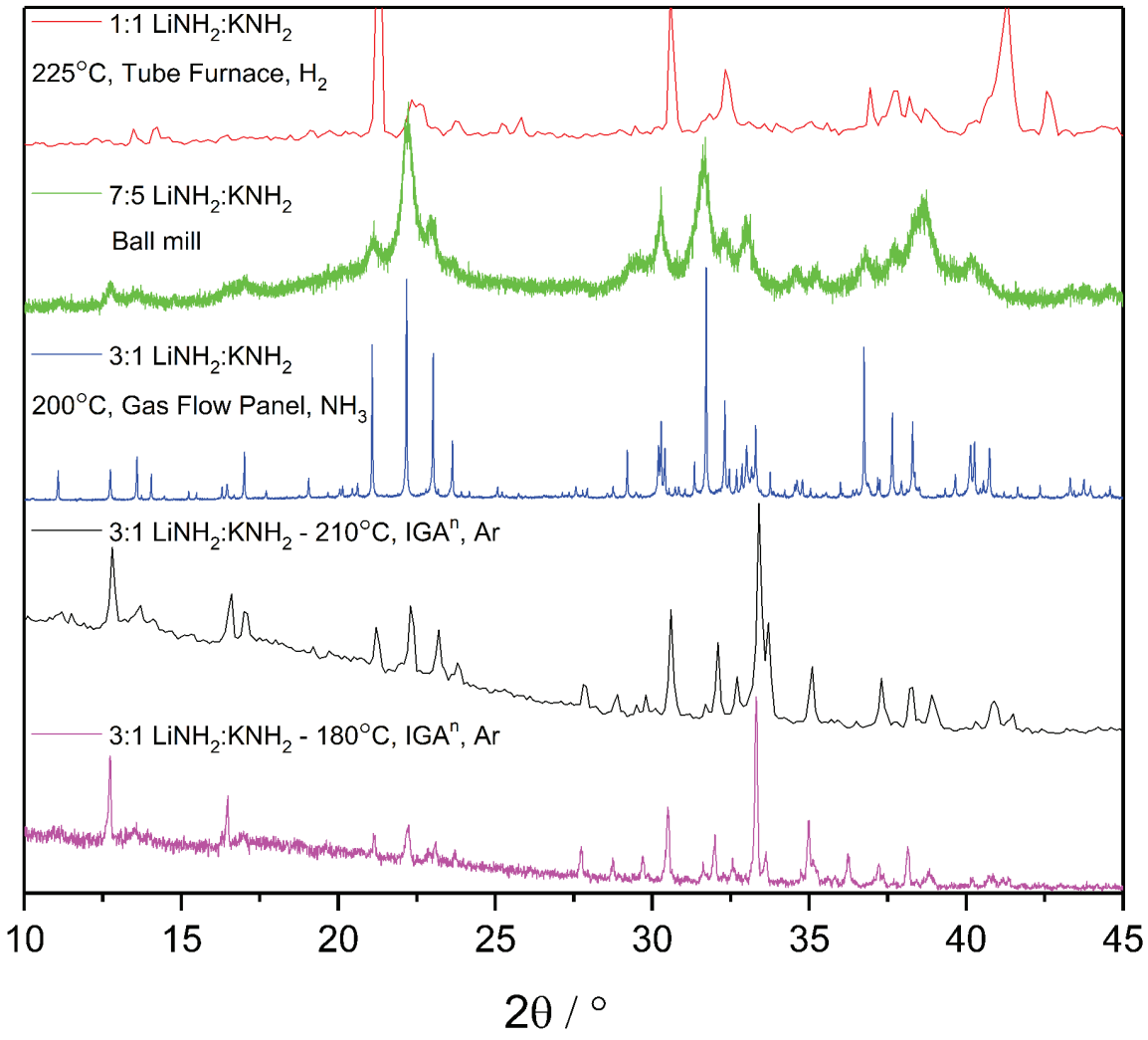


Figure 4.10: Powder X-ray diffraction data of the unknown phase formed under various conditions. Red (top) is the sample when $LiNH_2$:KNH_2 1:1 was heated to 225 °C in the tube furnace for 12 hours. Green is the sample when $LiNH_2$:KNH_2 7:5 was ball-milled at 400 rpm for 60 minutes. Blue is the sample when $LiNH_2$:KNH_2 3:1 was heated to 210 °C on the gas flow panel under NH_3. Purple and magenta (bottom) are the samples when $LiNH_2$:KNH_2 3:1 were heated to 210 °C and 180 °C respectively on the IGA^n under argon

In Figure 4.10 the different resolutions of the traces are due to the different diffractometers used. The red and black powder X-ray diffraction data was collected on the SAXS machine, the magenta diffraction data on the Smartlab (Section 2.6.4.2), the green diffraction data from a 10 minute scan on I11 at Diamond and the blue diffraction data from a 30 minute scan on I11 at Diamond (Section 2.6.4.4). Despite this, it can be qualitatively seen that the Bragg peaks line up, and it is the same phase present in each of the patterns despite the synthesis attempts being performed under a variety of conditions and the patterns being collected on a range of equipment. It is also clear that the samples synthesised on the gas flow panel and during IGA^n, which were just heated, have sharper peaks than those which relied on the mechanical grinding of the ball-mill, which has clearly lead to some amorphisation of the crystals which show significantly broader peaks. Since the half hour scan on I11 at Diamond for the sample of $3LiNH_2 + KNH_2$ heated on the gas flow panel under NH_3 has by far the best resolution, it is this pattern for the "unknown phase" that shall be used for indexing and characterisation attempts.

Recently there have been two literature reports of a similar, if not the same unknown phase. Goshome et al. [109] synthesised a "metal amide complex" from a 1:1 mixture of $LiNH_2$ and KNH_2 which was ball-milled for 10 hours under 0.1 MPa of Ar (analogous to the 6:6 $LiNH_2$:KNH_2 ball-milled sample in Figure 4.7). A Raman spectra collected for this compound shows stretches reported at $3280\,cm^{-1}$ and $3230\,cm^{-1}$, similar to those seen for the 7:5 and 6:6 ball-milled samples in Figure 4.8. Powder X-ray diffraction data of the sample synthesised in the literature also matches up well with the peaks assigned to the "unknown phase" in the 5:7-9:3 samples (Figure 4.7). Goshome et al. [109] suggest the unknown phase formed is a "coexistence of some different phases having a quite similar composition with $LiK(NH_2)_2$" which they describe as "complex $LiK(NH_2)_2$".

Li et al. also ball-milled a 1:1 mixture of $LiNH_2$:KNH_2 at 500 rpm for 12 hours to form a compound described as $LiK(NH_2)_2$ [178]. This compound shows Raman stretches at $3285\,cm^{-1}$, $3274\,cm^{-1}$, $3233\,cm^{-1}$ and $3221\,cm^{-1}$ which matches up well with those seen in [109] and those seen for the 7:5 and 6:6 ball-milled samples in Figure 4.8. The sample reported also shows similar peaks in the powder X-ray diffraction data to those assigned to the unknown phase in the 5:7-9:3 samples (Figure 4.7).

Although both of these papers tentatively suggested a compound "$LiK(NH_2)_2$", neither has made any attempts to index it or crystallographically characterise it and the powder X-ray diffraction data shown have poor resolution.

4.4.2 Raman

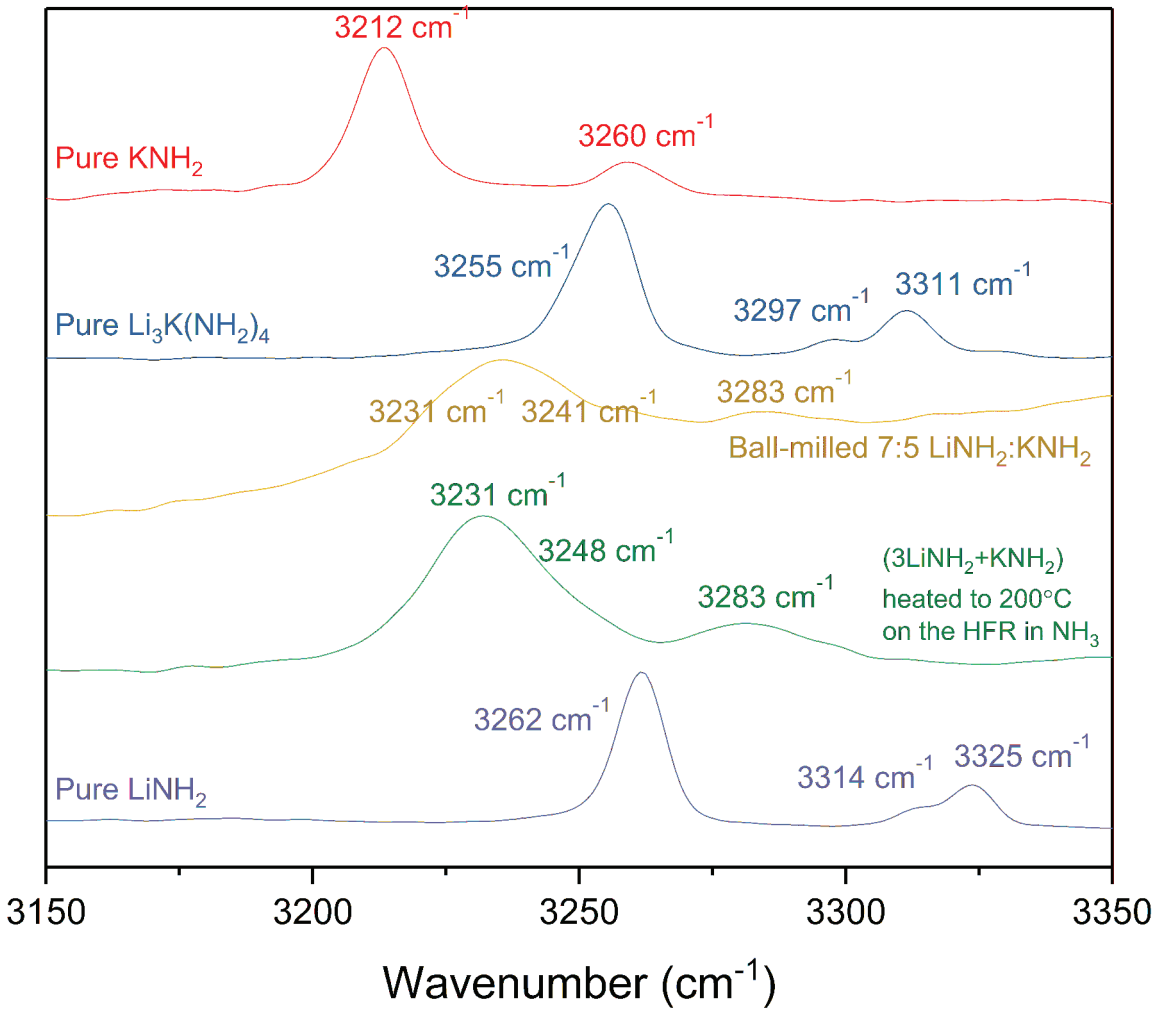


Figure 4.11: Raman spectra of the unknown phase compared those of known members of the Li-K-N-H system

Figure 4.11 shows that the ball-milled 7:5 $LiNH_2$:KNH_2 sample, and the sample formed when $LiNH_2$ and KNH_2 are mixed in a 3:1 ratio and heated under NH_3 on the gas flow panel produce similar Raman patterns. These are clearly different to the Raman spectra of $Li_3K(NH_2)_4$ but are similar to those shown for the "$LiK(NH_2)_2$" compounds discussed in recent literature [109, 178].

4.4.3 Structure solution

The powder X-ray diffraction data in Figure 4.10 (blue), for the sample synthesised when $LiNH_2$ and KNH_2 are mixed in a 3:1 ratio and heated under NH_3 on the gas flow panel (Section 2.2.4.2) is the only high quality powder X-ray diffraction data which can be used for further attempts to characterise this unknown phase.

91 of the powder X-ray diffraction peaks for this pattern (out to 23 Å) were fitted to pseudo-Voigt functions in TOPAS to get accurate peak positions. A Python program was then developed to look for cubic relationships between these peak positions but none were found. Attempts to index these peaks were therefore made in:

- TOPAS [229] with both charge flipping, simulated annealing and fourier difference maps
- DICVOL [44] which is better if there are multiple phases present
- DASH [73] with a variety of rigid body z-matrices based on motifs seen in $Li_3K(NH_2)_4$ and $LiK_2(NH_2)_3$ (Figure 4.12)
- FOX [97] which uses parallel tempering

A comprehensive search of DICVOL suggested a monoclinic structure with $a = 10.99$ Å, $b = 14.97$ Å, $c = 13.00$ Å and $\beta = 105.34°$. DASH was then used to predict the space group $P2_1/a$. Knowledge of volumes "per atom" in $LiNH_2$ and monoclinic KNH_2 (32.47 Å^3 and 55.42 Å^3 respectively) were used to predict the number of Li and K formula units in the unknown phase. A structure with the unit cell parameters predicted by DICVOL would have a volume of 2074.1 Å^3 and $P2_1/a$ structures have four asymmetric units per unit cell giving each asymmetric unit a volume of 518.5 Å^3. This value can then be compared to the sum of different quantities of Li and K units as shown in Table 4.2. The colours represent the similarity between the predicted volume of 518.5 Å^3 and the sum of different quantities of Li and K units. Red values are within 5 % of 518.5 Å^3, orange values are within 10 %, green values are within 15 %, blue values are within 20 %, and purple values are within 25 %. Squares highlighted in yellow represent values that have a 1:1 ratio of Li:K unit

components. A 6:6 ratio of $LiNH_2$:KNH_2 provides the closest fit to 100 % of all the ratios shown in Table 4.2 and particularly of the ratios highlighted along the 1:1 diagonal. A 7:7 ratio of $LiNH_2$:KNH_2 contains too many potassium ions to fit the observed X-ray scattering, whereas a 5:5 ratio leaves unfitted electron density (and 5 ions in an asymmetric unit is very unusual).

		Number of Li units			
		5	**6**	**7**	**8**
Number of K units	**3**	63%	70%	76%	82%
	4	74%	80%	87%	93%
	5	85%	91%	97%	104%
	6	95%	102%	108%	114%
	7	106%	112%	119%	125%

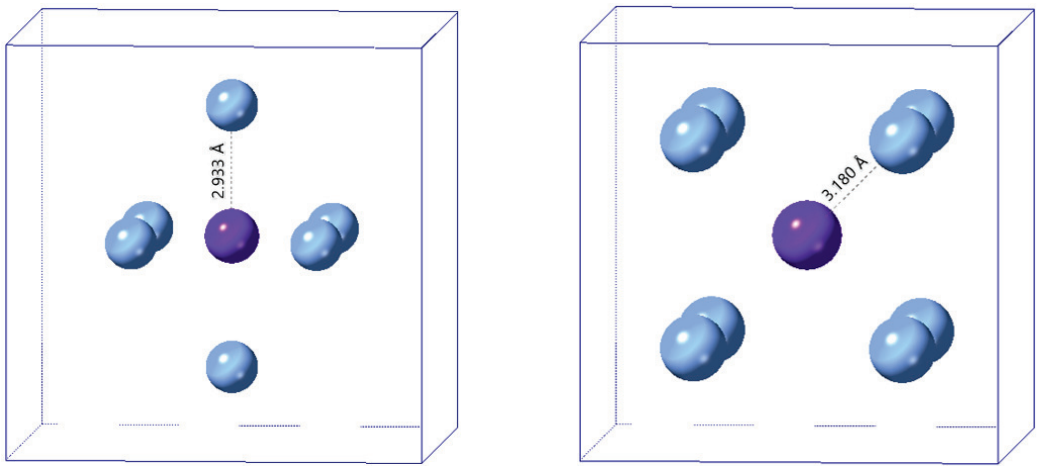
Table 4.2: Summed volume of different numbers of Li and K units compared to the volume of a $P2_1/a$ structure with a=10.99 Å, b=14.97 Å, c=13.05 Å and β=105.34 °

The $Li_3K(NH_2)_4$ and $LiK_2(NH_2)_3$ atom geometry and bond distances (Table 4.3) were used to add restrictions within the charge flipping and simulated annealing attempts in FOX to help refine the structure solution. Initially $[NH_2]^-$ units were modelled as $[F]^-$ units to aid refinement.

		$Li_3K(NH_2)_4$	**$LiK_2(NH_2)_3$**
Co-ordination environment:		6 N around each K in an almost octahedral fashion	8 N around each K in a bcc manner
Bond Distances:	N-K	4 x 2.8 Å 2 x 3.0 Å	4 x 3.0 Å 4 x 3.2 Å
	K-K	3.9 Å	3.6 Å
	Li-N	2.2 Å	2.2 Å

Table 4.3: Co-ordination environments and bond distances in the $Li_3K(NH_2)_4$ and $LiK_2(NH_2)_3$ structures

The bond distances and co-ordination environments shown in Table 4.3 for $Li_3K(NH_2)_4$ and $LiK_2(NH_2)_3$ were used to develop rigid body z-matrices shown as motifs in Figure 4.12, which could be used in DASH for attempts at structure solution.



(a) Octahedral z-matrix based on $Li_3K(NH_2)_4$ (b) Bcc z-matrix based on $LiK_2(NH_2)_3$

Figure 4.12: Rigid body z-matrices based on $Li_3K(NH_2)_4$ and $LiK_2(NH_2)_3$ motifs used in DASH for structure solution attempts. Purple = Potassium, Blue = Nitrogen

The best structures and solutions suggested by each of the programs are very similar, and Rietveld refinements in TOPAS produce good fits which are shown in Figure 4.13. The potassium ions present dominate the scattering and the consistency of their refinement to potassium layers and offset blocks, mean that their positions can be confidently predicted.

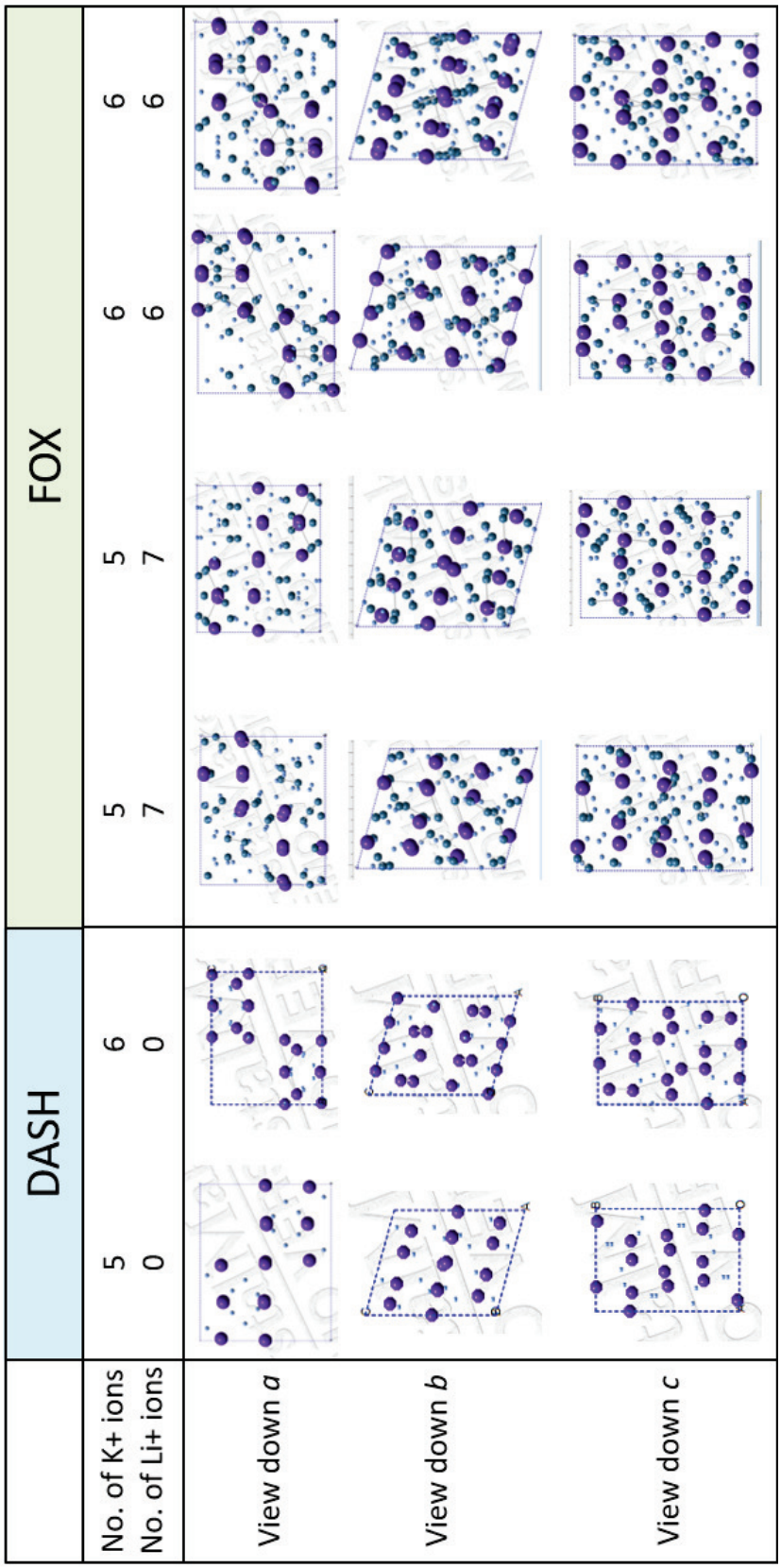


Figure 4.13: The best structures and solutions suggested for the unknown phase of the Li-K-N-H system from DASH and FOX

4.4.4 Summary and future work

Figure 4.9 shows that the unknown phase is most prevalent in the 6:6 $LiNH_2$:KNH_2 powder X-ray diffraction data and this ratio shows the closest fit to 100 % in Table 4.2. This is also consistent with the literature reports of an "$LiK(NH_2)_2$" phase [109, 178]. Therefore it is probable that the unknown phase has the main structural features shown by the potassium ions in Figure 4.13, and that Li:K are present in a 1:1 ratio. Therefore the unknown phase can be confidently described as $Li_nK_n(NH_2)_{2n}$.

Future work is necessary to successfully identify and crystallographically characterise this $Li_nK_n(NH_2)_{2n}$ phase. This could include synthesising the phase with ND_3 and using the POLARIS diffractometer at ISIS to help identify H/D positions. Figure 4.7 shows that varying the ratio of $LiNH_2$ and KNH_2 does not lead to the synthesis of $Li_nK_n(NH_2)_{2n}$ as a single phase. Successful characterisation may therefore include using the STA data shown in Figure 4.14 to identify a temperature to isolate it from $LiK_2(NH_2)_3$ and $Li_3K(NH_2)_4$.

4.5 STA traces for the phase space between $LiNH_2$ and KNH_2

Figure 4.14 shows STA traces of each of the mixed ratios of $LiNH_2$ and KNH_2 which were run from room temperature up to 400 °C and then cooled back to room temperature (all at 5 °C/min) to try and better identify temperatures for any synthetic, phase change or decomposition events.

Consideration of the liquid behaviour of these mixed-metal amide systems is very different to the limited research that has been done on the known mixed-metal amides before. This STA data shows how tuning the ratio of the metals present, impacts and changes the melting point of the samples as a whole.

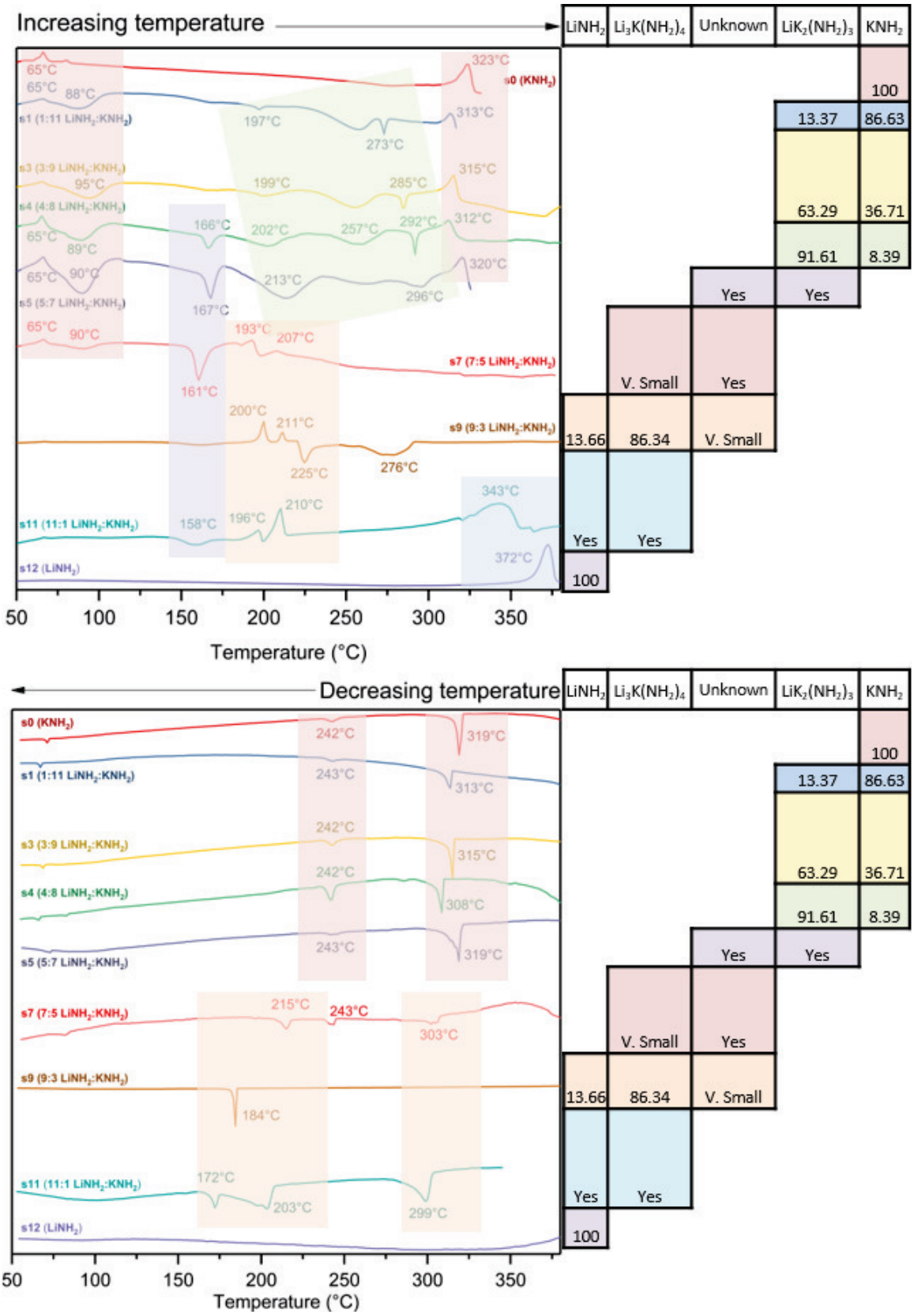


Figure 4.14: DSC traces for all of the ratios of $LiNH_2$:KNH_2 on heating (top) and cooling (bottom) alongside the percentage composition of each sample

Shaded Colour	**Likely Phase**	**Temperature (°C) Heating**	**Cooling**	**Possible thermal event**
Red	KNH_2	65 and 88		KNH_2 phase changes
		312-320		KNH_2 melting
			308-319	KNH_2 recrystallising
			242	KNH_2 thermal event
Green	$LiK_2(NH_2)_3$	197-213		Possible synthesis
		255-260		
		273-296		
Purple	Unknown	161-166		Synthesis of the unknown phase
Orange	$Li_3K(NH_2)_4$	161-166		Synthesis of $Li_3K(NH_2)_4$
		193-200		$Li_3K(NH_2)_4$ separates
		207-211		$Li_3K(NH_2)_4$ melts
			299-303	
			172-215	
Blue	$LiNH_2$	343-372		$LiNH_2$ melting

Table 4.4: Possible thermal events highlighted in Figure 4.14 for the Li-K-N-H system

The thermal events at 65 °C and 88 °C on heating are clearly visible in the s0-s7 traces and correspond to the phase changes for KNH_2 from monoclinic to tetragonal and tetragonal to cubic respectively. The thermal events visible in Figure 4.14 and highlighted in red on heating at 312 °C and 320 °C and on cooling at 308 °C, 319 °C and 242 °C are all related to KNH_2 as they are also present in the s0 sample for KNH_2 alone. KNH_2 has a known melting point of 338 °C. This suggests that the s1-s5 samples either did not form $LiK_2(NH_2)_3$, the reaction was incomplete, or the synthesised $LiK_2(NH_2)_3$ subsequently separated and recrystallised as KNH_2 and $LiNH_2$ rather than $LiK_2(NH_2)_3$.

There is clear evidence of the melting point shifting to higher temperature with in-

creasing $LiNH_2$ concentration from s1-s5 in the peaks highlighted in green. It is unclear what these exothermic events correlate to precisely, but they are likely to relate to the $LiK_2(NH_2)_3$ phase and will be discussed later with additional *ex-situ* data in Section 4.7.1 and *in-situ* data in Section 4.7.2.

The peaks highlighted in purple between 161 °C and 166 °C are likely to relate to the synthesis of the unknown phase and/or $Li_3K(NH_2)_4$ ($Li_3K(NH_2)_4$ was shown to be synthesised at 161 °C during the *in-situ* GEM experiment in Section 4.6.2.1). Given the $LiNH_2$:KNH_2 ratios during which these exotherms are observed and the powder X-ray diffraction analysis which has been performed on the post ball-milled versions of these samples, it is likely that the unknown phase and $Li_3K(NH_2)_4$ have a similar synthesis temperature.

$Li_3K(NH_2)_4$ is known to separate at 199 °C and subsequently melt at 211 °C (Figure 4.15) which are visible as the peaks highlighted in orange.

$LiNH_2$ has a known melting point of 375 °C which is visible as the peaks highlighted in blue.

Individually KNH_2 and $LiNH_2$ melt above 300 °C, but the simultaneous presence of both these amides means the melting point of the mixed-metal amide phases has been shifted down by over 100 °C.

Having analysed the whole phase space between $LiNH_2$ and KNH_2, despite the discovery of a new unknown phase, it is only $Li_3K(NH_2)_4$ and $LiK_2(NH_2)_3$ that could be made in high purity so it is these two compounds that were investigated in further depth.

4.6 $Li_3K(NH_2)_4$

4.6.1 *Ex-situ* thermal decomposition behaviour

STA focuses on examining the low temperature behaviour of this system. DSC traces taken for both pre-made $Li_3K(NH_2)_4$ (black) and a hand-ground mixture of $3LiNH_2 + NaNH_2$ (blue) are shown in Figure 4.15. The mass trace (green) comes from the reaction of $3LiNH_2 + KNH_2$ on the IGA^n.

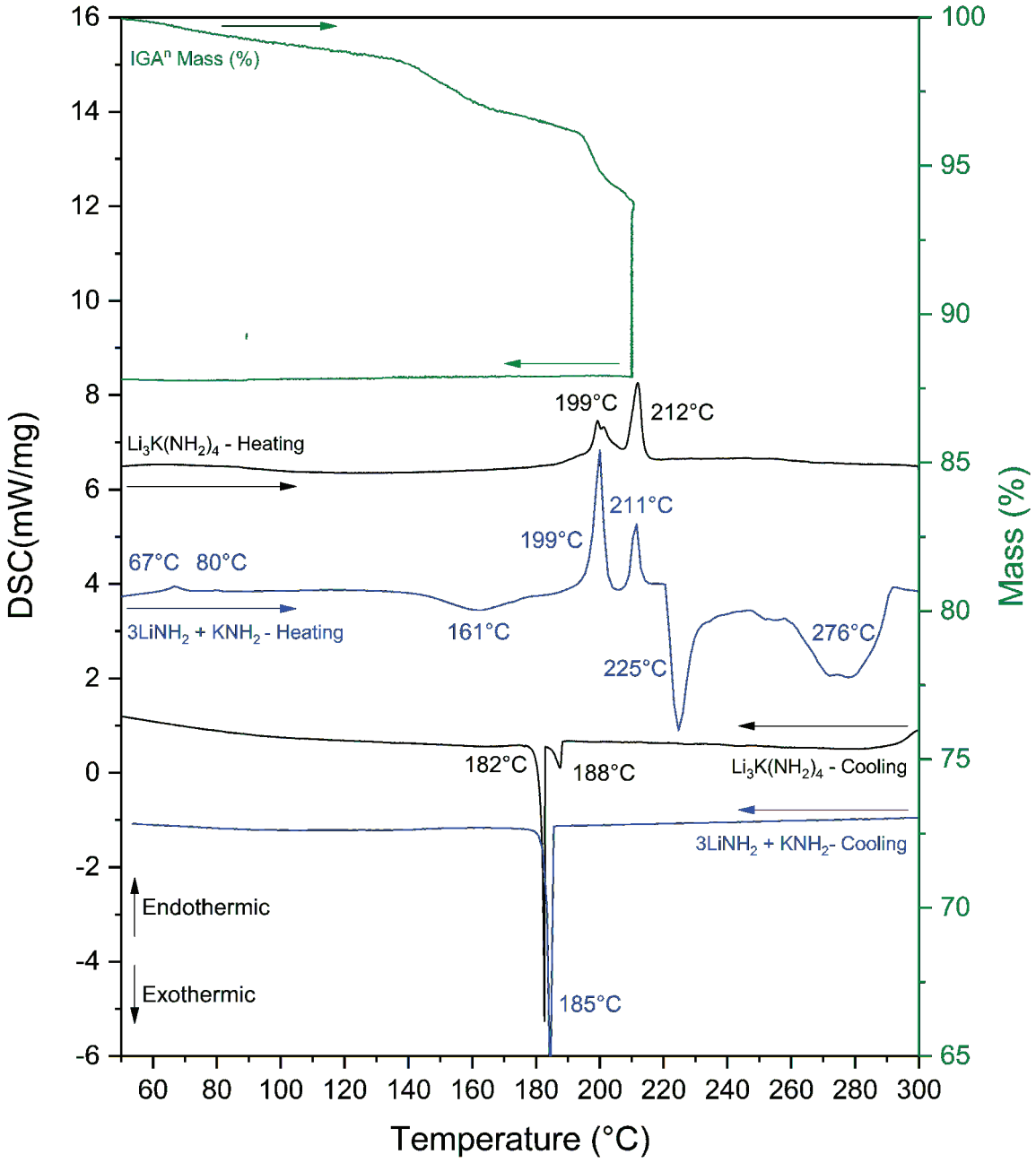


Figure 4.15: DSC traces for $Li_3K(NH_2)_4$ (black) and $3LiNH_2 + KNH_2$ (blue) and mass trace (green) for synthesis on the IGA^n.

The reported temperatures for the KNH_2 monoclinic to tetragonal and tetragonal to cubic phase changes are 53 °C [150] and 75 °C [211] respectively. From Figure 4.15 in the trace for $3LiNH_2 + KNH_2$ it can be seen that the analogous thermal events for these phase changes occur at 67 °C and 80 °C respectively. Comparison of the differences between the two STA traces enables the identification of the synthetic step for the formation of $Li_3K(NH_2)_4$ as from this point onwards the two traces should be identical. This is clearly visible as the broad exothermic event at 161 °C in the $3LiNH_2 + KNH_2$ STA trace. From the $3LiNH_2 + NaNH_2$ trace in Figure 3.5 it was deduced that the sharp exothermic event at 185 °C corresponded to the synthesis of $Li_3Na(NH_2)_4$. Comparatively, $Li_3K(NH_2)_4$ therefore forms at a lower temperature (161 °C) and the broader nature of the peak could be due to compositional variation (or impurities), as different parts of the sample are synthesised at slightly different temperatures.

The syntheses of both $Li_3Na(NH_2)_4$ and $Li_3K(NH_2)_4$ are exothermic as they correspond to opening out the $LiNH_2$ layered structure and inserting Na^+ or K^+ which is a low energy process. This does not require a total re-arrangement of the ions so there is little enthalpy difference between the starting and finishing structures. The synthesis of $Li_3Na(NH_2)_4$ and $Li_3K(NH_2)_4$ are topotactic transformations, as the $LiNH_2$ based structure does not change.

Analogously to the traces seen for $Li_3Na(NH_2)_4$ in Figure 3.5, it is thought that the two endothermic peaks seen in Figure 4.15 for $Li_3K(NH_2)_4$ correspond to separation (199 °C) and a whole sample melt (211 °C). At 199 °C, the structure falls apart and KNH_2 melts to form a structure approaching $3LiNH_{2(solid)} + KNH_{2(liquid)}$. This is the same temperature $NaNH_2$ separated out of $Li_3Na(NH_2)_4$ to form $Li_3Na_{(1-x)}(NH_2)_{(4-x)}$ $(0 < x < 1)$, suggesting the onset of separation is determined by the Li containing part of these mixed-metal amides. At 211 °C, the whole sample melts as $LiNH_2$ dissolves into the molten KNH_2, which is notable as KNH_2 alone does not melt until 338 °C.

This demonstrates that there is only a small temperature range (199 °C to 211 °C) for which the $Li_3K_{(1-x)}(NH_2)_{(4-x)}$ $(0 < x < 1)$ is in fact present as separate amides before forming a combined melt. Comparatively, the $Li_3Na_{(1-x)}(NH_2)_{(4-x)}$ based phase of $Li_3Na(NH_2)_4$ was present for a much wider temperature range (199 °C to 234 °C). This is because Li^+ and K^+ have a much greater difference in ionic radius than Li^+ and Na^+ (Table 4.1), so

$Li_3K_{(1\text{-}x)}(NH_2)_{(4\text{-}x)}$ is less stable than $Li_3Na_{(1\text{-}x)}(NH_2)_{(4\text{-}x)}$ and the same degree of compositional variation seen in the Li-Na-N-H system would not be expected for the potassium analogue. This would be reflected in the conductivity as in $Li_3K(NH_2)_4$ ionic mobility is suppressed due to the different cation environments.

The STA trace for $3LiNH_2 + KNH_2$ was repeated multiple times and each time showed the two broad exotherms at 225 °C and 276 °C. This was not expected as from 161 °C onwards the $3LiNH_2 + KNH_2$ and $Li_3K(NH_2)_4$ traces should be identical as it is the same inter-mixed molten phase that is present. This behaviour is unusual as these two broad exotherms are not seen in the $Li_3K(NH_2)_4$, $LiNH_2$ or KNH_2 STA traces.

The sharp exotherms on cooling at 182/185 °C are due to recrystallisation of the sample as the experiments were not heated high enough to cause complete decomposition of the samples.

Figure 4.15 also shows the mass trace recorded on the IGA^n as a sample of $3LiNH_2 + KNH_2$ was heated to 210 °C *ex-situ*. The small mass loss up to 150 °C of a few weight percent is due to desorption of physisorbed gases from within the particle grains. The synthesis at 161 °C is correlated with a $\sim 2\,\%$ mass loss. The separation endotherm at 199 °C is also correlated with a $\sim 2\,\%$ mass loss. The endotherm at 211 °C corresponds to the full sample melting and is correlated with a $\sim 6\,\%$ mass loss, most likely due to escape of the melted sample from the IGA^n bucket as the experimental set-up is not very effective at containing liquid samples.

The next step to further understand the decomposition of $Li_3K(NH_2)_4$ was to analyse its behaviour at high temperatures by looking at its decomposition on the gas flow panel under argon. Figure 4.16 shows the outlet gas flow mass spectrometry traces for the decomposition of $Li_3K(NH_2)_4$ and that of a hand-ground mixture of $3LiNH_2 + KNH_2$ under argon. The decomposition of pre-synthesised $Li_3K(NH_2)_4$ was compared to a hand ground mixture of the starting materials in a 3:1 ratio. A synthesis temperature of 161 °C was suggested from the DSC data for $Li_3K(NH_2)_4$ so it is likely that above this temperature the same materials are present in both cases, therefore the decomposition traces should look the same.

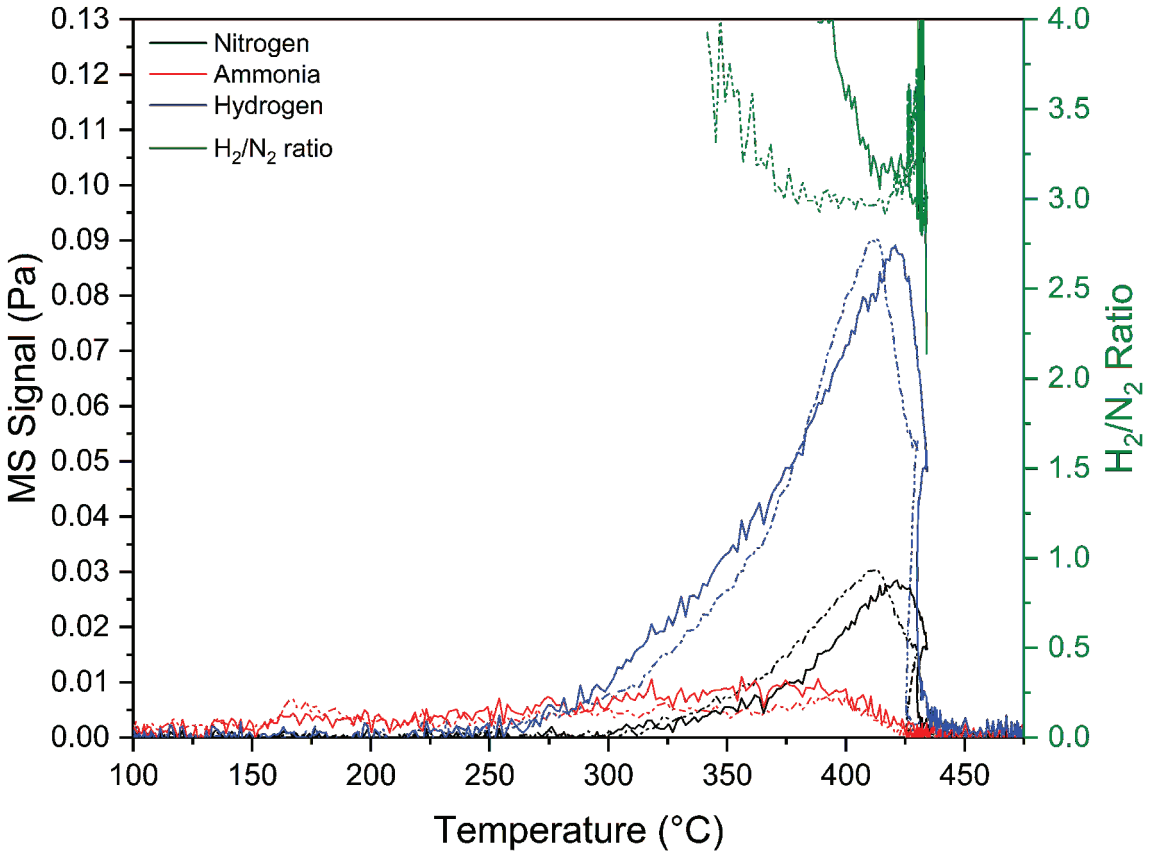


Figure 4.16: Decomposition of $Li_3K(NH_2)_4$ (solid lines) and $3LiNH_2 + KNH_2$ (dashed lines) on the gas flow panel under argon

Similarly to the MS trace seen for the decomposition of $Li_3Na(NH_2)_4$, the decomposition of $Li_3K(NH_2)_4$ shows that a very different gas profile is observed for this mixed-metal amide compared to either $LiNH_2$ or KNH_2 alone. As with $Li_3Na(NH_2)_4$, there is a massive favouring of hydrogen release over the NH_3 release seen for $LiNH_2$ decomposition. The presence of KNH_2 in the mixed molten phase is suppressing any NH_3 release from the $LiNH_2$ component. Both KNH_2 and $NaNH_2$ are known to decompose via the same mechanism so it is unsurprising that in both these mixed-metal systems, their presence is having a similar affect on $LiNH_2$. There are many similarities between the decomposition of $Li_3Na(NH_2)_4$ and $Li_3K(NH_2)_4$ but there is a shift in the actual decomposition temperatures for the two systems due to the different properties of KNH_2/K and $NaNH_2$/Na respectively.

Two peaks in the gases released during the decomposition of $Li_3Na(NH_2)_4$ under argon were postulated to result from the partial separation via $Li_3Na_{(1-x)}(NH_2)_{(4-x)}$ into its

constituent single metal amides which subsequently decompose at different temperatures. Similarly to the gas trace collected for the decomposition of $LiNa_2(NH_2)_3$ on the gas flow panel, although there is only one obvious peak in the H_2 and N_2 traces in Figure 4.16. Two pseudo-Voigt functions in TOPAS have been used to determine the "peak positions" of the decomposition reactions and Figure 4.17 shows that it may be more accurate to think of the H_2 MS signal as two overlapping peaks centred at ∼378 °C and 419 °C. This supports the theory that $Li_3K(NH_2)_4$ separates on melting into $LiNH_2$ and KNH_2 which then themselves decompose. The temperatures seen in Figure 4.17 are slightly raised compared to the single metal amides alone due to the slight interaction between the decomposition pathways for $LiNH_2$ and KNH_2. The pseudo-Voigt function centred at 378 °C and attributed to the decomposition of $LiNH_2$, correlate well with those seen at 365 °C and 376 °C from the decomposition of $LiNH_2$ in $Li_3Na(NH_2)_4$ (Figure 3.7) and $LiNa_2(NH_2)_3$ (Figure 3.10).

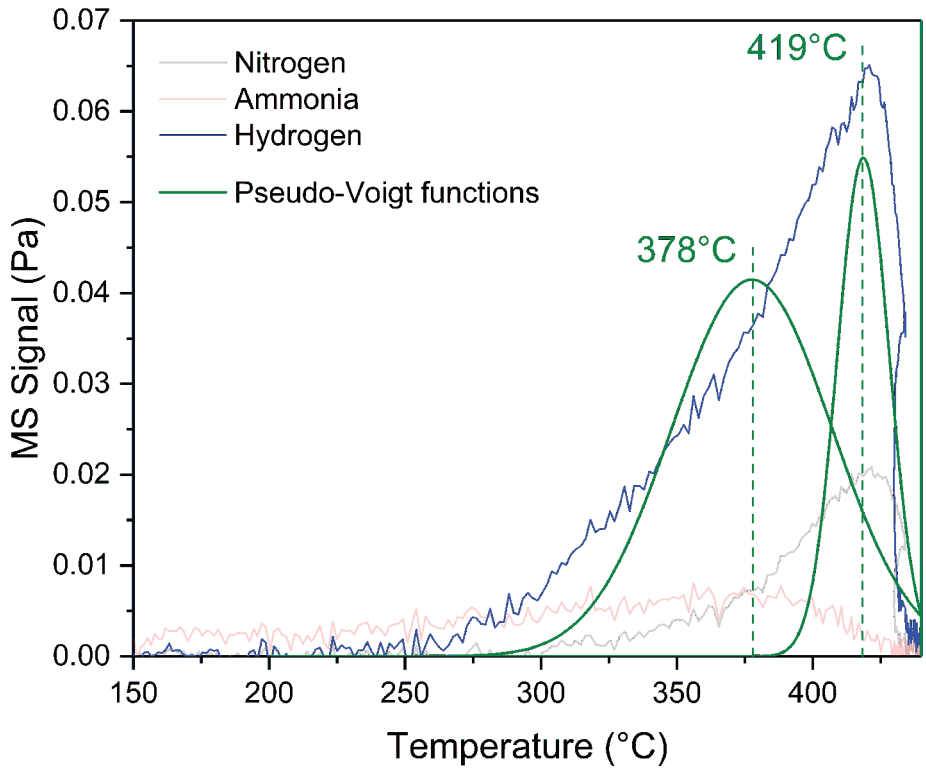


Figure 4.17: Two pseudo-Voigt functions have been used to determine the peak positions in the H_2 curve from Figure 4.16 during the decomposition of $Li_3K(NH_2)_4$

A hypothetical decomposition pathway for $Li_3K(NH_2)_4$ could therefore be proposed:

$Li_3K(NH_2)_4$	$\longrightarrow Li_3K_{(1-x)}(NH_2)_{(4-x)} + xKNH_2$	Partial separation
$Li_3K_{(1-x)}(NH_2)_{(4-x)}$	$\longrightarrow 3\,LiNH_2 + KNH_2$	Full separation
	$\longrightarrow \frac{3}{2}Li_2NH + \frac{1}{2}NH_3\uparrow + KNH_2$	$LiNH_2$ decomposes
	$\longrightarrow \frac{3}{2}Li_2NH + K + \frac{1}{2}N_2\uparrow + H_2\uparrow$	KNH_2 decomposes
	$\longrightarrow \frac{3}{2}Li_2NH + K\uparrow$	Gases lost
	$\longrightarrow \frac{3}{2}Li_2NH$	K volatilised

From the inter-mixed molten phase, $LiNH_2$ will decompose first producing Li_2NH and releasing NH_3. KNH_2 will then decompose to form K metal, releasing H_2 and N_2 (and possibly some NH_3) (Equation 4.1).

However, it is unlikely that the two constituent amides can be considered to be decomposing as independently as this decomposition pathway implies because they are present as one intermixed melt phase (the STA data showed it was only between 199 °C and 211 °C that they are present as distinct species). It is likely that the decomposition of $LiNH_2$ and KNH_2 occur fairly simultaneously and the NH_3 released from the decomposition of $LiNH_2$ would then be captured by the K metal that had been produced leading to the reformation of KNH_2 (leading to H_2 release from the system). KNH_2 would therefore cyclically decompose and reform until all of the $LiNH_2$ present in the sample had been converted to Li_2NH at which point it would decompose for the final time. It is clear from the mass spectrometry data that some NH_3 was released during the decomposition reaction of $Li_3K(NH_2)_4$, which suggests that ammonia capture by K was not 100 % effective, perhaps due to the experimental set-up of the gas flow over the powder grains. This would be an important consideration if this were to be scaled up for commercial applications.

It is clear that the decomposition of the mixed-metal amide is not simply a superposition of that of $LiNH_2$ and KNH_2, both from the nature of the gas species released and also the fact that the decomposition temperatures are substantially lowered here compared to the decomposition of either $LiNH_2$ or KNH_2 alone under argon. Instead it is the decomposition of the intermixed molten phase which must be considered.

Decomposition of $Li_3K(NH_2)_4$ (molar mass = 124.0) to $\frac{3}{2}Li_2NH$ (molar mass = 28.9) (assuming all other species were lost as gases and K volatilised) would result in a mass loss of 65.0 %. Decomposition of $Li_3K(NH_2)_4$ to $\frac{3}{2}Li_2NH$ and K (molar mass = 39.1) (assuming all other species were lost as gases) would result in a mass loss of 33.5%. Figure 4.15 shows a mass loss of 45 % which suggests that K is not being fully volatilised and lost and some of the K product from the decomposition is remaining in the reactor. This is therefore different to the decomposition of $Li_3Na(NH_2)_4$ during which all the Na decomposition product was volatilised and lost from the reactor. This is unexpected given K has a higher vapour pressure than Na so perhaps it is $NaNH_2$ that is more readily lost than KNH_2 (as $NaNH_2$ is more volatile) and any remaining KNH_2 is subsequently decomposed to K metal.

The final products of $Li_3K(NH_2)_4$ decomposition under flowing argon were determined by powder X-ray diffraction from the post decomposition residue remaining after the gas flow panel experiment. This was majority phase Li_2NH with a small amount of Li_2O present. No Bragg peaks were observed for any potassium containing material. It is possible that the K phase formed during the decomposition of $Li_3K(NH_2)_4$ was amorphous, or that the powder X-ray diffraction data was too poor quality (due to sample degradation and poor SAXS machine resolution) for determination of potassium metal.

Figure 4.16 also shows the H_2/N_2 ratio for the released gases above 330 °C, as below this temperature it is not reliable as there is only trace amounts of the gases present in the mass spectrometry trace. It is more appropriate to look qualitatively at trends in this ratio rather than quantitative absolute values. Figure 4.16 shows this ratio decreases with increasing temperature which indicates a change from NH_3 release (from $LiNH_2$ decomposing) to H_2 and N_2 release (from KNH_2 decomposition) which would lead to a decrease in the H_2/N_2 ratio from 3 to 2.

4.6.2 GEM experiments

Having explored the synthesis of Li-K mixed-metal amides and their decomposition by various *ex-situ* techniques, *in-situ* neutron powder diffraction experiments were performed to provide structural evidence to corroborate the conclusions made based on the *ex-situ* data.

Neutron powder diffraction is one of the best experimental techniques to help understand how the bulk structure of these materials behave under different conditions. *In-situ* structural techniques have been key to understanding form and function under reaction conditions [67, 196, 198].

The mass and temperature of the samples were recorded simultaneously as neutron diffraction data was collected using the IGA^n apparatus. Thermogravimetric readings of the sample mass, temperature and pressure were taken every 5 seconds, and neutron diffraction data were collected at 100 second intervals throughout the course of the experiments.

The diffraction data collected during these studies are presented as contour plots which are formed by stacking successive diffraction datasets next to each other, to provide a top down view of the diffraction data and a visual representation of the reaction progress. The lines observed correspond to the positions of the Bragg peaks at each point during the experiment. The colour of the lines reflects the relative intensities of the Bragg reflections. The colours range from dark red (weak intensity) through orange (medium intensity) and up to yellow/white (high intensity) and variation of these colours indicates changes in the relative proportions of the phases present.

Deviation in the gradient of the lines from the horizontal is indicative of variations in the lattice parameters of the phases. The appearance and disappearance of lines is consistent with formation and loss of crystalline phases respectively, whilst splitting or convergence of lines is indicative of phase transformations.

Vertical black bands denote periods of time when the synchrotron beam failed so no intensity was recorded. The aim is to maintain the sample under constant temperature and pressure during these malfunctions so as not to miss any crystallographic changes which would be recorded by the neutron diffraction.

Contour plots provide a convenient way of qualitatively viewing the crystallographic progress of a reaction; however, quantitative information regarding the crystal structures of the materials present cannot be obtained from the study of such diagrams. Values of lattice parameters, site occupancies and scale factors must be obtained from Rietveld analysis of each individual data set. Manual analysis of each of the datasets from variable temperature experiments such as these would be extremely time consuming. However, if the crystallographic variation between subsequent data sets is small, refinement of a large number of data sets can be semi-automated using the batch facility included in the TOPAS refinement package. A batch process uses the refined model from a previous diffraction dataset as the starting model for the successive diffraction datasets.

For all the GEM experiments, Rietveld analyses were performed in TOPAS and batch refinements were performed on the data collected from banks 3, 4 and 5 to ensure the greatest accuracy of the calculated parameters. The results of these refinements show species appear and disappear throughout the experiment and enables the correlation of structural changes with those seen in the mass data. Banks 1 and 2 have much poorer resolution than bank 3 and do not contain any additional Bragg peaks so have not been included. Because hydrogen has a large incoherent neutron scattering cross section, neutron diffraction studies require the synthesis of deuterium-enriched samples.

4.6.2.1 Synthesis of $Li_3K(ND_2)_4$

First the synthesis of $LiK_2(ND_2)_3$ from $3LiND_2 + KND_2$ was examined under argon using the IGA^n. In order to identify the temperatures of interest prior to the online neutron diffraction study, preliminary offline IGA^n measurements were performed on three samples of hand-ground $3LiNH_2 + KNH_2$ (Figure 4.18). The samples were heated to 200 °C, 210 °C and 180 °C respectively at a rate of 1 °C per minute under argon and the mass loss as a percentage of the starting mass was recorded as a function of temperature.

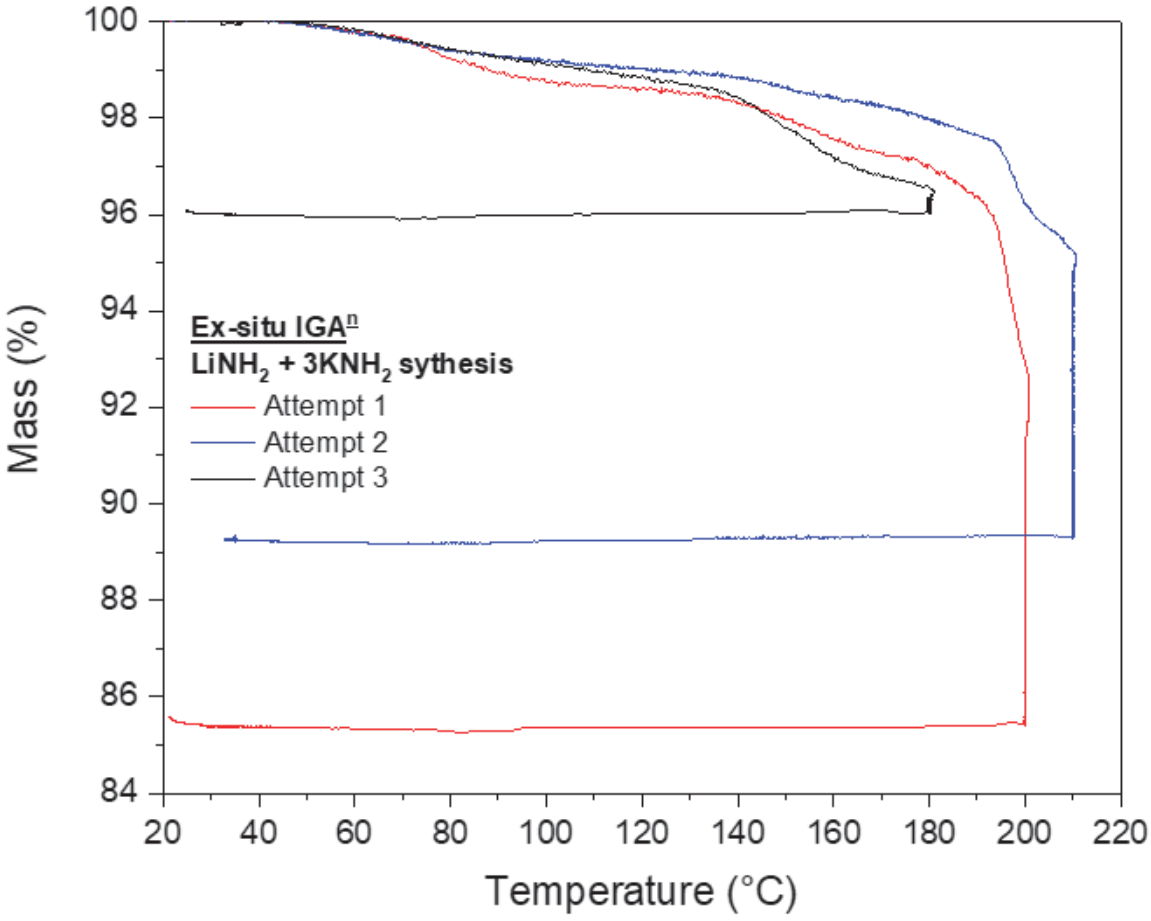


Figure 4.18: Three attempts at the off-line synthesis of $Li_3K(NH_2)_4$ using the IGA^n

From Figure 4.18, two mass loss steps can be observed in all three of the attempts, with midpoints at 85 °C and 153 °C. The mass loss at 85 °C is likely to be related to the KNH_2 tetragonal to cubic phase transition and the mass loss at 153 °C is likely to be related to the synthesis of $Li_3K(NH_2)_4$ as these events were determined to occur at 80 °C and 161 °C respectively from the STA data shown in Figure 4.15.

Larger mass losses of 14.5% (Attempt 1) and 11% (Attempt 2) correspond to escape of the melted sample from the IGA^n bucket, as $Li_3K(NH_2)_4$ is known to separate at 199 °C and melt at 211 °C from the STA data (Figure 4.15). The sharp change in gradient at 200 °C is indicative of melting. However, this did not occur on the third attempt when the sample was only heated to 180 °C, as it is below the initial separation temperature. These findings were used to plan the online IGA^n experiment.

Powder X-ray diffraction data collected from the residual samples remaining at the end

of these three off-line *ex-situ* IGA^n experiments. The experiment was designed to test the synthesis temperature for $Li_3K(NH_2)_4$ from $3LiNH_2 + KNH_2$ but rather than $Li_3K(NH_2)_4$ being formed as was expected, unknown powder X-ray diffraction data was obtained which is discussed further in Section 4.4.

For the *in-situ* synthesis experiment on GEM, 0.5 g of $3LiND_2 + KND_2$ (synthesised from $Li_3N + ND_3$ and $KH + ND_3$ respectively) was hand-ground for 5 minutes before being loaded into the vanadium IGA^n bucket and placed into the neutron beam under constant 1000 mbar argon.

A one hour scan was taken at room temperature to provide an accurate data set for the start of the batch process. Refinement of these diffraction data collected prior to heating indicated that the majority phase of the sample was $LiND_2$ (69.8 %), with a minor phase of $Li_3K(ND_2)_4$ (9.0 %) and an impurity phase of Li_2O (21.3 %) (Figure A.6 and Table A.3 in the Appendix). There is a very small amount of $Li_3K(ND_2)_4$ present initially which may be present as a result of the mechanical grinding to mix the starting materials. A small amount of Li_2O is also present which gradually increases in intensity as the experiment progresses and is likely due to a small amount of air present within the experimental equipment which led to the reaction of $LiND_2$ with oxygen.

It is the monoclinic KND_2 phase ($P2_1/m$) that is known to be stable below 63 °C however no KND_2 is seen in the neutron diffraction data despite its known presence in the reaction vessel. This is likely to be because monoclinic KNH_2 has a lower symmetry structure than $LiNH_2$ so the Bragg peaks will be at a lower intensity, and as $LiND_2$ and KND_2 are present in a 3:1 ratio, there is also less KND_2 in the reaction vessel to cause diffraction. Although not visible initially by diffraction, KND_2 is clearly present as $Li_3K(ND_2)_4$ is successfully synthesised. The two peaks at *d*-spacings of 3.1 Å and 3.2 Å remain un-indexed and do not fit to $LiNH_2$, KNH_2, $Li_3K(NH_2)_4$ or Li_2O but are present throughout the entire experiment.

The sample was heated at 1 °/min from room temperature. When it reached 100 °C the neutron beam failed, but the sample remained being heated until it reached 139 °C. It was set to cool at 1 °C/min so that no structural changes were missed by the lack of *in-situ* measurements. The neutron beam returned when the sample had reached a temperature of 124 °C but due to a lag time in the equipment, the sample was cooled to 118 °C. The sample

was then returned to being heated at 1 °C/min until 180 °C (as determined from the *ex-situ* IGA^n experiment) where it was held to dwell for 3 hours. It was then heated to 200 °C at 0.5 °C/min and once it reached this temperature it was cooled at 10 °C/min and it reached a temperature of 70 °C before the collection of neutron data was stopped.

Figure A.8 in the Appendix shows full contour plots for the data collected from banks 3, 4 and 5 for the $3LiND_2 + KND_2$ synthesis experiment. The diffraction data for bank 4 and the batch process refinement for banks 3, 4 and 5 (showing the scale of each species present throughout the experiment) are presented in Figure 4.19 alongside the corresponding thermogravimetric data. An SiO_2 background has been fitted because the silica tail was used. As expected, the lattice parameters of the unit cells track the temperature. This shows that on heating, the peaks corresponding to $LiND_2$ decrease in intensity, most clearly seen by the 2.93 Å (112) peak and this phase disappears at 180 °C. (112) are the Miller indices for $LiND_2$, a notation system in crystallography for planes in crystal lattices as explained in Section 2.6.2.1. The steepest drop off in $LiND_2$ intensity occurs between 155-180 °C and correlates with the second mass loss of $\sim 2\%$. This correlates well with the synthesis of $Li_3K(ND_2)_4$ which was determined from the STA data shown in Figure 4.15 to occur at 161 °C. The disappearance of $LiND_2$ from the GEM diffraction data corresponds with the appearance of peaks corresponding to $Li_3K(ND_2)_4$ at 175 °C confirming the successful synthesis (Figure A.7 and Table A.3 in the Appendix). There is a small degree of overlap between the start of the $Li_3K(ND_2)_4$ synthesis, a few minutes before the full disappearance of $LiND_2$.

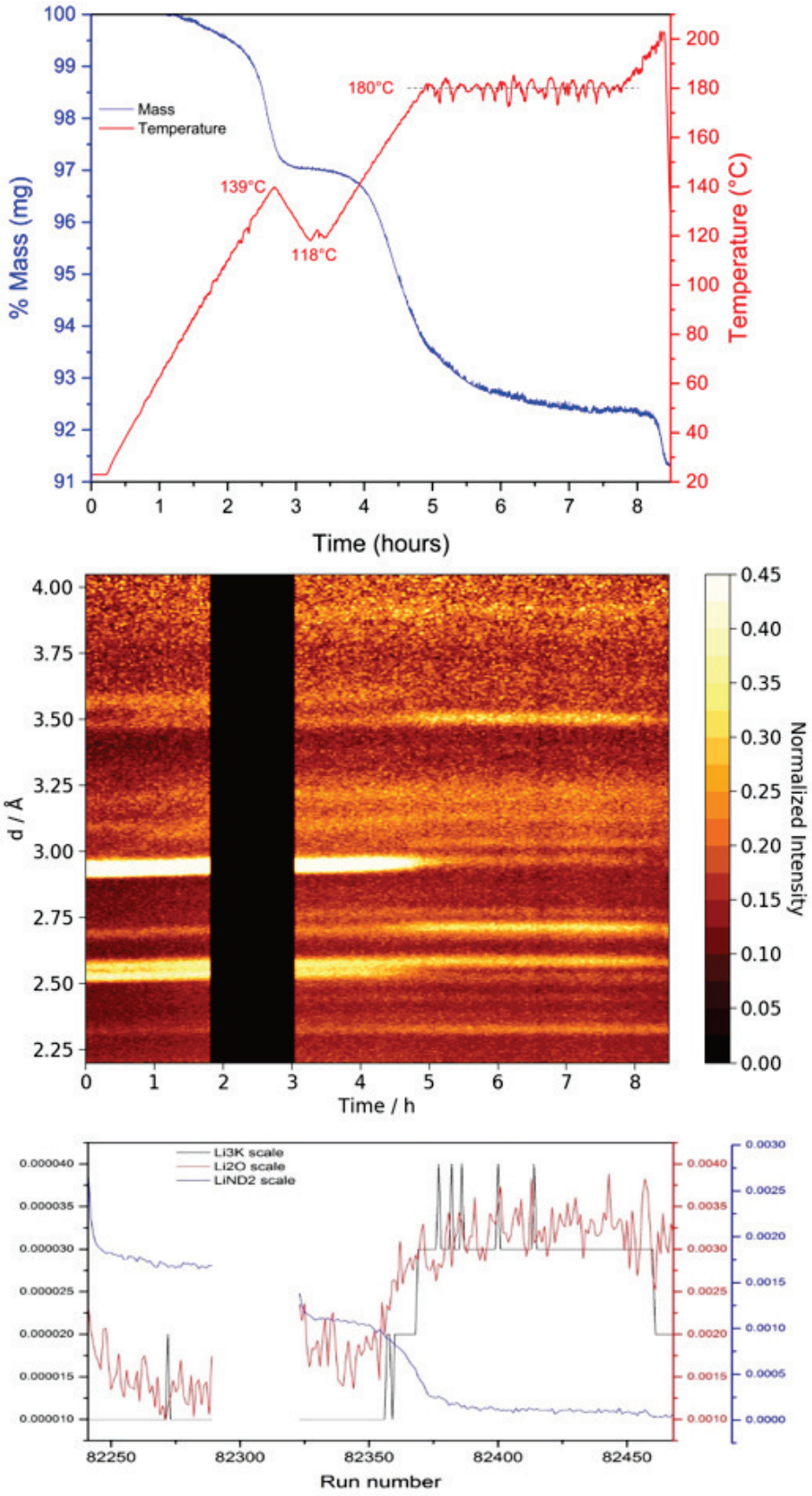


Figure 4.19: Diffraction data from bank 4 for the $Li_3K(ND_2)_4$ synthesis experiment, a batch refinement showing the species present alongside the corresponding thermogravimetric data

It is clear from the contour plot in Figure 4.19 that the synthesis of $Li_3K(ND_2)_4$ does not go through non-stoichiometric phases and $Li_3K(ND_2)_4$ simply forms as $LiND_2$ disappears. This is as expected, given the STA trace in Figure 4.15 shows the separating and melting temperatures are only 12 °C apart suggesting a $Li_3K_{(1-x)}(NH_2)_{(4-x)}$ phase is not as stable as the analogous component of the Li-Na-N-H system because Li^+ and K^+ have very different ionic radii whereas those of Li^+ and Na^+ are much more similar.

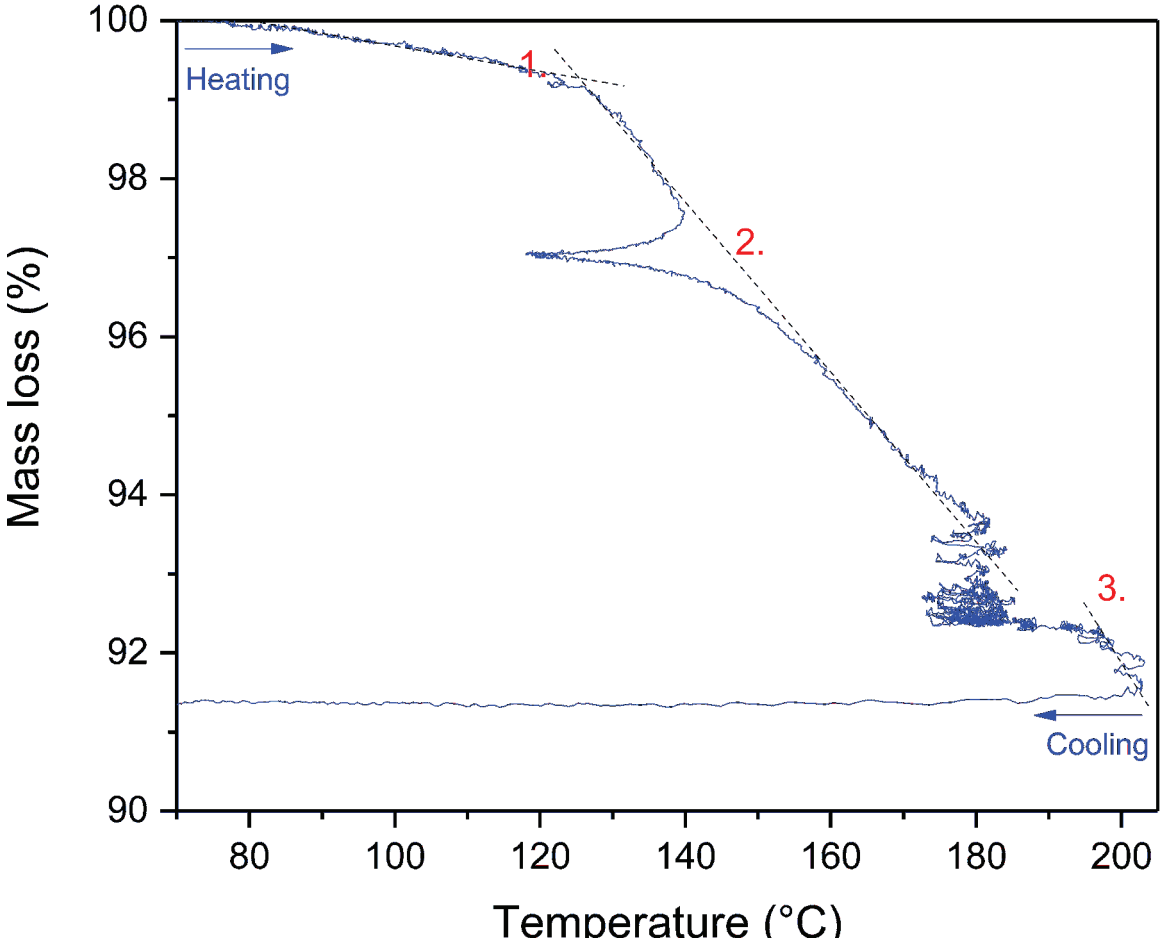


Figure 4.20: % Mass loss for the synthesis of $LiK_2(ND_2)_3$ on GEM plotted as a function of temperature

The percentage mass loss of the sample has been plotted as a function of temperature in Figure 4.20 and matches up well with that shown in Figure 4.15 which was collected *ex-situ*. Analysis of this *in-situ* thermogravimetric data implies that the reaction occurred via three distinct mass-releasing steps which are labelled. The first is a very gradual decrease in mass between 70 °C and 120 °C which is due to the desorption of physisorbed gases from within

the particle grains, most likely released during the KNH_2 phase changes. The second mass loss is much sharper and occurs between 125 °C and 180 °C and is likely to be related to $Li_3K(ND_2)_4$ synthesis. This second decrease in mass matches up with the small amount of NH_3 release seen in Figure 4.16 at 170 °C. The final mass loss observed at the very end of the experiment starts at 195 °C and is due to the whole sample melting and starting to escape from the IGA^n bucket. During this third mass loss, the $Li_3K(ND_2)_4$ peaks also show a corresponding decrease in intensity as the material is lost.

4.6.2.2 Decomposition of $Li_3K(ND_2)_4$

Despite the successful synthesis of $Li_3K(ND_2)_4$ *in-situ*, a separate pre-made sample (*ex-situ*) was used for this, a separate experiment to probe the decomposition of $Li_3K(ND_2)_4$ under argon using the IGA^n. This was synthesised by ball-milling $3LiND_2 + KND_2$ and was confirmed by powder X-ray diffraction (Figure A.9 in the Appendix).

Running these as two separate experiments enabled vanadium buckets to be utilised in the synthesis experiment where no H_2 is released. A quartz reactor could also be used to surrounded the sample which is advantageous as it produces no Bragg peaks. However, during this decomposition experiment, the sample was heated to 400 °C so the quartz cannot be used and a stainless steel reactor must be used instead. Hydrogen was expected to be produced which causes the decrepitation of vanadium, so additionally stainless steel buckets (which are unreactive towards alkali metal amides) had to be used. This meant that the decomposition experiment had the unavoidable consequence of steel peaks present throughout the experiment from where the neutron beam hits the steel on the way in and the way out. The peaks are separated because GEM is a time of flight diffractometer so the difference in d-spacing is the time taken for the neutron beam to travel from one side of the reactor to the other.

The sample of $Li_3K(ND_2)_4$ was heated from room temperature at 1 °C/min. There were four periods during which the beam failed during this experiment but only the first was long enough to warrant a change in the heating profile. The beam failed when the sample had reached 180 °C but it remained being heated until 190 °C at which point it was cooled back down to 180 °C. When the beam came back on, the sample was again heated up to

the target temperature of 400 °C. On reaching this temperature, the experimental set-up was such that the heater immediately turned off and so the sample crash cooled to 323 °C before this could be amended. The sample was heated back up to 400 °C at 2 °C/min where it was held for just under one hour before being cooled to 100 °C before neutron diffraction data stopped being collected.

Contour plots of the diffraction data and the corresponding thermogravimetric data collected from banks 3, 4 and 5 are presented in the Appendix in Figure A.10. The diffraction data collected from bank 4 and the batch process refinement for banks 3, 4 and 5 showing the scale of each species present throughout the experiment are presented in Figure 4.21 alongside the corresponding thermogravimetric data. Three batch process refinements were performed. The first refinement started with the initial hour long scan (taken at room temperature) and goes in the forwards direction tracking $Li_3K(ND_2)_4$ showing its disappearance at 205 °C. The second and third refinements were performed on the data collected from 4.5 hours into the experiment until the end of the experiment. The second refinement was performed in the forwards direction and tracks the scale of Li_2O, $Li_3K(ND_2)_4$ and $LiND_2$. The third refinement was performed in the reverse direction and tracks the scale of Li_2ND, as batch refinements works best when there is an appreciable amount of the phase present initially. These three batch refinements have been collated onto one graph shown in Figure 4.21.

Initially present at the start of the experiment, as expected, is a good refinement to $Li_3K(ND_2)_4$ (Table A.4 in the Appendix). The scale factor of $Li_3K(ND_2)_4$ (Figure 4.21) was observed to decrease slowly with increasing temperature, up to 203 °C. Above 203 °C a sharp, abrupt drop (to a negligible value) was observed in the $Li_3K(ND_2)_4$ scale factor, over the course of 9 runs. The *a*-lattice parameter of $Li_3K(ND_2)_4$ was observed to increase with temperature up to 203 °C from 7.24 Å to 7.31 Å and the *c*-lattice parameter increased from 24.01 Å to 24.23 Å in the same temperature range, which is consistent with the thermal expansion of the unit cell (Figure 4.22).

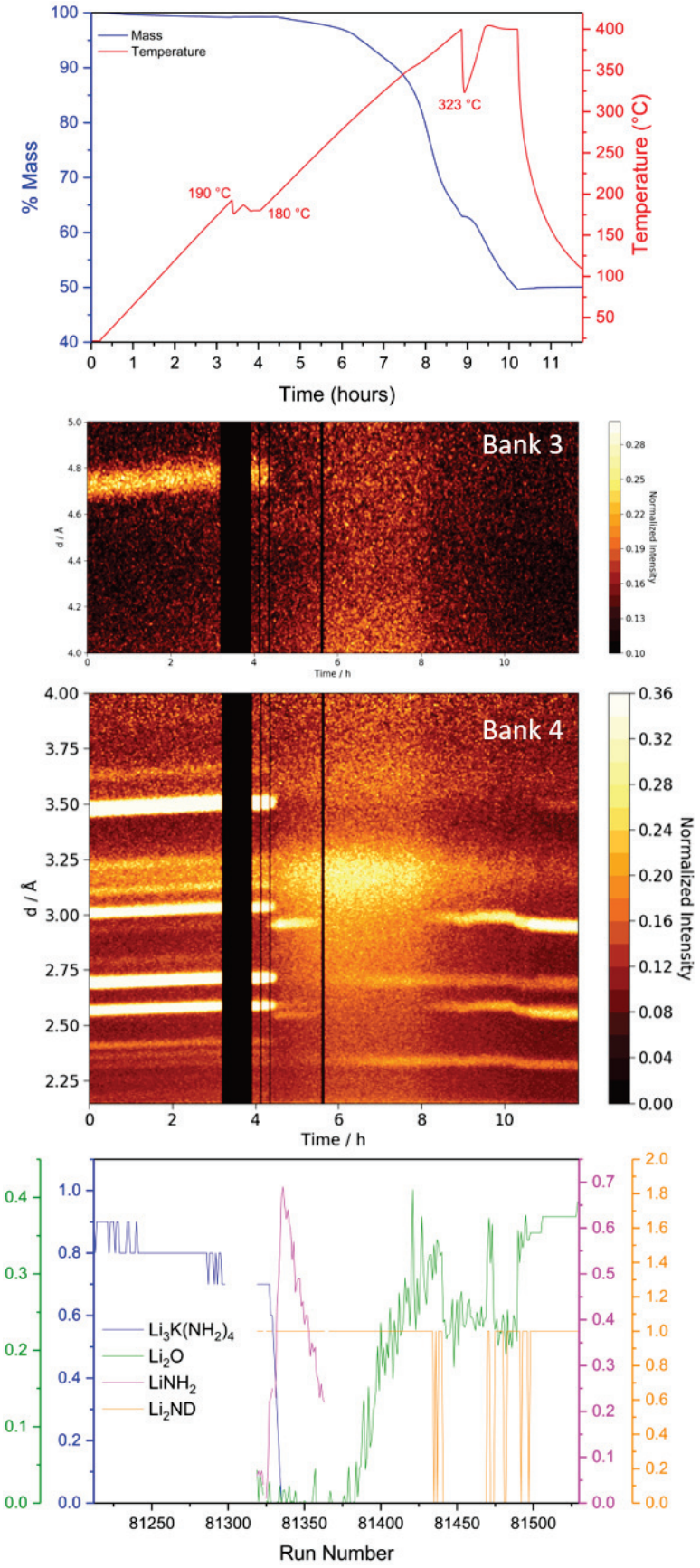


Figure 4.21: Diffraction data from bank 4 for the $Li_3K(ND_2)_4$ decomposition experiment, a batch refinement showing the species present alongside the corresponding thermogravimetric data

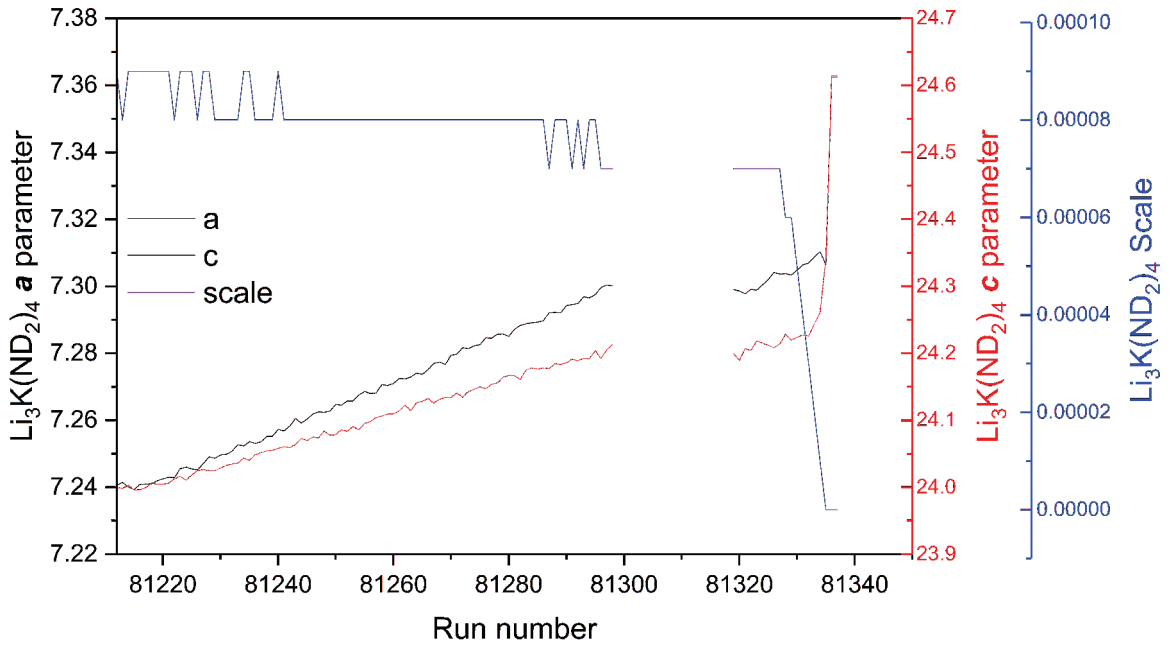


Figure 4.22: The a and c lattice parameters and scale of $Li_3K(ND_2)_4$ until it separates and melts

If $Li_3K(ND_2)_4$ does form a non-stoichiometric phase, it should be possible to see the K^+ occupancy decrease as a function of temperature and reaction progresses as it separates into constituent amide components prior to melting. This is often visible through analysis of the lattice parameters. A steady decrease in the observed K occupancy would be consistent with the separation of $Li_3K(ND_2)_4$ via a series of non-stoichiometric reaction intermediates of general formula $Li_3K_{1-x}(ND_2)_{4-x}$. If the potassium occupancy were to decrease with increasing temperature, to approach $Li_3K_{1-x}(ND_2)_{4-x}$, this would be expected to cause a unit cell contraction along the c-axis. However, if such a unit cell contraction is occurring, it appears to have been counter-balanced by thermal expansion of the phase, leading overall to a $Li_3K(ND_2)_4$ c-parameter that increased slightly with temperature up to 203 °C. Above 203 °C, no Bragg peaks were observed for $Li_3K(ND_2)_4$ indicating that the material had fully transformed towards a material of composition $3LiND_2 + KND_2$.

In Figure 4.21, it can be seen that peaks corresponding to $LiND_2$ appear at 197 °C which is slightly before $Li_3K(ND_2)_4$ fully disappears (7 run overlap). This corresponds to the initial endotherm (199 °C) in Figure 4.15 which was assigned to KNH_2 separating out of the structure possibly through varying compositions of an $Li_3K_{1-x}(ND_2)_{4-x}$ type solid

solution and tending ultimately towards a composition of $3LiND_2$ (solid) + KND_2 (liquid).

Whilst there is not the degree of non-stoichiometry seen in $Li_3Na(NH_2)_4$, which is known to support $Li_3Na_{(1-x)}(NH_2)_{(4-x)}$ $(0 < y < 1)$ phases, $Li_3K_{(1-x)}(ND_2)_{(4-x)}$ only exists for a small temperature range as some KND_2 separates out, before a full sample melt and loss of crystallinity. Analysis of the diffraction data shown in Figure 4.8 and the Raman spectra in Figure 4.7 shows there is reasonable evidence to suggest that $Li_3Ka_{(1-x)}(ND_2)_{(4-x)}$ does exist and a small degree of variable stoichiometry is being observed. The corresponding thermogravimetric data suggest that this phase transition was not accompanied by any change in mass.

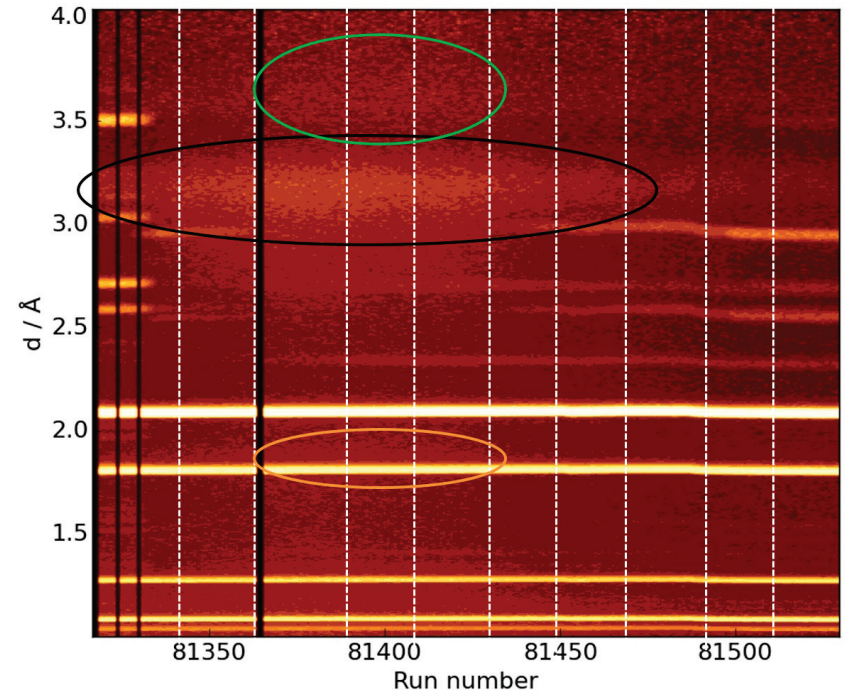
This leaves solid $LiND_2$ (for which Bragg peaks are visible) and molten KND_2 which is visible as amorphous bands in the contour plot and are discussed in more detail later. $LiND_2$ is the only crystalline species to form as the $Li_3K(ND_2)_4$ phase disappears. The $Li_3K_{1-x}(ND_2)_{4-x}$ and KND_2 phases formed as the K-content of $Li_3K(ND_2)_4$ decreased, were not observed by neutron diffraction, indicating that these materials were amorphous (and possibly molten) at the temperature of interest.

As expected, the $LiND_2$ formed is solid at this temperature, and Bragg peaks can be seen corresponding to this phase, especially the two peaks at 2.54 Å (200) and 2.59 Å (004) in addition to the other Bragg peaks at *d*-spacings of 2.86 Å (103) and 2.95 Å (112). The superlattice reflection 5.18 Å (002) of tetragonal $LiND_2$ appears as a consequence of the characteristic doubled cubic cell structure [145] and is used as one of the definitive indicators of the presence of tetragonal $LiND_2$ as opposed to Li_2ND. Although clearly visible in X-ray diffraction data, this peak is not visible in the neutron data collected from bank 3 as would expected, but it is likely that the super lattice peak is down in the noise compared to the size of the other peaks present. However, the (200)/(004) splitting visible in the contour plot is very indicative of tetragonal $LiND_2$ as opposed to cubic Li_2ND.

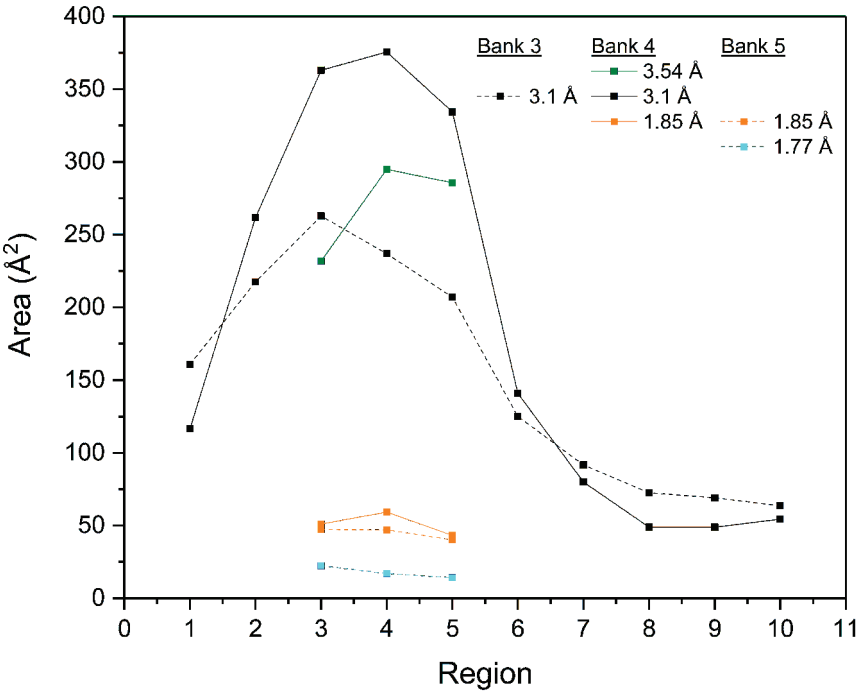
The scale of $LiND_2$ increases to 207 °C and then decreases to 258 °C at which point Bragg peaks corresponding to this phase disappear. This corresponds to the second endotherm in Figure 4.15 (211 °C) which corresponded to the full sample melting and forming one intermixed molten phase.

The melting points of KND_2 and $LiND_2$ are 338 °C and 375 °C respectively, which are well above the melting temperatures observed in this experiment (203 °C and 258 °C respectively) so it is clear a eutectic has formed [193]. The presence of both $LiND_2$ and KND_2 has lowered the melting points of each other in the mixture. This is consistent with the STA analysis into the $LiNH_2$:KNH_2 phase space in Section 4.5 which showed that the simultaneous presence of both these amides leads to the melting point of the mixed-metal amide phases being decreased in temperature by over 100 °C.

A particularly interesting feature of the contour plots are the broad features observed between 200 °C and 380 °C. In bank 3, there was one broad band identified centred around a *d*-spacing of ∼3.1 Å. In bank 4, there were three broad bands identified (highlighted by different coloured eclipses in Figure 4.23a), centred around *d*-spacings of ∼3.54 Å (green), ∼3.1 Å (black) and ∼1.85 Å (orange). In bank 5, there were two broad bands identified, centred around *d*-spacings of ∼1.85 Å and ∼1.77 Å. For each bank, the datasets between run numbers 81319 and 81530 were grouped into 10 regions (each approximately 20 runs) and the constituent datasets summed to provide 10 "sections" for each bank. The broad bands in the summed patterns for each of the 10 sections, were fitted to pseudo-Voigt peaks in TOPAS for which the area (Figure 4.23b), position and width were recorded.



(a) 10 regions for runs 81319-81530 for Bank 4 data and the 3 broad features identified



(b) Peak area for each of the broad features in banks 3, 4 and 5

Figure 4.23: Amorphous peak modelling

Equations 4.2 enable the particle size to be plotted (Figure 4.24), so the rate of growth of these particles can be tracked with temperature. Figure 4.23 shows that they are most prevalent (greatest area) in regions 3 and 4 which corresponds to a temperature range of 265 °C-320 °C. Only regions (2), 3, 4 and 5 have sufficiently large peaks to produce realistic particle size predictions and so have been included in Figure 4.24.

$$\frac{\Delta d}{d} = \frac{d}{p} \qquad \text{where d = } d\text{-spacing (Å) and } \Delta\text{d = Width} \tag{4.2a}$$

$$\frac{\text{Width}}{d\text{-spacing}} = \frac{d\text{-spacing}}{\text{Particle size}} \tag{4.2b}$$

$$\text{Particle size} = \frac{d\text{-spacing}^2}{\text{Width}} \tag{4.2c}$$

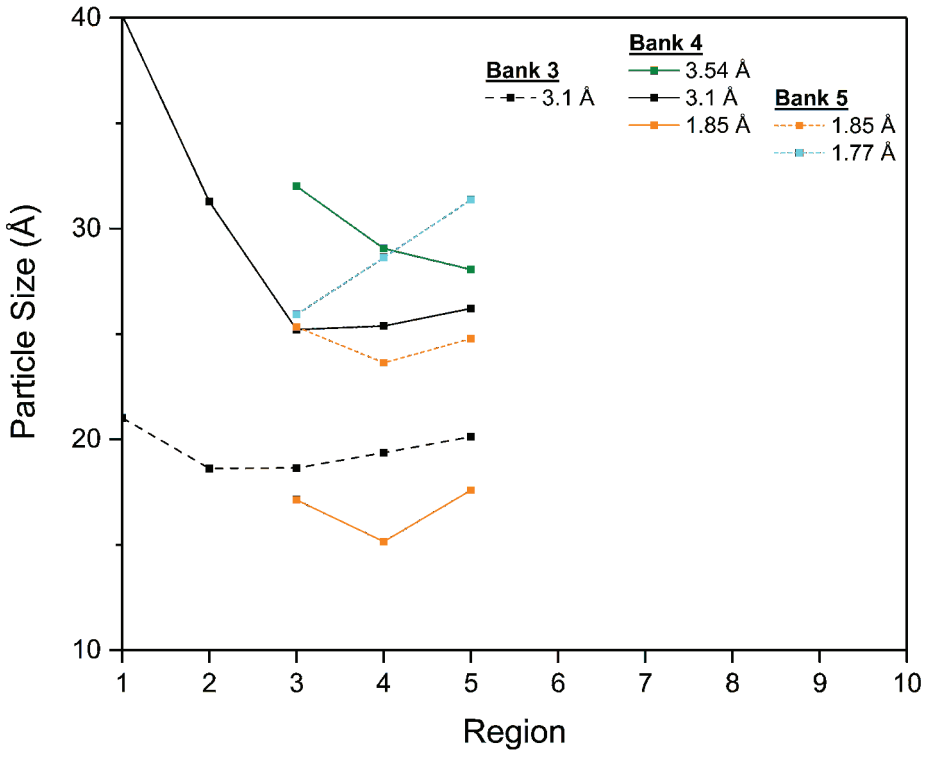


Figure 4.24: Particle size predicted by the broad features in banks 3, 4 and 5

It could be that the broad features correspond to amorphous nano-crystals of cubic KND_2 which are displaying local order, as the d values are similar to those for this material (d=3.54 Å (111) (green), d=3.06 Å (200) (black), d=1.85 Å (311) (orange), d=1.77 Å (222) (blue)). The melting points of KND_2 and $LiND_2$ are 338 °C and 375 °C respectively which corresponds to the disappearance of these features and a decrease in the background. However, $Li_3K(ND_2)_4$ separates prior to melting to form a molten phase approaching $3LiND_2 + KND_2$ not solid nano-crystals. It is possible to obtain amorphous background diffraction from liquids, so these broad features are more likely to correspond to liquid KND_2 in a molten phase. Liquids are structurally highly disordered but can contain some features of the solid structure if that is favoured by the coordination. The disappearance of these broad features at 380 °C would therefore correspond to decomposition of KND_2 which correlates well with the onset of gas release corresponding to the decomposition of $Li_3K(NH_2)_4$ on the gas flow panel in Figure 4.17.

At 260 °C a new set of Bragg peaks appears corresponding to a small amount of Li_2O (2.69 Å (111) and 2.33 Å (200)) are observed which gradually increase in intensity as the experiment progresses and are likely due to a small amount of air present within the experimental equipment. The Li_2O can be seen to form as soon as the Bragg peaks corresponding to $LiND_2$ disappear. After the initial increase due to the reaction of $LiND_2$ with any oxygen (or water) absorbed in the system, the Li_2O scale factor remained virtually constant during the remainder of the experiment, indicating that all the accessible oxygen had been utilised.

At 376 °C, there is a distinct change in the background, the amorphous features disappear and Bragg peaks appear. Whereas it was $LiND_2$ that formed initially on the decomposition of $Li_3K(ND_2)_4$, the Bragg peaks that appear at 376 °C correspond to lithium imide (2.58 Å (400) ($LiND_2$ would have two peaks here) and 2.98 Å (222)). The Li_2ND scale factor increased from zero as the amorphous phase disappears suggesting that Li_2ND was formed from decomposition of the amorphous phase. This fits with the decomposition sequence proposed in Section 4.6.1 which shows the concurrent decomposition of $LiND_2$ and KND_2 to ultimately form Li_2ND and K metal. The increase observed in the Li_2ND scale factor coincided with the second mass loss from 350 °C in the thermogravimetric data (Figure

4.26). The *d*-spacing of the Li_2ND Bragg peaks follows the temperature profile well from 8 hours onwards due to thermal expansion and contraction.

From 185 °C downwards on cooling, a Bragg peak at ∼3.51 Å becomes visible in banks 3 and 4. This correlates well with the sharp exotherms seen in the STA data in Figure 4.15 at this temperature which were attributed to recrystallisation of $Li_3K(NH_2)_4$. Therefore this peak could be the 3.46 Å (202) $Li_3K(ND_2)_4$ peak.

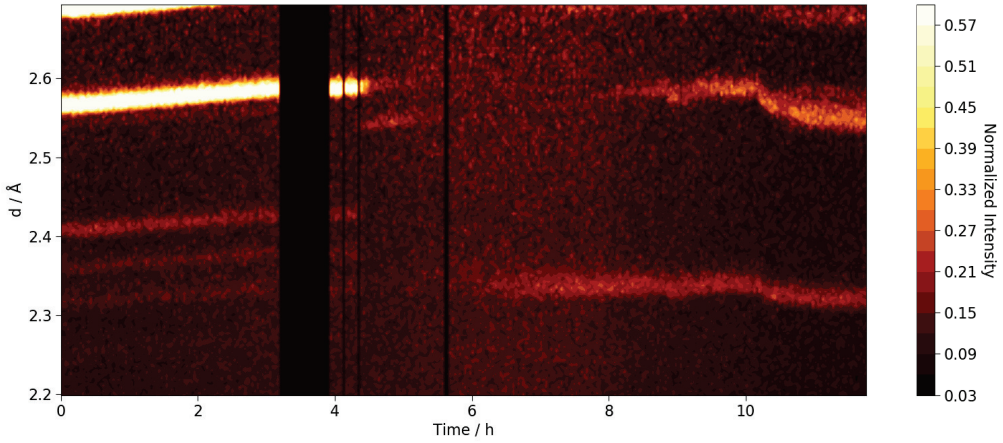


Figure 4.25: In Bank 5 the Li_2ND peak at 2.55 Å has a shoulder appear from 185 °C on cooling

In bank 5, a shoulder appears in the Li_2ND peak at 2.55 Å from 185 °C on cooling (Figure 4.25). This could be the 2.56 Å (220) peak of $Li_3K(ND_2)_4$ or it could be that lithium imide is becoming more amide like. Whereas cubic lithium imide has one peak at this *d*-spacing, (2.58 Å (400)) tetragonal lithium amide has two peaks here at 2.54 Å (200) and 2.59 Å (004). Li_2NH is known to undergo a transition between a high temperature disordered structure and a low temperature ordered structure but this has been reported to be at much lower temperatures of 80 °C to 87 °C [26, 100].

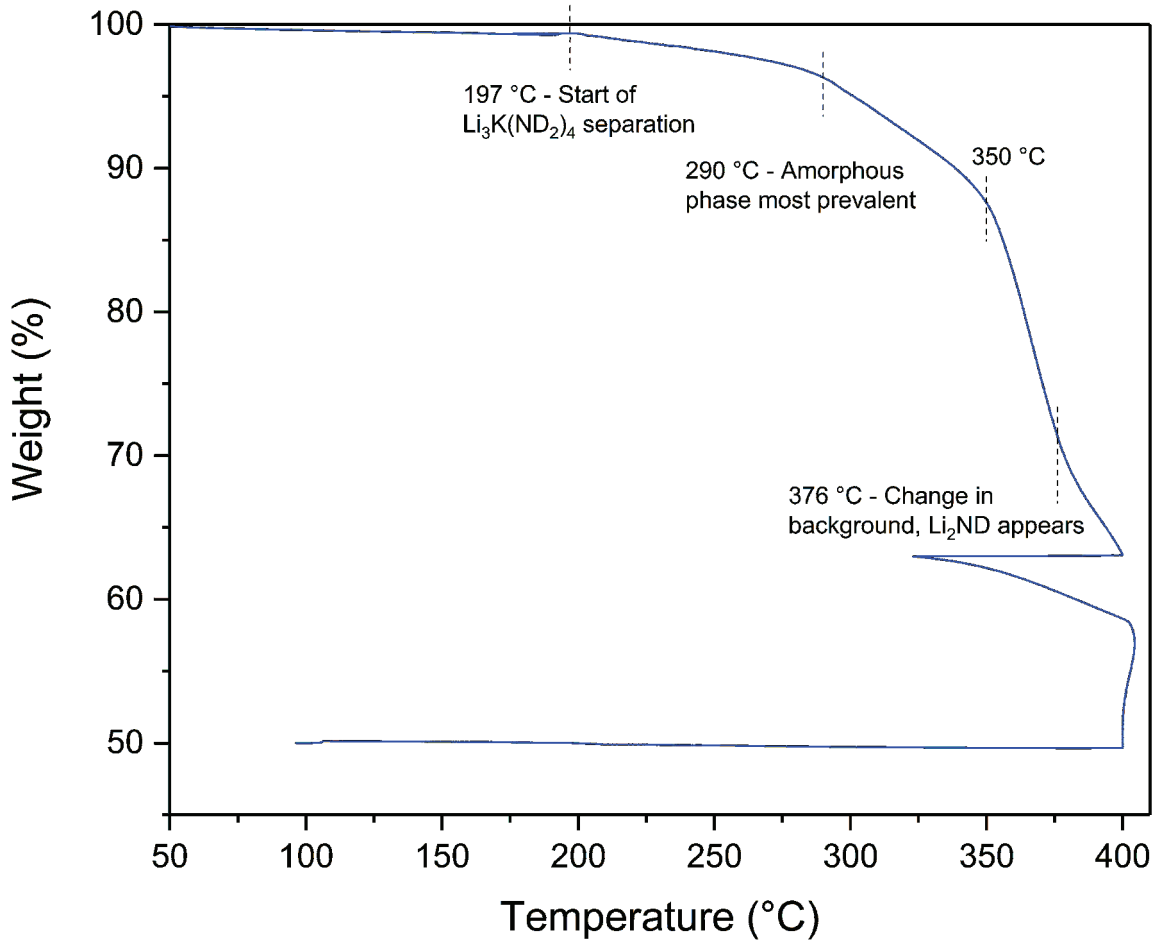


Figure 4.26: Percentage mass loss from $Li_3K(ND_2)_4$ during the decomposition experiment on GEM

Figure 4.26 shows a near constant mass up to 197 °C, and then the onset of mass loss which aligns with the disappearance of Bragg peaks from $Li_3K(ND_2)_4$ and the appearance of $LiND_2$ and amorphous KND_2 (separation).

Comparison of the crystallographic and thermogravimetric data indicates that the mass loss step from 70 %-50 % was accompanied by in increase in the Li_2ND scale factor. It therefore appears that the amorphous KND_2 and $LiND_2$ produced from the separation of $Li_3K(ND_2)_4$ decomposed to form Li_2ND and an amorphous K phase, releasing gas.

The final products of $Li_3K(ND_2)_4$ decomposition under flowing argon after the gas flow panel experiment showed that Li_2ND was produced with a small amount of Li_2O also present, which is supported by this *in-situ* experimental analysis.

Decomposition of $Li_3K(ND_2)_4$ (molar mass = 124.0) to $\frac{3}{2}Li_2NH$ (molar mass = 28.9)

(assuming all other species were lost as gases and K volatilised) would result in a mass loss of 65 %. Figure 4.26 shows a mass loss of 50 % (which correlates well with Figure 4.27) and suggests that K is not being fully volatilised and lost. Decomposition of $Li_3K(NH_2)_4$ to $\frac{3}{2}Li_2ND$ and K (molar mass = 39.1) would result in a mass loss of 33 % therefore some of the K product from $Li_3K(ND_2)_4$ decomposition is remaining in the reactor either as K metal or KND_2.

4.6.3 Inert gas summary for $Li_3K(NH_2)_4$

Figure 4.27 shows the superposition of the mass trace when $Li_3K(NH_2)_4$ was heated on the IGA, the MS trace for the gases released when heated on the gas flow panel and the DSC trace when heated on the STA. The key results from the GEM decomposition experiment have also been summarised at the relevant temperatures.

It is evident from both the *in-situ* and *ex-situ* data that there are different individual events taking place in the complex multi-step thermal decomposition, and it is clear that a different mechanism is occurring compared to a simple superposition of the individual behaviours of $LiNH_2$ and KNH_2. Looking holistically at all the data collected together suggests $Li_3K(NH_2)_4$ separates and melts into a combined melt and the presence of KNH_2 in this mixture lowers the decomposition temperature and leads to H_2 and N_2 release rather than NH_3.

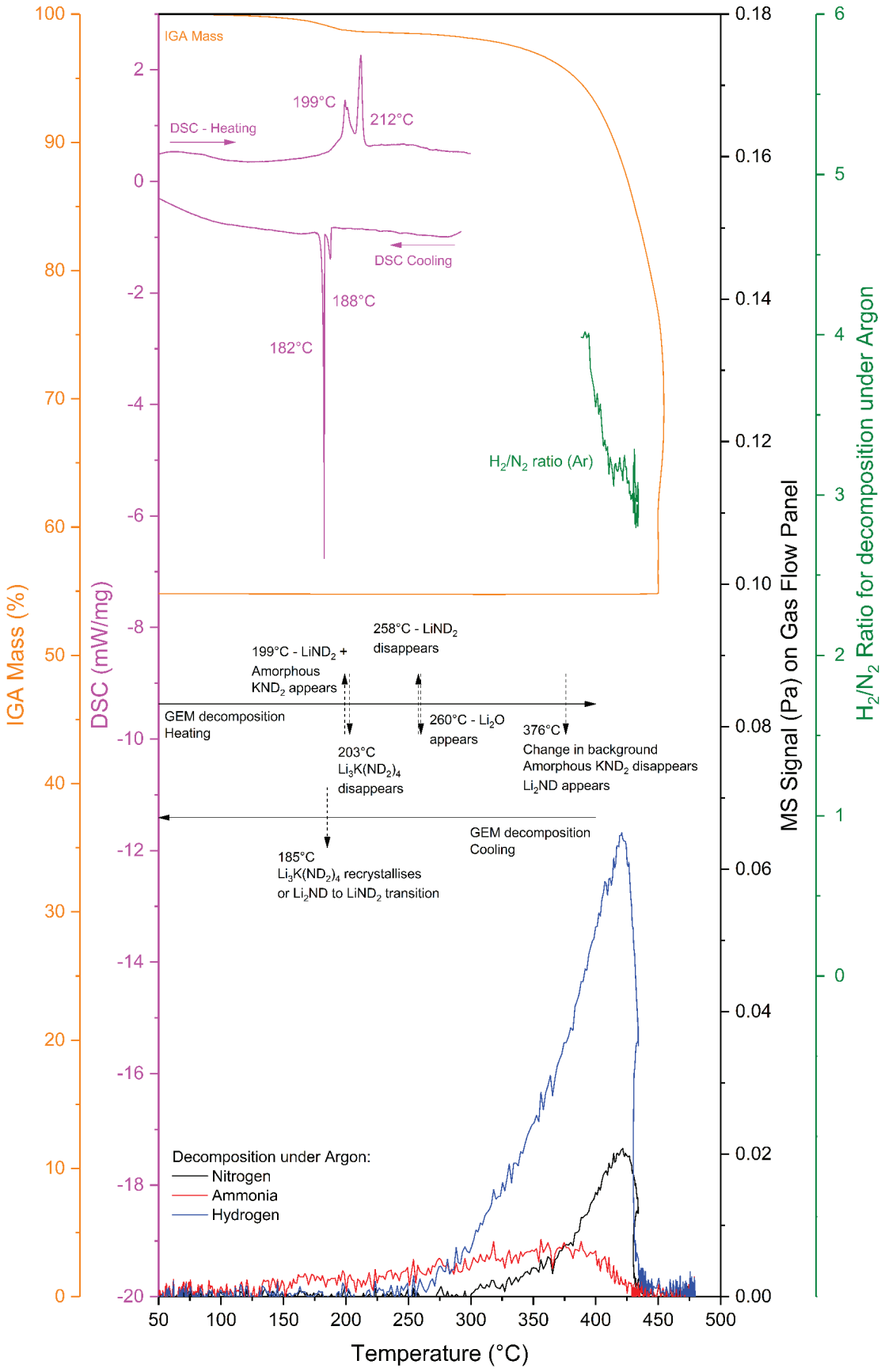


Figure 4.27: Thermodynamic properties measured during the decomposition of $Li_3K(NH_2)_4$ under inert gas

4.7 $LiK_2(NH_2)_3$

4.7.1 *Ex-situ* thermal decomposition behaviour

Having developed a novel and successful method for the high purity synthesis of $LiK_2(NH_2)_3$, the first step to understanding its decomposition and how it behaves, was to analyse its activity under inert gas at low temperatures by STA and at high temperatures on the gas flow panel.

The STA trace of $LiK_2(NH_2)_3$ was compared to that of a hand ground mixture of $LiNH_2 + 2KNH_2$ (Figure 4.28). STA is a particularly important tool for investigating $LiK_2(NH_2)_3$ as it was not successfully synthesised during the *in-situ* GEM experiment (Section 4.7.2.1).

The STA traces for pre-made $LiK_2(NH_2)_3$ and $LiNH_2 + 2KNH_2$ are vastly different which suggests that in the $LiNH_2 + 2KNH_2$ STA experiment, no $LiK_2(NH_2)_3$ was actually made, as other than the initial synthetic thermal event, these traces should otherwise be identical. This is not surprising given the difficulty with which $LiK_2(NH_2)_3$ was synthesised in the tube furnace and on the gas flow panel (Section 2.2.4.2) and during the *in-situ* GEM experiment (Section 4.7.2.1). The undulations seen in the $LiNH_2 + 2KNH_2$ trace are unusual and drawing conclusions from these STA data alone is quite difficult. Key points have been extracted and discussed, but it is more instructive to consider this data in conjunction with that collected both *in-situ* and *ex-situ* by other techniques to understand this system more fully.

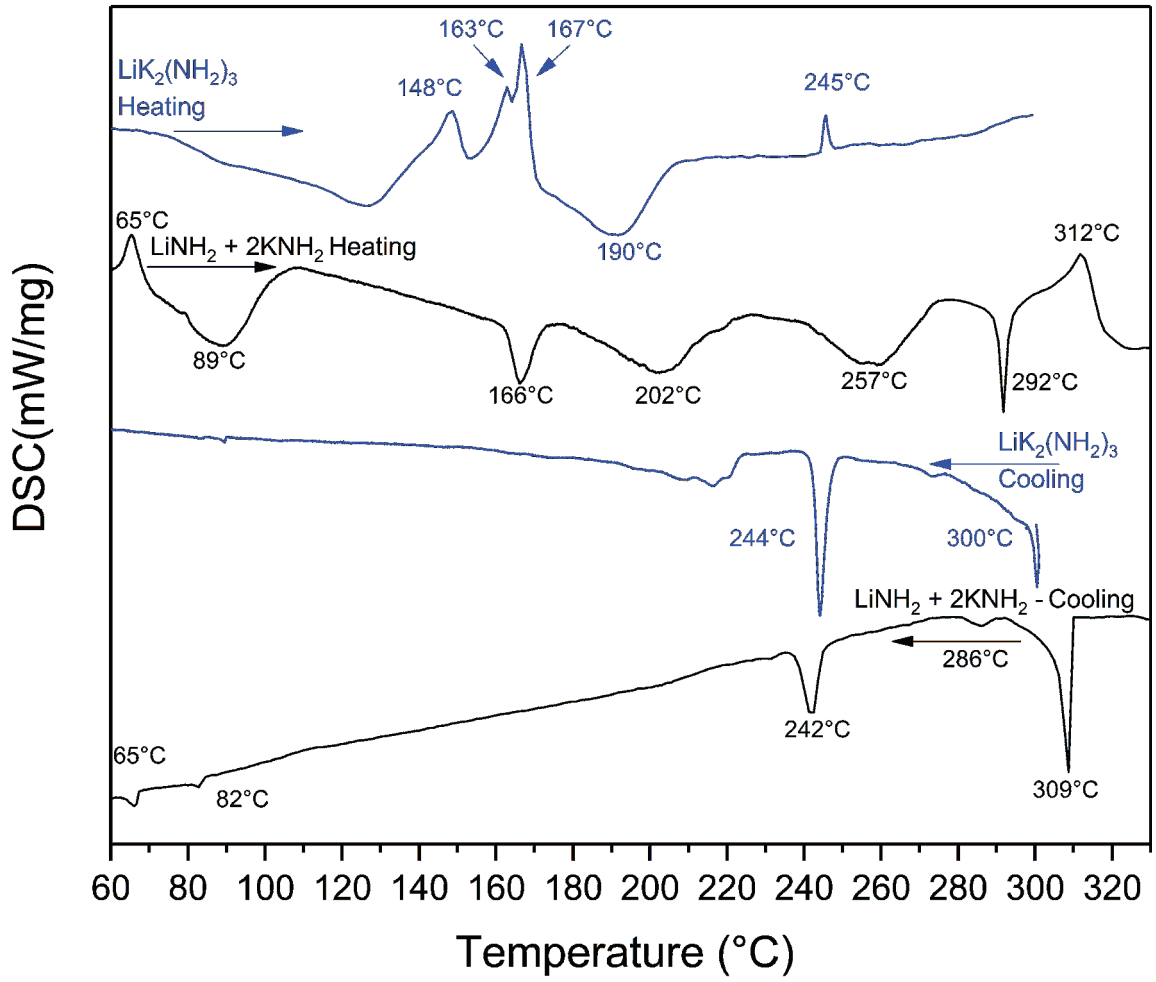


Figure 4.28: DSC traces for $LiK_2(NH_2)_3$ (blue) and $LiNH_2 + 2KNH_2$ (black)

The thermal event at 148 °C could potentially be an endothermic synthesis peak as a result of incomplete synthesis in the ball-mill. It could also relate to desorption of physisorbed gases from within the powder grains because Figure 4.39 shows that the thermal event at 148 °C occurs alongside a $\sim$1% mass loss in the trace recorded by the IGA^n during the *in-situ* GEM decomposition experiment.

Analysis of Figure 4.28 suggests that the endotherm at 163 °C corresponds to the separation of $LiK_2(NH_2)_3$ into $LiNH_2$ and KNH_2 and the endotherm at 167 °C is the combined melt of the whole sample. This is analogous to the STA for $LiNa_2(NH_2)_3$ shown in Figure 3.8 which showed separation and melt endotherms at 201 °C and 204 °C respectively. For both these materials, there is only a small temperature range $\sim$4 °C for which the material is present as separate components, as molten KNH_2 and solid $LiNH_2$, before the $LiNH_2$

dissolves into the liquid KNH_2 and a molten phase approaching $LiNH_2 + 2KNH_2$ is formed.

The unknown endotherm at 245 °C correlates with exotherms in the cooling traces of both $LiK_2(NH_2)_3$ and $2LiNH_2 + KNH_2$. From analysis of the GEM experiment for the decomposition of $LiK_2(ND_2)_3$ (Section 4.7.2.2) it can be seen that at 230 °C KND_2 starts to loose its crystallinity and the endotherm at 245 °C could therefore relate to this.

The sharp exotherm at 300 °C seen in the cooling trace of $LiK_2(NH_2)_3$ (blue) is consistent with $LiK_2(NH_2)_3$ separating and some KNH_2 recrystallising on cooling. The GEM diffraction data in Figure 4.36 shows some KND_2 cubic regains its crystallinity on cooling at 300 °C. During the STA experiment for $LiNH_2 + 2KNH_2$ (black), $LiK_2(NH_2)_3$ did not form, so KNH_2 is still present and is therefore seen to recrystallise at 309 °C. Figure 4.1 shows KNH_2 has a small exotherm at 242 °C on cooling, therefore the presence of exotherms at 244 °C/242 °C on cooling in Figure 4.28 suggest that KNH_2 has separated out of $LiK_2(NH_2)_3$ and is behaving independently on cooling. The presence of these two exotherms on cooling were also seen in the 1:11, 3:9, 4:8 and 5:7 $LiNH_2$:KNH_2 STA traces shown in Figure 4.4 and detailed in Table 4.14. These exotherms are particularly interesting as they are not temperatures expected for crystallisation of either $LiNH_2$ or KNH_2.

The high temperature decomposition behaviour under argon on the gas flow panel of both pre-synthesised $LiK_2(NH_2)_3$ and a hand ground mixture of $LiNH_2 + 2KNH_2$ were compared (Figure 4.29). Previous synthesis attempts on the gas flow panel under argon (Section 2.2.4.2) showed at 200 °C $LiK_2(NH_2)_3$ was only formed in $\sim$40% purity. However, it is possible that at higher temperatures, the same materials will be present in both cases, as a result of the decomposition of the pre-formed $LiK_2(NH_2)_3$ into a combined melt of the constituent single metal amides. The decomposition traces should therefore look the same as the same molten phase will be present in both experiments.

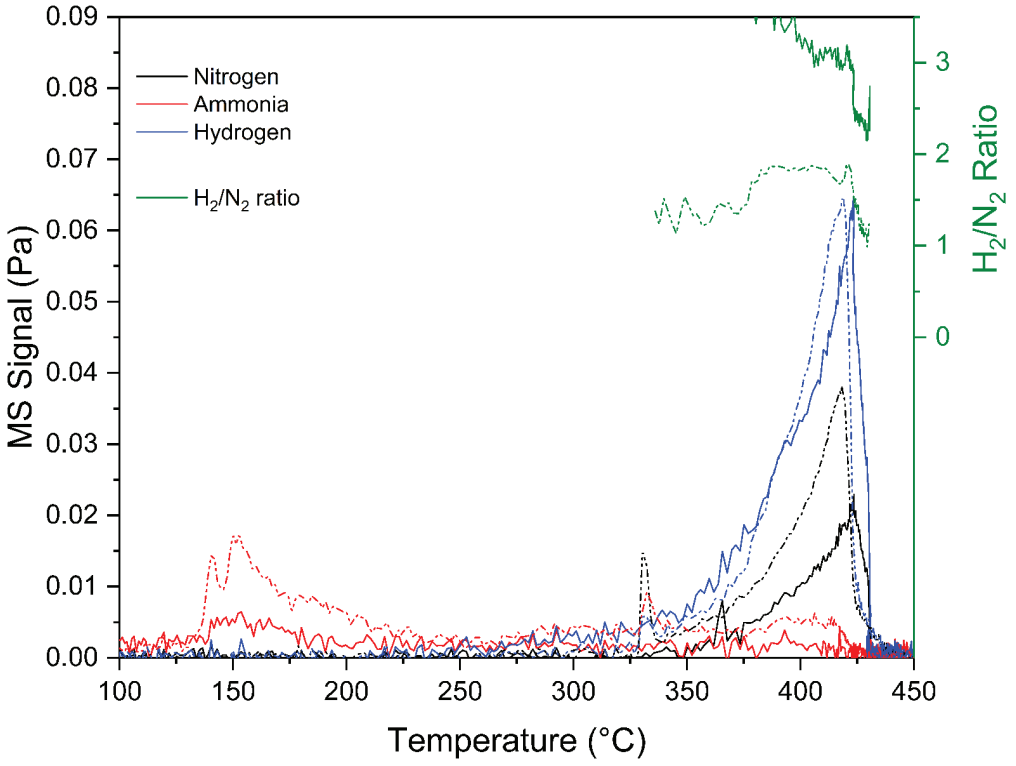


Figure 4.29: Decomposition of $LiK_2(NH_2)_3$ (solid lines) and $LiNH_2 + 2KNH_2$ (dashed lines) on the gas flow panel under argon

Again, qualitatively it can be seen that it is H_2 and N_2 that is released rather than NH_3. $LiNH_2$ and KNH_2 decompose at 350 °C and over 400 °C respectively so this mixed-metal system is not simply a superposition of their individual amide components post separation.

The trace for $LiNH_2 + 2KNH_2$ shows an NH_3 release at 150 °C which correlates with the thermal event observed at 166 °C in the $LiNH_2 + 2KNH_2$ STA trace. $LiK_2(NH_2)_3$ also shows an NH_3 release at this temperature but to a smaller extent and this could correlate with the endotherm seen at 148 °C in the $LiK_2(NH_2)_3$ STA trace (Figure 4.28). This had been assigned to the desorption of physisorbed gases due to concurrent mass loss recorded by the IGA^n at this temperature in the GEM decomposition experiment. However, as the thermal event in the $LiNH_2 + 2KNH_2$ STA trace is exothermic and that in the $LiK_2(NH_2)_3$ STA trace is endothermic, it is likely that they correspond to different crystallographic events/processes despite both leading to NH_3 gas release at similar temperatures. A small amount of ammonia is also released at 150 °C during the decomposition of $LiNa_2(NH_2)_3$ (Figure 3.9).

There are sharp spikes in the N_2 trace for both $LiNH_2 + 2KNH_2$ (330 °C) and $LiK_2(NH_2)_3$ (365 °C). The STA experiments were not heated so high meaning it cannot be seen if there are corresponding exotherms. These may relate to the decomposition of KNH_2 which is known to decompose to K metal and N_2 and H_2 gases (Equation 4.1).

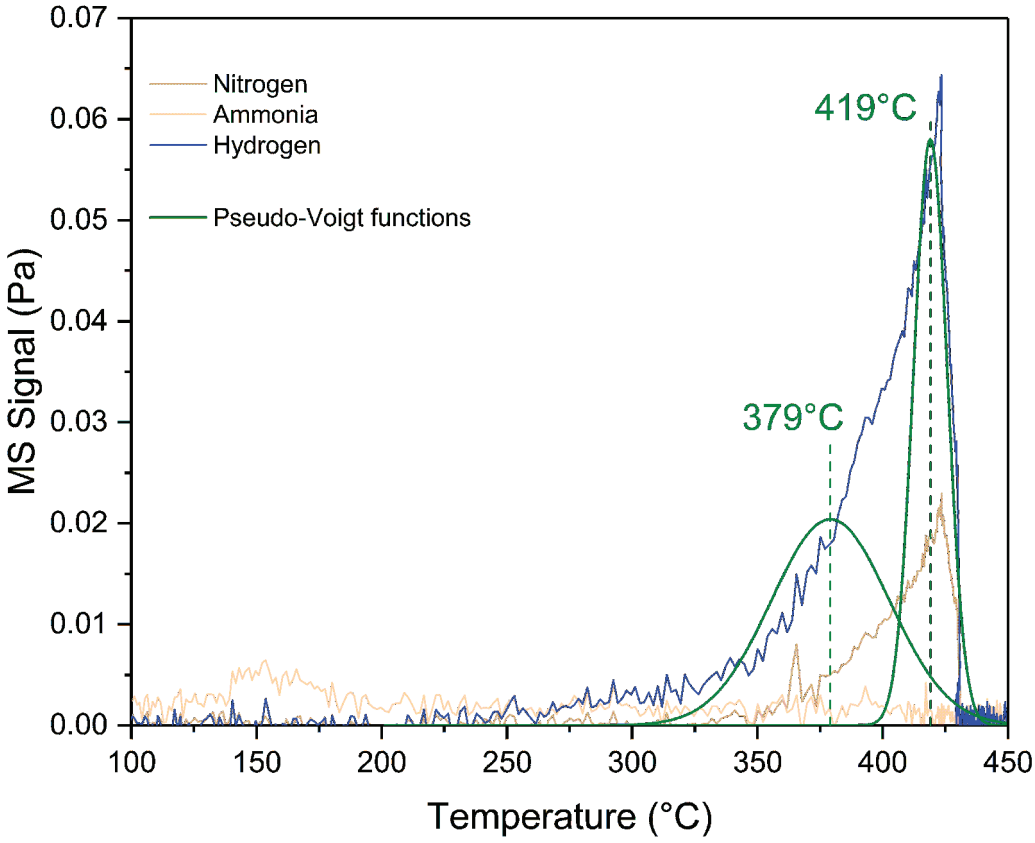


Figure 4.30: Two pseudo-Voigt functions have been used to determine the peak positions in the H_2 curve from Figure 4.29 during the decomposition of $LiK_2(NH_2)_3$

Pseudo-Voigt functions (in TOPAS) have been used to determine the "peak positions" in the H_2 curve observed during the decomposition of $LiK_2(NH_2)_3$ under argon on the gas flow panel (Figure 4.30). This shows that it may be more accurate to think of the MS signal for $LiK_2(NH_2)_3$ in Figure 4.29 as two overlapping peaks centred at 379 °C and 419 °C. These two temperatures correspond to separate events during the decomposition of the combined "melt phase" and are likely due to the constituent single metal amides decomposing at different temperatures.

The MS traces for the decomposition of $Li_3Na(NH_2)_4$ and $LiNa_2(NH_2)_3$ under argon on the gas flow panel each had peak positions in the H_2 curve determined to be at $\sim$370 °C and 404 °C. The lower temperature (370 °C) here is therefore likely due to the decomposition of $LiNH_2$ and correlates well with the H_2 peak position of 378 °C seen for $Li_3K(NH_2)_4$.

Comparison of Figure 4.17 for $Li_3K(NH_2)_4$ and Figure 4.30 for $LiK_2(NH_2)_3$ shows that the two pseudo-Voigt functions for each mixed-metal amide are centred about the same temperatures, $\sim$378 °C and 419 °C. This is consistent with both mixed-metal amides forming a molten phase of $LiNH_2$ and KNH_2 which are then themselves decomposing. This would mean that the molten phase of $LiNH_2 + 2KNH_2$ is decomposing in an analogous manner to the molten phase of $3LiNH_2 + KNH_2$.

It can be seen that the shape of the gas profiles is markedly different for the two different ratios. For the 3:1 ratio (Figure 4.16) it can be seen that H_2 and N_2 are produced from 280 °C and increase in pressure over $\sim$140 °C, whereas for the 1:2 ratio (Figure 4.29) H_2 and N_2 are only produced from 350 °C and the pressure increases much more steeply over 70 °C. This is likely to be due to the different ratios of the single metal amides present in each mixture as $LiNH_2$ decomposes at lower temperatures than KNH_2, which will affect the overall shape of the traces of the gases released.

The different shapes of the H_2 gas profiles for $Li_3K(NH_2)_4$ and $LiK_2(NH_2)_3$ mean the areas of the two pseudo-Voigt functions for each mixed-metal amide are also different. $Li_3K(NH_2)_4$ forms a 3:1 molten phase of $LiNH_2$:KNH_2 which would be expected to have a larger peak at $\sim$378 °C due to the decomposition of $LiNH_2$, the dominant single metal amide. By comparison, $LiK_2(NH_2)_3$ forms a molten phase of majority KNH_2 so the respective areas of the two pseudo-Voigt functions has inverted and the pseudo-Voigt function centred at 419 °C has a larger area due to the greater gas release originating from the more prevalent KNH_2. The difference ratios to which each single metal amide is present means that the gas release for "$Li_3K(NH_2)_4$" (from the decomposition of $LiNH_2$) starts at a lower temperature and has a shallower rise to the peak gas release temperature, whereas the gas release has a much steeper gradient for "$LiK_2(NH_2)_3$" due to the decomposition of KNH_2.

Figure 4.29 also shows the H_2/N_2 ratio for the released gases from 330 °C which would be expected to approach 3. Whereas for $LiK_2(NH_2)_3$ the H_2/N_2 ratio is $\sim$3, for $LiNH_2$

$+\,2KNH_2$ the N_2 signal is relatively higher than that of H_2 so the H_2/N_2 ratio is much lower and is less than 2. This could suggest the products of decomposition are different for the two experiments as the overall amount of each gas released is different, however it is more likely that the calibration of the H_2 trace from the gas flow panel is not accurate. It is therefore more instructive to analyse the qualitative trends in the H_2/N_2 ratios rather than their absolute values.

A mechanism could be proposed for the decomposition of $LiK_2(NH_2)_3$ envisaging the combined separation and melt of $LiK_2(NH_2)_3$ into a molten phase of $LiNH_2$ $+\,2KNH_2$. $LiNH_2$ would then decompose first into Li_2NH followed by KNH_2 decomposition into K.

$$
\begin{aligned}
LiK_2(NH_2)_3 &\longrightarrow LiNH_2 + 2\,KNH_2 && \text{Combined separation and melt}\\
&\longrightarrow \tfrac{1}{2}Li_2NH + \tfrac{1}{2}NH_3\uparrow + 2\,KNH_2 && LiNH_2 \text{ decomposes}\\
&\longrightarrow \tfrac{1}{2}Li_2NH + 2\,K + N_2\uparrow + 2\,H_2\uparrow && KNH_2 \text{ decomposes}\\
&\longrightarrow \tfrac{1}{2}Li_2NH + 2\,K\uparrow && \text{All gases lost}\\
&\longrightarrow \tfrac{1}{2}Li_2NH && \text{K volatalised}
\end{aligned}
$$

Decomposition of $LiK_2(NH_2)_3$ (molar mass = 133.2) to $\frac{1}{2}Li_2NH$ (molar mass = 28.9) and 2K (molar mass = 39.1) would correspond to a mass loss of 30.4 %. The 29.4 % mass loss seen during the *in-situ* decomposition on GEM (Figure 4.38) is therefore in good agreement with this. This implies that whereas during the decomposition of $LiNa_2(NH_2)_3$, some of the Na (decomposition product of $NaNH_2$) was volatilised, the K resulting from the decomposition of KNH_2 was not, which has beneficial impacts on improved containment, an important characteristic for a catalyst. This is similar to the recovery of $Li_3K(NH_2)_4$ compared to $Li_3Na(NH_2)_4$ which also showed K had not been fully volatilised and lost, but Na had.

The final products of $LiK_2(NH_2)_3$ decomposition under flowing argon were determined by powder X-ray diffraction from the post decomposition residue remaining after the gas flow panel experiment. Similarly to all the other mixed-metal amides, this was majority phase Li_2NH (which would be expected as the product of $LiNH_2$ decomposition under argon) with a small amount of Li_2O present. No K containing products were identified by powder X-ray diffraction.

4.7.2 GEM experiments

In analogous experiments to those described in Section 4.6.2, first the synthesis of $LiK_2(ND_2)_3$ from $LiND_2 + 2KND_2$ was studied followed by the subsequent decomposition of $LiK_2(ND_2)_3$ under argon using the IGA^n on the GEM diffractometer at ISIS.

Thermogravimetric readings of the sample mass, temperature and pressure were recorded every 5 seconds (however the mass trace did not work for the synthesis experiment). *In-situ* neutron diffraction data was collected every 100 seconds. Rietveld refinements were performed in TOPAS and batch refinements performed on the data collected from banks 3, 4 and 5 to track the scale of each deuterium-enriched species throughout the course of the reactions.

4.7.2.1 Synthesis of $LiK_2(ND_2)_3$

First the synthesis of $LiK_2(ND_2)_3$ from $LiND_2 + 2KND_2$ was investigated. 0.5 g of $LiND_2$:KND_2 in a 1:2 ratio was hand ground for 5 minutes before being loaded into the IGA^n bucket and placed into the neutron beam under constant 1000 mbar argon. It was then heated to 190 °C at 1 °C/min where it was held for 40 minutes before being cooled to 50 °C. A vanadium can and quartz tail were used so there are no steel peaks visible in the diffraction data.

An hour long scan was taken at room temperature to obtain an accurate refinement for the start of the batch process. Refinement of these diffraction data indicated that the majority phase of the sample was KND_2 (41.6 % monoclinic and 47.6 % tetragonal), with 11.0 % $LiND_2$ present (Table A.5 in the Appendix). Both monoclinic and tetragonal KND_2 (mainly signified by the presence of the (110) peak at 3.04 Å and the (101) peak at 3.53 Å) were present. It is the monoclinic phase of KND_2 ($P2_1/m$) that is known to be stable at room temperature and this undergoes a phase transition to tetragonal (P4/nmm) at 53 °C [150]. The presence of tetragonal KND_2 before heating commenced, may be due to the energy input from the mechanical grinding of the starting materials in the pestle and mortar being sufficient to cause a small amount of the phase change to occur.

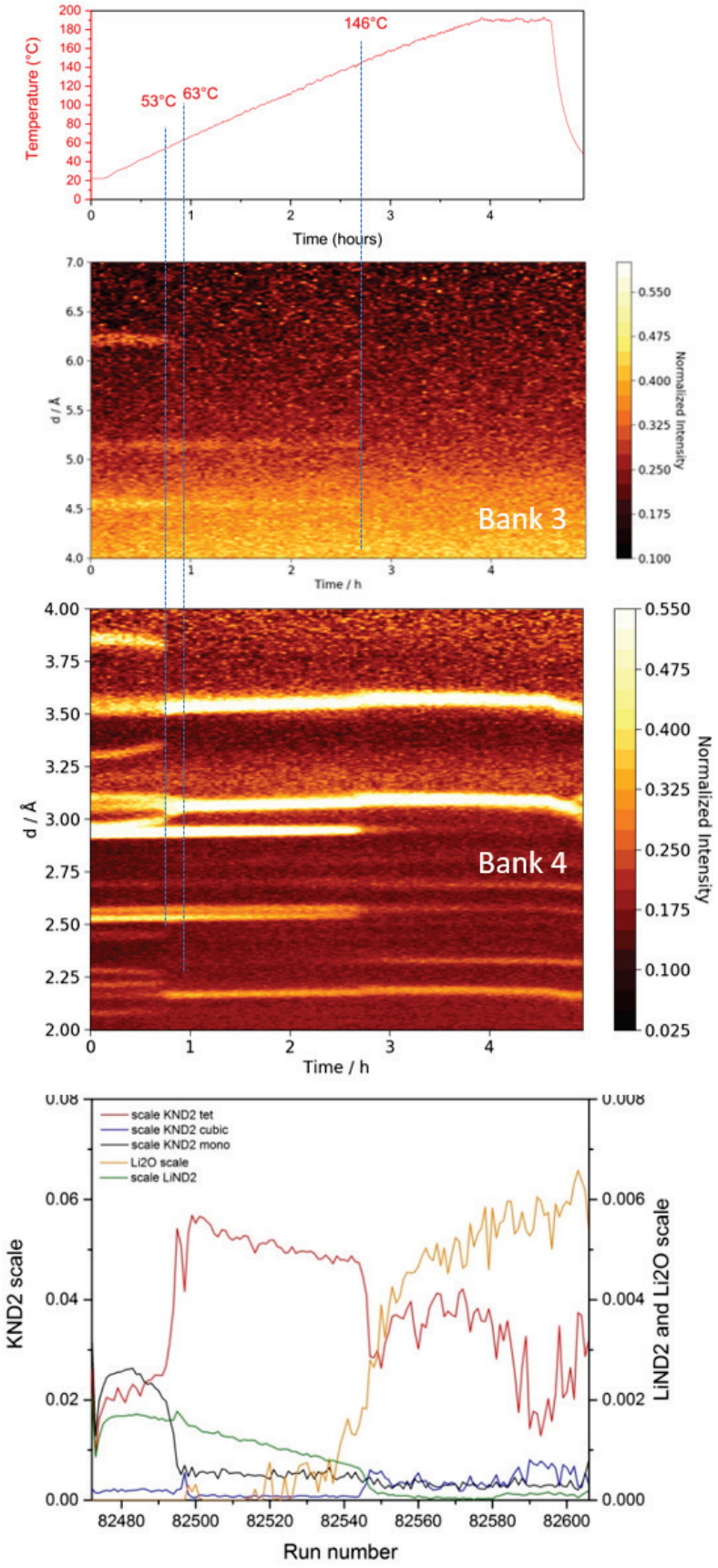


Figure 4.31: Diffraction data from bank 4 for the $LiK_2(ND_2)_3$ synthesis experiment, a batch refinement showing the species present alongside the the temperature profile

Contour plots of the diffraction data collected from banks 3, 4 and 5 and the corresponding temperature profile is presented in the Appendix in Figure A.12. Selected regions of the diffraction data collected from banks 3 and 4 and the batch process refinement for banks 3, 4 and 5 showing the scale of each species present throughout the experiment are presented in Figure 4.31 alongside the temperature profile.

On heating, the monoclinic KND_2 peaks can be seen to disappear at 53 °C as it undergoes a phase change to tetragonal KND_2 (reported value of 53 °C [150]), most clearly signified by the loss of the peaks at 3.85 Å (10-1), 3.29 Å (011), 3.09 Å (002), 2.96 Å (110), and 2.44 Å (102). The tetragonal KND_2 peaks at 3.53 Å (101), 3.04 Å (110) and 3.09 Å (002) also increase in intensity. During the monoclinic to tetragonal phase change, the a and c lattice parameters decrease as b and β increase to enable the $P2_1/m$ to P4/nmm unit cell symmetry change. This explains why the monoclinic (10-1) peak at 3.85 Å shifts to a smaller d-spacing on heating, but the (110) at 2.96 Å shifts to a larger d-spacing as the temperature is increased.

The tetragonal to cubic phase change for KND_2 is visible at 63 °C which correlates well with the reported value of 75 °C [211]. Above 63 °C it is cubic KND_2 (3.54 Å (111), 3.06 Å (200), 2.17 Å (220) and 1.85 Å (311)) and $LiND_2$ that is present in the reactor.

No $LiK_2(ND_2)_3$ appeared to have been synthesised during the experiment. The hour long scan at the start of the $LiK_2(ND_2)_3$ decomposition experiment (Section 4.7.2.2) shows $LiK_2(ND_2)_3$ has distinct peaks at 5.99 Å (101), 4.53 Å (111), 4.50 Å (102), 3.47 Å (200), 3.11 Å (210), 3.07 Å (113), 3.00 Å (211, 202), 2.75 Å (212), 2.53 Å (114), 2.46 Å (220), 2.44 Å (213) and 2.40 Å (221) which are not visible at all throughout the diffraction data collected during this experiment. This is consistent with the findings in Section 2.2.4.2 that $LiK_2(NH_2)_3$ requires mechanical grinding in the ball-mill to form and was not synthesised successfully under heat treatment alone on the tube furnace or gas flow panel.

In Figure 4.31, at 146 °C Bragg peaks corresponding to $LiND_2$ disappeared and Li_2O forms (2.68 Å (111) and 2.32 Å (200)), likely due to a small amount of air in the experimental set-up. This a low temperature for $LiND_2$ to melt (which has a known melting point of 375 °C (Table 4.1)). This suggests that the melting point of $LiND_2$ is being heavily influenced by the presence of KND_2.

At the same temperature that the $LiND_2$ disappears, the *d*-spacings of the Bragg peaks corresponding to cubic KND_2 increase by ~ 0.02 Å (Figure 4.32). The peak at 3.54 Å (111) shifts to 3.56 Å, the peak at 3.06 Å (200) shifts to 3.09 Å and the peak at 2.17 Å (220) shifts to 2.18 Å.

It is believed that a small amount of Li may have been incorporated into the solid KND_2 cubic structure, as at this temperature Li will be liquid and mobile, and this has caused a unit cell expansion and the slight step change in lattice parameter. This is supported by the Raman data for the cases where a small amount of $LiNH_2$ is ball-milled with pre-dominantly KNH_2 (Section 4.3.2 and Figure 4.8). It has been reported that the dissolution of KH into cubic KNH_2 leads to an anionic substitution and a metal amide–hydride solid solution, so it is possible that something similar is happening here but with Li^+ cations instead [246]. As cubic KNH_2 has previously been shown to accommodate and support some compositional variation, this may explain the change in lattice parameter when $LiND_2$ disappears as Li^+ can also possibly move into the KND_2 structure.

On cooling, at 47 °C cubic KND_2 undergoes a phase change to tetragonal KND_2, particularly visible as the 3.06 Å (200) peak splits into the tetragonal 3.09 Å (002) and 3.04 Å (110) peaks. The experiment was not cooled down further, so monoclinic KND_2 was not observed. It appears that tetragonal KND_2 is stable down to lower temperatures than is reported for the phase change for a small amount of time. Li_2O remains visible until the end of the experiment and no $LiND_2$ reforms. This leaves the peak at 2.58 Å seen in banks 4 and 5 unfitted.

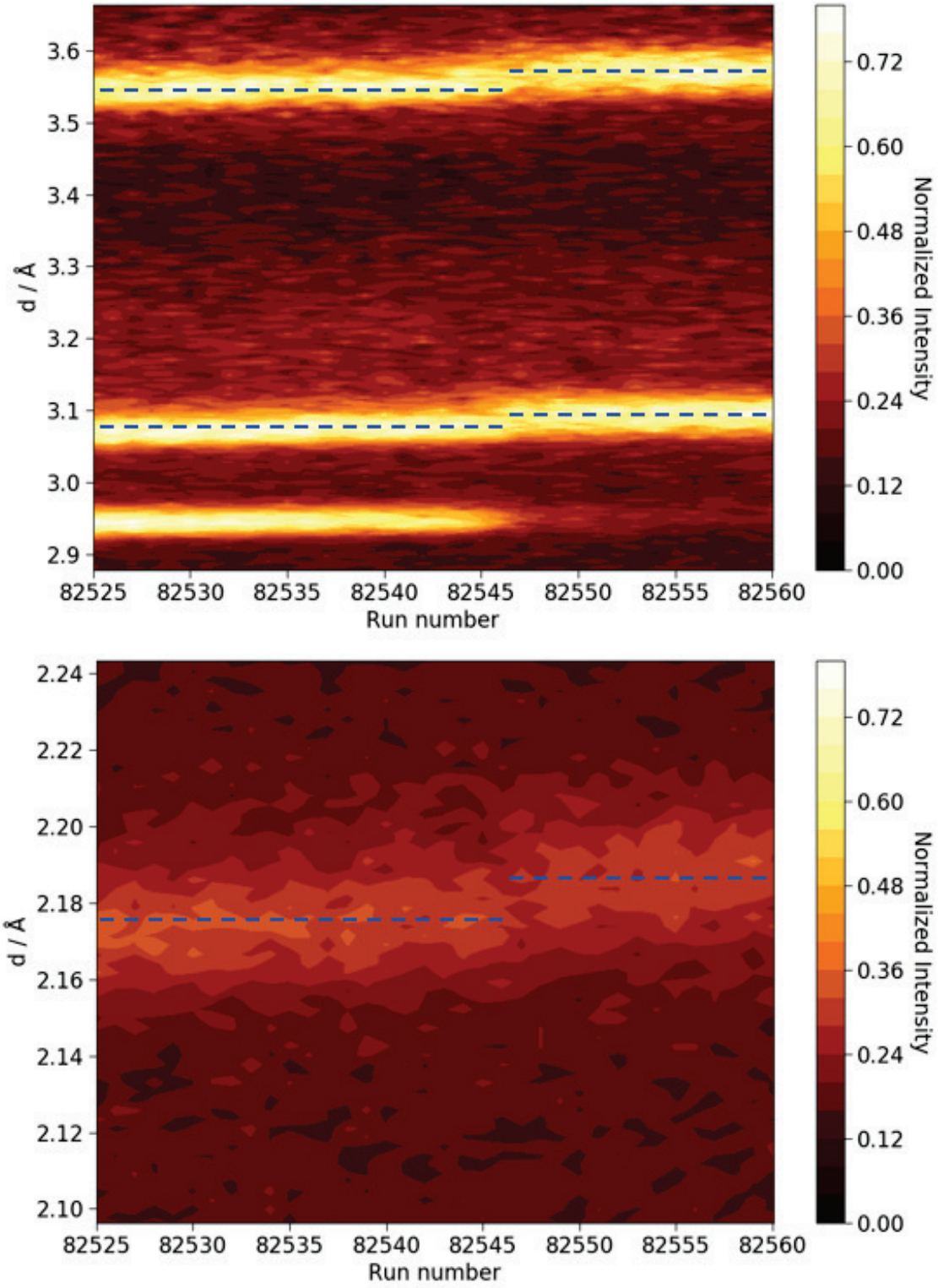


Figure 4.32: Step change seen in Bragg peaks of KND_2 cubic peaks as $LiND_2$ Bragg peaks disappear

4.7.2.2 Decomposition

As no $LiK_2(ND_2)_3$ was formed in the synthesis experiment on GEM described above, (and so that a vanadium can and quartz tail could be used in the synthesis experiment), a separate pre-made sample (*ex-situ*) was used for this experiment to probe the decomposition of $LiK_2(ND_2)_3$. This $LiK_2(ND_2)_3$ sample was synthesised by ball-milling $LiND_2$ and KND_2 (1:2) and was confirmed by powder X-ray diffraction (Figure A.11 in the Appendix). A stainless steel reactor had to be used as the sample was heated to 400 °C (as discussed in Section 4.6.2.2) so there are unavoidable steel peaks in the contour plots.

A contour plot of the diffraction data collected from bank 4 and the corresponding thermal and gravimetric data is presented in Figure 4.33. The sample of $LiK_2(ND_2)_3$ was heated from room temperature at 1 °C/min and the neutron beam failed when it reached 285 °C. The sample continued to be heated until it reached 320 °C at which point the heating was stopped and it was cooled to 260 °C where it was held for one hour. At this point it was determined that the beam would not come back on soon, so to prevent any degradation of the sample, it was cooled to room temperature. In total the beam was off for 24 hours. When the beam came back on, the sample was heated at 5 °C/min to 120 °C as neutron diffraction data for this temperature range had already been collected, and then more slowly at 1 °C/min from 120 °C to 400 °C. Once the sample reached 400 °C it was cooled to 90 °C before the experiment was ended. Throughout the course of the experiment there were three additional very short periods of beam failure but these only lasted for one or two runs so were inconsequential to the data analysis. Due to the severe length of the 24 hour beam off in the middle, the analysis will be treated in two separate sections before finally looking at the overall experiment.

Analysis of Section 1 from Figure 4.33 shown in Figure 4.34

Contour plots of the diffraction data collected before the 24 hours of beam failure from banks 3 and 4 are presented in Figure 4.34 alongside the lattice parameters and scale of $LiK_2(ND_2)_3$, and the corresponding thermogravimetric data. This graph plots the result of the batch refinement for the data collected from banks 3, 4 and 5. Full contour plots from banks 3, 4 and 5 for this section are shown in the Appendix in Figure A.13.

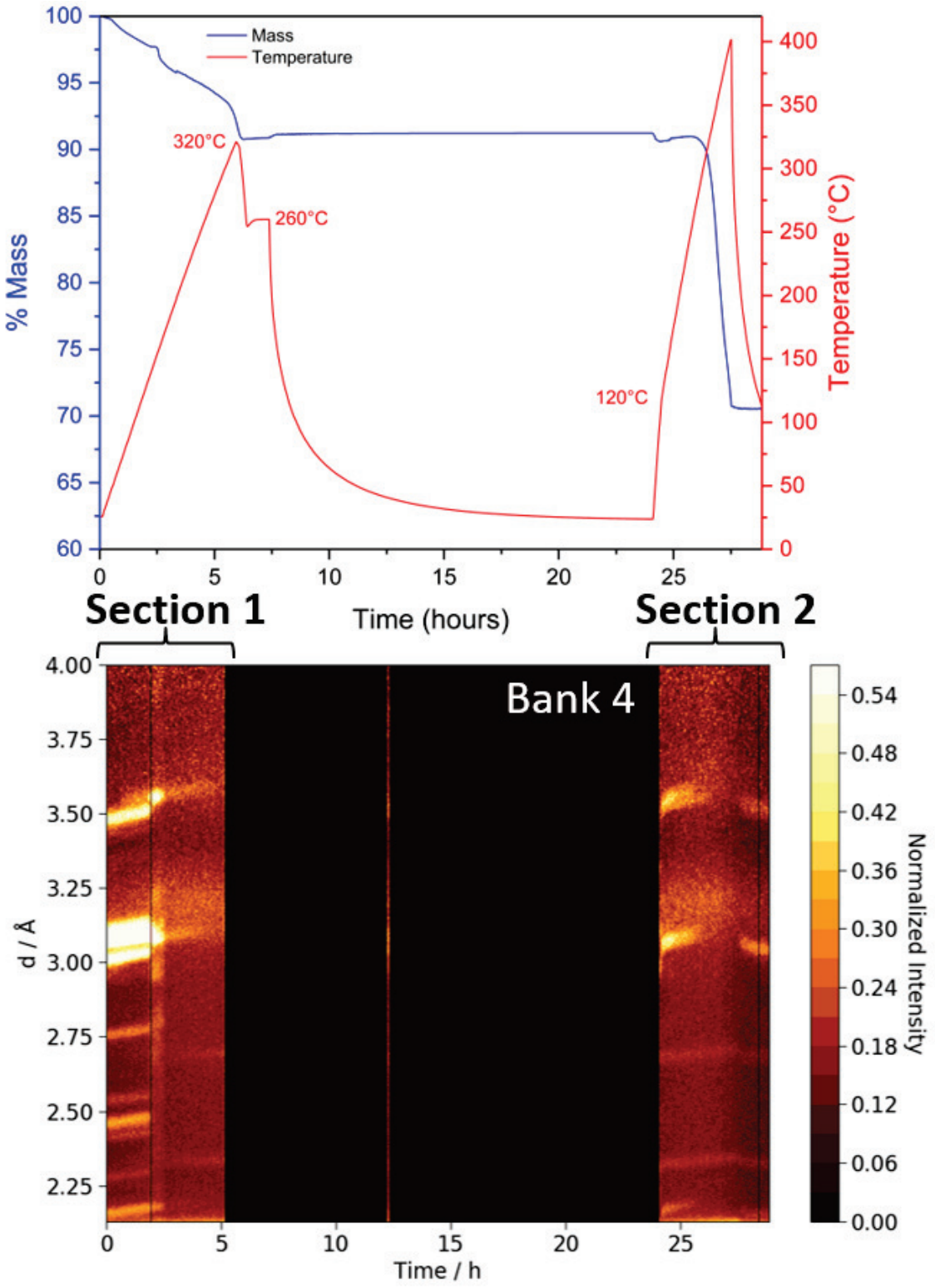


Figure 4.33: Contour plot for bank 4 for the whole $LiK_2(ND_2)_3$ decomposition experiment alongside corresponding thermogravimetric data

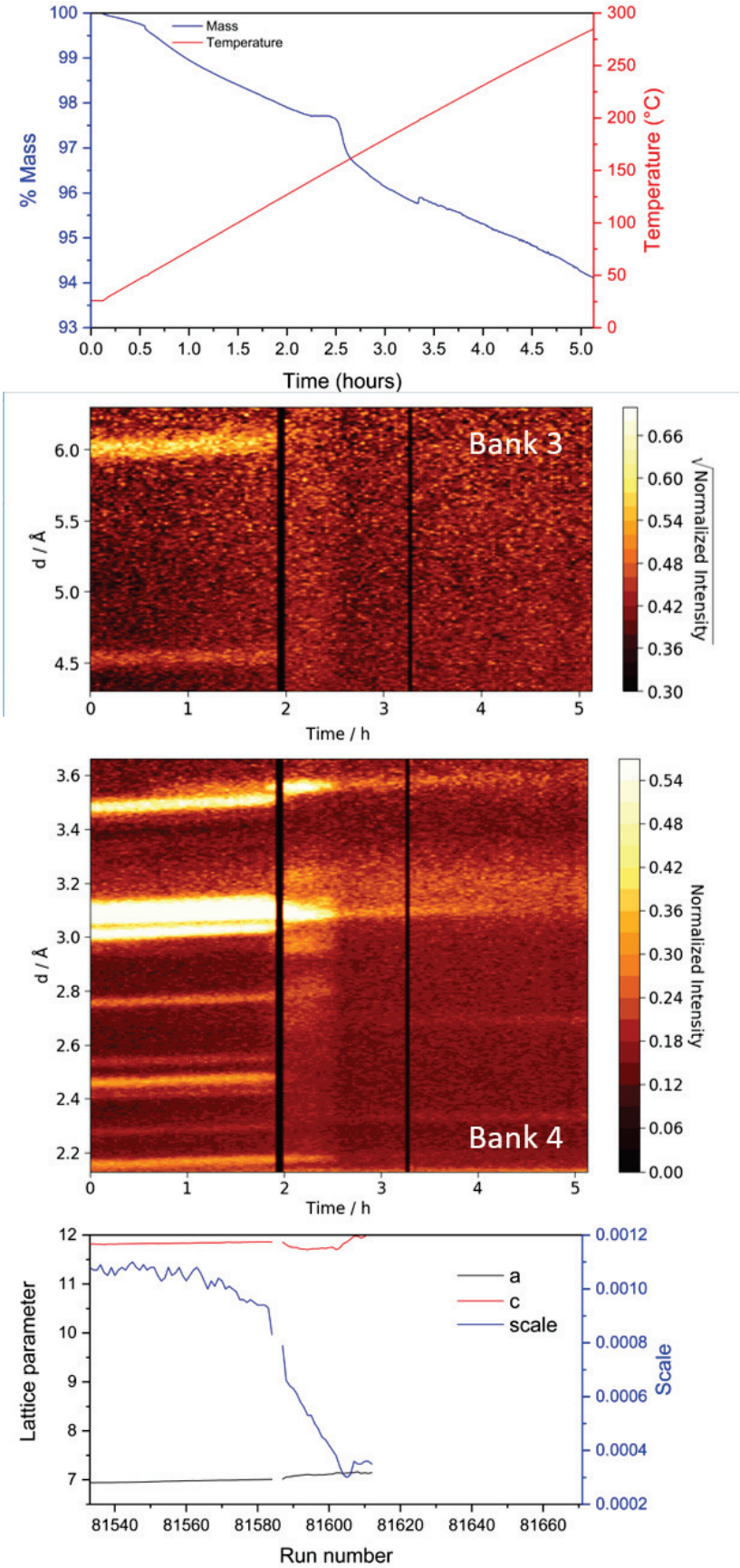


Figure 4.34: Contour plots from banks 3 and 4, the batch refinement showing the scale and lattice parameters of $LiK_2(ND_2)_3$ alongside the thermogravimetric data for the period before the beam failed

An hour long scan was taken at room temperature to get an accurate refinement for the start of the batch process which refines to pure $LiK_2(ND_2)_3$ (Table A.6 in the Appendix).

A new set of Bragg peaks appear at 118 °C which index to cubic KND_2 (3.55 Å (111), 3.08 Å (200) and 2.18 Å (220)). Bragg peaks corresponding to $LiK_2(ND_2)_3$ disappear at 129 °C due to $LiK_2(ND_2)_3$ melting (which unfortunately coincides with two runs of beam failure). This temperature is much lower than the exotherms in the STA trace (Figure 4.28) at 163 °C and 167 °C which had been assigned to the initial separation and overall melt steps respectively.

There is a five run overlap for which $LiK_2(ND_2)_3$ and cubic KND_2 are both present. This therefore supports the idea that mixed-metal amides separate into their constituent single metal amides prior to a full sample melt, but due to the crystal structure of $LiK_2(ND_2)_3$, this phase is transient and is better thought of as a combined separation and melt. Similarly to $Li_3K(ND_2)_4$ and $LiNa_2(NH_2)_3$, $LiK_2(ND_2)_3$ only retains its crystallinity for a very short period of time once separation has started before decomposing (compared to $Li_3Na(NH_2)_4$). $LiNa_2(NH_2)_3$ and $LiK_2(NH_2)_3$ have the same crystal structure and are known to be line phases so cannot tolerate any non-stoichiometry.

As the temperature of the $LiK_2(ND_2)_3$ sample increased, $LiK_2(ND_2)_3$ melts to form a molten phase approaching a composition of $LiND_2 + 2KND_2$. Whereas for $Li_3K(ND_2)_4$ it was Bragg peaks corresponding to $LiND_2$ that appeared, for $LiK_2(ND_2)_3$ it is Bragg peaks corresponding to KND_2 that are observed prior to $LiK_2(ND_2)_3$ disappearing. This is unsurprising given this is a more KND_2 rich phase than $Li_3K(ND_2)_4$ which is more $LiND_2$ rich. The separation and melting of $LiK_2(ND_2)_3$ does not correspond to any mass loss. $Li_3K(ND_2)_4$ was seen to begin separating and melting at 203 °C (much higher than the 118 °C seen here) suggesting $Li_3K(ND_2)_4$ is much more thermally stable than $LiK_2(ND_2)_3$. This is analogous to the Li-Na-N-H system for which the STA data showed that $Li_3Na(NH_2)_4$ melts at 234 °C and $LiNa_2(NH_2)_3$ melts at 203 °C showing that $LiNa_2(NH_2)_3$ is less stable than $Li_3Na(NH_2)_4$. This also shows the Li-K-N-H system is less stable on heating compared to the Li-Na-N-H system.

In addition to the cubic KND_2 Bragg peaks, from 2 hours to 2.5 hours there are some broad features visible in the contour plots at *d*-spacings of 2.70 Å, 2.96 Å, 3.22 Å and 3.98 Å

(Figure 4.35). These broad shoulders do not correspond to monoclinic or tetragonal KND_2 (which is unsurprising given the temperature of 130-160 °C), $LiND_2$ or Li_2ND. The fact they are broad suggests they have a poorly crystalline quality. These broad shoulders are seen to start forming when the $LiK_2(ND_2)_3$ Bragg peaks disappear and themselves disappear at 159 °C which corresponds to a decrease in the scale of the cubic KND_2 Bragg peaks, a marked change in the background and a mass loss of $\sim 2\%$ seen in the IGA^n mass trace (Figure 4.38). This change in background correlates with the small ammonia bump at about 150 °C seen in the gas flow panel decomposition of $LiK_2(NH_2)_3$ under argon (Figure 4.29) so is likely due to desorption/loss of NH_3 as physisorbed gas from the powder grains.

These observations in the GEM data at 159 °C also correlate with the exotherm in the STA trace for pre-formed $LiK_2(NH_2)_3$ (Figure 4.28) at 167 °C which had been assigned to the full sample melting.

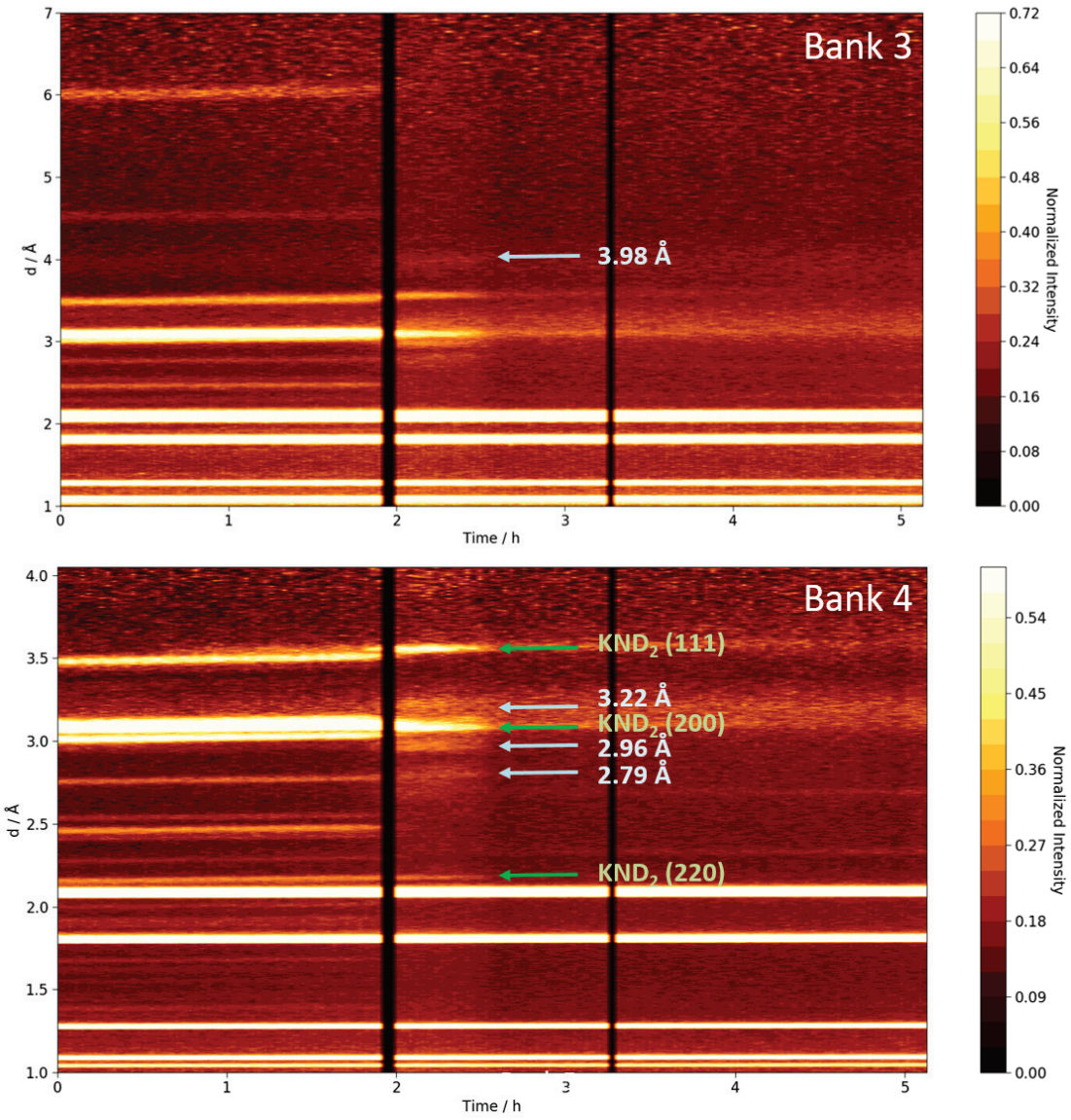


Figure 4.35: Unaccounted for amorphous peaks (blue)

From 159 °C (2.5 hours) onwards, two very small Bragg peaks corresponding to Li_2O at d-spacings of 2.33 Å (200) and 2.70 Å (111) appear which remain present for the rest of the experiment. When the beam fails at 285 °C there is Li_2O and cubic KND_2 present, which is starting to go amorphous, as shown by the broadening of the Bragg peaks (the melting point of KND_2 is 338 °C).

Analysis of Section 2 from Figure 4.33 shown in Figure 4.36

A contour plot of the diffraction data collected after the 24 hours of beam failure collected from bank 4 is presented in Figure 4.36 together with the corresponding thermogravimetric data. Contour plots of the diffraction data collected from banks 3, 4 and 5 and the corresponding thermogravimetric data for this region is presented in the Appendix in Figure A.14.

The last pattern taken at 283 °C before the beam failed was run number 81671. 3 patterns managed to be collected about 6 hours into the 24 hour period of beam failure (run numbers 81863-81865), by which point the sample had cooled to 40 °C. As soon as the beam came back on, a 30 minute scan (run number 81866) was taken at room temperature to get an accurate refinement of the sample present. From Figure 4.36 it can be seen that the Bragg peaks for the first two runs of the contour plot (run numbers 81867 and 81868) are different (particularly at d-spacings of 3.0-3.1 where there are clearly two peaks visible rather than one) to the peaks observed from run number 81869 onwards. The data collected from bank 4 for these runs are shown in Figure 4.37 alongside simulated patterns for monoclinic, tetragonal and cubic KND_2 for visual comparison.

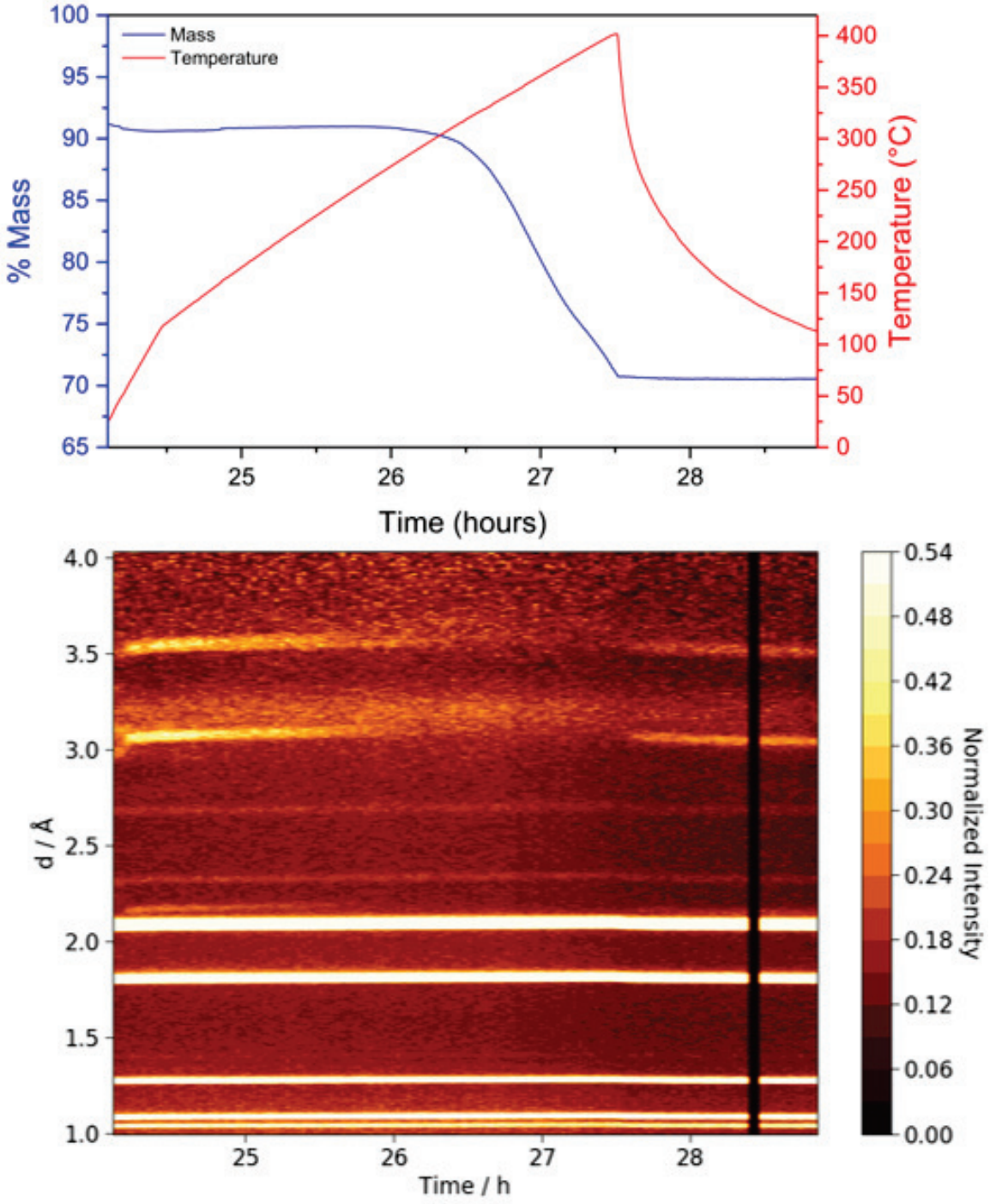


Figure 4.36: Contour plot from bank 4 and the thermogravimetric data for the period after the beam failure for the $LiK_2(ND_2)_3$ decomposition experiment

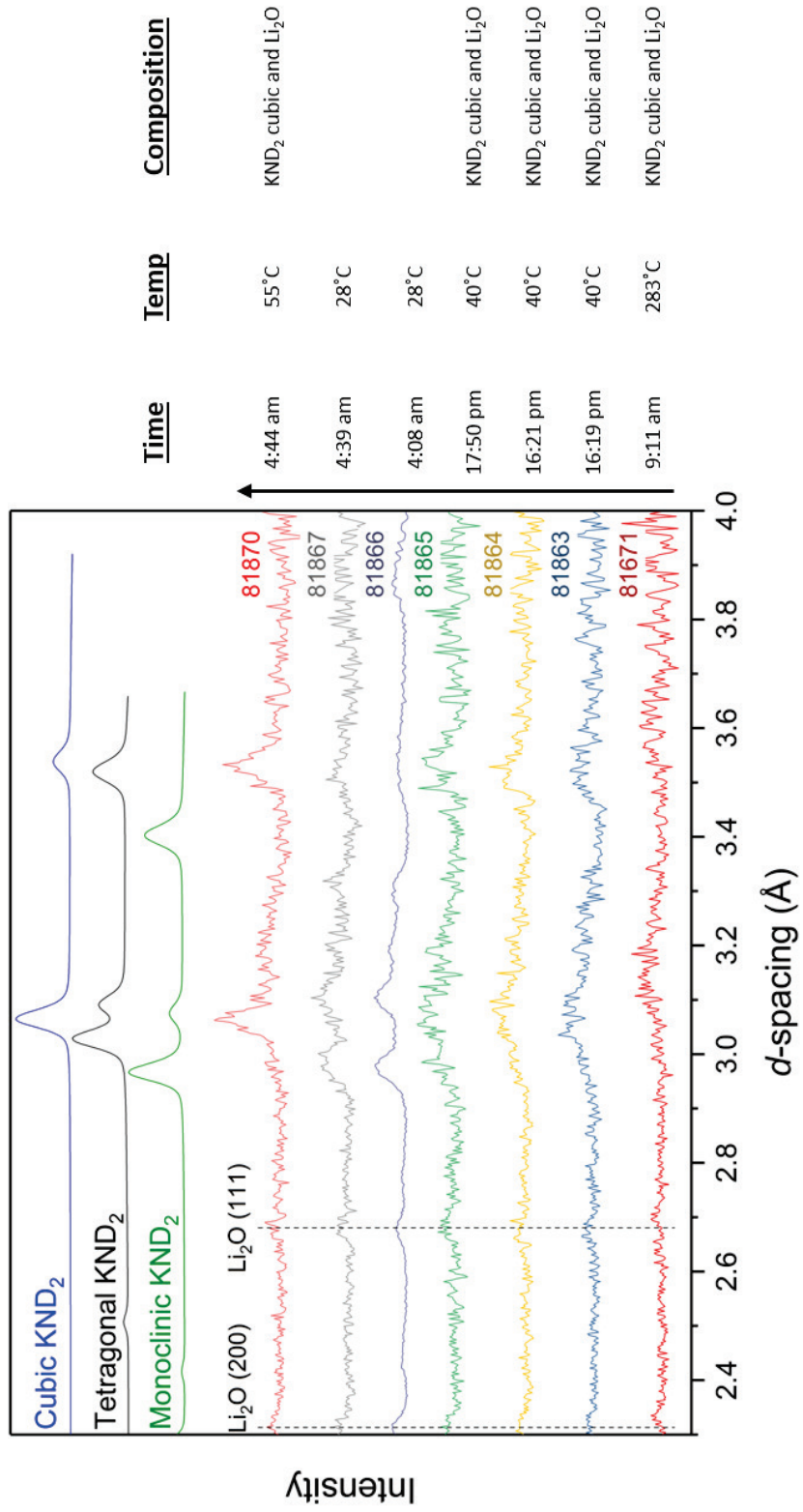


Figure 4.37: Bank 4 TOF data from the last run before the beam failed (run number 81671) until a consistent pattern returns when the beam comes back on (run number 81870)

Figure 4.37 shows that until at least 6 hours into the period of beam failure, despite the sample having cooled to 40 °C, the Bragg peaks in the pattern remain unchanged and fit to Li_2O (2.67 Å (111) and 2.31 Å (200)) and cubic KND_2 (3.53 Å (111), 3.06 Å (200) and 2.16 Å (220)). The *d*-spacings have just shifted due to thermal contraction as a result of the lower temperature. This is unexpected given monoclinic KND_2 is known to be the stable phase at this temperature not cubic KND_2. It may be that cubic KND_2 here may be metastable and takes a long time to relax back to the monoclinic phase and is perhaps stabilised by the presence of $LiND_2$.

It has been reported that the addition of potassium hydride can stabilise the cubic geometry of KNH_2, which retains the rotation of the amide anions even at room temperature during the formation of a metal amide-hydride solid solution [246]. The dissolution of KH into KNH_2 leads to an anionic substitution, which decreases the interaction among NH_2^- ions. The rotational properties of the high temperature cubic polymorph of KNH_2 is retained down to room temperature and the coexistence of the cubic and monoclinic phases of KNH_2 is observed, suggesting the presence of a two phase field at room temperature. It is therefore likely that something similar is occurring here, but with the dissolution of $LiND_2$ rather than KH into KND_2.

In bank 4, monoclinic KND_2 would have two peaks at 3.07 Å (101) and 2.97 Å (011 and 110), tetragonal KND_2 would have two peaks at 3.03 Å (110) and 3.09 Å (002), and cubic KND_2 has one peak at 3.06 Å (200). Looking at the data in this region, monoclinic KND_2 would seem to fit well but a peak at 3.43 Å (10-1) would be predicted which is not observed in the neutron diffraction data. This therefore supports the idea that the patterns collected for run numbers 81866 (and 81867 and 81868) might fit to a version of KND_2 with some Li incorporated.

The diffraction data in run number 81870 (60 °C) fits to cubic KND_2 and Li_2O. This is a low temperature for cubic KND_2 to be present but there may be a hysteric memory effect. The sharper peaks in run number 81870 compared to the broader ones at run number 81671 (for the same phases present) show that at the lower temperature the cubic KND_2 is more crystalline and at the higher temperature it is more amorphous.

The cubic KND_2 Bragg peaks lose their crystallinity around 230 °C and gradually become more amorphous until 350 °C. This is expected as 338 °C is the reported melting point for KND_2. Figure 4.38 shows the percentage mass loss as a function of temperature and it can be seen that the mass loss starts at 310 °C and is continuous until the peak temperature of 400 °C. The mass loss is likely to correlate with the decomposition of KND_2 which will release gases. At 350 °C, half way through the mass loss there is a change in the background of the neutron diffraction data.

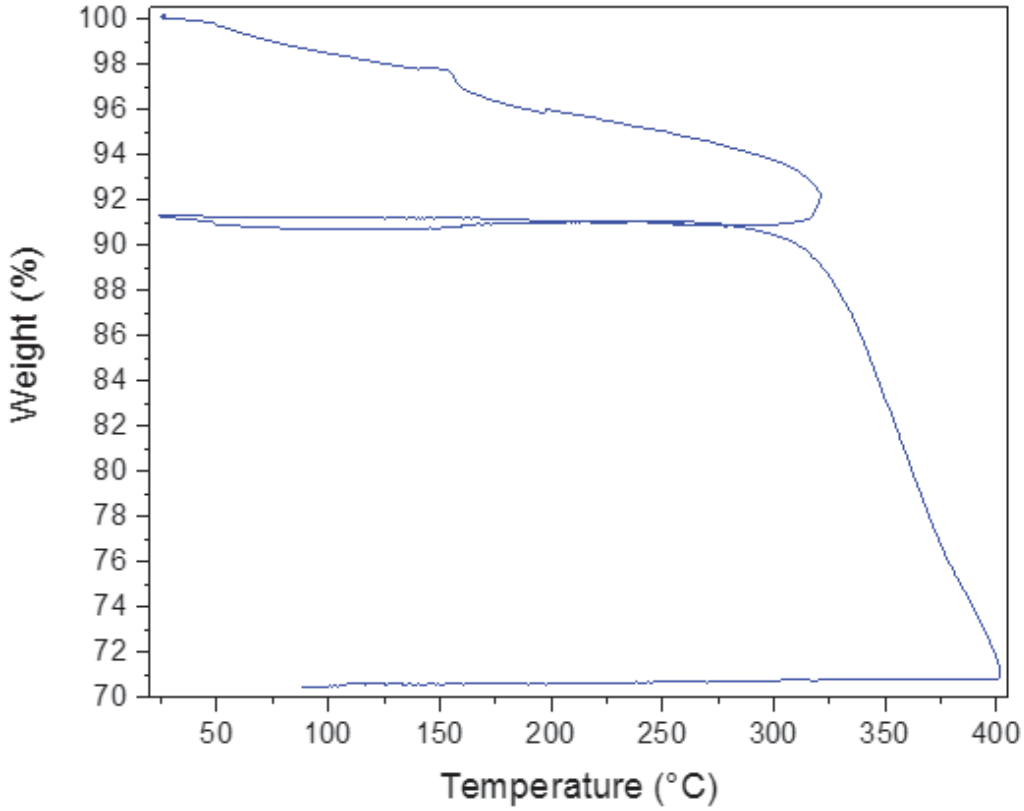


Figure 4.38: Percentage mass of the $LiK_2(ND_2)_3$ sample as a function of temperature during the $LiK_2(ND_2)_3$ decomposition experiment on GEM

If $LiK_2(ND_2)_3$ decomposed fully to $\frac{1}{2}Li_2ND + 2K$ this would give a mass loss of 30.4 %. Figure 4.38 shows that over the course of the experiment 29.5 % of the initial sample mass is lost. The diffraction data shows some cubic KND_2 regains its crystallinity on cooling at 300 °C, so KND_2 decomposition to K metal is not complete. The experiment is only cooled to 113 °C which is not low enough to see if tetragonal or monoclinic KND_2 reform at lower temperatures.

$LiK_2(ND_2)_3$ GEM decomposition summary

Overall Figure 4.33 shows that $LiK_2(ND_2)_3$ melts at 129 °C. Cubic KND_2 appears slightly before this at 118 °C alongside some broad amorphous (unfitted) features. There is a change in the background at 159 °C which correlates with a small mass loss. Cubic KND_2 peaks loose their crystallinity at 230 °C and gradually become more amorphous until they disappear at 340 °C. This correlates with a mass loss of 22.35%. Cubic KND_2 regains its crystallinity at 300 °C on cooling. These findings are consistent with the conclusions drawn on how $LiK_2(NH_2)_3$ was observed to decompose *ex-situ* in Section 4.7.1 by undergoing a combined separation and melt to form an intermediate molten phase of $LiNH_2 + 2KNH_2$ which subsequently decomposes.

4.7.3 Inert gas summary for $LiK_2(NH_2)_3$

Figure 4.39 shows the superposition of all the experiments starting with pre-made $LiK_2(NH_2)_3$. This includes the mass trace from the IGA^n when $LiK_2(NH_2)_3$ was heated during the GEM decomposition experiment, the MS trace for the gases released when heated on the gas flow panel and the DSC trace when heated on the STA. The key results from the GEM decomposition experiment have also been summarised at the relevant temperatures.

It is clear from both the *in-situ* and *ex-situ* data that there are different individual events taking place in the complex multi-step thermal decomposition, and it is clear that a different mechanism is occurring compared to a simple superposition of the individual behaviours of $LiNH_2$ and KNH_2.

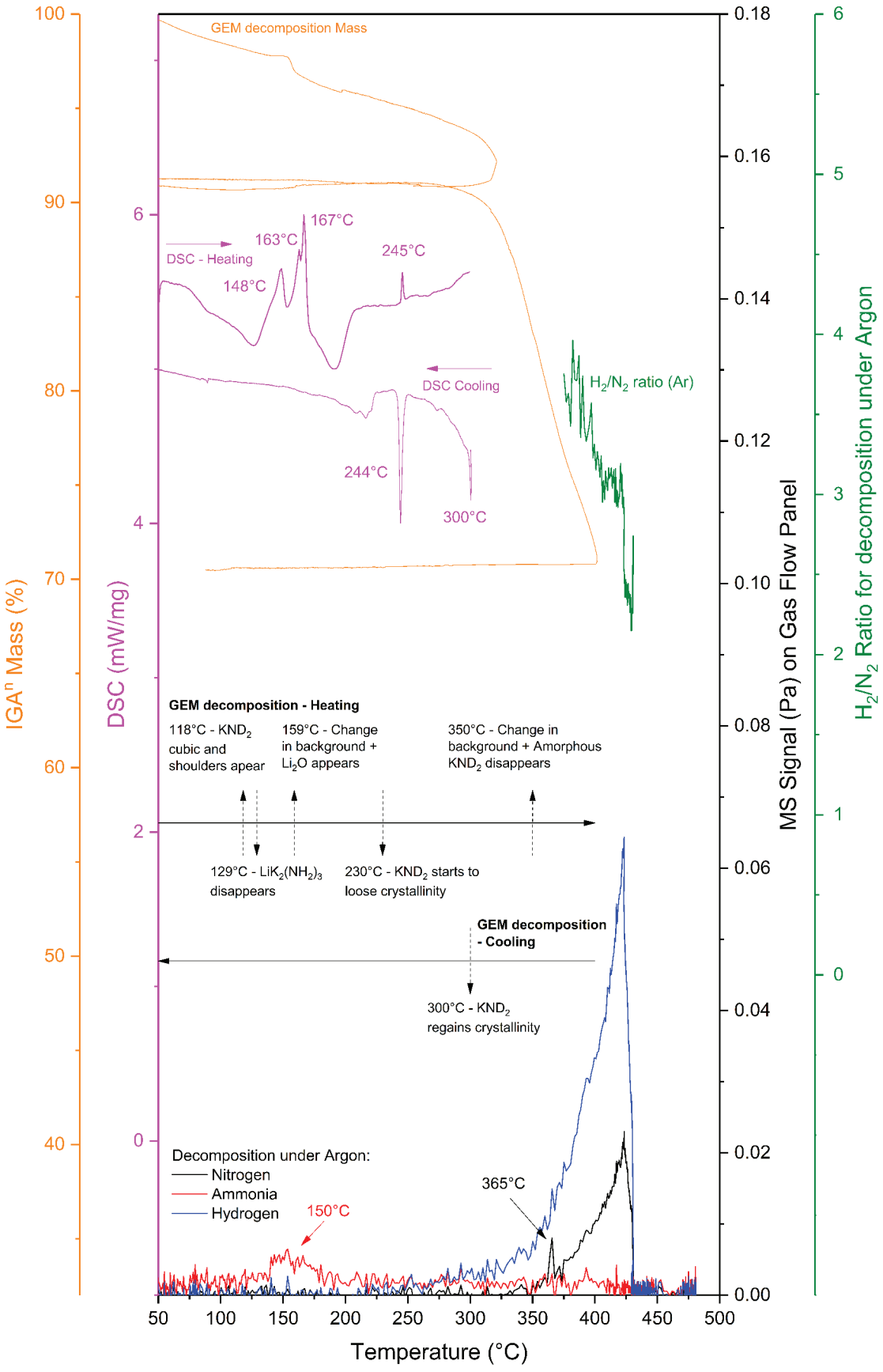


Figure 4.39: Thermodynamic properties measured during the decomposition of $LiK_2(NH_2)_3$ under inert gas

4.8 Ammonia decomposition

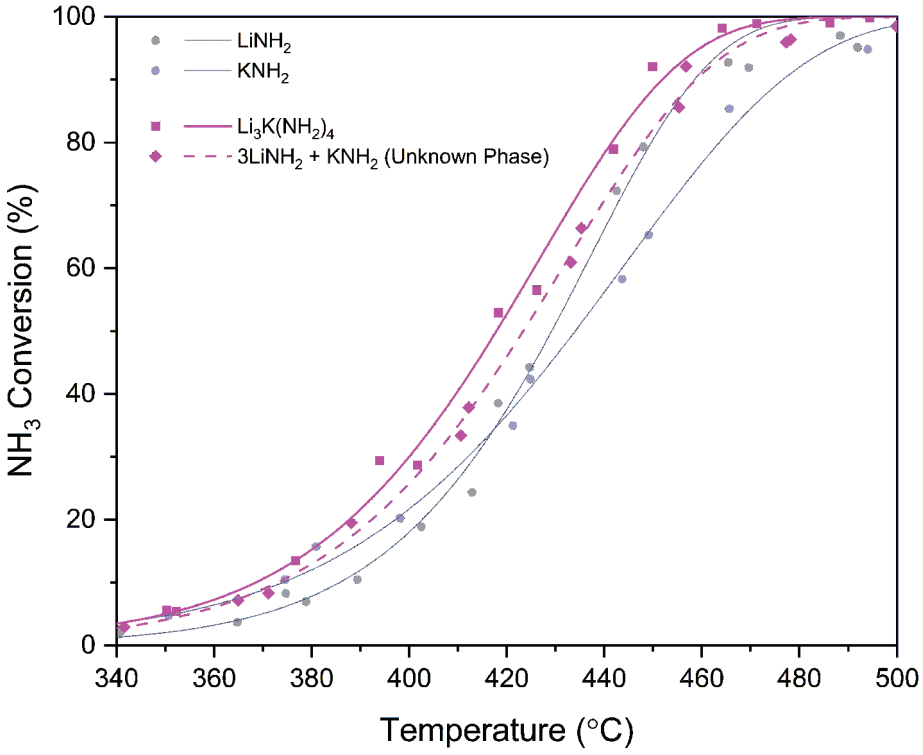
Mixed-metal Group 1/2 light metal amides are being investigated as a new class of inexpensive and effective catalyst for the decomposition of ammonia into nitrogen and hydrogen for energy applications (Equation 3.3) and they show superior activities to optimised transition metal based catalysts. Building on the success of the Li-Na-N-H system in Section 3.5, the ammonia decomposition ability of $Li_3K(NH_2)_4$ and $LiK_2(NH_2)_3$ was investigated. Ammonia conversion efficiencies were analysed using the same experimental setup described in detail in Section 3.5.

4.8.1 Quantitative fitting and analysis

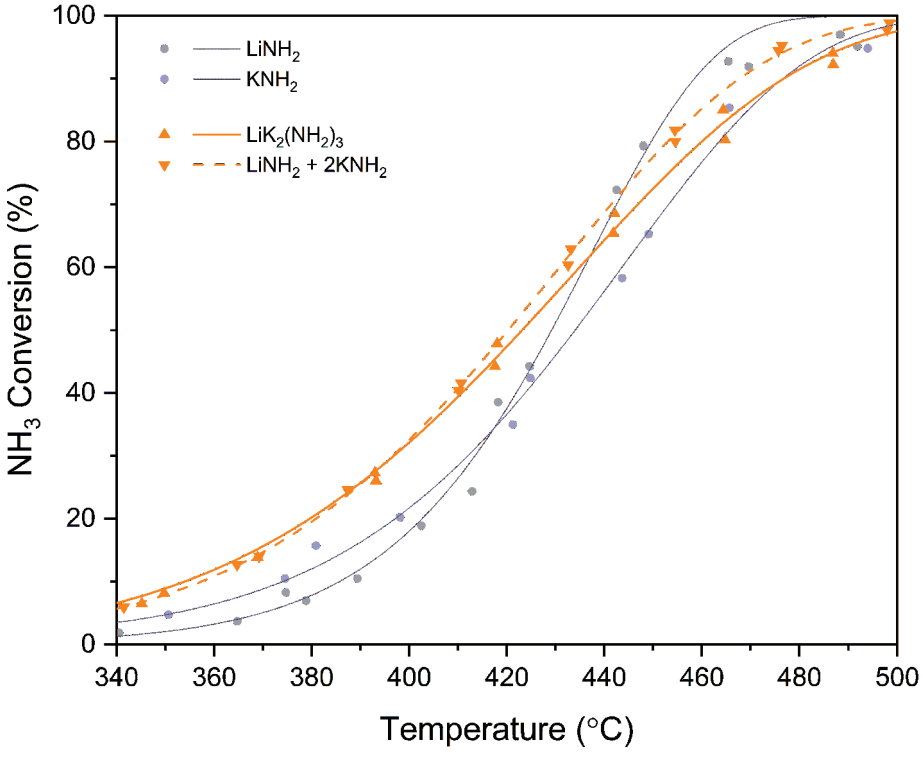
Figure 4.40 shows the ammonia conversion percentage calculated from the MS data shown in Figure 4.41. It compares the NH_3 decomposition ability of the pre-formed mixed-metal amides with the analogous behaviour of ground-up mixtures of their constituent single metal amides in the relevant ratios. Results for equivalent masses of pure $LiNH_2$ and KNH_2 have been included for comparison.

The plotted points are the recorded experimental results and the line of best fit has been drawn using the two process sigmoidal Gompertz function (Equation 3.4) with the parameters listed in Table 4.5 which were themselves generated using the sigmoid fit calculated in TOPAS (Section 3.5.1). Uncertainties for T_e and E_A are estimated to be on the order of $\pm 2\,°C$ and $\pm 3\,kJ/mol$ respectively.

Figure 4.40 shows that, as with the Li-Na-N-H system, from looking at the single metal amides alone it can be seen that $LiNH_2$ is a higher performing NH_3 decomposition catalyst and has a steeper curve (indicative of higher activation energy) than KNH_2. $LiNH_2$ is also significantly easier to maintain in the reactor and shows much higher post-reaction recovery than KNH_2 (85 % and 25 % respectively). Whereas $LiNH_2$ decomposes to Li_2NH which is solid until its own decomposition at around 600 °C, KNH_2 melts at 338 °C and decomposes to K which is harder to contain due to its high volatility. However, KNH_2 does show improved containment over $NaNH_2$ which is beneficial for onboard catalytic applications.



(a) $Li_3K(NH_2)_4$ and $3LiNH_2 + KNH_2$



(b) $LiK_2(NH_2)_3$ and $LiNH_2 + 2KNH_2$

Figure 4.40: Ammonia decomposition sigmoids for the Li-K-N-H system as potential catalysts on the gas flow panel

Qualitatively it can be seen that $Li_3K(NH_2)_4$ out-performs $LiNH_2$ and KNH_2 across the entire temperature range and particularly at moderate temperatures. $LiK_2(NH_2)_3$ outperforms $LiNH_2$ and KNH_2 at low temperature, but above 440 °C it is a less effective catalyst than $LiNH_2$ alone. $LiK_2(NH_2)_3$ outperforms $Li_3K(NH_2)_4$ until 410 °C, from which point onwards $Li_3K(NH_2)_4$ demonstrates the best NH_3 decomposition ability. Unsurprisingly, the more Li rich systems ($Li_3K(NH_2)_4$ and $3LiNH_2 + KNH_2$) have curves that are shaped much more like $LiNH_2$ and the more K rich systems ($LiK_2(NH_2)_3$ and $LiNH_2 + 2KNH_2$) have curves much more similar to that of KNH_2.

There is little deviation between the two traces for each respective ratio, which suggests there is no benefit to pre-forming the mixed-metal amides from an activity perspective. The synthesis temperatures for $Li_3K(NH_2)_4$ and $LiK_2(NH_2)_3$ under argon determined by STA are 161 °C and 148 °C respectively (Figure 4.28 and Figure 4.15) which are well below the start of the ammonia decomposition activity. However, it is important to note that synthesis attempts to form both $Li_3K(NH_2)_4$ and $LiK_2(NH_2)_3$ from their constituent amides in the relevant ratios under NH_3 on the gas flow panel were unsuccessful. $3LiNH_2 + KNH_2$ under NH_3 formed a sample which produced unknown powder X-ray diffraction data, rather than $Li_3K(NH_2)_4$. This is discussed further in Section 4.4. $LiNH_2 + 2KNH_2$ under NH_3 formed 25.4 % $Li_3K(NH_2)_4$, 59.9 % $LiNH_2$ and 14.8 % Li_2O (Figure A.4 in the Appendix). However, it is known that $Li_3K(NH_2)_4$ and $LiK_2(NH_2)_3$ separate and melt into a combined molten phase of $LiNH_2$ and KNH_2 in the relevant ratios at 199 °C/211 °C and 201 °C/204 °C respectively. These temperatures are well below those required for the onset of NH_3 decomposition so by the point NH_3 decomposition starts, the same materials will be present in the reactor regardless of whether it was the pre-formed mixed-metal amide or the constituent single metal amides that was started with.

As with the Li-Na-N-H system, these decomposition reactions fit to a single process (Equation 3.4). There is no obvious change in RDS across the temperature range and they are thought to be successive stoichiometric reactions within the bulk, rather than surface-mediated mechanisms (Section 3.5.1).

	Constant	T_e (°C)	E_A (kJ/mol)	Recovery by mass (%)
Blank	0.000(1)	547	102	n/a
$LiNH_2$	0.000(5)	439	184	88
KNH_2	0.009(2)	449	132	25
$Li_3K(NH_2)_4$	0.007(3)	429	153	85
$3LiNH_2 + KNH_2$	0.002(8)	435	150	80
$LiK_2(NH_2)_3$	0.000(2)	440	101	74
$LiNH_2 + 2KNH_2$	0.000(4)	436	112	68

Table 4.5: Li-K-N-H system Gompertz curve output values. Uncertainties for T_e and E_A are estimated to be on the order of ± 2 °C and ± 3 kJ/mol respectively and have been calculated from the TOPAS fitting process

The sigmoid for $LiNH_2$ is the steepest (highest E_A) followed by $Li_3K(NH_2)_4/3LiNH_2 + KNH_2$. Interestingly, similarly to $LiNa_2(NH_2)_3/LiNH_2 + 2NaNH_2$, $LiK_2(NH_2)_3/LiNH_2 + 2KNH_2$ has a lower E_A and a shallower slope than KNH_2 (or $LiNH_2$) individually. Somehow the presence of KNH_2 and $NaNH_2$ is lowering the activation energy of the NH_3 decomposition process compared to either single metal process independently. It could be that this lower activation energy may relate to differences in the decomposition under inert gas seen in terms of the presence of KNH_2 lowering the decomposition temperature of $LiNH_2$ and promoting the release of H_2 and N_2 rather than NH_3. $LiK_2(NH_2)_3$ is better at decomposing NH_3 at low temperatures but is worse at high temperatures. However, the overall conversion depends on a combination of the activation energy and the pre-exponential term as activation energy alone only provides information on the slope.

For both ratios, it is the Li-K-N-H amide that has the lower E_A value than the Li-Na-N-H analogue. The improved performance of the Li-K-N-H system compared to the Li-Na-N-H may be rationalised in terms of the way the KNH_2 behaves as it is heated compared to $NaNH_2$. KNH_2 decomposes at a lower temperature than $NaNH_2$, with an onset temperature of around 300 °C compared with 420 °C for sodium amide. The decomposition of the amide is likely to be the RDS which may explain why potassium amide has faster ammonia decomposition kinetics than sodium amide. Potassium amide melts at a higher

temperature than sodium amide (330 °C and 210 °C respectively) [159]. Molten potassium amide is therefore less mobile than sodium amide, resulting in a greater proportion of the sample remaining in the hot zone where it can decompose the ammonia. This is also reflected in the recovery post ammonia decomposition reaction.

4.8.2 Catalyst recovery

The catalyst recovery is the average percentage of the starting mass of the catalyst recovered from the reactor at the end of the experiment, and is a guide to the volatility of the catalyst. A high percentage recovery is an important characteristic for potential practical applications within on-board NH_3 cracking systems to produce H_2 on demand and is crucially important in order to maintain efficiency and improve lifetimes.

The results in Table 4.5 indicate that the pre-formed mixed-metal amides have better recovery than the mixed starting materials, again emphasising the potential benefits of mixed-metal amides, and also indicates that there may be some practical value in pre-forming mixed amides, even though there was not a significant difference in their observed activity compared to starting with a mixture of the single metal amides in the relevant ratios.

The recovery of both $Li_3K(NH_2)_4$ and $LiK_2(NH_2)_3$ is quite high, especially in comparison to KNH_2 alone. The Li-K-N-H system shows catalyst recoveries which are $\sim$15-20% higher than those for the Li-Na-N-H system. The investigation into this system started with the question of whether KNH_2 melting at a higher temperature than $NaNH_2$, or the fact K has a higher vapour pressure than Na would have a dominant affect on the recovery of the catalysts. It therefore appears that the fact the amide is stable to a higher temperature range is the dominant effect on the recovery during these experiments.

Powder X-ray diffraction analysis of the residues left in the reactors at the end of the ammonia decomposition reactions was performed in order to identify the decomposition products, an important step to help determine the mechanism by which each catalyst decomposes ammonia.

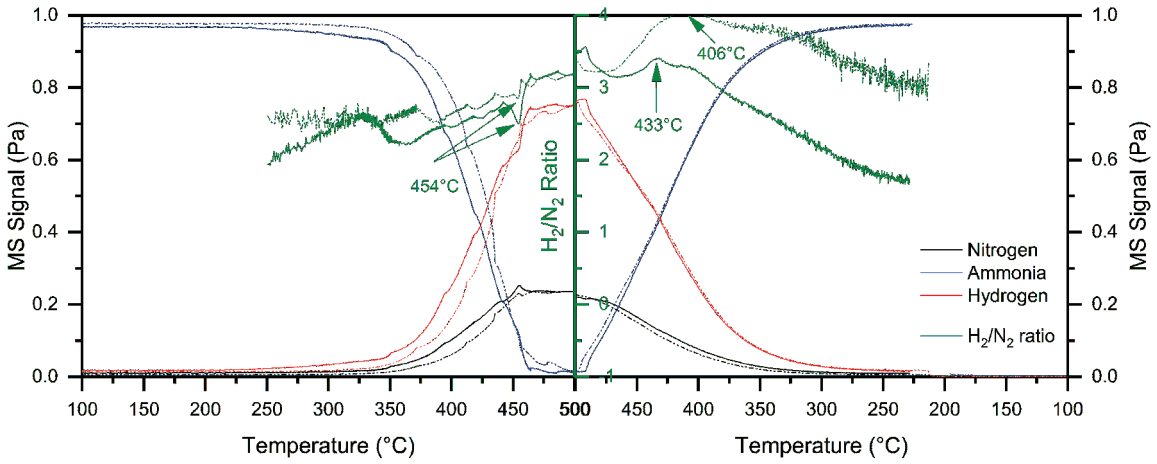
Decomposition of both mixed-metal amides under argon suggested the separation and subsequent decomposition of each constituent single metal amide; $LiNH_2$ and KNH_2. Under

NH_3, $LiNH_2$ and KNH_2 would be expected as the decomposition products. Powder X-ray diffraction analysis has shown that $LiNH_2$ is present in all the post-reaction products, which is consistent with the fact that the samples have separated under NH_3 decomposition conditions as it is $LiNH_2$ that is recovered at the end not a mixed-metal amide. No potassium containing components were detected but this does not necessarily meaning it had been volatilised and therefore lost from the reactor. The mass recovery actually implies that KNH_2 has not been lost from the reactor. There are still some issues of containment as seen in the Li-Na-N-H system, although there is some improvement from replacing $NaNH_2$ with KNH_2.

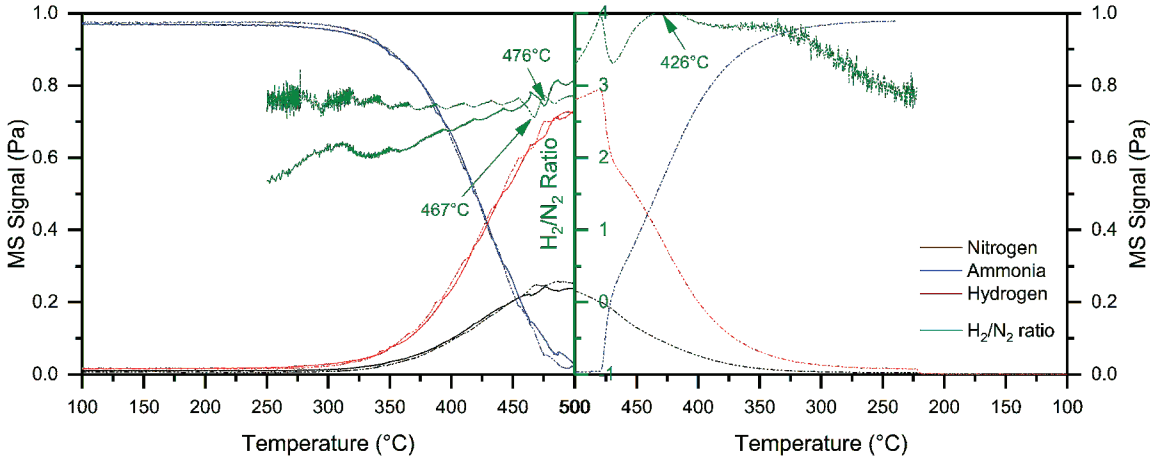
4.9 Decomposition under ammonia

Figure 4.41 shows the outlet gas flow MS traces for the decomposition of $Li_3K(NH_2)_4$ and $LiK_2(NH_2)_3$ as well as hand-ground mixtures of the constituent single metal amides in the relevant ratios under ammonia during the experiments described in Section 4.8. Analysis of these MS traces is important to get an idea of what the active form of the catalyst is at the temperatures of interest for NH_3 decomposition. It is useful to relate the thermal decomposition behaviour of these materials under ammonia to how they are likely to perform as catalysts.

In Figure 4.41 the H_2/N_2 ratio is shown above 250 °C by which point $Li_3K(NH_2)_4$ and $LiK_2(NH_2)_3$ will both have separated and melted forming intermixed molten phases of $LiNH_2$ and KNH_2 in the relevant ratios. The decomposition of $LiNH_2$ to Li_2NH leads to the release of NH_3 (Equation 3.1a) which will itself decompose to H_2 and N_2 in a 3:1 ratio, so will not change the observed H_2/N_2 ratio to that seen for NH_3 decomposing alone. However, KNH_2 decomposes analogously to $NaNH_2$ into H_2 and N_2 in a 2:1 ratio (Equation 4.1) as it does not decompose via the production of NH_3. The decomposition of KNH_2 will therefore affect the overall ratio of observed H_2/N_2 as there is relatively less H_2 and more N_2. The suppression seen in the H_2/N_2 ratio on heating under NH_3 in Figure 4.41 is therefore indicative of the production of K metal and overall decomposition of KNH_2 in the "melt phase".



(a) $Li_3K(NH_2)_4$ (solid lines) and $3LiNH_2 + KNH_2$ (dashed lines)



(b) $LiK_2(NH_2)_3$ (solid lines) and $LiNH_2 + 2KNH_2$ (dashed lines)

Figure 4.41: Decomposition on the gas flow panel under ammonia

The decomposition temperature under NH_3 for $Li_3K(NH_2)_4$ and $3LiNH_2 + KNH_2$ of 454 °C is higher than those seen under Ar (412/421 °C). The decomposition temperatures under NH_3 for $LiK_2(NH_2)_3$ and $LiNH_2 + 2KNH_2$ of 467 °C/476 °C are also higher than those seen under Ar (418/423 °C). Whereas under argon the peaks in the gas traces of the mass spectrometry data were modelled to two pseudo-Voigt peaks in TOPAS, under NH_3, $Li_3K(NH_2)_4$ and $LiK_2(NH_2)_3$ appear to decompose in a single step.

The peaks in the H_2/N_2 ratio on cooling at 406 °C/433 °C and 426 °C for the 3:1 and 1:2 systems respectively correspond to extra H_2 (relatively less N_2) due to the reformation of some KNH_2 from K (the reverse of Equation 4.1).

4.10 Summary

Investigation of the Li-K-N-H system started with the development of the novel ball-mill synthesis method for the formation of high purity $Li_3K(NH_2)_4$ and $LiK_2(NH_2)_3$. A thorough analysis of the phase space between $LiNH_2$ and KNH_2 led to the identification of a new phase, nominally "$LiK(NH_2)_2$" which is close to being crystallographically characterised. In depth *ex-situ* and *in-situ* analysis of $Li_3K(NH_2)_4$ and $LiK_2(NH_2)_3$ has shown that both mixed-metal amides show an almost simultaneous separation (of KNH_2) followed by a full sample melt. $Li_3K(NH_2)_4$ can support a small degree of non-stoichiometry as $Li_3K_{(1-x)}(NH_2)_{(4-x)}$ but only for a very small temperature range. The resulting inter-mixed molten phases decompose through the interaction of $LiNH_2$ and KNH_2. The different ratios to which these are present in $Li_3K(NH_2)_4$ and $LiK_2(NH_2)_3$ leads to slightly different gas releases observed for the two phases on decomposition. However, both ultimately show H_2 and N_2 gas release (rather than NH_3) and do so at lower temperatures than have been observed for $LiNH_2$ or KNH_2 decomposing alone.

Both $Li_3K(NH_2)_4$ and $LiK_2(NH_2)_3$ are better NH_3 decomposition catalysts than $LiNH_2$. $LiK_2(NH_2)_3$ is particularly high performing below $\sim 430\,^{\circ}C$ whereas $Li_3K(NH_2)_4$ is the best catalyst above this temperature. A more detailed analysis of this behaviour can be found in Chapter 7. This system also shows much better catalyst recovery post-reaction than the Li-Na-N-H system as KNH_2 is stable to higher temperatures than $NaNH_2$. This an important finding for future commercial applications.

Chapter 5

Mixed Sodium-Potassium system

Contents

5.1 Background 256

5.1.1 Crystallography 258

5.1.2 Chapter overview 258

5.2 Phase space between $NaNH_2$ and KNH_2 259

5.2.1 Powder X-Ray Diffraction (PXRD) on I11 259

5.2.1.1 Principal Component Analysis (PCA) 261

5.2.1.2 Unknown Phase 264

5.2.2 Raman 265

5.2.3 Simultaneous Thermal Analysis (STA) 268

5.3 *Ex-situ* thermal decomposition behaviour 271

5.4 GEM data 276

5.4.1 $NaND_2 + 2KND_2$ synthesis 277

5.4.2 $NaK_2(ND_2)_3$ decomposition 281

5.5 Inert Gas Summary 285

5.6 Ammonia decomposition 286

5.6.1 Quantitative analysis and fitting 286

5.6.2 Catalyst recovery 289

5.7 Decomposition under ammonia 289

5.8 Summary 291

5.1 Background

Having investigated the Li-Na-N-H and Li-K-N-H systems, the next step in the analysis of Group 1 mixed-metal amide systems as a whole is to explore the Na-K-N-H system. Preceding research for other mixed-metal systems has been focused around hydrogen storage applications, however this system has not been previously explored in this regard. Precedent literature on the Na-K-N-H system only exists in the context of a sodium amide-potassium amide eutectic mixture [35, 193].

Only one mixed-metal amide has been reported, $NaK_2(NH_2)_3$ [168] due to its isostructural relationship to $LiK_2(NH_2)_3$. This work therefore presents for the first time an investigation into the Na-K-N-H system as a potential NH_3 decomposition catalyst. There is a cost advantage of using $NaNH_2$ over KNH_2 due to a significantly greater supply.

The Na-K-N-H system is particularly interesting, because while $LiNH_2$ is known to decompose under argon to Li_2NH (Equation 3.1a), both $NaNH_2$ and KNH_2 are known to decompose via a different mechanism, straight to the metal (Equation 4.1 and Equation 3.2). This difference has had marked effects on the behaviour of the mixed-metal amide systems in the preceding chapters so the Na-K-N-H system, where neither component can form an imide will form an interesting extension and comparison.

Table 5.1 details the key thermodynamic properties of $NaNH_2$, KNH_2 and $NaK_2(NH_2)_3$ which are the components of the Na-K-N-H system and have been included here as a reference guide.

	Synthesis	**Melting**	**Onset of decomposition**
$NaNH_2$		210 °C	420 °C
KNH_2		338 °C	400 °C
$NaK_2(NH_2)_3$	89 °C	141 °C	325 °C

Table 5.1: Key thermodynamic temperatures (± 1 °C) of the single metal amides and mixed-metal amide of the Na-K-N-H system

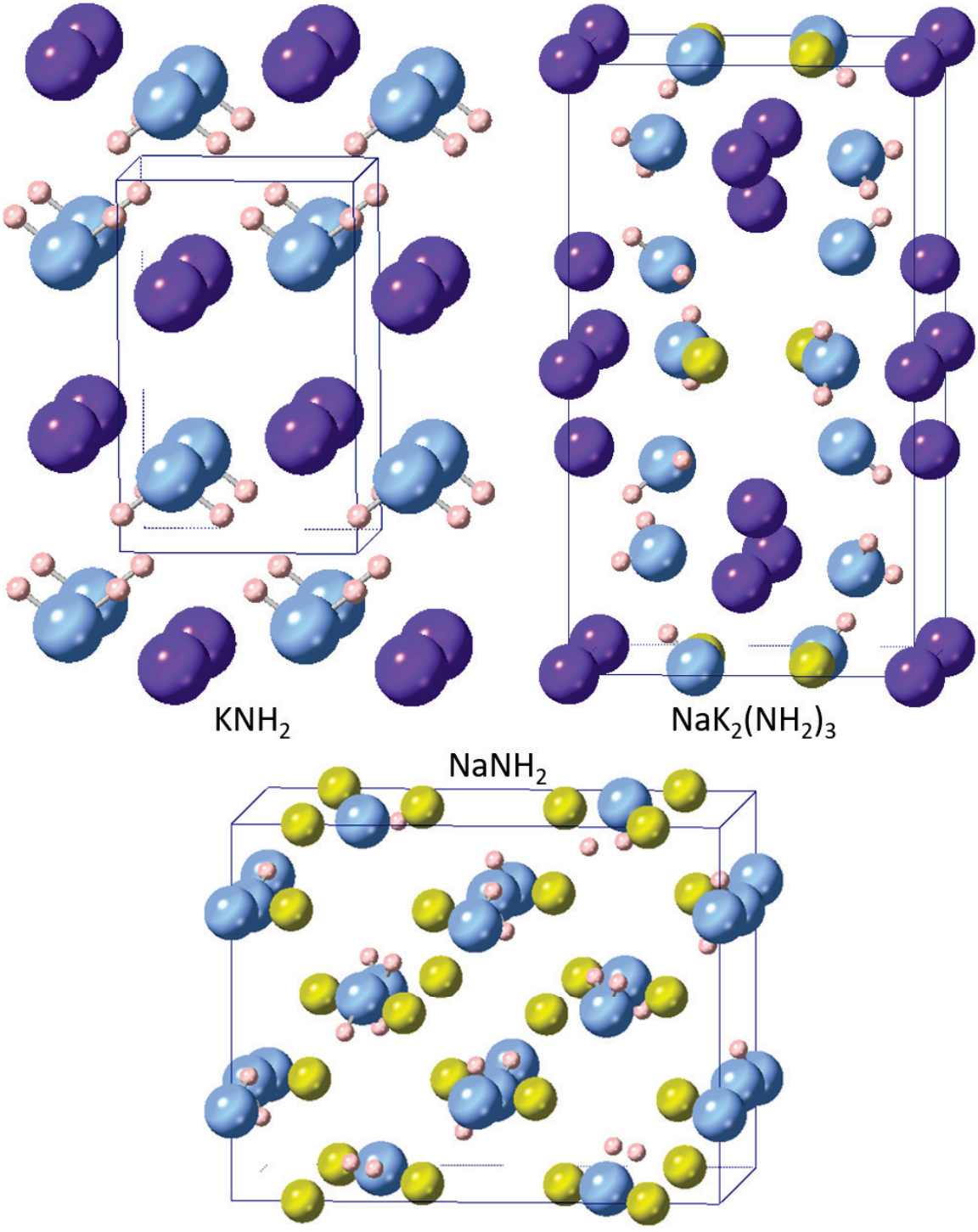


Figure 5.1: Crystallographic unit cells for $NaNH_2$, $NaK_2(NH_2)_3$ and monoclinic KNH_2 roughly proportional in size. Yellow = Sodium, Purple = Potassium, Blue = Nitrogen, Pink = Hydrogen

5.1.1 Crystallography

$NaK_2(NH_2)_3$ is isostructural with $LiNa_2(NH_2)_3$ and $LiK_2(NH_2)_3$ and all crystallise in the $P4_2/m$ space group [168]. Figure 5.1 shows the crystallographic unit cells for $NaNH_2$, $NaK_2(NH_2)_3$ and monoclinic KNH_2 (for which multiple unit cells have been shown for a more accurate comparison of scale).

The ion arrangement and coordination in $NaK_2(NH_2)_3$ is analogous to that observed for $LiNa_2(NH_2)_3$ (Section 3.2.1) and $LiK_2(NH_2)_3$ (Section 4.1.2). In $NaK_2(NH_2)_3$, $\frac{3}{4}$ of the K^+ cations display octahedral coordination and $\frac{1}{4}$ show tetrahedral coordination, and are all situated in environments too large for Na^+ cations. The Na^+ cations are tetrahedrally coordinated by NH_2^- ions in environments too small for K^+ cations. Cross occupation of the metal sites in $NaK_2(NH_2)_3$ is not possible and there is no clear cation migration pathway so ionic mobility is suppressed and $NaK_2(NH_2)_3$ only exists as a pure, single and fully stoichiometric line phase.

5.1.2 Chapter overview

The solid state reaction of $NaNH_2 + 2KNH_2$ in the tube furnace, ball-mill and on the gas flow panel under argon and ammonia as detailed in Table 2.5 in Section 2.2.4.3 shows $NaK_2(NH_2)_3$ can be routinely made to over 90% purity. The novel, low temperature, mild synthesis route involving ball-milling the constituent amides together in the relevant ratios is the best method to routinely form $NaK_2(NH_2)_3$, so this was used to prepare the samples analysed in the remainder of this chapter. The whole phase space between $NaNH_2$ and KNH_2 was investigated, which similarly to the Li-K-N-H system, led to the discovery of a previously unreported phase within the Na-K-N-H system.

A thorough investigation of the thermal decomposition behaviour of high-purity samples of $NaK_2(NH_2)_3$ under inert gas was performed. This was done both by a number of *ex-situ* techniques and also *in-situ* on the GEM beamline at ISIS and was used as a basis for understanding how the system behaves. Finally the catalytic activity of $NaK_2(NH_2)_3$ for NH_3 decomposition was investigated.

5.2 Phase space between $NaNH_2$ and KNH_2

No research in the literature exists on the phase space between $NaNH_2$ and KNH_2 so this was investigated through ten molar ratios between the two end members with $NaNH_2$:KNH_2 of 11:1, 10:2, 9:3, 8:4, 7:5, 6:6, 5:7, 4:8, 3:9, 1:11. 0.5 g of each ratio was hand-ground and 3 mg of this mixture was separated for STA in order to identify temperatures for the synthesis and phase changes of the mixed-metal amides in each case (Figure 5.6). The remainder of each hand-ground mixture was ball-milled for 1 hour. For each resulting sample, powder X-ray diffraction data was collected on I11 at Diamond (Figure 5.2) and a Raman spectrum obtained (Figure 5.4).

5.2.1 Powder X-Ray Diffraction (PXRD) on I11

Figure 5.2 shows the powder X-ray diffraction data collected on I11 at Diamond for each of the ball-milled samples. Rietveld analysis was performed using TOPAS and the patterns fitted to different proportions of $NaNH_2$, KNH_2 and $NaK_2(NH_2)_3$ as was expected. Additional peaks highlighted in red were identified which correspond to an unknown phase. Therefore a more in depth compositional analysis was performed by principal component analysis.

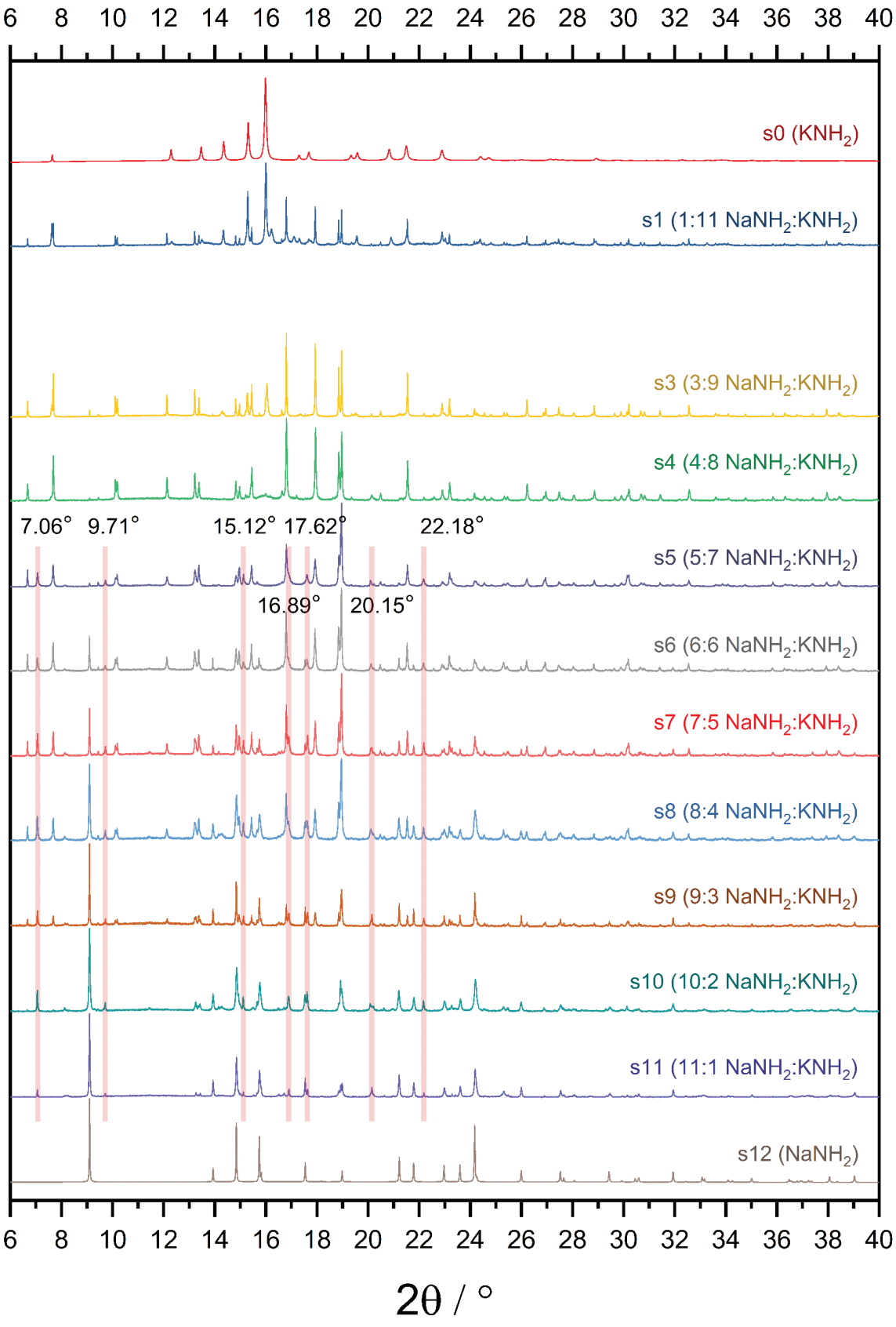


Figure 5.2: I11 powder X-ray diffraction data for the phase space between $NaNH_2$ and KNH_2 with the main peaks of the unknown phase highlighted in red

5.2.1.1 Principal Component Analysis (PCA)

The percentage compositions of the K-rich samples labelled s0, s1, s3 and s4 could be easily determined in TOPAS as all the peaks corresponded to the known phases of $NaNH_2$, KNH_2 and $NaK_2(NH_2)_3$. The sample which was a ball-milled mixture of $NaNH_2$:KNH_2 in a 4:8 ratio (s4) fitted to 100% $NaK_2(NH_2)_3$ as was expected.

For the remaining samples (s5-s11), peaks corresponding to an unknown phase (U.P.) were identified at 2θ and d-spacing values listed in Table A.7 in the Appendix. The main peaks of this unknown phase are highlighted in red in Figure 5.2. A manual principle component analysis was performed in order to determine the percentage composition of each sample. The peaks identified for this principal component analysis and listed in Table 5.2 were chosen as they were clearly present in some of the powder X-ray diffraction data but had gone in others and were easily distinguishable.

For each of the peaks listed in Table 5.2, the area was calculated by fitting a pseudo-Voigt function in TOPAS. The total area of the peaks corresponding to each phase was then summed. Summing all the peaks for each sample enabled the percentage composition of each phase to be calculated for each sample, shown graphically in Figure 5.3.

		Peak area for each $NaNH_2$:KNH_2 ratio						
	Peak 2θ value	**5:7**	**6:6**	**7:5**	**8:4**	**9:3**	**10:2**	**11:1**
Unknown Phase	7.07	136.2	55.1	90.7	70.2	30.2	63.0	23.2
	9.72	52.7	19.7	35.5	29.3	22.1	28.9	18.5
	15.13	108.2	47.4	56.6	68.5	31.5	58.0	24.0
	17.61	247.5	87.5	124.3	153.7	58.2	110.4	42.0
	22.2	63.1	27.2	48.6	36.1	17.0	35.4	10.5
Total Phase Area		607.7	236.9	355.7	357.8	158.9	295.7	118.3
% phase composition		38%	25%	33%	28%	27%	30%	12%
$NaNH_2$	9.10	22.9	75.8	122.4	272.0	165.0	432.4	542.0
	13.93	11.8	9.6	14.2	62.7	24.4	106.0	125.3
	21.22	82.0	30.0	46.9	87.1	58.2	131.2	162.4
Total Phase Area		116.6	115.4	183.4	421.8	247.6	669.6	829.7
% Phase Composition		7%	12%	17%	33%	43%	68%	88%
$NaK_2(NH_2)_3$	7.67	24.3	109.7	97.1	64.7	22.9	2.1	0
	12.14	6.2	47.5	41.3	50.9	44.3	4.0	0
	16.81	616.5	298.5	270.2	295.1	82.0	7.5	0
	21.5	176.8	103.42	93.2	73.4	20.1	1.8	0
	26.21	47.0	32.7	27.3	17.8	6.2	0.6	0
Total Phase Area		870.7	591.7	529.1	501.8	175.4	15.9	0
% Phase Composition		55%	63%	50%	39%	30%	2%	0%
Total Sample Area		1595.1	944.0	1068.2	1281.5	582.0	981.3	948.0

Table 5.2: Peak positions and areas for Na-K-N-H manual PCA

A combination of the principal component analysis and the Rietveld refinement for each ratio, enabled the plot of starting material stoichiometry against percentage composition (by peak area) shown in Figure 5.3 to be constructed. This shows the composition of both $NaNH_2$ and KNH_2 decrease from 100 % at opposite ends of the graph to 0 % at the 4:8 $NaNH_2$:KNH_2 ratio, which is where pure $NaK_2(NH_2)_3$ was synthesised. $NaK_2(NH_2)_3$ was present to a degree in all the samples with $NaNH_2$:KNH_2 of 1:11 to 10:2. The unknown phase was present in all the samples between $NaNH_2$:KNH_2 of 5:7 and 11:1.

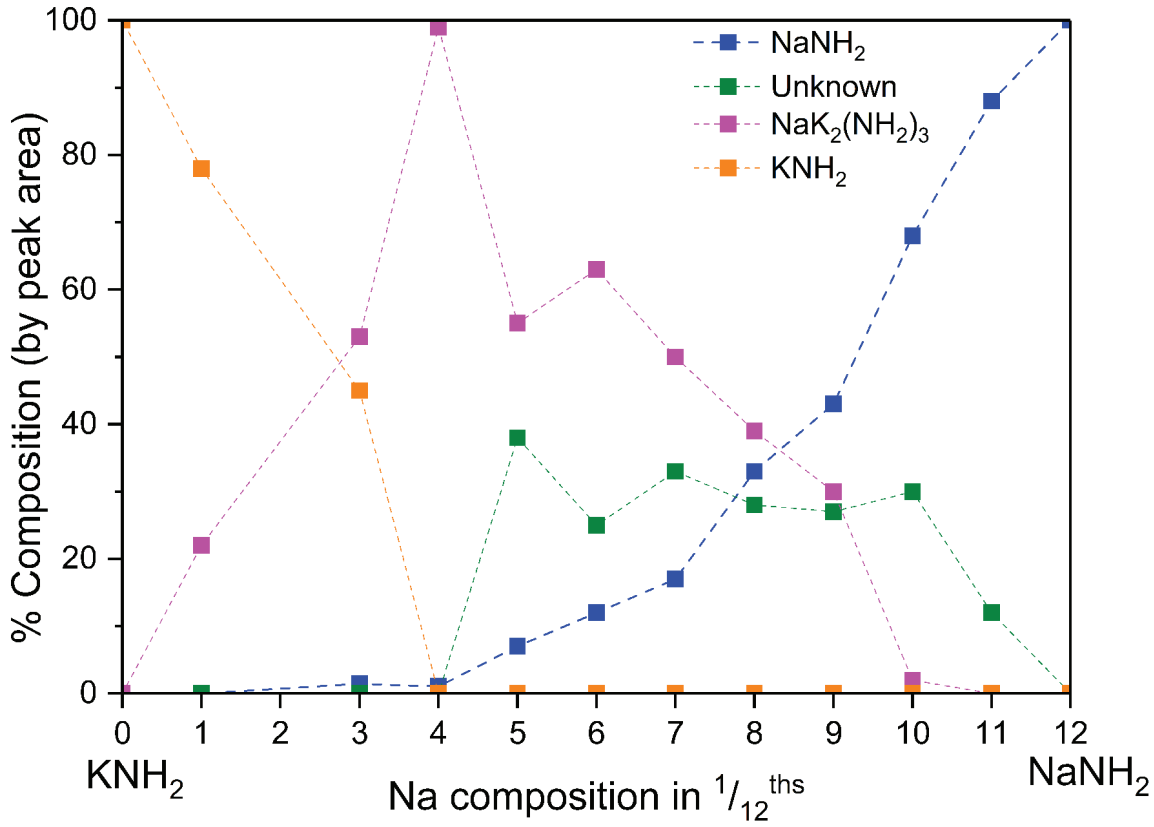


Figure 5.3: Principal component analysis for the Na-K-N-H system showing the percentage composition by peak area for each ratio analysed

5.2.1.2 Unknown Phase

Comparing the Na-K-N-H system with the Li-Na-N-H and Li-K-N-H systems, whilst $NaK_2(NH_2)_3$ is iso-structural with $LiNa_2(NH_2)_3$ and $LiK_2(NH_2)_3$ ($P4_2/m$), the Li-Na-N-H and Li-K-N-H systems have an additional mixed-metal amide, in a 3:1 ratio ($Li_3Na(NH_2)_4$ or $Li_3K(NH_2)_4$). It is likely that the unknown phase for the Na-K-N-H system has a similar composition of $NaNH_2$:KNH_2 based on the ratios in which it is seen to be present. However, $Li_3Na(NH_2)_4$ and $Li_3K(NH_2)_4$ are derived from expanded versions of $LiNH_2$. $NaNH_2$ has a different structure to $LiNH_2$ and since $LiNH_2$ is not present in the Na-K-N-H system, the unknown phase cannot be an analogous version of "$Na_3K(NH_2)_4$" although the ratio of constituent amide components is likely to be similar. It is possible that "$Na_3K(NH_2)_4$" has a similar structure to the equivalent oxide, with an "AB_3O_4" type structure as it is unlikely that this unknown phase is going to be layered.

Figure 5.3 shows that $NaK_2(NH_2)_3$ is the dominant phase for the ratios of $NaNH_2$:KNH_2 from 5:7 to 9:3 and only for the 10:2 and 11:1 ratios is the unknown phase present at a greater weight percent than $NaK_2(NH_2)_3$. $NaK_2(NH_2)_3$ is known to exist as a line-phase so may be trapping Na^+ and K^+ ions in an irreversible process so they are unable to form this additional unknown phase. $NaK_2(NH_2)_3$ is likely to be synthesised first as it has a very low synthesis temperature as determined from STA analysis (Figure 5.7).

Table 5.3 lists the total unit cell volumes for different numbers of constituent metal amide units. $NaNH_2$ and monoclinic KNH_2 have a volumes of 756.7 Å^3 and 110.8 Å^3 with 16 and 2 formula units per unit cell respectively. This gives the formula units of $NaNH_2$ and KNH_2 volumes of 47.3 Å^3 and 55.4 Å^3. The known structure of $NaK_2(NH_2)_3$ would be predicted by this method to have a volume of 632.5 Å^3 and in actual fact it has a volume of 606.5 Å^3 which is 95.9% of the predicted volume.

		Number of $NaNH_2$ units						
		5	**6**	**7**	**8**	**9**	**10**	**11**
Number of KNH_2 units	**1**	291.9	339.2	386.5	433.8	481.0	528.3	575.6
	2	347.3	394.6	441.9	489.2	536.5	583.8	631.0
	3	402.7	450.0	497.3	544.6	591.9	639.2	686.5
	4	458.1	505.4	552.7	600.0	647.3	694.6	741.9
	5	513.6	560.8	608.1	655.4	702.7	750.0	797.3
	6	569.0	616.3	663.6	710.9	758.1	805.4	852.7
	7	624.4	671.7	719.0	766.3	813.6	860.9	908.1

Table 5.3: Predicted unit cell volumes in $Å^3$ for different numbers of $NaNH_2$ and KNH_2 units

"$Na_3K(NH_2)_4$" would be predicted by this method to have a volume of 591.9 $Å^3$ (highlighted in yellow). This value could be used to guide characterisation and lattice parameter values of a potential "AB_3O_4" based unit cell.

5.2.2 Raman

Figure 5.4 shows the Raman spectra of some of the ball-milled ratios of $NaNH_2$:KNH_2 alongside the percentage composition data derived from the principal component analysis and Rietveld refinement of the I11 powder X-ray diffraction data. Each spectrum has been fitted to pseudo-Voigt peaks in TOPAS to identify the position of different stretches.

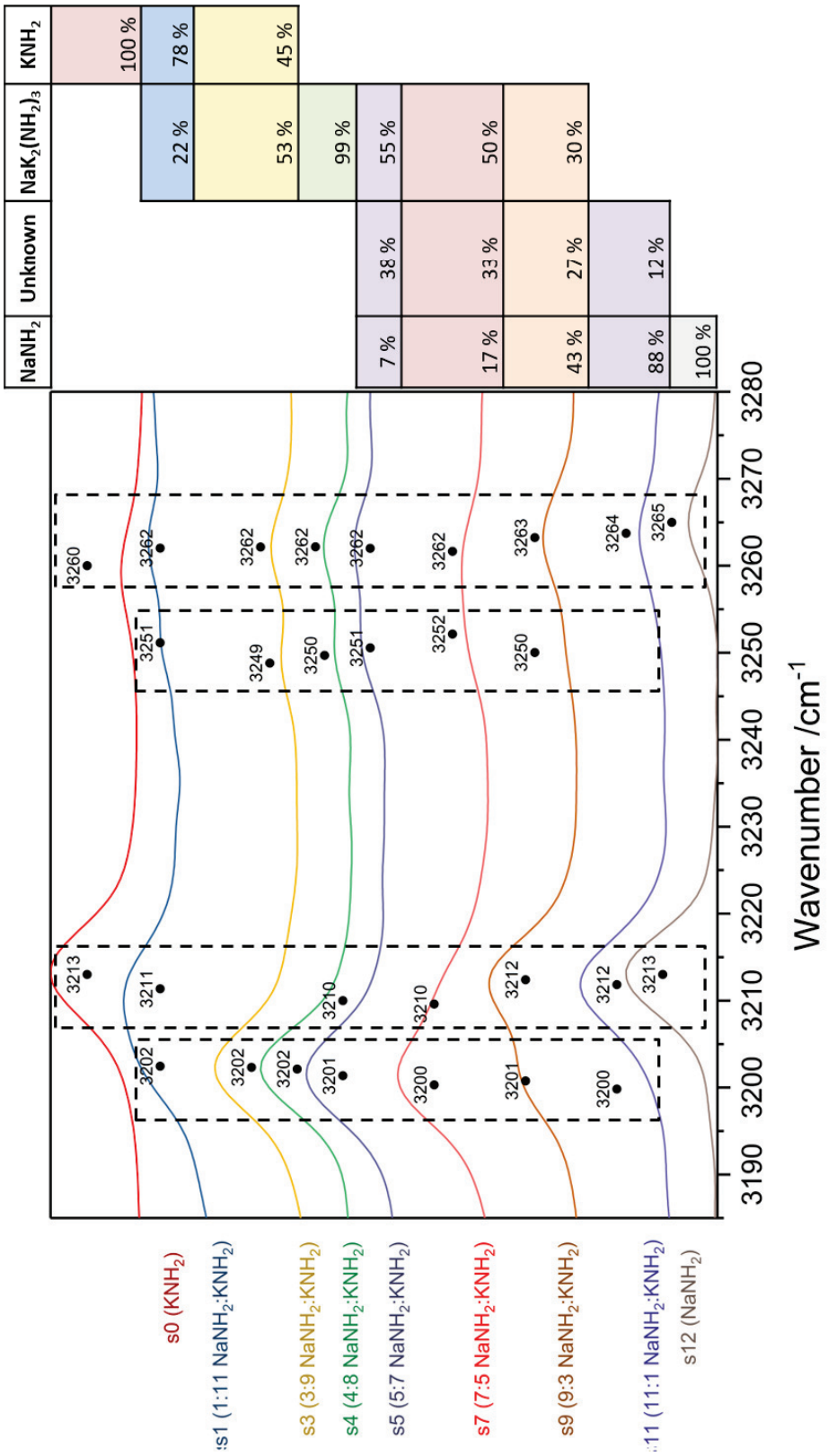


Figure 5.4: Raman spectrum for the Na-K-N-H system

The pseudo-Voigt peaks fitted and annotated on Figure 5.4 show there are four key wave-number ranges where peaks appear throughout the range of patterns and these have been highlighted by dashed boxes. Figure 5.5 plots the area of these peaks for each of the samples so it can be seen in which ratio each peak is most prevalent. This will aid assignment of the different Raman stretches to the different phases present in each sample.

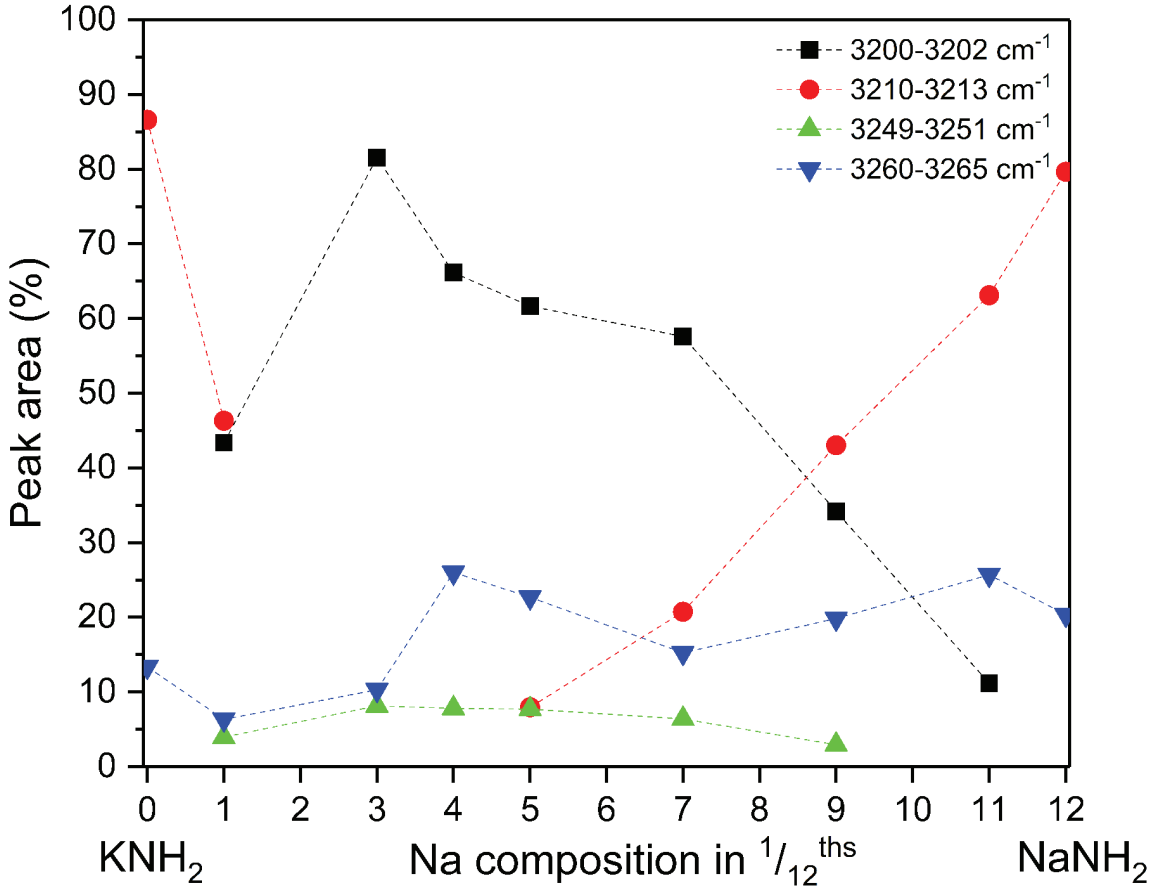


Figure 5.5: Fitted pseudo-Voigt peak areas for different Raman stretches for the Na-K-N-H system

The Raman stretches in the region of 3210-3213 cm^{-1} come from the symmetric N−H stretch of either $NaNH_2$ or KNH_2 as they are known to occur within this range. The Raman stretches of the unknown phase appear to be similar to those of $NaK_2(NH_2)_3$, as the Raman stretches in the regions of 3200-3202 cm^{-1} and 3249-3251 cm^{-1} are all fairly consistent in percentage area despite the varying composition between $NaK_2(NH_2)_3$ and the unknown phase across the ratios. This suggests that the local environment of the amide ions in the

unknown phase is similar to that in $NaK_2(NH_2)_3$. Analysis of Figure 5.5 also shows that both $NaK_2(NH_2)_3$ and the unknown phase are present as line phases (rather than with variable stoichiometry) as the Raman stretches at specific wave numbers are either present or they are not, there is not a varying wave number across the different ratios. This is consistent with the fact that both $LiNa_2(NH_2)_3$ or $LiK_2(NH_2)_3$ have been considered to be line phases and all three compounds have the same structure.

5.2.3 Simultaneous Thermal Analysis (STA)

The thermal behaviour of the hand-ground mixtures of $NaNH_2$:KNH_2 for each ratio was characterised by STA from 20 °C to 400 °C and then back to 20 °C at 5 °C/min. Figure 5.6 shows the DSC traces for each of these experiments alongside the predicted phase composition. The traces for the heating and cooling sections of the experiment have been separated and those for each sample off-set for clarity of presentation and ease of analysis. Dashed boxes have been used to group together thermal events that are possibly related and their possible origin is discussed in more detail.

All of the K-rich samples show the endothermic events at 66 °C and 78 °C which are known to correspond to the phase transitions of KNH_2 from monoclinic to tetragonal and tetragonal to cubic respectively. The KNH_2 phase change events are most prominent in the samples with the highest proportion of KNH_2 (s0-s5). The presence of thermal events at similar temperatures in both the heating and cooling traces suggest reversible phase changes. Cubic KNH_2 is reported to have a melting point of 338 °C so the reversible endo/exo-therms highlighted as “a” and “b” are likely to correspond to the melting and re-crystallisation of KNH_2.

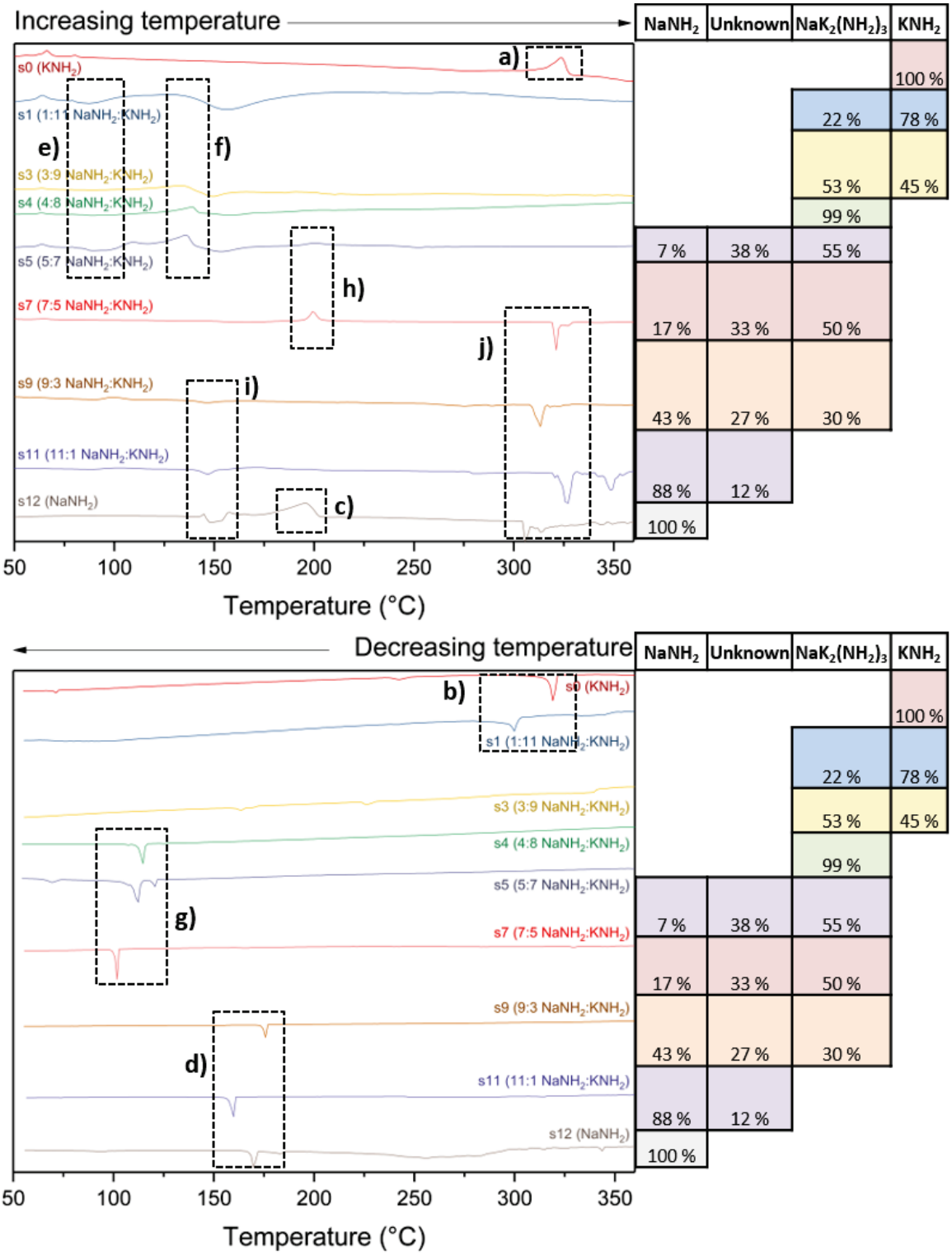


Figure 5.6: DSC traces for the Na-K-N-H system with analogous peaks grouped together in dashed boxes

The DSC data for $NaNH_2$ rich samples show thermal events labelled as "i" which are probably due to N_2 release, as this is often observed in the gas stream during gas flow panel experiments for $NaNH_2$ at this temperature (Section 3.3.1.2). There is also a stronger endothermic peak at 198 °C (labelled "c") due to the melting of $NaNH_2$ [155] ($NaNH_2$ is reported to have a melting point of 210 °C). The exo-therms in s9/s11/s12 at ∼170 °C (labelled "d") are likely to correspond to the re-crystallisation of $NaNH_2$.

The exotherms at 70 °C in s2/3/4/5 (labelled "e") correspond to the synthesis of $NaK_2(NH_2)_3$ and the large endotherms at 140 °C (labelled "f") in these samples correspond to the melting of $NaK_2(NH_2)_3$. The large exotherm at 110 °C ((labelled "g") in s4/5/7 corresponds to the re-crystallisation of $NaK_2(NH_2)_3$ on cooling. This is unexpected given that none of the mixed-metal amides from the Li-Na-N-H or Li-K-N-H systems re-crystallised on cooling, but the lack of peaks at 110 °C in either the $NaNH_2$ or KNH_2 STA traces alone suggest that their presence in the s4/5/7 samples is arising from a mixed-metal amide. From the decomposition experiments under argon on the gas flow panel it is known that "$NaK_2(NH_2)_3$ " decomposes at 427 °C, a temperature not reached in this experiment to protect the equipment.

Based on the PCA of the powder X-ray diffraction data shown in Figure 5.2 it is expected that the STA traces of s1-s9 would show the synthesis of $NaK_2(NH_2)_3$ and the STA traces of s5-s11 would show the synthesis of the unknown phase. The traces for s1/s3/s4/s5 have similar features in the 80-150 °C region, both on the way up and the way down, and support the result that $NaK_2(NH_2)_3$ melts and re-crystallises around 130 °C. It is possible that the small endotherm at 190 °C (labelled "h") in s5 and s7 on heating is a phase change between $NaK_2(NH_2)_3$ and the unknown phase. The traces for s7/s9/s11 show similarities with each other and are more similar to the STA trace of pure $NaNH_2$ so support the idea that the unknown phase is more Na rich.

5.3 *Ex-situ* thermal decomposition behaviour

Having analysed the phase space between $NaNH_2$ and KNH_2, despite the discovery of a new unknown phase, it is only $NaK_2(NH_2)_3$ that could be made in high purity so it is this compound which was investigated in further depth.

The behaviour of the single metal amides $NaNH_2$ and KNH_2 has previously been discussed in Section 3.3.1 and Section 4.1.1. The *ex-situ* thermal decomposition of $NaK_2(NH_2)_3$ was investigated at low temperatures by STA and at high temperatures on the gas flow panel under argon. Together these give a holistic view of how the mixed-metal amide behaves.

Figure 5.7 shows DSC traces for both pre-made $NaK_2(NH_2)_3$ (black) and a hand-ground mixture of $NaNH_2 + 2KNH_2$ (blue). The mass trace (green) comes from the TGA part of the STA experiment for pre-made $NaK_2(NH_2)_3$ (black).

The reported temperatures for the KNH_2 monoclinic to tetragonal and tetragonal to cubic phase changes are 53 °C [150] and 75 °C [211] respectively which can be seen in Figure 5.7 at 63 °C and 79 °C respectively. The slight difference in temperature is likely to be attributable to differences in sample size, heating ramp rate and gas flow amongst others.

Comparison of the two traces in Figure 5.7 enables the identification of the synthetic step for the formation of $NaK_2(NH_2)_3$ as from this point onwards the two traces should be identical. This is visible in the $NaNH_2 + 2KNH_2$ trace as the broad exothermic event at 89 °C. This is interesting as the thermal events for the synthesis of $LiNa_2(NH_2)_3$ and $LiK_2(NH_2)_3$ were determined to be endothermic and at much higher temperatures of 187 °C (Figure 3.8) and 148 °C (Figure 4.28) respectively.

STA traces for $LiNa_2(NH_2)_3$ and $LiK_2(NH_2)_3$ have shown separation and melting steps which occur almost simultaneously, with only a 3 °C difference in temperatures as the crystal structures cannot accommodate ionic mobility or non-stoichiometry. $NaK_2(NH_2)_3$ is also a line phase but in Figure 5.7 distinct separation and melting steps are not observed.

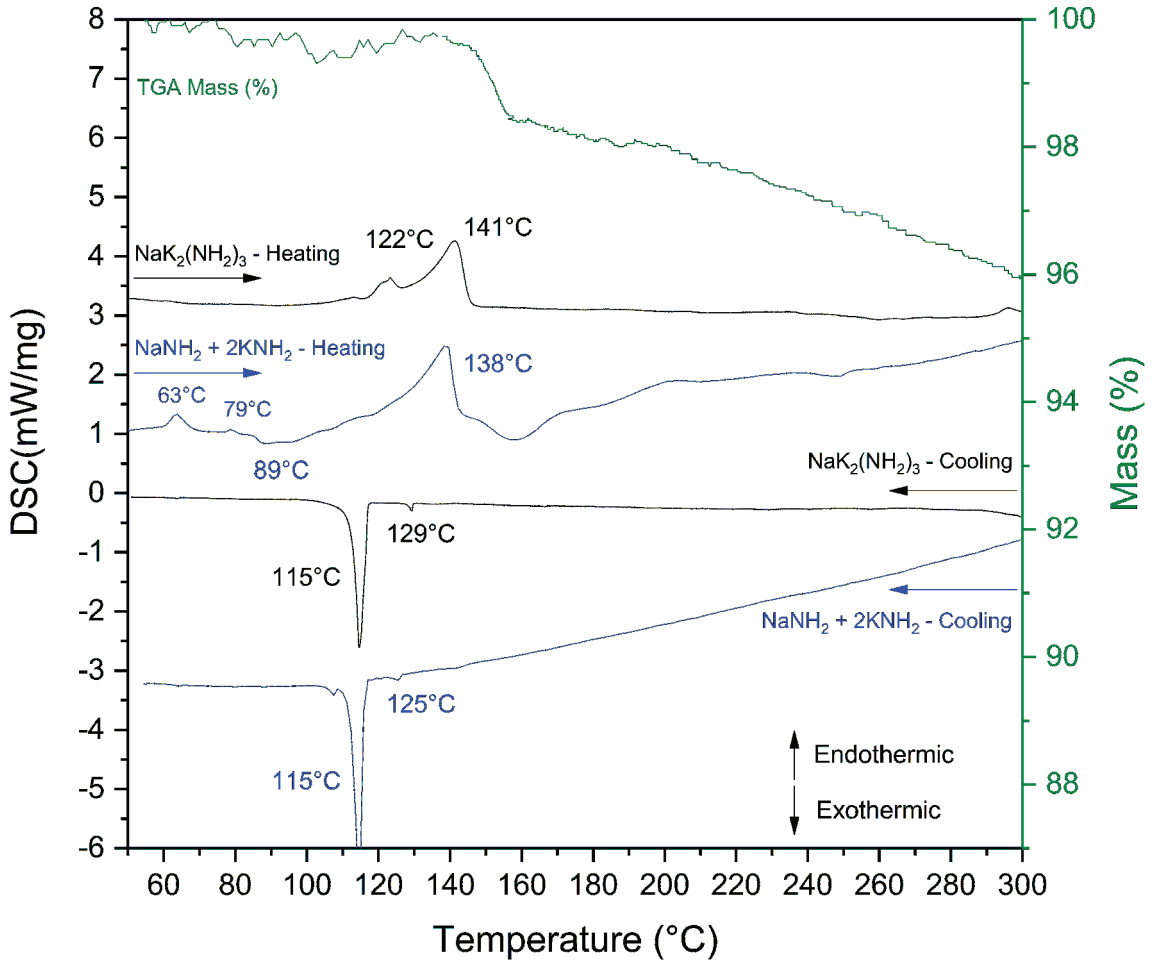


Figure 5.7: DSC traces for $NaK_2(NH_2)_3$ (black) and $NaNH_2 + 2KNH_2$ (blue) and mass trace (green) from the TGA part of the STA experiment for $NaK_2(NH_2)_3$ (black)

It could be that these two steps are occurring simultaneously but the exothermic event at 115 °C has been attributed to the re-crystallisation of $NaK_2(NH_2)_3$. The synthesis experiment performed on GEM (Section 5.4.1) also supports the idea that $NaK_2(NH_2)_3$ does not separate on melting, and a molten $NaK_2(NH_2)_3$ structure is maintained up to 200 °C. It is therefore likely that the endotherm at 141 °C only corresponds to $NaK_2(NH_2)_3$ melting and not consecutively separating.

The mass loss was recorded throughout these experiments by TGA and a 2 % mass loss is observed which correlates with the thermal event at 141 °C. This is the desorption of physisorbed gases which are released from the powder grains when the whole sample melts.

Many of the mixed-metal amides discussed in this thesis show hysteresis through a slight

off-set of corresponding thermal events between heating and cooling. This is not unusual in thermal analysis and is simply a product of the kinetics of the experiment, as sometimes it takes longer to nucleate crystallisation. With a slower heating rate the off-set would be expected to decrease.

There is a notable difference in peak shape between the broad melting event at $\sim 140\,^{\circ}C$ and the sharp recrystallisation at 115 °C. It is interesting that in this system, it is $NaK_2(NH_2)_3$ that is solidifying out of the molten high temperature combined solution (rather than $NaNH_2$ or KNH_2) and it is doing so at a particularly low temperature.

It has been reported that "thoroughly mixing the proper weights of the two amides" ($NaNH_2$ and KNH_2) leads to the preparation of a eutectic mixture [35, 193]. Whereas the melting points of $NaNH_2$ and KNH_2 are known to be 220 °C and 338 °C respectively, this eutectic mixture has a reported melting point of 92 °C, lower than the endothermic events seen in Figure 5.7 but not dissimilar to the thermal events seen in Figure 5.6 which had been assigned to the re-crystallisation of $NaK_2(NH_2)_3$.

Below 300 °C, (the peak temperature reached in this STA experiment), there are no sharp exotherms signifying the start of the decomposition of the molten phase as was seen for the Li-Na-N-H and Li-K-N-H systems. This implies that perhaps due to the lack of an imide forming amide ($LiNH_2$) the molten $NaK_2(NH_2)_3$ is stable to higher temperatures.

The gas flow panel was used to investigate the high temperature thermal decomposition of both pre-formed $NaK_2(NH_2)_3$ and a hand-ground mixture of $NaNH_2 + 2KNH_2$ under argon from 20 °C to 480 °C. Figure 5.8 shows the outlet gas flow MS traces of $NaK_2(NH_2)_3$ (solid lines) and $NaNH_2 + 2KNH_2$ (dashed lines).

When heated on the gas flow panel under argon, $LiNa_2(NH_2)_3$ and $LiK_2(NH_2)_3$ both show low temperature NH_3 release at $\sim 150\,^{\circ}C$ but $NaK_2(NH_2)_3$ does not show any gas release until the onset of N_2 and H_2 release at $\sim 300\,^{\circ}C$. $LiNH_2$ decomposes to Li_2NH with the release of NH_3, but $\sim 150\,^{\circ}C$ is too low a temperature for this to occur.

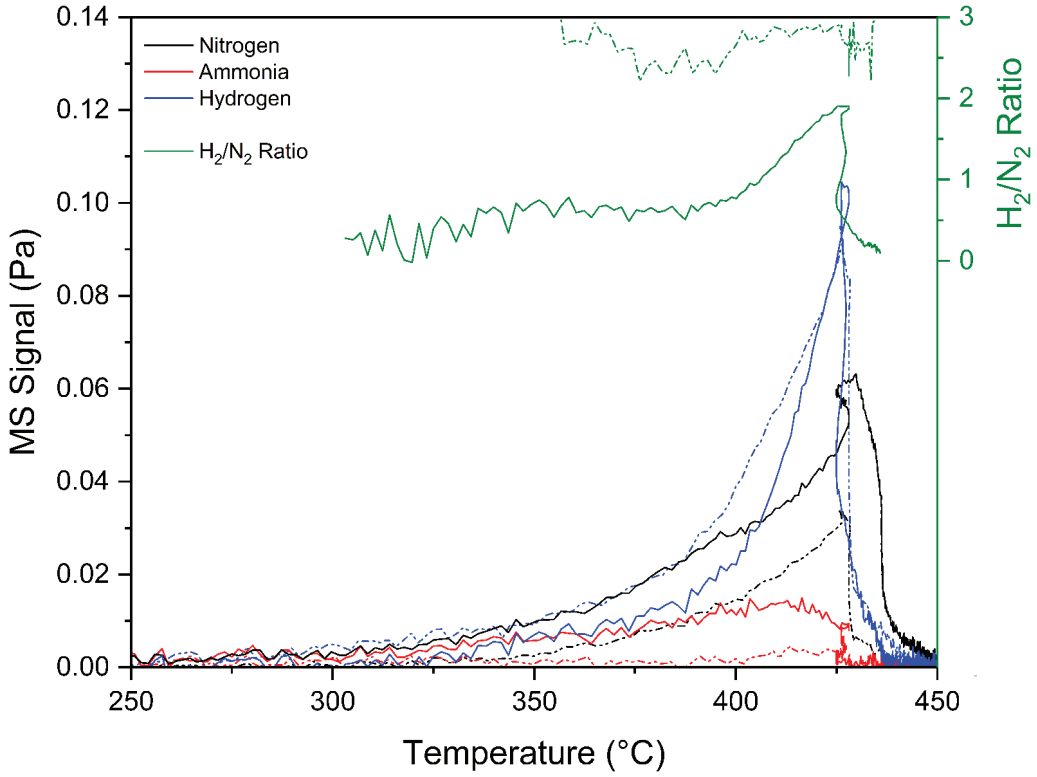


Figure 5.8: Decomposition of $NaK_2(NH_2)_3$ (solid lines) and $NaNH_2 + 2KNH_2$ (dashed lines) on the gas flow panel under argon

Two pseudo-Voigt functions in TOPAS have been used to determine "peak positions" of the decomposition reactions from the N_2 curves for the $NaK_2(NH_2)_3$ trace (Figure 5.9) in an analogous manner to the Li-Na-N-H and Li-K-N-H systems. This shows that it may be more accurate to think of the MS signal as two overlapping peaks centred at $\sim$404 °C and 430 °C.

$NaNH_2$ was seen to decompose at 404 °C during the decomposition of $Li_3Na(NH_2)_4$ and $LiNa_2(NH_2)_3$ and KNH_2 was seen to decompose at 419 °C during the decomposition of $Li_3K(NH_2)_4$ and $LiK_2(NH_2)_3$. The pseudo-Voigt functions in Figure 5.9 are therefore consistent with $NaNH_2$ decomposing first at 404 °C and KNH_2 decomposing at 430 °C. This is unexpected given that alone KNH_2 is known to decompose at a lower temperature than $NaNH_2$.

It has been suggested from the STA data that $NaK_2(NH_2)_3$ melted at 141 °C and did not separate below 300 °C. The consistency of the pseudo-Voigt "peak positions" in Figure 5.9 with those seen for the Li-Na-N-H and Li-K-N-H systems suggest that it is ultimately

$NaNH_2$ and KNH_2 that is decomposing above 400 °C. Molten $NaK_2(NH_2)_3$ must therefore separate into a molten phase of $NaNH_2 + 2KNH_2$ between 300 °C and 400 °C before the onset of decomposition and gas release.

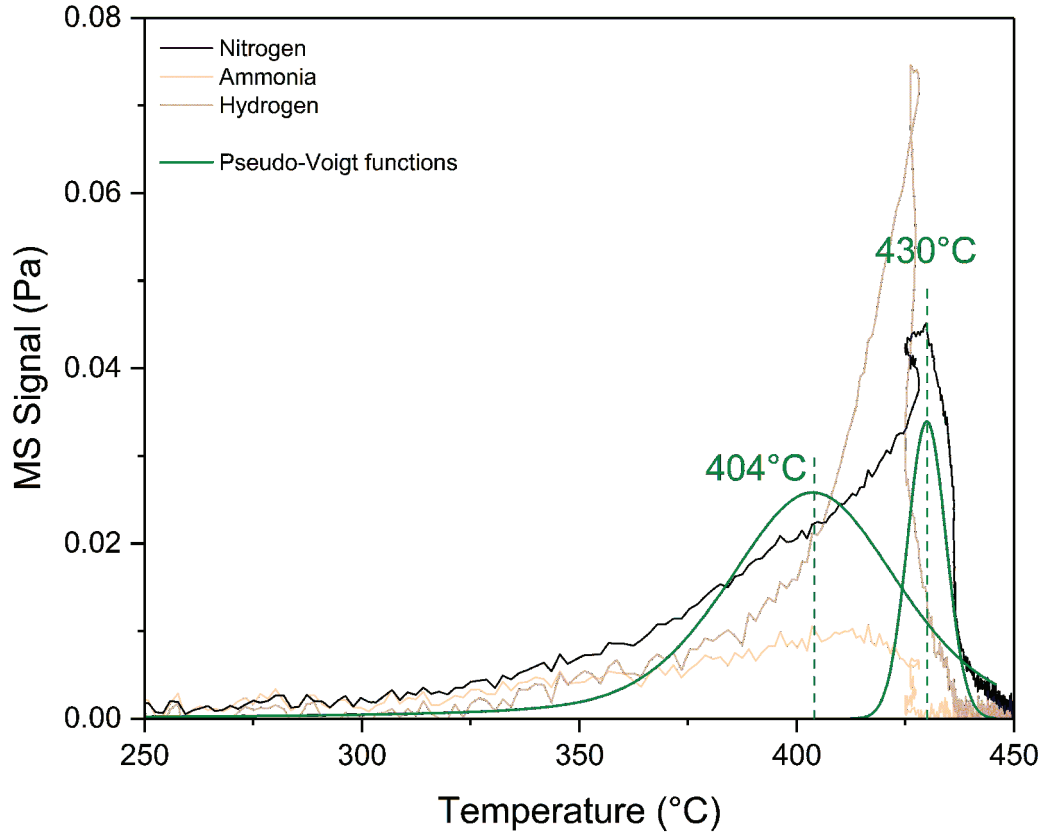


Figure 5.9: Two pseudo-Voigt functions have been used to determine the peak positions in the N_2 curve from Figure 5.8 during the decomposition of $NaK_2(NH_2)_3$

A mechanism could be proposed for the overall decomposition envisaging the initial melt of $NaK_2(NH_2)_3$ followed by its separation into $NaNH_2 + 2KNH_2$. $NaNH_2$ would then decompose first into Na metal closely followed by the decomposition of KNH_2 into K metal. It is possible that the sodium-potassium alloy NaK forms which is used as a coolant in fast reactors as it is a liquid at room temperature. NaK was not detected in these experiments but if it were to be present it may explain the unusual peak shapes in Figure 5.8 as it would be behaving as an inbuilt cooling mechanism.

Solid $NaK_2(NH_2)_3$	$\longrightarrow$ Liquid $NaK_2(NH_2)_3$	Melt
Liquid $NaK_2(NH_2)_3$	$\longrightarrow NaNH_2 + 2\,KNH_2$	Separation
	$\longrightarrow Na + \frac{1}{2}N_2\uparrow + H_2\uparrow + 2\,KNH_2$	$NaNH_2$ decomposes
	$\longrightarrow Na + 2\,K + N_2\uparrow + 2\,H_2\uparrow$	KNH_2 decomposes
	$\longrightarrow Na + 2\,K$	All gases lost
	$\longrightarrow$ Empty reactor	Na and K volatilised

No recoverable sample was present at the end of either of the decomposition experiments for $NaK_2(NH_2)_3$ or $NaNH_2 + 2KNH_2$ under Ar so powder X-ray diffraction could not be done to determine the residual products in each case. It is Na and K metals that are the products of $NaNH_2$ and KNH_2 under argon and both have been observed to have been lost from the reactors and unable to be identified when investigating the Li-Na-N-H and Li-K-N-H systems, so it is unsurprising that they are also volatilised during these experiments. Low mass recovery is a poor property for a catalyst.

5.4 GEM data

Analogous to the experiments described in Section 4.6.2 and Section 4.7.2, the synthesis of $NaK_2(ND_2)_3$ from $NaND_2 + 2KND_2$ was investigated followed by the subsequent decomposition of $NaK_2(ND_2)_3$ under argon on the GEM beamline at ISIS using the IGA^n equipment.

The mass and temperature of the samples were recorded simultaneously as neutron diffraction data was collected using the IGA^n apparatus (however, the mass trace did not work for the synthesis experiment). The temperature and pressure were recorded every 5 seconds, and neutron diffraction data were collected at 100 second intervals throughout the course of the experiment.

Rietveld refinements were performed in TOPAS and batch refinements done for the data collected from banks 3, 4 and 5 to track the scale of each species as it changes throughout the reactions.

5.4.1 $NaND_2 + 2KND_2$ synthesis

For the *in-situ* synthesis experiment, 0.5 g of a hand ground mixture of $NaND_2 + 2KND_2$ was placed in a vanadium bucket which was hung from a tungsten wire from the IGA^n balance under an inert atmosphere and sealed with a quartz tail before being loaded into the GEM beamline. An initial hour long scan of the sample was taken, before the sample was heated at a ramp rate of 1 °C/min to 200 °C where it was held for 3 hours. The sample was then cooled at 10 °C/min.

Figure A.15 in the Appendix shows the full contour plots for banks 3, 4 and 5 for the whole of the $NaND_2 + 2KND_2$ synthesis experiment. Figure 5.10 shows the diffraction data collected from bank 4 and a selected *d*-spacing range from bank 3 alongside the temperature profile. The results of the batch refinement for this initial section when Bragg peaks are visible are also shown.

From Figure 5.10, it can be seen that there are three different regions within the contour plot:

1. Bragg peaks from 20 °C to 125 °C
2. From 125 °C as the sample was heated to 200 °C and then cooled to 110 °C for which there are only broad amorphous peaks visible
3. On cooling Bragg peaks reappear at 105 °C

Refinement of the hour long scan of the sample taken prior to heating indicated that the majority phase of the sample was monoclinic KND_2 (37.6 %) and $NaND_2$ (35.8 %) with (26.6 %) tetragonal KND_2 also present (Table A.9 in the Appendix). Monoclinic KND_2 is the phase known to be stable below 53 °C [150] but there is also a small amount of tetragonal KND_2 visible which may be metastable and present as a result of the mechanical grinding to mix the starting materials. It has been reported that the mechanochemical treatment of KH and KNH_2 from manual grinding is enough to promote the formation of detectable amounts of a $K(NH_2)_xH_{(1-x)}$ solid solution [246] enabling the coexistence of multiple phases of KNH_2 at room temperature. It is therefore possible that a similar interaction is occurring here.

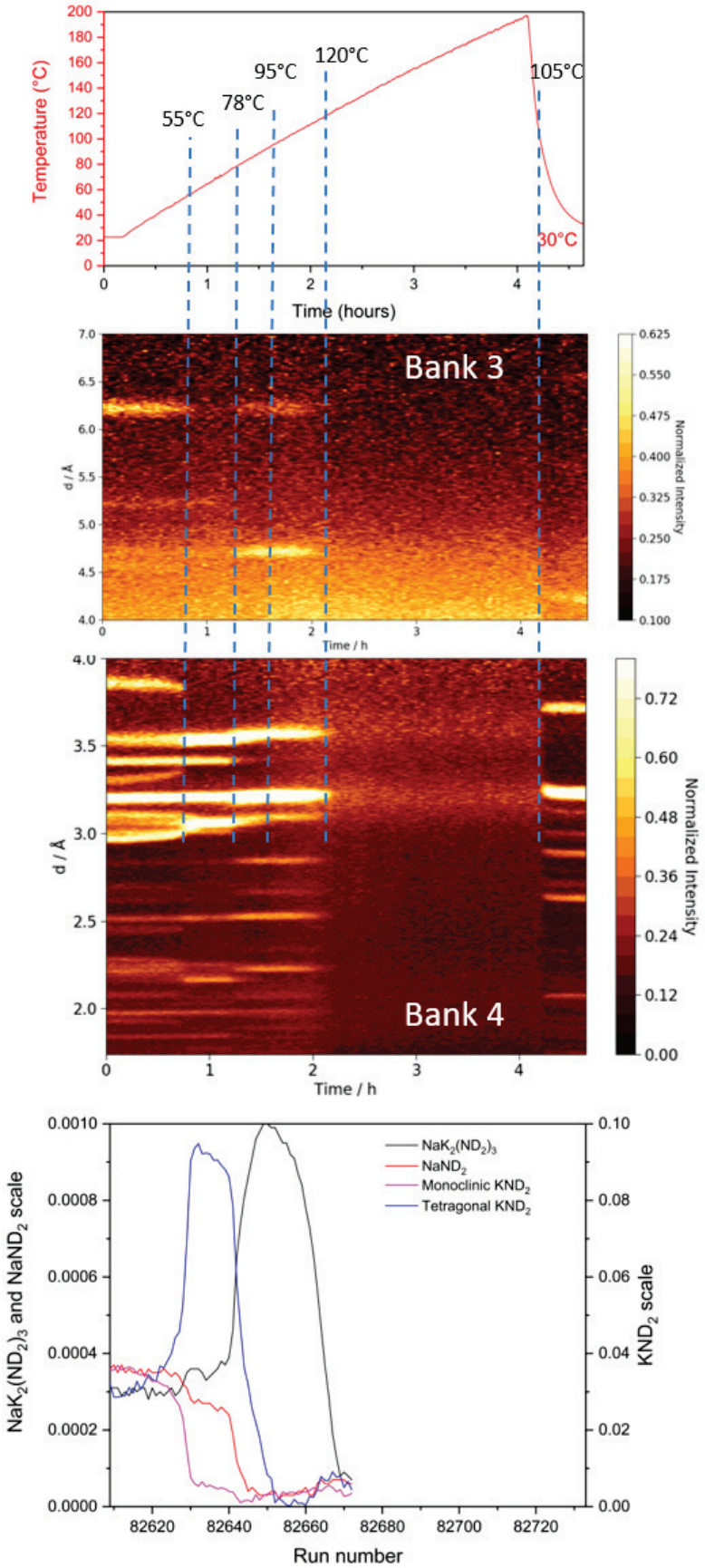


Figure 5.10: Bank 4, a selected range of Bank 3 and the temperature profile for the $NaND_2 + 2KND_2$ synthesis experiment on GEM alongside the results of the batch process refinement showing which phases are present for the initial part of the experiment until the Bragg peaks disappear

As expected, on heating, monoclinic KND_2 undergoes a phase change to tetragonal KND_2 at 55 °C, most clearly signified by the loss of the peaks at 3.84 Å (10-1), 3.30 Å (011), 3.09 Å (002), 2.96 Å (110) and 2.45 Å (102). The tetragonal KND_2 peak at 3.55 Å (101) also increases in intensity as do the peaks at 3.11 Å (002), 3.05 Å (110) and 2.18 Å (112). During the monoclinic to tetragonal KND_2 phase change the a and c lattice parameters decrease as b and β increase to enable the $P2_1/m$ to P4/nmm unit cell symmetry change which explains why the monoclinic 3.84 Å (10-1) peak shifts to a smaller d-spacing on heating, but the 2.96 Å (110) shifts to larger d-spacing as the temperature is increased. $NaK_2(ND_2)_3$ is synthesised at a lower temperature than that known for the phase change from tetragonal KND_2 to cubic KND_2 so no cubic KND_2 is observed.

At 78 °C, $NaK_2(ND_2)_3$ is synthesised which is an unusually low temperature for mixed-metal amide formation. The distinctive $NaND_2$ peaks at 3.40 Å (220), 3.19 Å (022), and 3.01 Å (131) disappear and new $NaK_2(ND_2)_3$ peaks appear (Table A.9 in the Appendix). There is a distinct change in the background at 95 °C, half-way through the section of the contour plot for which $NaK_2(ND_2)_3$ Bragg peaks are visible.

The Bragg peaks corresponding to $NaK_2(ND_2)_3$ disappear at 120 °C as the sample melts alongside a change in the background as a whole and broad peaks appear at d-spacings of 3.23 Å and 3.61 Å in bank 4, 1.64 Å and 1.93 Å in bank 5 and 4.00 Å in bank 3. These features have retained some aspects and elements of the $NaK_2(ND_2)_3$ structure so could correspond to molten $NaK_2(ND_2)_3$. This supports the STA data in Figure 5.7 which showed $NaK_2(NH_2)_3$ re-crystallised at 110 °C and did not separate on melting.

This experiment was only heated to 200 °C and Figure 5.8 shows the onset of gas release corresponding to the start of decomposition is 300 °C. Therefore this amorphous $NaK_2(ND_2)_3$ does not appear to decompose and the amorphous bands are visible up to the peak temperature of 200 °C and on cooling until the sample reaches 120 °C again. This suggests that $NaK_2(ND_2)_3$ is not separating on melting and does not decompose below 200 °C.

As the sample is cooled, Bragg peaks reappear in a single step in the contour plot at 105 °C (Figure 5.11). This is consistent with a single recrystallisation event rather than two events if $NaK_2(ND_2)_3$ had separated into $NaND_2$ and KND_2 as they would be expected to

recrystallise at different temperature. The observed Bragg peaks listed in Table A.9 in the Appendix do not match any known Na-N-(-H), K-N(-H) or Na-K-N-(H) phases or expected oxidation products, so corresponds to an unknown phase. The appearance of this unknown phase at 105 °C correlates well with the single exothermic event at 115 °C seen in the STA data in Figure 5.7.

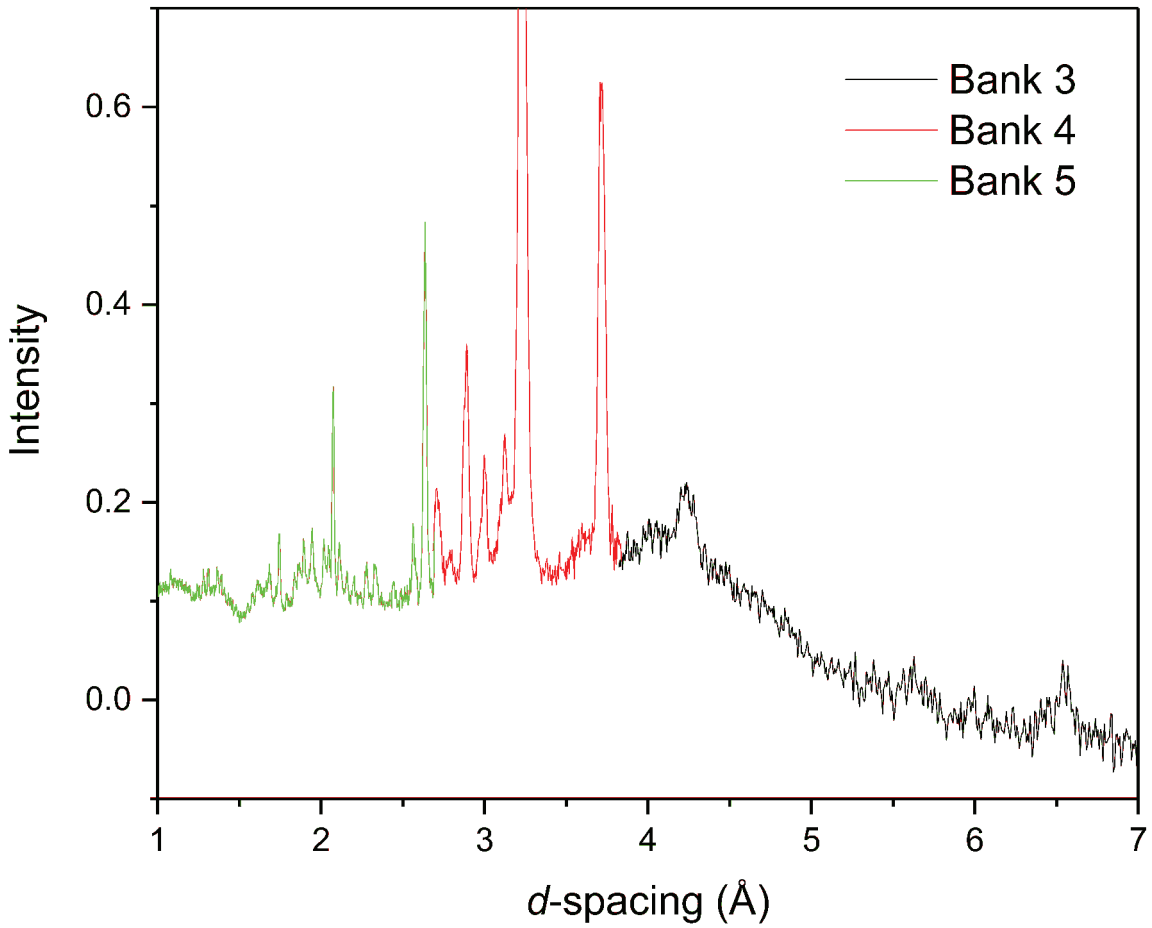


Figure 5.11: Neutron diffraction data from banks 3, 4 and 5 for the unknown phase formed on cooling during $NaND_2 + 2KND_2$ synthesis experiment on GEM from 105 °C

This unknown phase is different to the one observed in the ball-milled ratios discussed in Section 5.2.1.2. Future work would be to successfully identify and characterise both of these phases. Experiments were performed on the gas flow panel with the same temperature profile and starting materials as the *in-situ* experiment to try and replicate the conditions. It was hoped that this unknown phase could be formed again in order for a powder X-ray diffraction to be taken. However, in each case it is only $NaK_2(NH_2)_3$ that forms.

5.4.2 $NaK_2(ND_2)_3$ decomposition

Although $NaK_2(ND_2)_3$ was successfully synthesised *in-situ*, a separate pre-made sample (*ex-situ*) was used for this separate experiment to probe the decomposition of $NaK_2(ND_2)_3$. This was synthesised by ball-milling $NaND_2 + 2KND_2$ and was confirmed by *ex-situ* powder X-ray diffraction.

During this decomposition experiment, the sample was heated to 400 °C so the quartz reactor cannot be used and a stainless steel reactor must be used instead. The stainless steel bucket was also used leading to the unavoidable consequence of steel peak present as doublets throughout the experiment.

The sample of $NaK_2(ND_2)_3$ was heated from room temperature at 1 °C/min to 380 °C when the heater was turned off and it was cooled at 10 °C/min to 35 °C. There were two short periods of beam off throughout this experiment but neither was long enough to warrant a change in the heating profile.

Full contour plots of the diffraction data and the corresponding thermogravimetric data collected from banks 3, 4 and 5 is presented in the Appendix in Figure A.16. The diffraction data for bank 4 and a selected *d*-spacing range from bank 3, the temperature profile and the batch process refinement from banks 3, 4 and 5 data (showing the scale, *a* and *c* parameters of $NaK_2(ND_2)_3$ throughout the experiment) are presented in Figure 5.12.

An initial hour long room temperature scan was taken to get an accurate dataset for the start of the batch refinement which refines to $NaK_2(ND_2)_3$ (Table A.10 in the Appendix). Figure 5.12 shows that on heating, the reflections from $NaK_2(ND_2)_3$ slowly decrease in intensity up to 100 °C and faster between 100 °C and 125 °C. They disappear as $NaK_2(ND_2)_3$ melts at 125 °C and no new reflections appear before the heating was stopped at 380 °C and the sample was cooled. The batch process Rietveld refinement on the *a* and *c* unit cell parameters shows an approximately linear thermal expansion in both the *a*, (*b*) and *c* directions. The $NaND_2 + 2KND_2$ GEM synthesis experiment shows $NaK_2(ND_2)_3$ melts at 120 °C which is in good agreement with the melting temperature of 125 °C seen here.

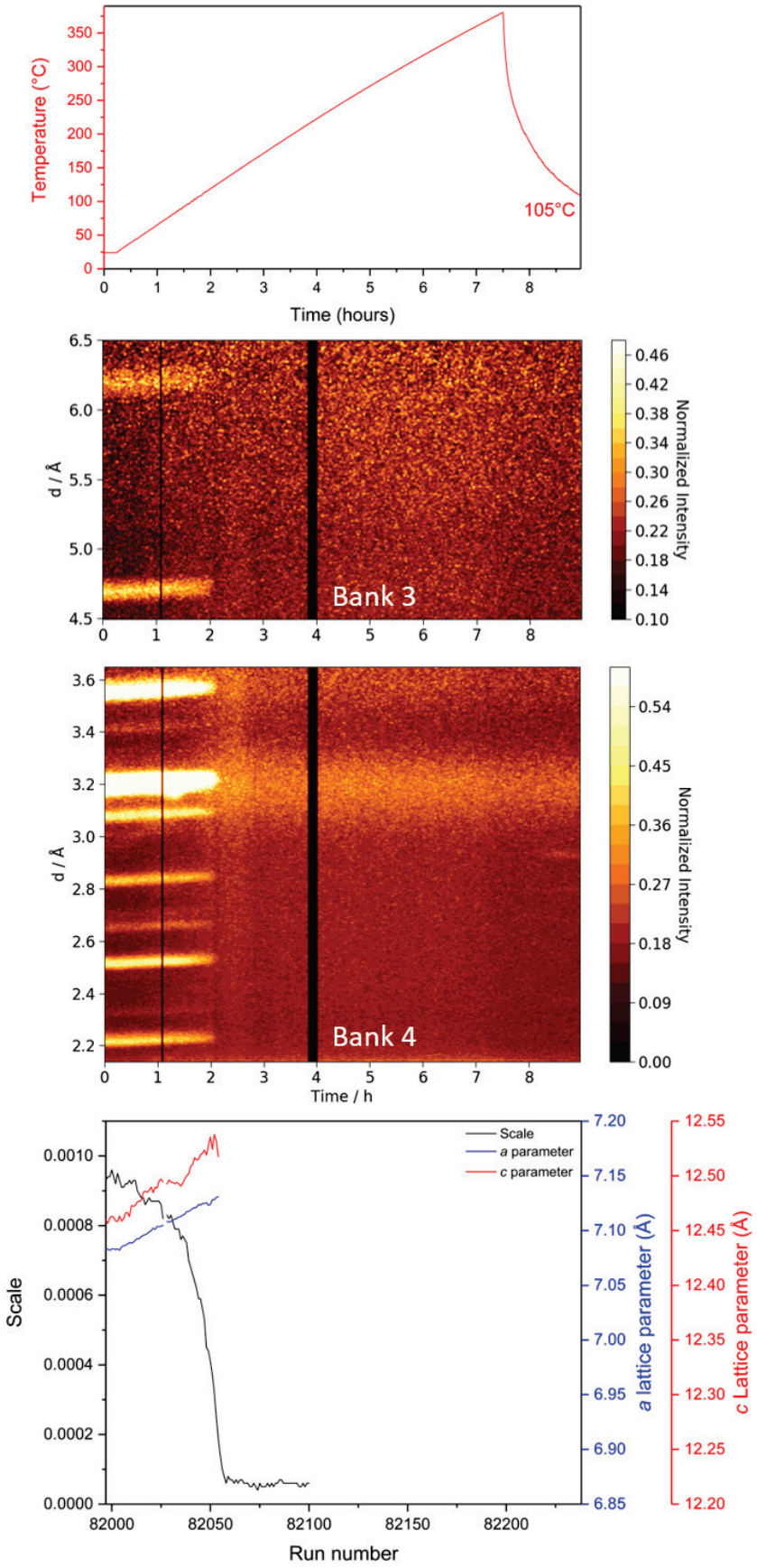


Figure 5.12: Neutron diffraction data from banks 3 and 4 and the temperature profile for the $NaK_2(ND_2)_3$ decomposition experiment on GEM alongside the results of the batch process refinement showing the scale, a and c parameters of $NaK_2(ND_2)_3$ throughout the experiment

Beyond 125 °C, there is a change in the background and broad peaks appear at *d*-spacings of 3.98 Å and 3.23 Å (bank 3), 3.61 Å and 3.23 Å (bank 4) and 1.64 Å (bank 5). These are all at the same *d*-spacings as the broad peaks that appeared in the GEM synthesis experiment at 120 °C (Figure 5.10) and are attributed to molten $NaK_2(ND_2)_3$.

Figure 5.8 shows when $NaK_2(ND_2)_3$ is heated, gas release does not occur until $\sim$320 °C, with a peak gas release temperature of 429 °C. This *in-situ* experiment was heated to 380 °C so it is possible the sample was not heated high enough for full decomposition to be observed, although it was heated enough for the onset of decomposition to occur. The amorphous $NaK_2(ND_2)_3$ peaks are therefore visible for the duration of the experiment.

From Figure 5.12 it can be seen that on cooling, faint Bragg peaks appear in banks 4 and 5 at 160 °C at *d*-spacings of 2.93 Å and 2.81 Å, 2.69 Å and 2.37 Å. The experiment was only cooled to 108 °C before neutron patterns stopped being collected so it is possible this phase would have gained crystallinity if it was cooled further. The faint Bragg peaks observed do not correspond to, KND_2, $NaK_2(ND_2)_3$ or the unknown phase in the $NaND_2 + 2KND_2$ GEM synthesis experiment which crystallised on cooling at 120 °C (Figure 5.11). They could fit to $NaND_2$ as they are appearing at the same temperature as the exothermic events seen for the $NaNH_2$ rich samples in the STA traces shown in Figure 5.6.

This is different to the decomposition experiments ran on the gas flow panel under argon for which no recoverable sample was present at the end of either experiment as full decomposition had occurred. The experiments on the gas flow panel were heated to much higher temperatures, which were obviously required for full decomposition and volatilisation of the decomposition products.

Figure 5.13 plots the change in mass as recorded by the IGA^n against the reaction temperature and shows the on-set of mass loss in this GEM decomposition experiment is $\sim$320 °C which therefore correlates well with the temperature for the onset of gas release during the decomposition under argon on the gas flow panel (Figure 5.8).

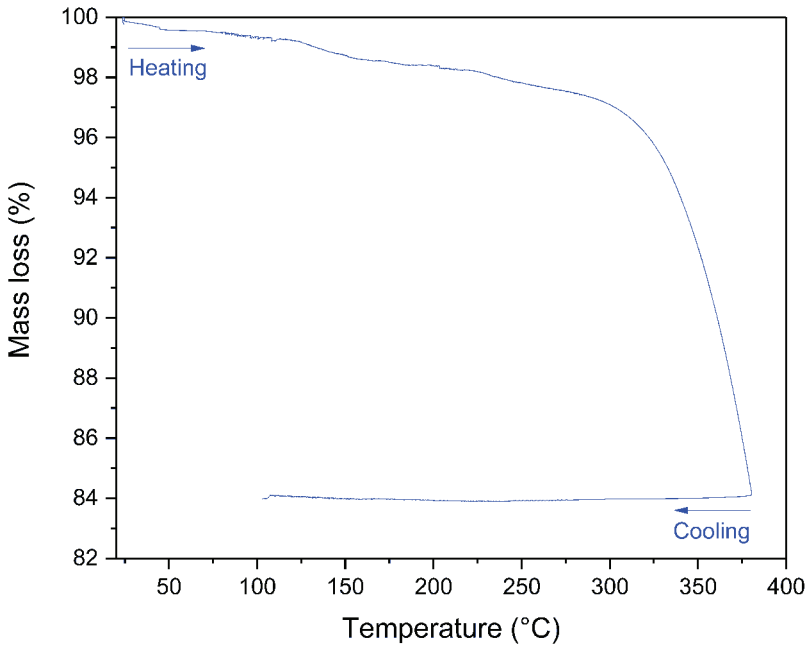


Figure 5.13: Percentage mass loss as a function of temperature for the $NaK_2(ND_2)_3$ decomposition experiment on GEM

Figure 5.13 shows that during the experiment only 16 % of the starting mass was lost. If the $NaK_2(ND_2)_3$ sample is molten, it will not be contained well in the IGA^n bucket which is consistent with the steady mass loss seen over time up to $\sim$320 °C. Beyond 320 °C there is a some additional mass loss due the onset of decomposition. The trajectory of the mass loss between 320 °C and 380 °C (the peak temperature reached) shows that the sample did not fully decompose and had not completely lost mass when cooling started, as the mass loss had not plateaued or finished.

Decomposition of $NaK_2(ND_2)_3$ into solely Na and K metals would lead to a mass loss of 32 %. A mass loss of only 16 % of that of the initial sample mass is observed during this GEM decomposition experiment which is consistent with only partially decomposition of $NaK_2(ND_2)_3$. A higher temperature would need to be achieved to effect full and complete decomposition.

5.5 Inert Gas Summary

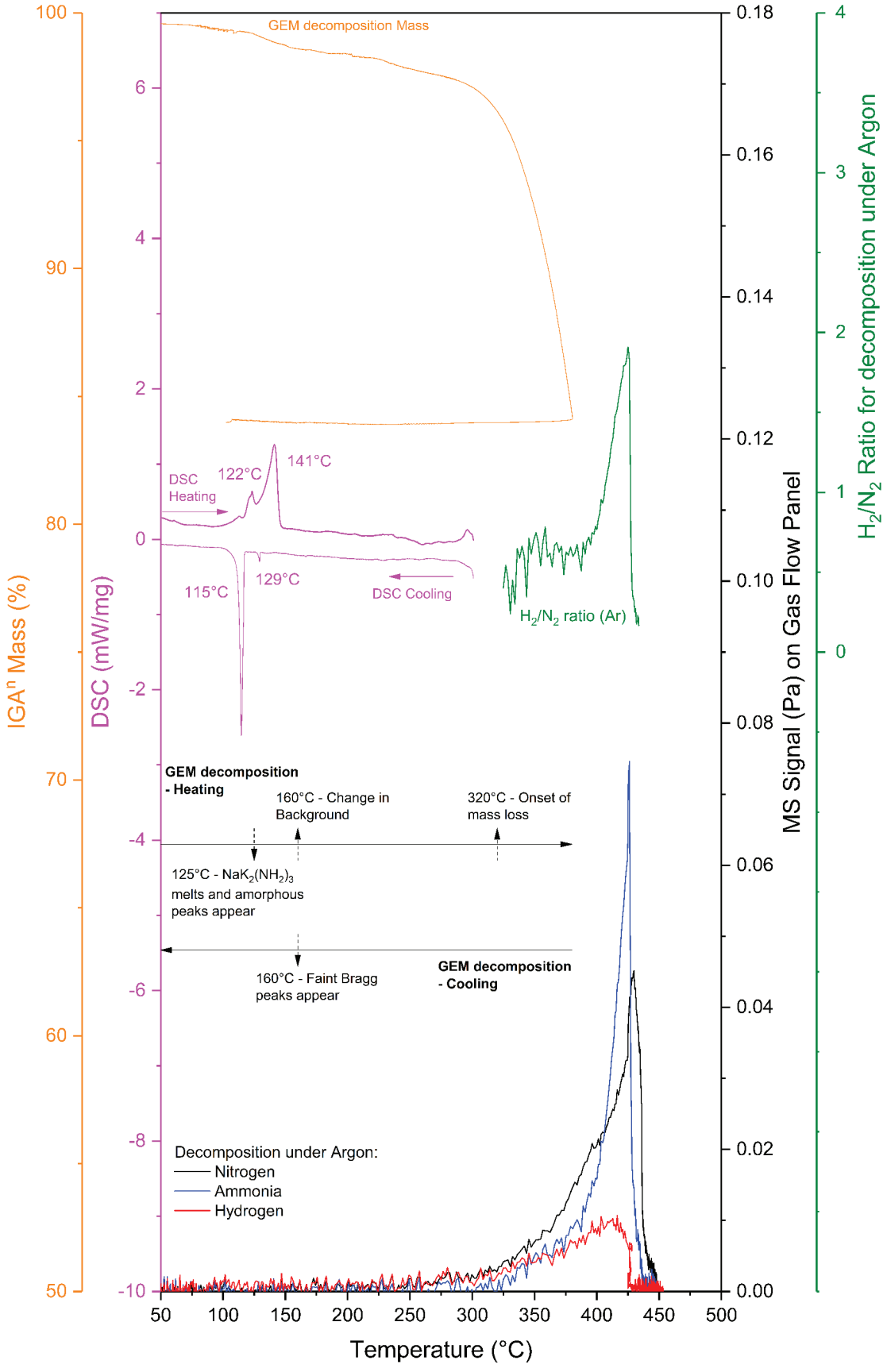


Figure 5.14: Thermodynamic properties measured during the decomposition of $NaK_2(NH_2)_3$ under inert gas

Figure 5.14 shows the superposition of the mass trace when $NaK_2(NH_2)_3$ was heated on the IGA^n during the GEM decomposition experiment, the MS trace for the gases released when heated on the gas flow panel and the DSC trace during STA. The key results from the GEM decomposition experiment have also been summarised at the relevant temperatures.

It is clear that a different mechanism is occurring compared to a superposition of the individual behaviours of $NaNH_2$ and KNH_2. Significant NH_3 production is observed above 300 °C during the decomposition of $NaK_2(NH_2)_3$ which is not seen during the decomposition of $NaNH_2$ or KNH_2 alone. The overall behaviour of $NaK_2(NH_2)_3$ is summarised in Section 5.8.

5.6 Ammonia decomposition

Group 1 mixed-metal amides have been shown to be a new class of inexpensive and effective catalysts for the decomposition of ammonia into nitrogen and hydrogen (Section 3.5 and Section 4.8).

Ammonia conversion efficiencies of these materials were analysed by loading 0.5 g of the catalyst powder into a 46.9 cm^3 stainless steel reactor, attached to the gas flow panel as described in Section 2.2.1.1 and Section 2.3 [310]. The temperature was varied as ammonia as passed over the sample whilst the out gas from the cell was monitored by mass spectrometry using the gas flow panel as described in Section 2.3.

5.6.1 Quantitative analysis and fitting

Figure 5.15 compares the ammonia conversion percentage for $NaK_2(NH_2)_3$ and a hand-ground mixture of $NaNH_2 + 2KNH_2$ calculated from the MS data shown in Figure 5.16. Data for equivalent masses of pure $NaNH_2$ and KNH_2 have been included for comparison. The plotted points are the recorded experimental results and the line of best fit has been drawn using the two process sigmoidal Gompertz function (Equation 3.4) with the parameters listed in Table 5.4 which were themselves generated using the sigmoid fit calculated in TOPAS (Section 3.5.1). Uncertainties for T_e and E_A are estimated to be on the order of ± 2 °C and ± 3 kJ/mol respectively.

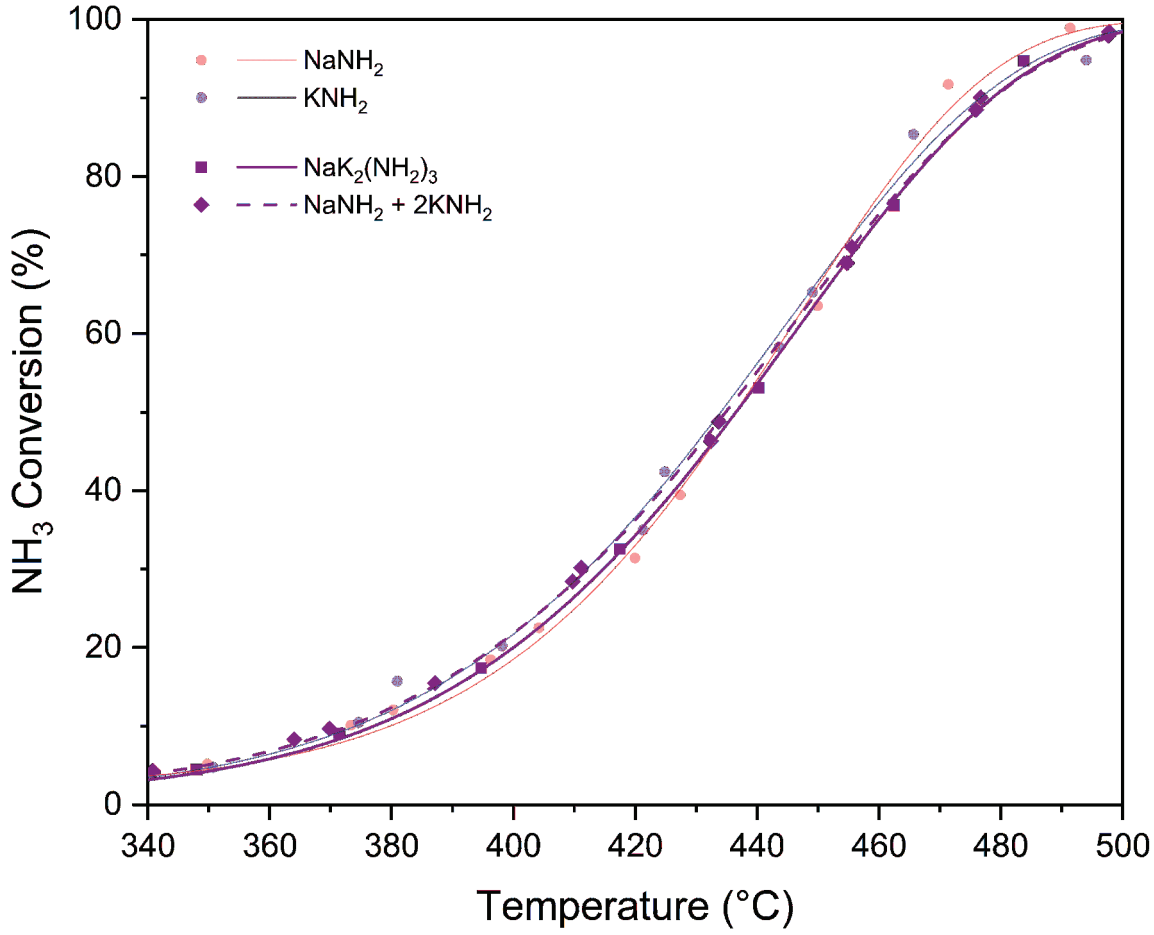


Figure 5.15: NH_3 decomposition sigmoids for the Na-K-N-H system as a potential catalyst on the gas flow panel

As detailed in Section 2.2.4.3 the synthesis of $NaK_2(NH_2)_3$ under NH_3 was confirmed on the gas flow panel so it is unsurprising that the decomposition sigmoids for pre-made $NaK_2(NH_2)_3$ and a mixture of the single-metal amides in the relevant ratios are identical, as the same material will be present in both cases. This is most likely molten $NaNH_2 + 2KNH_2$ as the temperatures required for NH_3 decomposition are high enough to cause the separation of molten $NaK_2(NH_2)_3$.

The similarity in the NH_3 decomposition ability of $NaK_2(NH_2)_3$ with that of $NaNH_2$ or KNH_2 alone is consistent with a relative lack of interaction between the two single metal amides. This is reasonable as $NaNH_2$ and KNH_2 have the same decomposition pathway and is in contrast to the NH_3 decomposition behaviour seen for the lithium containing mixed-metal systems.

	Constant	T_e (°C)	E_A (kJ/mol)	Recovery by mass (%)
Blank	0.000(1)	547	102	n/a
$NaNH_2$	0.021(7)	450	154	6
KNH_2	0.009(2)	449	132	25
$NaK_2(NH_2)_3$	0.009(2)	451	135	18
$NaNH_2$ + 2KNH_2	0.012(6)	450	129	15

Table 5.4: Na-K-N-H system Gompertz curve output values. Uncertainties for T_e and E_A are estimated to be on the order of ± 2 °C and ± 3 kJ/mol respectively and have been calculated from the TOPAS fitting process

Comparing the results for T_e and E_A shown in Table 5.4, it can be seen that KNH_2 and $NaNH_2$ have the same T_e value (449 °C) but $NaNH_2$ has a higher E_A than KNH_2 (154 °C and 132 °C respectively). KNH_2 has a higher vapour pressure than $NaNH_2$ and is known to decompose at a lower temperature than $NaNH_2$ which may explain why potassium amide has faster ammonia decomposition kinetics than sodium amide. As with the Li-Na-N-H and Li-K-N-H systems, these decomposition reactions fit to a single process and there is no obvious change in RDS across the temperature range. They are thought to be successive stoichiometric reactions within the bulk, rather than surface-mediated mechanisms (Section 3.5.1).

$NaK_2(NH_2)_3$ has a T_e value of 451 °C which is slightly higher those that of $LiNa_2(NH_2)_3$ and $LiK_2(NH_2)_3$ (both 440 °C). $NaK_2(NH_2)_3$ also has a higher E_A value of 134 kJ/mol compared to 120 kJ/mol and 105 kJ/mol for $LiNa_2(NH_2)_3$ and $LiK_2(NH_2)_3$ respectively. Whereas $LiNa_2(NH_2)_3/LiNH_2$ + 2$NaNH_2$ and $LiK_2(NH_2)_3/LiNH_2$ + 2KNH_2 both had a lower E_A than $LiNH_2$, $NaNH_2$ or KNH_2 individually, $NaK_2(NH_2)_3$ has an E_A comparable to KNH_2, the more dominant single metal amide in the mixed-metal composite.

It is important to compare the NH_3 decomposition ability of the Na-K-N-H system to the Li-Na-N-H and Li-K-N-H systems because here both single metal amides decompose to their respective metals and there is no imide forming amide present. A comprehensive comparison of these systems is discussed more thoroughly in Section 7.

5.6.2 Catalyst recovery

The results in Table 5.4 show little recoverable sample was present after either decomposition experiment for the Na-K-N-H system. Powder X-ray diffraction data could not be collected to characterise the residue, so decomposition products could not be identified. This would be an important step to help determine the mechanism by which the catalyst decomposes ammonia.

Table 5.4 shows that $NaK_2(NH_2)_3$ has better recovery than $NaNH_2 + 2KNH_2$, again emphasising the potential benefits of mixed-metal amides and there may be some practical value in pre-forming mixed-metal amides, even though there was not a significant improvement in their catalytic activity.

Decomposition of molten $NaK_2(NH_2)_3$ under inert gas has been shown to proceed through the separation and subsequent decomposition of molten $NaNH_2 + 2KNH_2$ to Na and K metals which have previously shown to have suffer from containment issues. This is particularly enhanced in this system where there is no imide forming amide present which may help to stabilise the otherwise volatile metals.

5.7 Decomposition under ammonia

Thermal decomposition was performed under NH_3 during the experiment described in Section 5.6 and the MS trace can be used to ascertain the active form of the catalyst at the temperatures required for NH_3 decomposition. Figure 5.16 shows the outlet gas flow MS traces for the decomposition of $NaK_2(NH_2)_3$ and a hand ground mixture of $NaNH_2 + 2KNH_2$ under ammonia.

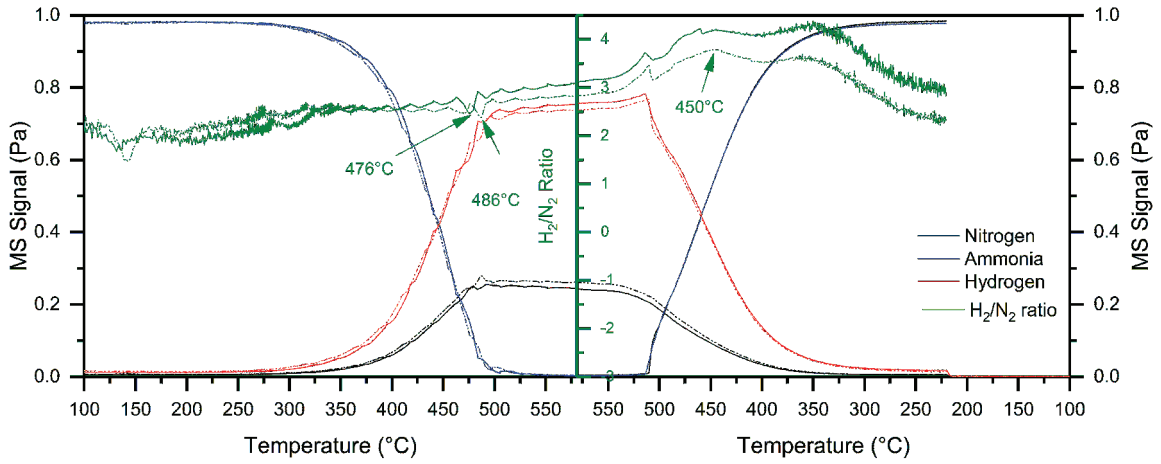


Figure 5.16: Decomposition of $NaK_2(NH_2)_3$ (solid lines) and $NaNH_2 + 2KNH_2$ (dashed lines) on the gas flow panel under ammonia

If molten $NaK_2(NH_2)_3$ separates into $NaNH_2 + 2KNH_2$ which subsequently decompose, H_2 and N_2 would be released in a 2:1 ratio (Equation 3.2 and Equation 4.1). This will affect the overall ratio of H_2 and N_2 observed from the decomposition of NH_3 alone (3:1) and is evident as a suppression in the H_2/N_2 ratio at $\sim$480 °C as relatively less H_2 is produced. This suppression is therefore indicative of the production of Na and/or K metal and the overall decomposition of the "melt phase".

As expected, the decomposition temperatures are higher under NH_3 than under argon, at 476 °C and 486 °C for $NaK_2(NH_2)_3$ and $NaNH_2 + 2KNH_2$ respectively. Whereas, under argon, the peaks in the gas traces of the mass spectrometry data were modelled to two pseudo-Voigt peaks in TOPAS (at 430 °C and 404 °C), under NH_3, the decomposition appears to occur in a single step.

The regions of higher H_2/N_2 ratio on cooling between 500 °C and 400 °C (centred at 450 °C) correspond to extra H_2 (relatively less N_2) due to the reformation of some $NaNH_2$ and/or KNH_2 from Na and/or K. It had been suggested that the faint Bragg peaks that formed at 160 °C on cooling in the *in-situ* decomposition experiment at GEM (Figure 5.12) were due to the re-crystallisation of $NaND_2$.

5.8 Summary

The ball-mill preparation method was used to develop a routine and consistent synthesis route for high purity $NaK_2(NH_2)_3$. Investigation into the phase space between $NaNH_2$ and KNH_2 led to the discovery of an unknown phase within the Na-K-N-H system which is likely to have a composition of "$Na_3K(NH_2)_4$" with an "AB_3O_4" type structure. The STA traces and Raman spectrum collected for each ratio of $NaNH_2$:KNH_2 investigated, supported the presence of the different amide components identified in each of the powder X-ray diffraction data.

Investigation into the low temperature behaviour of $NaK_2(NH_2)_3$ suggests that unlike any of the previously discussed mixed-metal amides, $NaK_2(NH_2)_3$ does not separate on melting and instead forms molten $NaK_2(NH_2)_3$ which is stable to at least 300 °C and will re-crystallise on cooling. Above this temperature this phase separates into an inter-mixed molten phase of $NaNH_2 + 2KNH_2$. This will ultimately decompose releasing H_2 and N_2 to Na and K metals which suffer from poor containment so low catalyst recovery is observed.

$NaK_2(NH_2)_3$ is a poor NH_3 decomposition catalyst compared to the mixed-metal amides of the Li-Na-N-H and Na-K-N-H systems as there is no imide forming component which appears crucial to optimising the NH_3 decomposition ability. A detailed comparison of the NH_3 decomposition ability of the intra Group 1 mixed-metal systems is presented in Chapter 7.

Chapter 6

Group 1 triple mixed-metal amides

Contents

6.1 Chapter overview 293

6.2 Crystallography 294

6.3 Simultaneous Thermal Analysis (STA) 296

6.3.1 6:1:1 mixture of $LiNH_2$:$NaNH_2$:KNH_2 296

6.3.2 1:1:1 and 2:3:4 mixtures of $LiNH_2$:$NaNH_2$:KNH_2 299

6.4 Synthesis 301

6.4.1 6:1:1 mixture of $LiNH_2$:$NaNH_2$:KNH_2 301

6.4.2 1:1:1 and 2:3:4 mixtures of $LiNH_2$:$NaNH_2$:KNH_2 303

6.5 Raman spectra 306

6.6 Summary 307

6.1 Chapter overview

Having analysed mixed-metal amide systems with two different Group 1 cations, the next step is to envisage "triple mixed-metal amide" systems with three different Group 1 cations. This chapter compares such structures to those known for the binary mixed-metal amide systems and discusses the STA and synthesis experiments performed to ascertain if these species could indeed exist.

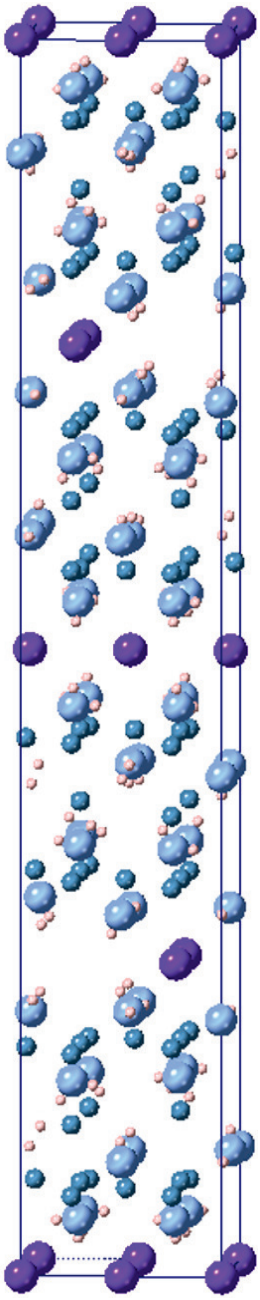
6.2 Crystallography

The known structures of $Li_3Na(NH_2)_4$ and $Li_3K(NH_2)_4$ are based on expanded versions (along the *c* axis) of the $LiNH_2$ unit cell where a quarter of the Li^+ lattice sites have been replaced by Na^+ or K^+ ions via non-stoichiometric amides of general formula $Li_{4-y}R_y(NH_2)_4$ where R=Na/K and $0 < y < 1$. Therefore the structures can be considered as a series of solely lithium-containing blocks (essentially $LiNH_2$) separated by layers of Na^+ or K^+ cations.

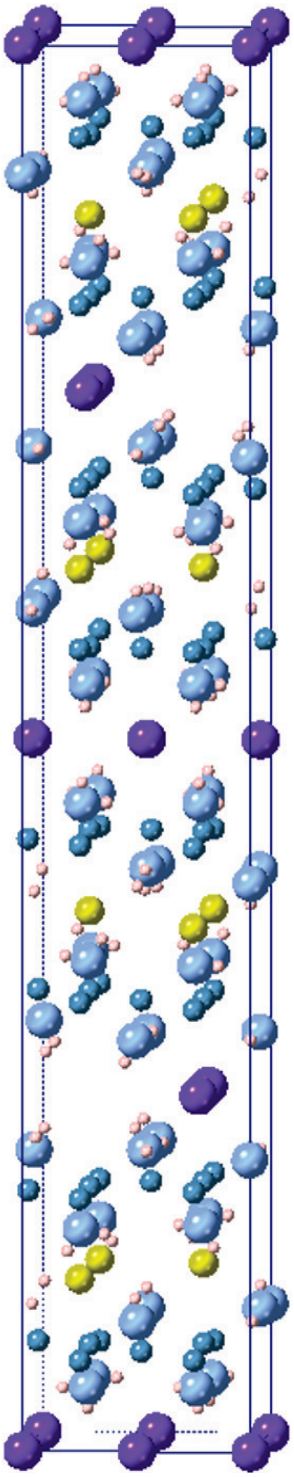
Phases of general formula $Li_nR(NH_2)_{n+1}$ for n = 3–15 (and beyond) with R = Na or K are therefore feasible where the Na^+/K^+ layers are separated by ever larger lithium containing blocks. Indeed, both $Li_5Na(NH_2)_6$ [147] (not successfully synthesised in this work) and $Li_7K(NH_2)_8$ have been reported [148].

A logical extension to this idea would be to try and form a novel triple mixed-metal amide $Li_xNa_yK_z(NH_2)_{(x+y+z)}$ which may have interesting ammonia decomposition properties. Figure 6.1 shows a hypothesised structure for one such material, $Li_6NaK(NH_2)_8$ which is based on the known structure of $Li_7K(NH_2)_8$ where one of the partial filled Li^+ layers has been replaced with Na^+ ions. The Li^+ chosen for this swap were those making up the $\frac{1}{4}$ filled $[Li_3(NH_2)_4]^-$ layers rather than those that are part of the $\frac{3}{4}$ filled $[Li_3(NH_2)_4]^-$ layers in the original $Li_7K(NH_2)_8$ structure, as because the layers are less full, they are more likely to be able to accommodate the larger Na^+ ions.

Approximate unit cell parameters for the hypothesised $Li_6NaK(NH_2)_8$ structure can be estimated by analysis of the $LiNH_2$ and $Li_3Na(NH_2)_4$ structures. On replacement of Li^+ for Na^+, the *c* parameter elongates from 10.23 Å in $LiNH_2$ to 11.48 Å in $Li_3Na(NH_2)_4$ whilst the *a* (and *b*) parameters remain similar at 5.04 Å and 5.07 Å respectively. On forming $Li_6NaK(NH_2)_8$ from $Li_7K(NH_2)_8$ it is therefore likely that the *c* axis will elongate by a similar proportion. Equations A.1 (in the Appendix) therefore lead to estimated unit cell parameters of $c = 47.50$ Å and $a = b = 7.20$ Å.



(a) $Li_7K(NH_2)_8$
$a = b = 7.18\,\text{Å},\ c = 44.39\,\text{Å}$



(b) Hypothesised $Li_6NaK(NH_2)_8$ structure with estimated lattice parameters of
$a = b = 7.20\,\text{Å},\ c = 47.50\,\text{Å}$

Figure 6.1: Crystallographic unit cells for $Li_7K(NH_2)_8$ and a hypothesised $Li_6NaK(NH_2)_8$ structure, roughly proportional in size. Teal = Lithium, Purple = Potassium, Yellow = Sodium, Blue = Nitrogen, Pink = Hydrogen

6.3 Simultaneous Thermal Analysis (STA)

The first step towards discovering if the synthesis of triple mixed-metal amides was possible was running STA experiments of hand-ground mixtures of different ratios of Group 1 metal amides to enable the determination of potential synthesis temperatures.

Three ratios of $LiNH_2$:$NaNH_2$:KNH_2 were investigated:

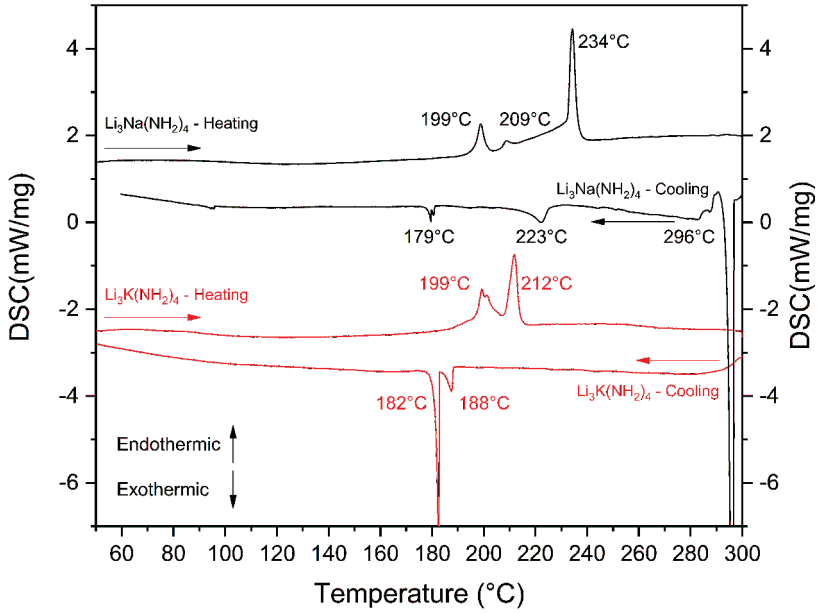
- 6:1:1 – based on $Li_3K(NH_2)_4$ + $Li_3Na(NH_2)_4$
- 1:1:1 - based on $LiNa_2(NH_2)_3$ + $LiK_2(NH_2)_3$
- 2:3:4 – based on $LiNa_2(NH_2)_3$ + $LiK_2(NH_2)_3$ + $NaK_2(NH_2)_3$

The 1:1:1 $LiNH_2$:$NaNH_2$:KNH_2 ratio arises from combining the $LiNa_2(NH_2)_3$ and $LiK_2(NH_2)_3$ known phases and the 2:3:4 ratio comes from adding into this the $NaK_2(NH_2)_3$ structure to test different stoichiometry mixtures within the the 1:2 mixed-metal ratio regime. There are therefore similarities between the results from the 1:1:1 and 2:3:4 experiments so these are discussed together.

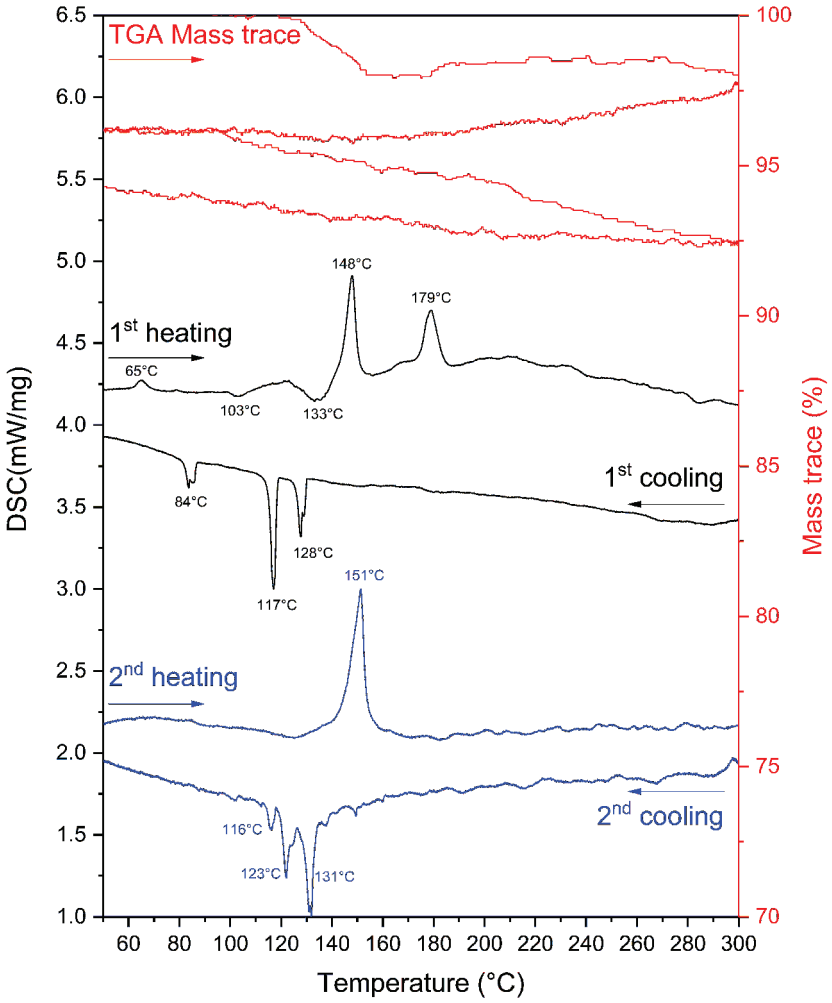
6.3.1 6:1:1 mixture of $LiNH_2$:$NaNH_2$:KNH_2

A hypothetical triple mixed-metal amide $Li_6NaK(NH_2)_8$ could be envisaged based on $Li_3K(NH_2)_4$ + $Li_3Na(NH_2)_4$ which would require a 6:1:1 ratio of $LiNH_2$:$NaNH_2$:KNH_2. The STA trace collected for the 6:1:1 ratio of $LiNH_2$:$NaNH_2$:KNH_2 (Figure 6.2b) is therefore compared to those for $Li_3Na(NH_2)_4$ and $Li_3K(NH_2)_4$ (Figure 6.2a).

Figure 6.2b shows the STA trace when 3 mg of a 6:1:1 mixture of hand-ground $LiNH_2$:$NaNH_2$:KNH_2 was heated to 300 °C and cooled to room temperature twice. Two sequential heating cycles were used to determine if in the first cycle a triple mixed-metal amide formed and then if this phase behaved differently when itself was heated the second time. This is indeed the case as it can be seen that in the first cycle (black) there are two endothermic events on heating at 148 °C and 179 °C, whereas in the second cycle (blue) there is only one at 151 °C.



(a) Comparison of the STA traces of $Li_3Na(NH_2)_4$ (black) and $Li_3K(NH_2)_4$ (red)



(b) Two sequential heating cycles for an STA of a 6:1:1 mixture of hand-ground $LiNH_2$:$NaNH_2$:KNH_2

Figure 6.2: STA traces

The peaks at 55 °C and 65 °C seen in the first heating cycle correspond to the monoclinic to tetragonal to cubic phase transitions for KNH_2. However, they are absent in the second heating cycle indicating that a mixed-metal amide must have formed.

Comparing these DSC traces to Figure 6.2a, it can be seen that when all three single metal amides are present, it is not the case that $Li_3Na(NH_2)_4$ or $Li_3K(NH_2)_4$ form, as none of the thermal events observed in Figure 6.2a are present in Figure 6.2b.

The synthesis of $Li_3Na(NH_2)_4$ and $Li_3K(NH_2)_4$ were both exothermic events due to the relatively low energy synthesis derived from opening the layers of the $LiNH_2$ structure and inserting Na^+ or K^+ ions. It is therefore likely that a hypothetical triple mixed-metal amide also based on this layered structure (Figure 6.1) would also be formed in an exothermic synthesis. Either of the exothermic events in Figure 6.2b, at 103 °C or 133 °C, could correspond to the synthesis of a hypothetical triple mixed-metal amide. $Li_3Na(NH_2)_4$ and $Li_3K(NH_2)_4$ were synthesised at 185 °C and 161 °C respectively so it is more likely that the exothermic peak at 133 °C in the initial heating cycle corresponds to the synthesis of the triple mixed-metal amide. The slight suppression at this temperature in the second heating cycle will then correspond to annealing of the sample where any unreacted starting material is being used to synthesise additional triple mixed-metal amide.

There are endothermic peaks visible in the first (black) and second (blue) heating cycles at 148 °C and 151 °C respectively which possibly correspond to the synthesised triple mixed-metal amide phase melting. Analogous to the distinct separation and melt temperatures seen for $Li_3Na(NH_2)_4$ and $Li_3K(NH_2)_4$, the two endothermic events at 148 °C and 179 °C in the first cycle (black) could correspond to these two distinct steps. However, the exothermic peaks at $\sim$120 °C on cooling in the initial cycle (black) are likely to correspond to recrystallisation of the mixed-metal amide in which case separation could not occur on melting. The replicability of the endothermic melting peak at $\sim$150 °C on heating and the exothermic recrystallisation peaks at $\sim$120 °C on cooling in the second heating cycle (blue) suggest that the triple mixed-metal amide formed is not decomposing below 300 °C. This is supported by the mass trace in Figure 6.2b which shows there is not a significant mass loss from any decomposition induced gas release.

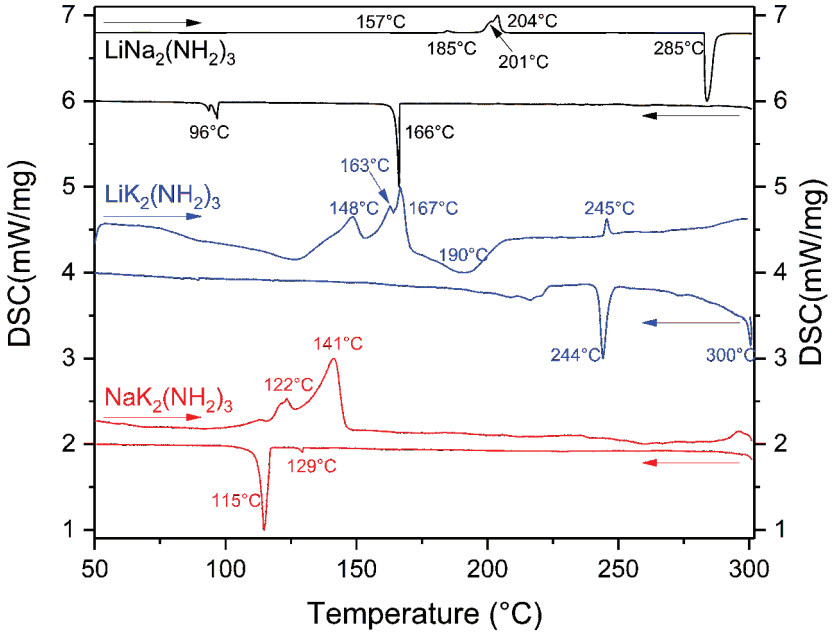
6.3.2 1:1:1 and 2:3:4 mixtures of $LiNH_2$:$NaNH_2$:KNH_2

Other hypothetical triple mixed-metal amide could be envisaged based on combinations of $LiNa_2(NH_2)_3$ + $LiK_2(NH_2)_3$ or $LiNa_2(NH_2)_3$ + $LiK_2(NH_2)_3$ + $NaK_2(NH_2)_3$ which would require a 1:1:1 or 2:3:4 ratio of $LiNH_2$:$NaNH_2$:KNH_2 respectively. The STA traces collected for these two ratios (Figure 6.3b) were therefore compared to those for $LiNa_2(NH_2)_3$, $LiK_2(NH_2)_3$ and $NaK_2(NH_2)_3$ (Figure 6.3a). Qualitatively it can be seen that there are quite significant differences between the thermal behaviour seen in Figure 6.3a and Figure 6.3b which is indicative of the potential formation of a triple mixed-metal phase.

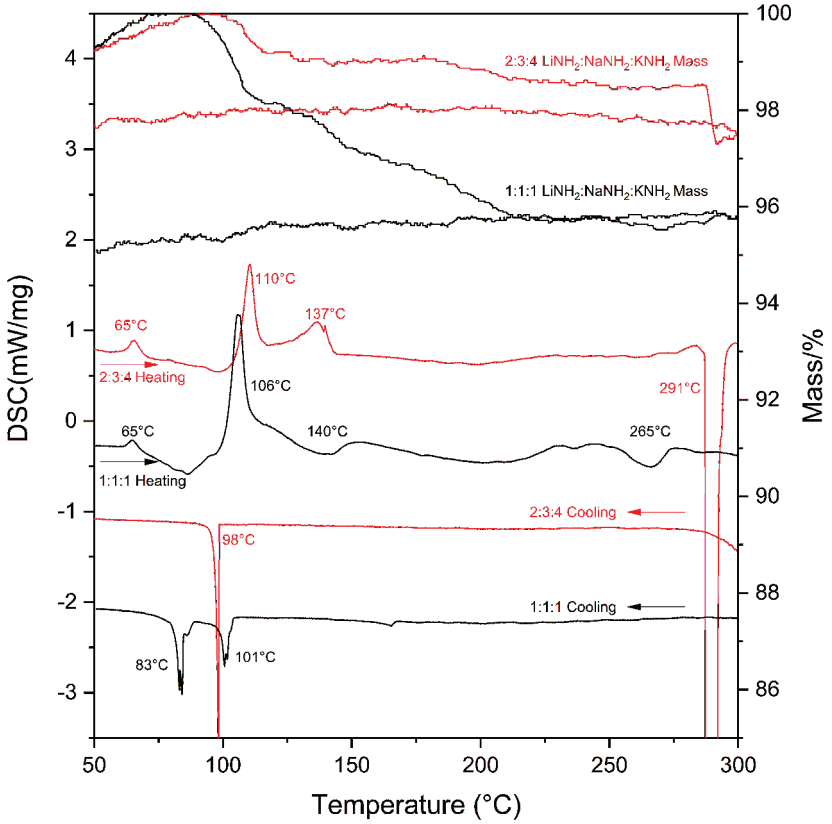
Figure 6.3b shows that the STA traces for the 2:3:4 and 1:1:1 mixtures of hand-ground $LiNH_2$:$NaNH_2$:KNH_2 are very similar. Small exothermic suppressions can be seen in both the 2:3:4 and 1:1:1 traces at $\sim$80°C which may correspond to the synthesis of a triple mixed-metal amide. The endothermic events at 106 °C and 110 °C on heating are associated with a very small mass loss (1-2%) and possibly relate to the separation/melt of the triple mixed-metal amide. The 2:3:4 ratio trace has an additional endotherm at 137 °C which correlates well with the temperature seen for the full sample melt for $NaK_2(NH_2)_3$ of 141 °C in Figure 6.3a. This suggests that some $NaK_2(NH_2)_3$ is synthesised in addition to any triple mixed-metal amide and this has been confirmed by powder X-ray diffraction (Figure 6.5b). The large exotherm seen in the 2:3:4 trace at 291 °C correlates with the exotherm at 291 °C seen for $LiNa_2(NH_2)_3$ in Figure 6.3a which had been attributed to the onset of decomposition. Powder X-ray diffraction has shown $LiNa_2(NH_2)_3$ and $NaK_2(NH_2)_3$ are present after heating both the 2:3:4 and 1:1:1 samples (Figure 6.5).

The exothermic peaks at 99,°C and 101,°C on cooling for the 2:3:4 and 1:1:1 ratios respectively may correspond to the recrystallisation of the triple mixed-metal amide.

Whereas $LiNa_2(NH_2)_3$ and $NaK_2(NH_2)_3$ have similar shaped DSC traces, that of $LiK_2(NH_2)_3$ has added features at 245 °C. This may be because whereas the Li-Na-N-H and Na-K-N-H systems are known to have two mixed-metal amides ($LiNa_2(NH_2)_3$/$Li_3Na(NH_2)_4$ and $NaK_2(NH_2)_3$/unknown), the Li-K-N-H system has three mixed-metal amides; $Li_3K(NH_2)_4$, $LiK_2(NH_2)_3$ and the unknown phase. Therefore there is a greater propensity for phase changes between the greater number of components.



(a) STA traces for $LiNa_2(NH_2)_3$ (black), $LiK_2(NH_2)_3$ (blue) and $NaK_2(NH_2)_3$ (red)



(b) STA traces for 2:3:4 (red) and 1:1:1 (black) mixtures of hand-ground $LiNH_2$:$NaNH_2$:KNH_2

Figure 6.3: STA traces

6.4 Synthesis

As a result of the analysis of the STA traces in Figure 6.2b and Figure 6.3b, synthesis attempts for triple mixed-metal amides were performed in the tube furnace and powder X-ray diffraction data was collected of the products.

6.4.1 6:1:1 mixture of $LiNH_2$:$NaNH_2$:KNH_2

0.5 g of a hand-ground mixture of 6:1:1 $LiNH_2$:$NaNH_2$:KNH_2 was heated to 210 °C for 12 hours in the tube furnace. The powder X-ray diffraction data shown for the resulting sample in Figure 6.4 was initially fitted to $Li_7K(NH_2)_8$. This is noteworthy considering the inability to synthesise $Li_7K(NH_2)_8$ from $7LiNH_2 + KNH_2$ using a variety of methods as described in Section 4.2.3. This suggests that the low melting point of $NaNH_2$ (210 °C) creates the molten environment needed for such a structure to form. However, as predicted by the equations shown in Section A.1 in the Appendix, when $Li_7K(NH_2)_8$ is fitted to the data, significant expansion along the c axis is observed.

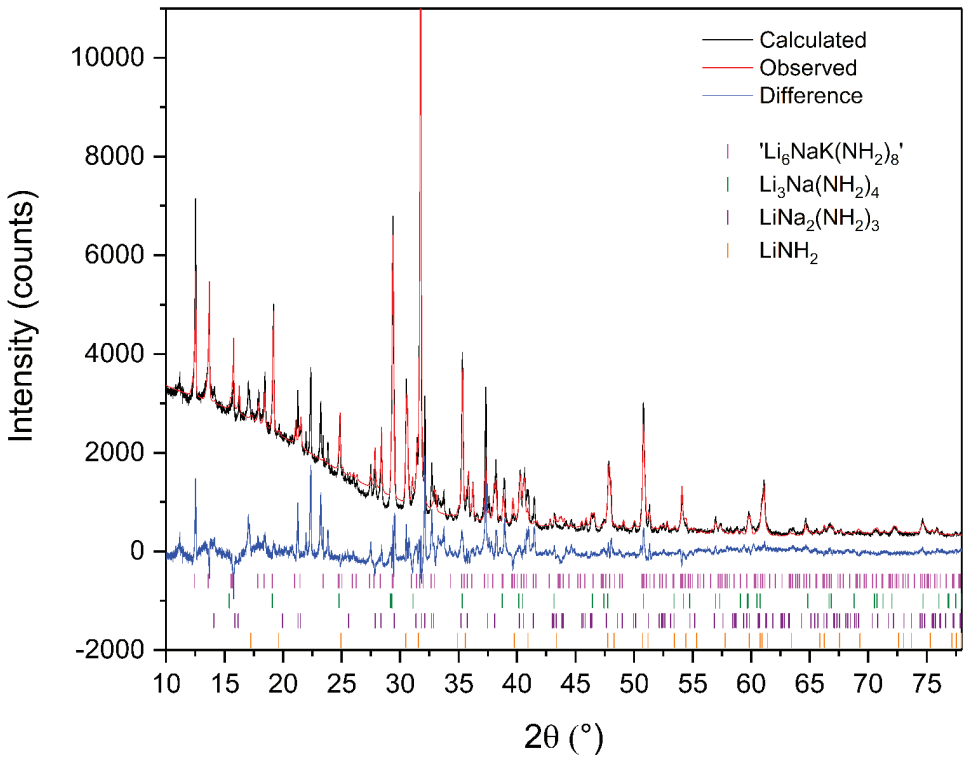


Figure 6.4: Powder X-ray diffraction data collected for a sample of 6:1:1 $LiNH_2$:$NaNH_2$:KNH_2 heated to 210 °C in the tube furnace for 12 hours

Therefore this X-ray diffraction data can be more accurately fitted to the CIF for the $Li_6NaK(NH_2)_8$ structure shown in Figure 6.1b, where one of the Li^+ has been substituted by a larger Na^+ cation. A fit to this structure is confirmed by the 2 low angle peaks at 2θ values of 12.38 ° (101) (d-spacing of 7.11 Å) and 13.54 ° (103) (d-spacing of 6.51 Å). A parameter has been included to allow for possible split stoichiometry at the new Na^+ cation site as there may be stacking defects. The best fit to the data gives a value of 0.51(2) for the occupancy of this position. The powder X-ray diffraction data in Figure 6.4 therefore fits to 55.7 % $Li_6NaK(NH_2)_8$, 21.1 % $Li_3K(NH_2)_4$, 11.8 % $LiNa_2(NH_2)_3$ and 11.4 % $LiNH_2$.

Compared to the published structure for $Li_7K(NH_2)_8$, the a (and b) axes of the novel $Li_6NaK(NH_2)_8$ phase fitted in Figure 6.4 have increased from 7.18 Å to 7.21 Å (as predicted). The c axis was observed to expand significantly from 44.39 Å (in $Li_7K(NH_2)_8$) to 47.39 Å, which is consistent with the c parameter of 47.50 Å (Section 6.2 and Section A.1 in the Appendix) estimated for a hypothetical $Li_6NaK(NH_2)_8$ structure. This increase confirms the formation of a triple mixed-metal amide through sodium substitution or insertion at some of the vacant sites and indicates a degree of non-stoichiometry. There are still some peaks which remain unfitted in Figure 6.4 which may mean $Li_6NaK(NH_2)_8$ crystallises in a slightly different space group to $Li_7K(NH_2)_8$, although they clearly have very similar structures.

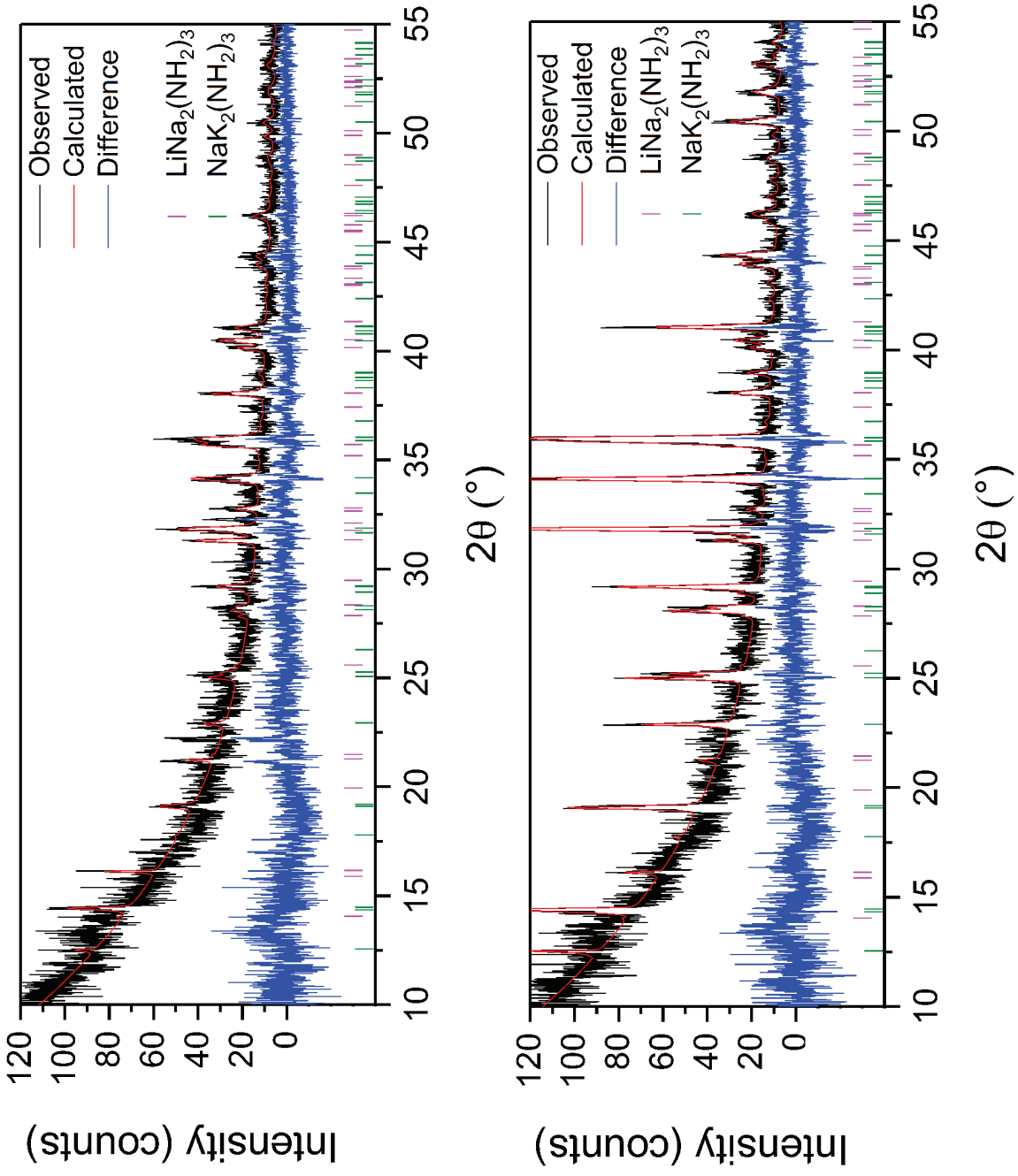
A synthesis reaction for $Li_7K(NH_2)_8$ was subsequently attempted on the gas flow panel, with 7:1 $LiNH_2$:KNH_2 heated to 390 °C for 12 hours under NH_3 to try and replicate the molten conditions provided by $NaNH_2$. Although this temperature could have been reached on the tube furnace, an NH_3 atmosphere was required to ensure $LiNH_2$ melted at high temperature rather than decomposing to the imide and this is only possible on the gas flow panel. However no $Li_7K(NH_2)_8$ was synthesised and the composition of the product obtained was almost identical to that formed from the tube furnace reactions as shown in Figure A.5 (in the Appendix) of 55.0 % $Li_3K(NH_2)_4$ and $\sim$45.0 % $LiNH_2$.

6.4.2 1:1:1 and 2:3:4 mixtures of $LiNH_2$:$NaNH_2$:KNH_2

A hand-ground mixture of 1:1:1 $LiNH_2$:$NaNH_2$:KNH_2 was heated to 220 °C in the tube furnace and powder X-ray diffraction data was collected for the product (Figure 6.5a). This fitted to 49.9 % $LiNa_2(NH_2)_3$ and 50.1 % $NaK_2(NH_2)_3$ with a small number of unfitted peaks.

A hand-ground mixture of 2:3:4 $LiNH_2$:$NaNH_2$:KNH_2 was heated to 230 °C in the tube furnace and a powder X-ray diffraction taken of the product (Figure 6.5b). This fits to $LiNa_2(NH_2)_3$ (19.3 %) and $NaK_2(NH_2)_3$ (80.7 %) with a few peaks unaccounted for.

Considered together, the powder X-ray diffraction data collected from the products formed from the 1:1:1 and 2:3:4 ratios are very similar and peaks fit to a mixture of $LiNa_2(NH_2)_3$ and $NaK_2(NH_2)_3$. Interestingly no peaks corresponding to $LiK_2(NH_2)_3$ were observed in either pattern. This is perhaps unsurprising given the synthesis of $LiK_2(NH_2)_3$ was much more challenging than that of $LiNa_2(NH_2)_3$ or $NaK_2(NH_2)_3$. It is therefore unlikely that $LiK_2(NH_2)_3$ will form if two more stable compounds can form instead. There are still unfitted peaks in both patterns, which may be due to the formation of a novel triple-mixed amide that has similarities to the structures of $LiNa_2(NH_2)_3$ and $NaK_2(NH_2)_3$.



(a) A sample of 1:1:1 $LiNH_2$:$NaNH_2$:KNH_2 heated to 220 °C

(b) A sample of 2:3:4 $LiNH_2$:$NaNH_2$:KNH_2 heated to 230 °C

Figure 6.5: Powder X-ray diffraction data for samples of 1:1:1 and 2:3:4 $LiNH_2$:$NaNH_2$:KNH_2 heated to 220 °C and 230 °C respectively in the tube furnace for 12 hours

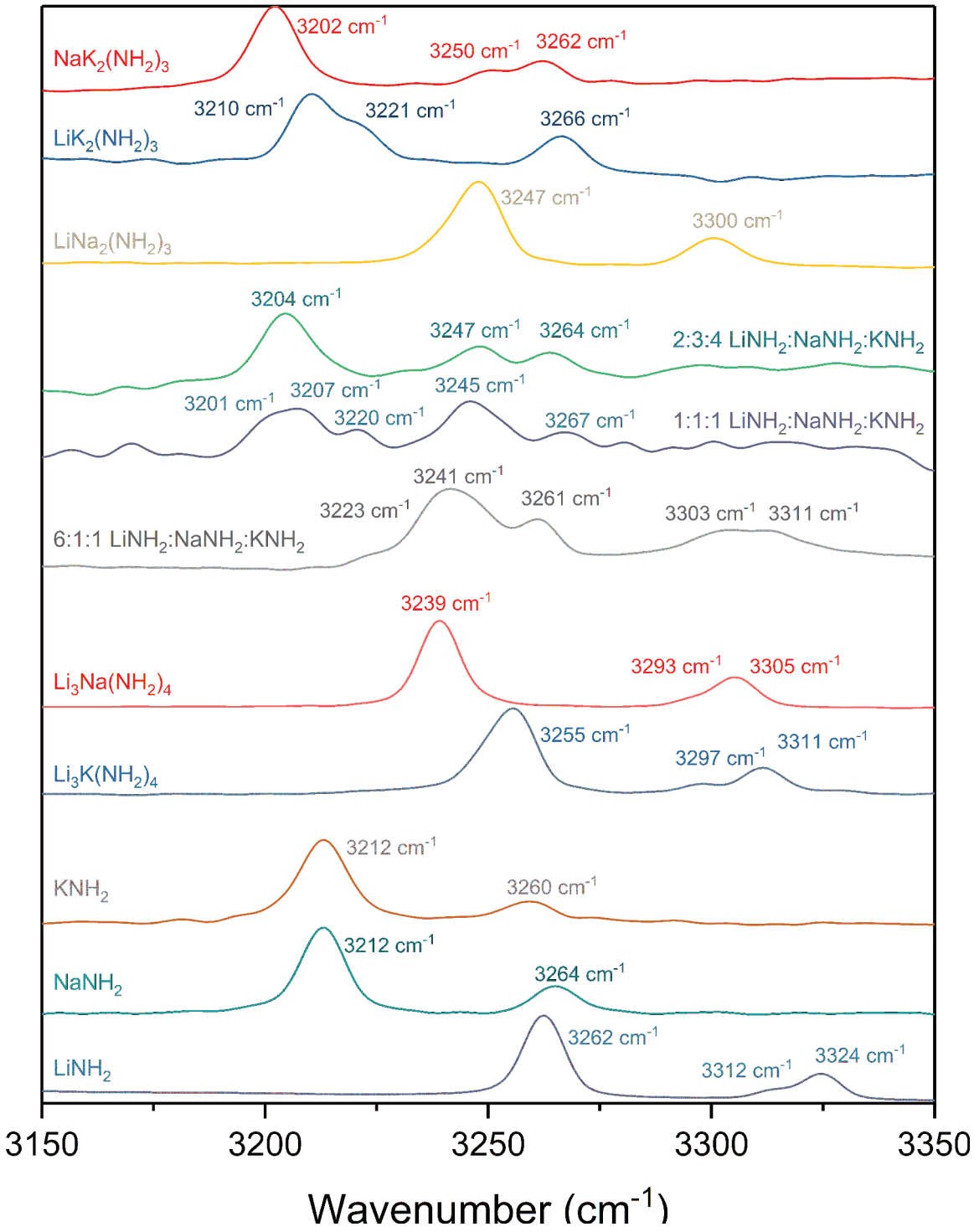


Figure 6.6: Raman stretches for all Group 1 mixed and single metal amides

6.5 Raman spectra

The Raman spectra of all the known mixed-metal amide phases for intra Group 1 systems as-well as those for the triple mixed-metal amide attempts were collected as outlined in Section 2.5.1 and are presented in Figure 6.6.

It can be clearly seen that $Li_3Na(NH_2)_4$ and $Li_3K(NH_2)_4$ have similar stretches to $LiNH_2$ which is expected as their structures are based on expanded versions of $LiNH_2$. All three spectra have the same shape with a shoulder in the asymmetric stretch. There is a greater shift in wavenumber for both the symmetric and asymmetric stretches of $Li_3Na(NH_2)_4$ compared to $Li_3K(NH_2)_4$ away from those of $LiNH_2$ due to the differences in the Pauling electronegativity for K (0.82), Na (0.93) and Li (0.98).

$LiNa_2(NH_2)_3$, $LiK_2(NH_2)_3$ and $NaK_2(NH_2)_3$ have the same structure but very different Raman spectra. Whereas $LiNa_2(NH_2)_3$ shows just one peak for both the asymmetric and symmetric amide stretches, $LiK_2(NH_2)_3$ has a shoulder in the symmetric stretch and $NaK_2(NH_2)_3$ has a shoulder in the asymmetric stretch. It would be expected that the mixed-metal systems would have amide stretches with energies between those of the parent compounds, however it can be seen that the asymmetric stretches of both $NaK_2(NH_2)_3$ and $LiK_2(NH_2)_3$ are at a lower wavenumber than those of $NaNH_2$ or KNH_2.

Peaks corresponding to the single metal amides $LiNH_2$, $NaNH_2$ and KNH_2 do not appear to be present in the Raman patterns for any of the triple mixed-metal amide ratios, which suggests mixed-metal amides of some description have formed.

The patterns collected for the 1:1:1 and 2:3:4 ratios are harder to interpret due to noise but the larger peaks can still be distinguished and occur at similar wavenumbers. This is consistent with their similar powder X-ray diffraction data (Figure 6.5) which fitted to $LiNa_2(NH_2)_3$ and $NaK_2(NH_2)_3$ and possibly a triple mixed-metal amide. The Raman spectra for the 1:1:1 and 2:3:4 ratios could correspond to the superposition of the Raman spectra observed for $LiNa_2(NH_2)_3$ and $NaK_2(NH_2)_3$ independently,

The sample containing a 6:1:1 ratio of $LiNH_2$:$NaNH_2$:KNH_2 has been predicted to contain "$Li_6NaK(NH_2)_8$". The local environment of the amide ions in this triple mixed-metal amide are likely to be similar to those in $Li_3Na(NH_2)_4$ and $Li_3K(NH_2)_4$ and the Raman

pattern for the 6:1:1 ratio does appear to be a linear combination of $Li_3Na(NH_2)_4$ and $Li_3K(NH_2)_4$. No $Li_3K(NH_2)_4$ was observed in the powder X-ray diffraction data for the 6:1:1 sample in Figure 6.4 so the presence of Raman stretches at similar wavenumbers to those in $Li_3K(NH_2)_4$ supports the formation of a triple mixed-metal amide with regions of local "$Li_3K(NH_2)_4$" type coordination.

6.6 Summary

The data collected is consistent with the synthesis of a novel triple mixed-metal amide with a composition of $Li_6NaK(NH_2)_8$, and a structure very similar to that shown in Figure 6.1b. This is supported by the successful fitting of this "$Li_6NaK(NH_2)_8$" structure (based on an expanded version of $LiNH_2$) to X-ray powder diffraction data (Figure 6.4) collected for a heated sample of $LiNH_2$:$NaNH_2$:KNH_2 in a 6:1:1 ratio. This structure shows unit cell expansion along the c axis compared to $Li_7K(NH_2)_8$ due to substitution of larger Na^+ cations for some of the Li^+ ions. The Raman spectra collected for this sample also suggests this structure has local symmetry similar to that of $Li_3Na(NH_2)_4$ and $Li_3K(NH_2)_4$ (Figure 6.6) but the STA data for the 6:1:1 ratio is clearly different to that of $Li_3Na(NH_2)_4$ or $Li_3K(NH_2)_4$ independently (Figure 6.2). Future work would include isolating and crystallographically characterising this "$Li_6NaK(NH_2)_8$" structure before investigating its potential as an NH_3 decomposition catalyst.

2:3:4 and 1:1:1 ratios of $LiNH_2$:$NaNH_2$:KNH_2 produce similar STA, powder X-ray diffraction and Raman patterns to each other. Whilst these appear to have features which could correspond to $LiNa_2(NH_2)_3$ and $NaK_2(NH_2)_3$ it is also possible that a novel triple mixed-metal amide has formed with a structure that incorporates the local features of $LiNa_2(NH_2)_3$ and $NaK_2(NH_2)_3$ and also crystallises in the $P4_2/m$ space group.

Chapter 7

NH_3 decomposition summary for Group 1 mixed-metal amides

Contents

7.1 Chapter overview 308

7.2 Analysis 309

7.3 Future work 317

7.4 Conclusions 318

7.1 Chapter overview

This chapter provides an overview of the NH_3 decomposition behaviour of all the intra Group 1 mixed-metal systems discussed so far. Combining the analysis already discussed for the Li-Na-N-H (Chapter 5), Li-K-N-H (Chapter 4) and Na-K-N-H systems (Chapter 3) independently means that important over-arching conclusions can be drawn.

It is clear that qualitatively, mixed-metal amide systems out-perform single metal amides at low temperatures, and $Li_3Na(NH_2)_4$ and $Li_3K(NH_2)_4$ also do at high temperatures. This provides evidence that there is added value of the mixed-metal amides as NH_3 decomposition catalysts compared to single metal amides. There is very little difference between the NH_3 decomposition performance of the pre-formed mixed-metal amides and the ground-up mixtures of their constituent single metal amides in the relevant ratios. This close correlation suggests that, at the temperatures required for NH_3 decomposition, the same material is present, most likely as a combination of constituent starting amides in an inter-mixed molten phase. It is the differences in the subsequent decomposition of $LiNH_2$, $NaNH_2$ and KNH_2 from this molten phase and the ratios to which they are present, that appears most important in determining the NH_3 decomposition ability of the mixed-metal amide.

7.2 Analysis

Lithium amide shows NH_3 mediated thermal decomposition to lithium imide:

$$LiNH_2(l) \longrightarrow Li_2NH(s) + NH_3(g) \tag{7.1a}$$

$$x LiNH_2(s) + Li_2NH(s) \longrightarrow 2\,Li_{2-x}NH_{1+x}(s) \tag{7.1b}$$

Whereas sodium amide and potassium amide decompose to the respective metals:

$$RNH_2(l) \longrightarrow R(l) + \frac{1}{2}N_2(g) + H_2 \qquad \text{(R=Na or K)} \tag{7.2a}$$

$$R(s) + NH_3(l) \longrightarrow RNH_2(s) + \frac{1}{2}H_2(g) \tag{7.2b}$$

The mixed-metal amides for which NH_3 decomposition sigmoids are shown in Figure 7.1 and Figure 7.2 therefore fall into three categories:

1. $Li_3Na(NH_2)_4$ and $Li_3K(NH_2)_4$ with a 3:1 ratio of imide (Li_2NH) to metal (Na or K) under NH_3 decomposition conditions (Figure 7.1). These materials show particularly good high temperature conversion and have the steepest slopes, indicative of a higher activation energy for NH_3 decomposition.

2. $LiNa_2(NH_2)_3$ and $LiK_2(NH_2)_3$ (Figure 10.2a) which show the best low temperature conversion (even better than ruthenium shown in Figure 1.16). There is still both an imide and a metal component present at the point of NH_3 decomposition but these are now present in a 1:2 not a 3:1 ratio of Li_2NH:R (R=Na or K).

3. $NaK_2(NH_2)_3$ (Figure 10.2b) is unique because both $NaNH_2$ and KNH_2 decompose to the respective metals under NH_3 decomposition conditions so there is no imide component present. This emphasises the importance of stable imides for good NH_3 decomposition catalysts.

This demonstrates the effect of mixing Group 1 amides which have different decomposition pathways under NH_3 and shows that two factors govern the NH_3 decomposition ability of a catalyst:

1. Active form of the original amides catalytic surface under NH_3 decomposition conditions (imide or metal)

2. Stoichiometry ratio of the constituent amides

The initial crystal structure of the mixed-metal amide does not affect the NH_3 decomposition ability of the catalyst as these have separated and melted into the constituent metal amides. These have subsequently decomposed into the imide or metal (the active forms of the catalyst) below the temperatures required for NH_3 decomposition.

Figure 7.1 and Figure 7.2 show the NH_3 decomposition performance of all the mixed-metal amide catalysts discussed so far.

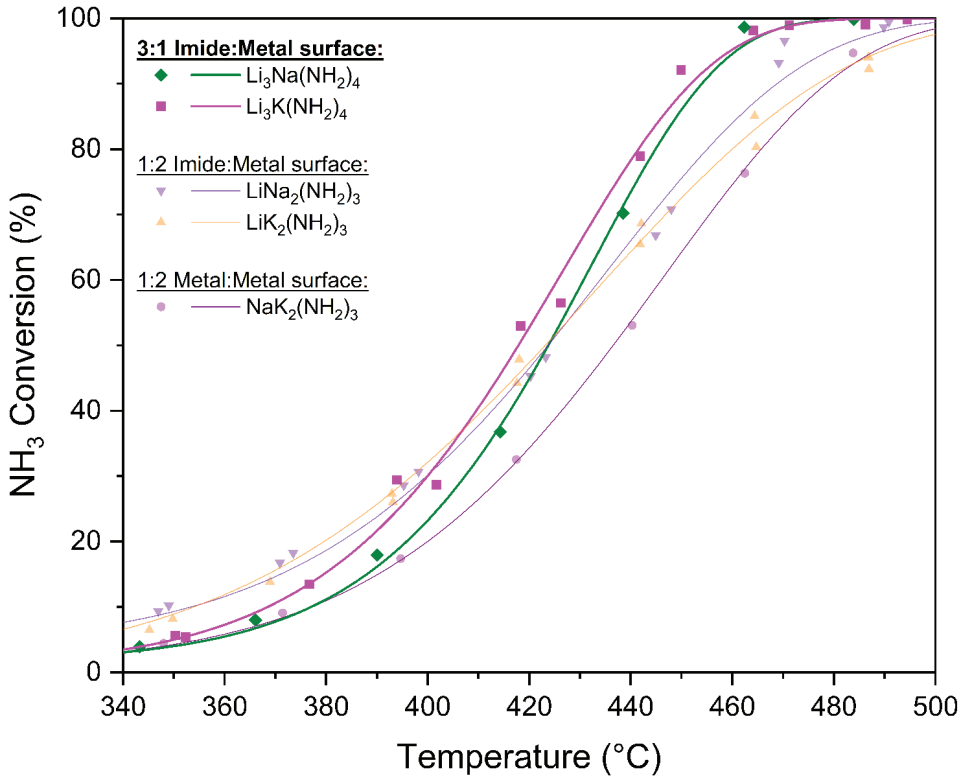
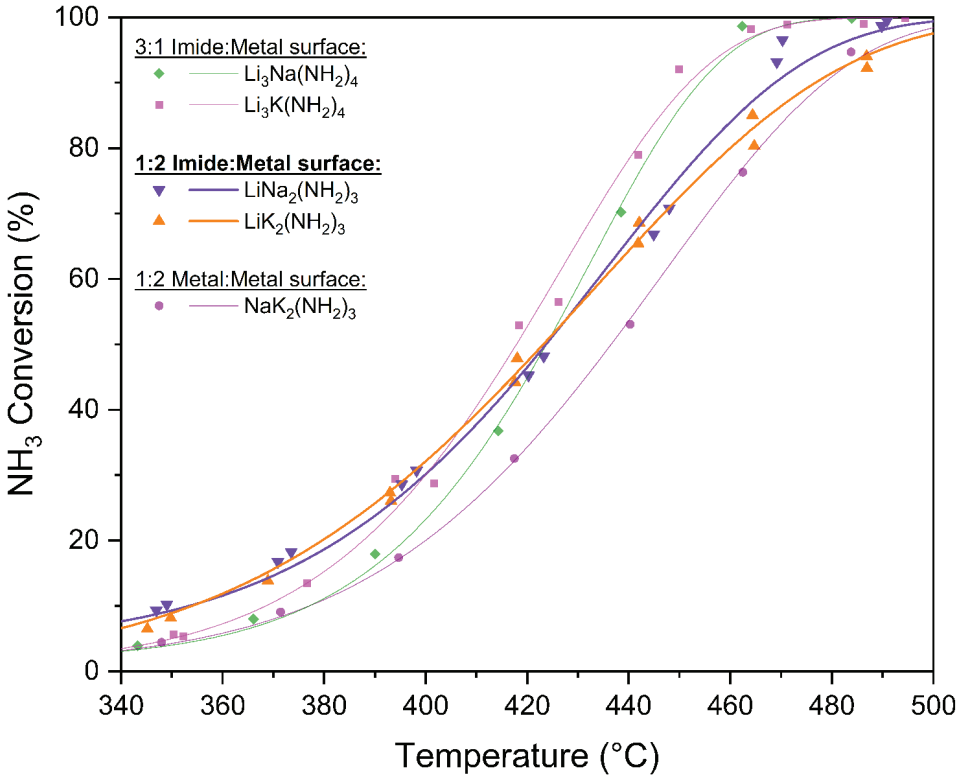
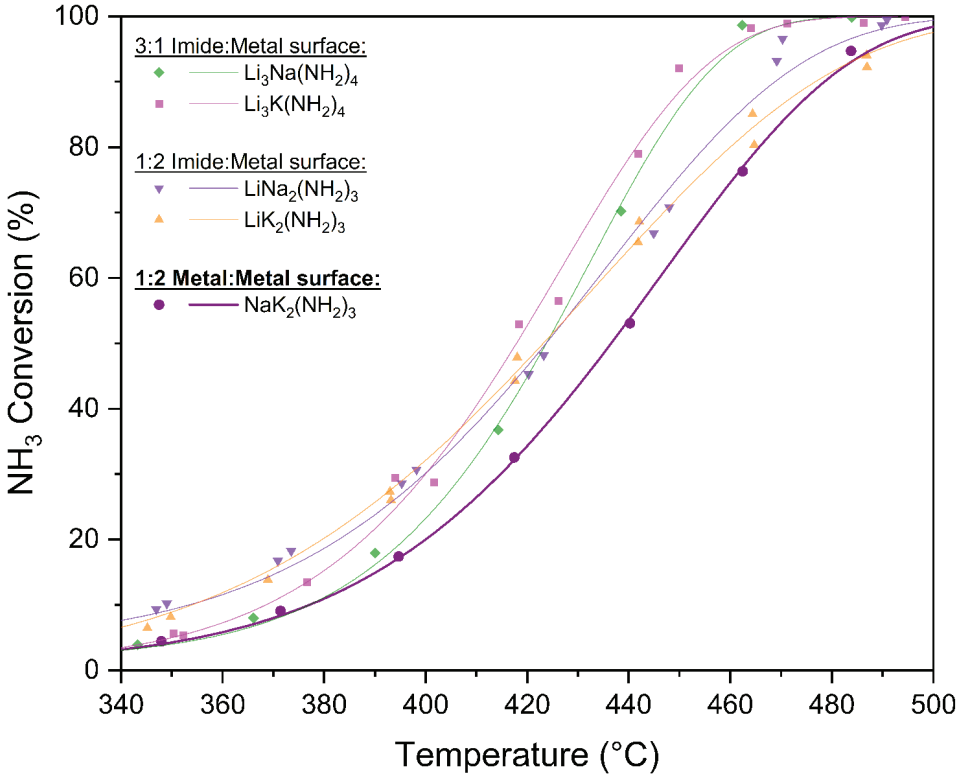


Figure 7.1: Ammonia decomposition ability of catalysts with a 3:1 imide:metal surface on decomposition



(a) Catalysts with a 1:2 imide:metal surface on decomposition



(b) Catalysts with a 1:2 metal:metal surface on decomposition

Figure 7.2: Ammonia decomposition ability of catalysts with a 1:2 amide component ratio

Quantitative analysis from fitting by a least-squares procedure to the two process sigmoidal function known as the Gompertz curve (Equation 3.4 in Section 3.5.1) gives rise to the values of E_A, Constant and T_e detailed in Table 7.1. Uncertainties for T_e and E_A are estimated to be on the order of $\pm 2\,°C$ and $\pm 3\,kJ/mol$ respectively.

	Constant	**T_e (°C)**	**E_A (kJ/mol)**	**Recovery by mass (%)**
Blank	0.000(1)	547	102	n/a
$LiNH_2$	0.000(5)	439	184	88
$NaNH_2$	0.021(7)	450	154	6
KNH_2	0.009(2)	449	132	25
$Li_3Na(NH_2)_4$	0.015(6)	434	177	73
$3LiNH_2 + NaNH_2$	0.017(8)	431	180	65
$LiNa_2(NH_2)_3$	0.039(2)	440	123	56
$LiNH_2 + 2NaNH_2$	0.019(4)	439	116	48
$Li_3K(NH_2)_4$	0.007(3)	429	153	85
$3LiNH_2 + KNH_2$	0.002(8)	435	150	80
$LiK_2(NH_2)_3$	0.000(2)	440	101	74
$LiNH_2 + 2KNH_2$	0.000(4)	436	112	68
$NaK_2(NH_2)_3$	0.009(2)	451	135	18
$NaNH_2 + 2KNH_2$	0.012(6)	450	129	15

Table 7.1: Gompertz curve output values. Uncertainties for T_e and E_A are estimated to be on the order of $\pm 2\,°C$ and $\pm 3\,kJ/mol$ respectively and have been calculated from the TOPAS fitting process

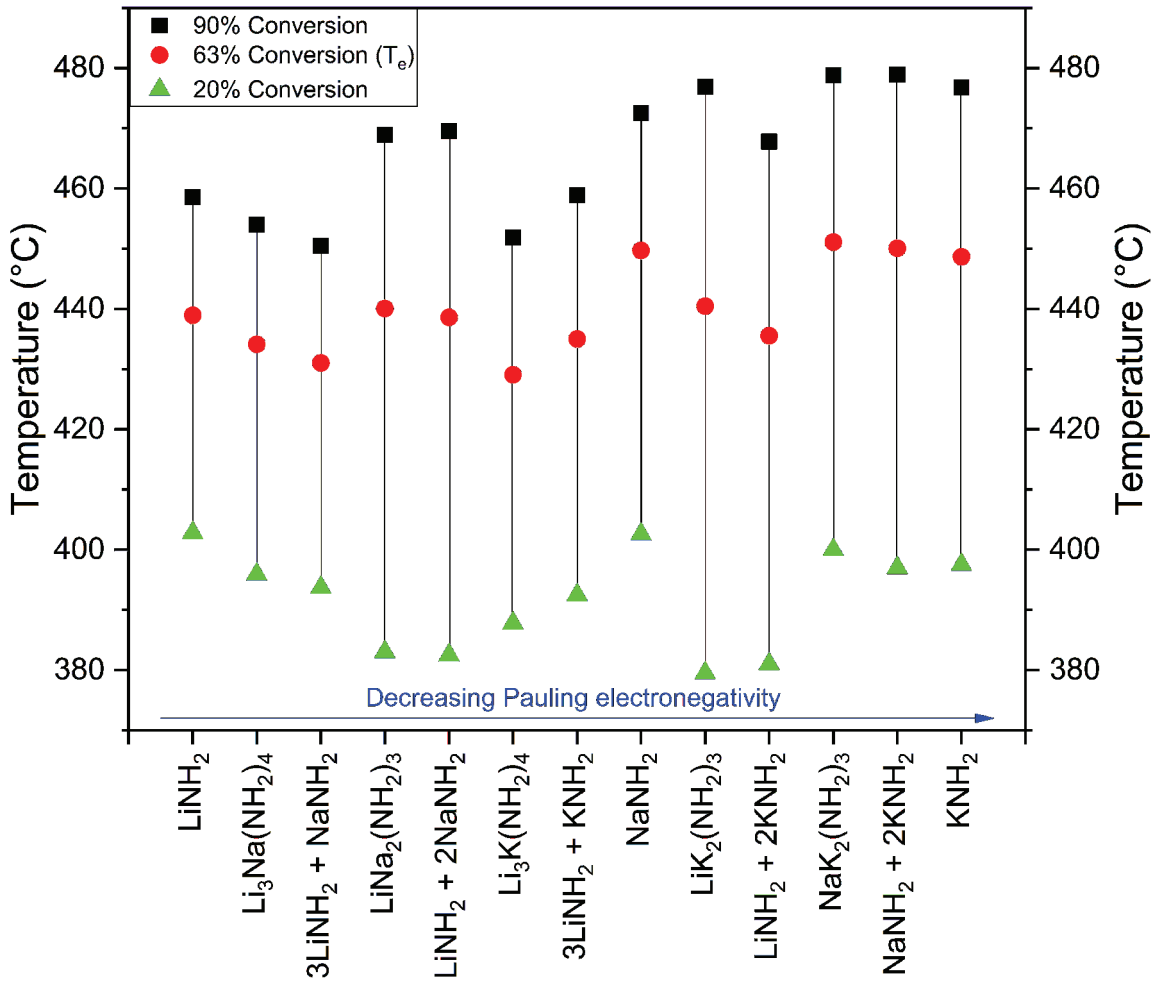


Figure 7.3: Plot to show the temperature at which each single metal/mixed-metal/composite leads to 90 %, 63 % (T_e), and 20 % conversion of NH_3 into $\frac{1}{2}N_2$ and $\frac{3}{2}H_2$

T_e is the temperature at which $\sim$63 % of NH_3 has been decomposed and can be a useful number for comparing the activity of different catalysts as it indicates where the sigmoid is increasing most rapidly. Figure 7.3 plots the temperature at which each catalyst causes 90 %, 63 % (T_e), and 20 % conversion of NH_3 into $\frac{1}{2}N_2$ and $\frac{3}{2}H_2$. The catalysts are arranged in order of decreasing average Pauling electronegativity from left to right. The value of T_e reported in Table 7.1 is very specific and is based on the assumption that the Gompertz equation (Equation 3.4) is exactly the right model to use whereas the ranges shown in Figure 7.3 are more indicative of the behaviour of each catalyst.

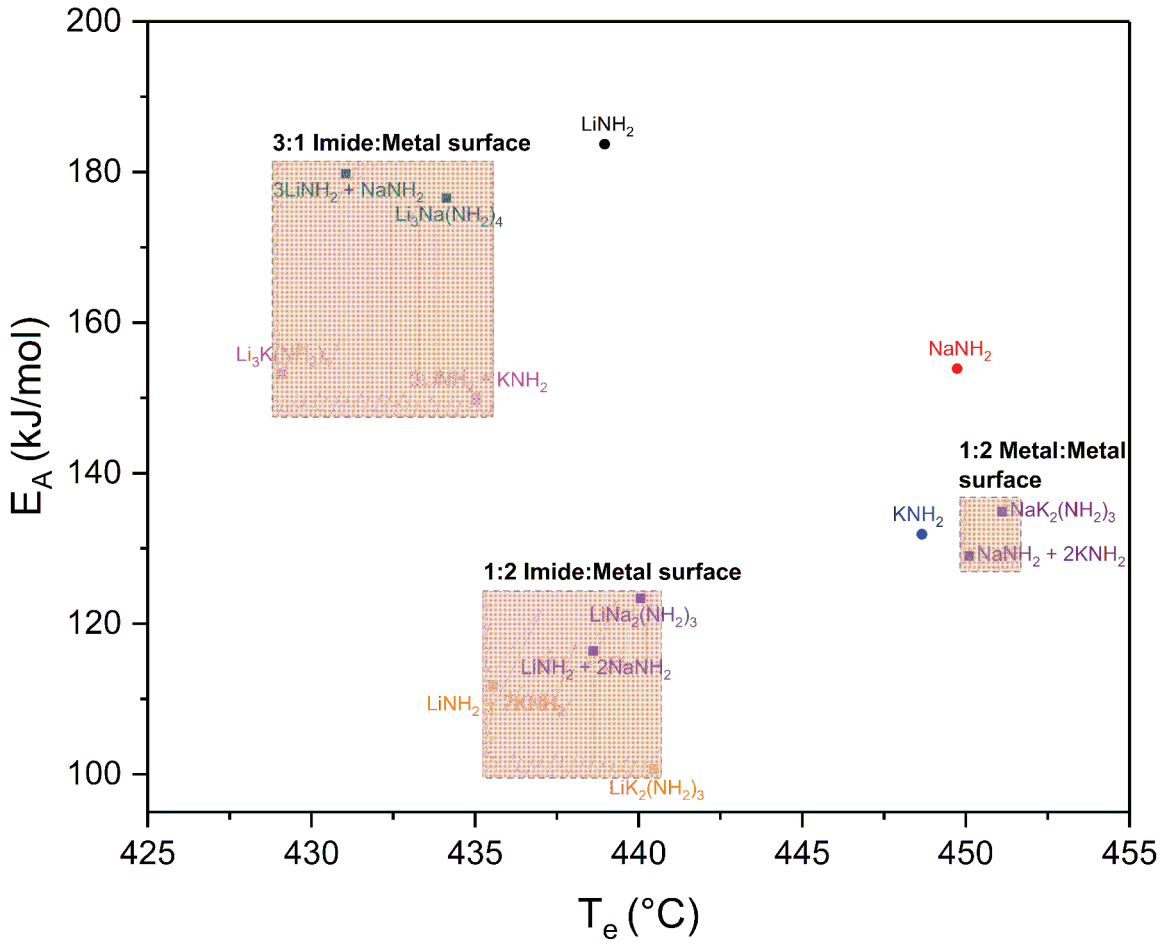


Figure 7.4: Activation energy (E_A) against T_e for all the catalysts listed in Table 7.1

For a given value of T_e, the steepness of the sigmoid function is indicative of higher activation energy (E_A) for NH_3 decomposition (but both the activation energy and the pre-exponential factor within the empirical Arrhenius relationship must be considered as the determinants of reaction kinetics). Correlations between E_A and T_e are small. Figure 7.4 plots the activation energy (E_A) against T_e for all the catalysts listed in Table 7.1. An ideal catalyst would have a high E_A and low T_e so $Li_3Na(NH_2)_4$, $LiNH_2 + 3NaNH_2$, $Li_3K(NH_2)_4$ and $LiNH_2 + 3KNH_2$ are all better than $LiNH_2$ alone.

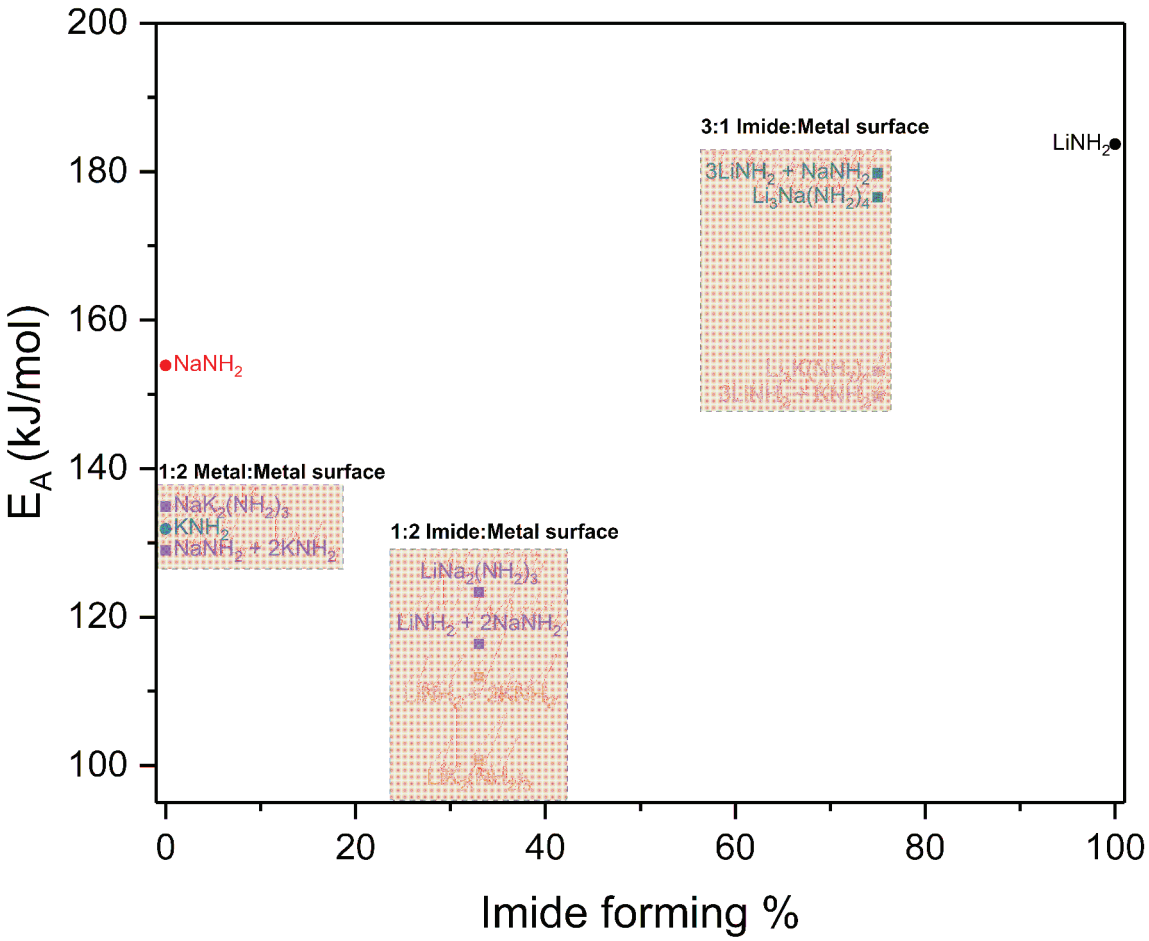


Figure 7.5: Activation energy (E_A) against percentage composition of the imide forming component for all the catalysts listed in Table 7.1

Figure 7.5 plots the activation energy (E_A) against the percentage of the imide forming component of all the catalysts listed in Table 7.1. In both graphs against activation energy (E_A), a clear distinction can be observed between the mixed-metal amide catalysts which have decomposed to form a 3:1 imide:metal surface, 1:2 imide:metal surface or 1:2 metal:metal surface at the temperatures required for NH_3 decomposition.

The percentage recovery of the catalyst is also crucially important in order to maintain efficiency and improve lifetimes. Figure 7.6 plots the percentage recovery of the catalyst against the percentage of the imide forming component of all the catalysts listed in Table 7.1. This demonstrates how crucial the imide forming component (Li_2NH derived from from $LiNH_2$), is in improving the percentage recovery of the catalyst from the reactor.

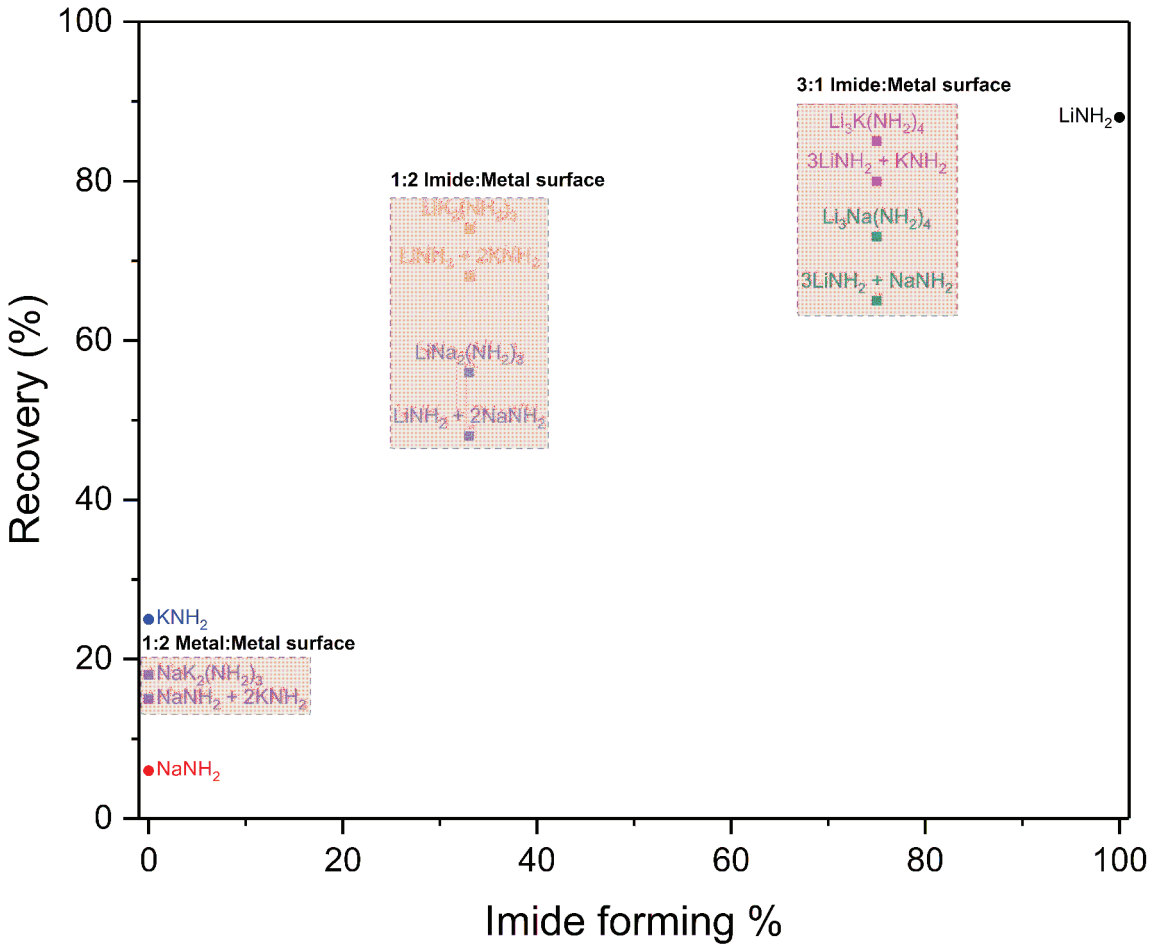


Figure 7.6: Percentage recovery against the percentage of the imide forming component of all the catalysts listed in Table 7.1

Figure 7.6 shows that the pre-formed mixed-metal amides have better recovery than the mixed starting materials in the relevant ratios, indicating there is a practical value in pre-forming the mixed amide, even though there was not a significant difference in the observed activity.

Powder X-ray diffraction data was collected for the residues left in the reactor at the end of each ammonia decomposition reaction in order to identify the decomposition products. Analysis has shown that $LiNH_2$ is present in all the post-reaction products for lithium containing mixed-metal amides, however no sodium or potassium containing components were detected suggesting they may have been volatilised and therefore lost from the reactor.

7.3 Future work

Containment of the active catalyst appears to be the principal practical hurdle for the use of lithium, sodium and potassium mixed-metal amides due to poor recovery of the catalyst post-reaction. Enhancing NH_3 conversion efficiencies is predicated on improving catalyst containment and increasing the active reaction surface area of the catalysts. Without a transparent reactor to monitor the behaviour of the sample *in-situ*, it is difficult to know exactly what would be the best strategy to contain the amides. At the temperatures of operation, $NaNH_2$, KNH_2, Na and K are expected to be molten and $NaNH_2$ and KNH_2 are likely to be volatile (with boiling points of $\sim 400\,°C$ [230]) and therefore likely to be present as aerosols within the reactor. Experiments have been performed with a 1.6 mm thick nickel-foam baffle placed 5 mm above the bottom of the NH_3 inlet tube [72] to improve both material containment and reaction surface area. This inclusion increases the NH_3 conversion efficiency by $\sim 10\%$ for $NaNH_2$ [71] and future reactor designs could lead to further improved performance. It is possible that a reflux environment develops, with $NaNH_2$ volatilising and then condensing at the top of the reactor, or in the exhaust pipe where the temperature is below the melting point of both Na and $NaNH_2$ [294]. A heating design in which the lower part of the reactor is heated to the reaction temperature, and the upper part is heated to slightly above the melting point of the amide, may help to contain the sample.

Chemical containment could also trap sodium, potassium, $NaNH_2$ and KNH_2, whilst also potentially enhancing the activity through a higher surface area and more favourable interactions with the scaffold. Containment in porous carbon materials has been achieved through various means for the Li-N-H system, resulting in lower decomposition temperatures and altered decomposition pathways compared with the bulk sample [74, 300, 308]. Similar containment and enhancement of sodium amide may be a productive future research focus for improving the overall NH_3 performance of the mixed-metal amide systems.

The trends discussed here could be explored more fully by extending the research to include the examination of the behaviour and NH_3 decomposition behaviour of rubidium amide, caesium amide and any mixed-metal amides these may form with other group 1

metal amides. Mixed-metal amides have been reported for the Rb-Li-N-H system [151] and Cs-Li-N-H system [149]. However, there are particularly significant hazards associated with working with rubidium and caesium due to their high reactivity. It may therefore be more instructive to tailor future research efforts towards less volatile materials such as *p*-block metals or purely ionic materials.

7.4 Conclusions

It is the presence of $LiNH_2$, which decomposes to the imide (the active form of the catalyst) rather than the metal, that has a significant influence on the way the parent mixed-metal amides decompose NH_3. $LiNH_2$ has to be present in the mixed-metal amide for it to be an effective NH_3 decomposition catalyst. $LiNa_2(NH_2)_3$ and $LiK_2(NH_2)_3$ are currently the best low temperature catalysts and $Li_3Na(NH_2)_4$ and $Li_3K(NH_2)_4$ show the best conversion at high temperatures to date. The importance of the imide led to the study of the K-Mg-N-H system (Chapter 8) and Na-Mg-N-H system (Chapter 9) as the mixed-metal amides of these systems have been reported to form mixed amide-imide phases $KMg(NH_2)(NH)$ and $NaMg(NH_2)(NH)$. As "imide forming" mixed-metal amides, it will therefore be important to understand how these systems behave in comparison to these intra Group 1 systems.

Chapter 8

Mixed Potassium-Magnesium system

Contents

8.1 Background 320

8.1.1 Chapter overview 321

8.1.2 Crystallography 321

8.2 Synthesis 323

8.2.1 $K_2Mg(NH_2)_4$ 323

8.3 *Ex-situ* thermal decomposition 325

8.3.1 $Mg(NH_2)_2$ 325

8.3.2 $K_2Mg(NH_2)_4$ 327

8.4 POLARIS experiments under inert gas 333

8.4.1 Synthesis of $K_2Mg(ND_2)_4$ 333

8.4.1.1 Preliminary offline study 333

8.4.1.2 POLARIS experiment 335

8.4.2 Decomposition of $K_2Mg(ND_2)_4$ 339

8.5 Inert gas summary 345

8.6 Ammonia decomposition (*ex-situ*) 347

8.6.1 Quantitative fitting and analysis 347

8.6.2 Catalyst Recovery 353

8.7 Decomposition under ammonia 353

8.8 POLARIS experiment - Ammonia decomposition (*in-situ*) . . 354

8.9 Summary 361

8.1 Background

There are two key goals in the development of metal amide-imide catalysts: first, to design new catalysts which display higher NH_3 decomposition activity and will help catalogue periodic behaviour of these materials as catalysts; secondly, to develop materials which remain solid and stable across the range of NH_3 decomposition reaction conditions. Imides generally have higher melting points than their corresponding amides, so an imide which forms at low temperatures and remains solid over a wide range of operating conditions would be an ideal candidate for a practical NH_3 decomposition catalyst.

Lithium-calcium imide ($Li_2Ca(NH)_2$) currently shows the best variable temperature conversion and specifically the highest low-temperature activity towards NH_3 decomposition reported for any metal amide/imide system studied to date (Figure 1.17) [196]. It also shows substantially improved containment of the catalyst mass within the reactor hot-zone with almost complete mass recovery (98 % after heating to 500 °C). However, despite being stable in the temperature range used for NH_3 decomposition under inert gas, one of the challenges presented by $Li_2Ca(NH)_2$ is the difficulty in keeping it solid at intermediate temperatures under NH_3, in part due to its decomposition into $LiNH_2$ and CaNH.

Building on this success, there are other Group 1 and Group 2 based mixed-metal systems which are known and could be considered as catalysts. Magnesium based imides and amides, Mg-N-H ([80, 126, 213]), Li-Mg-N-H [213, 219] and Rb-Mg-N-H [148], have to date, been investigated mainly as H_2 storage materials. The K-Mg-N-H, and Na-Mg-N-H systems (Chapter 9), are of particular chemical interest as the tetra-amides ($K_2Mg(NH_2)_4$ and $Na_2Mg(NH_2)_4$) are reported to be metastable kinetic products [291]. These can be annealed above 300 °C to form thermodynamically stable, novel mixed amide-imide phases $KMg(NH_2)(NH)$ and $NaMg(NH_2)(NH)$ which are stable to higher temperatures (360 °C) (Equation 8.1).

$$K_2Mg(NH_2)_4 \longrightarrow KMg(NH)(NH_2) + KNH_2 + NH_3 \tag{8.1}$$

The presence of these amide-imide complexes constitutes a new class of NH_3 decomposition catalysts, bridging the intra-Group 1 systems studied so far (Li-Na-N-H (Chapter 3), Li-K-N-H (Chapter 4) and Na-K-N-H (Chapter 5)) for which no mixed-metal imide exists and those for which only an imide is known ($Li_2Ca(NH)_2$ and $Li_2Mg(NH)_2$).

The amide-imide complex may be an important route to stabilising the system to the temperatures required for catalytic NH_3 decomposition reflected by the high mass recovery rates for $K_2Mg(NH_2)_4$ and $Na_2Mg(NH_2)_4$ from catalyst tests (89 % and 87 % respectively). Previously studied ternary imides are considered to behave as a combination of the two imide components [196], but these new systems may act differently to a simple combination of $Mg(NH_2)_2$ with KNH_2 or $NaNH_2$.

8.1.1 Chapter overview

The K-Mg-N-H system is chemically important due to the reported formation of the novel mixed amide-imide complex $KMg(NH_2)(NH)$ at high temperatures. The variable-temperature structural behaviour of the systems under both inert gas and NH_3 decomposition conditions will be described. A combination of *in-situ* and *ex-situ* data, will provide a more complete understanding of the behaviour and dynamics arising from the co-existence of amide-imide groups within the system.

8.1.2 Crystallography

The crystal structures of $K_2Mg(NH_2)_4$ (P 2_1/c) and $KMg(NH_2)(NH)$ (P nma) can both be described as a combination of hepta-coordinated potassium ions (KN_7) forming linear chains by sharing a face, and magnesium-nitrogen tetrahedra (MgN_4). The arrangement of these building units is different in the two structures, with a more dense packing of potassium inside the $K_2Mg(NH_2)_4$ structure, where KN_7 forms linear chains of face-sharing polyhedra, while in $KMg(NH_2)(NH)$ the KN_7 polyhedral chains share only one face and one edge with each other. The larger space available in between potassium chains in the crystal structure of $KMg(NH_2)(NH)$ permits a higher fraction of magnesium cations [214].

$KMg(NH_2)(NH)$ is crystallographically particularly interesting due to the presence of imide groups bonded to potassium cations. No inorganic potassium imide phase is known

so $KMg(NH_2)(NH)$ offers for the first time evidence for the occurrence of a potassium-containing compound associated with imide groups [214]. The presence of preferential bonding of magnesium ions with imide groups is retained inside the $KMg(NH_2)(NH)$ structure. Magnesium atoms are bonded to three imide groups and just one amide group while potassium cations are coordinated by four amide groups and three imide groups.

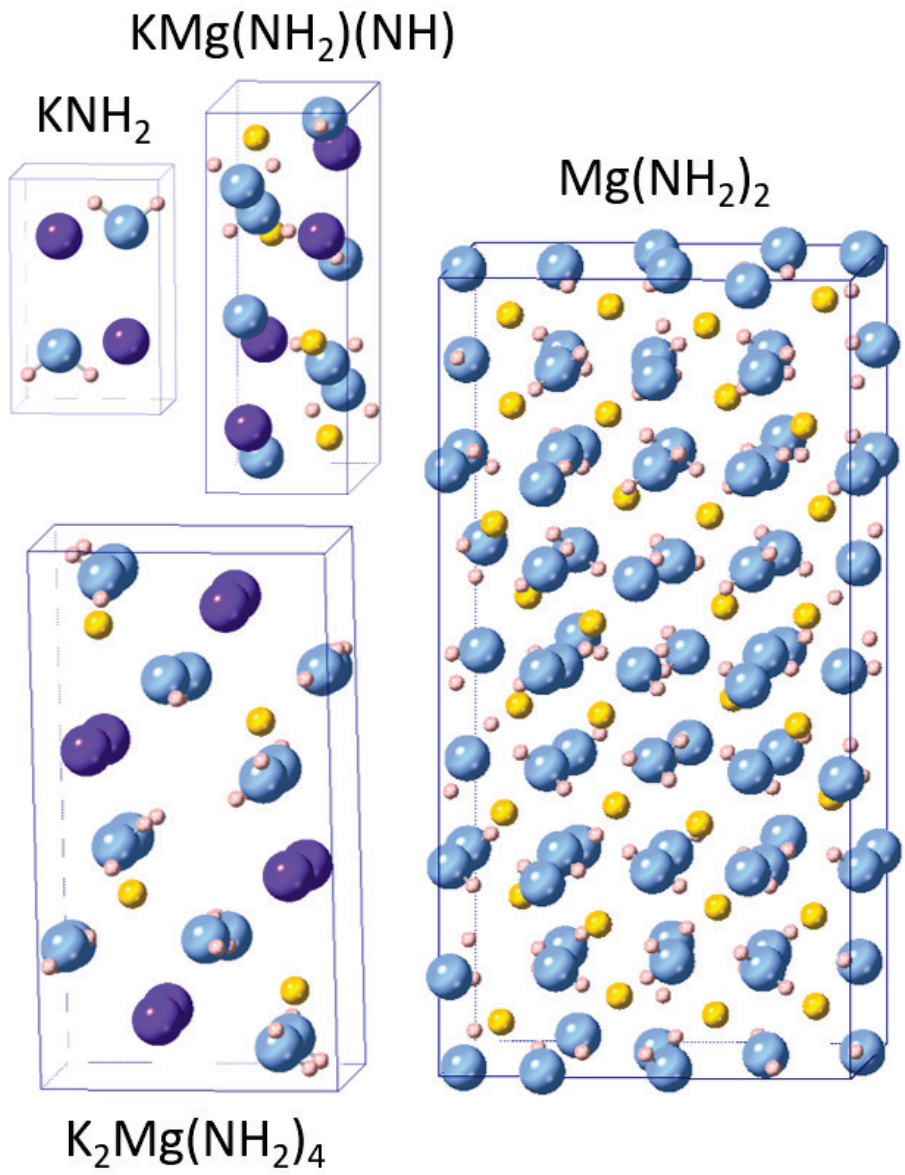


Figure 8.1: Crystallographic unit cells for monoclinic KNH_2, $K_2Mg(NH_2)_4$, $KMg(NH)(NH_2)$ and $Mg(NH_2)_2$ roughly proportional in size. Purple = Potassium, Yellow = Magnesium, Blue = Nitrogen, Pink = Hydrogen

8.2 Synthesis

8.2.1 $K_2Mg(NH_2)_4$

Novel synthetic methods for the formation of $K_2Mg(NH_2)_4$ directly from KNH_2 and $Mg(NH_2)_2$ have been developed using both tube furnace and ball-mill preparations and are discussed in Section 2.2.4.4.

For the synthesis of the metastable mixed amide-imide phase $KMg(NH_2)(NH)$, an annealing reaction was attempted on the gas flow panel in which a sample of pre-made $K_2Mg(NH_2)_4$ was heated to 250 °C and held for 10 hours under argon. Analysis of the exhaust gas stream throughout the experiment showed no NH_3, N_2 or H_2 was given off which would be expected if Equation 8.1 were to occur. However, analysis of the powder X-ray diffraction data collected for the sample after this reaction fitted to $KMg(NH_2)(NH)$ (61.5 %) and monoclinic KNH_2 (38.5 %) but not to $K_2Mg(NH_2)_4$ showing the annealing reaction had been successful (Figure 8.2).

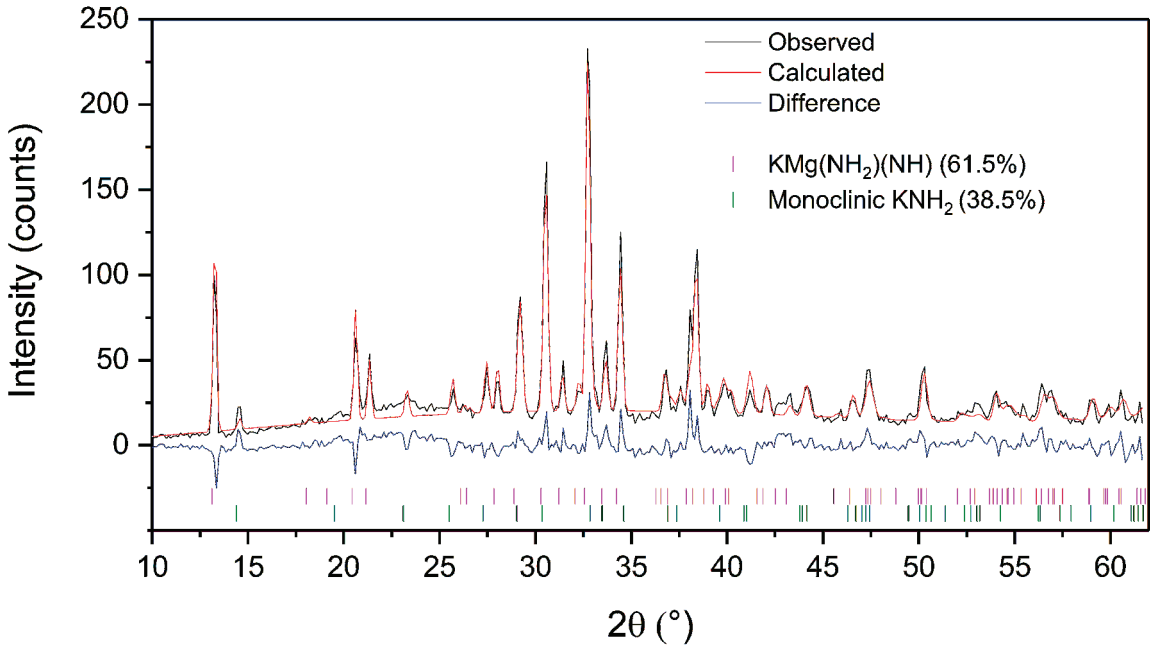


Figure 8.2: Post-reaction powder X-ray diffraction data of the sample of $K_2Mg(NH_2)_4$ which had been heated to 300 °C for 10 hours under argon to form $KMg(NH_2)(NH)$ (Wavelength = 1.5418 Å)

The bonding in the sample of $K_2Mg(NH_2)_4$ synthesised in both the tube furnace and ball-mill was probed by Raman spectroscopy and collected as outlined in Section 2.5.1. Raman spectroscopy can be used to follow the conversion between amide (NH_2^-), imide (NH^{2-}), and nitride (N^{3-}) phases by examining the change in the vibrational modes. The N−H stretching region for each of the phases is shown in Figure 8.3 along with those of KNH_2 and $Mg(NH_2)_2$ for reference.

In Figure 8.3 it can be seen that $Mg(NH_2)_2$ shows characteristic infrared absorption bands of N−H stretches at wavenumbers of 3275 cm^{-1} and 3329 cm^{-1} and $K_2Mg(NH_2)_4$ shows stretches at wavenumbers of 3227 cm^{-1}, 3234 cm^{-1}, 3287 cm^{-1}, 3302 cm^{-1}, 3332 cm^{-1} and 3354 cm^{-1}. These match up well with data reported in the literature [291], showing that $K_2Mg(NH_2)_4$ was successfully synthesised in both the tube furnace and ball-mill (despite the lack of crystallinity in the latter sample).

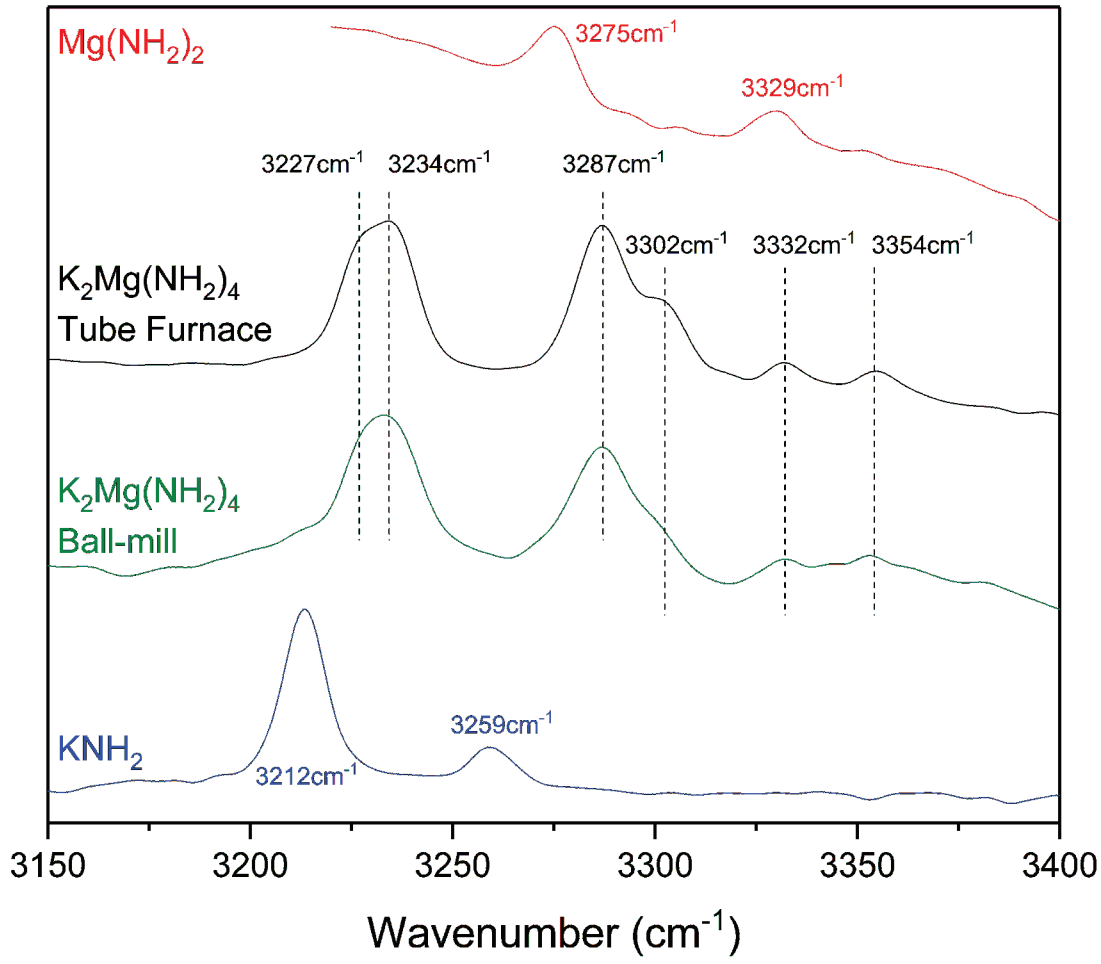


Figure 8.3: Raman stretches for the K-Mg-N-H system

8.3 *Ex-situ* thermal decomposition

8.3.1 $Mg(NH_2)_2$

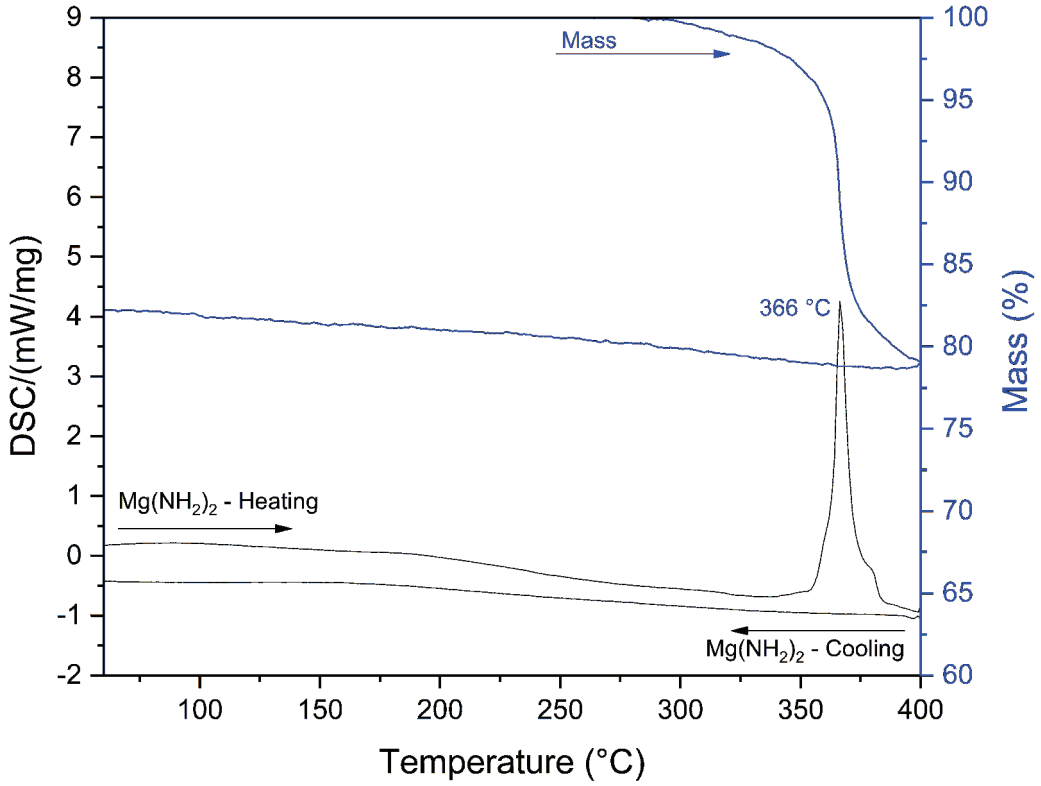
In order to evaluate the decomposition properties of the mixed-metal amides, understanding the behaviour of the constituent single metal amides is an important first step. KNH_2 alone has already been analysed in Section 4.5 as part of the Li-K-N-H system. The STA experiment looking at the low temperature behaviour of KNH_2 (Figure 4.1) showed a (reversible) endothermic event at 324 °C on heating and 319 °C on cooling which correlates with the known melting point of KNH_2 (338 °C) and during this experiment there was no mass loss up to 380 °C, showing KNH_2 decomposes above this temperature.

$Mg(NH_2)_2$ is known to decompose first to magnesium imide releasing NH_3 (Equation 8.2a) which is itself unstable to magnesium nitride formation (Equation 8.2b) [80, 301]. This is an analogous decomposition pathway to $LiNH_2$ but is different to that for $NaNH_2$ and KNH_2 which decompose to the respective metals.

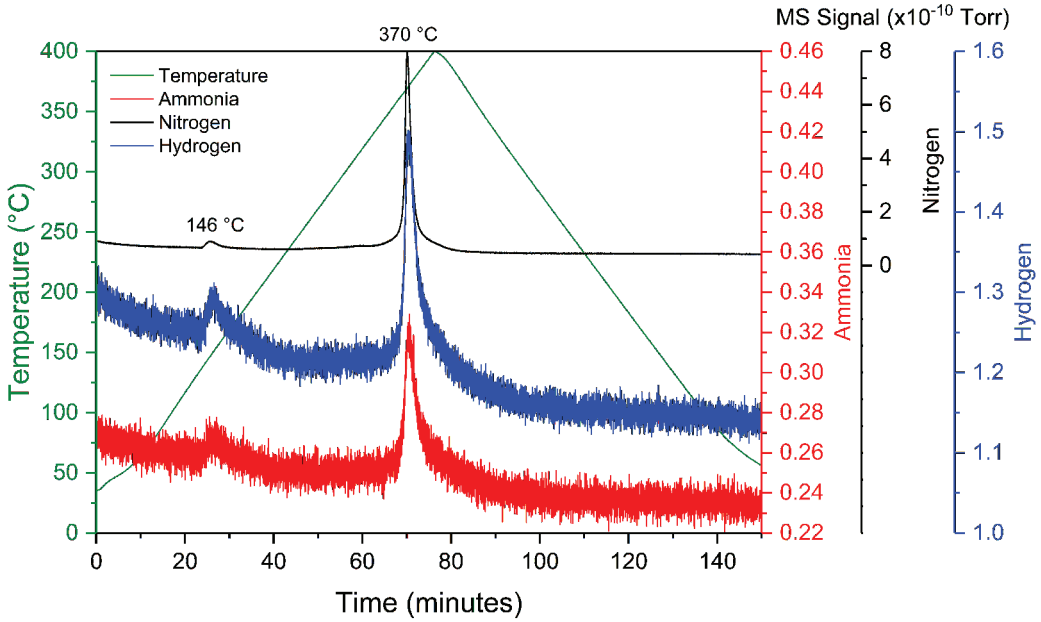
$$Mg(NH_2)_2 \longrightarrow MgNH + NH_3 \tag{8.2a}$$

$$3\,MgNH \longrightarrow Mg_3N_2 + NH_3 \tag{8.2b}$$

Figure 8.4 shows a non-reversible endotherm for $Mg(NH_2)_2$ at 366 °C which occurs alongside a 21 % mass loss due to the release of N_2, H_2 and NH_3 gas which is likely to correspond to the $Mg(NH_2)_2$ to MgNH phase change, as the MgNH to Mg_3N_2 decomposition is known to occur at higher temperatures (490 °C) [80]. A full phase change from $Mg(NH_2)_2$ to MgNH would correspond to 30 % mass loss so this process is only partially complete during this experiment.



(a) STA trace for $Mg(NH_2)_2$ (black) and mass trace (blue)



(b) QGA data from the STA trace for $Mg(NH_2)_2$

Figure 8.4: STA traces for $Mg(NH_2)_2$

8.3.2 $K_2Mg(NH_2)_4$

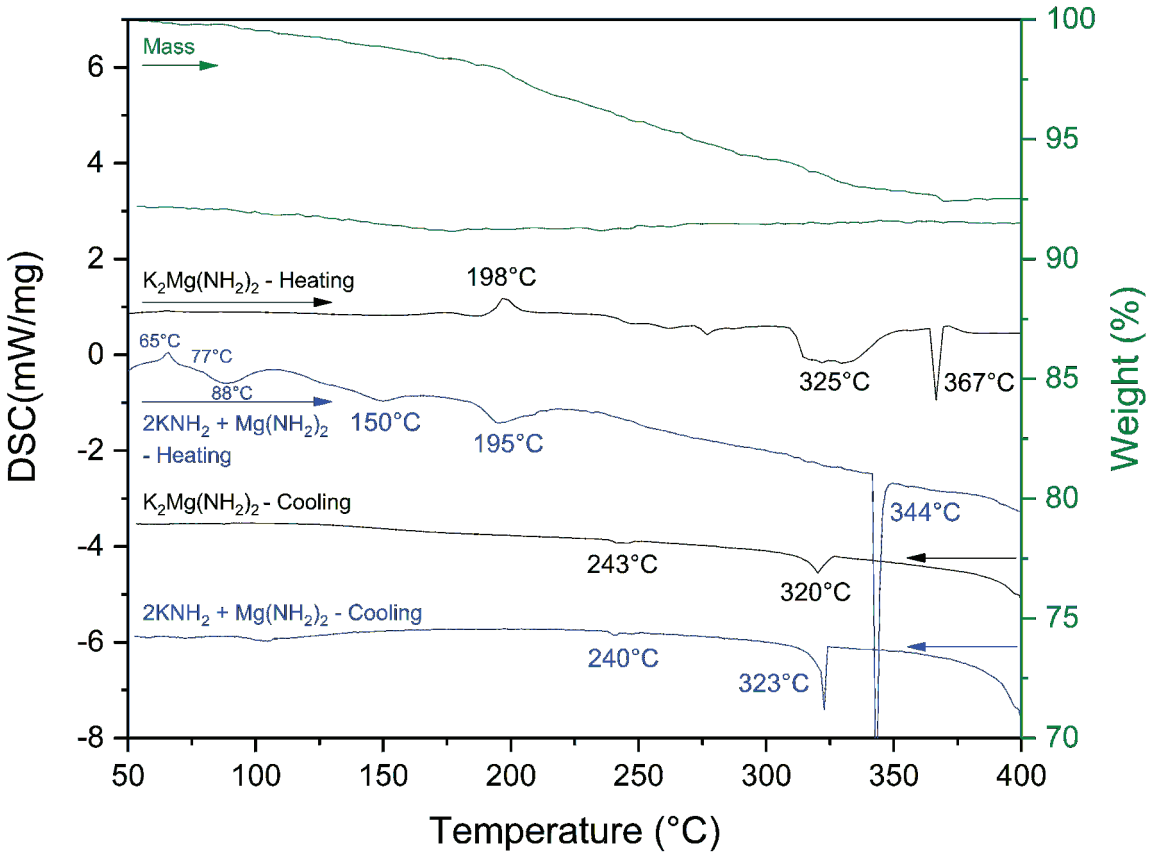
In order to probe the inert gas synthesis and decomposition of $K_2Mg(NH_2)_4$, the low temperature behaviour was investigated using Simultaneous Thermal Analysis (STA). A detailed analysis of the low temperature behaviour is particularly important for understanding the phase change behaviour in these systems in relation to the melt phase. Complementary high temperature measurements were performed on the gas flow panel under argon in order to provide insight into the whole decomposition process.

DSC traces were taken for both pre-made $K_2Mg(NH_2)_4$ (black) and a hand-ground mixture of $2KNH_2 + Mg(NH_2)_2$ (blue) and are shown in Figure 8.5a. The mass trace (green) has been determined from the TGA component of this STA experiment.

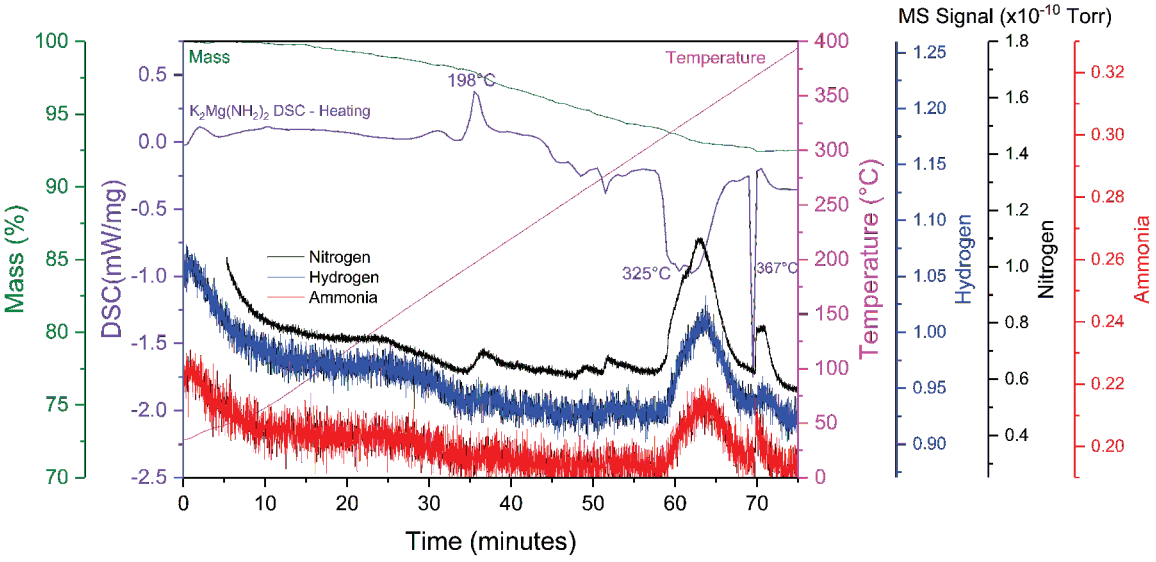
The reported temperatures for the monoclinic to tetragonal and tetragonal to cubic phase changes for KNH_2 are 53 °C [150] and 75 °C [211] respectively. From Figure 8.5a in the trace for $2KNH_2 + Mg(NH_2)_2$ it can be seen that the analogous thermal events for these phase changes occur here at 67 °C and 77 °C respectively.

Comparison of the differences between these two traces suggests the synthesis of $K_2Mg(NH_2)_4$ corresponds to the exothermic event at 150 °C and the material subsequently melts at 198 °C. The synthesis and subsequent melting temperatures of $K_2Mg(NH_2)_4$ have been reported to be 195 °C and 234 °C from the interaction of KNH_2 with $Mg(NH_2)_2$ when investigated by *in-situ* powder X-ray diffraction [245].

For previous Group 1 mixed-metal amide systems in this thesis, two endothermic peaks have been observed on heating which have been suggested to correspond to a separation followed by a full sample melt. Only one endothermic peak is seen in the STA trace for pre-made $K_2Mg(NH_2)_4$ in Figure 8.5a, indicating that a full phase separation to the single metal amides does not occur. The exotherm at 198 °C therefore only corresponds to a full sample melt and not a concurrent separation. It is the decomposition of this molten $K_2Mg(NH_2)_4$ that then leads to the formation of $KMg(NH_2)(NH)$.



(a) STA traces for $K_2Mg(NH_2)_4$ (black) and $2KNH_2 + Mg(NH_2)_2$ (blue) alongside the mass trace (green) from the TGA



(b) DSC trace for $K_2Mg(NH_2)_4$ (purple), mass trace (green), temperature profile (magenta) and QGA data for N_2, H_2 and NH_3 (black, blue and red)

Figure 8.5: STA traces for $K_2Mg(NH_2)_4$

During the decomposition of $K_2Mg(NH_2)_4 \longrightarrow KMg(NH)(NH_2) + KNH_2 + NH_3$, one molecule of NH_3 is released which is observed as an exothermic event at 325 °C in Figure 8.5b. This is confirmed by the mass loss of ∼9 % seen in the TGA trace (a complete phase change would correspond to a mass loss of 10 %). There is a smooth mass loss observed from the start of the heating process and an increased slope from the melting point at 198 °C. Figure 8.5b shows the largest gas releases occur alongside the exotherms at 325 °C (and 367 °C). However, the mass loss has plateaued by this point which implies some stability in the system and that these exotherms do not correspond to decomposition steps. MS analysis of the exhaust gas shows that it is not NH_3 that is released, but H_2 and N_2 in a 3:1 ratio suggesting that $KMg(NH_2)(NH)$ is acting as an NH_3 decomposition catalyst at this temperature.

The sharp exotherm at 367 °C in the heating traces of $K_2Mg(NH_2)_4$ could correspond to crystallisation of the newly formed $KMg(NH_2)(NH)$. As the molten $K_2Mg(NH_2)_4$ finishes decomposing to $KMg(NH_2)(NH)$, this will then solidify. The melting point of $KMg(NH_2)(NH)$ alone is not known but it is likely that this system is behaving analogously to $LiNH_2$ which is known to melt and decompose to Li_2NH which then solidifies as it has a higher melting point. $K_2Mg(NH_2)_4$ decomposes to $KMg(NH_2)(NH)$ in an exothermic process with the release of gas (positive entropy) therefore in a non-reversible transformation, which may bode well for $KMg(NH_2)(NH)$ being stable under NH_3 decomposition conditions. This is useful, as one of the premises for a successful NH_3 decomposition catalyst is an unstable amide which could ideally not be reformed.

The exotherms on cooling correspond to phase transitions of the KNH_2 which is formed as a by-product during the decomposition of $K_2Mg(NH_2)_4$. These thermal events occur at the same temperature as those seen in the KNH_2 dominant ratios in Figure 4.14 where the exotherms at ∼320 °C correlate to the recrystallisation of KNH_2 and the thermal events at ∼240 °C to a KNH_2 phase change. The fact that no additional thermal events are seen on cooling corroborates the theory that $KMg(NH_2)(NH)$ solidifies as it is formed on heating at 367 °C, as no recrystallisation events for $KMg(NH_2)(NH)$ are seen on cooling.

The high temperature decomposition of pre-synthesised $K_2Mg(NH_2)_4$ was analysed under argon on the gas flow panel. Figure 8.6 shows that the outlet gas flow mass spectrometry traces for this experiment from which it can be seen the start of H_2 and N_2 gas release occurs from $\sim 275\,°C$.

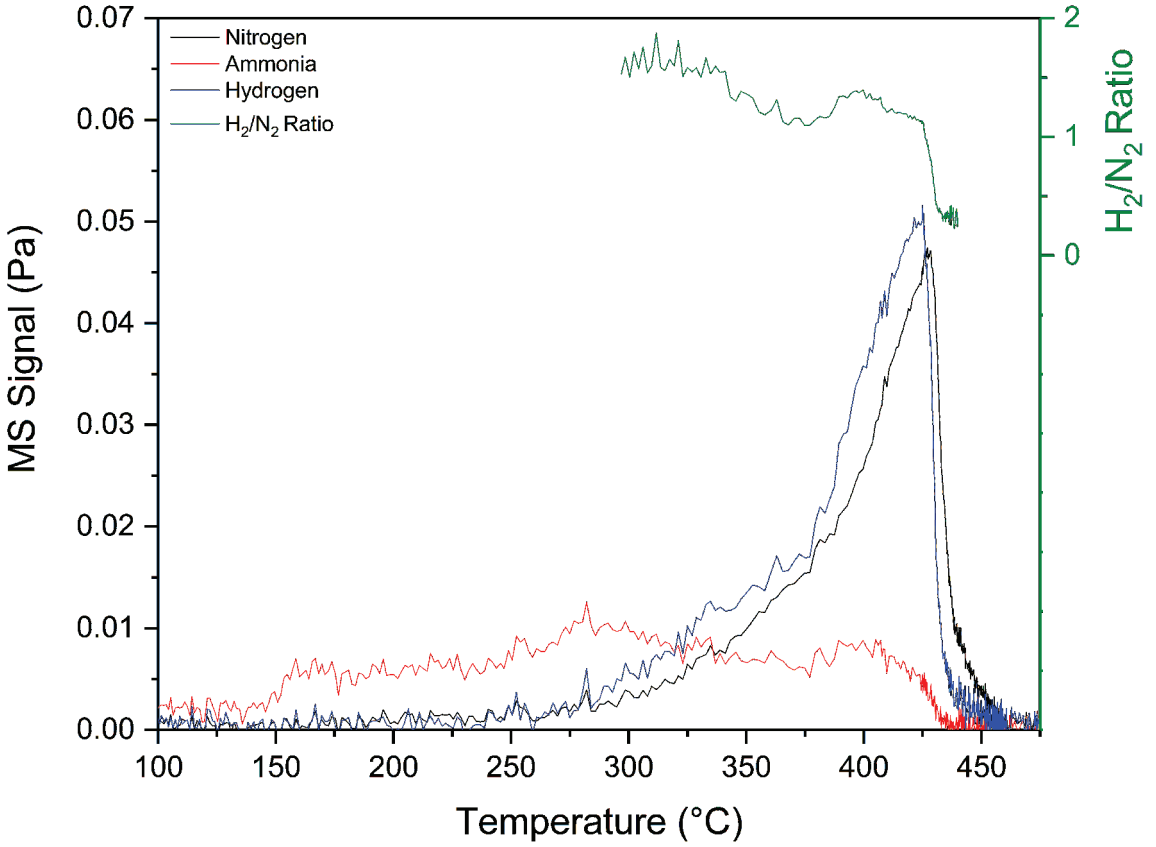


Figure 8.6: Decomposition of $K_2Mg(NH_2)_4$ on the gas flow panel under argon

Similarly to the Group 1 mixed-metal systems, Figure 8.7 shows pseudo-Voigt functions in TOPAS have been used to determine "peak positions" in the H_2 MS trace shown in Figure 8.6. However, whereas for the Group 1 mixed-metal systems two pseudo-Voigt functions were used, for the K-Mg-N-H system, three pseudo-Voigt functions were used due to the different decomposition pathway occurring due to the presence of the amide/imide complex.

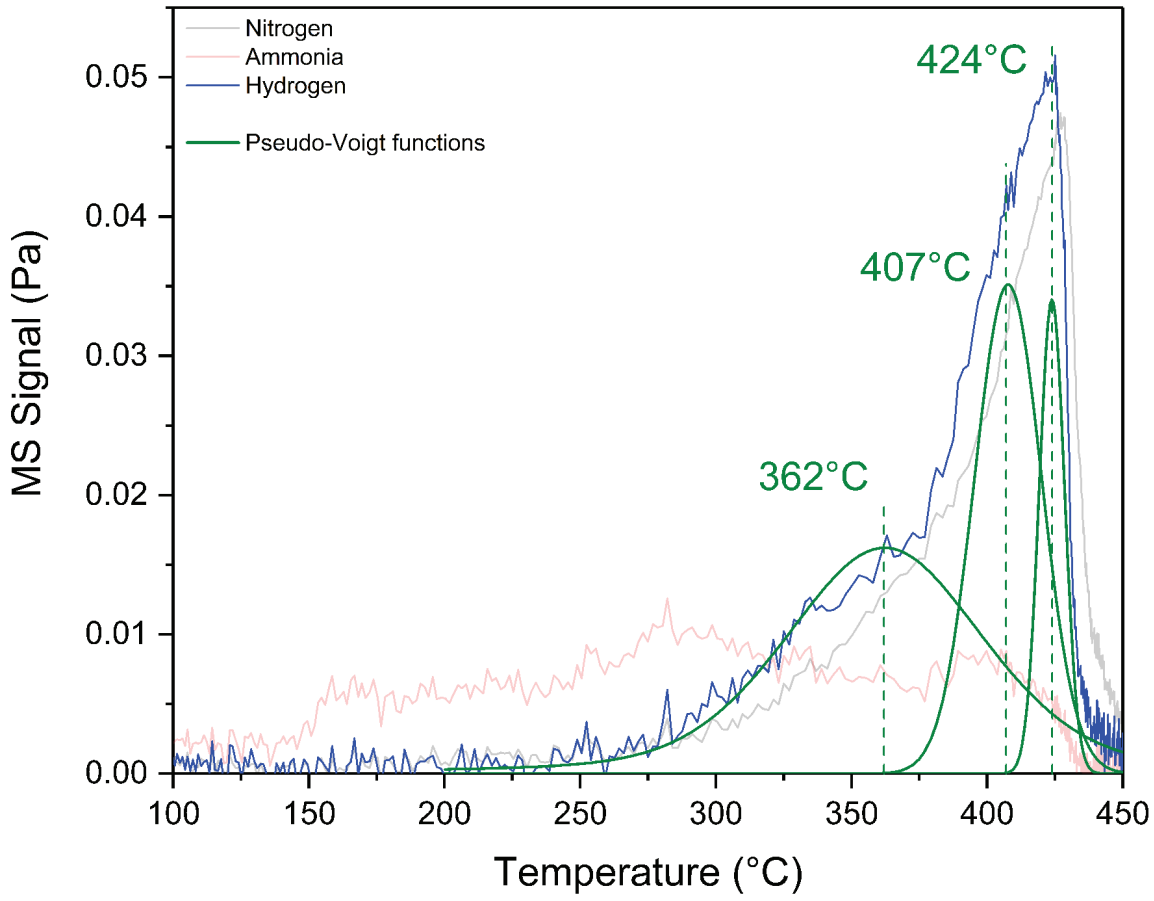


Figure 8.7: Three pseudo-Voigt functions have been used to determine the peak positions in the H_2 curve from Figure 8.6 during the decomposition of $K_2Mg(NH_2)_4$

The peak at 362 °C is likely due to the gas released as $K_2Mg(NH_2)_4$ decomposes to $KMg(NH_2)(NH)$ (this exothermic event was determined to be at 325 °C from the STA experiment in Figure 8.5b). Whilst Equation 8.1 would suggest it is NH_3 that would be expected to be given off, the K-Mg-N-H phases present are acting as an NH_3 decomposition catalyst and it is H_2 and N_2 that are in fact observed.

Santoru et al. [245] performed an *in-situ* powder X-ray diffraction experiment which showed that $K_2Mg(NH_2)_4$ melted and decomposed into $KMg(NH_2)(NH)$, which itself decomposed at 420 °C, in accordance with Wang et al. [291]. Mg_3N_2 was observed to have formed as an end product with MgNH proposed as a likely intermediate. This therefore suggests that $KMg(NH_2)(NH)$ itself decomposes by separating into the constituent single metal amides/imides which could subsequently decompose at different temperatures. Potassium imide is not known, so KNH_2 and MgNH must form. KNH_2 would decompose first (likely

the peak at 407 °C) as magnesium imide is stable to higher temperatures, before being known to decompose to Mg_3N_2 (likely the peak at 424 °C). A hypothetical decomposition pathway could be proposed for $K_2Mg(NH_2)_4$:

$K_2Mg(NH_2)_4$	$\longrightarrow KMg(NH)(NH_2) + KNH_2 + NH_3\uparrow$	Decomposition
	$\longrightarrow KMg(NH)(NH_2) + K + \frac{1}{2}N_2\uparrow + H_2\uparrow$	KNH_2 decomposes
	$\longrightarrow KNH_2 + MgNH + K$	Mixed-metal amide-imide separates
	$\longrightarrow MgNH + 2\,K + \frac{1}{2}N_2\uparrow + H_2\uparrow$	KNH_2 decomposes
	$\longrightarrow \frac{1}{3}\,Mg_3N_2 + \frac{1}{3}\,NH_3\uparrow + 2\,K$	MgNH decomposes
	$\longrightarrow \frac{1}{3}\,Mg_3N_2 + 2\,K$	All gases lost
	$\longrightarrow \frac{1}{3}\,Mg_3N_2$	K metal volatalised

Santoru et al. also observed potassium metal, monoclinic KNH_2 and a new cubic phase as end products [245]. The peak positions of this new cubic phase do not match the cubic phases of KH (a = 5.70 Å) or KNH_2 (a = 6.13 Å) since a cell parameter of 6.06 Å was found. This new cubic phase is most probably a solid solution of cubic KNH_2 and KH (both $Fm\overline{3}m$), of variable stoichiometry $K(NH_2)_xH_{(1-x)}$ and the different extent of substitution of amide–hydride anions is responsible for the intermediate cell parameter. A potassium amide-hydride solid solution has been previously reported [246] and its formation is favourable due to structural similarities between the two cubic polymorphs. A linear relationship was found between the unit cell parameter of the cubic phase at 270 °C and the molar fraction of amide anions, as expected from Vegard's law. No K metal, monoclinic KNH_2 or a solid solution of $K(NH_2)_xH_{(1-x)}$ was observed in Figure A.18. This was expected based on the study of the Li-K-N-H and Na-K-N-H systems, during which no K containing species were observed as end products after decomposition experiments on the gas flow panel, most likely due to decomposition of KNH_2 to K metal which was subsequently volatilised.

8.4 POLARIS experiments under inert gas

Having explored the synthesis of $K_2Mg(NH_2)_4$ and $KMg(NH_2)(NH)$ and their subsequent decomposition by various *ex-situ* techniques, combined neutron powder diffraction and gravimetric *in-situ* structural work on POLARIS were planned to corroborate these results. POLARIS, like GEM, is a neutron powder diffractometer at the ISIS facility which is used for *in-situ* structural analysis and was used to understand how the bulk structures of these materials behave under operating conditions. The IGA^n apparatus was used to determine the variable-temperature structural behaviour of the systems under argon and the *in-situ* sample stick was used to look at the structure of $K_2Mg(ND_2)_4$ while decomposing ammonia.

The high quality diffraction data from POLARIS correlated with mass changes recorded by the IGA^n instrument enables the determination of each structural transformation during these multi-step processes, and it was hoped that specifically the transformation from $K_2Mg(ND_2)_4$ to the novel mixed amide-imide phase $KMg(ND_2)(ND)$ could be observed and investigated.

The use of neutrons aids the assignment of deuterium positions during the transformation from amide to imide groups which may help probe the subtlety of whether the amide-imide complex is formed in a fixed stoichiometry or with a varied ratio.

8.4.1 Synthesis of $K_2Mg(ND_2)_4$

The synthesis of $2\,KND_2 + Mg(ND_2)_2 \longrightarrow K_2Mg(ND_2)_4$ was examined under argon using the IGA^n.

8.4.1.1 Preliminary offline study

In order to identify the temperatures of interest prior to the online neutron diffraction study, preliminary offline IGA^n measurements were performed on three samples of hand-ground $2KNH_2 + Mg(NH_2)_2$. Figure 8.8 shows the mass loss as a percentage of the starting mass as a function of temperature when a sample of $2KNH_2 + Mg(NH_2)_2$ was heated to 200 °C at a rate of 2 °C per minute where it was held for 5.5 hours under argon. 200 °C was chosen

because it had been reported that the desorption properties of $K_2Mg(NH_2)_4$ were slow below 200 °C but became vigorous above 210 °C when H_2 and N_2 (rather than NH_3) were released [245].

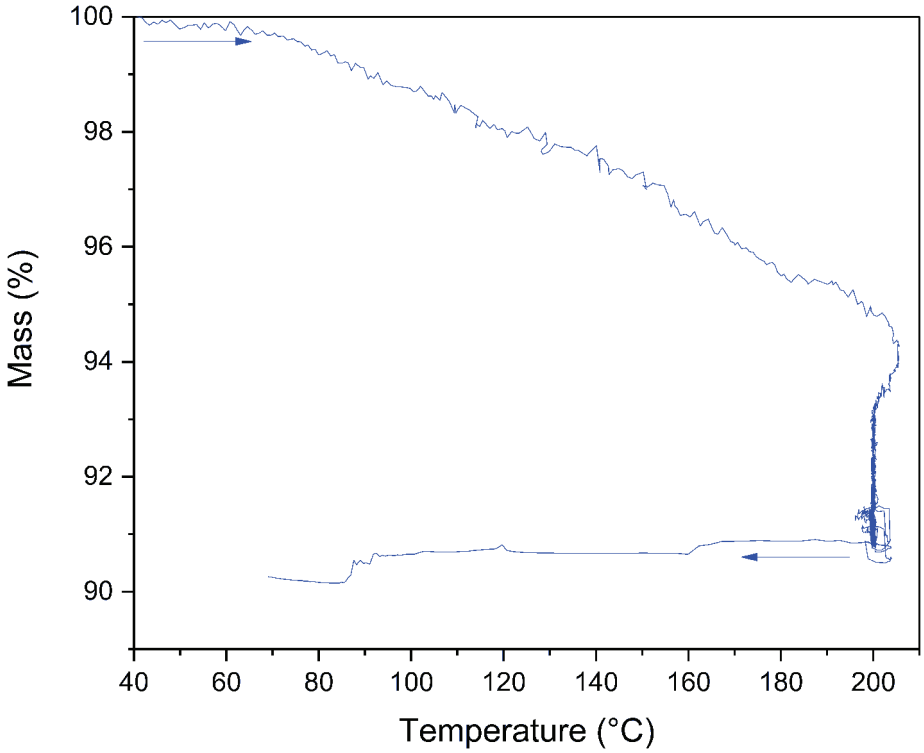


Figure 8.8: Mass trace (%) for a preliminary offline attempt at $K_2Mg(NH_2)_4$ synthesis using the IGA^n

Figure 8.8 shows a gradual mass loss of ∼6% up to 200 °C where it was held, during which there was a further ∼3.5% mass loss.

Although a full phase change for $K_2Mg(NH_2)_4 \longrightarrow KMg(NH)(NH_2) + KNH_2 + NH_3$ would correspond to an overall mass loss of 10 %, previous experiments have shown that the equipment set-up of the IGA^n apparatus means that it is prone to melted sample escaping from the bucket, which may have lead to the mass loss observed here. The annealing reaction was heated to 300 °C for 12 hours for the $K_2Mg(NH_2)_4$ to $KMg(NH_2)(NH)$ phase change to occur (Figure 8.2) and this had been assigned to the thermal event at 325 °C in Figure 8.5b, which are much higher temperatures than the peak temperature of 200 °C reached in this experiment.

8.4.1.2 POLARIS experiment

For the synthesis of $K_2Mg(ND_2)_4$, 0.5 g of a hand-ground mixture of the deuterated amides $2KND_2 + Mg(ND_2)_2$ was transferred into the vanadium IGA^n bucket within a quartz reactor before it was craned into the POLARIS diffractometer under constant 1000 mbar argon.

The sample was heated at 1 °C/min to 200 °C where it was held for 1 hour before being cooled to room temperature at 5 °C/min. Thermogravimetric readings of the sample mass, temperature and pressure were taken every 5 seconds, and neutron diffraction data were collected at 100 second intervals throughout the course of the experiment. This enabled the monitoring of the reaction progress of the samples as a function of temperature. Figure A.19 in the Appendix shows contour plots for data collected from banks 2, 3, 4 and 5 for the $2KND_2 + Mg(ND_2)_2$ synthesis experiment with corresponding thermogravimetric data.

An hour long scan was taken at room temperature to get a high quality data set which indicated that the sample was 73.0 % monoclinic KND_2 and 27.0 % $Mg(ND_2)_2$. Table A.11 in the Appendix lists the *d*-spacings and indices for the peaks present in this scan from both monoclinic KND_2 and $Mg(ND_2)_2$ which are shown in Figure 8.9 as red and blue arrows respectively.

Figure 8.9 shows the thermogravimetric data, a bank 4 contour plot and key temperatures and regions highlighted for the $2KND_2 + Mg(ND_2)_2$ synthesis experiment. It can be seen that qualitatively the diffraction data can be split into six different regions which are detailed in Table 8.1 alongside the phase composition.

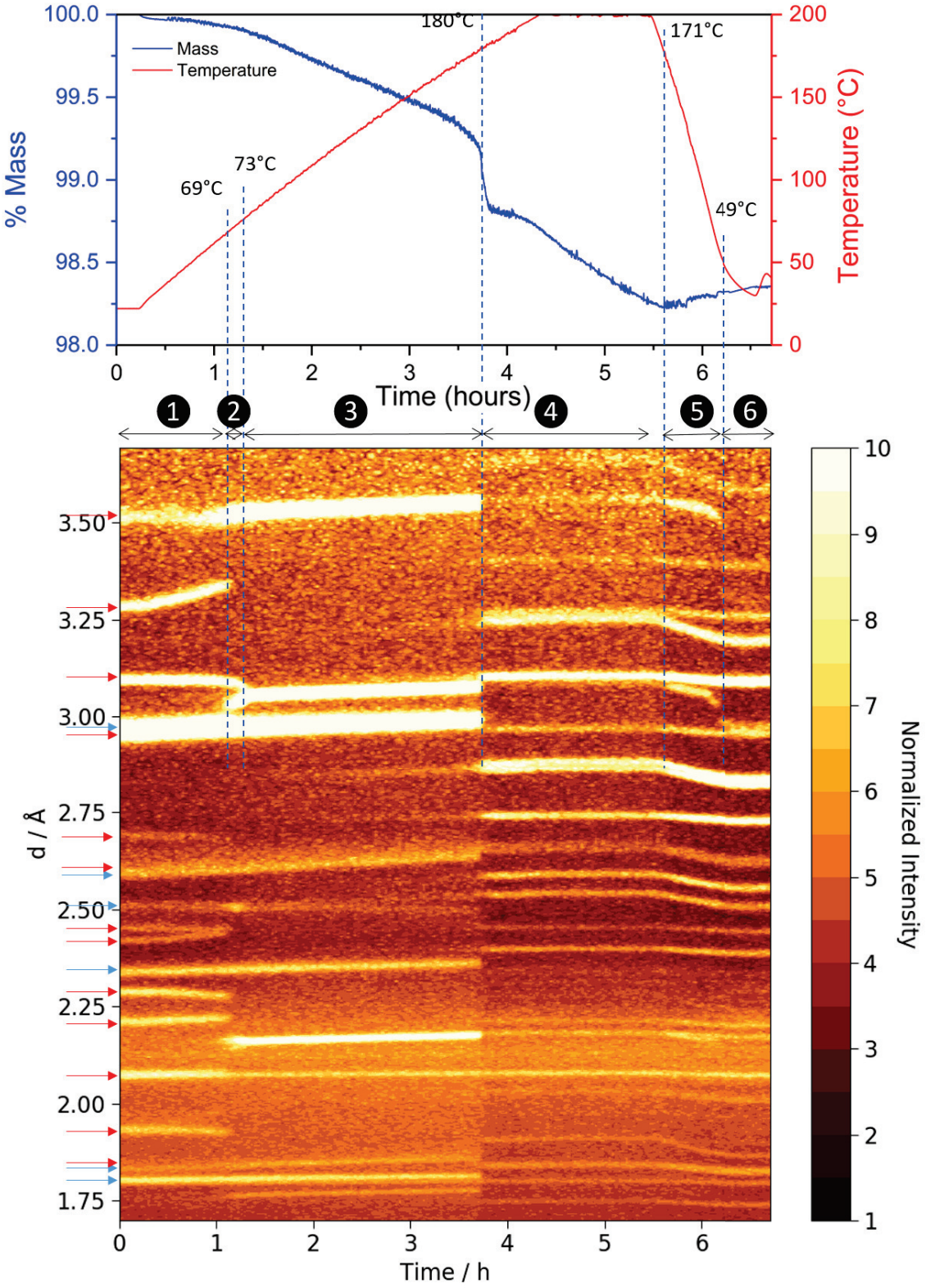


Figure 8.9: Thermogravimetric data, a bank 4 contour plot and key temperatures and regions highlighted for the $2KND_2 + Mg(ND_2)_2$ synthesis experiment. Red and blue arrows correspond to KND_2 and $Mg(ND_2)_2$ peaks respectively in the initial hour long scan

Region	Temperature Range	Run numbers	Phases present
1	RT-69°C	106945-106975	$Mg(ND_2)_2$ and monoclinic KND_2
2	69°C-73°C	106976-106982	$Mg(ND_2)_2$ and tetragonal KND_2
3	73°C-180°C	106982-107048	$Mg(ND_2)_2$ and cubic KND_2
4	180°C-200°C-171°C	107051-107102	$K_2Mg(ND_2)_4$, cubic KND_2, MgO and some unfitted peaks
5	171°C-49°C	107103-107119	$K_2Mg(ND_2)_4$, cubic KND_2, MgO and some unfitted peaks
6	49°C-RT	107120-107134	$K_2Mg(ND_2)_4$, monoclinic KND_2, MgO and some unfitted peaks

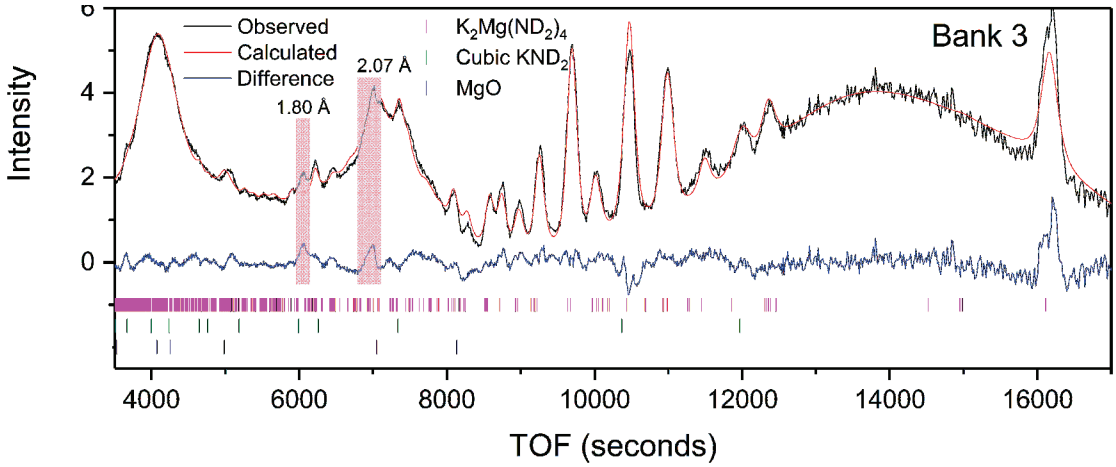
Table 8.1: Six regions for the POLARIS $2KND_2 + Mg(ND_2)_2$ synthesis experiment

At 69 °C monoclinic KND_2 undergoes a phase change to tetragonal KND_2, most clearly signified by the loss of the monoclinic KND_2 peaks at 3.29 Å (011) and 3.09 Å (002). The tetragonal KND_2 peaks at 3.52 Å (101), 3.08 Å (002), 3.04 Å (110), 2.50 Å (102), 2.15 Å (200) and 2.16 Å (112) also appear. During the monoclinic to tetragonal phase change for KND_2, a and c decrease as b and β increase during the $P2_1/m$ to $P4/_nmm$ unit cell symmetry change. This explains why the monoclinic (10-1) peak at 3.86 Å shifts to a smaller d-spacing on heating, but the (011) peak at 3.29 Å shifts to larger d-spacing as the temperature is increased.

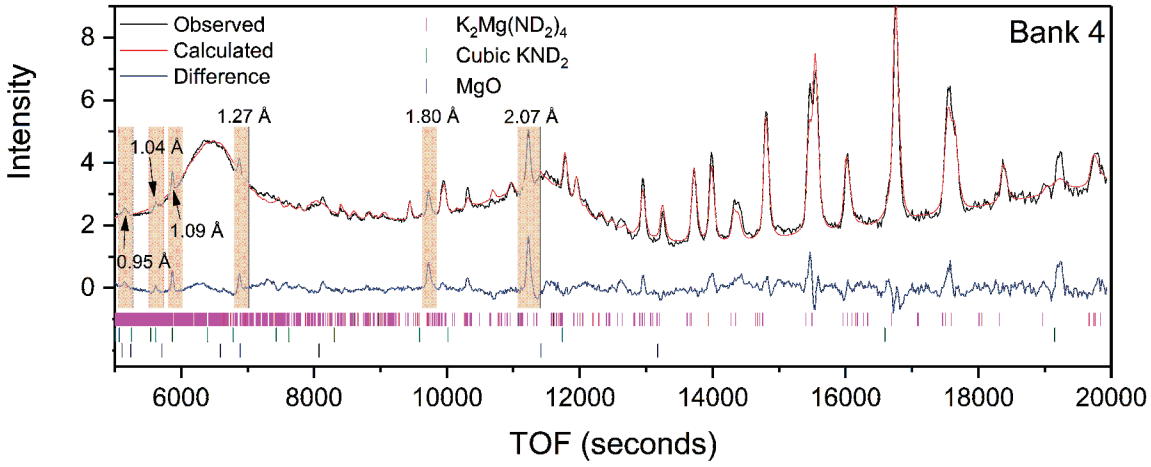
The tetragonal to cubic KND_2 phase change is visible at 73 °C which correlates well with the reported value of 75 °C [211]. This is most clearly seen by the loss of the tetragonal KND_2 peaks at 3.08 Å (002), 3.04 Å (110), 2.15 Å (200) and 2.16 Å (112) and the appearance of the cubic KND_2 peaks at 3.06 Å (200) and 2.16 Å (220).

Between 73 °C and 180 °C $Mg(ND_2)_2$ and cubic KND_2 are present and at 180 °C there is a distinct change in the contour plot as the Bragg peaks corresponding to $Mg(ND_2)_2$ and cubic KND_2 disappear and those corresponding to $K_2Mg(ND_2)_4$ appear. The STA trace for $2KNH_2 + Mg(NH_2)_2$ showed an exothermic event at 150 °C which had been attributed to the synthesis of $K_2Mg(NH_2)_4$ (Figure 8.5a). 195 °C was the reported synthesis temperature of $K_2Mg(NH_2)_4$ by Santoru et al. [245]. There is also a small amount of MgO present as indicated by the very small Bragg peaks at 2.13 Å (200) and 1.51 Å (220). This synthesis step coincides with a mass loss of 2.1 mg (0.4 %) which is most likely due to the desorption of a small amount of physisorbed gases.

In Region 4, the data from banks 3 and 4 fit well to a majority phase of $K_2Mg(ND_2)_4$ (63.9 %) with cubic KND_2 (11.7 %) and MgO (24.4 %) also present. Figure 8.10 shows the summed powder X-ray diffraction data from banks 3 and 4 for this region. An SiO_2 background has been fitted because the silica tail was used which accounts for the broad features seen in Figure 8.10. There are a few un-fitted peaks at *d*-spacings of 2.07 Å, 1.80 Å, 1.27 Å, 1.09 Å, 1.04 Å and 0.95 Å which are highlighted.



(a) Bank 3



(b) Bank 4

Figure 8.10: Summed powder X-ray diffraction data for Region 4 with un-fitted peaks highlighted

During Regions 4, 5 and 6, $K_2Mg(ND_2)_4$ is the main phase present throughout (Figure 8.9). From 171 °C on cooling (the start of Region 5), it can be seen that the cubic KND_2 peaks at *d*-spacings of 3.57 Å (111), 3.07 Å (200) and 2.17 Å (220) initially gain intensity but

then disappear at 49 °C (start of region 6) as the cubic KND_2 present in Regions 4 and 5 undergo a phase change to monoclinic KND_2 present in Region 6. This can be clearly seen from the loss of the peak at a *d*-spacing of 3.57 Å which is the cubic KND_2 (111) peak. Additionally, the cubic KND_2 (200) peak at a *d*-spacing of 3.07 Å decreases to 3.04 Å and then disappears at 49 °C as simultaneously the monoclinic KND_2 (110) peak at 2.99 Å appears which then decreases to 2.97 Å as the sample is cooled.

On cooling, during Region 5, it can be seen that the single $K_2Mg(ND_2)_4$ peak at $\sim$3.26 Å gradually separates into two peaks which end up at 3.26 Å (weak) which corresponds to the $K_2Mg(ND_2)_4$ (004) Bragg peak, and 3.19 Å (strong) which corresponds to the $K_2Mg(ND_2)_4$ (210) and (21-2) Bragg peaks.

Ex-situ powder X-ray diffraction data was collected of the final sample remaining at the end of this decomposition experiment on POLARIS and a Rietveld refinement in TOPAS showed it consisted of 89.0 % $K_2Mg(ND_2)_4$ and 11.0 % monoclinic KND_2 (Figure A.20).

8.4.2 Decomposition of $K_2Mg(ND_2)_4$

Despite the successful synthesis of $K_2Mg(ND_2)_4$ *in-situ*, a separate pre-made sample (*ex-situ*) was used to probe the decomposition of $K_2Mg(ND_2)_4$ under argon using the IGA^n. This sample was synthesised by ball-milling $2KND_2 + Mg(ND_2)_2$ and was confirmed by powder X-ray diffraction. A one hour neutron diffraction scan at room temperature was taken in a vanadium can (Figure 8.11) which fits to a majority phase of $K_2Mg(ND_2)_4$ (76.9 %), with minor phases of $Mg(ND_2)_2$ (15.8 %) and monoclinic KND_2 (7.3 %).

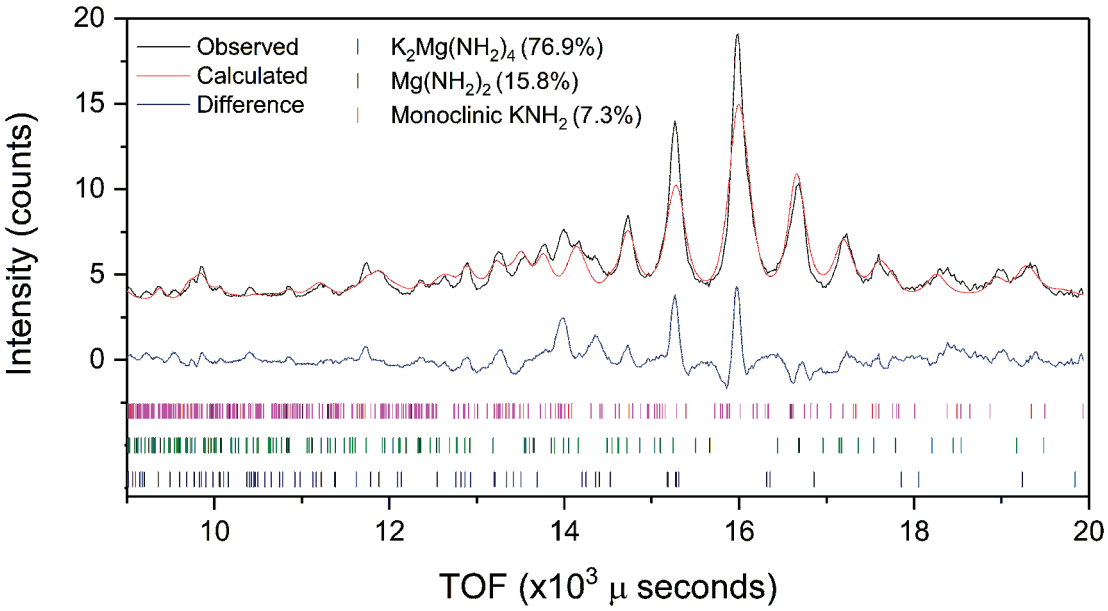


Figure 8.11: Bank 4 neutron diffraction data collected in a vanadium can of the of the fresh sample of $K_2Mg(ND_2)_4$ synthesised *ex-situ* before any *in-situ* experiments had been performed

During this decomposition experiment, the sample was heated to 300 °C so a stainless steel bucket and reactor were used, leading to the unavoidable consequence of steel peaks present throughout the experiment present as two sets of doublets, listed in Table A.12 in the Appendix.

The sample of $K_2Mg(ND_2)_4$ was heated from room temperature to 100 °C at 1 °C/min and then from 100 °C to 300 °C at 0.5 °C/min. Contour plots of the diffraction data collected from banks 2, 3, 4 and 5 for the entire experiment and the corresponding thermogravimetric data are shown in the Appendix in Figure A.21. Due to the long period for which there are no Bragg peaks, followed by an extensive period of beam off, the analysis is focused on 2 sections. The first, on heating from room temperature to 212 °C (Figure 8.12) for which the initial Bragg peaks are present, and the second section on cooling from 300 °C from after the beam off period (Figure 8.13). Figure 8.12 and Figure 8.13 show the thermogravimetric data, key temperatures and contour plots from banks 3 and 4. They also show that the overall experiment can be split into six different regions shown in Table 8.2.

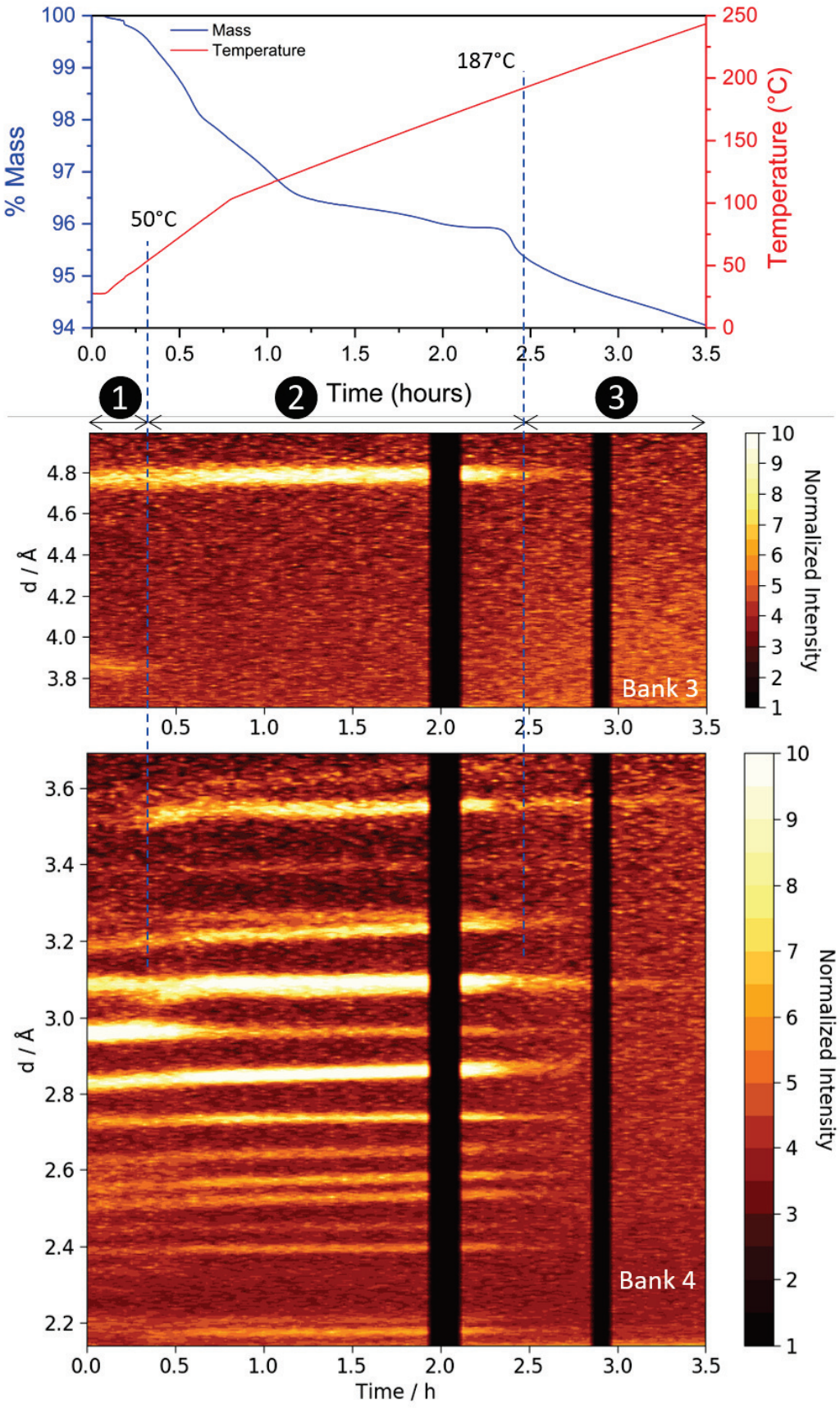


Figure 8.12: Thermogravimetric data, contour plots for banks 3 and 4 and key temperatures and regions highlighted for the first section of the $K_2Mg(ND_2)_4$ decomposition experiment

Region	Temperature Range	Run numbers	Phases present
1	RT-60°C	17606-107613	69.2 % $K_2Mg(ND_2)_4$, 11.5 % $Mg(ND_2)_2$ and 19.3 % monoclinic KND_2
2	60°C-187°C	107616-107677	71.2 % $K_2Mg(ND_2)_4$ and 28.8 % cubic KND_2
3	187°C-237°C	107679-107707	Cubic KND_2
4	260°C-186°C	107933-107939	Cubic KND_2
5	173°C	107939-107941	Unknown peaks at 3.00 Å and 3.02 Å
6	170°C-RT	107941-107923	22.5 % $K_2Mg(ND_2)_4$ and 77.5 % KND_2 cubic

Table 8.2: Six regions for the POLARIS $K_2Mg(ND_2)_4$ decomposition experiment

Figure 8.12 shows at 50 °C an annealing step happens and any un-reacted monoclinic KND_2 and $Mg(ND_2)_2$ forms $K_2Mg(ND_2)_4$. This is shown by loss of the KND_2 monoclinic peak at 3.86 Å (10-1) and a decrease in intensity of the peak at $\sim$2.9 Å due to loss of the 2.96 Å (110) $Mg(ND_2)_2$ peak and an increase in intensity of the $K_2Mg(ND_2)_4$ (022) peak at 3.08 Å. The increased intensity of the $K_2Mg(ND_2)_4$ peaks could also be as a result of recrystallisation of any amorphous $K_2Mg(ND_2)_4$ produced during the original synthesis of the sample in the ball-mill.

In Region 2, the Bragg peaks fit to $K_2Mg(ND_2)_4$ (71.2 %) and cubic KND_2 (28.8 %) and Miller indices for each *d*-spacing is listed in Table A.12 in the Appendix. The reported phases changes for KND_2 from monoclinic to tetragonal to cubic are at 53 °C [150] and 75 °C [211] respectively. These KND_2 phase changes can be seen in Figure 8.12 from the change in peak positions in the region between 3.04-3.10 Å with tetragonal KND_2 visible only briefly for 6 runs.

At 187 °C there is an increase in the rate of mass loss and a sharp decrease in the intensity of the $K_2Mg(ND_2)_4$ Bragg peaks signifying the melting of $K_2Mg(ND_2)_4$ (Figure 8.12). This is in contrast to the $2KND_2 + Mg(ND_2)_2$ synthesis experiment (Figure 8.9) in which $K_2Mg(ND_2)_4$ formed at 180 °C and was present from this temperature throughout the remainder of the experiment up to the peak temperature of 200 °C and on cooling back down to room temperature. In this $K_2Mg(ND_2)_4$ decomposition experiment, $K_2Mg(ND_2)_4$ begins to melt at 187 °C so that by 236 °C there are only Bragg peaks corresponding to cubic KND_2 present.

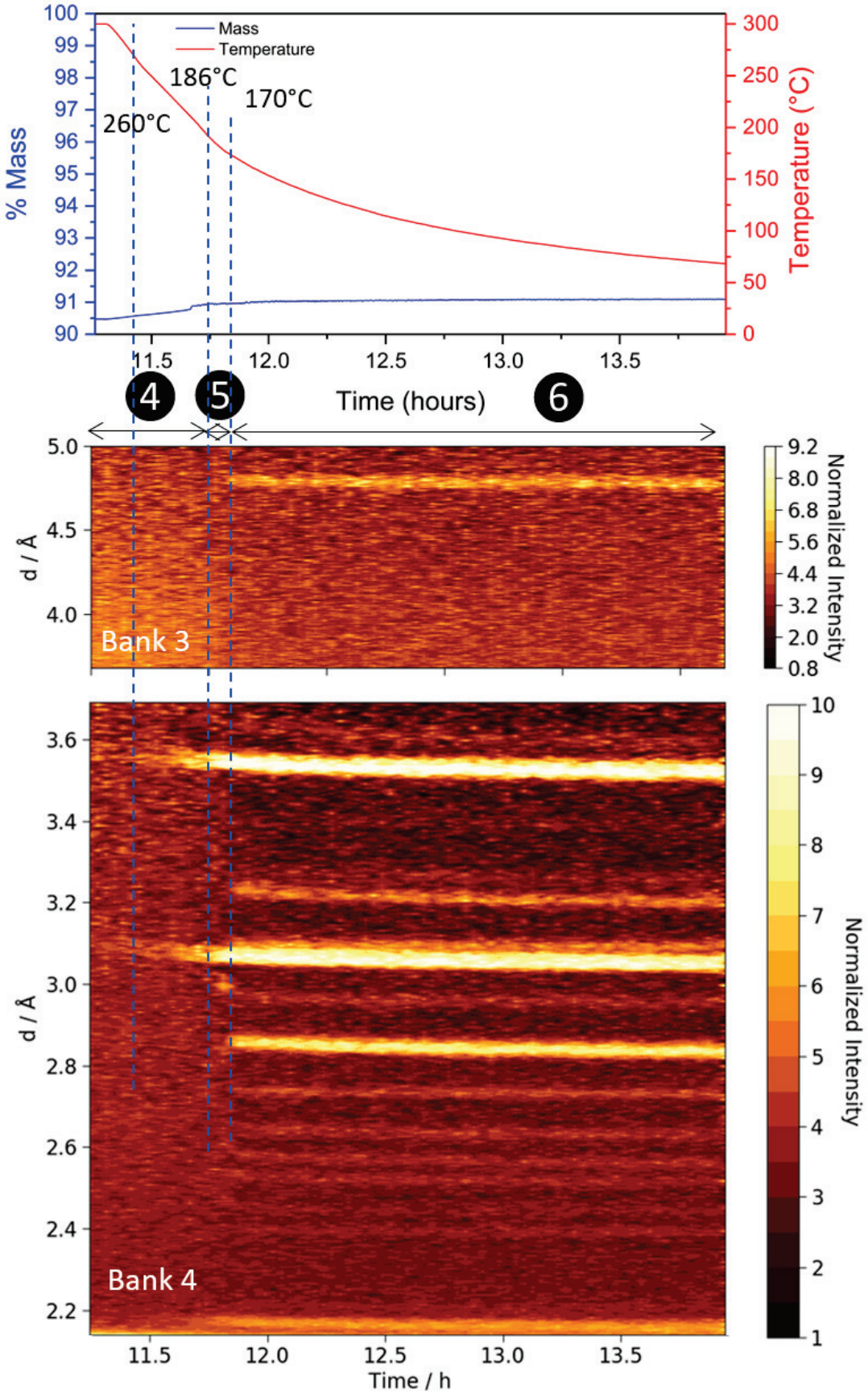


Figure 8.13: Thermogravimetric data, contour plots for banks 3 and 4 and key temperatures and regions highlighted for the second section of the $K_2Mg(ND_2)_4$ decomposition experiment

Figure 8.13 shows that on cooling, at ∼260 °C Bragg peaks according to KND_2 start to appear. At 186 °C, for 3 runs, there are faint Bragg peaks that appear at 3.00 Å and 3.02 Å. Tetragonal KND_2 has two peaks in this region compared to only one seen for either cubic KND_2 or monoclinic KND_2 but a temperature of 186 °C is much too high for tetragonal KND_2 to be observed. It is only once these peaks at ∼3.00 Å disappear that Bragg peaks corresponding to $K_2Mg(ND_2)_4$ re-appear at 170 °C as this phase re-crystallises. Region 6 fits to 22.5 % $K_2Mg(ND_2)_4$ and 77.5 % cubic KND_2. It appears that the mixed amide-imide phase $KMg(ND_2)(ND)$ did not form during this experiment, perhaps unsurprising as the experiment was only heated to 300 °C and previously $KMg(NH_2)(NH)$ has been observed to form above this temperature.

Ex-situ powder X-ray diffraction data was collected of the final sample remaining at the end of this decomposition experiment on POLARIS and a Rietveld refinement in TOPAS showed it consisted of 44.2 % $K_2Mg(ND_2)_4$ and 55.8 % monoclinic KND_2 (Figure A.22 in the Appendix).

During this experiment $K_2Mg(ND_2)_4$ melted on heating at 187 °C and recrystallised on cooling at 170 °C despite being heated to 300 °C. Crucially this is the first mixed-metal system for which the mixed-metal amide itself was recovered after the experiment. The intra Group 1 mixed-metal amides studied, melted and irreversibly separated to ultimately form a combined molten phase of the two constituent amides. The fact that the $K_2Mg(NH_2)_4$ is recoverable post experiment despite being heated to 300 °C suggests it is the most stable mixed-metal amide studied so far which is advantageous for catalysis.

Figure 8.12 and Figure 8.13 show that during the decomposition experiment under argon the final mass was 90.5 % of the starting mass. Loss of one formula unit of ND_3 from the system would correspond to a mass loss of 11 % but it is more likely that the mass loss observed is due to a combination of the sample melting out of the IGA^n bucket and the desorption of physisorbed gases rather than the mass loss being associated with decomposition.

Comparing the composition of the initial sample before heating, to the sample that recrystallises and is recovered on cooling, shows that the percentage of $K_2Mg(ND_2)_4$ has decreased and that of KND_2 has increased. This suggests that on heating the sample retains

the $K_2Mg(ND_2)_4$ crystal structure but gradually looses the fully amide composition as the decomposition to $KMg(NH_2)(NH)$ partially occurs (Equation 8.1) and KND_2 is produced. This is consistent with the STA experiment (Figure 8.5) which showed $KMg(NH_2)(NH)$ only crystallised right at the end of the mass loss and at a much higher temperature. This is supported by a change in the lattice parameters between the $K_2Mg(ND_2)_4$ structure on heating and the $K_2Mg(ND_2)_4$ structure that is observed to recrystallise on cooling at 170 °C. At comparable temperatures the *a*, *b* and *c* lattice parameters have decreased by 1-1.5 % which is indicative of a sample with the same structure but with a slightly different composition, showing that $K_2Mg(ND_2)_4$ can support a degree of stoichiometry variation as KND_2 is lost from the structure. This percentage variation is a similar size to that observed in $Li_3Na_{(1-x)}(NH_2)_{(4-x)}$ compared to $Li_3Na(NH_2)_4$ [189].

8.5 Inert gas summary

In depth analysis of the thermal decomposition of these materials under inert gas is used as a basis for understanding how these systems perform as NH_3 decomposition catalysts. Figure 8.14 shows the superposition of key results from the experiments performed under inert gas for the K-Mg-N-H which have already been discussed.

The low temperature behaviour of the samples was probed through the DSC traces recorded on the STA machine as the samples were heated to 400 °C. The high temperature thermal decomposition behaviour was analysed through the percentage mass loss recorded on the IGA^n and the MS signal of the outlet gas flow recorded on the gas flow panel as the samples were heated to 475 °C. The onset and peak temperatures of these decomposition events may differ slightly for the three traces due to the different conditions (sample size, heating rate and reaction pressure) used during the studies, but correlations can still be observed.

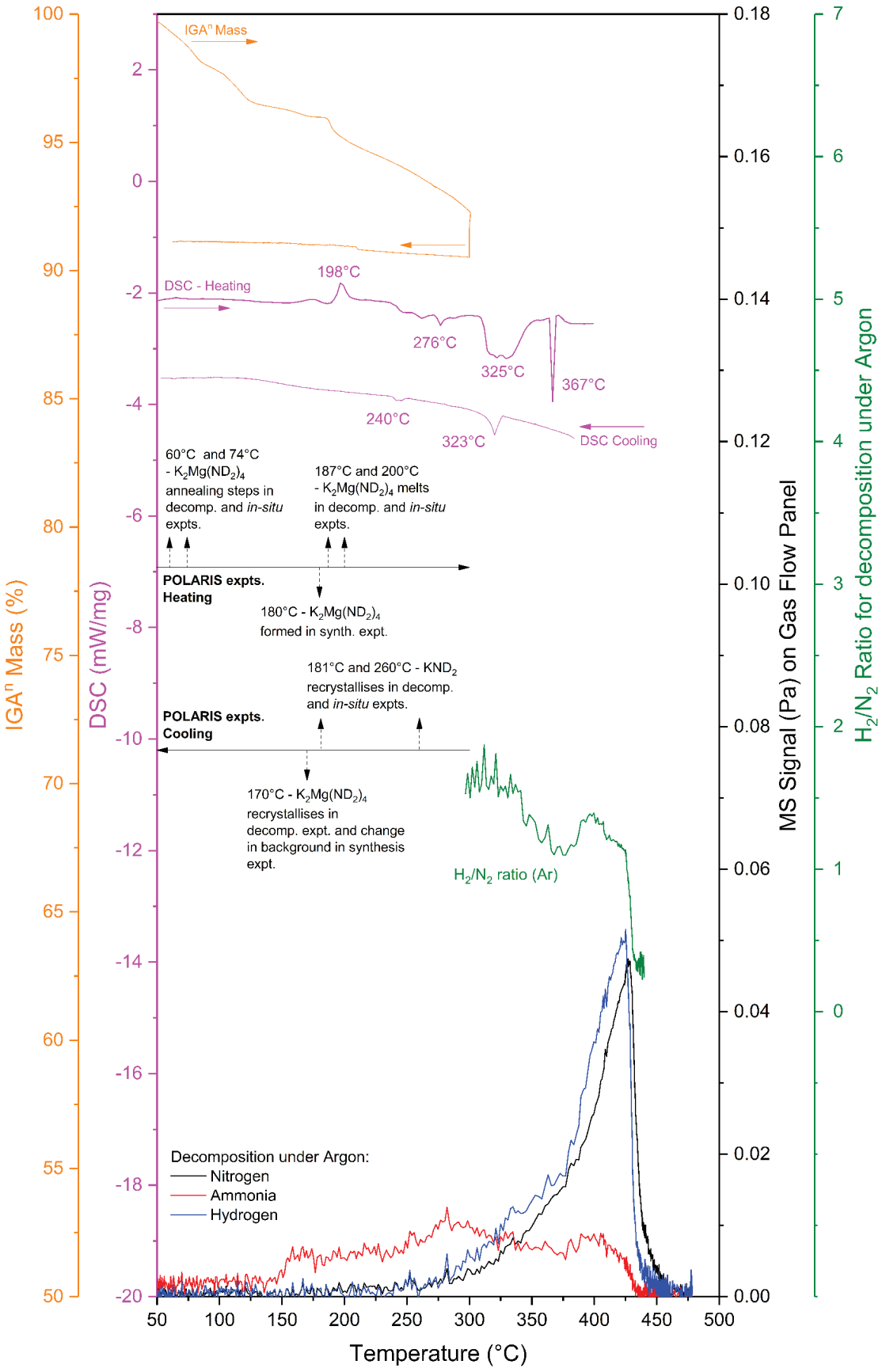


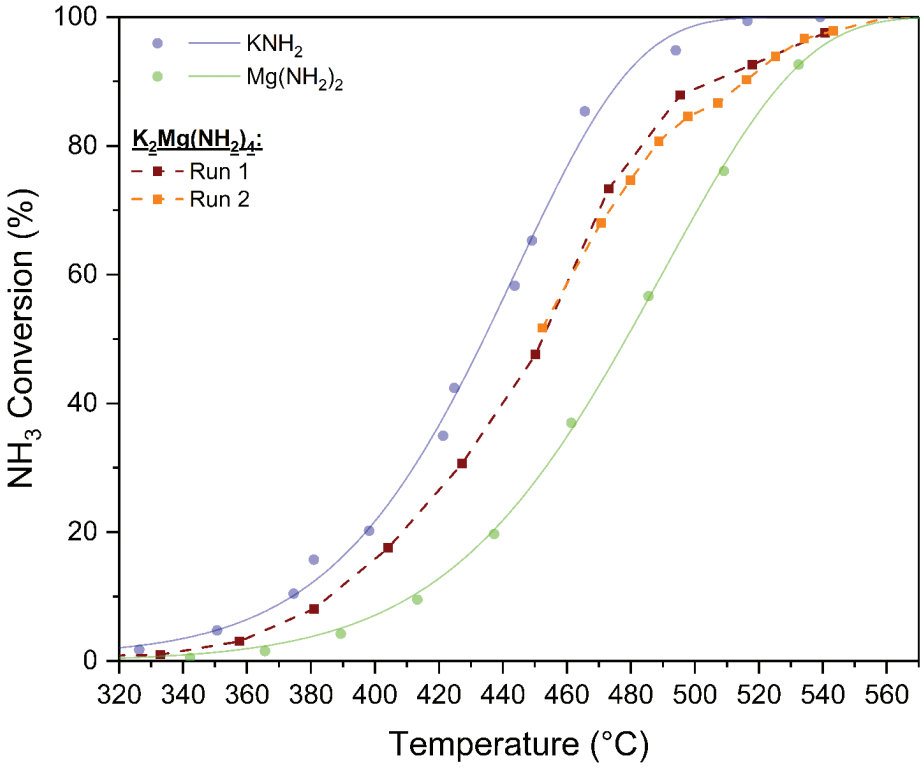
Figure 8.14: Thermodynamic properties measured during the decomposition of $K_2Mg(NH_2)_4$ under inert gas

8.6 Ammonia decomposition (*ex-situ*)

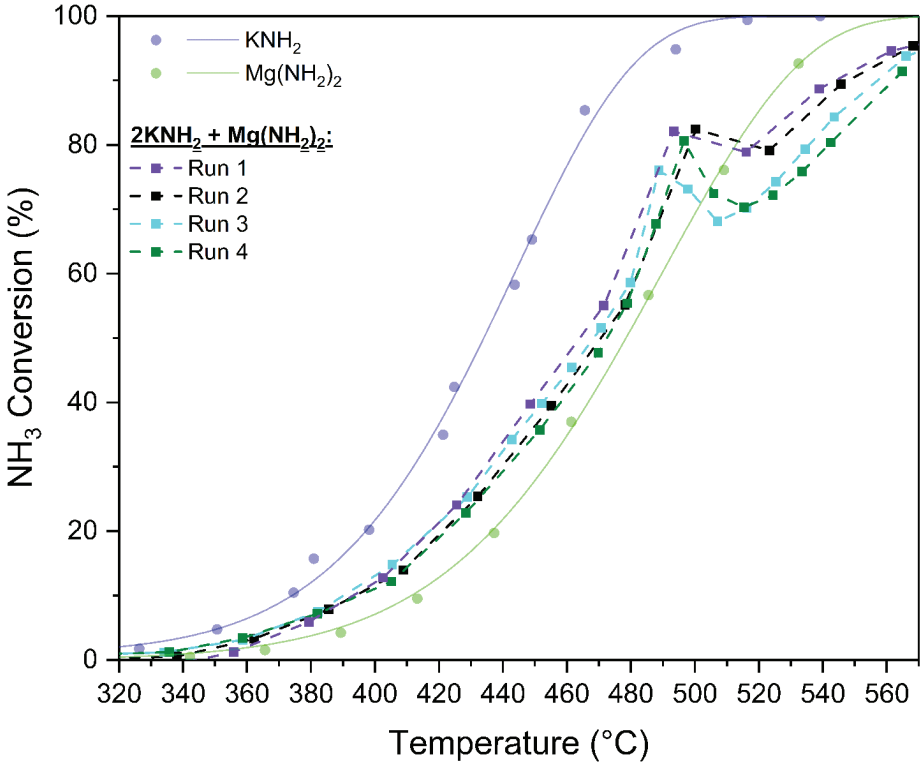
The NH_3 decomposition ability of the K-Mg-N-H, and Na-Mg-N-H systems (Chapter 9), are of particular chemical interest due to the potential novel mixed amide-imide phases ($KMg(NH_2)(NH)$ and $NaMg(NH_2)(NH)$) (Equation 8.1) which may provide stabilisation of the tetra-amides to the temperatures required for NH_3 decomposition. Previously studied ternary imides are considered to behave as a combination of the two imide components [196]. However, as $K_2Mg(NH_2)_4$ has been shown to recrystallise as the mixed-metal amide despite being heated to 300 °C (Figure 8.13) these new systems may offer a divergence from a simple superposition as they may not separate into the constituent single metal amides.

8.6.1 Quantitative fitting and analysis

Ammonia conversion efficiencies of these materials were analysed for 0.5 g of the catalyst powder in a reactor, attached to the gas flow panel as described in Section 2.2.1.1 and Section 2.3. The temperature was varied for a given ammonia inlet flow (60 sccm) whilst the out gas from the sample cell was monitored by mass spectrometry using the Quantitative Gas Analyser described in Section 2.3. Conversion efficiencies were calculated using a customised computer program by determining the ammonia signal as a percentage of the total signal [310].



(a) $K_2Mg(NH_2)_4$



(b) $2KNH_2 + Mg(NH_2)_2$

Figure 8.15: Ammonia decomposition ability of the K-Mg-N-H system as potential catalysts on the gas flow panel

Figure 8.15 shows the ammonia conversion percentages calculated from the MS data for the K-Mg-N-H system. Figure 8.15a shows the NH_3 decomposition ability of the pre-formed mixed-metal amide $K_2Mg(NH_2)_4$ and Figure 8.15b shows the analogous behaviour of ground-up mixtures of $2KNH_2 + Mg(NH_2)_2$. Results for equivalent masses of pure KNH_2 and $Mg(NH_2)_2$ have been included for comparison.

The plotted points are the recorded experimental results and the lines of best fit for KNH_2 and $Mg(NH_2)_2$ have been drawn using the two process sigmoidal Gompertz function (Equation 3.4) with the parameters listed in Table 8.3 which were themselves generated using the sigmoid fit calculated in TOPAS (Section 3.5.1).

Figure 8.15b shows that the data points for $2KNH_2 + Mg(NH_2)_2$ have a bump in the NH_3 decomposition activity between 480 °C and 520 °C which has not been seen in any of the previously studied systems. This is a relatively large temperature range and has been repeatedly seen in all four experimental runs. Qualitatively it can be seen that if all the data points for $2KNH_2 + Mg(NH_2)_2$ are included, they do not form sigmoid shaped curves which would mean the sigmoid fit could not be calculated in TOPAS.

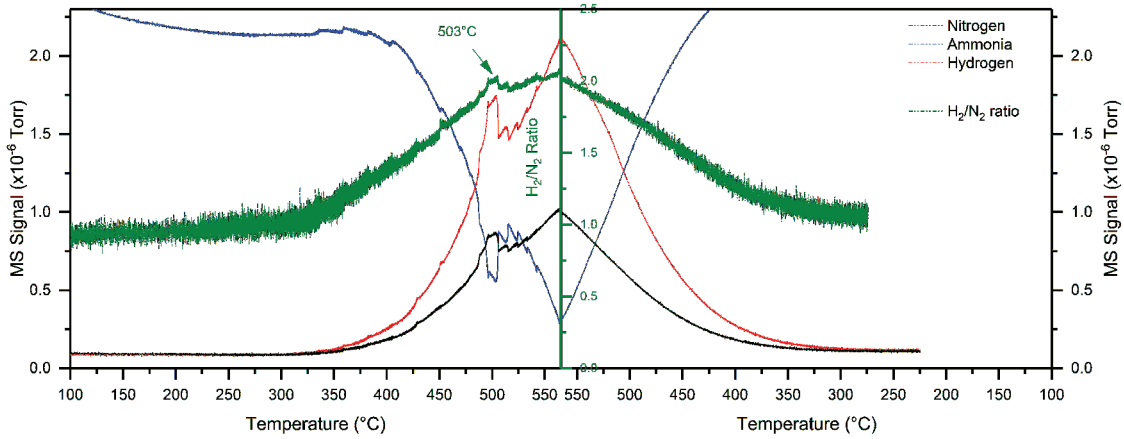


Figure 8.16: Raw MS data for the decomposition of $2KNH_2 + Mg(NH_2)_2$ experiment - Run 4

However, if the raw MS data is analysed for the $2KNH_2 + Mg(NH_2)_2$ experiments (shown in Figure 8.16 for the "Run 4" experiment), it can be seen that there is an additional release of H_2 and N_2 from the samples between 485 °C and 515 °C. During this temperature range, there is clearly some transformation occurring within the catalyst itself which involves a

release of H_2 and N_2, in addition to the NH_3 being decomposed catalytically, which is leading to an inflated conversion.

If the initial $2KNH_2 + Mg(NH_2)_2$ formed $K_2Mg(NH_2)_4$ under NH_3, this additional gas release could be due to the subsequent decomposition of $K_2Mg(NH_2)_4$ to $KMg(NH_2)(NH)$ as this is accompanied by the release of NH_3. However, this effect is not observed for the pre-formed $K_2Mg(NH_2)_4$ samples as it is only present to a very small degree in one of the runs ("Run 2" in Figure 8.15a).

It is therefore much more likely that this additional gas release is arising from unreacted $Mg(NH_2)_2$ starting material decomposing to Mg_3N_2 (Equation 8.2). KNH_2 decomposes to K metal with release of H_2 and N_2 (Equation 4.1), but under NH_3 this is only one component of the catalytic cycle, so net gas release is not expected. However, decomposition of $Mg(NH_2)_2$ to Mg_3N_2 is an irreversible transformation resulting in net NH_3 gas release, and this is then being cracked to the observed H_2 and N_2. The points observed in Figure 8.15 can therefore be thought of as two curves merged together, those representing the ability of KNH_2 and $Mg(NH_2)_2$ to decompose ammonia.

If the data points in Figure 8.15 between 485 °C and 515 °C are ignored, this would leave only the data points corresponding to the underlying conversion, which does indeed form a smooth line (Figure 8.17). Sigmoid fits can therefore be calculated in TOPAS and the T_e, E_A and "constant" values are shown in Table 8.3. Uncertainties for T_e and E_A are estimated to be on the order of ± 2 °C and ± 3 kJ/mol respectively.

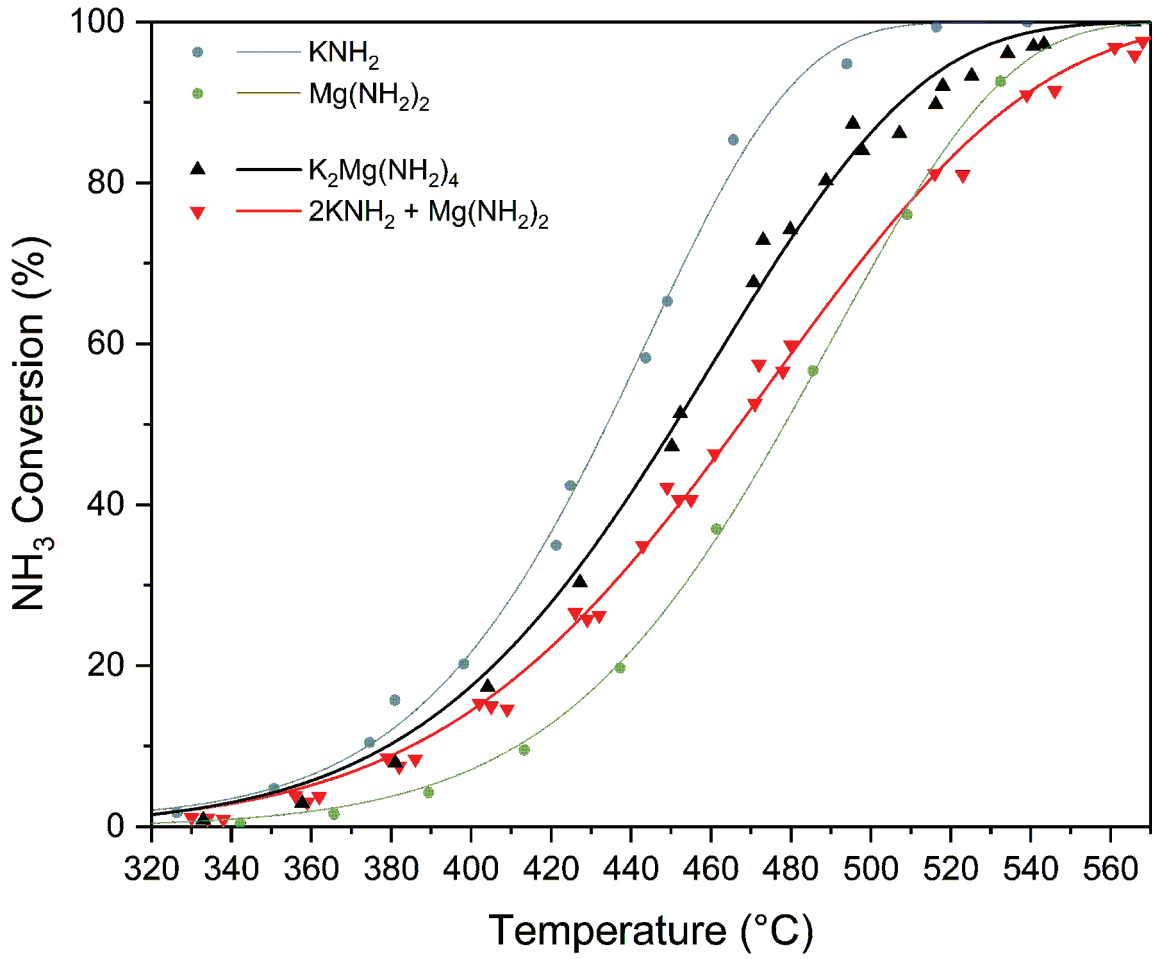


Figure 8.17: Ammonia decomposition ability of $K_2Mg(NH_2)_4$ and $2KNH_2 + Mg(NH_2)_2$ as potential catalysts on the gas flow panel

	Constant	T_e (°C)	E_A (kJ/mol)	Recovery by mass (%)
Blank	0.000(1)	547	102	n/a
KNH_2	0.009(2)	449	132	25
$Mg(NH_2)_2$	0.000(2)	500	144	60
$K_2Mg(NH_2)_4$	0.000(1)	471	108	89
$2KNH_2 + Mg(NH_2)_2$	0.000(2)	494	96	32

Table 8.3: K-Mg-N-H system Gompertz curve output values. Uncertainties for T_e and E_A are estimated to be on the order of ± 2 °C and ± 3 kJ/mol respectively and have been calculated from the TOPAS fitting process

Analysing the NH_3 decomposition ability of the single metal amides alone, it can be seen that KNH_2 is a higher performing NH_3 decomposition catalyst and has a steeper curve (indicative of higher activation energy) than $Mg(NH_2)_2$. Although $K_2Mg(NH_2)_4$ is not known to separate into KNH_2 and $Mg(NH_2)_2$, Figure 8.15a shows that the NH_3 decomposition ability of $K_2Mg(NH_2)_4$ is between that of KNH_2 and $Mg(NH_2)_2$ at all temperatures. However, it is more similar to that of KNH_2, as expected given KNH_2 and $Mg(NH_2)_2$ are still present in a 2:1 ratio, just as the mixed-metal amide rather than in a molten phase of the individual amides.

The NH_3 decomposition ability of $2KNH_2 + Mg(NH_2)_2$ is quite different to that of $K_2Mg(NH_2)_4$ which contrasts the behaviour seen for all the intra Group 1 mixed-metal systems for which there was very little difference between the traces of the pre-formed mixed-metal amides and the ground-up mixtures of the constituent single metal amides in the relevant ratios. The intra Group 1 mixed-metal systems were considered to separate and melt into the constituent single metal amides and it was this combined melt that decomposed NH_3, (so the same melt phase was present regardless of the initial material present in the reactor), this separation does not occur for $K_2Mg(NH_2)_4$.

It is clear that the material present in the reactor for the $K_2Mg(NH_2)_4$ and $2KNH_2 + Mg(NH_2)_2$ experiments is not the same at the temperatures required for NH_3 decomposition, as they are not behaving in the same way with respect to NH_3 decomposition. This supports the possibility that under NH_3, $2KNH_2 + Mg(NH_2)_2$ has not reacted fully, if at all, to form $K_2Mg(NH_2)_4$ and therefore there is some $Mg(NH_2)_2$ remaining in the reactor which is known to be a low performing NH_3 decomposition catalyst. The sigmoid for the $2KNH_2 + Mg(NH_2)_2$ experiment is more similar to that of $Mg(NH_2)_2$ than to that of $K_2Mg(NH_2)_4$.

The NH_3 decomposition ability of $K_2Mg(NH_2)_4$ is better than that of $2KNH_2 + Mg(NH_2)_2$ which is reflected by the different shaped curves observed in Figure 8.17 and the different T_e and E_A values in Table 8.3. There is therefore a requirement to pre-form $K_2Mg(NH_2)_4$ if it is to be used as an NH_3 decomposition catalyst.

8.6.2 Catalyst Recovery

Recovery of KNH_2 and $Mg(NH_2)_2$ are 25 % and 60 % respectively, but $K_2Mg(NH_2)_4$ shows a high mass recovery rate of 89 %, possibly due to stabilisation provided by the amide-imide complex $KMg(NH_2)(NH)$. KNH_2 melts at 338 °C and decomposes to K metal which is hard to contain due to its high volatility.

The experiment starting with $2KNH_2 + Mg(NH_2)_2$ shows a recovery of 32 %. If these single metal amides were present in this ratio, not interacting and were to show the same percentage recoveries as observed alone, an overall recovery of 37 % would be expected. This therefore supports the fact that $2KNH_2 + Mg(NH_2)_2$ does not form $K_2Mg(NH_2)_4$ under NH_3, so decomposition during this experiment is effectively a superposition of that seen for KNH_2 and $Mg(NH_2)_2$ separately.

8.7 Decomposition under ammonia

Figure 8.16 and Figure 8.18 show the raw data from the outlet gas flow of the MS traces for the decomposition of ammonia on the gas flow panel for $2KNH_2 + Mg(NH_2)_2$ and $K_2Mg(NH_2)_4$ respectively. Analysis of these MS traces provides important insights into what the active form of the catalyst is at the temperatures of interest for NH_3 decomposition.

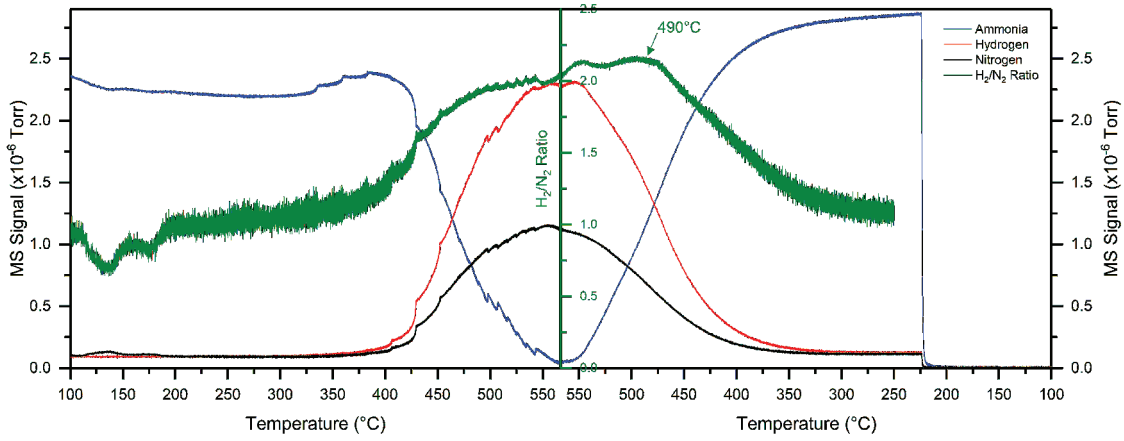


Figure 8.18: Raw MS data for the decomposition of $K_2Mg(NH_2)_4$ on the gas flow panel under ammonia

The analogous traces for the intra Group 1 system showed peaks in the H_2/N_2 ratios on cooling which corresponded to extra H_2 (relatively less N_2) due to the reformation of some $NaNH_2$ and/or KNH_2 from Na and/or K (the reverse of Equation 4.1). Figure 8.18 shows a peak on cooling in the H_2/N_2 ratio at 490 °C which could correspond to the reformation of KNH_2 from K. However, Figure 8.16 does not show a peak in the H_2/N_2 ratio on cooling suggesting during this experiment there is a different decomposition pathway.

8.8 POLARIS experiment - Ammonia decomposition (*in-situ*)

Having analysed and investigated the ability of the K-Mg-N-H system to decompose ammonia *ex-situ* on the gas flow panel, the *in-situ* sample stick was used to simulate ammonia decomposition conditions on POLARIS. Analysing the ND_3 decomposition ability of $K_2Mg(ND_2)_4$ *in-situ* enables the identification of any structural changes in the catalyst throughout the experiment to help determine the active form of the $K_2Mg(ND_2)_4$ catalyst under ND_3 decomposition conditions.

Despite the commercial importance of mixed light metal amide catalysts, only the NH_3 decomposition ability of $LiND_2$ [198, 296] and $Li_2Ca(ND)_2$ [196] have been investigated *in-situ*. The chemical transformations of amide materials under ammonia are intimately related to their activity as NH_3 decomposition catalysts and the lack of any *in-situ* data on the crystalline structure and amide-imide ratio of these systems under ammonia decomposition conditions precludes understanding the optimal catalyst composition. Monitoring ND_3 conversion efficiency *in-situ* will enable identification of the microstructure and phase composition as an *in-situ* probe is the most reliable means for determining the active state of the system.

The experimental set-up is described in Section 2.6.3.4. 3 g of a pre-made $K_2Mg(ND_2)_4$ sample (*ex-situ*) was loaded into the cylindrical through-flow cell in an argon-filled glove bag (Figure 2.13). ND_3 flows into the stainless steel through-flow cell via a pipe which extends 14.5 mm down from the top of the cell into the cell volume, and out through a hole in the top of the cell. This minimises the potential for a blockage of the cell and enables maximum exposure of the sample to flowing ND_3 gas.

The sample cell was attached to the same gas delivery panel used in the *ex-situ* ammonia decomposition experiments (Section 2.2.1.1) and was equipped with Ar and ND_3. The *in-situ* sample stick was placed within the standard furnace housed in the POLARIS sample tank and an initial 1 hour diffraction dataset was collected at room temperature under flowing Ar (20 sccm). Neutron diffraction data were collected in 100 second intervals as the sample was heated under flowing argon before being exposed to ND_3 at 400 °C. Neutron powder diffraction datasets were collected of the as prepared sample (Figure 8.11) and the recovered sample post-experiment (Figure A.23) in 8 mm i.d. vanadium cans over 3 hours each at room temperature.

$K_2Mg(ND_2)_4$ was initially heated under argon to 400 °C at which point it was exposed to ND_3 (at 550 minutes) as it was further heated to a peak temperature of 480 °C as the rate of ND_3 decomposition was analysed (Figure 8.21). The system was heated under argon rather than ND_3 because if $K_2Mg(ND_2)_4$ was unstable, it would decompose to form $KMg(ND_2)(ND)$. It would then be $KMg(ND_2)(ND)$ that would be exposed to ND_3 to explore how this behaves as an ammonia cracking catalyst. Previous *in-situ* experiments have shown issues arising from melting amides under ND_3 which then block up the system [198, 296].

Figure A.24 in the Appendix shows contour plots for banks 2, 3, 4 and 5 for the whole experiment and Figure A.25 in the Appendix shows the MS data and temperature profile alongside the contour plot from the bank 4 data for the whole of the experiment. Figure 8.19 shows the MS data, temperature profile, and the bank 4 and bank 2 contour plots for the first part of the experiment (up to 238 °C) as this is the only temperature range for which Bragg peaks are present.

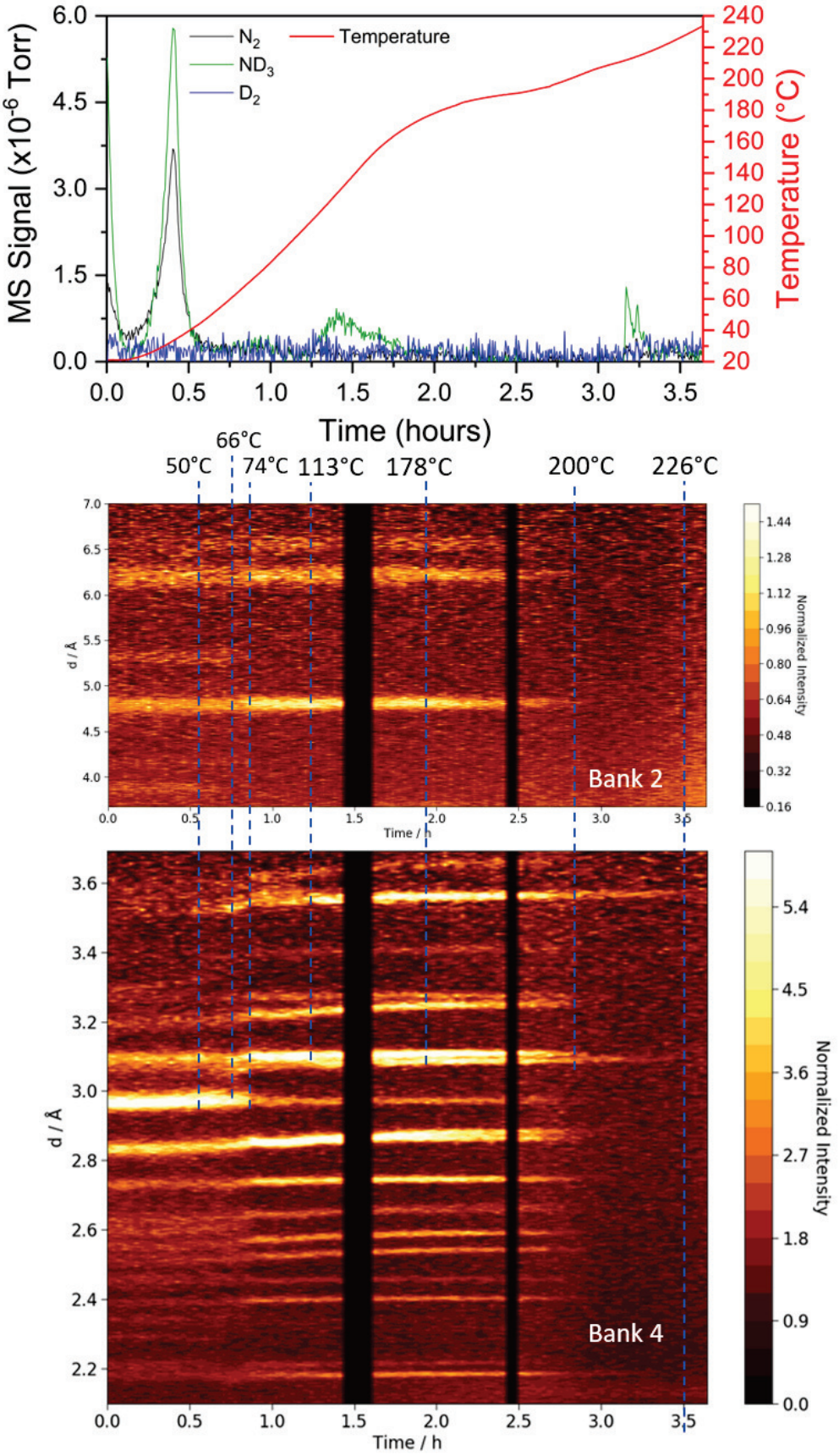


Figure 8.19: Mass spectrometry data, temperature profile and the bank 4 and bank 2 contour plots for the first part of the $K_2Mg(ND_2)_4$ ND_3 decomposition experiment

Analysis of the diffraction data shown in Figure 8.19 is very similar to that in Figure 8.12 from the *in-situ* decomposition experiment under argon, which is unsurprising as the experiments are analogous apart from the equipment used. The initial neutron diffraction data collected in a vanadium can (one hour at room temperature) (Figure 8.11) for the "fresh" sample synthesised *ex-situ* in the ball-mill fits to a majority phase of $K_2Mg(ND_2)_4$ (76.9 %), with minor phases of $Mg(ND_2)_2$ (15.8 %) and monoclinic KND_2 (7.3 %).

From Figure 8.19 it can be seen that from room temperature to 50 °C a release of ND_3 and N_2 is seen in the MS data. At 66 °C the phase change of monoclinic KND_2 to tetragonal KND_2 can be seen, most clearly from the appearance of the tetragonal KND_2 (110) peak at 3.05 Å (in addition to the tetragonal KND_2 (002) peak at 3.09 Å and the (022) peak $K_2Mg(ND_2)_4$ at 3.10 Å. At 74 °C the phase change of tetragonal KND_2 to cubic KND_2 is observed; the peak at 3.52 Å (tetragonal KND_2 (101)) shifts to 3.54 Å (cubic KND_2 (111)) and the cubic KND_2 (200) peak appears at 3.10 Å. This occurs alongside an annealing step as seen in the POLARIS experiment looking at the decomposition of $K_2Mg(ND_2)_4$ under argon (Figure 8.12 at 60 °C). Peaks corresponding to any un-reacted $Mg(ND_2)_2$ starting material disappear (the $Mg(ND_2)_2$ (224) peak at 2.97 Å looses intensity) and Bragg peaks corresponding to $K_2Mg(ND_2)_4$ sharpen. Additional $K_2Mg(ND_2)_4$ peaks (3.62 Å (200), 3.40 Å (021) and 3.26 Å (004)) become visible as the sample gains crystallinity because initial synthesis in the ball-mill is likely to have led to a degree of amorphisation. From 74 °C to 200 °C it is $K_2Mg(ND_2)_4$ and cubic KND_2 that are present.

Figure 8.20 shows that there are peaks (which start to appear at about 180 °C) located at *d*-spacings of 3.41 Å, 2.14 Å, 1.52 Å, 1.24 Å, 0.96 Å, 0.87 Å which remain present for the remainder of the experiment. These unfitted peaks are observed in banks 3, 4 and 5 in addition to the strong steel peaks located at *d*-spacings of 2.09 Å, 1.81 Å, 1.28 Å, 1.09 Å, 1.17 Å, 1.05 Å (the geometry of the *in-situ* cell means that only bank 4 does not directly have steel peaks). These unknown peaks do not correspond to BN (from the boron-nitride collimation shell), Gd (from the gadolinium shielding) or steel (from the steel *in-situ* reactor).

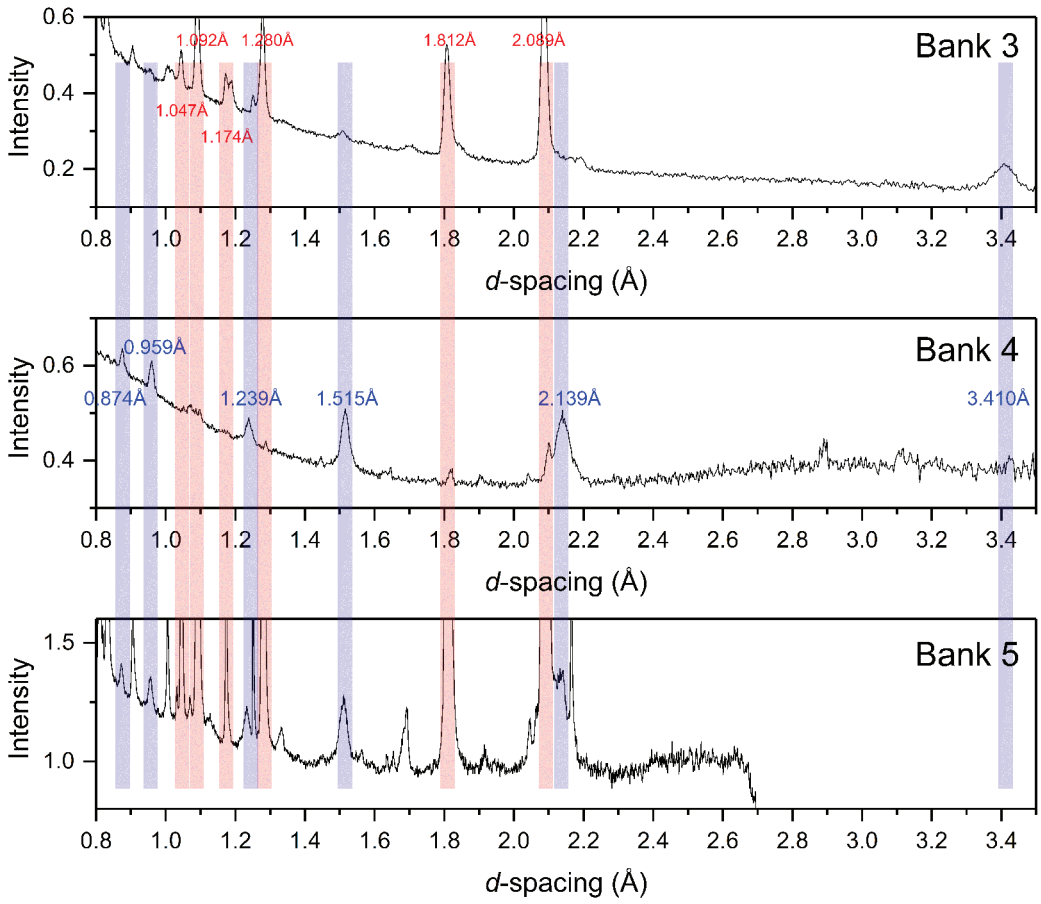


Figure 8.20: Summed patterns for Banks 4 and 5 between 300 °C on heating and 200 °C on cooling where blue bands denote unknown peaks and red bands denote steel peaks

Figure 8.19 shows that at 200 °C $K_2Mg(ND_2)_4$ melts and it is cubic KND_2 and the unknown peaks highlighted in Figure 8.20 that are left visible in the contour plot. In the POLARIS experiment looking at the decomposition of $K_2Mg(ND_2)_4$ under argon (Figure 8.12), $K_2Mg(ND_2)_4$ was seen to melt at 187 °C and the STA trace for pre-formed $K_2Mg(NH_2)_4$ showed it melted at 198 °C (Figure 8.5b). However, the POLARIS experiment looking at the synthesis of $K_2Mg(ND_2)_4$ under argon (Figure 8.9) showed $K_2Mg(ND_2)_4$ was stable up to 200 °C (the peak temperature reached in the experiment). Figure 8.19 shows at 226 °C, KND_2 melts and there is a small ND_3 release associated with this step and from this temperature, it is only the unknown peaks that are present in the contour plots for the remainder of the experiment. Cubic KND_2 was seen to melt at 237 °C in the POLARIS experiment looking at the decomposition of $K_2Mg(ND_2)_4$ under argon (Figure 8.12).

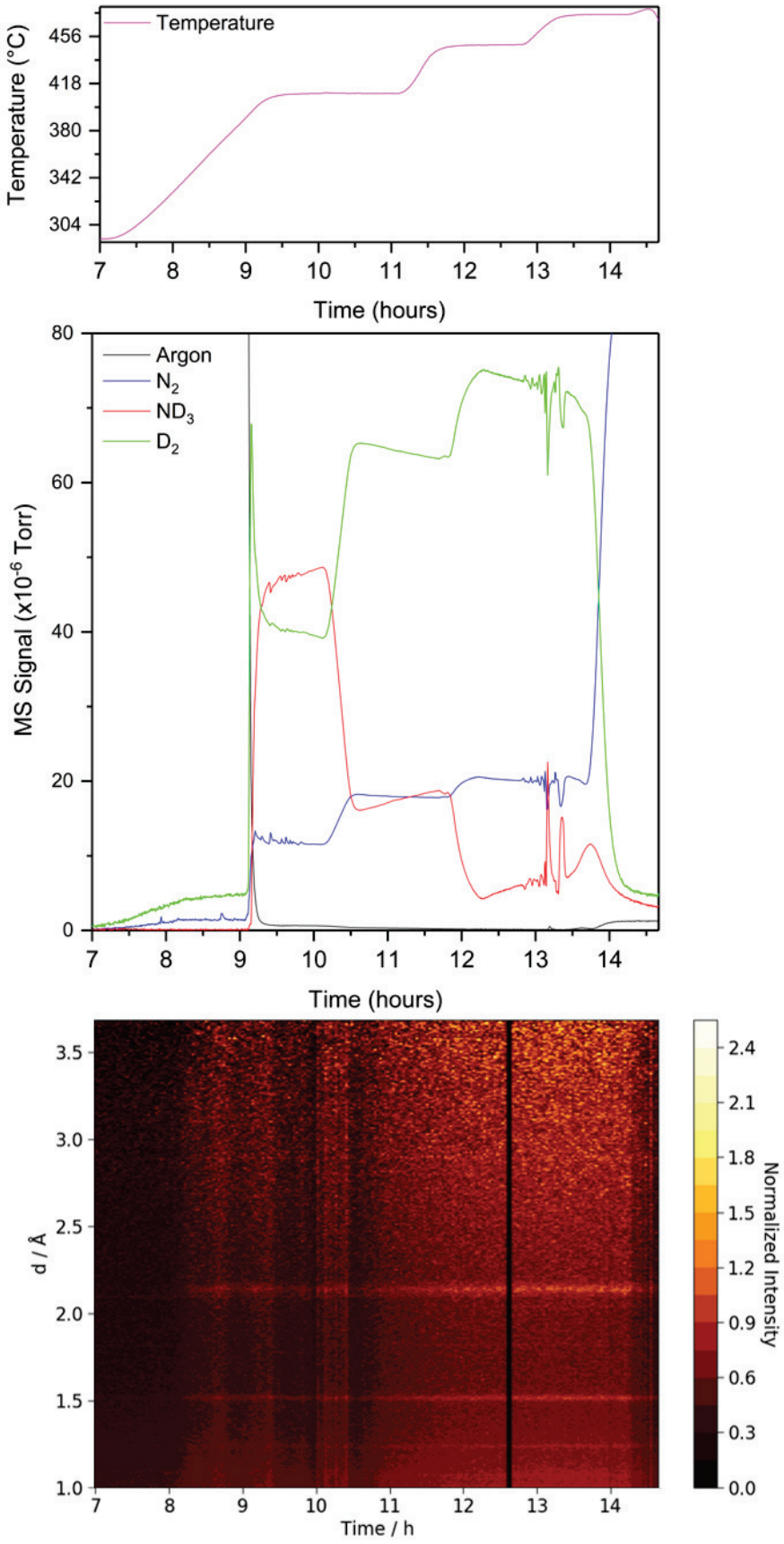


Figure 8.21: Temperature, MS trace and Bank 4 contour plot for the portion of the experiment under ND_3 decomposition conditions

Figure 8.21 shows that at 290 °C (7 hours) N_2 and D_2 start to be given off whilst the sample is still being heated under argon. This is consistent with the onset decomposition temperature seen in Figure 8.6 of 275 °C when the decomposition of $K_2Mg(NH_2)_4$ was investigated on the gas flow panel under argon *ex-situ*. When the sample reaches 400 °C, the gas was switched and the sample was held at 410 °C under ND_3 for 80 minutes. It was then heated at 1 °C/min to 450 °C where it was held for 70 minutes before being heated at 1 °C/min to 475 °C where it was held for 60 minutes. Figure 8.6 for the decomposition of $K_2Mg(NH_2)_4$ on the gas flow panel under argon showed a peak gas release at 423°C, however decomposition under NH_3 has been seen to occur $\sim$50 °C higher than under argon in other systems. Figure 8.21 shows the catalyst present is clearly effective at decomposing ammonia as it is mostly D_2 and N_2 that is observed, rather than ND_3.

Pulses of gas are observed in the traces for D_2, N_2 and ND_3 from 12 hours 50 minutes into the experiment which is where the equipment is starting to block and there is constricted flow. Figure 8.21 shows the equipment blocked at 825 minutes so the remainder of the experiment was performed under N_2 as the sample was cooled (this is the cause of the change in background observed in the contour plot). There are no Bragg peaks visible in the contour plot during ND_3 decomposition which makes understanding any structural changes in the catalyst more challenging. One of the aims of this experiment was to investigate *in-situ* the formation of the novel $KMg(ND_2)(ND)$ mixed-metal amide-imide phase; however, this was not observed. Either the $KMg(ND_2)(ND)$ phase did not form during the experiment or it formed in a molten phase for which no Bragg peaks could be observed.

Figure A.24 shows that on cooling, very faint Bragg peaks appear in Banks 2, 3 and 5 at 181 °C due to recrystallisation of cubic KND_2 (3.57 Å (111), 3.08 Å (200) and 2.18 Å (220)). *Ex-situ* powder X-ray diffraction data and neutron diffraction data (collected in a vanadium can for one hour at room temperature) were obtained of the sample recovered at the end of this experiment (Figure A.23 in the Appendix). This fits to $K_2Mg(ND_2)_4$ (45.1 %), monoclinic KND_2 (21.0 %) and MgO (33.9 %) and is consistent with the composition of the sample remaining at the end of the POLARIS experiment looking at the decomposition of $K_2Mg(ND_2)_4$ under argon (Figure A.22). As in the decomposition experiment under argon (Section 8.4.2), the $K_2Mg(ND_2)_4$ structure fitted in Figure A.23 shows similar shifts in the

lattice parameters which points to stoichiometry variation within the $K_2Mg(ND_2)_4$ crystal structure.

Unlike the mixed Group 1 systems for which non of the mixed-metal amides themselves were recovered post heating, $K_2Mg(ND_2)_4$ is the first mixed-metal amide to have not decomposed via separation and has been successfully recovered despite being heated to 300 °C under argon and 475 °C under ND_3.

8.9 Summary

High purity $K_2Mg(NH_2)_4$ has been prepared by ball-mill preparations and by heat treatment ($\sim$180 °C), and this has been shown to melt at $\sim$190 °C. No separation occurs on melting and this mixed-metal amide is stable under argon until 325 °C when it irreversibly decomposes to form $KMg(NH_2)(NH)$. However, $K_2Mg(NH_2)_4$ has been shown to be able to support a degree of non-stoichiometry as KNH_2 is slowly lost from the structure between the onset of it melting and the formation of $KMg(NH_2)(NH)$. Solid $KMg(NH_2)(NH)$ crystallises out of solution at 367 °C due to its higher melting point, and decomposes by separating into KNH_2 and MgNH which subsequently decompose to K metal and Mg_3N_2. $K_2Mg(NH_2)_4$ is the first mixed-metal amide to be recovered despite being heated to 300 °C under argon and 475 °C under ND_3. Despite showing the highest mass recovery for a mixed-metal amide catalyst to date, $K_2Mg(NH_2)_4$ is the worst performing catalyst in terms of its NH_3 decomposition ability.

Chapter 9

Mixed Sodium-Magnesium system

Contents

9.1 Background 364

9.1.1 Chapter overview 364

9.2 Synthesis/ Crystallography/ Phase Space/ Raman 365

9.3 *Ex-situ* thermal decomposition 372

9.4 POLARIS experiments under inert gas 377

9.4.1 Synthesis of $Na_2Mg(ND_2)_4$ 377

9.4.2 Decomposition of "$Na_2Mg(ND_2)_4$" 380

9.5 Inert gas summary 389

9.6 Ammonia decomposition 389

9.6.1 Quantitative fitting and analysis 389

9.6.2 Catalyst Recovery 391

9.7 Decomposition under ammonia 392

9.8 Summary 393

9.1 Background

The Na-Mg-N-H system is believed to be analogous to the K-Mg-N-H system (Chapter 8) in that the tetra-amides ($Na_2Mg(NH_2)_4$) are both reported to be metastable kinetic products which can be annealed above 300 °C to form thermodynamically stable novel mixed amide-imide phases ($NaMg(NH_2)(NH)$), stable to higher temperatures (Equation 9.1) [232, 291].

$$Na_2Mg(NH_2)_4 \longrightarrow NaMg(NH)(NH_2) + NaNH_2 + NH_3 \tag{9.1}$$

Precedent literature on the Na-Mg-N-H system has focused on hydrogen absorption and desorption from the $NaNH_2 + MgH_2$ system in the context of hydrogen storage and the phase transformations during this process. Sodium amide (5.1 % (weight) H_2 content) has received little attention as a possible component in a hydrogen storage system as unlike lithium and magnesium, sodium imide is not known to exist, which limits possible destabilization reaction pathways. Therefore, similarly to $KMg(NH_2)(NH)$, $NaMg(NH_2)(NH)$ is particularly interesting due to the presence of imide groups bonded to sodium cations.

9.1.1 Chapter overview

It has been suggested that $Na_2Mg(NH_2)_4$ and $NaMg(NH_2)(NH)$ exist based on analogies drawn between the K-Mg-N-H and Na-Mg-N-H systems, and although different structures have been proposed in the literature, neither $Na_2Mg(NH_2)_4$ nor $NaMg(NH_2)(NH)$ have yet been isolated and crystallographically characterised. Experiments have therefore been performed in order to better understand the structural behaviour of the Na-Mg-N-H system at both low and high temperatures, and under both inert and NH_3 decomposition conditions. *In-situ* experiments on POLARIS were carried out to compliment the *ex-situ* data obtained to try and better understand the behaviour and dynamics of the system as a whole and the potential role of the amide-imide complex.

9.2 Synthesis/ Crystallography/ Phase Space/ Raman

Novel synthetic methods for the formation of "$Na_2Mg(NH_2)_4$" directly from $NaNH_2$ and $Mg(NH_2)_2$ have been developed using tube furnace and ball-mill procedures (Section 2.2.4.5). To address the lack of crystallographic structures for the Na-Mg-N-H system, a survey of the whole phase space was performed. $NaNH_2$ and $Mg(NH_2)_2$ (synthesised as in Section 2.2.2.2) were ball-milled together in a range of molar ratios (11:1, 9:3, 8:4, 7:5, 5:7, 3:9 and 1:11) for 1 hour. For each resulting sample, powder X-ray diffraction data was collected on the I11 beam-line at the Diamond Light Source (Figure 9.1).

No known structures exist for the Na-Mg-N-H system but within the powder X-ray diffraction data for the different ratios shown in Figure 9.1, two phases (in addition to $NaNH_2$ and $Mg(NH_2)_2$) have been detected by principal component analysis. These have been labelled as unknown phase X (U.P X) and unknown Phase Y (U.P Y) with the main peaks highlighted in blue and orange respectively in Figure 9.1 and detailed in Figure 9.1.

U.P X is present at 2θ values and d-spacings listed in Table A.13 in the Appendix and has been indexed to tungsten carbide (WC) which arises from the ball-milling procedure. This makes sense as it is present in every mixed-metal ratio shown in Figure 2.6. WC is only present in these ball-milled samples (as opposed to those reported for other systems in this thesis) as these have been synthesised more recently, and over time there has been degradation of the ball-mill to some extent.

Ex-situ powder X-ray diffraction data collected for the sample of "$Na_2Mg(NH_2)_4$" synthesised from $2NaNH_2 + Mg(NH_2)_2$ in the tube furnace should be identical to that of the (*in-situ*) 8:4 $NaNH_2$:$Mg(NH_2)_2$ ratio shown in Figure 9.1. Figure 2.6 plots the observed powder X-ray diffraction data from these samples (although the ball-milled 7:5 $NaNH_2$:$Mg(NH_2)_2$ sample has been chosen as this sample appeared to have the greatest proportion of U.P Y compared to the other species present), plotted in terms of d-spacing (Å) to account for the different wavelengths of the diffractometers used. As for the K-Mg-N-H system, the pattern collected from the sample synthesised in the tube furnace has a slightly better resolution, as the ball-mill has lead to reduced crystallinity of the sample. However Figure 2.6 shows that the peak positions are still the same.

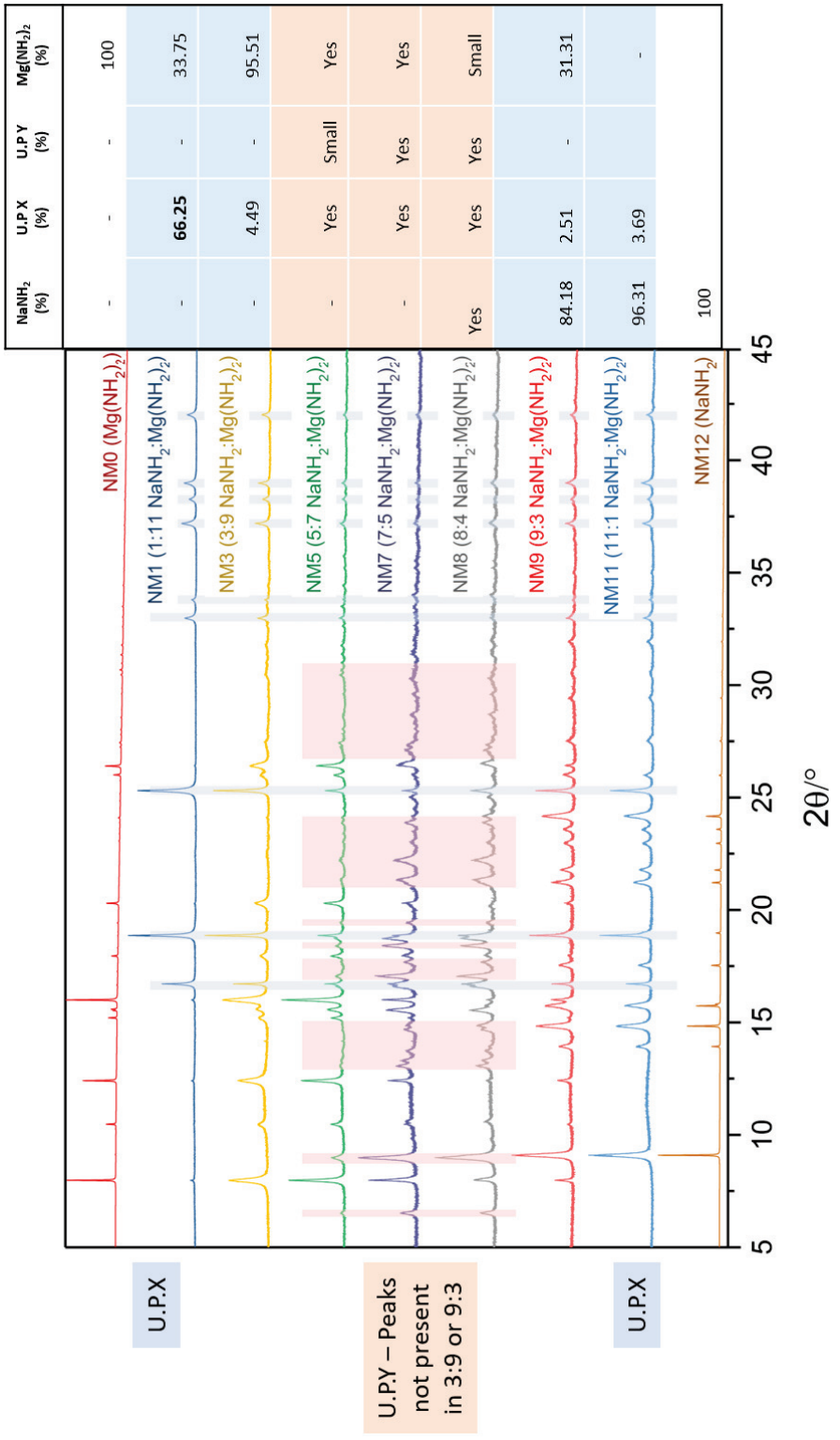


Figure 9.1: I11 powder X-ray diffraction data for the phase space between $NaNH_2$ and $Mg(NH_2)_2$ and suggested composition of each pattern. Unknown phase X is highlighted in blue and unknown phase Y is highlighted in orange. Wavelength = 0.8248901 Å

The ball-milled samples for the 1:11, 3:9, 9:3 and 11:1 ratios fit to WC, $NaNH_2$ and/or $Mg(NH_2)_2$ with no unfitted peaks. Unknown phase Y is a new phase with extra peaks present in the 8:4, 7:5 and 5:7 ratios and it is this unknown phase that is likely to be attributable to "$Na_2Mg(NH_2)_4$". Unknown phase Y has peaks at 2θ values and d-spacings shown in Table 9.1. Future work would be to fully identify this phases using a combination of TOPAS, DICVOL, DASH and FOX software.

$Li_3Na(NH_2)_4$ and $Li_3K(NH_2)_4$ have related structures and $LiNa_2(NH_2)_3$, $LiK_2(NH_2)_3$ and $NaK_2(NH_2)_3$ have the same structure (Table 2.6). It is therefore not unrealistic to propose that the structures of $Na_2Mg(NH_2)_4$ and $NaMg(NH_2)(NH)$ are related to those of $K_2Mg(NH_2)_4$ and $KMg(NH_2)(NH)$. Figure 8.1 shows the unit cells of $K_2Mg(NH_2)_4$ and $KMg(NH_2)(NH)$ and Figure 2.5 shows the powder X-ray diffraction of $K_2Mg(NH_2)_4$ collected on the I11 beam-line at Diamond. However, comparison of the peak positions for the trace of the 8:4 $NaNH_2$:$Mg(NH_2)_2$ ratio shown in Figure 9.1 with that for $K_2Mg(NH_2)_4$ (Figure 2.5) shows that the peak positions are different.

A more quantitative approach to seeing if the powder X-ray diffraction data collected for "$Na_2Mg(NH_2)_4$" fit to the same structure observed for $K_2Mg(NH_2)_4$, takes into account the fact that K has a larger ionic radii than Na. KNH_2 and $Mg(NH_2)_2$ have volumes of 55.4 Å^3 and 67.7 Å^3 per formula unit, so $2KNH_2 + Mg(NH_2)_2$ would be expected to have a volume of 178.55 Å^3. The known structure of $K_2Mg(NH_2)_4$ has a volume of 170.8 Å^3 which is 96 % of the expected volume. Analogously, $2NaNH_2 + Mg(NH_2)_2$ would therefore be expected to have a volume per formula unit of 162.3 Å^3 and 96 % of this is 155.2 Å^3. If $Na_2Mg(NH_2)_4$ were to have the same P 12_1/c1 structure, this would give a total unit cell volume of 620.9 Å^3. If β were to stay the same as in $K_2Mg(NH_2)_4$, this would give $Na_2Mg(NH_2)_4$ a, b and c parameters of 7.22 Å, 6.80 Å and 13.11 Å respectively.

Although this approach goes one step further than simply acknowledging that the peak positions are different, even when the volume change is accounted for it still does not appear that $Na_2Mg(NH_2)_4$ has the same structure as $K_2Mg(NH_2)_4$ because an $Na_2Mg(NH_2)_4$ structure with the unit cell parameters listed above does not fit the powder X-ray diffraction data shown in Figure 2.6 or the unknown phase Y shown in Figure 9.1.

U.P Y (I11 data - Figure 9.1)		**Literature *d*-spacing values (Å)**		
2 θ (°)	***d*-spacing (Å)**	**[301]**	**[260]**	**[232]**
6.52	7.25			
9.00	5.26	5.21	5.24	
10.61	4.46	4.53	4.53	4.67
13.07	3.63		4.41	
13.31	3.56			
13.73	3.45	3.41	3.41	
14.69	3.23			
14.85	3.19	3.19		3.18
		3.07	3.03	
			3	
			2.98	
			2.87	2.88
17.06	2.78			
17.67	2.69			
18.4	2.58	2.54	2.53	
19.43	2.44	2.45		2.40
		2.33	2.32	2.37
21.35	2.23	2.24	2.24	
22.21	2.14	2.15	2.14	2.15
23.04	2.07		2.03	
23.88	1.99			
25.01	1.09		1.82	
27.12	1.76	1.78	1.76	1.79
27.35	1.74			1.71
28.68	1.66	1.67	1.66	
29.57	1.62			
30.26	1.58			
		1.51		
		1.39	1.40	
		1.41		
		1.36		

Table 9.1: U.P Y 2 θ (°) and *d*-spacing (Å). Unknown phase *d*-spacings (Å) from the literature

The Raman spectra for $K_2Mg(NH_2)_4$ (Figure 8.3) and $Na_2Mg(NH_2)_4$ (Figure 9.2) are very similar, which supports the fact these mixed-metal amides may be similar on a local level despite having different structures in terms of average symmetry.

Table 9.2 shows that $NaNH_2$ and $Mg(NH_2)_2$ have volumes of 47.29 Å^3 and 67.71 Å^3 per formula unit respectively. Table 9.3 calculates the predicted volume of a mixed Na-Mg-N-H amide with different numbers of constituent Na and Mg units. Analysis of Figure 9.1 shows the unknown phase Y is present in the 8:4, 7:5 and 5:7 ratios for which the total unit cell volumes have been highlighted in red in Table 9.3.

	Space Group	Formula Units per unit cell	a (Å)	b (Å)	c (Å)	Total Volume (Å^3)	Volume per formula unit (Å^3)
$NaNH_2$	Fddd	16	8.96	10.46	8.07	756.66	47.29
$Mg(NH_2)_2$	I 4_1/acd	16	10.37	10.37	20.15	2166.87	67.71

Table 9.2: Volume per formula unit for $NaNH_2$ and $Mg(NH_2)_2$

		Number of Na units				
		5	**6**	**7**	**8**	**9**
Number of Mg units	**3**	439.6	486.9	534.2	581.5	628.7
	4	507.3	554.6	601.9	649.2	696.5
	5	575.0	622.3	669.6	716.9	764.2
	6	642.7	690.0	737.3	784.6	831.9
	7	710.4	757.7	805.0	852.3	899.6

Table 9.3: Predicted volume for an unknown Na-Mg-N-H phase

There have been some crystallographic structures for Na-Mg-N-H phases suggested in the literature. Xiong et al, [301], Dolotko et al, [81] and Sheppard et al. [260] all report the same unknown phase with peaks at d-spacings shown in Table 9.1. This unknown phase has been suggested to be an imide with either a previously unknown MgNH structure, or an imide comprised of both Na and Mg (with $NaMg(NH_2)(NH)$ suggested). A trigonal phase has been proposed with possible space group P3c1 and lattice constants $a = b = 6.11$ Å

and $c = 17.9\,\text{Å}$ [260]. Pireddu et al. [232] also report an unknown structure (believed to be the same as that in the three papers above) but propose an orthorhombic cell with $a = 3.6149\,\text{Å}$, $b = 15.1739\,\text{Å}$ and $c = 9.4289\,\text{Å}$ and also believe this unknown phase to be $NaMg(NH_2)(NH)$. Neither of these proposed structures fit the powder X-ray diffraction data collected for the different ratios shown in Figure 9.1.

Magnesium, when combined with lithium, is known to form non-stoichiometric amides $Li_xMg_{2-x}(NH_2)_{2+x}$ for $0 < x < 1$ [159], a stoichiometric imide $Li_2Mg(NH)_2$ [241] and non-stoichiometric nitrides $(Li_xMg_{1-x})_3N_{2-x}$ for $0 < x < 0.2$ and $(Li_xMg_{1-x})_2N_{(2-x)2/3}$ for $0.5 < x < 0.6$ [302]. Sodium, when combined with lithium, is known to form both a stoichiometric amide $LiNa_2(NH_2)_3$ and a solid solution amide $Li_{4-y}Na_y(NH_2)_4$ $(0 < y < 1)$ [189]. There is some evidence in the literature that suggests that $NaMg(NH_2)(NH)$ is a solid solution, due to a $0.5\,°\,2\theta$ shift in the peak positions of the unknown phase reported in [260] between powder X-ray diffraction data collected at 165 °C and 267 °C. This could be due to compositional changes in the $NaMg(NH_2)(NH)$ structure arising from Na or Mg migration to or from the phase, as a function of reaction and/or temperature.

Sheppard et al. [260] report a second unknown phase, likely to be a magnesium and sodium containing nitride, but structurally different from Mg_3N_2 (Fourier-transform infrared spectroscopy excludes it from being an amide or imide). This phase has been suggested to be monoclinic with possible space group C2 and lattice constants $a = 13.92\,\text{Å}$, $b = 3.58\,\text{Å}$, $c = 12.39\,\text{Å}$ and $\beta = 115.8\,°$. This proposed structure also does not fit the powder X-ray diffraction data for the different ratios shown in Figure 9.1.

Pireddu et al. [232] report a second unknown phase which has been proposed to be $Na_2Mg(NH_2)_4$ but there is no powder X-ray diffraction data to support this, only Fourier-transform infrared spectroscopy data which shows N−H stretches at $3297\,\text{cm}^{-1}$, $3285\,\text{cm}^{-1}$, $3274\,\text{cm}^{-1}$, $3257\,\text{cm}^{-1}$, $3243\,\text{cm}^{-1}$, $3209\,\text{cm}^{-1}$ and $3167\,\text{cm}^{-1}$. These stretches are at not dissimilar wavenumbers to the peak sequences shown for "$Na_2Mg(NH_2)_4$" synthesised in the tube furnace and ball-mill shown in Figure 9.2.

Due to the lack of crystallographic data, Raman spectroscopy is a particularly important technique for characterising the Na-Mg-N-H system. Raman spectroscopy can be used to follow the conversion between amide (NH_2^-) and imide (NH^{2-}) phases by examining the

change in the vibrational modes. Raman stretches for "$Na_2Mg(NH_2)_4$" synthesised by both tube furnace and ball-mill preparations were collected as outlined in Section 2.5.1. Raman spectra for $NaNH_2$ and $Mg(NH_2)_2$ are included for comparison.

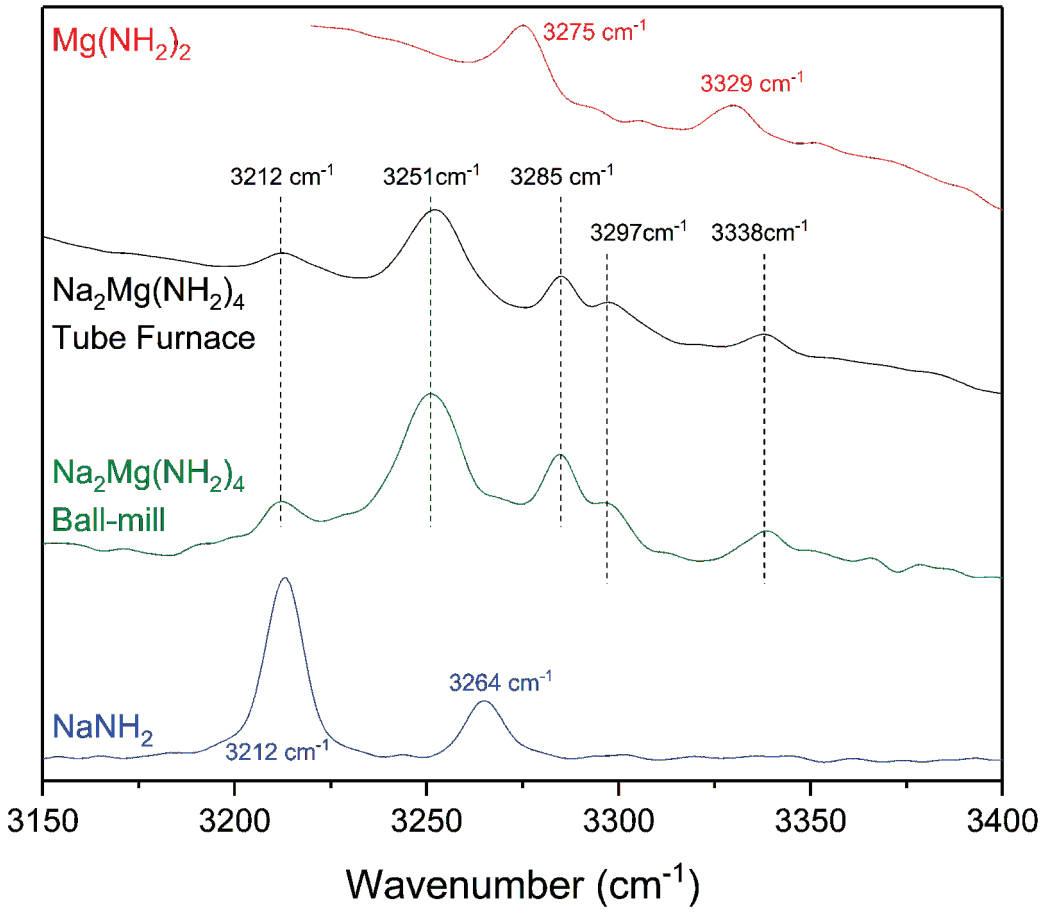


Figure 9.2: Raman stretches for the Na-Mg-N-H system

$Mg(NH_2)_2$ shows characteristic infrared absorption bands ascribed to amide N−H stretching at wavenumbers of $3275\,cm^{-1}$ and $3329\,cm^{-1}$, and $NaNH_2$ shows the characteristic asymmetric N−H stretch at $3264\,cm^{-1}$ and symmetric stretch at $3212\,cm^{-1}$.

The products synthesised in the tube furnace and ball-mill from $2NaNH_2 + Mg(NH_2)_2$ show stretches at wavenumbers of $3212\,cm^{-1}$, $3251\,cm^{-1}$, $3281\,cm^{-1}$, $3297\,cm^{-1}$ and $3338\,cm^{-1}$ which match up well with with each other and those in the literature [232] and are in the range expected for amide groups. They are also clearly different from a simple superposition of the peaks seen in $NaNH_2$ and $Mg(NH_2)_2$ independently. Figure 9.2 shows the absence of imide peaks at $3171/3167\,cm^{-1}$ which had been ascribed to $NaMg(NH_2)(NH)$ in

[260] and [232] respectively. This suggests that the samples synthesised in the tube furnace and ball-mill are not an imide ($NaMg(NH_2)(NH)$) but an amide, most likely $Na_2Mg(NH_2)_4$.

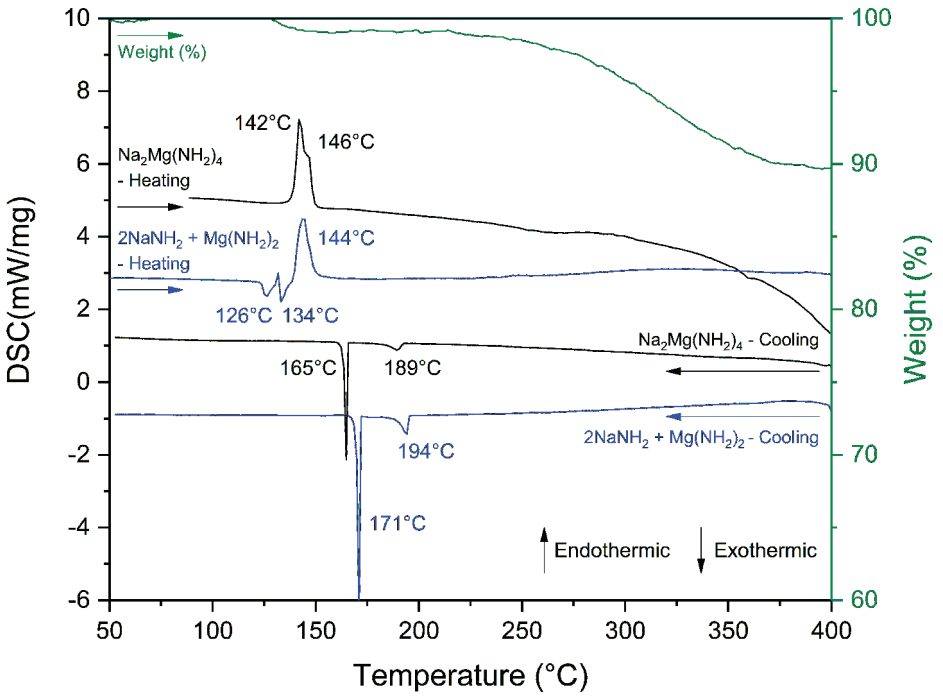
$NaNH_2$ and KNH_2 show almost identical Raman stretches to each other, so if $Na_2Mg(NH_2)_4$ and $K_2Mg(NH_2)_4$ were to have the same structure, it is likely that these mixed-metal amides would also have comparable Raman spectra. $K_2Mg(NH_2)_4$ shows stretches at wavenumbers of $3227\,cm^{-1}$, $3234\,cm^{-1}$, $3287\,cm^{-1}$, $3302\,cm^{-1}$, $3332\,cm^{-1}$ and $3354\,cm^{-1}$ (Figure 8.3). Comparison of Figure 8.3 and Figure 9.2 shows a similar peak sequence, but whereas $K_2Mg(NH_2)_4$ has peaks at $3227\,cm^{-1}$ and $3234\,cm^{-1}$, "$Na_2Mg(NH_2)_4$" has peaks at $3212\,cm^{-1}$ and $3251\,cm^{-1}$.

9.3 *Ex-situ* thermal decomposition

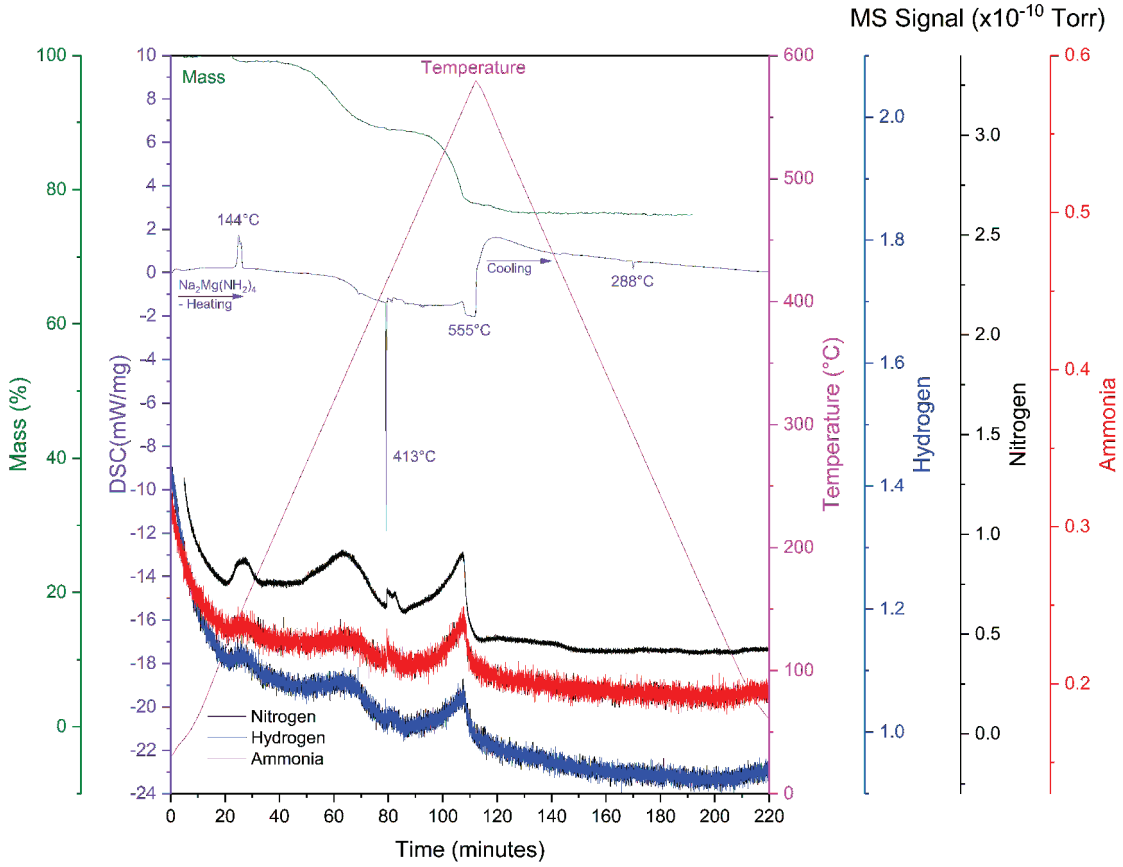
STA particularly focuses on the low temperature behaviour of the system. DSC traces taken for both pre-made "$Na_2Mg(NH_2)_4$" (black) and a hand-ground mixture of $2NaNH_2 + Mg(NH_2)_2$ (blue) are shown in Figure 9.3a. The mass trace (green) comes from the TGA part of the STA experiment for pre-made "$Na_2Mg(NH_2)_4$" (black).

Comparison of the differences between the two STA traces in Figure 9.3a enables the identification of the synthetic step for the formation of "$Na_2Mg(NH_2)_4$", as from this point onwards the two traces should be identical. This synthetic step is clearly visible as the exothermic events between 126 °C and 134 °C in the $2NaNH_2 + Mg(NH_2)_2$ STA trace. It is likely that the Na-Mg-N-H system is behaving analogously to the K-Mg-N-H system and the endotherms at $\sim$144 °C correspond to $Na_2Mg(NH_2)_4$ melting and not a concurrent separation as was seen for the Group 1 mixed-metal amides.

An additional STA experiment was performed on a pre-made sample of "$Na_2Mg(NH_2)_4$" and heated to 580 °C (Figure 9.3b). Similarly to Figure 9.3a, endothermic events can be seen at $\sim$144 °C corresponding to a sample melt. These thermal events correspond to a small amount of N_2, H_2 and NH_3 release, possibly from desorption of physisorbed gases from within the particle grains which has caused the small mass loss observed up to this temperature.



(a) STA traces for "$Na_2Mg(NH_2)_4$" (black) and $2NaNH_2 + Mg(NH_2)_2$ (blue) and the mass trace (green) from the TGA



(b) DSC trace for "$Na_2Mg(NH_2)_4$" (purple), mass trace (green), temperature (magenta) and QGA data for H_2, N_2 and NH_3 (blue, black and red) from the TGA

Figure 9.3: STA traces for pre-made "$Na_2Mg(NH_2)_4$"

The decomposition from $Na_2Mg(NH_2)_4$ to $NaMg(NH_2)(NH)$ (Equation 9.1) would correspond to a mass loss of 13 % if only NH_3 was lost. Both Figure 9.3a and Figure 9.3b show a mass loss of just over 10 % from 260 °C to 400 °C, so this phase change could be occurring. Interestingly there are no obvious thermal events shown in either DSC trace during this mass loss indicating a small ΔH for the $Na_2Mg(NH_2)_4$ to $NaMg(NH_2)(NH)$ decomposition.

The mass and DSC traces seen in Figure 9.3a also look analogous to the K-Mg-N-H system (Figure 8.5) as a mass loss (possibly incomplete) is seen without any thermal events. When this is combined with the *in-situ* diffraction data, (Figure 9.7) where $NaMg(NH_2)(NH)$ is not seen, this may suggest $Na_2Mg(NH_2)_4$ has not fully decomposed to $NaMg(NH_2)(NH)$ when only heated to 400 °C. Therefore the exotherms on cooling in Figure 9.3a could correspond to recrystallisation of a small amount of $NaNH_2$ at 189 °C and 194 °C (produced as a by-product in Equation 9.1) and $Na_2Mg(NH_2)_4$ recrystallising at 165 °C and 171 °C as it has not fully decomposed and is still the major phase present.

However, if the Na-Mg-N-H system is heated to higher temperatures (Figure 9.3b) then there is a sharp exotherm seen at 413 °C which could correlate to crystallisation of the newly formed $NaMg(NH_2)(NH)$ at the end of the mass loss (analogous to the K-Mg-N-H system). It is likely $NaMg(NH_2)(NH)$ has a higher melting point than $Na_2Mg(NH_2)_4$, so as the molten $Na_2Mg(NH_2)_4$ finishes decomposing to $NaMg(NH_2)(NH)$, this may then solidify. All the $Na_2Mg(NH_2)_4$ in Figure 9.3b has decomposed to $NaMg(NH_2)(NH)$ whereas this process was incomplete in Figure 9.3a (not heated to as high a temperature) and was therefore seen to recrystallise on cooling at 165 °C and 171 °C. $Na_2Mg(NH_2)_4$ decomposes to $NaMg(NH_2)(NH)$ in an exothermic process with the release of gas (positive entropy) which is therefore a non reversible transformation so no thermal events corresponding to $Na_2Mg(NH_2)_4$ are observed on cooling if this process is complete.

In order for the exotherm at 413 °C to correspond to the decomposition of $Na_2Mg(NH_2)_4$ to $NaMg(NH_2)(NH)$, then the endotherms at $\sim$144 °C can only correspond to a melting step and not a concurrent separation step. The Na-Mg-N-H system is therefore behaving more analogously to the K-Mg-N-H system than the Group 1 mixed-metal systems.

Figure 9.3b shows the mass trace had stabilised between 413 °C and 555 °C and the exotherm at 555 °C which occurs alongside an $\sim$10 % mass loss (due to the release of N_2

and H_2) may correspond to $NaMg(NH_2)(NH)$ itself decomposing. It could also correlate to the decomposition of the $NaNH_2$ formed, as alone this is known to do so at 539 °C from Figure 3.4.

An irreversible decomposition has occurred in Figure 9.3b, as on cooling, there is only one very small exotherm seen at 288 °C whereas in Figure 9.3a there are two exotherms at 189 °C and 165 °C. Additionally, the mass trace shows a greater mass loss above 500 °C than would be expected from the $Na_2Mg(NH_2)_4$ to $NaMg(NH_2)(NH)$ decomposition alone.

$NaMg(NH_2)(NH)$ could decompose into $NaNH_2$ and MgNH (a sodium imide is not known). $NaNH_2$ would decompose to Na and MgNH would decompose to magnesium nitride (reported to occur at ∼490 °C [80]) which could correspond to the thermal event at 555 °C.

The gas flow panel was used for a more in-depth analysis of the high temperature behaviour of the Na-Mg-N-H system under argon. Figure 9.4 shows the outlet gas flow MS trace for the decomposition of "$Na_2Mg(NH_2)_4$" under argon.

The shapes of the MS traces for the K-Mg-N-H system (Figure 8.6) and the Na-Mg-N-H system are very different (Figure 9.4). Where as the H_2 and N_2 curves for the K-Mg-N-H system have almost the same magnitude to each other at all temperatures, the Na-Mg-N-H system in Figure 9.4 shows two peak releases of H_2 at 365 °C and 426 °C but only one of N_2. From 375 °C, the H_2/N_2 ratio is close to 2. The decomposition of the K-Mg-N-H system under argon on the gas flow panel showed a "peak position" at 362 °C which had been attributed to the decomposition of $K_2Mg(NH_2)_4$ into $KMg(NH_2)(NH)$. Analogously, the peak at 365 °C in Figure 9.4 could be due to the decomposition of $Na_2Mg(NH_2)_4$ into $NaMg(NH_2)(NH)$ and the peak at 426 °C due to the subsequent decomposition of $NaMg(NH_2)(NH)$, possibly into $NaNH_2$ and MgNH. Figure A.26 in the Appendix shows the powder X-ray diffraction data collected for the sample recovered after $Na_2Mg(NH_2)_4$ was heated on the gas flow panel to 450 °C. This fits to Mg_3N_2 and it is likely another phase is present but no $NaNH_2$ or $Mg(NH_2)_2$ is present. This suggests, as seen for the K-Mg-N-H system, that the MgNH has decomposed.

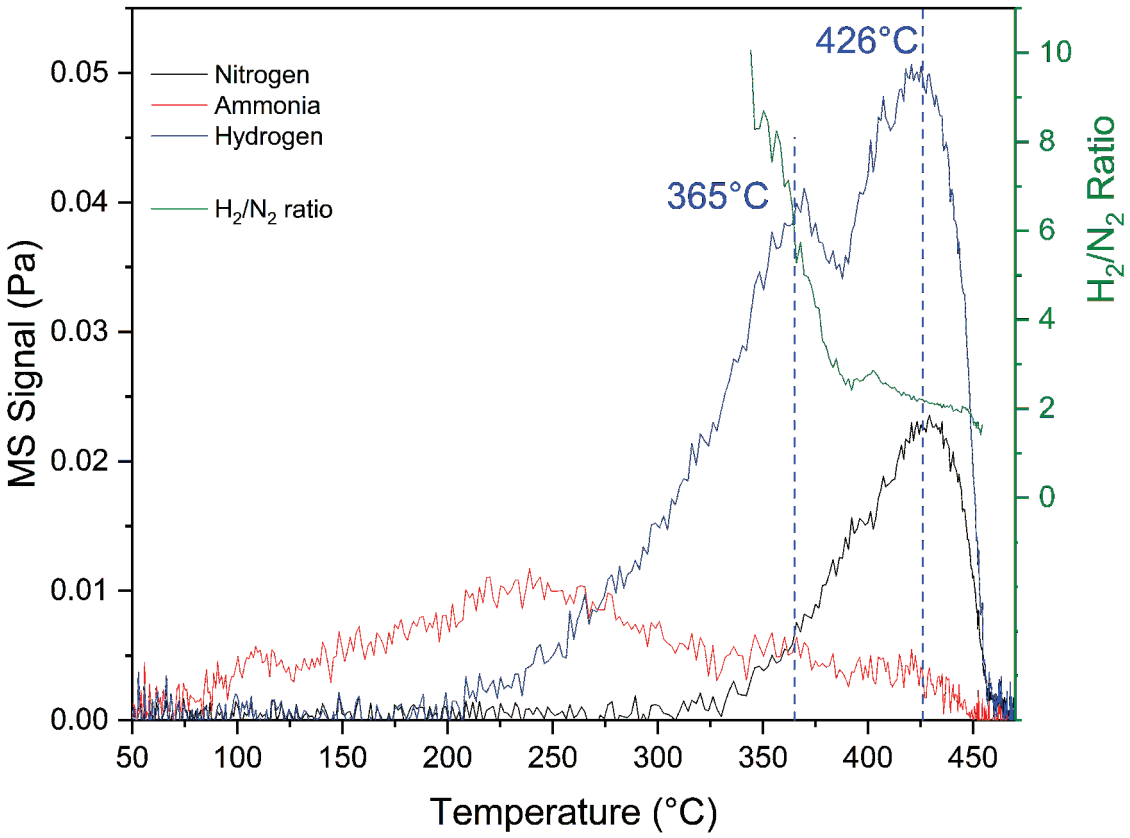


Figure 9.4: Decomposition of "$Na_2Mg(NH_2)_4$" on the gas flow panel under argon

A hypothetical decomposition pathway for $Na_2Mg(NH_2)_4$ could therefore be proposed, although it appears that these steps occur fairly simultaneously at high temperature:

$Na_2Mg(NH_2)_4$	$\longrightarrow NaMg(NH)(NH_2) + NaNH_2 + NH_3\uparrow$	Decomposition
	$\longrightarrow NaMg(NH)(NH_2) + Na + \frac{1}{2}N_2\uparrow + H_2\uparrow$	$NaNH_2$ decomposes
	$\longrightarrow NaNH_2 + MgNH + Na$	$NaMg(NH_2)(NH)$separates
	$\longrightarrow Na + \frac{1}{2}N_2\uparrow + H_2\uparrow + MgNH + Na$	$NaNH_2$ decomposes
	$\longrightarrow 2\,Na + \frac{1}{3}Mg_3N_2 + \frac{1}{3}NH_3\uparrow$	MgNH decomposes
	$\longrightarrow 2\,Na + \frac{1}{3}Mg_3N_2$	All gases lost
	$\longrightarrow \frac{1}{3}Mg_3N_2$	Na volatilised

9.4 POLARIS experiments under inert gas

The Na-Mg-N-H system is structurally under-explored as neither $Na_2Mg(NH_2)_4$ or $NaMg(NH_2)(NH)$ have been crystallographically characterised, so this experiment provides the opportunity to gain greater insight into the behaviour of these novel materials by investigating the variable-temperature structural behaviour of the system under argon. In conjunction with *ex-situ* data, it was hoped these experiments would provide a more complete understanding of the behaviour and dynamics arising from the co-existence of amide and imide groups in the Na-Mg-N-H system. The POLARIS experiments combine neutron powder diffraction and gravimetric studies for the *in-situ*, synthesis and subsequent thermal decomposition of "$Na_2Mg(ND_2)_4$".

9.4.1 Synthesis of $Na_2Mg(ND_2)_4$

The *in-situ* synthesis of $Na_2Mg(ND_2)_4$ from $2NaND_2 + Mg(ND_2)_2$ was examined under argon using the IGA^n. 0.5 g of a hand-ground mixture of the deuterated amides $2NaND_2 + Mg(ND_2)_2$ was transferred to the vanadium IGA^n bucket before it was craned into the POLARIS diffractometer under constant 1000 mbar argon. The steel reactor was used so there is one set of steel peaks present in the contour plots throughout the reaction (Table A.14 and Figure A.27 in the Appendix).

The sample was heated at 1 °C/min under 1 bar Ar to 200 °C where it was held for 3 hours before being cooled to room temperature at 5 °C/min. Thermogravimetric readings of the sample mass, temperature and pressure were taken every 5 seconds, and neutron diffraction data were collected at 100 second intervals throughout the course of the experiment to monitor the reaction progress.

Rietveld refinements to the $NaND_2$ and $Mg(ND_2)_2$ phases were performed in TOPAS. However, a batch refinement could not be performed because "$Na_2Mg(ND_2)_4$" does not, as yet, have a crystallographically solved structure.

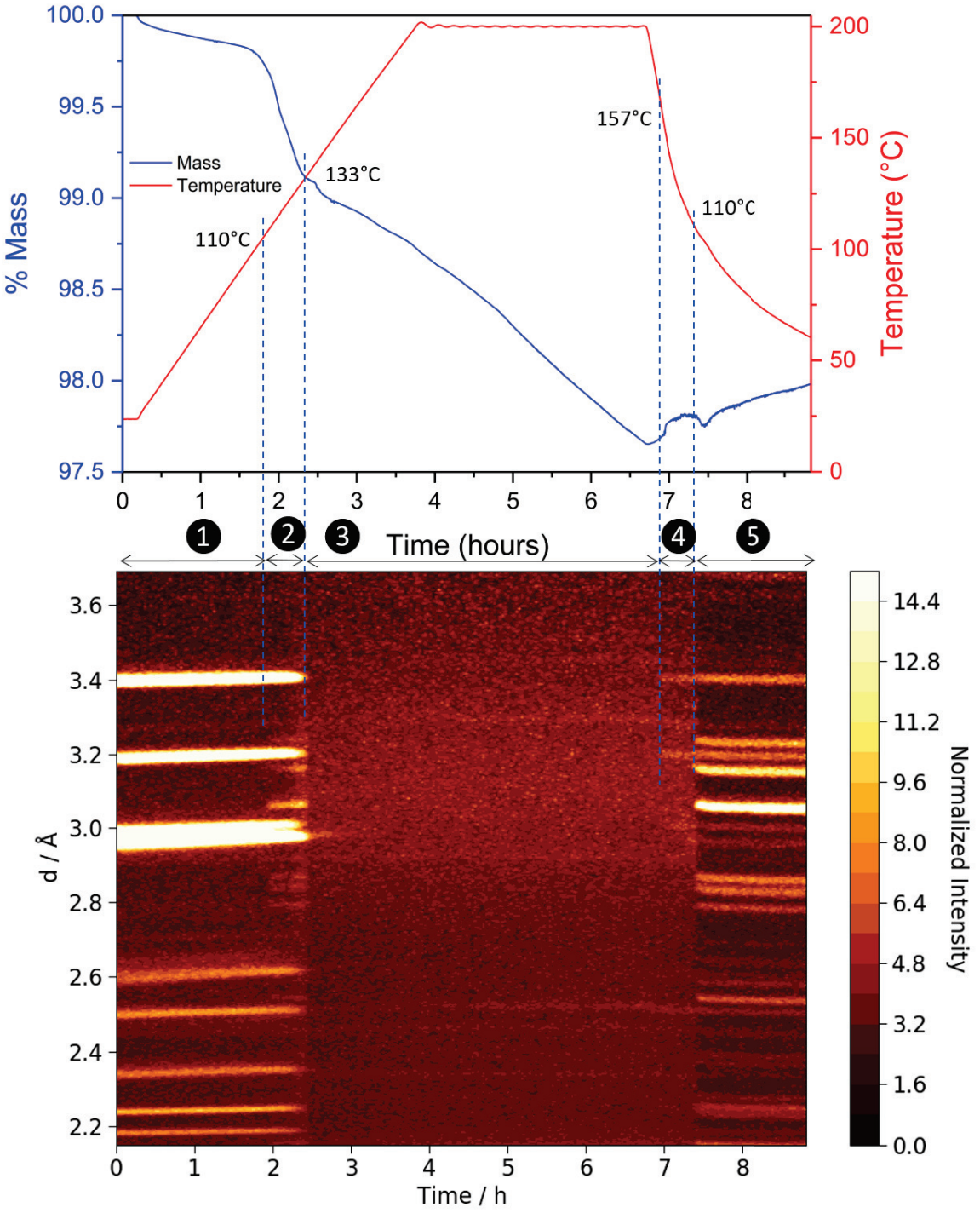


Figure 9.5: Thermogravimetric data, a bank 4 contour plot and key temperatures and regions highlighted for the $2NaND_2 + Mg(ND_2)_2$ synthesis experiment

Contour plots of the diffraction data collected from banks 2, 3, 4 and 5 and the corresponding thermogravimetric data for the whole $2NaND_2 + Mg(ND_2)_2$ synthesis experiment are presented in Figure A.27 in the Appendix. Figure 9.5 shows thermogravimetric data, a bank 4 contour plot and key temperatures and regions highlighted for the $2NaND_2 + Mg(ND_2)_2$ synthesis experiment. The diffraction data can be split into 5 different regions which are detailed in Table 9.4.

Region	**Temperature Range**	**Run numbers**	**Phases present**
1	RT-110°C	107137-107191	59.0 % $NaND_2$ and 41.0 % $Mg(ND_2)_2$
2	110°C-133°C	107192-107205	"$Na_2Mg(ND_2)_4$"
3	133°C-200°C-157°C	107206-107331	-
4	157°C-110°C	107332-107344	$NaND_2$
5	110°C-60°C	107345-107386	"$Na_2Mg(ND_2)_4$" + $NaND_2$

Table 9.4: Five regions for the POLARIS $2NaND_2 + Mg(ND_2)_2$ synthesis experiment

An hour long scan was taken at room temperature to get an accurate data set for the materials present at the start of the experiment. Refinement of the diffraction data collected prior to heating indicated that the sample was 59.0 % $NaND_2$ and 41.0 % $Mg(ND_2)_2$ (Table A.14 in the Appendix).

Between 110 °C and 133 °C there is a 0.75 % mass loss (Figure 9.5) and new Bragg peaks appear. It therefore appears that "$Na_2Mg(ND_2)_4$" is synthesised at 110 °C and melts at 133 °C in one step and there is no evidence of either $NaND_2$ or $Mg(ND_2)_2$ separating out of the mixed-metal amide. At this point there is also a marked change in the background. These temperature values match up well with the STA experiment in Figure 9.3a from which it had been suggested that $Na_2Mg(NH_2)_4$ was synthesised at $\sim$130 °C and melts at $\sim$144 °C.

This synthesis experiment was not heated high enough for any Bragg peaks corresponding to a phase change to the proposed $NaMg(ND_2)(ND)$ structure to be seen. The sample was held at 200 °C for 3 hours during which there was only a 1.5 % mass loss. If the

"$Na_2Mg(ND_2)_4$" to $NaMg(ND_2)(ND)$ transition were to occur (Equation 9.1), one molecule of ND_3 would be released which would correspond to a 13 % mass loss. It is therefore unlikely this decomposition has occurred even if the $NaMg(ND_2)(ND)$ produced was amorphous (no visible Bragg peaks).

On cooling, faint Bragg peaks re-appear at 157 °C which correspond to $NaND_2$ and at 110 °C there is a clear change in the background and additional sharp Bragg peaks appear. These are most likely due to "$Na_2Mg(ND_2)_4$" recrystallising (Figure 9.9) as they are at the same *d*-spacings as the Bragg peaks that appear on heating at 110 °C (region 2) which had been attributed to the synthesis of $Na_2Mg(ND_2)_4$. This is consistent with the STA data in Figure 9.3a which shows two exothermic events at ∼190 °C (small) and ∼170 °C (large), which had been attributed to the recrystallisation of $NaNH_2$ and "$Na_2Mg(NH_2)_4$" respectively, which therefore match up with the Bragg peaks that appear at 157 °C (weak) and 110 °C (strong).

Figure A.28 in the Appendix shows the powder X-ray diffraction data collected for the remaining sample at the end of this *in-situ* synthesis experiment which has peaks corresponding to $NaND_2$ and peaks at similar 2θ values to those shown in Figure 2.6 (fresh $Na_2Mg(ND_2)_4$).

9.4.2 Decomposition of "$Na_2Mg(ND_2)_4$"

0.5 g of a separate pre-made sample of "$Na_2Mg(ND_2)_4$" (*ex-situ* in the ball-mill from $2NaND_2 + Mg(ND_2)_2$) was used for this decomposition experiment. Although there is no CIF file as the $Na_2Mg(ND_2)_4$ structure is as yet unknown, powder X-ray diffraction data was collected to prove the phase formed was consistent with that seen previously.

The pre-made "$Na_2Mg(ND_2)_4$" sample was placed in a vanadium can for an hour long neutron diffraction dataset to be collected in the POLARIS beam to get an accurate pattern to use for attempts at structure solution. Due to the different resolutions/ranges of each bank, an amalgamated spectrum was produced which included the best resolution parts from each bank (Figure 9.6). *d*-spacings above 5.5 Å came from Bank 2 and include the peak at 5.89 Å, the *d*-spacing region from 3.5-5.5 Å came from Bank 3 and includes the peaks at 5.19 Å, 4.82 Å and 3.66 Å, the region from 2.7-3.5 Å came from Bank 4 and includes the

peaks at 3.40 Å, 3.20 Å, 3.15 Å, 3.05 Å, 2.97 Å, 2.96 Å, 2.86 Å, 2.83 Å and 2.78 Å and the region for *d*-spacings below 2.7 Å was taken from Bank 5. The peak positions of "unknown phase Y" listed in Table 9.1 show similar *d*-spacings to those observed in Figure 9.6.

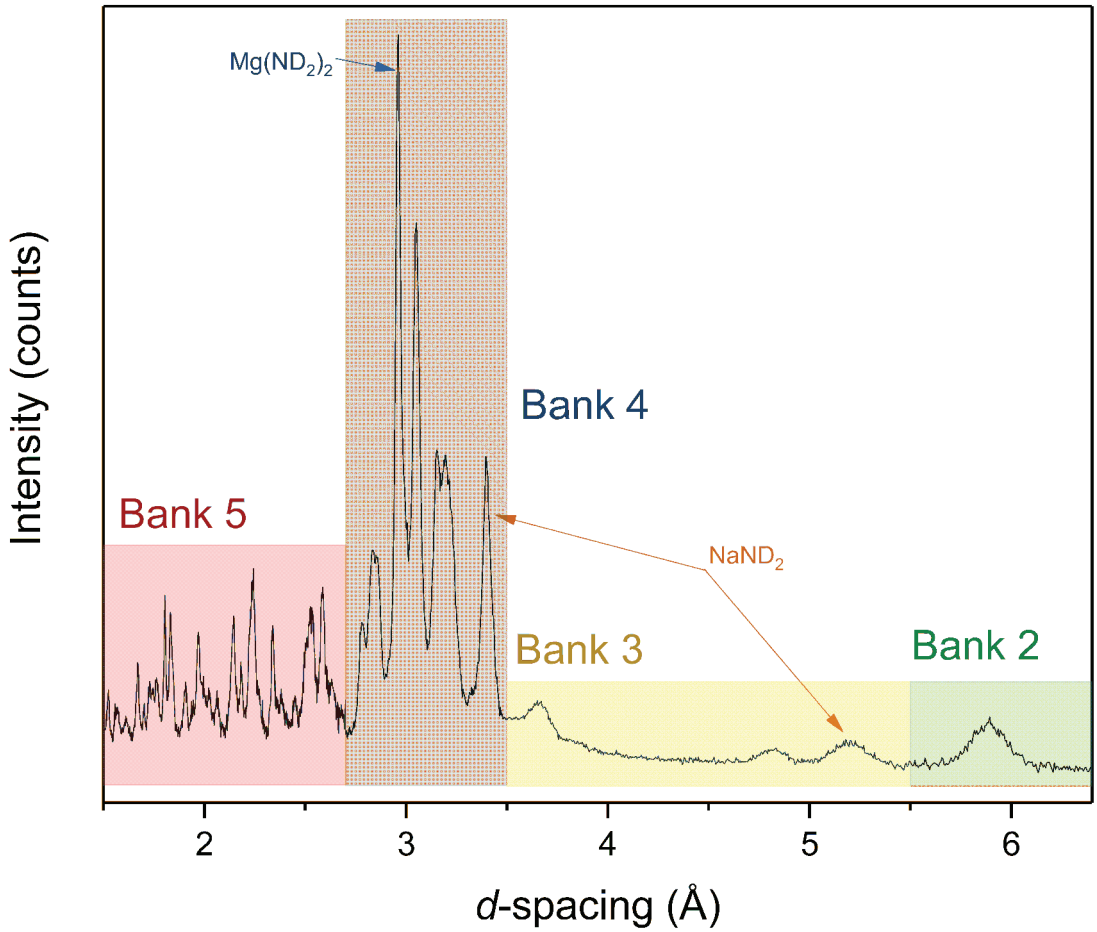


Figure 9.6: Amalgamated *in-situ* neutron diffraction data for "$Na_2Mg(ND_2)_4$" synthesised from $2NaND_2 + Mg(ND_2)_2$ in the ball-mill and collected in a vanadium can

During this *in-situ* decomposition experiment, the sample was heated to 300 °C so the quartz reactor cannot be used and a stainless steel reactor must be used instead. Hydrogen was expected to be produced, which causes the decrepitation of vanadium whereas stainless steel is unreactive towards alkali metal amides. This meant that the decomposition experiment had the unavoidable consequence of steel peaks present throughout the experiment, present as two sets of doublets, one from the beam entry and one from the beam exit positions of the bucket.

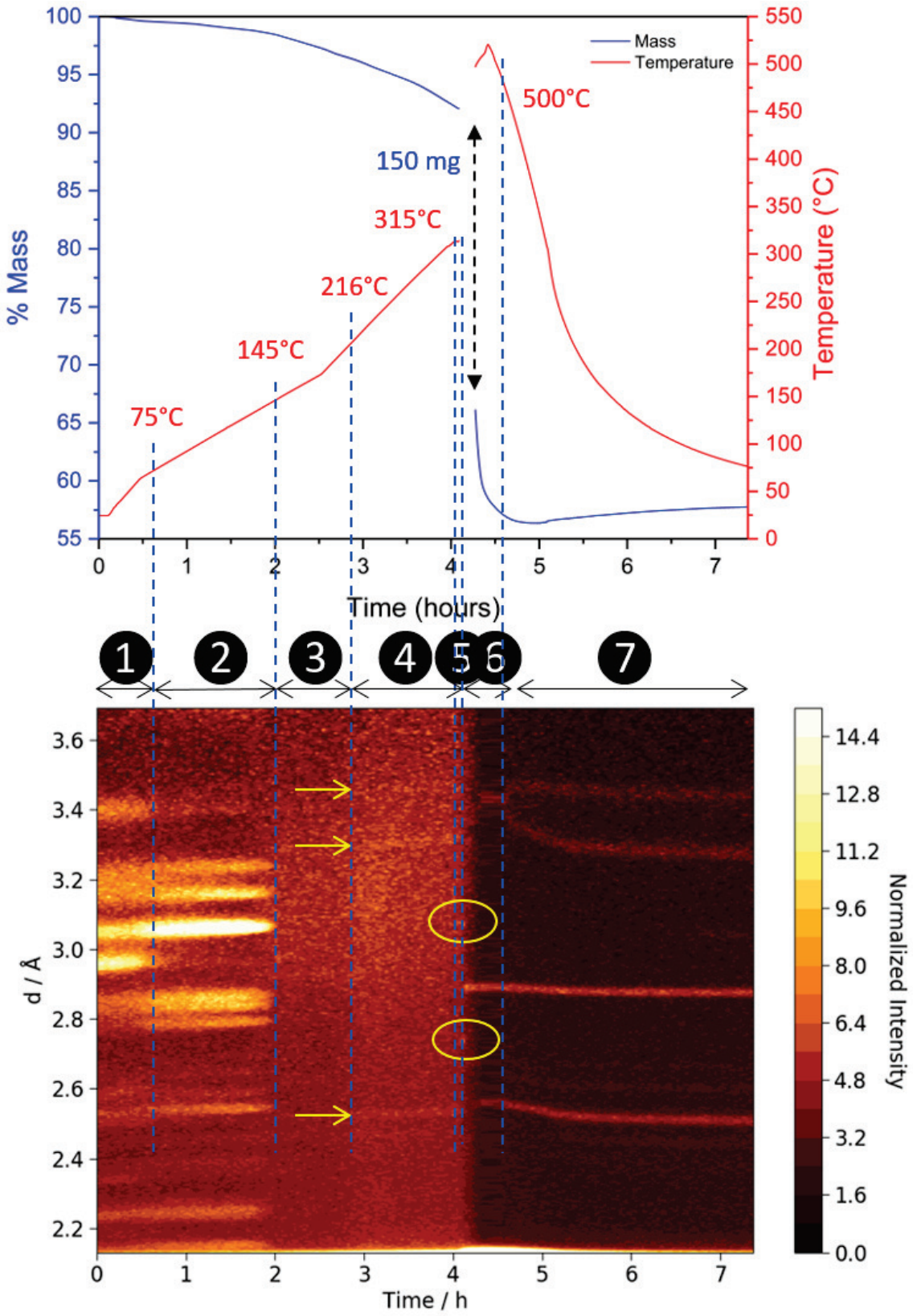


Figure 9.7: Contour plot for bank 4 for the "$Na_2Mg(ND_2)_4$" decomposition experiment with corresponding thermogravimetric data

Contour plots of the diffraction data collected from banks 2, 3, 4 and 5 and the corresponding thermogravimetric data for the $Na_2Mg(ND_2)_4$ decomposition experiment are presented in the Appendix in Figure A.30. Figure 9.7 shows the contour plot for bank 4 for the "$Na_2Mg(ND_2)_4$" decomposition experiment with corresponding thermogravimetric data. The sample of "$Na_2Mg(ND_2)_4$" was heated from room temperature to 60 °C at 2 °C/min and then from 60 °C to 170 °C at 1 °C/min and then from 170 °C to 315 °C at 2 °C/min. At this point there was an unexpected drop in pressure from 1000 mbar to 124 mbar and a rapid rise in the temperature from 315 °C to 500 °C which led to a sharp mass loss of 153.8 mg.

Region	**Temperature Range**	**Run numbers**	**Phases present**
1	RT-75°C	107388-107400	"$Na_2Mg(ND_2)_4$" and some unreacted $NaND_2$ and $Mg(ND_2)_2$
2	75°C-145°C	107408-107443	Annealed "$Na_2Mg(ND_2)_4$"
3	144°C-216°C	107444-107467	No peaks
4	216°C-315°C	107468-107500	Unidentified Bragg peaks
5	500°C	107501-107503	Two Bragg peaks at 3.07 Å and 2.74 Å
6	500°C-520°C-470°C	107504-107510	Peak at 3.43 Å
7	470°C-78°C	107535-107590	Same unidentified Bragg peaks as Region 4

Table 9.5: Seven regions for the POLARIS "$Na_2Mg(ND_2)_4$" decomposition experiment

Table 9.5 details the components of the 7 different regions identified in Figure 9.7. Initially present at the start of the decomposition experiment is the phase tentatively assigned to "$Na_2Mg(ND_2)_4$". During the analogous experiment on POLARIS for the decomposition of $K_2Mg(ND_2)_4$, it can be seen in Figure 8.12 and Figure 8.19 that at 60 °C and 74 °C annealing steps occur and any un-reacted monoclinic KND_2 and $Mg(ND_2)_2$ form $K_2Mg(ND_2)_4$. A similar annealing step can be seen to occur in Figure 9.7 between Regions 1 and 2 which is shown more clearly in Figure 9.8 by the difference in the neutron diffraction data collected from the starting sample collected in a vanadium can (room temperature for one hour) and Region 2, beyond 75 °C. It is therefore likely that at 75 °C, any un-reacted $NaND_2$ and $Mg(ND_2)_2$ is forming $Na_2Mg(ND_2)_4$ (although this is a lower temperature than the synthesis at $\sim$130 °C seen in Figure 9.3a). However, the annealing steps for $K_2Mg(ND_2)_4$

were also seen to occur at lower temperatures than the initial $K_2Mg(ND_2)_4$ synthesis temperature. The increased intensity of the "$Na_2Mg(ND_2)_4$" peaks could also be as a result of recrystallisation of any amorphous sample produced during the original synthesis of the sample in the ball-mill.

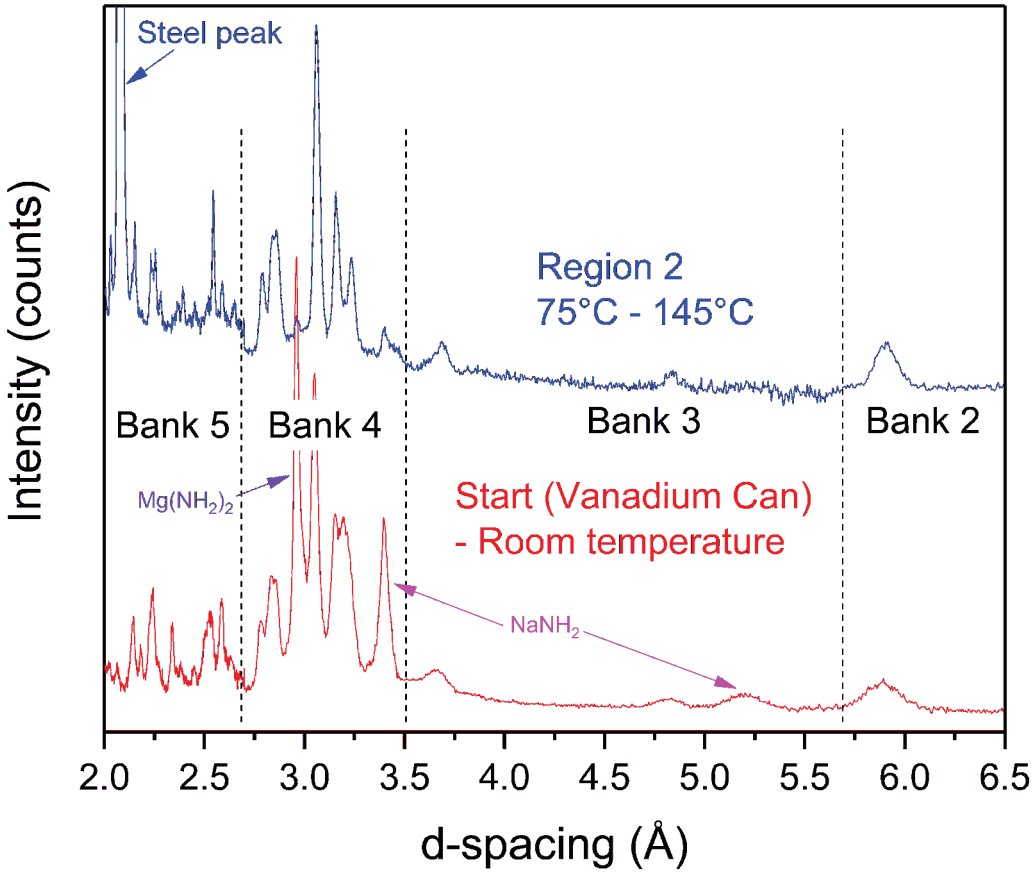


Figure 9.8: Neutron pattern of the starting "$Na_2Mg(ND_2)_4$" sample synthesised in the ball-mill collected in a vanadium can and Region 2, beyond 75 °C when this sample has annealed

Figure 9.8 compares the neutron diffraction data collected for the initial sample at the start of the experiment (collected in a vanadium can) with the summed pattern for Region 2 by which point the sample has undergone an annealing step. It is therefore likely that the summed neutron pattern from Region 2 is actually the best neutron pattern to index and use in conjunction with the powder X-ray diffraction diffraction data (shown in Figure 2.6 for the sample of $Na_2Mg(NH_2)_4$ made in the tube furnace), to try and index and solve the "$Na_2Mg(NH_2)_4$" structure. However, this has not yet been successful.

The difference between the diffraction data collected in the vanadium can and the summed pattern from Region 2 is that on heating, the $NaND_2$ peaks at 5.19 Å (111) and 3.40 Å (222) and the $Mg(ND_2)_2$ (224) peak at 2.96 Å have been lost and the peak at ~3.23 Å (amongst others) have gained intensity. The annealing step in the decomposition of $K_2Mg(ND_2)_4$ (Figure 8.12) also saw a decrease in intensity of the peak at ~2.9 Å due to loss of the 2.96 Å (110) $Mg(ND_2)_2$ peak.

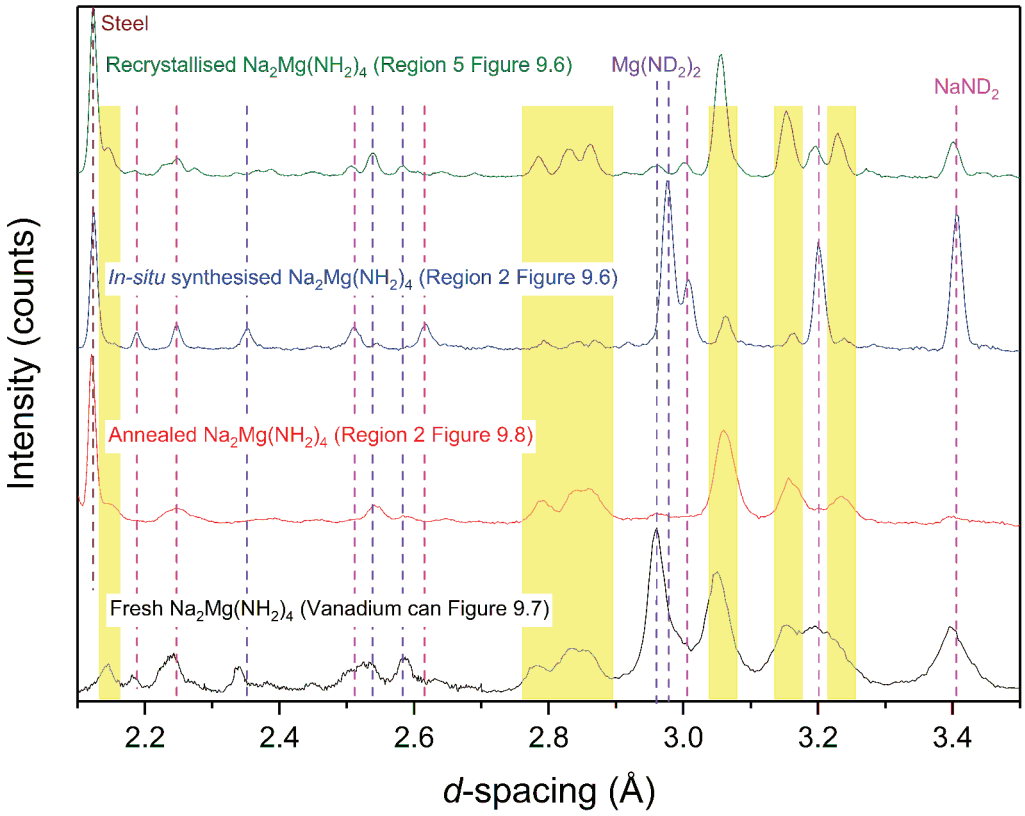


Figure 9.9: Selected Bank 4 neutron diffraction data for the summed regions shown in Figure 9.5, Figure 9.7 and Figure 9.8 for samples which are all expected to be $Na_2Mg(ND_2)_4$. Dashed lines in maroon, purple and magenta denote steel, $Mg(ND_2)_2$ and $NaND_2$ peaks respectively.

Figure 9.9 focuses on the diffraction data collected from bank 4 in the *d*-spacing range from 2.7 Å to 2.5 Å as Figure 9.8 shows this is where the greatest number of peaks are observed. The blue trace is from region 2 (initial synthesis) and the green trace is from region 5 (re-crystallisation) during the *in-situ* synthesis of $Na_2Mg(NH_2)_4$ (Figure 9.5). The black trace was collected of the starting sample of "$Na_2Mg(ND_2)_4$" (synthesised in the ball-

mill) at room temperature in a vanadium can prior to the start of the *in-situ* decomposition experiment (Section 9.4.2). Similar to the K-Mg-N-D system, this initial "$Na_2Mg(ND_2)_4$" sample appears to undergo an annealing step at 75 °C (Figure 9.7). The red trace in Figure 9.9 is therefore from region 2 of the *in-situ* decomposition experiment of $Na_2Mg(ND_2)_4$ as this is a more accurate pattern for "$Na_2Mg(ND_2)_4$".

Having performed both the *in-situ* synthesis and decomposition experiments of "$Na_2Mg(ND_2)_4$" and collected a pattern from a "fresh" sample in a vanadium can, Figure 9.9 enables the comparison of the neutron diffraction data collected for the different samples which are all expected to be $Na_2Mg(ND_2)_4$. Dashed lines in maroon, purple and magenta denote steel, $Mg(ND_2)_2$ and $NaND_2$ peaks respectively. Once the presence of these has been accounted for, the peaks corresponding to $Na_2Mg(ND_2)_4$ can be identified and have been highlighted by yellow boxes and are clearly present in each of the samples at *d*-spacings which had previously been identified as corresponding to $Na_2Mg(NH_2)_4$ in Table 9.1. It can be seen that the Bragg peaks in regions 2 and 5 during the synthesis experiment correspond to the same phase formed in the ball-mill from $2NaND_2 + Mg(ND_2)_2$ which had been assigned to "$Na_2Mg(ND_2)_4$".

At 145 °C in Figure 9.7 the phase assigned to "$Na_2Mg(ND_2)_4$" appears to melt due to loss of the observed Bragg peaks. This temperature corresponds very well with that seen in the STA experiment (Figure 9.3a) where the endotherms at $\sim$144 °C corresponded to the full sample melt. In the $2NaND_2 + Mg(ND_2)_2$ synthesis on POLARIS the "$Na_2Mg(ND_2)_4$" sample was seen to melt at 133 °C (Figure 9.5).

From 145 °C-216 °C (Region 3) there are no Bragg peaks. This suggests that "$Na_2Mg(ND_2)_4$" melts entirely and no separation of $NaND_2$ and $Mg(ND_2)_2$ has occurred. At 216 °C there is a distinct change in the background and a few Bragg peaks appear (highlighted by yellow arrows in Figure 9.7). The Bragg peaks present in Region 4 are at the same *d*-spacings as those in Region 7, where they are stronger and easier to distinguish due to the change in background at 4 hours from the sharp jump in pressure, temperature and mass. The Bragg peaks are at *d*-spacings of 1.5 Å, 2.51 Å, 2.88 Å, 3.28 Å and 3.44 Å and as yet remain unidentified as they do not correspond to MgO, MgOH, MgNH, $Mg(ND_2)_2$, $NaND_2$, Na_2O or $NaMgH_3$.

Mg_3N_2 crystallises in the $Ia\overline{3}$ space group under ambient conditions, but a high-pressure phase with the monoclinic C2/m structure has been observed above 20.6 GPa and a hexagonal $P\overline{3}m_1$ structure has been theoretically predicted above 67 GPa [119]. However none of these three phases of Mg_3N_2 fit to the Bragg peaks observed in regions 6 or 7 in Figure 9.7. Sheppard et al. [260] reported an unknown phase, suggested to have a "monoclinic C2 structure and likely to be a magnesium and sodium containing nitride but structurally different from Mg_3N_2". However, this proposed structure also does not fit the unknown Bragg peaks in Figure 9.7.

Figure 9.7 shows that in Banks 3 and 4, just before the pressure and mass drop and the temperature spikes, there are two Bragg peaks that appear at *d*-spacings of 3.07 Å and 2.74 Å in one run (Region 5). These are highlighted by yellow ellipses in Figure 9.7 and their identity remains unknown.

As the temperature is cooled from 500 °C, it is likely that there is only one material present which undergoes a phase change from a simple structure (possibly cubic) in Region 6, to one of lower symmetry in Region 7 (such as tetragonal). This is due to the presence of a single peak at 3.43 Å which splits into two at 3.45 Å and 3.28 Å. The sharp mass loss of 153 mg corresponds to 28.8 % of the starting mass. The phase change from "$Na_2Mg(ND_2)_4$" to $NaMg(NH_2)(NH)$ (Equation 9.1) would correspond to a mass loss of 13 % if one mole of ND_3 was lost, so additional gases/species have been lost during this experiment.

If the hypothetical decomposition pathway for $Na_2Mg(ND_2)_4$ proposed in Section 9.3 is occurring, then subsequent decomposition of $NaMg(ND_2)(ND)$ and $NaND_2$, to Mg_3N_2 and Na would lead to a mass loss of 60% so this reaction is not going to completion if it is occurring. It is also very possible that due to the high temperature reached, additional mass was lost simply by the sample melting or volatilising out of the bucket.

Figure A.29 in the Appendix shows the powder X-ray diffraction data collected for the remaining sample at the end of the *in-situ* decomposition experiment. This fits to Mg_3N_2 (as in Figure A.26 for the decomposition of $Na_2Mg(NH_2)_4$ under argon on the gas flow panel) and MgO. There is no $NaND_2$ present as there was in the pattern collected for the sample collected at the end of the POLARIS synthesis experiment (Figure A.28) and there are no peaks which correspond to those seen in Figure 2.6 from fresh $Na_2Mg(NH_2)_4$.

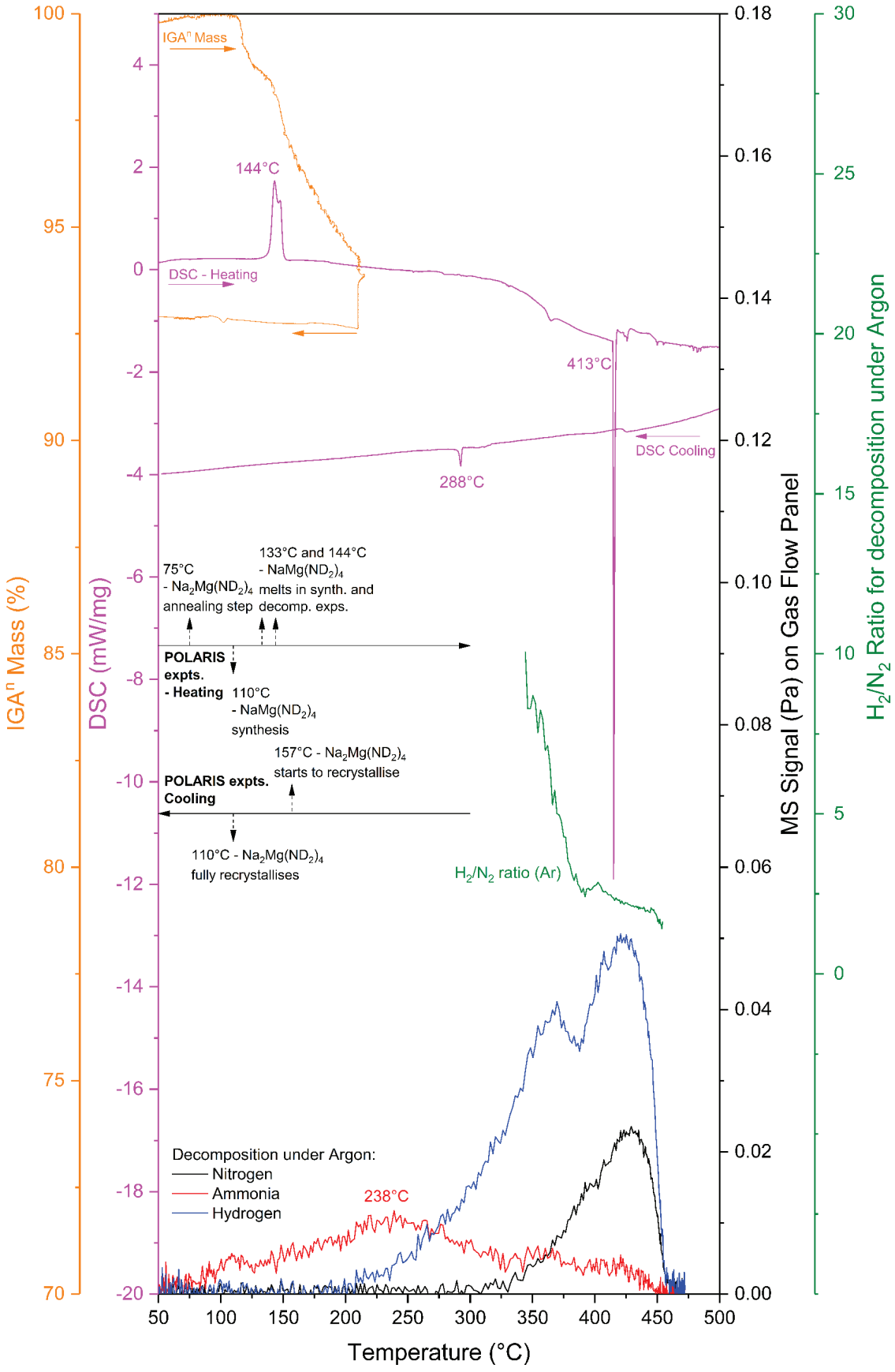


Figure 9.10: Thermodynamic properties measured during the decomposition of $Na_2Mg(NH_2)_4$ under inert gas

9.5 Inert gas summary

Figure 9.10 shows the thermodynamic properties measured during the decomposition of $Na_2Mg(NH_2)_4$ under inert gas through the superposition of key results from a variety of experiments. The low temperature behaviour of the samples was probed through the DSC traces recorded on the STA machine as the samples were heated to 400 °C. The high temperature thermal decomposition behaviour was analysed through the percentage mass loss recorded on the IGA^n and the MS signal of the outlet gas flow recorded on the gas flow panel as the samples were heated to 475 °C.

9.6 Ammonia decomposition

9.6.1 Quantitative fitting and analysis

As with the preceding systems, ammonia conversion efficiencies were calculated as described in Section 2.2.1.1 and Section 2.3. Figure 9.11 shows the ammonia conversion percentages calculated from the MS data for both the pre-formed mixed-metal amide "$Na_2Mg(NH_2)_4$" and a ground-up mixture of $2NaNH_2 + Mg(NH_2)_2$. Results for equivalent masses of pure $NaNH_2$ and $Mg(NH_2)_2$ have been included for comparison.

The plotted points are the recorded experimental results and the lines of best fit have been drawn using the two process sigmoidal Gompertz function (Equation 3.4) with the parameters listed in Table 9.6, which were themselves generated using the sigmoid fit calculated in TOPAS (Section 3.5.1). Uncertainties for T_e and E_A are estimated to be on the order of ± 2 °C and ± 3 kJ/mol respectively.

From looking at the single metal amides alone it can be seen that $NaNH_2$ is a higher performing NH_3 decomposition catalyst and has a steeper curve (indicative of higher activation energy) than $Mg(NH_2)_2$. Figure 9.11 shows that the NH_3 decomposition ability of "$Na_2Mg(NH_2)_4$" is intermediate to that of $NaNH_2$ and $Mg(NH_2)_2$ at all temperatures, which reflects the composition of the mixed-metal amide.

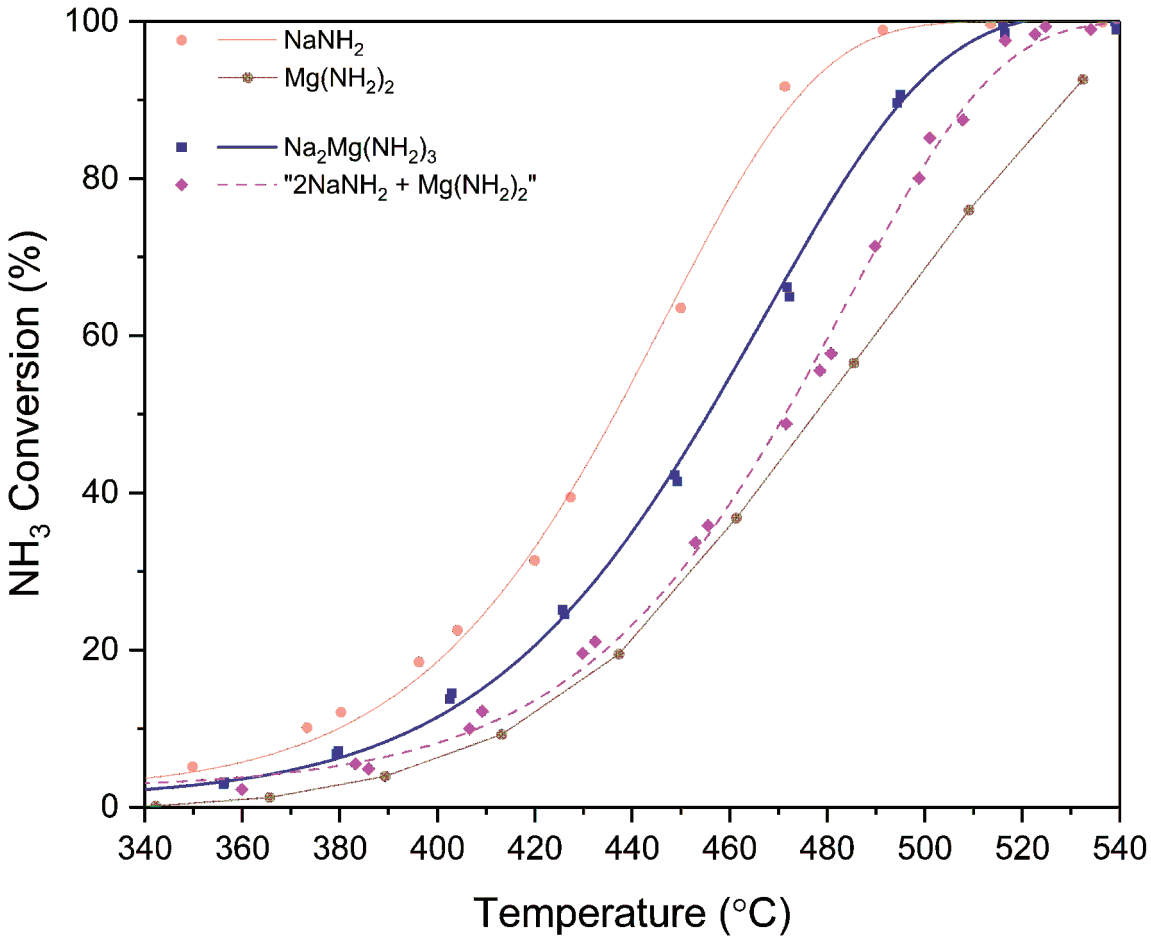


Figure 9.11: Ammonia decomposition ability of the Na-Mg-N-H system as potential catalysts on the gas flow panel

	Constant	T_e (°C)	E_A (kJ/mol)	Recovery by mass (%)
Blank	0.000(1)	547	102	n/a
$NaNH_2$	0.021(7)	450	154	6
$Mg(NH_2)_2$	0.000(2)	500	144	60
"$Na_2Mg(NH_2)_4$"	0.011(9)	472	152	87
$2NaNH_2 + Mg(NH_2)_2$	0.023(2)	488	181	24

Table 9.6: Na-Mg-N-H system Gompertz curve output values. Uncertainties for T_e and E_A are estimated to be on the order of ± 2 °C and ± 3 kJ/mol respectively and have been calculated from the TOPAS fitting process

Similarly to the K-Mg-N-H system, the NH_3 decomposition ability of $Na_2Mg(NH_2)_4$ is not the same as that as $2NaNH_2 + Mg(NH_2)_2$. Comparing the results for T_e and E_A shown in Table 9.6 and the shape of the curves (Figure 9.11), it can be seen that $2NaNH_2 + Mg(NH_2)_2$ has higher T_e and E_A value than "$Na_2Mg(NH_2)_4$" (by 16 °C and 8 °C respectively) which means the two NH_3 decomposition curves do not sit on top of each other. It is likely, that analogously to the K-Mg-N-H system, $2NaNH_2 + Mg(NH_2)_2$ does not form $Na_2Mg(NH_2)_4$ under NH_3 so for the two experiments it is not the same material that is present at the temperatures required for NH_3 decomposition.

The NH_3 decomposition ability of $2NaNH_2 + Mg(NH_2)_2$ is very similar to that of $Mg(NH_2)_2$ alone, especially up until 440 °C. At higher temperatures it is a better NH_3 decomposition catalyst, possibly as the $NaNH_2$ component takes over.

Whereas the trace for $2KNH_2 + Mg(NH_2)_2$ showed a bump in the NH_3 decomposition activity between 480 °C and 520 °C (Figure 8.15b), this is not seen for $2NaNH_2 + Mg(NH_2)_2$ in Figure 9.11. However, Figure 9.12 shows that there is a similar, additional gas release of H_2 and N_2 as seen in Figure 8.16. In both these experiments the gas release is occurring at the same temperature ($\sim$505 °C) which points to the fact it is resulting from decomposition of $Mg(NH_2)_2$, as this is common to both experiments. For the K-Mg-N-H system, this gas release is occurring when there is still a significant proportion of NH_3 present, so this therefore manifests as a bump in the NH_3 decomposition sigmoid between 480 °C and 520 °C (Figure 8.15b). However, the Na-Mg-N-H system appears to be a more active catalyst, so at this same temperature, the NH_3 conversion is nearly 100 % and there is effectively no NH_3 present (Figure 9.12). Therefore there is no effect of this additional gas release on the observed sigmoid for the $2NaNH_2 + Mg(NH_2)_2$ experiment.

9.6.2 Catalyst Recovery

Recovery of $NaNH_2$ is 5 % as Na is highly volatile and difficult to contain, and $Mg(NH_2)_2$ shows a recovery of 60 %. "$Na_2Mg(NH_2)_4$" shows a high mass recovery rate of 87 %, possibly due to stabilisation from the amide-imide complex $NaMg(NH_2)(NH)$.

The experiment starting with $2NaNH_2 + Mg(NH_2)_2$ shows a recovery of 24 %. If these single metal amides were present in this ratio, not interacting, and were to show the same

percentage recoveries as observed alone, an overall recovery of 29 % would be expected. This therefore supports the fact that $2NaNH_2 + Mg(NH_2)_2$ does not form $Na_2Mg(NH_2)_4$ under NH_3.

$K_2Mg(NH_2)_4$ and $Na_2Mg(NH_2)_4$ are the first amide/imide materials to show high NH_3 decomposition activity with no lithium content; potassium, sodium and magnesium are cheaper and more plentiful than Li which is an important consideration when designing a new catalyst.

9.7 Decomposition under ammonia

Thermal decomposition was also investigated under NH_3 during the experiment described in Section 9.6 to try and ascertain the active form of the catalysts at the temperatures required for NH_3 decomposition. Figure 9.12 shows the outlet gas flow MS traces for the decomposition of $Na_2Mg(NH_2)_4$ and a hand ground mixture of $2NaNH_2 + Mg(NH_2)_2$ under ammonia.

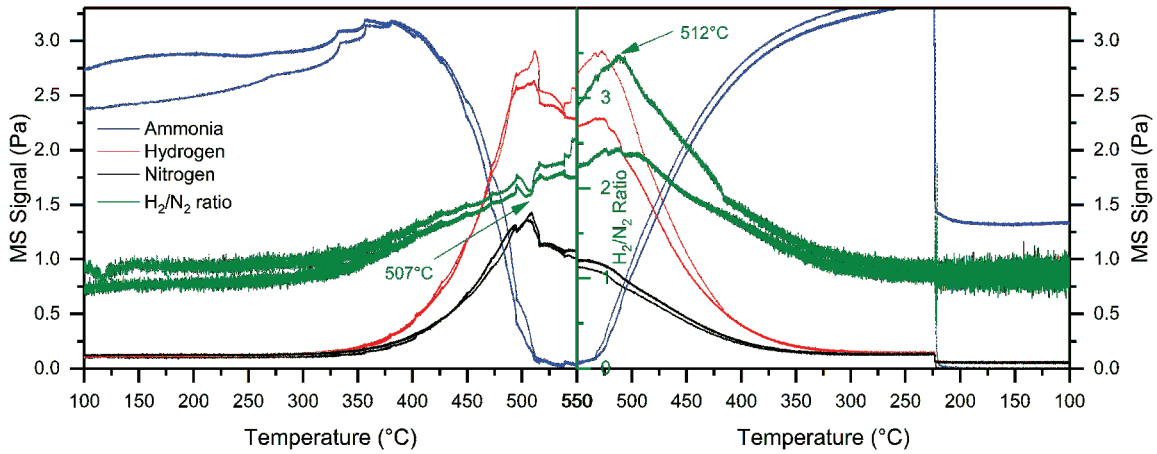


Figure 9.12: Decomposition of $Na_2Mg(NH_2)_4$ (solid lines) and $2NaNH_2 + Mg(NH_2)_2$ (dashed lines) on the gas flow panel under ammonia

There is a suppression in the H_2/N_2 ratio during both experiments at 507 °C suggesting at this temperature, the materials present are decomposing. This suggests that by this temperature, the initial $Na_2Mg(NH_2)_4$ has decomposed to $NaMg(NH_2)(NH)$ which itself has decomposed to $NaNH_2$ and MgNH and so the same materials are now present in the

reactor regardless of whether it was $Na_2Mg(NH_2)_4$ or $2NaNH_2 + Mg(NH_2)_2$ that was started with.

Powder X-ray diffraction data collected on the remaining samples of $Na_2Mg(NH_2)_4$ and $2NaNH_2 + Mg(NH_2)_2$ after decomposition under NH_3 on the gas flow panel were almost identical. Figure A.31 in the Appendix shows the powder X-ray diffraction data collected for the $Na_2Mg(NH_2)_4$ sample fits well to Mg_3N_2 and MgO as would be expected.

Figure 9.12 shows a peak at 512 °C on cooling, in the H_2/N_2 ratio for the $2NaNH_2 + Mg(NH_2)_2$ experiment which suggests that a small amount of Na is being observed to reform $NaNH_2$.

9.8 Summary

Consistent powder X-ray patterns have been collected for samples tentatively assigned to $Na_2Mg(NH_2)_4$, synthesised both in the ball-mill and on the tube furnace. These have been indexed but have not yet been crystallographically characterised so no CIF exists for this structure. Raman analysis suggests this phase is $Na_2Mg(NH_2)_4$ based on analogies drawn to the K-Mg-N-H system and $K_2Mg(NH_2)_4$. $Na_2Mg(NH_2)_4$ melts at $\sim$140 °C but does not separate during this process. It is likely that $Na_2Mg(NH_2)_4$ irreversibly decomposes to $NaMg(NH_2)(NH)$ which crystallises at 413 °C but will ultimately separate on decomposition into $NaNH_2$ and MgNH. Na and Mg_3N_2 are therefore the final recoverable decomposition products if the sample is heated to sufficiently high temperature. $Na_2Mg(NH_2)_4$ does decompose NH_3, but does not show high activity (although it is better than $K_2Mg(NH_2)_4$), but shows high catalytic mass recovery due to the stabilisation provided by $NaMg(NH_2)(NH)$.

Chapter 10

Conclusions and Future Work

Contents

10.1 New phases **399**

10.2 Ball-mill synthesis **399**

10.3 Thermal behaviour **400**

10.4 Implications for NH_3 decomposition **401**

10.5 Future work **407**

10.6 Conclusions **409**

There is, without a doubt, an urgent global need to revolutionise the way in which we source and store our energy. The consequences of the unprecedented rise in greenhouse gas emissions, originating from the over-exploitation of fossil fuels, is proving to be one of the greatest crises of the 21^{st} century. Our current reliance on coal, oil and natural gas is highly unsustainable due to their limited supply and environmental impact. The need to re-design the energy, and transportation sector in particular, is imminently approaching a crossroads beyond which carbon emissions will cause irreversible damage to the living systems of the planet.

Hydrogen is undoubtedly going to play a role in a future energy system due to its high gravimetric energy density, the vast abundancy of H_2O from which it can originate, and its clean emissions profile at the point of use. However, there are significant barriers preventing its widespread implementation, such as long term storage issues due to its low energy content per unit volume as well as the capital cost burden and large investment in infrastructure that would be required for its production, safe transportation and distribution. These challenges can be overcome by the reversible chemical storage of hydrogen as ammonia which can then be accessed on demand for use, for example, in fuel cells or combustion engines in cars. This has the potential to revolutionise the current energy sector towards that of a sustainable energy system. Many of the commonly discussed renewable energy sources such as solar

and wind are intermittent, so it is the storage of energy for load balancing in electric grids and transportation that has become as important as developing clean synthetic fuels.

The potential of ammonia is currently under appreciated. There are both real and perceived safety issues, for example with regard to toxicity, and its compatibility with PEM fuel cells which are irreparably degraded by low ppm concentrations of NH_3. Nevertheless, NH_3 will play a vital role in realising the potential benefits of the hydrogen economy. It is only through coupling the benefits of hydrogen as a fuel with the indisputable merits of ammonia as a hydrogen vector and large scale inter-seasonal energy store, that the required overhaul of the energy sector will be achieved.

The ammonia economy is conceptually the logical development of the hydrogen economy. Ammonia provides all of the benefits of hydrogen as a fuel whilst also having characteristics which enable some of the challenges faced by hydrogen to be overcome. Ammonia has a high hydrogen content of 17.8 % (by weight) and a greater volumetric hydrogen density than even liquid hydrogen itself. Ammonia is easily liquefied at room temperature and mild pressure and as the second most commonly produced chemical in the world, it is already widely distributed through mature transportation networks due to its use as a fertiliser precursor and in cleaning products. It is this existing infrastructure that is necessary to hasten the transition to hydrogen and ammonia as alternative fuels.

Ammonia is a flexible fuel that can be directly used in solid oxide fuel cells/internal combustion engines or cracked either to release all the hydrogen for low temperature fuel cells, or to promote combustion. However, with the current systems, ammonia cracking catalysts have poor hydrogen release kinetics which require high operating temperatures compromising the efficiency of the energy cycle.

In order to kick start hydrogen fuel cells in cars, NH_3 is the crucial step in terms of getting a hydrogen fuel cell fleet on the road. The main reason ammonia's potential as a carbon free hydrogen vector at the point of use has yet to be realized is largely because of the unavailability of an efficient, cheap and effective means for accessing its hydrogen content at scale. An ideal scenario would involve storing H_2 as NH_3 and producing hydrogen on-demand within the car only when it is needed.

Recent and drastic cost reductions from renewable energy sources such as solar and wind offer new possibilities for competitive green NH_3 production in large-scale plants based on electrolysis of water using surplus renewable electricity. Whilst the adoption of such energy sources is a necessary end-goal to eliminate the economic and political monopoly of oil and gas in addition to the environmental benefits, the key process is NH_3 cracking in terms of getting the hydrogen infrastructure in place. The infrastructure for NH_3 exists, its widespread implementation is simply predicated on the discovery and development of an effective ammonia cracking catalyst which can be utilised on an industrial scale.

There are three key goals for the development of more effective NH_3 cracking catalysts:

1. To design new systems which display higher NH_3 decomposition activity at low operating temperatures (ideally 300 - 400 °C just operating on waste heat)

2. To develop materials which are easier to maintain as a solid and remain stable across the range of NH_3 decomposition reaction conditions and up to maximum operating temperature

3. To identify materials that are tolerant to small amounts of water and limited exposure to air

These goals can be embodied by two challenges:

- Chemistry challenge: To discover and characterise an imide/amide system where the amide decomposes at room temperature or below and the imide is stable and solid up to maximum operating temperature

- Chemical engineering challenge: To develop a solid catalyst and support which is maintained within the catalyst reactor

The focus of this thesis has been to address these goals and overcome these challenges by synthesising, characterising and optimising new highly active and effective ammonia cracking catalysts. The function and potential of inexpensive earth abundant Group 1 and 2 based mixed-metal amide catalysts was explored. Mixed-metal amides are clearly among the most highly active NH_3 decomposition catalysts at modest temperatures and

have matched or surpassed the performance of optimised transition metal based catalysts. A progression of different systems was studied to investigate the ability of mixed-metal amide systems to tailor the active form and activity of the catalyst.

1. Intra Group 1 mixed-metal amides:
    - Mixing metals with different decomposition pathways:
        - Lithium-sodium amides: These were chosen based on their close crystallographic similarity to $LiNH_2$
        - Lithium-potassium amides: KNH_2 thermally decomposes via the same route as $NaNH_2$ but has a higher melting point leading to less significant catalyst loss
    - Mixing metals with the same decomposition pathway:
        - Sodium-potassium amides: $LiNa_2(NH_2)_3$, $LiK_2(NH_2)_3$ and $NaK_2(NH_2)_3$ are isostructural but there is a cost advantage of using $NaNH_2$ over $LiNH_2$
2. Mixed Group 1 and Group 2 metal amides:
    - Potassium-magnesium amides
    - Sodium-magnesium amides

    Mixed amide-imide phases have been reported for these systems meaning they are a new class of mixed-metal NH_3 decomposition catalyst. They bridge the intra-Group 1 amide systems for which no mixed-metal imide exists and the Li-Ca-N-H and Li-Mg-N-H systems for which only an imide is known.

The widespread application of mixed-metal amide systems as NH_3 cracking catalysts is predicated on understanding how the decomposition mechanisms observed under argon are correlated with their NH_3 decomposition activity. The study of these Group 1/2 mixed-metal systems has led to some important overarching lessons being learnt from these materials.

10.1 New phases

The crystallography of most of these systems had not previously been investigated in detail. The crystallographic structure of a catalyst plays an important role in dictating its properties in terms of the thermal behaviour of a sample. A number of new phases were discovered in this thesis:

- Li-K-N-H system (Figure 4.10) - Likely to consist of Li:K in a 1:1 ratio ("$LiK(NH_2)_2$") with layers of potassium ions
- Na-K-N-H system (Figure 5.2) - Likely to consist of Na:K in a 3:1 ratio ("$Na_3K(NH_2)_4$")
- Na-K-N-H system (Figure 5.11) - Formed during the $NaND_2 + 2KND_2$ synthesis experiment on GEM on cooling from 105 °C
- Li-Na-K-N-H system (Figure 6.1) - $Li_6NaK(NH_2)_8$ synthesised from a 6:1:1 ratio of $LiNH_2$:$NaNH_2$:KND_2 in the tube furnace
- Na-Mg-N-H system (Figure 2.6) - Sample of "$Na_2Mg(NH_2)_4$" synthesised from $2NaNH_2 + Mg(NH_2)_2$ in the tube furnace.
- Na-Mg-N-H system - Possibility of crystalline $NaMg(NH_2)(NH)$

Despite multiple attempts by a variety of methods, whilst progress was made in crystallographically characterising these unknown phases, these structures have not yet been completely solved.

10.2 Ball-mill synthesis

This thesis presents successful attempts to synthesise the mixed-metal amides of all the systems studied by novel ball-mill preparations. For the first time, it has been shown that a wide range of mixed-metal amides can be successfully synthesised by straightforward ball-milling of the constituent single metal amides in the respective ratios. This synthesis method is simple, quick, reliable and much less energy intensive than previously reported syntheses. Feasibility studies to scale up NH_3 cracking will involve working with ~ 100 g catalyst, so

improved performance means upscaling to commercial quantities which can be consistently and routinely made. Using the ball-mill therefore presents an attractive synthesis method to facilitate this.

10.3 Thermal behaviour

Analysing how these mixed-metal amides behave under inert gas and elucidating their reaction mechanisms under argon is crucial to understanding their behaviour. STA was used to focus on the low temperature behaviour of the systems (synthesis, separation and melting) and the behaviour at high temperatures (mainly decomposition) was investigated on the gas flow panel. The combination of neutron diffraction data with mass changes recorded by the IGA^n instrument gave valuable *in-situ* insight into the structure and mechanisms during the synthesis and decomposition of each of the mixed-metal amides. Correlating changes in the structures of the forming or decomposing mixed-metal amides with variations in the mass of the sample as a function of temperature have enabled, in conjunction with the *ex-situ* data, a more complete description of the behaviour and dynamics of the systems to be obtained.

Investigation of the low temperature behaviour of $Li_3Na(NH_2)_4$ and $Li_3K(NH_2)_4$ under argon, showed initially $NaNH_2$ or KNH_2 melts and separates out of the structure via non-stoichiometric $Li_3R_{(1\text{-}x)}(NH_2)_{(4\text{-}x)}$ (R=Na or K). This is due to the fact their structures are based on expanded, layered versions of $LiNH_2$ which allow facile (de)intercalation of sodium or potassium. There is then a small temperature range for which the amides are present as separate components, before the solid $LiNH_2$ dissolves into the liquid $NaNH_2$ or KNH_2 to form an inter-mixed molten phase with a composition approaching that of the constituent amides. $LiNa_2(NH_2)_3$ and $LiK_2(NH_2)_3$ are line phases and cannot support non-stoichiometry so show a single, combined separation and melt temperature, but ultimately forming analogous inter-mixed molten phases. Stable phases of these mixed-metal amides were not observed. $NaK_2(NH_2)_3$ does not separate on melting and instead forms molten $NaK_2(NH_2)_3$ which is stable to at least 300 °C, and only separates above this temperature into a molten phase approaching $NaNH_2 + 2KNH_2$.

The Li-Na-N-H, Li-K-N-H and Na-K-N-H systems all ultimately form an intermixed molten phase of the single metal amides present in the relevant ratios, as the structures of the mixed-metal amides fall apart at high temperatures. These molten phases are behaving similarly to ionic liquids and exhibit different properties and decomposition behaviour to those of the solid mixed-metal amides. Ionic liquids are a broad category of salts and typically contain a larger organic cation and either an inorganic or organic smaller anion. They are poorly coordinated, so have a low melting point and are generally liquid at room temperature and are non-volatile, thermally stable, and non-flammable.

At high temperatures it is the decomposition the two amides of these inter-mixed molten phases that is observed and there is a degree of interaction between these two concurrent processes. This is observed through lowered decomposition temperatures of the single metal amides when part of this combined melt phase compared to their individual decomposition. Furthermore, when these intermixed molten phases are decomposing, it is H_2 and N_2 release that is observed rather than NH_3 which is seen for $LiNH_2$ alone.

$K_2Mg(NH_2)_4$ and $Na_2Mg(NH_2)_4$ are metastable kinetic products and do not readily separate, instead displaying a single melt temperature. They are stable to much higher temperatures before they decompose to novel molten mixed amide-imide phases, $KMg(NH_2)(NH)$ or $NaMg(NH_2)(NH)$ which crystallise out of solution at 367 °C and 413 °C respectively and do not themselves decompose until over 500 °C into KNH_2/$NaNH_2$ and MgNH.

It is the correlation of this behaviour under inert gas with the catalytic activity of each mixed-metal amide towards NH_3 that is crucial to improving their performance and understanding how to optimise NH_3 decomposition conditions.

10.4 Implications for NH_3 decomposition

Mixed-metal amides are highly active and effective NH_3 decomposition catalysts at modest temperatures and have surpassed the performance of optimised transition metal catalysts.

Lithium amide shows NH_3 mediated thermal decomposition to lithium imide:

$$LiNH_2(l) \longrightarrow Li_2NH(s) + NH_3(g) \tag{10.1a}$$

$$x LiNH_2(s) + Li_2NH(s) \longrightarrow 2\,Li_{2-x}NH_{1+x}(s) \tag{10.1b}$$

Sodium amide and potassium amides decompose to the metals:

$$RNH_2(l) \longrightarrow R(l) + \frac{1}{2}N_2(g) + H_2 \qquad (R{=}Na \text{ or } K) \tag{10.2a}$$

$$R(s) + NH_3(l) \longrightarrow RNH_2(s) + \frac{1}{2}H_2(g) \tag{10.2b}$$

Magnesium amide decomposes via magnesium imide to magnesium nitride:

$$Mg(NH_2)_2 \longrightarrow MgNH + NH_3 \tag{10.3a}$$

$$3\,MgNH \longrightarrow Mg_3N_2 + NH_3 \tag{10.3b}$$

The NH_3 decomposition sigmoids shown in Figure 10.1 and Figure 10.2 fall into three categories:

1. $Li_3Na(NH_2)_4$ and $Li_3K(NH_2)_4$, with a 3:1 ratio of imide (Li_2NH) to metal (Na or K) under NH_3 decomposition conditions. These materials show the best high temperature conversion and have the steepest slopes, indicative of higher activation energy for NH_3 decomposition.

2. $LiNa_2(NH_2)_3$ and $LiK_2(NH_2)_3$, with a 1:2 ratio of imide (Li_2NH) to metal (Na or K) under NH_3 decomposition conditions. These materials are the best low temperature catalysts to date (superior to ruthenium shown in Figure 1.16).

3. $NaK_2(NH_2)_3$ is unique because both $NaNH_2$ and KNH_2 decompose to the respective metals under NH_3 decomposition conditions so there is no imide component present. This emphasises the importance of stable imides for good NH_3 decomposition catalysts due to the fact $NaK_2(NH_2)_3$ is the worst mixed-metal amide NH_3 catalyst shown at both low and high temperatures.

Figure 10.1 and Figure 10.2 therefore demonstrate the effect of mixing Group 1 amides which have different decomposition pathways under NH_3. From analysis of the NH_3 decomposition ability of all three Group 1 mixed-metal amide systems, it can be deduced that two factors govern the NH_3 decomposition ability of these catalysts:

1. Active form of the constituent metal catalyst surface under NH_3 decomposition conditions

2. Stoichiometry ratio of the constituent amides

The dominant factor in the NH_3 decomposition ability of the catalyst, appears to be the active form of the constituent metal catalyst surface under NH_3 decomposition conditions. This is both in terms of identity (whether it is imide or metal) and the ratio of the constituent metal amides from which it is derived. The initial crystal structure of the mixed-metal amide does not affect the NH_3 decomposition ability of the catalyst, as these materials have undergone a separation and melt before the temperatures required for NH_3 decomposition.

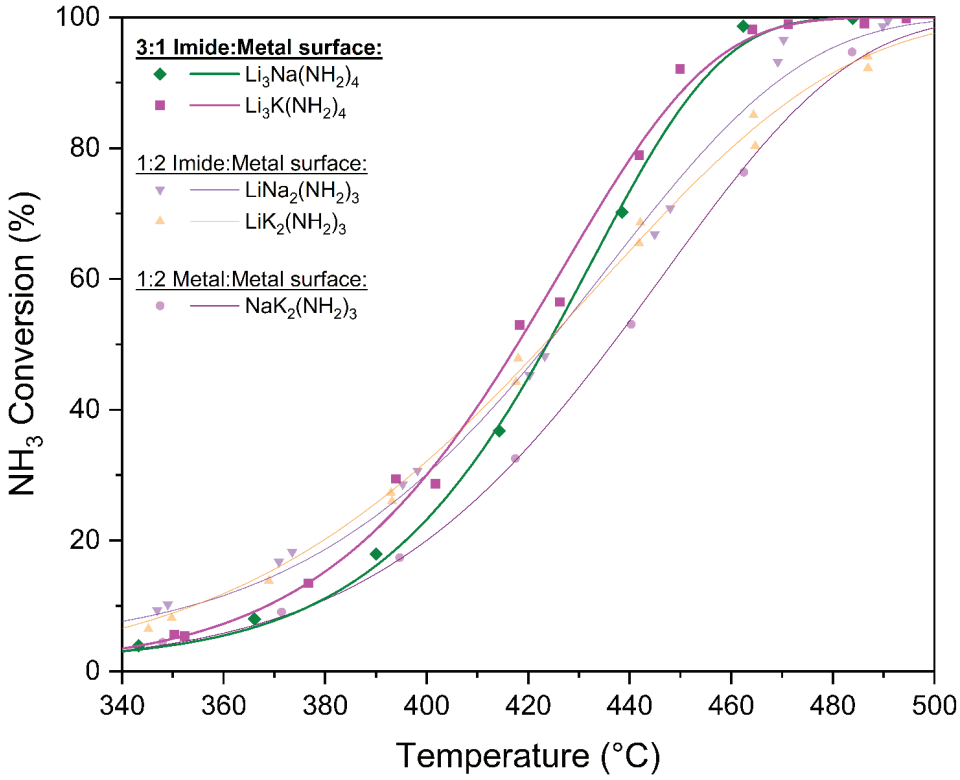
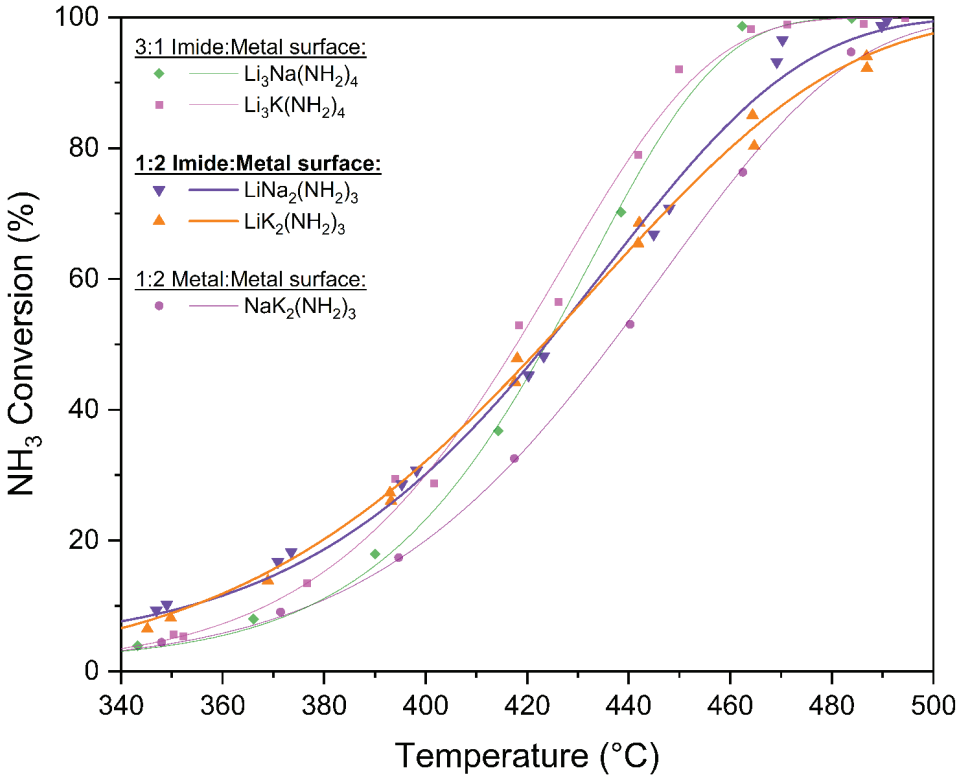
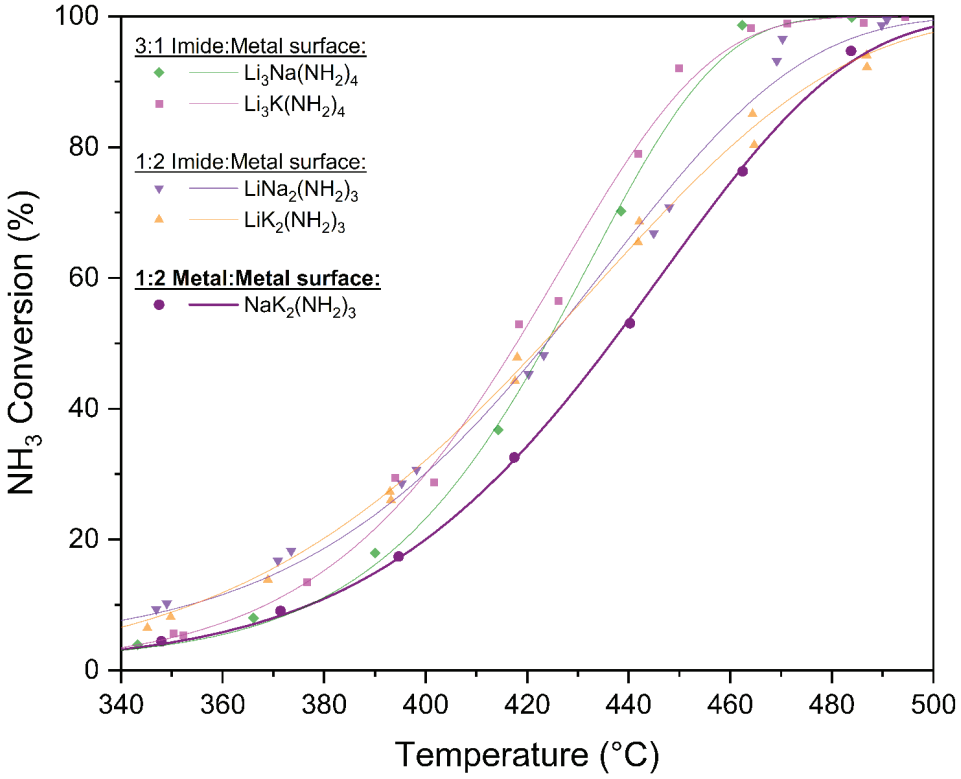


Figure 10.1: Ammonia decomposition ability of catalysts with a 3:1 imide:metal surface on decomposition



(a) Catalysts with a 1:2 imide:metal surface on decomposition



(b) Catalysts with a 1:2 metal:metal surface on decomposition

Figure 10.2: Ammonia decomposition ability of catalysts with a 1:2 amide component ratio

In terms of finding uses, if 20 % of the NH_3 needs to be cracked at a low temperature ($\sim$350 °C) then $LiNa_2(NH_2)_3$ or $LiK_2(NH_2)_3$ are the best catalysts, but if complete conversion is required in a single pass and higher temperatures are being used then $Li_3Na(NH_2)_4$ and $Li_3K(NH_2)_4$ are the best catalysts.

The NH_3 decomposition ability of the K-Mg-N-H and Na-Mg-N-H systems (Figure 10.3) are entirely different to that of the Group 1 mixed-metal amides, and significantly worse. Figure 10.2b shows that $NaK_2(NH_2)_3$ was the poorest performing Group 1 mixed-metal amide at all temperatures, and it has been shown that $NaNH_2$, KNH_2 and $NaK_2(NH_2)_3$ have almost identical NH_3 decomposition ability (Figure 5.15). Figure 10.3 shows that $K_2Mg(NH_2)_4$ and $Na_2Mg(NH_2)_4$ are both poorer NH_3 decomposition catalysts than $NaNH_2$ or KNH_2 alone, at both low temperatures, and particularly high temperatures. For these systems it is likely that it is the mixed amide-imide phases $KMg(NH_2)(NH)$ and $NaMg(NH_2)(NH)$ that are the active forms of the catalyst at the temperatures required for NH_3 decomposition.

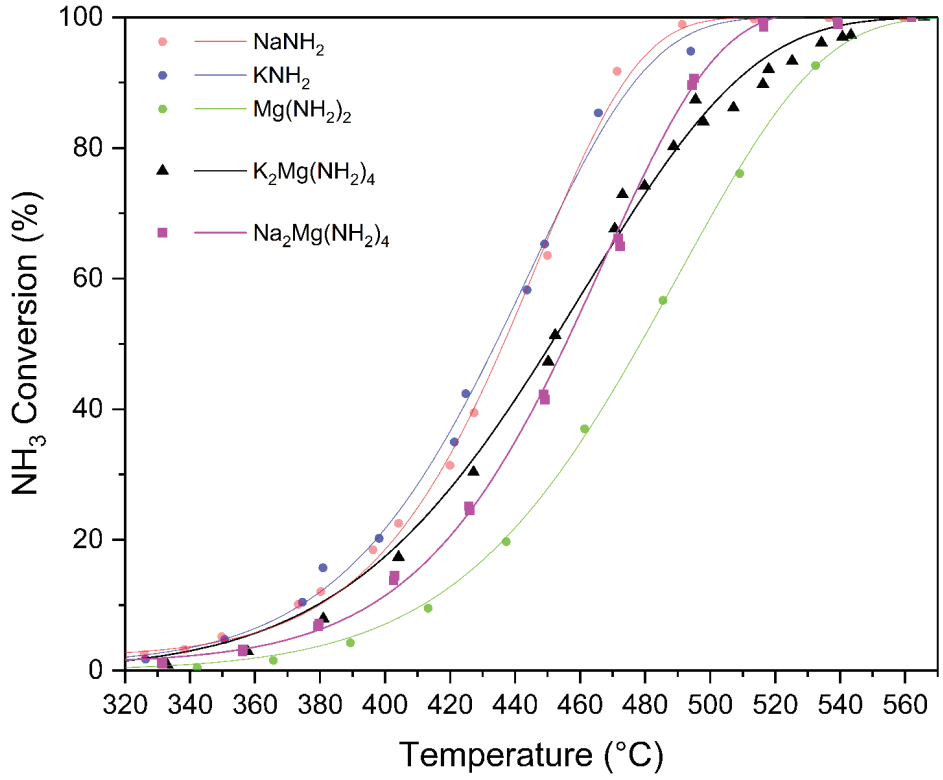


Figure 10.3: Ammonia decomposition ability of $K_2Mg(NH_2)_4$ and $Na_2Mg(NH_2)_4$

Quantitative analysis from fitting by a least-squares procedure to the two process sigmoidal Gompertz function (Equation 3.4) gives rise to the values of E_A, Constant and T_e detailed in Table 7.1. Uncertainties for T_e and E_A are estimated to be on the order of $\pm 2\,°C$ and $\pm 3\,kJ/mol$ respectively.

	Constant	T_e (°C)	E_A (kJ/mol)	Recovery by mass (%)
Blank	0.000(1)	547	102	n/a
$LiNH_2$	0.000(5)	439	184	88
$NaNH_2$	0.021(7)	450	154	6
KNH_2	0.009(2)	449	132	25
$Mg(NH_2)_2$	0.000(2)	500	144	60
$Li_3Na(NH_2)_4$	0.015(6)	434	177	73
$3LiNH_2 + NaNH_2$	0.017(8)	431	180	65
$LiNa_2(NH_2)_3$	0.039(2)	440	123	56
$LiNH_2 + 2NaNH_2$	0.019(4)	439	116	48
$Li_3K(NH_2)_4$	0.007(3)	429	153	85
$3LiNH_2 + KNH_2$	0.002(8)	435	150	80
$LiK_2(NH_2)_3$	0.000(2)	440	101	74
$LiNH_2 + 2KNH_2$	0.000(4)	436	112	68
$NaK_2(NH_2)_3$	0.009(2)	451	135	18
$NaNH_2 + 2KNH_2$	0.012(6)	450	129	15
$K_2Mg(NH_2)_4$	0.000(1)	471	108	89
$2KNH_2 + Mg(NH_2)_2$	0.000(2)	494	96	32
"$Na_2Mg(NH_2)_4$"	0.011(9)	472	152	87
$2NaNH_2 + Mg(NH_2)_2$	0.023(2)	488	181	24

Table 10.1: Gompertz curve output values and catalyst recovery. Uncertainties for T_e and E_A are estimated to be on the order of $\pm 2\,°C$ and $\pm 3\,kJ/mol$ respectively and have been calculated from the TOPAS fitting process

The percentage recovery of the catalyst is crucially important in order to maintain efficiency and improve lifetimes. Na and K are volatile so the Li-Na-N-H and Li-K-N-H systems suffer from poor containment and reversibility of such materials is clearly limited under these conditions. However, $K_2Mg(NH_2)_4$ and $Na_2Mg(NH_2)_4$ show the highest catalytic mass recovery rates of close to 90 %, due to stabilisation provided by the amide-imide complexes.

A high activation energy is seen for lithium dominated systems and a low activation

energy is observed for metal dominated systems. For a given value of T_e, the steepness of the sigmoid function is indicative of higher activation energy (E_A) for NH_3 decomposition. $NaNH_2$ and KNH_2 have very similar NH_3 decomposition ability but $LiNH_2$ and $Mg(NH_2)_2$ are very different. It is the presence of $LiNH_2$, which decomposes to the imide, that has a significant influence on the way the mixed-metal amides behave. $LiNH_2$ has to be present in the mixed-metal amide for it to be an effective NH_3 decomposition catalyst.

10.5 Future work

There are some subtleties in the reactions with NH_3 of the catalytic systems discussed in this thesis which have not yet been fully elucidated. Future investigations should focus on a more generic understanding of these materials. Most of the structural behaviour of the mixed-metal systems discussed in this thesis has been focused on diffraction experiments, such as the *in-situ* experiments on GEM and POLARIS at ISIS in addition to analysis of the powder X-ray diffraction data collected on the I11 beamline at Diamond. However, spectroscopic techniques such as NMR could also be used to analyse the local structure of the non-stoichiometric phases $Li_{4-y}Na_y(NH_2)_4$ and $Li_{4-y}K_y(NH_2)_4$ $(0 < y < 1)$. The collection of high-temperature *in-situ* NMR data can be experimentally challenging, but could provide important and complementary information to the diffraction data reported here. Ionic mobility studies using methods such as variable temperature solid state NMR and four-point probe conductivity analysis could also be used to look at the non-stoichiometry observed in these materials. Another important *in-situ* experiment would be time and temperature resolved mid IR spectroscopy measurements which would enable analysis of the interaction of the bulk of the catalyst with NH_3 via H-D isotopic exchange.

Additional avenues for further investigation could also be pursued. Within the systems studied so far, the effect of mixing these materials with iron could be studied. This may provide a method to dilute the catalyst, providing a bigger surface area and therefore more active sites. There is also scope for attempting to encapsulate these amide and imide materials, and to decorate the solid systems onto support architectures.

The most effective mixed-metal NH_3 decomposition catalysts to date, $Li_3Na(NH_2)_4$ and $Li_3K(NH_2)_4$ (Figure 7.1) and $Li_2Ca(NH)_2$ are layered materials. $Li_3Na(NH_2)_4$ and $Li_3K(NH_2)_4$ consist of alternating $LiNH_2$ blocks and layers of Na^+ or K^+ cations and $Li_2Ca(NH)_2$ consists of alternating layers of lithium and calcium imide. Whilst these layered systems are effective catalysts, they do not appear to be particularly thermally stable, as the separation of these layers into constituent amide/imide phases does not require a large input of energy. These materials are known to undergo partial separation followed by a full sample melt to form a molten phase with a composition approaching that of the constituent single metal amides.

In order to design mixed-metal systems which are stable to higher temperatures, it may therefore be beneficial to investigate systems where more integrated ion structures are observed. Progression from analysis of intra group 1 mixed-metal amides to the the K-Mg-N-H and Na-Mg-N-H systems was therefore interesting as for these systems the unstable amide does not separate on melting and instead decomposes to form a mixed amide-imide phase. Whilst these systems show better catalyst recovery, the NH_3 decomposition ability is much lower.

Future research efforts should therefore be focused on finding a balance between these two competing effects through utilising metals which give both high activity but also have the character of an unstable amide and a stable imide or amide/imide. One such system could be the Na-Ca-N-H system, for which sodium-calcium amide ($NaCa(NH_2)_3$) is known (Figure 10.4). $NaCa(NH_2)_3$ has a very different, non-layered structure of the $KEu(NH_2)_3$ structure type, with both Na^+ and Ca^{2+} cations in octahedral holes. $NaCa(NH_2)_3$ may therefore exhibit a higher thermal stability as with no layers, it would be less prone to separation on heating.

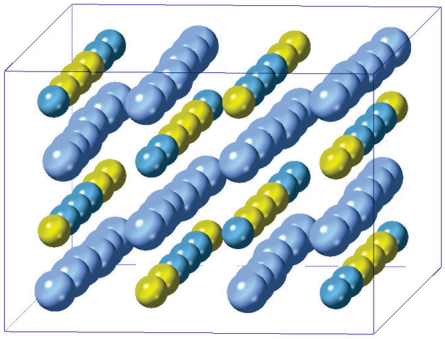


Figure 10.4: Crystallographic unit cell for $NaCa(NH_2)_3$. Teal = Calcium, Yellow = Sodium, Blue = Nitrogen

10.6 Conclusions

The overall purpose of this work was to deepen the understanding of the fundamental chemistry and reaction mechanisms of amide-imide catalysts for ammonia decomposition whilst simultaneously endeavouring to develop a highly active, low temperature NH_3 decomposition catalyst for application in the transport and energy sectors. Analysis of the information gained has assisted in determining the important elements required to help target future research efforts into designing a new generation of cheap and effective ammonia decomposition catalysts with improved potential and performance for the production of hydrogen.

Mixed-metal amides have the potential to play an important role in the implementation of a sustainable energy system which uses hydrogen as a fuel. The requirement to find unstable amides that exothermically decompose to a stable imide is crucial to improving the design of mixed-metal amide/imide catalyst systems. The future development of imide-based catalysts is key to facilitating the affordable and effective production of H_2 from NH_3 for sustainable energy applications.

The need for a renewable based H_2 carrier has been highlighted as paramount and it is hoped this work may contribute in helping to facilitate a transition to a future sustainable energy economy where the potential of ammonia is exploited to play a dominant role in transporting and storing clean and carbon free energy.

Appendix

Appendix

Contents

A.1 Chapter 3 - Li-Na-N-H System 414

A.2 Chapter 4 - Li-K-N-H System 416

A.3 Chapter 5 - Na-K-N-H System 430

A.4 Chapter 6 - Group 1 triple mixed-metal amides 435

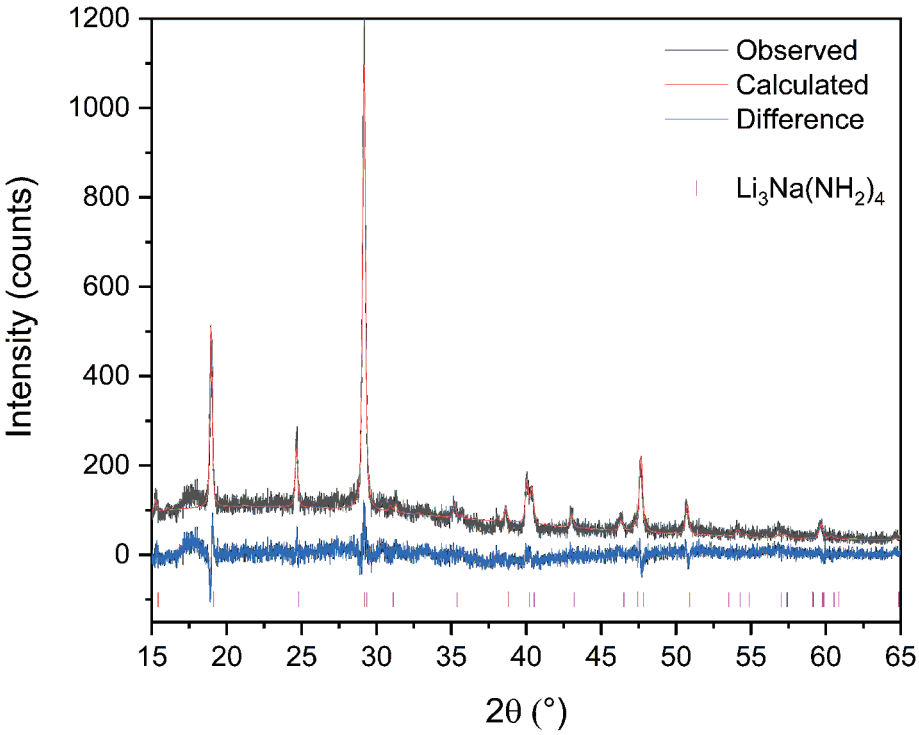
A.5 Chapter 8 - K-Mg-N-H System 436

A.6 Chapter 9 - Na-Mg-N-H System 445

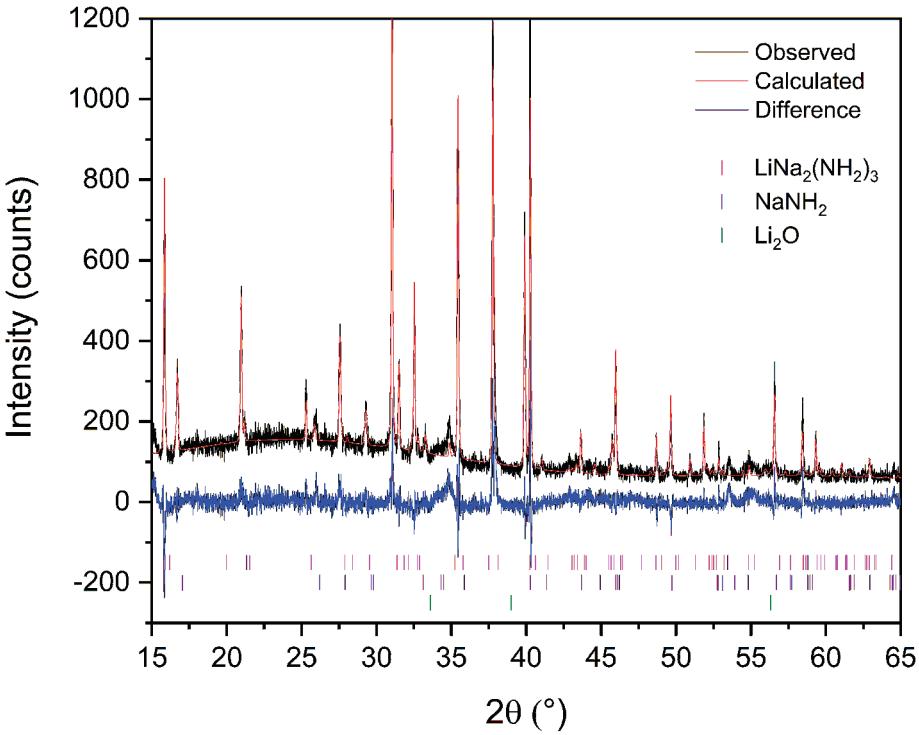
A.1 Chapter 3 - Li-Na-N-H System

Sample Number	Heating Method	Ramp Rate °C/ min	Starting materials % purity	Total sample mass/ g	Composition for 3:1 ratio (weight %)			Composition for 1:2 ratio (weight %)			
					$Li_3Na(NH_2)_4$	$LiNa_2(NH_2)_3$	$LiNH_2$	$LiNa_2(NH_2)_3$	$NaNH_2$	Li_2O
1	Sealed cylindrical reactor	5	95	1	76.59	12.7	10.71	-	-	-
2	Tube furnace	2	95	1	75.69	10.39	13.93	84.29	9.93	5.78
3		1	95	1	77.35	17.00	5.65	85.87	10.82	3.31
4		1	99	1	68.55	14.44	17.00	87.50	11.24	1.27
5		1	95	0.5	96.96	3.04	0	89.74	8.36	1.9
6	Gas flow panel - argon	1	95	0.5	95.45	4.55	-	88.76	11.24	-
7	Gas flow panel - ammonia	1	95	0.5	97.33	-	-	67.91	25.52	6.57
8	BM	-	95	0.5	∼100	-	-	71.83	28.17	-

Table A.1: Synthesis conditions for the Li-Na-N-H system



(a) Powder X-ray diffraction data for $Li_3Na(NH_2)_4$



(b) Powder X-ray diffraction data for $LiNa_2(NH_2)_3$

Figure A.1: Powder X-ray diffraction data of the main phases of the Li-Na-N-H system

A.2 Chapter 4 - Li-K-N-H System

Tube furnace										
						TF temp	% Composition			
Sample						(°C)	KNH_2	$LiK_2(NH_2)_3$	$LiNH_2$	
A						70	55.4	-	44.6	
B						130	73.9	9.3	16.8	
C						190	64.5	35.4	-	
D						200	58.0	42.0	-	
E						275	56.7	43.3	-	
Gas flow panel					**Gas flow panel gas**	**Gas flow panel temp**	**% Composition**			
Sample						**(°C)**	**KNH_2**	**$LiK_2(NH_2)_3$**	**$LiNH_2$**	
R					Argon	200	39.0	61.0	-	
S					NH_3	200	25.0% $Li_3K(NH_2)_4$, 59.9% $LiNH_2$, 15.1 % Li_2O			
Ball-mill	**Reactor**	**Ball**	**Quantity**	**RPM**	**Time**	**PXRD**	**TF temp**	**% Composition**		
Sample	**Vol (ml)**	**Diameter (mm)**	**of balls**		**(mins)**	**vs. TF**	**(°C)**	**KNH_2**	**$LiK_2(NH_2)_3$**	**$LiNH_2$**
F	125	4	5	200	60	Pre	-	5.37	61.47	33.16
G	125	4	5	200	60	Post	225	42.81	16.98	40.21
H	80	2	45g	200	60	Pre	-	-	66.80	33.2
I	80	2	45g	200	60	Post	225			
J	80	2	45g	200	60	Post	160			
K	80	2	30g	200	60	Pre	-	-	66.31	33.69
L	80	2	30g	200	60	Post	160	V. poor PXRD, only some KNH_2 discernible		
M	80	2	30g	400	60	Pre	-	-	100	-
N	80	2	30g	400	60	Post	160	V. poor PXRD, only some KNH_2 discernible		
P	80	2	30g	200	120	Pre	-	-	56.56	43.44
Q	80	2	30g	200	120	Post	160	V. poor PXRD, only some KNH_2 discernible		

Table A.2: $LiK_2(NH_2)_3$ synthesis conditions

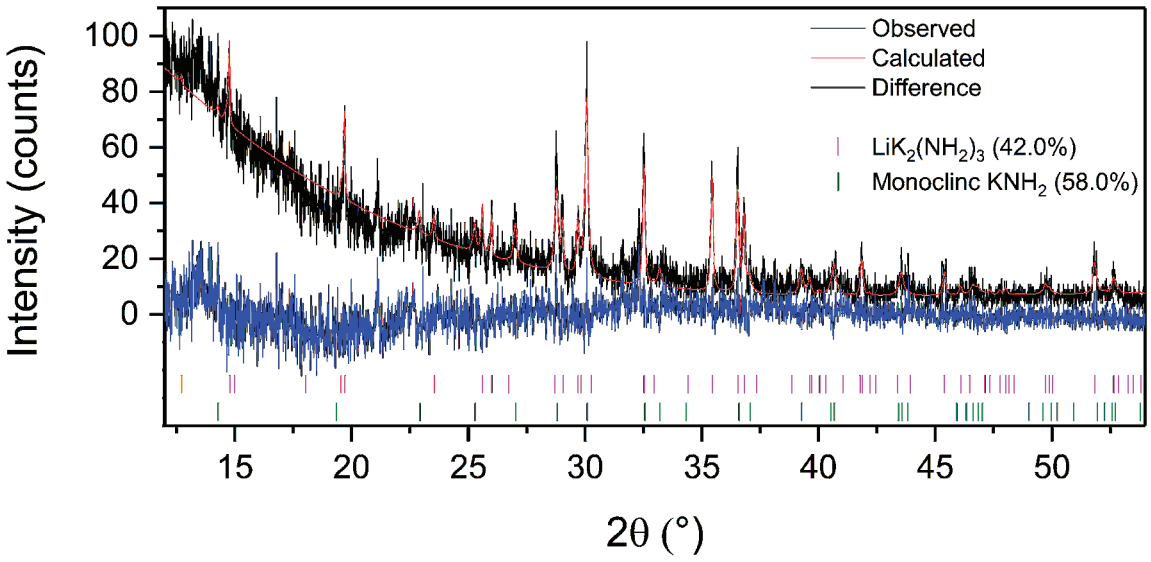


Figure A.2: Powder X-ray diffraction data collected for the sample resulting from the synthesis of $LiK_2(NH_2)_3$ in the tube furnace for 12 hours at 200 °C

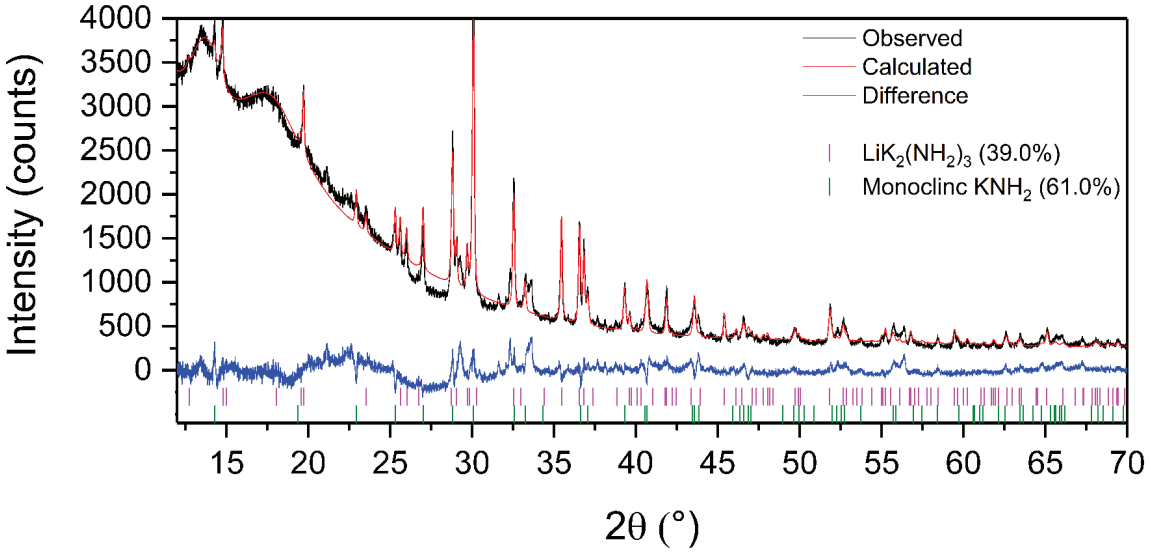


Figure A.3: Powder X-ray diffraction data collected for the sample resulting from the synthesis of $LiK_2(NH_2)_3$ on the Gas Flow Panel for 12 hours at 200 °C under argon

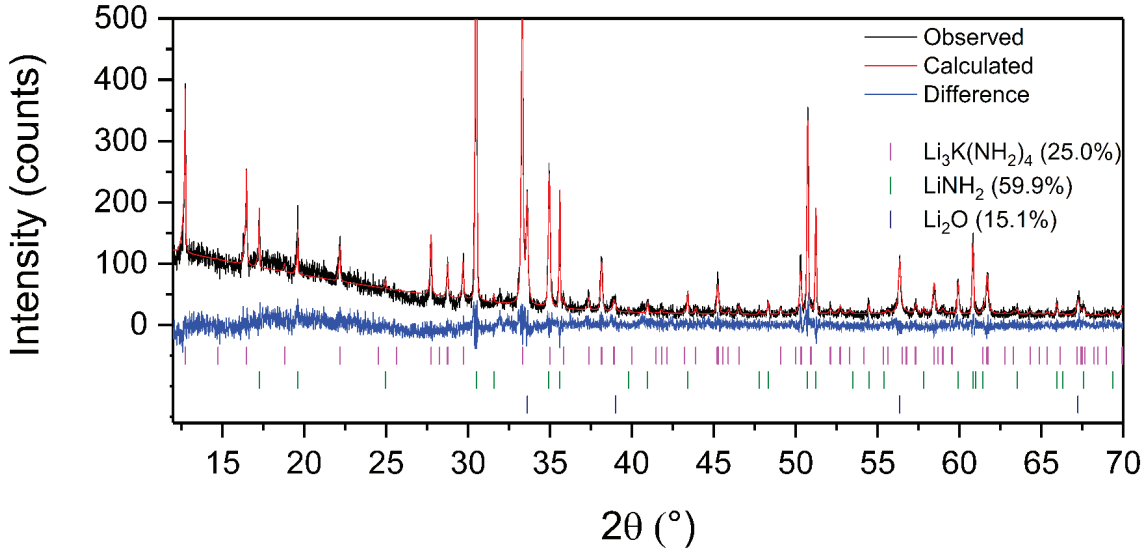


Figure A.4: Powder X-ray diffraction data collected for the sample resulting from the synthesis of $LiK_2(NH_2)_3$ on the Gas Flow Panel for 12 hours at 200 °C under ammonia

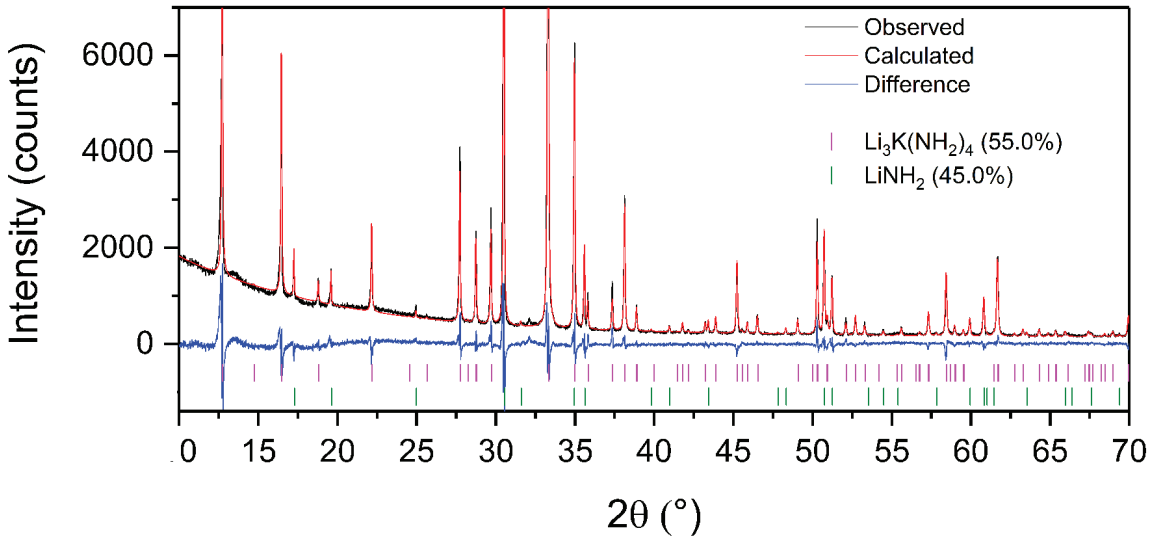


Figure A.5: Powder X-ray diffraction data collected for the sample resulting from the synthesis of $Li_7K(NH_2)_8$ in the tube furnace for 12 hours at 200 °C

Initial hour long scan						**$Li_3K(NH_2)_4$ synthesis at 175 °C**	
$LiND_2$		**$Li_3K(ND_2)_4$**		**Li_2O**		**$Li_3K(ND_2)_4$**	
d-spacing (Å)	Miller indices (*hkl*)	*d*-spacing (Å)	Miller indices (*hkl*)	*d*-spacing (Å)	Miller indices (*hkl*)	*d*-spacing (Å)	Miller indices (*hkl*
5.12	(002)	3.47	(202)	2.67	(111)	4.74	(112)
4.52	(101)	2.69	(215)	2.31	(002)	3.49	(202)
3.57	(110)	2.57	(220)			3.23	(211)
2.93	(112)					3.18	(116)
2.56	(004)					3.12	(204, 207)
2.52	(200)					3.03	(008, 213)
2.20	(211)					2.71	(206, 215)
1.90	(105)					2.58	(220)
1.88	(213)					2.53	(109)
						2.37	(217, 224)
						2.33	(303, 208)

Table A.3: Peak positions and indexing for the $3LiND_2 + KND_2$ synthesis experiment on GEM seen in Figure A.6, Figure A.7 and Figure A.8

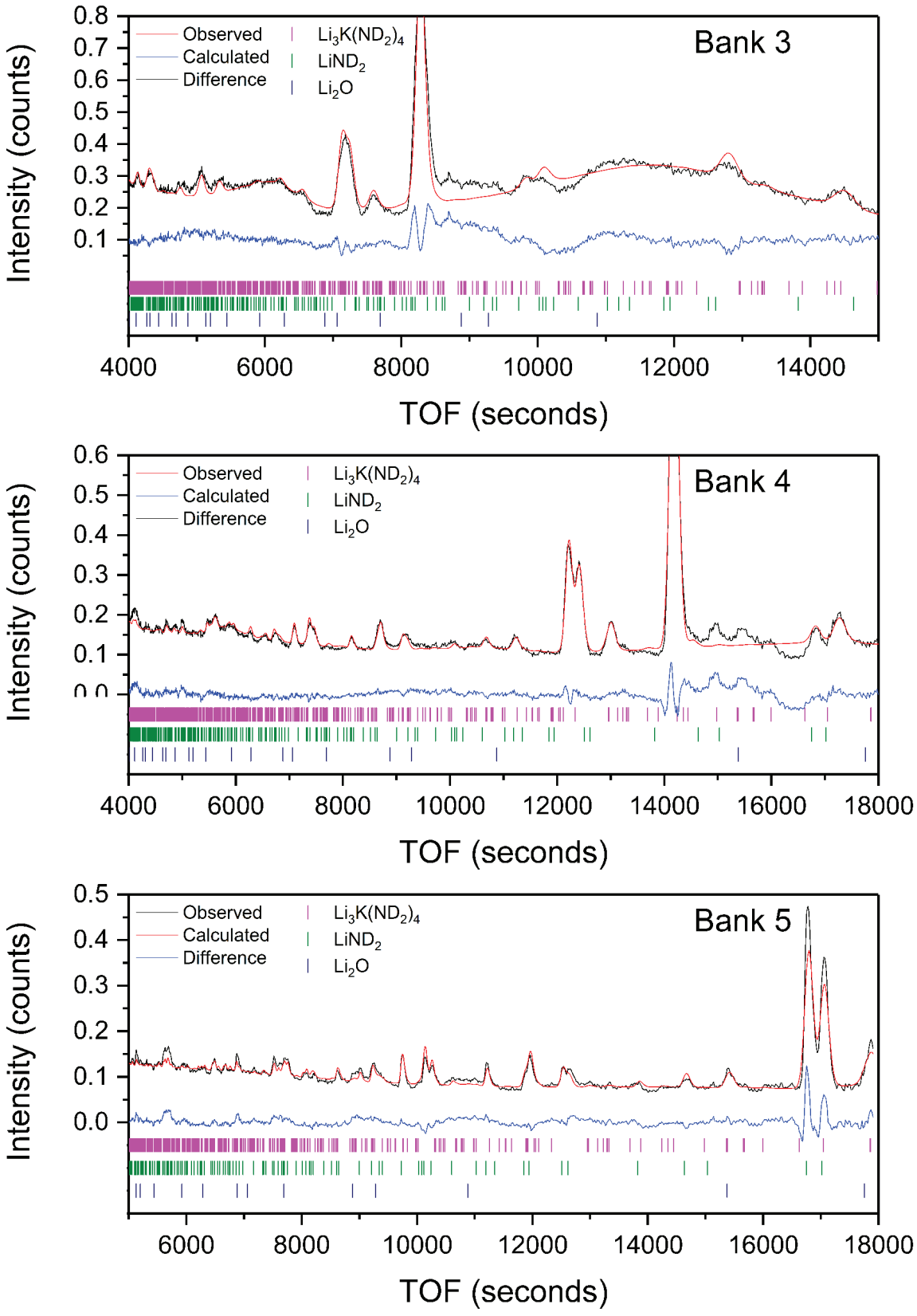


Figure A.6: Long run (82240) at the start of the $3LiND_2 + KND_2$ synthesis experiment on GEM which fits to $LiND_2$ (69.8 %), Li_2O (21.3 %) and $Li_3K(ND_2)_4$ (9.0 %)

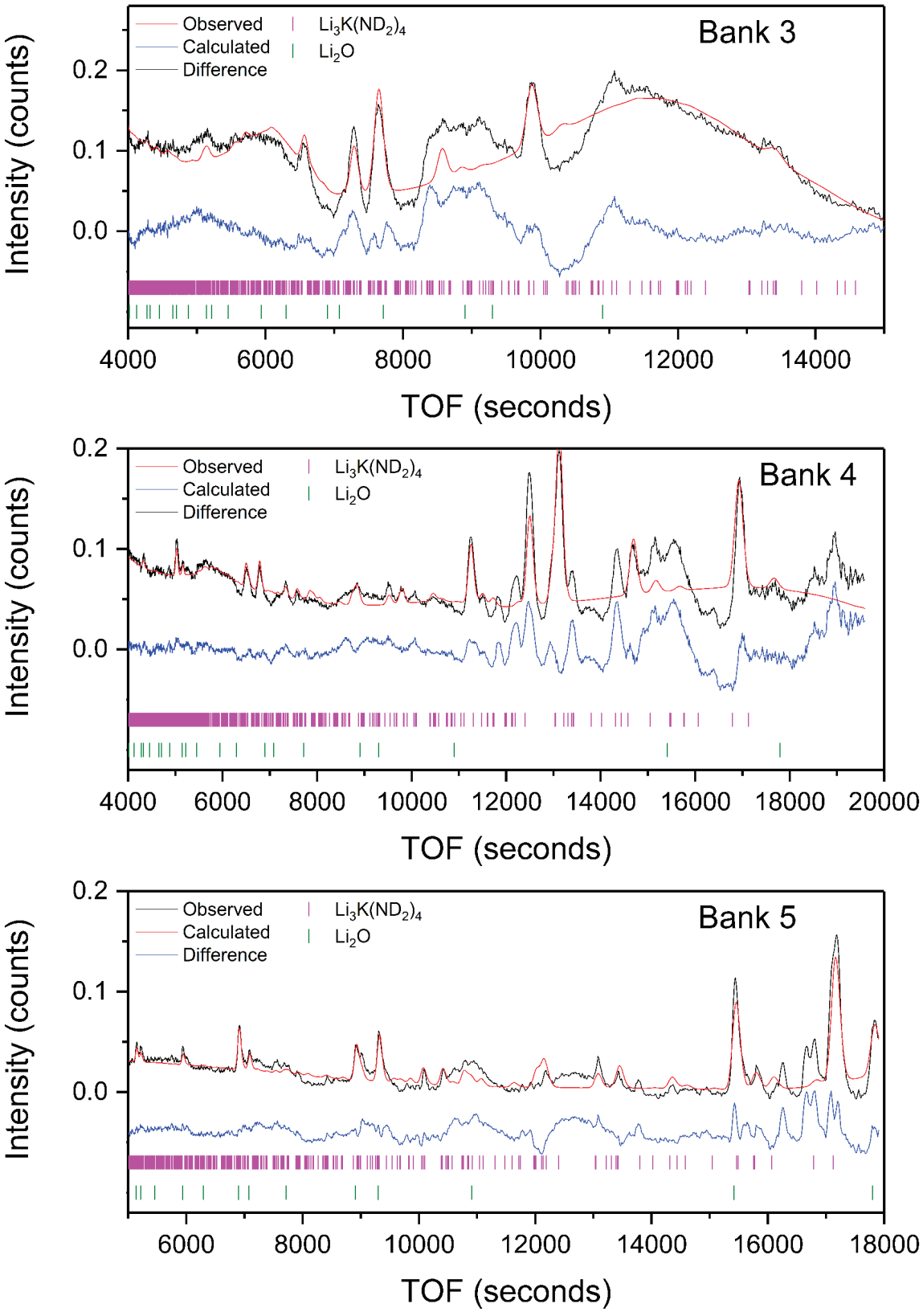


Figure A.7: Runs 82373-82468 (from 175 °C onwards)from the $3LiND_2 + KND_2$ synthesis experiment on GEM once $Li_3K(ND_2)_4$ was synthesised which fits to $Li_3K(ND_2)_4$ (66.1 %) and Li_2O (33.9 %)

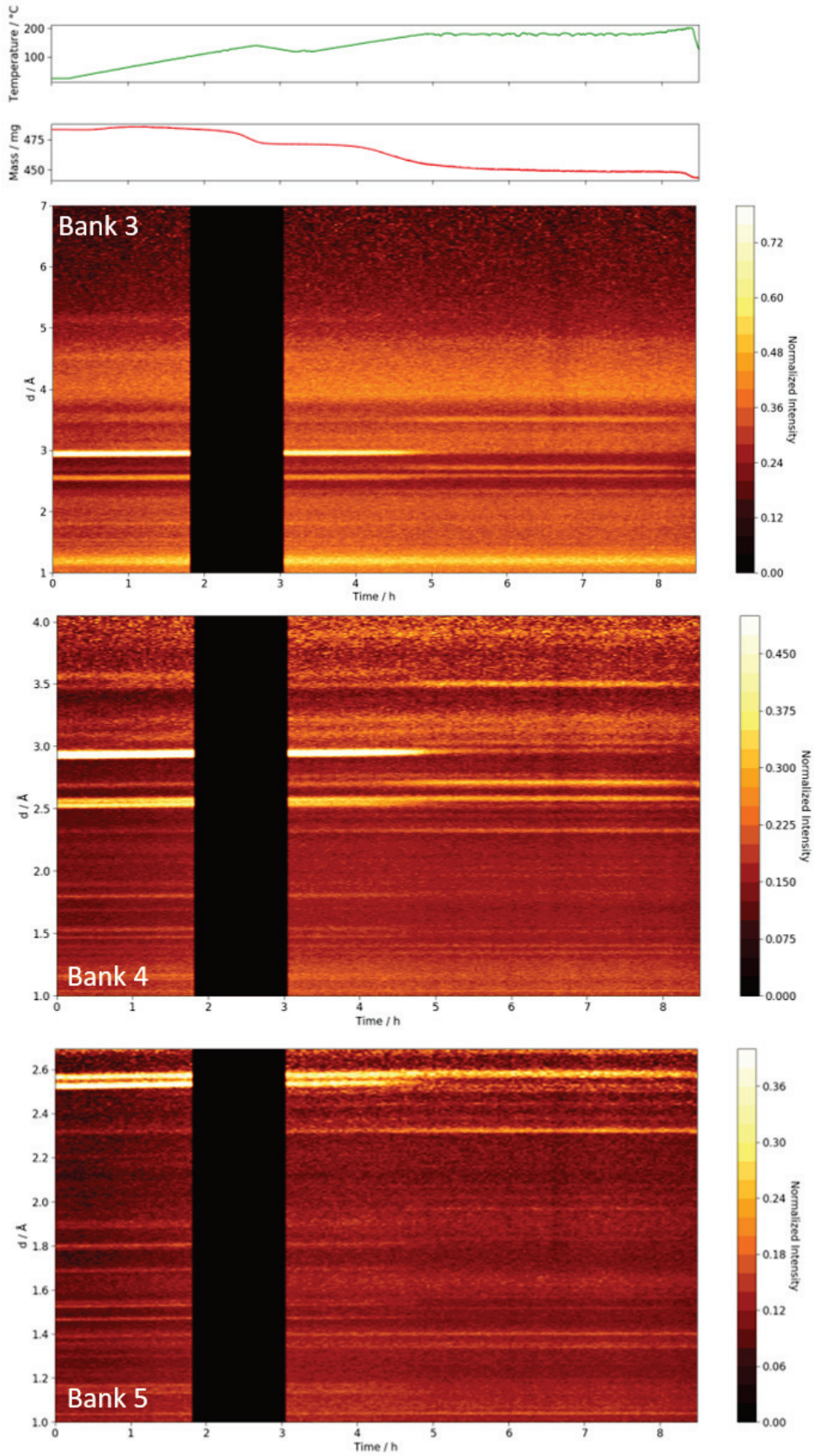


Figure A.8: Contour plots of the diffraction data collected from banks 3, 4 and 5 together with the corresponding thermogravimetric data for the $3LiND_2$ +KND_2 synthesis experiment on GEM

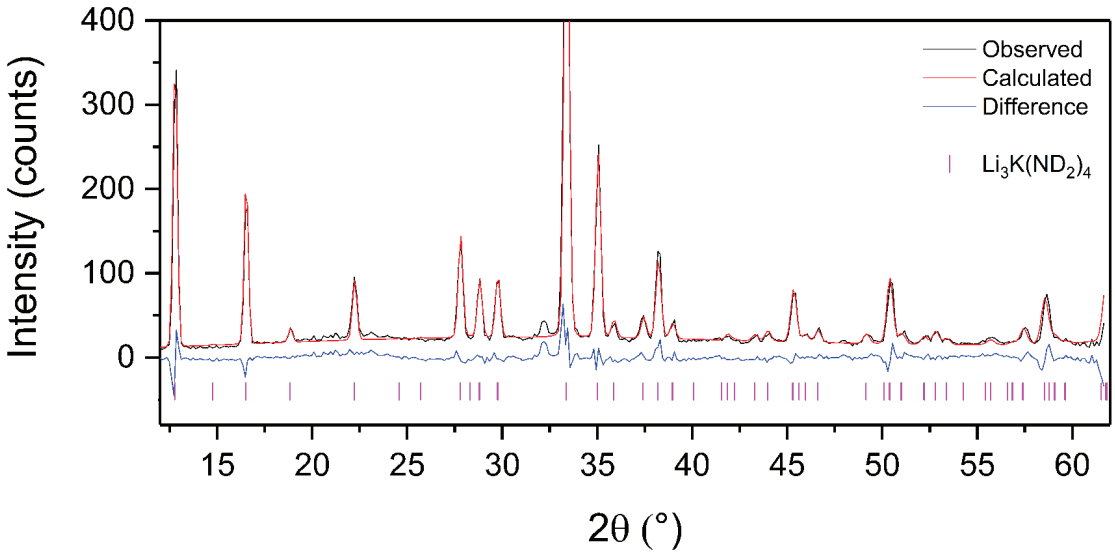


Figure A.9: Powder X-ray diffraction data collected for the ball-milled sample of $Li_3K(ND_2)_4$ used for the $Li_3K(ND_2)_4$ decomposition experiment on GEM

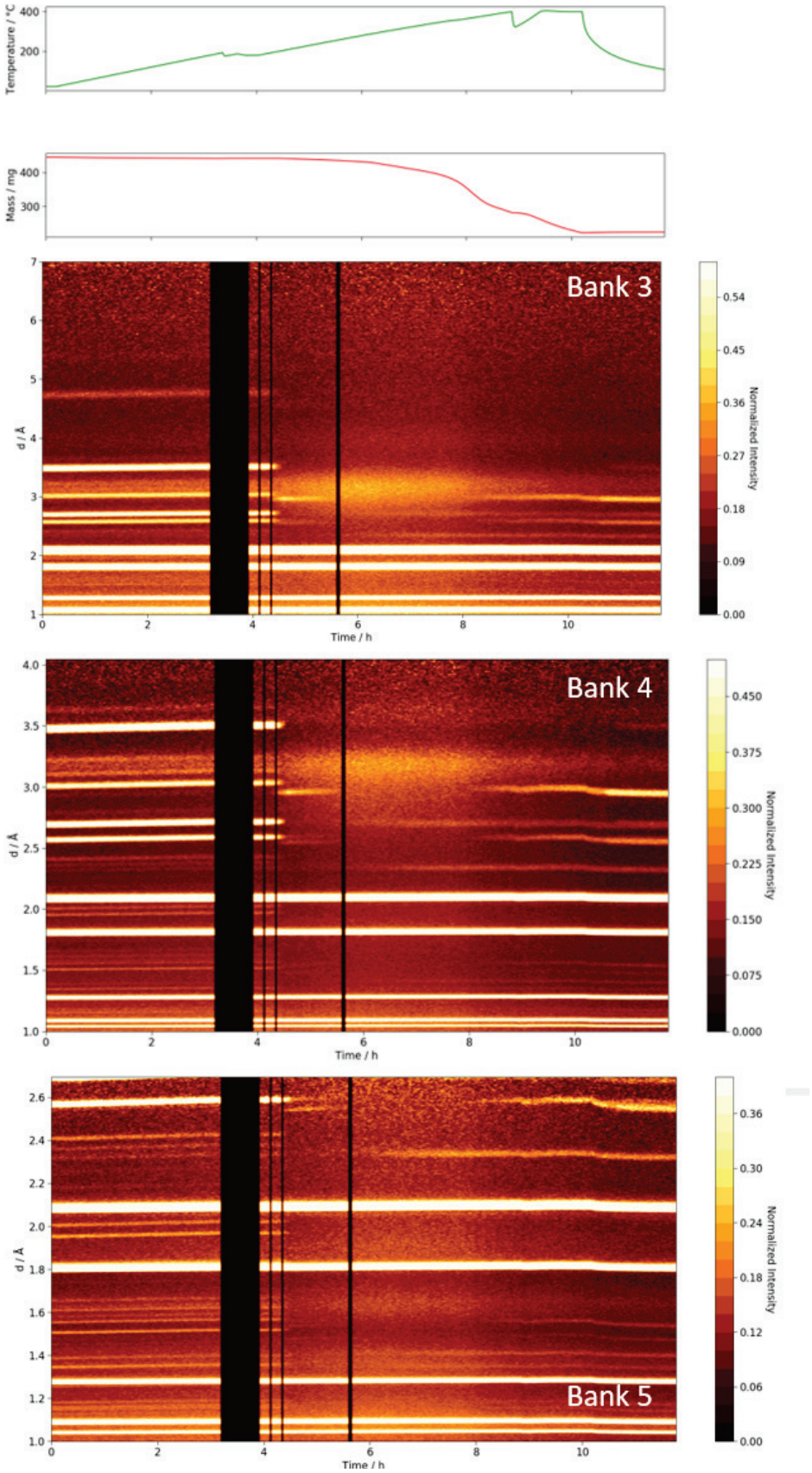


Figure A.10: Contour plots for banks 3, 4 and 5 for the $Li_3K(ND_2)_4$ decomposition experiment

Steel doublets			**$Li_3K(ND_2)_4$**	
d-spacing (Å)		Miller indices (*hkl*)	*d*-spacing (Å)	Miller indices (*hkl*)
2.08	2.07	(111)	4.71	(112)
1.80	1.79	(002)	3.62	(200)
1.28	1.27	(022)	3.46	(202)
1.09	1.08	(311)	3.21	(211)
1.04	1.03	(222)	3.15	(116)
			3.10	(107, 204)
			3.00	(213, 008)
			2.68	(215, 200)
			2.56	(220)
			2.40	(301)
			2.35	(224, 217)

Table A.4: Peak positions and indexing for the $Li_3K(ND_2)_4$ decomposition experiment on GEM shown in Figure A.10

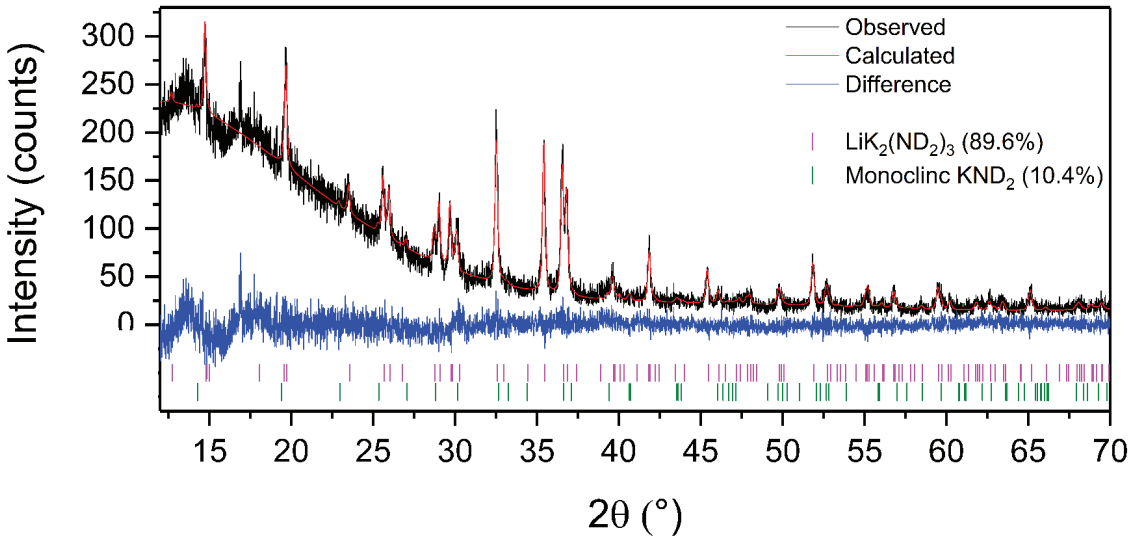


Figure A.11: Powder X-ray diffraction data collected for the sample of $LiK_2(ND_2)_3$ synthesised by ball-milling $LiND_2$ and KND_2 in a 1:2 molar ratio

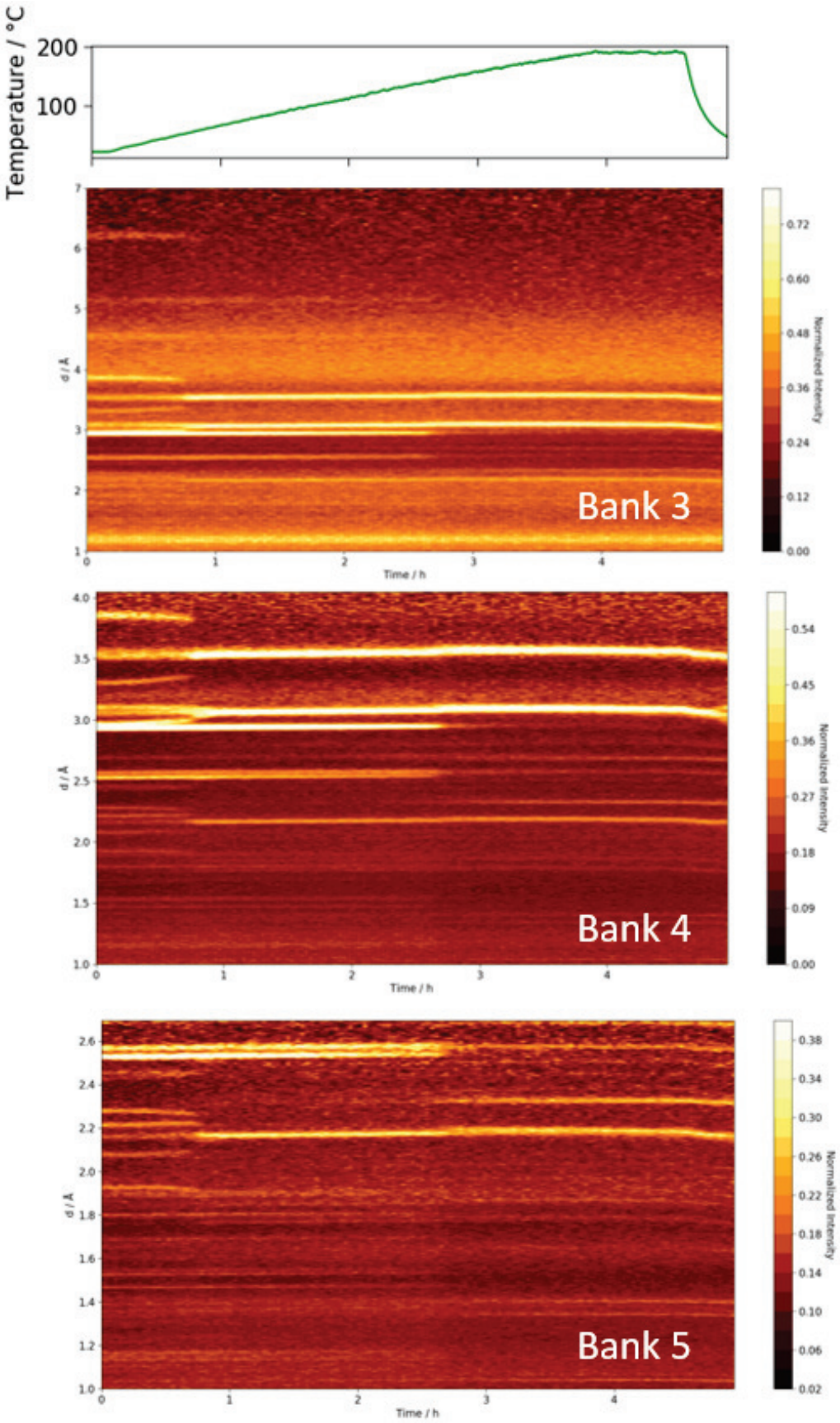


Figure A.12: Contour plots for banks 3, 4 and 5 for the $LiND_2$ +2KND_2 synthesis experiment

Monoclinic KND_2		**Tetragonal KND_2**		**$LiND_2$**	
d-spacing (Å)	Miller indices (*hkl*)	*d*-spacing (Å)	Miller indices (*hkl*)	*d*-spacing (Å)	Miller indices (*hkl*)
6.18	(001)	3.53	(101)	5.13	(002)
4.55	(100)	3.09	(002)	4.53	(101)
3.85	(10-1)	3.04	(110)	3.57	(110)
3.50	(101)	2.51	(102)	2.93	(112)
3.29	(011)			2.56	(004)
3.09	(002)			2.52	(200)
2.96	(110)				
2.69	(10-2)				
2.44	(102)				

Table A.5: Peak positions and indexing for the $LiND_2$ + $2KND_2$ synthesis experiment on GEM shown in Figure A.12

$LiK_2(ND_2)_3$			
d-spacing (Å)	Miller indices (*hkl*)	*d*-spacing (Å)	Miller indices (*hkl*)
5.99	(101)	3.00	(211, 202)
4.53	(111)	2.75	(212)
4.50	(102)	2.53	(114)
3.47	(200)	2.46	(220)
3.11	(210)	2.44	(213)
3.07	(113)	2.40	(221)

Table A.6: Peak positions and indexing for the initial hour long scan at the start of the $LiK_2(ND_2)_3$ decomposition experiment on GEM as shown in Figure A.13

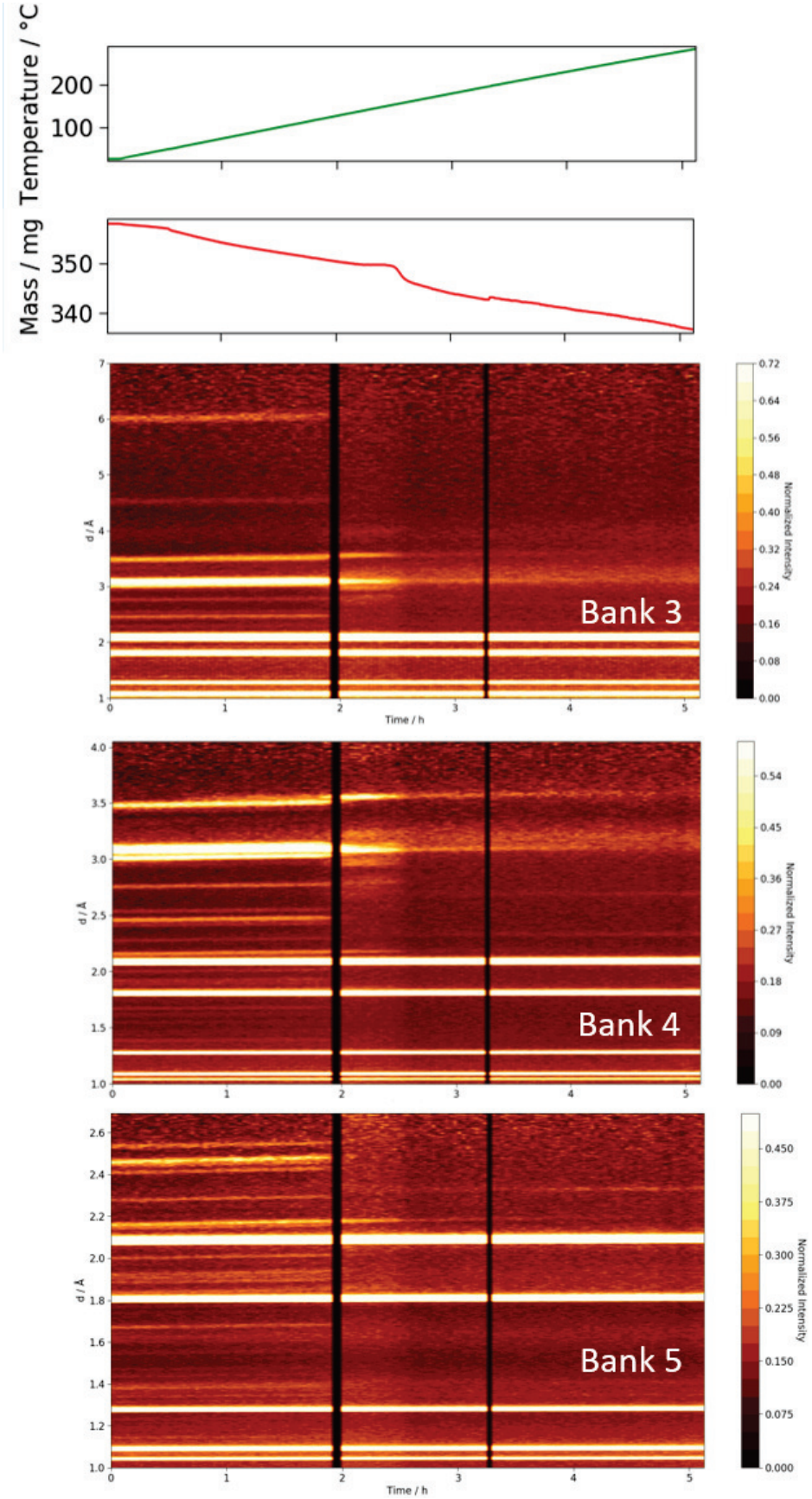


Figure A.13: $LiK_2(ND_2)_3$ decomposition experiment bank 3, 4 and 5 diffraction data and thermogravimetric data before the long beam off

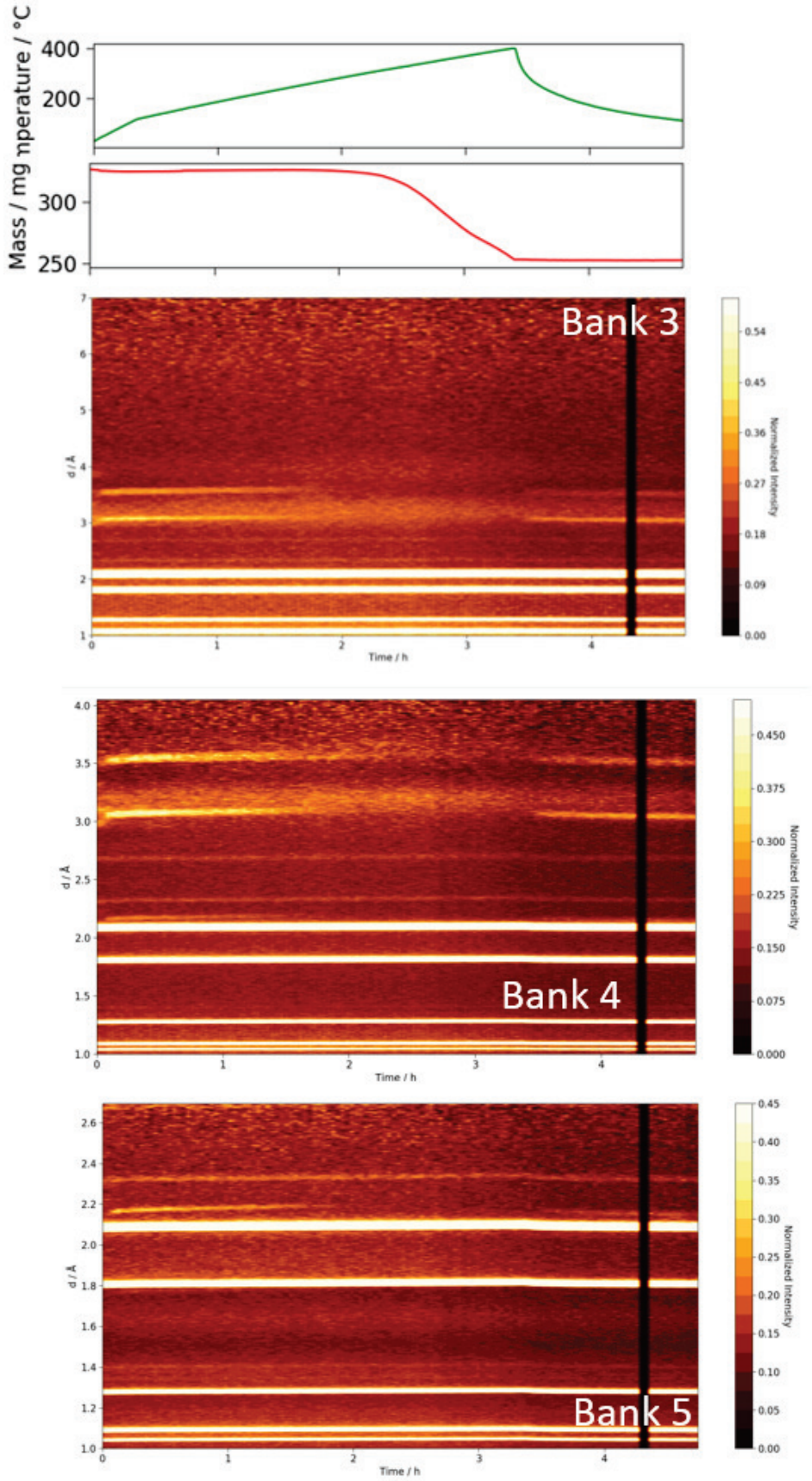


Figure A.14: $LiK_2(ND_2)_3$ decomposition experiment bank 3, 4 and 5 diffraction data and thermogravimetric data after the long beam off

A.3 Chapter 5 - Na-K-N-H System

2 θ	***d*-spacing**
7.07	6.69
8.13	5.82
9.44	5.01
9.72	4.87
11.45	4.13
13.37	3.54
14.15	3.35
14.95	3.17
15.13	3.13
15.66	3.03
16.50	2.87
16.90	2.81
17.61	2.69
18.95	2.51
20.15	2.37
20.64	2.30
20.96	2.27
22.17	2.15
23.27	2.04
23.40	2.03
24.23	1.96
24.32	1.96
24.56	1.94
25.48	1.87

Table A.7: 2 θ and d-spacing values for peaks corresponding to the unknown phase (U.P.) in the s5-s11 samples in Figure 5.2 (highlighted in red)

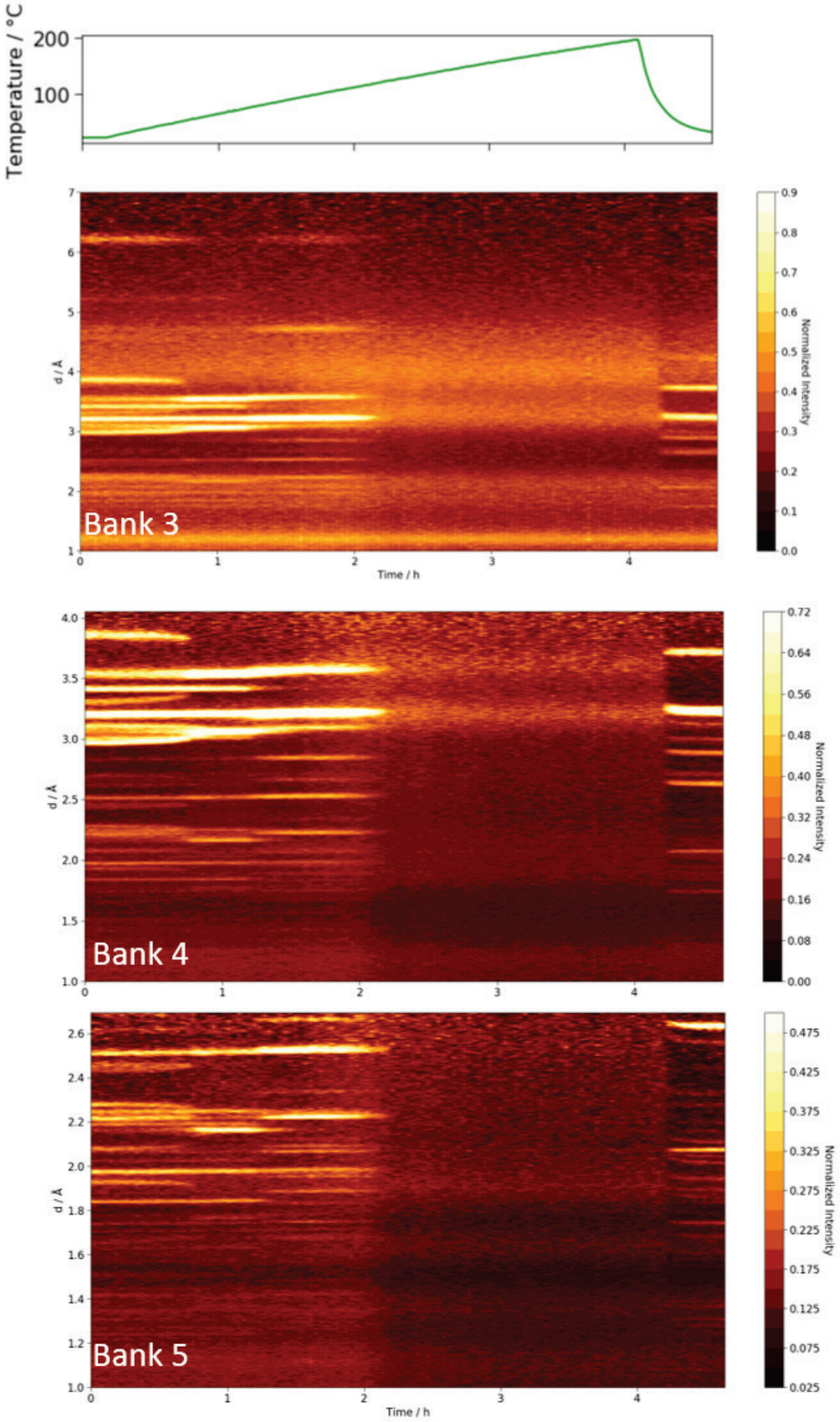


Figure A.15: Contour plots for banks 3, 4 and 5 for $NaND_2$ + $2KND_2$

$NaND_2$		**Monoclinic KND_2**		**Tetragonal KND_2**	
d-spacing (Å)	Miller indices (*hkl*)	*d*-spacing (Å)	Miller indices (*hkl*)	*d*-spacing (Å)	Miller indices (*hkl*)
5.19	(111)	6.19	(001)	3.55	(101)
3.40	(220)	4.54	(100)	3.11	(002)
3.19	(022)	3.84	(10-1)	3.05	(110)
3.01	(131)	3.50	(101)		
3.00	(202)	3.30	(011)		
2.71	(311)	3.09	(002)		
2.61	(040)	2.96	(110)		
2.60	(222)	2.68	(10-2)		
2.50	(113)	2.61	(111)		
		2.45	(102)		

Table A.8: Peak positions and indexing for the initial hour long scan at the start of the $NaK_2(ND_2)_3$ synthesis experiment on GEM as shown in Figure A.15

$NaK_2(ND_2)_3$ formed at 78 °C		**Unknown Phase formed at 105 °C on cooling**	
d-spacing (Å)	Miller indices (*hkl*)	*d*-spacing (Å)	
7.11	(100)	6.55	2.56
6.26	(002)	4.22	2.44
6.19	(101)	3.73	2.33
4.70	(102)	3.72	2.28
4.67	(111)	3.24	2.2
3.60	(103)	3.23	2.16
3.56	(200)	3.12	2.11
3.21	(113)	3.00	2.07
3.18	(210)	2.90	2.06
3.09	(202, 211)	2.89	2.05
2.86	(014)	2.71	2.02
2.84	(212)	2.66	1.95
2.66	(114)	2.64	1.90
2.53	(213)	2.63	1.86

Table A.9: Peak positions and indexing for $NaK_2(ND_2)_3$ formed at 78 °C and the Unknown Phase formed at 105 °C on cooling in the $NaK_2(ND_2)_3$ synthesis experiment on GEM as shown in Figure A.15

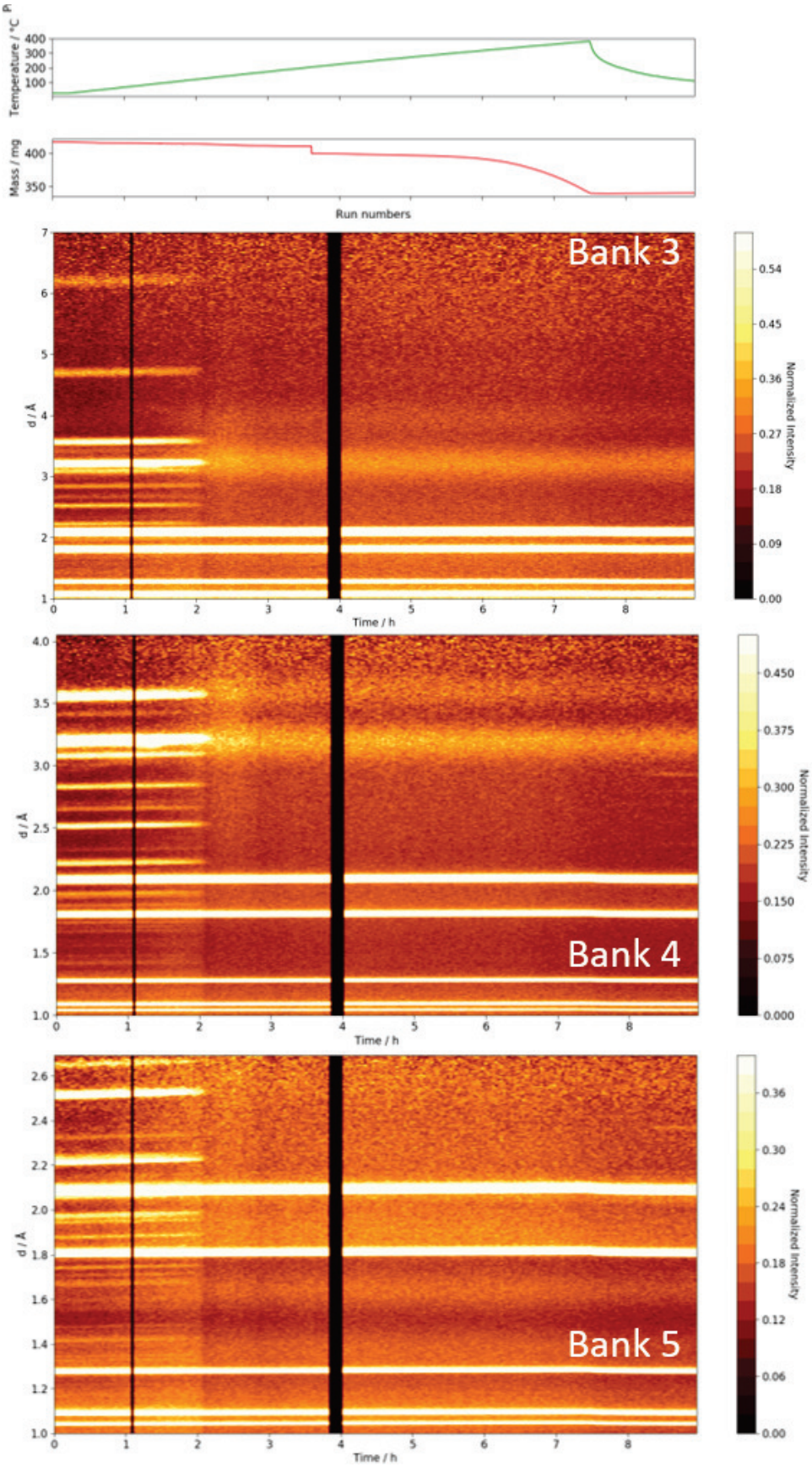


Figure A.16: Contour plots for banks 3, 4 and 5 for the $NaK_2(ND_2)_3$ decomposition experiment

Steel doublets			**$NaK_2(ND_2)_3$**	
d-spacing (Å)		Miller indices (*hkl*)	*d*-spacing (Å)	Miller indices (*hkl*)
2.08	2.07	(111)	7.08	(100)
1.80	1.08	(002)	6.23	(002)
1.04	1.27	(022)	6.16	(101)
1.09	1.08	(311)	4.65	(111)
1.04	1.04	(222)	4.08	(102)
			3.58	(103)
			3.54	(200)
			3.41	(201)
			3.20	(113)
			3.08	(202)
			2.85	(104)
			2.64	(114)
			2.52	(213)

Table A.10: Peak positions and indexing for the initial hour long scan at the start of the $NaK_2(ND_2)_3$ decomposition experiment on GEM as shown in Figure A.16

A.4 Chapter 6 - Group 1 triple mixed-metal amides

$$\frac{[Li_3Na]}{[Li_4]} = \frac{1}{4}\alpha = r_c = \frac{\Delta c}{c} \tag{A.1a}$$

$$r_c = \frac{11.48 - 10.23}{10.23} = 0.122 \tag{A.1b}$$

$$\frac{[Li_6NaK]}{[Li_7K]} = \frac{1}{7}\alpha = r_c' = \frac{4}{7}r_c \tag{A.1c}$$

$$r_{c'} = \frac{4}{7} \times 0.122 = 0.0699 \tag{A.1d}$$

$$\Delta c\text{'} = r_{c'} \times c' = 0.0699 \times 44.39 = 3.11 \tag{A.1e}$$

$$c'' = c' + \Delta c\text{'} = 47.50\,\mathring{A} \tag{A.1f}$$

$LiNH_2$ = [Li_4], $Li_3Na(NH_2)_4$ = [Li_3Na], $Li_7K(NH_2)_8$ = [Li_7], $Li_6NaK(NH_2)_8$ = [Li_6Na], Δc = change in c between $LiNH_2$ and $Li_3Na(NH_2)_4$, c is the lattice parameter of $LiNH_2$, Δc' = change in c between $Li_7K(NH_2)_8$ and $Li_6NaK(NH_2)_8$, c' is the lattice parameter of $Li_7K(NH_2)_8$ and c" is the lattice parameter of $Li_6NaK(NH_2)_8$.

A.5 Chapter 8 - K-Mg-N-H System

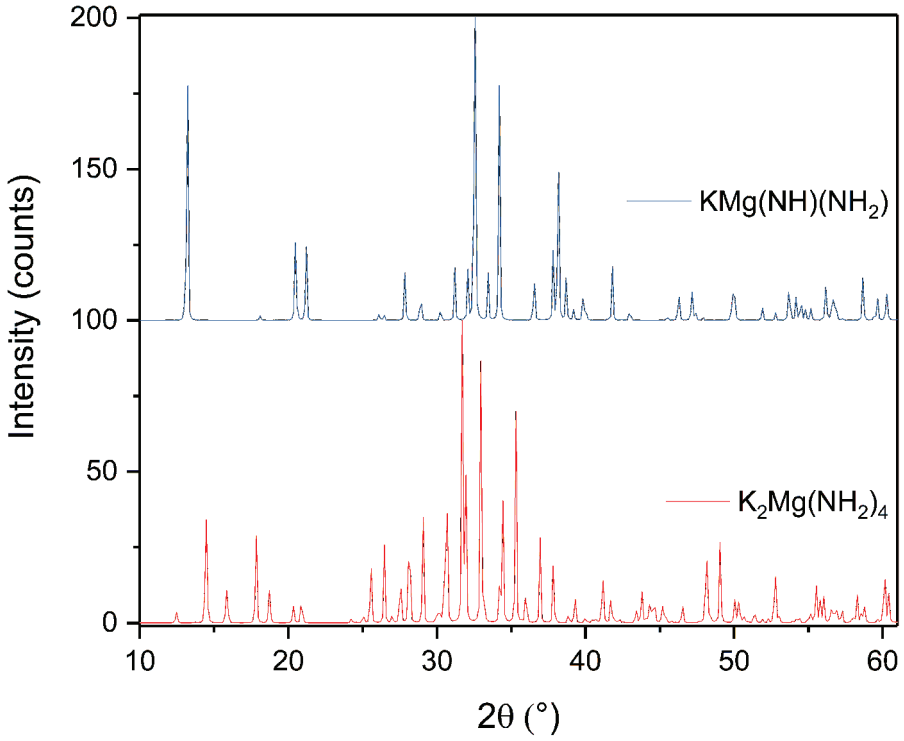


Figure A.17: Simulated powder X-ray diffraction data for $K_2Mg(NH_2)_4$ and $KMg(NH_2)(NH)$ (Normalized and offset from each other, wavelength = 1.5418 Å)

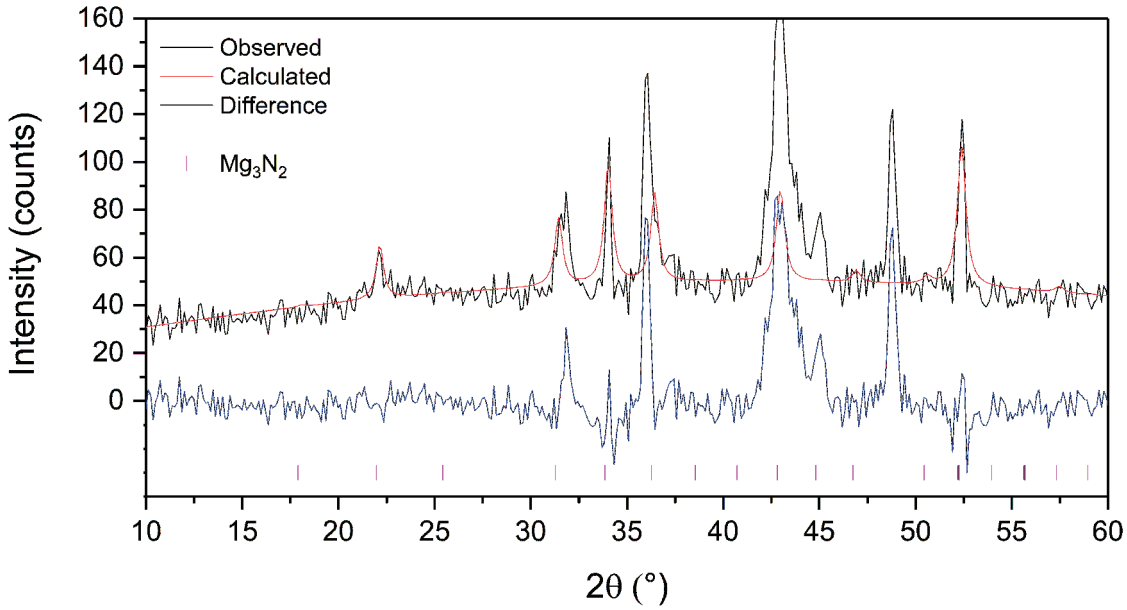


Figure A.18: Powder X-ray diffraction data collected for the sample remaining in the reactor at the end of the decomposition experiment of $K_2Mg(NH_2)_4$ under argon on the gas flow panel (Figure 8.6)

KND_2		$Mg(ND_2)_2$	
d-spacing (Å)	(*hkl*)	*d*-spacing (Å)	(*hkl*)
3.51	(101)	2.96	(224)
3.29	(011)	2.59	(400)
3.09	(002)	2.51	(008, 402)
2.96	(110)	2.34	(316)
2.69	(10-2)	1.83	(440)
2.60	(111)	1.80	(408)
2.45	(102)		
2.41	(012)		
2.28	(200)		
2.21	(20-1)		
2.07	(201, 112)		
1.93	(20-2, 020)		
1.85	(021)		

Table A.11: *d*-spacings for KND_2 and $Mg(ND_2)_2$ present in the hour long scan taken prior to the $K_2Mg(ND_2)_4$ synthesis experiment

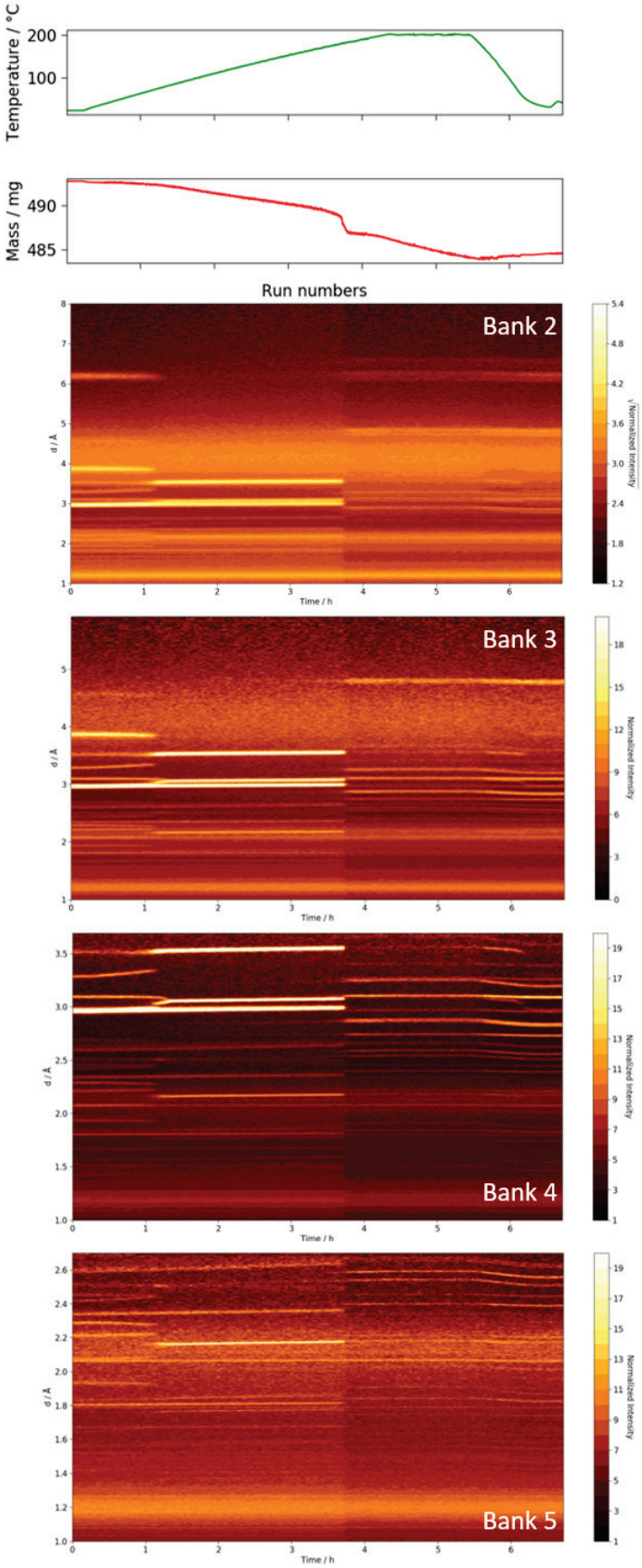


Figure A.19: Contour plots for banks 2, 3, 4 and 5 for the $2KND_2$ +$Mg(ND_2)_2$ synthesis experiment with corresponding thermogravimetric data

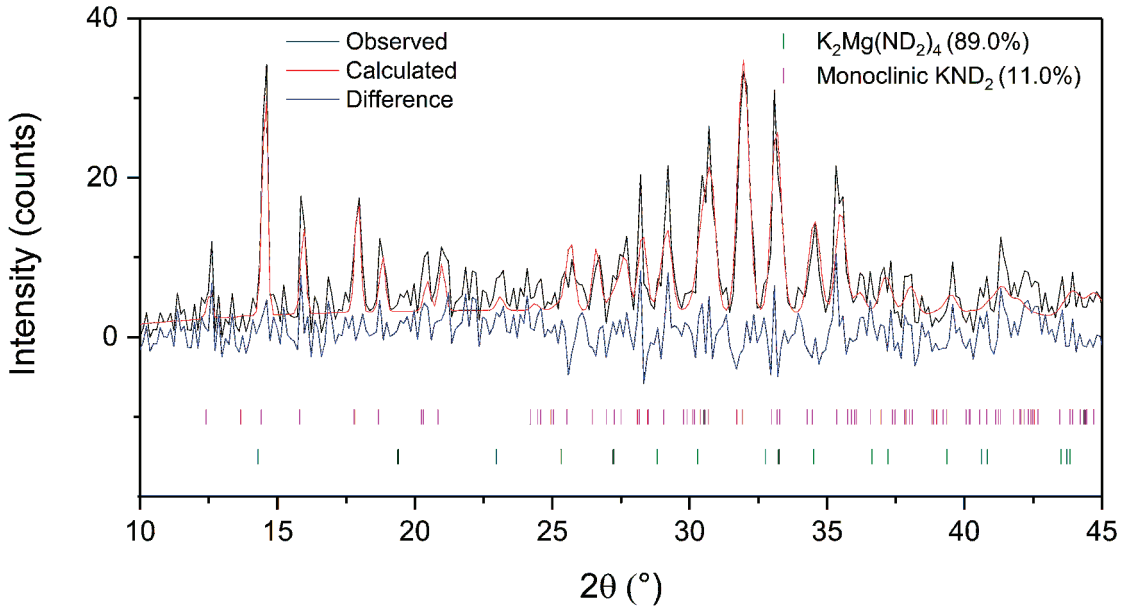


Figure A.20: Powder X-ray diffraction data collected from the final sample remaining at the end of the synthesis experiment on POLARIS

Steel doublets			**Region 2: $K_2Mg(ND_2)_4$**		**Region 2: Cubic KND_2**	
d-spacing (Å)		Miller indices (*hkl*)	*d*-spacing (Å)	Miller indices (*hkl*)	*d*-spacing (Å)	Miller indices (*hkl*)
2.12/2.04	2.08/2.06	(111)	4.79	(012)	3.54	(111)
1.84/1.80	1.79/1.76	(002)	3.63	(200)	3.07	(200)
1.30/1.25	1.27/1.26	(022)	3.40	(021)	2.17	(220)
1.07/1.06	1.09/1.08	(311)	3.27	(004)	1.85	(311)
			3.22	(210)		
			3.10	(022)		
			2.97	(211)		
			2.86	(202)		
			2.84	(20-4)		
			2.74	(023)		
			2.65	(212)		
			2.57	(22-1)		
			2.53	(114)		
			2.45	(015)		
			2.40	(221)		

Table A.12: *d*-spacings for the steel doublets as well as $K_2Mg(ND_2)_4$ and cubic KND_2 present in Region 2 of the $K_2Mg(ND_2)_4$ decomposition experiment shown in Figure A.21

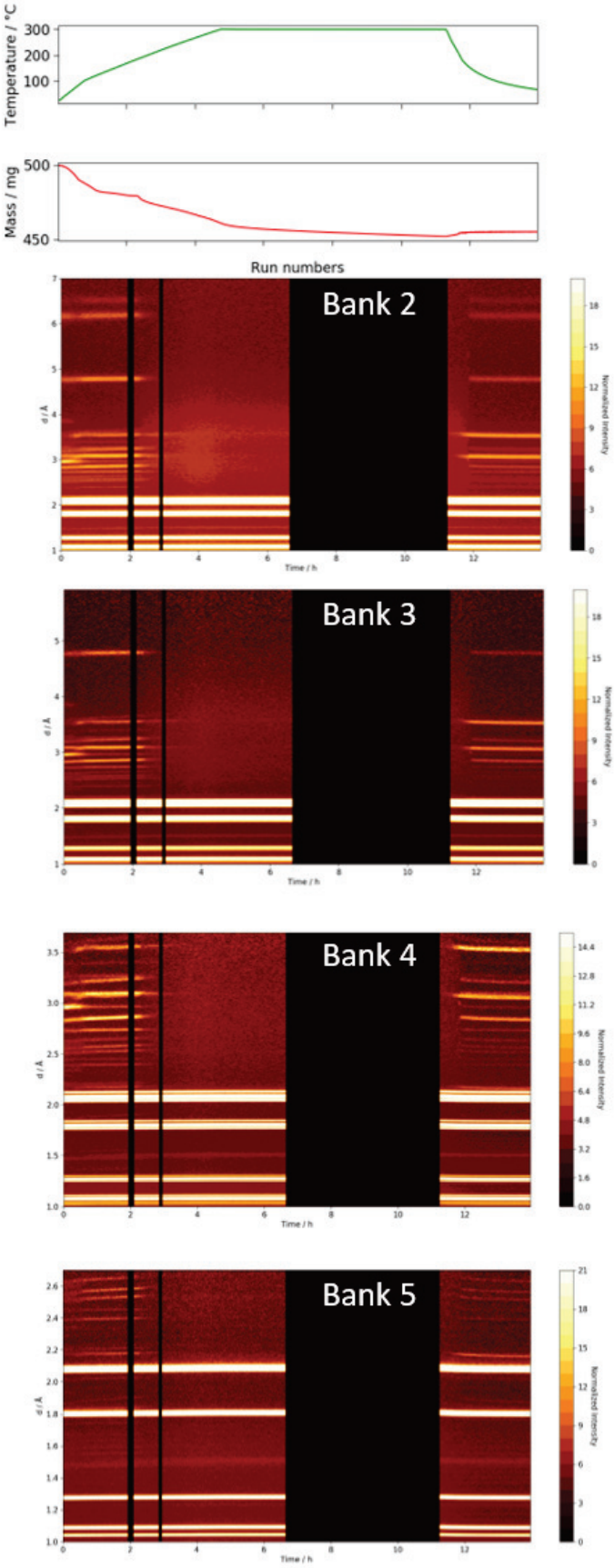


Figure A.21: Contour plots for banks 2, 3, 4 and 5 for the $K_2Mg(ND_2)_4$ decomposition experiment with corresponding thermogravimetric data

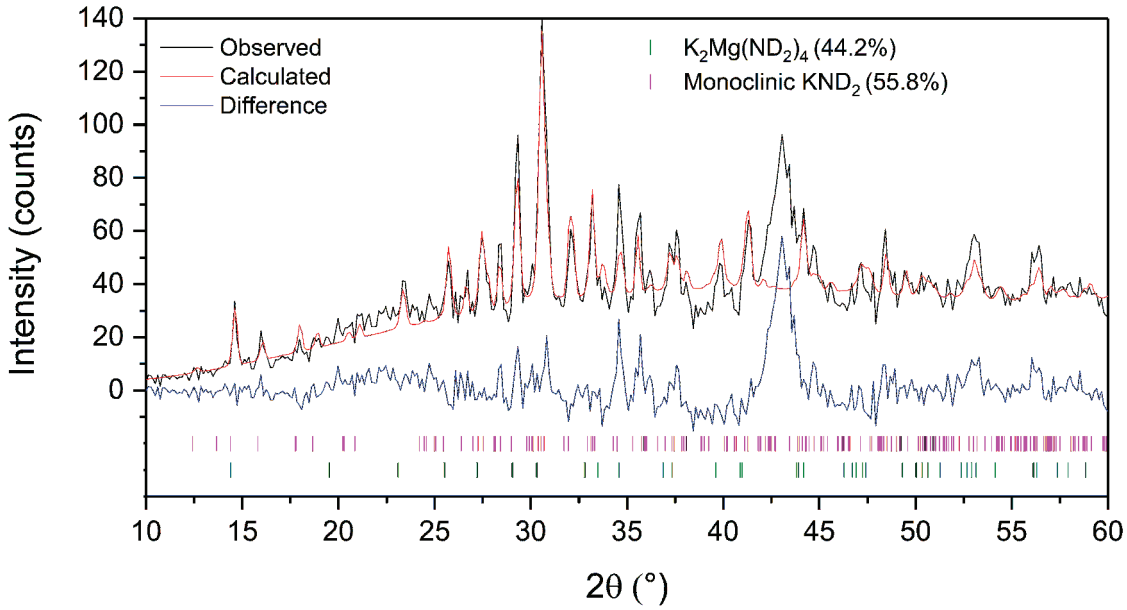


Figure A.22: Powder X-ray diffraction data collected for the final sample remaining at the end of the decomposition experiment on POLARIS

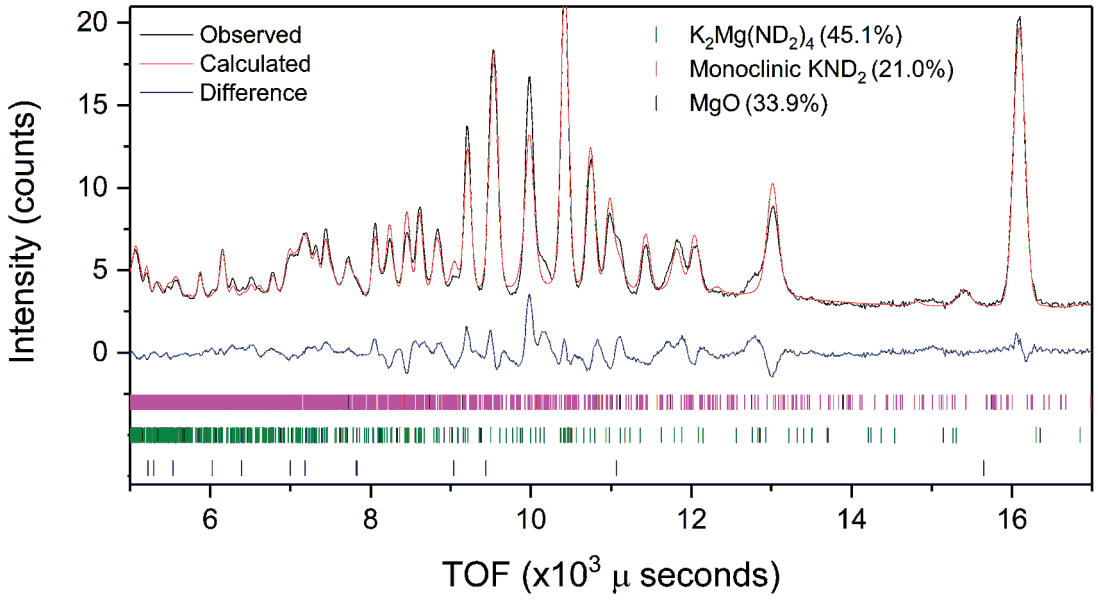


Figure A.23: Bank 3 post-experiment neutron diffraction data collected in a vanadium can of the sample recovered from the $K_2Mg(ND_2)_4$ decomposition experiment

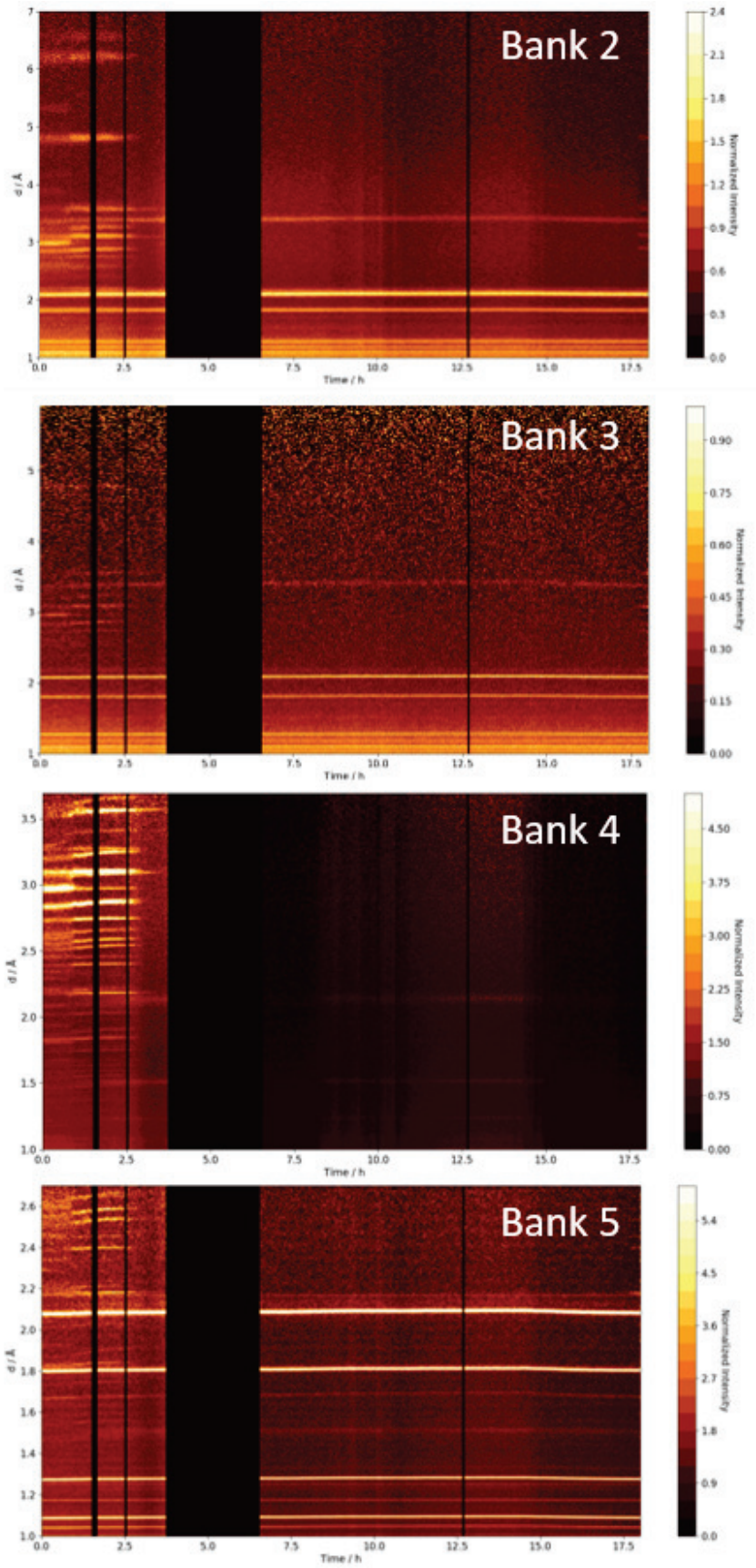


Figure A.24: Contour plots for banks 2, 3, 4 and 5 for the experiment looking at the ND_3 decomposition ability of $K_2Mg(ND_2)_4$

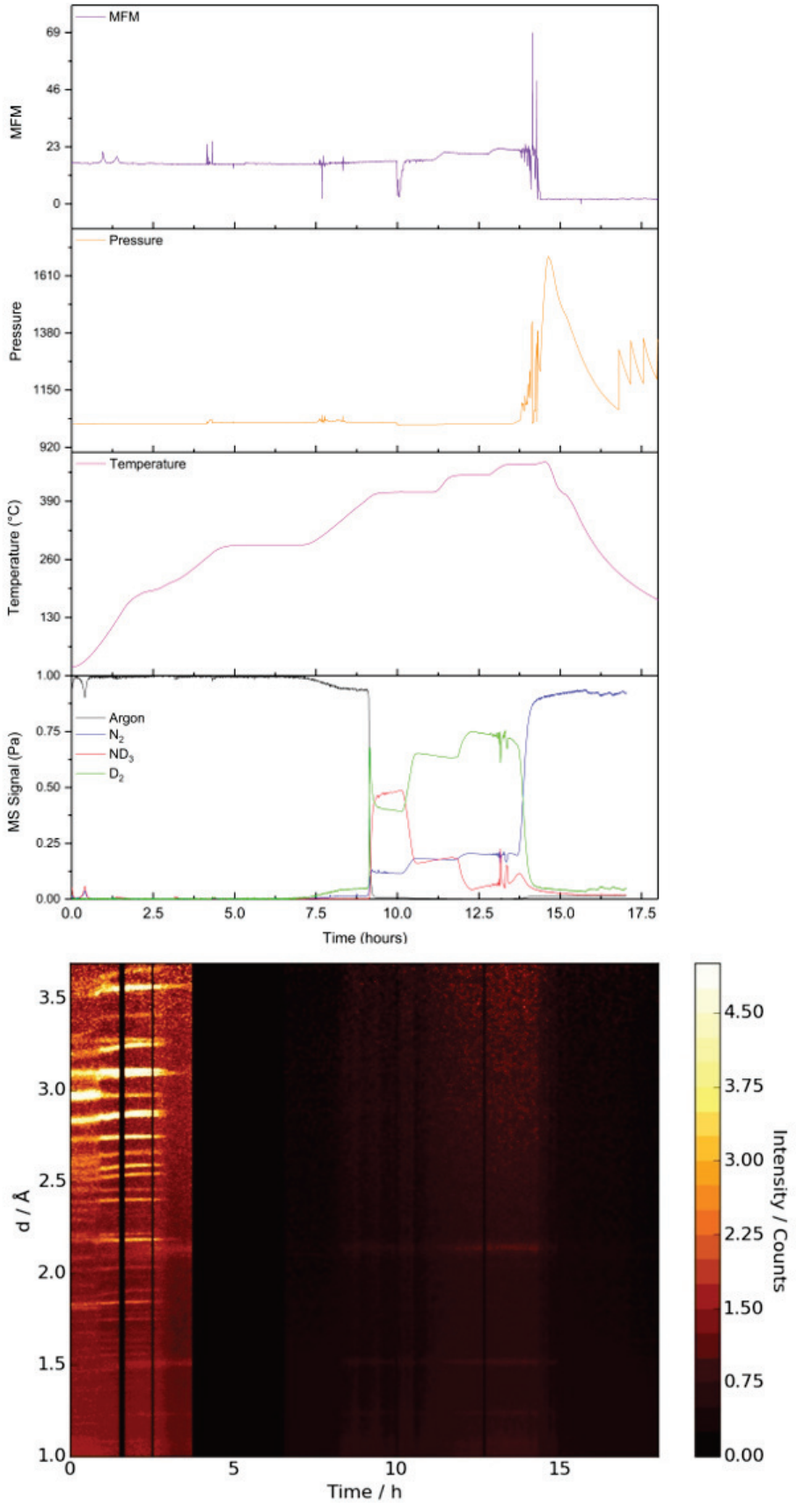


Figure A.25: Mass Spectrometry data, temperature profile and the bank 4 contour plot for the experiment looking at the ND_3 decomposition ability of $K_2Mg(ND_2)_4$

A.6 Chapter 9 - Na-Mg-N-H System

U.P. X		
2 θ (°)	***d*-spacing (Å)**	**WC Index**
16.71	2.84	001
18.86	2.52	100
25.30	1.88	101
32.97	1.45	2-10
33.78	1.42	002
37.18	1.29	2-11
38.26	1.26	200
38.97	1.24	102
42.01	1.15	201
47.93	1.02	2-12
51.38	0.95	3-10
51.68	0.95	003
51.95	0.94	202
54.41	0.90	3-11
55.50	0.89	103

Table A.13: U.P X (WC) 2 θ (°), *d*-spacing (Å) and indexing

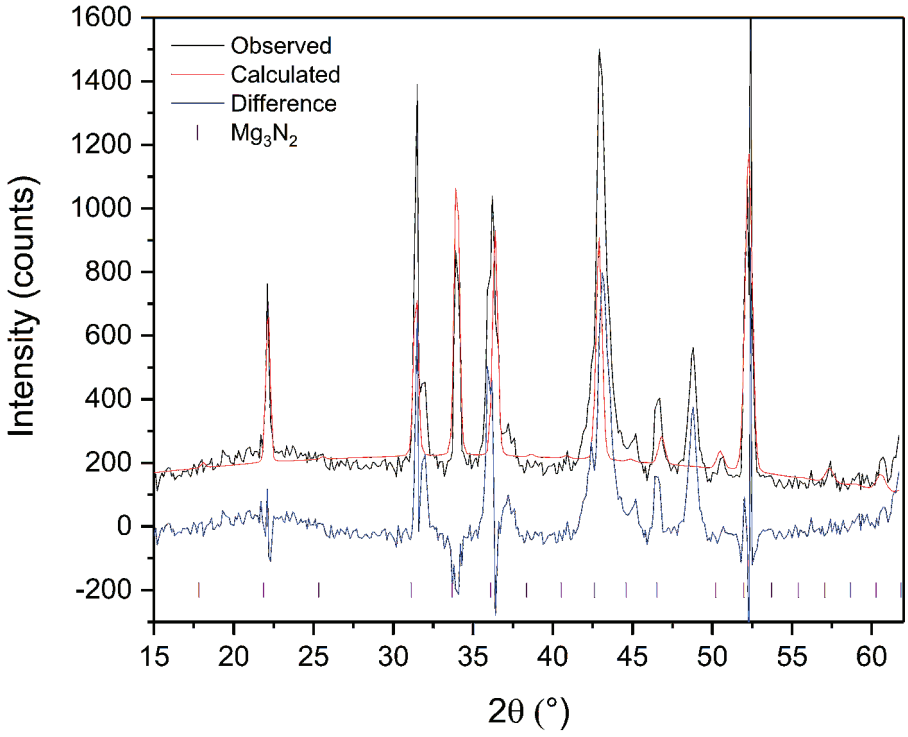


Figure A.26: Powder X-ray diffraction data collected for the sample recovered after $Na_2Mg(NH_2)_4$was heated on the gas flow panel to 450 °C

Steel doublets			**$NaND_2$**		**$Mg(NH_2)_2$**	
d-spacing (Å)		Miller indices (*hkl*)	*d*-spacing (Å)	Miller indices (*hkl*)	*d*-spacing (Å)	Miller indices (*hkl*)
2.12	2.04	(111)	5.21	(111)	2.97	(224)
1.84	1.76	(002)	3.40	(220)	2.62	(400)
1.30	1.25	(022)	3.20	(022)	2.52	(411)
1.11	1.06	(311)	3.01	(202/131)	2.35	(325)
1.06	1.02	(222)	2.70	(311)	1.80	(408)
			2.61	(040)		
			2.50	(113)		
			2.24	(400)		
			2.18	(331)		
			1.97	(151/242)		

Table A.14: *d*-spacings and indexing for the steel doublets as well as $NaND_2$ and $Mg(ND_2)_2$ present in the hour long scan at the start of the synthesis experiment shown in Figure A.27

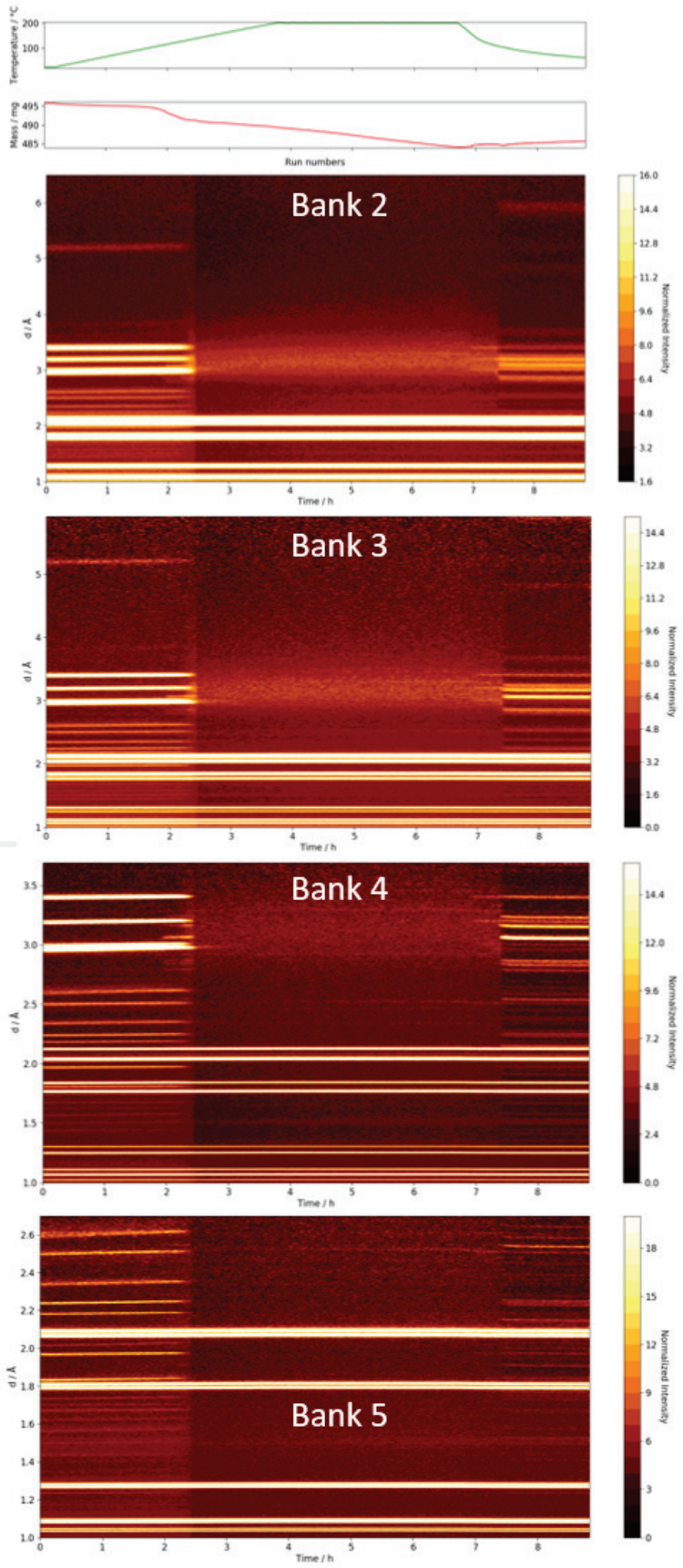


Figure A.27: Contour plots for banks 2, 3, 4 and 5 for the $2NaND_2$ $+Mg(ND_2)_2$ synthesis experiment with corresponding thermogravimetric data

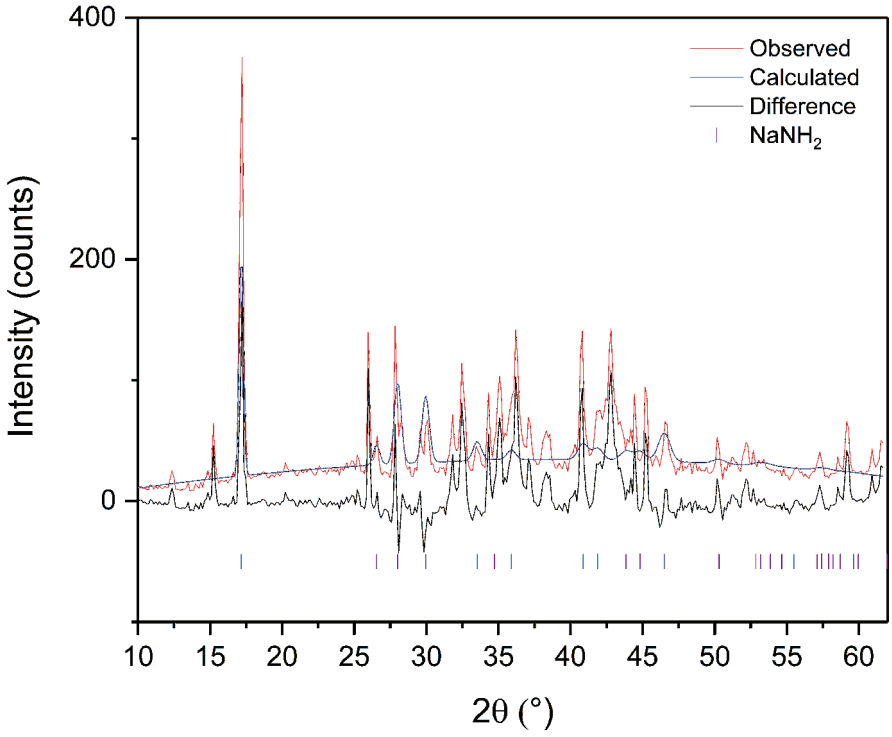


Figure A.28: Powder X-ray diffraction data collected of the remaining sample at the end of the *in-situ* synthesis experiment shown in Figure 9.5

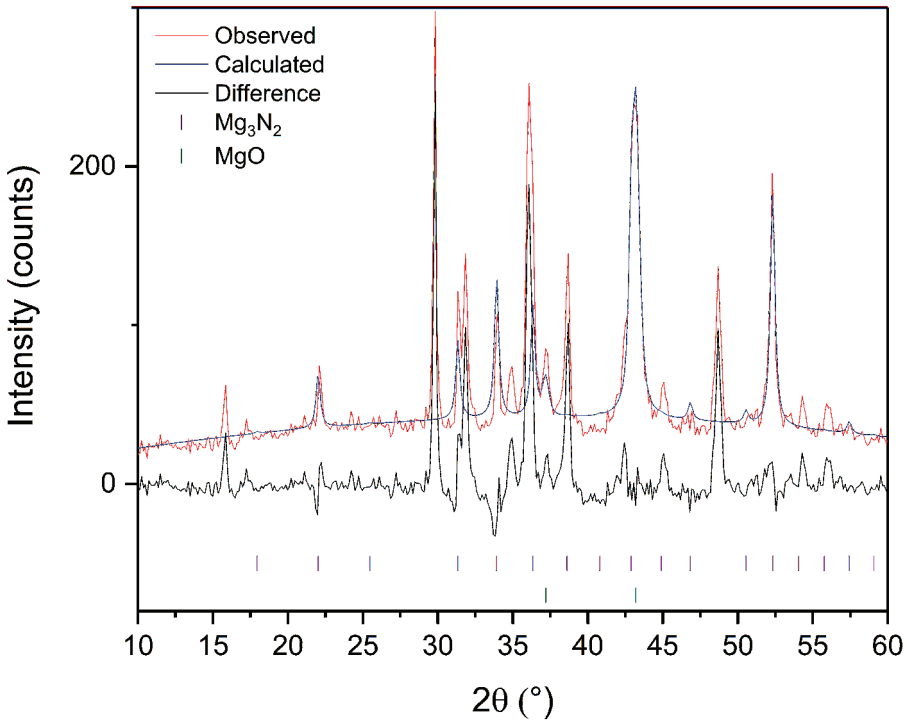


Figure A.29: Powder X-ray diffraction data collected of the remaining sample at the end of the *in-situ* decomposition experiment shown in Figure 9.7

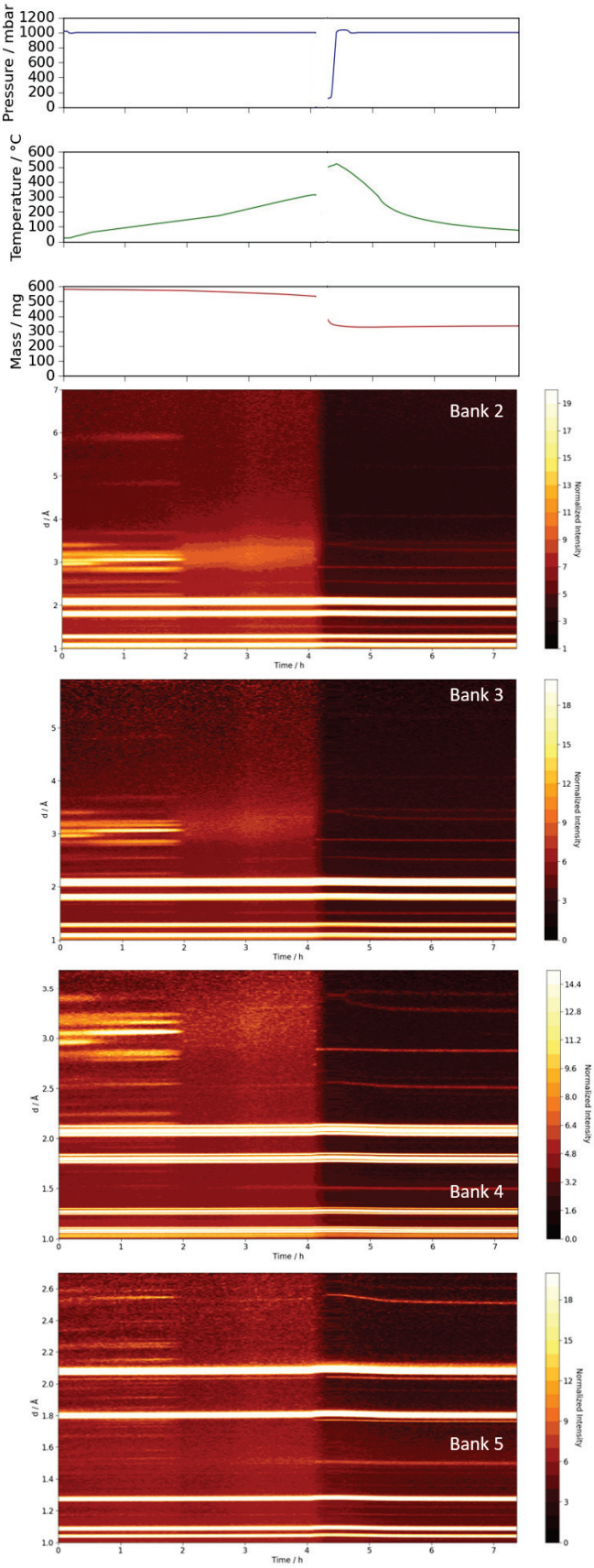


Figure A.30: Contour plots for banks 2, 3, 4 and 5 for the "$Na_2Mg(ND_2)_4$" decomposition experiment with corresponding thermogravimetric data

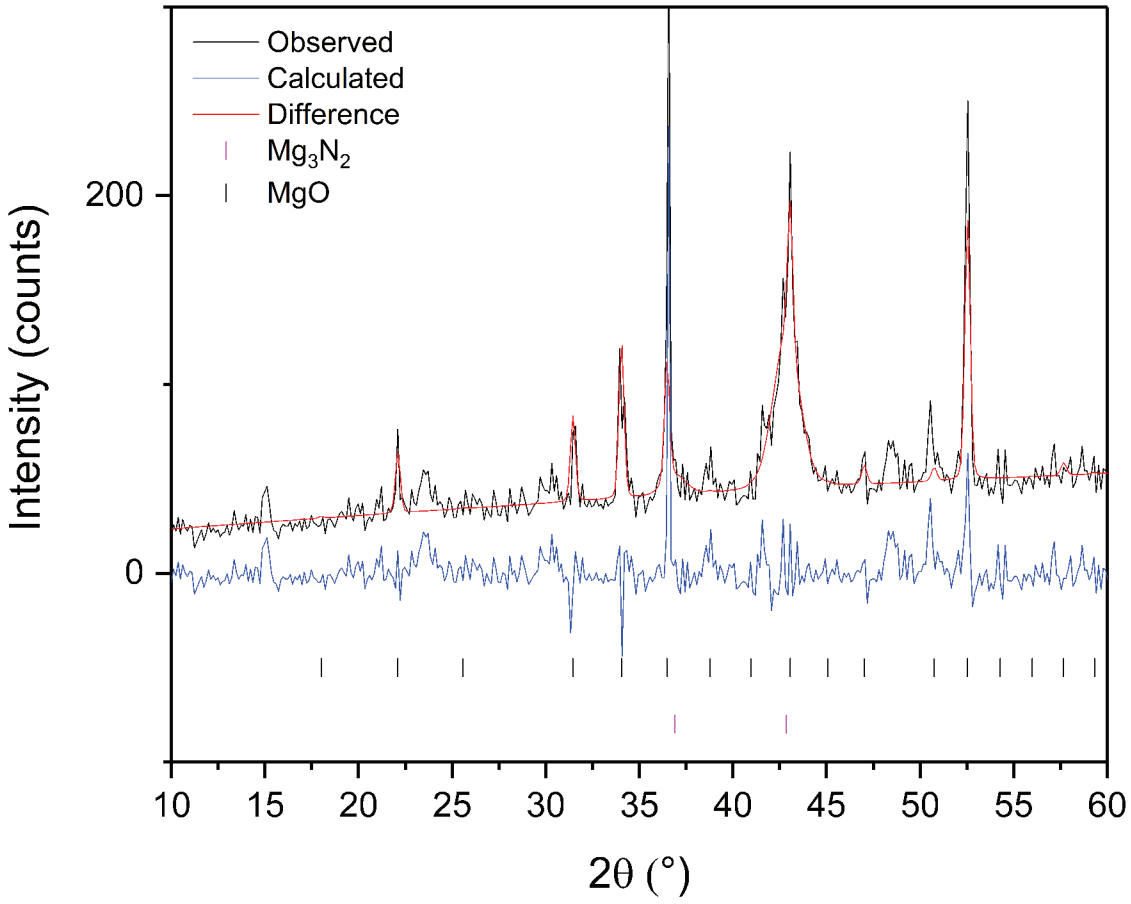


Figure A.31: Powder X-ray diffraction data collected for the sample recovered after $Na_2Mg(NH_2)_4$was heated on the gas flow panel under NH_3

References

[1] Battery Megafactory Forecast: 400% Increase to 1 TWh by 2028.

[2] Breaking ground: efficient lithium-air battery demonstrator unveiled - Power Technology.

[3] Clean tech transition could generate 65 million jobs, save $26 trillion – study – pv magazine International.

[4] Hydrogen fuel cell trains to run on British railways from 2022.

[5] Hydrogen Storage in Liquid Organic Hydrogen Carriers - Advanced Science News.

[6] Kawasaki Moving Ahead with LH2 Tanker Project – Ammonia Energy.

[7] Nitrogen — Nutrien.

[8] Storage solutions — McPhy.

[9] World′s first hydrogen train rolls out in Germany — News — DW — 17.09.2018.

[10] Australian solar-ammonia exports to Germany, 1990.

[11] Global carbon emissions hit record high in 2012, 2013.

[12] Nuvera demonstrates FCEV electrochemical hydrogen compressor. *Fuel Cells Bull.*, 2016(11):7, nov 2016.

[13] Renewables 2017. Technical Report October, 2017.

[14] Päivi T. Aakko-Saksa, Chris Cook, Jari Kiviaho, and Timo Repo. Liquid organic hydrogen carriers for transportation and storing of renewable energy – Review and discussion. *J. Power Sources*, 396:803–823, aug 2018.

[15] ACIL Allen Consulting. Opportunities for Australia from Hydrogen Exports. Technical Report August, 2018.

[16] Kerry Ann Adamson and Peter Pearson. Hydrogen and methanol: A comparison of safety, economics, efficiencies and emissions. *J. Power Sources*, 86(1):548–555, mar 2000.

[17] William L. Ahlgren. The dual-fuel strategy: An energy transition plan. *Proc. IEEE*, 100(11):3001–3052, nov 2012.

[18] U. v. Alpen, M. F. Bell, and T. Gladden. Lithium ion conduction in lithium nitride single crystals and sinters. *Electrochim. Acta*, 24(7):741–744, jul 1979.

[19] Ibrahim A. Amar, Rong Lan, Christophe T.G. Petit, and Shanwen Tao. Solid-state electrochemical synthesis of ammonia: A review. *J. Solid State Electrochem.*, 15(9):1845–1860, sep 2011.

[20] Adnan Z. Amin. Renewable Power Generation Costs in 2014 : An Overview. Technical Report January, IEA, 2015.

[21] Max Appl. Ammonia, 2. Production Processes. In *Ullmann's Encycl. Ind. Chem.* Wiley-VCH Verlag GmbH & Co. KGaA, Weinheim, Germany, oct 2011.

[22] Singanahally T. Aruna and Alexander S. Mukasyan. Combustion synthesis and nanomaterials. *Curr. Opin. Solid State Mater. Sci.*, 12(3-4):44–50, 2008.

[23] Mohammad Asadi, Baharak Sayahpour, Pedram Abbasi, Anh T. Ngo, Klas Karis, Jacob R. Jokisaari, Cong Liu, Badri Narayanan, Marc Gerard, Poya Yasaei, Xuan Hu, Arijita Mukherjee, Kah Chun Lau, Rajeev S. Assary, Fatemeh Khalili-Araghi, Robert F. Klie, Larry A. Curtiss, and Amin Salehi-Khojin. A lithium-oxygen battery with a long cycle life in an air-like atmosphere. *Nature*, 555(7697):502–506, mar 2018.

[24] W. H. Avery. A role for ammonia in the hydrogen economy. *Int. J. Hydrogen Energy*, 13(12):761–773, jan 1988.

[25] S. Badwal, S.P.S.; Kulkarni, A.P.; Ju, H.; Giddey. Solar Fuels. In Electrochemical Science for a Sustainable Society. *Springer*, a tribute, 2017.

[26] Michael P. Balogh, Camille Y. Jones, J. F. Herbst, Louis G. Hector, and Matthew Kundrat. Crystal structures and phase transformation of deuterated lithium imide, Li2ND. *J. Alloys Compd.*, 420(1-2):326–336, aug 2006.

[27] René Bañares-Alcántara, Gerard Dericks III, Maurizio Fiaschetti, Philipp Grünewald, Joaquín Masa Lopez, Edman Tsang, Aidong Yang, Lin Ye, and Shangyi Zhao. Analysis of Islanded Ammonia-based Energy Storage Systems. Technical Report October, 2014.

[28] Pierluigi Barbaro and Claudio Bianchini. *Catalysis for Sustainable Energy Production.* Wiley-VCH, 2009.

[29] Jerry Barker. Progress in the Commercialization of Faradion's Na-ion Battery Technology. Technical report, 2017.

[30] Eleanor Bash. `[U+6E08][U+7121]` No Title No Title. *PhD Propos.*, 1(October):287–301, 2015.

[31] Diana Bauer, David Diamond, Jennifer Li, David Sandalow, Paul Telleen, and Brent Wanner. US Department of Energy: Critical Materiasl Strategy, December 2010. Technical Report December, USDOE Office of Energy Efficiency and Renewable Energy (EE) (United States), dec 2010.

[32] T. E. Bell and L. Torrente-Murciano. H2 Production via Ammonia Decomposition Using Non-Noble Metal Catalysts: A Review. *Top. Catal.*, 59(15-16):1438–1457, sep 2016.

[33] José M. Bellosta Von Colbe, Oliver Metz, Gustavo A. Lozano, P. Klaus Pranzas, Heinz W. Schmitz, Felix Beckmann, Andreas Schreyer, Thomas Klassen, and Martin Dornheim. Behavior of scaled-up sodium alanate hydrogen storage tanks during sorption. *Int. J. Hydrogen Energy*, 37(3):2807–2811, feb 2012.

[34] M. Ben Amar, J. M. Allain, N. Puff, and M. I. Angelova. Stokes instability in inhomogeneous membranes: Application to lipoprotein suction of cholesterol-enriched domains, 2007.

[35] F. W. Bergstrom, H. G. Sturz, and H. W. Tracy. The use of the fused eutectic of sodium amide and potassium amide in organic syntheses. *J. Org. Chem.*, 11(3):239–246, may 1946.

[36] Polly A. Berseth, Andrew G. Harter, Ragaiy Zidan, Andreas Blomqvist, C. Moysés Araújo, Ralph H. Scheicher, Rajeev Ahuja, and Puru Jena. Carbon nanomaterials as catalysts for hydrogen uptake and release in NaAIH 4. *Nano Lett.*, 9(4):1501–1505, apr 2009.

[37] A. Blomqvist, C. Moysás Araújo, P. Jena, and R. Ahuja. Dehydrogenation from 3d -transition-metal-doped NaAl H4: Prediction of catalysts. *Appl. Phys. Lett.*, 90(14), 2007.

[38] Bloomberg. Electric Vehicles on the Road Are Set to Triple in Two Years - Bloomberg.

[39] Borislav Bogdanović, Richard A. Brand, Ankica Marjanović, Manfred Schwickardi, and Joachim Tölle. Metal-doped sodium aluminium hydrides as potential new hydrogen storage materials. *J. Alloys Compd.*, 302(1-2):36–58, apr 2000.

[40] Borislav Bogdanović and Manfred Schwickardi. Ti-doped alkali metal aluminium hydrides as potential novel reversible hydrogen storage materials. *J. Alloys Compd.*, 253-254:1–9, may 1997.

[41] J. P.O. Bohger, R. R. Eßmann, and H. Jacobs. Infrared and Raman studies on the internal modes of lithium amide. *J. Mol. Struct.*, 348:325–328, mar 1995.

[42] Alexander Böhmer. Organisation for economic cooperation and development. *Handb. Transnatl. Econ. Gov. Regimes*, pages 227–241, 2009.

[43] Astrid Boisen, Søren Dahl, Jens K. Nørskov, and Claus Hviid Christensen. Why the optimal ammonia synthesis catalyst is not the optimal ammonia decomposition catalyst. *J. Catal.*, 230(2):309–312, mar 2005.

[44] Ali Boultif and Daniel Louër. Powder pattern indexing with the dichotomy method. *J. Appl. Crystallogr.*, 37(5):724–731, oct 2004.

[45] Hujun Cao, Jianhui Wang, Yongshen Chua, Han Wang, Guotao Wu, Zhitao Xiong, Jieshan Qiu, and Ping Chen. NH3 mediated or ion migration reaction: The case study on halide-amide system. *J. Phys. Chem. C*, 118(5):2344–2349, feb 2014.

[46] CB&I. {QAFCO} {Ammonia} {Storage} {Tanks} - {CB}\&{I}, 2017.

[47] Center for Global Development. Grading Power Africa — Center For Global Development.

[48] A. S. Chellappa, C. M. Fischer, and W. J. Thomson. Ammonia decomposition kinetics over Ni-Pt/Al2O3 for PEM fuel cell applications. *Appl. Catal. A Gen.*, 227(1-2):231–240, mar 2002.

[49] Jiuling Chen, Zhong Hua Zhu, Shaobin Wang, Qing Ma, Victor Rudolph, and Gao Qing Lu. Effects of nitrogen doping on the structure of carbon nanotubes (CNTs) and activity of Ru/CNTs in ammonia decomposition. *Chem. Eng. J.*, 156(2):404–410, jan 2010.

[50] Ping Chen, Zhitao Xiong, Jizhong Luo, Jianyi Lin, and Kuang Lee Tan. Interaction of hydrogen with metal nitrides and imides. *Nature*, 420(6913):302–304, nov 2002.

[51] Xuan Cheng, Zheng Shi, Nancy Glass, Lu Zhang, Jiujun Zhang, Datong Song, Zhong Sheng Liu, Haijiang Wang, and Jun Shen. A review of PEM hydrogen fuel cell contamination: Impacts, mechanisms, and mitigation. *J. Power Sources*, 165(2):739–756, mar 2007.

[52] Steven Chiuta, Raymond C. Everson, Hein W J P Neomagus, Percy Van Der Gryp, and Dmitri G. Bessarabov. Reactor technology options for distributed hydrogen generation via ammonia decomposition: A review. *Int. J. Hydrogen Energy*, 38(35):14968–14991, nov 2013.

[53] Krzysztof Chłopek, Christoph Frommen, Aline Léon, Oleg Zabara, and Maximilian Fichtner. Synthesis and properties of magnesium tetrahydroborate, Mg(BH <inf>4</inf>)<inf>2</inf>. *J. Mater. Chem.*, 17(33):3496–3503, aug 2007.

[54] Marina Chong, Abhi Karkamkar, Tom Autrey, Shin Ichi Orimo, Satish Jalisatgi, and Craig M. Jensen. Reversible dehydrogenation of magnesium borohydride to magnesium triborane in the solid state under moderate conditions. *Chem. Commun.*, 47(4):1330–1332, jan 2011.

[55] T. V. Choudhary, C. Sivadinarayana, and D. W. Goodman. Production of COx-free hydrogen for fuel cells via step-wise hydrocarbon reforming and catalytic dehydrogenation of ammonia. *Chem. Eng. J.*, 93(1):69–80, may 2003.

[56] Claus Hviid Christensen, Tue Johannessen, Rasmus Zink Sørensen, and Jens K. Nørskov. Towards an ammonia-mediated hydrogen economy? *Catal. Today*, 111(1-2):140–144, jan 2006.

[57] Claus Hviid Christensen, Rasmus Zink Sørensen, Tue Johannessen, Ulrich J. Quaade, Karoliina Honkala, Tobias D. Elmøe, Rikke Køhler, and Jens K. Nørskov. Metal ammine complexes for hydrogen storage. *J. Mater. Chem.*, 15(38):4106–4108, sep 2005.

[58] Hailiang Chu, Zhitao Xiong, Guotao Wu, Teng He, Chengzhang Wu, and Ping Chen. Hydrogen storage properties of Li-Ca-N-H system with different molar ratios of LiNH2/CaH2. *Int. J. Hydrogen Energy*, 35(15):8317–8321, aug 2010.

[59] Yong Shen Chua, Guotao Wu, Zhitao Xiong, and Ping Chen. Investigations on the solid state interaction between LiAlH4 and NaNH2. *J. Solid State Chem.*, 183(9):2040–2044, sep 2010.

[60] J. Clark. Atomic and Ionic Radius.

[61] Accelerating Climate, Action In, and Urgent Times. [U+65B0][U+6C14][U+5019][U+7ECF][U+6D4E]nce_2018_[U+6267][U+884C] Technical report, 2018.

[62] A. A. Coelho. A bound constrained conjugate gradient solution method as applied to crystallographic refinement problems. *J. Appl. Crystallogr.*, 38(3):455–461, 2005.

[63] A. A. Coelho. A charge-flipping algorithm incorporating the tangent formula for solving difficult structures. *Acta Crystallogr. Sect. A Found. Crystallogr.*, 63(5):400–406, sep 2007.

[64] Paul T. Cunningham and Victor A. Maroni. Laser Raman spectra of solid and molten NaNH2: Evidence for hindered rotation of the NH2-1ion. *J. Chem. Phys.*, 57(4):1415–1418, aug 1972.

[65] Gopi Krishna Phani Dathar and Daniela Silvia Mainardi. Kinetics of hydrogen desorption in NaAlH4 and Ti-containing NaAlH4. *J. Phys. Chem. C*, 114(17):8026–8031, may 2010.

[66] W. R.W. Daud, R. E. Rosli, E. H. Majlan, S. A.A. Hamid, R. Mohamed, and T. Husaini. PEM fuel cell system control: A review. *Renew. Energy*, 113:620–638, dec 2017.

[67] W. I.F. David, S. K. Callear, M. O. Jones, P. C. Aeberhard, S. D. Culligan, A. H. Pohl, S. R. Johnson, K. R. Ryan, J. E. Parker, P. P. Edwards, C. J. Nuttall, and A. Amieiro-Fonseca. The structure, thermal properties and phase transformations of the cubic polymorph of magnesium tetrahydroborate. *Phys. Chem. Chem. Phys.*, 14(33):11800–11807, aug 2012.

[68] William I.F. David. Effective hydrogen storage: A strategic chemistry challenge. *Faraday Discuss.*, 151(0):399–414, aug 2011.

[69] William I.F. David. Effective hydrogen storage: A strategic chemistry challenge. *Faraday Discuss.*, 151(0):399–414, aug 2011.

[70] William I.F. David, Martin O. Jones, Duncan H. Gregory, Catherine M. Jewell, Simon R. Johnson, Allan Walton, and Peter P. Edwards. A mechanism for non-stoichiometry in the lithium amide/lithium imide hydrogen storage reaction. *J. Am. Chem. Soc.*, 129(6):1594–1601, 2007.

[71] William I.F. David, Joshua W. Makepeace, Samantha K. Callear, Hazel M.A. Hunter, James D. Taylor, Thomas J. Wood, and Martin O. Jones. Hydrogen production from ammonia using sodium amide. *J. Am. Chem. Soc.*, 136(38):13082–13085, sep 2014.

[72] William I.F. David, Joshua W. Makepeace, Samantha K. Callear, Hazel M.A. Hunter, James D. Taylor, Thomas J. Wood, and Martin O. Jones. Hydrogen production from ammonia using sodium amide. Technical Report 38, 2014.

[73] William I.F. David, Kenneth Shankland, Jacco Van De Streek, Elna Pidcock, W. D.Samuel Motherwell, and Jason C. Cole. DASH: A program for crystal structure determination from powder diffraction data. *J. Appl. Crystallogr.*, 39(6):910–915, dec 2006.

[74] Rezan Demir-Cakan, Wan Si Tang, Ali Darwiche, and Raphaël Janot. Modification of the hydrogen storage properties of Li3N by confinement into mesoporous carbons. *Energy Environ. Sci.*, 4(9):3625–3631, aug 2011.

[75] Umit B. Demirci. Ammonia borane, a material with exceptional properties for chemical hydrogen storage. *Int. J. Hydrogen Energy*, 42(15):9978–10013, apr 2017.

[76] Energy & Industrial Strategy Department for Business. Erratum: Electron rescattering in strong-field photodetachment of F- (Physical Review A (2016) 93 (069901) DOI: 10.1103/PhysRevA.93.069901). *Phys. Rev. A*, 94(2), 2016.

[77] Department for Transport. Energy and Environment: Data Tables, 2018.

[78] Department of Agricultural and Consumer Economics. Nitrogen Prices, Rates Cuts, and 2018 Fertilizer Costs • farmdoc daily, 2018.

[79] A. C. Dillon, K. M. Jones, T. A. Bekkedahl, C. H. Kiang, D. S. Bethune, and M. J. Heben. Storage of hydrogen in single-walled carbon nanotubes. *Nature*, 386(6623):377–379, mar 1997.

[80] Francesco Dolci, Emilio Napolitano, Eveline Weidner, Stefano Enzo, Pietro Moretto, Michela Brunelli, Thomas Hansen, Maximilian Fichtner, and Wiebke Lohstroh. Magnesium imide: Synthesis and structure determination of an unconventional alkaline

earth imide from decomposition of magnesium amide. *Inorg. Chem.*, 50(3):1116–1122, feb 2011.

[81] Oleksandr Dolotko, Neil Paulson, and Vitalij K. Pecharsky. Thermochemical transformations in 2MNH2-3MgH2 systems (M = Li or Na). *Int. J. Hydrogen Energy*, 35(10):4562–4568, may 2010.

[82] Bao Xia Dong, Jing Jing Gao, Yun Lei Teng, Hui Tian, and Long Zheng Wang. A novel hydrogen storage system of KLi3(NH2)4-4LiH with superior cycling stability. *Int. J. Hydrogen Energy*, 41(11):5371–5377, mar 2016.

[83] Bao Xia Dong, Liang Song, Jun Ge, Yun Lei Teng, and Shi Yang Zhang. The ternary amide KLi3(NH2)4: An important intermediate in the potassium compound-added Li-N-H systems. *RSC Adv.*, 4(21):10702–10707, 2014.

[84] Bao Xia Dong, Yun Lei Teng, Jun Ge, Liang Song, and Shi Yang Zhang. The interesting and superior hydrogenation properties of potassium-doped LiNH2and its ternary mixed-cationic amide. *RSC Adv.*, 3(38):16977–16980, sep 2013.

[85] Xuezhi Duan, Gang Qian, Xinggui Zhou, Zhijun Sui, De Chen, and Weikang Yuan. Tuning the size and shape of Fe nanoparticles on carbon nanofibers for catalytic ammonia decomposition. *Appl. Catal. B Environ.*, 101(3-4):189–196, jan 2011.

[86] Xuezhi Duan, Jinghong Zhou, Gang Qian, Ping Li, Xinggui Zhou, and De Chen. Carbon nanofiber-supported Ru catalysts for hydrogen evolution by ammonia decomposition. *Cuihua Xuebao/Chinese J. Catal.*, 31(8):979–986, aug 2010.

[87] Ulrich Eberle, Michael Felderhoff, and Ferdi Schüth. Chemical and physical solutions for hydrogen storage. *Angew. Chemie - Int. Ed.*, 48(36):6608–6630, aug 2009.

[88] Mohamed Eddaoudi, Jaheon Kim, Nathaniel Rosi, David Vodak, Joseph Wachter, Michael O'Keeffe, and Omar M. Yaghi. Systematic design of pore size and functionality in isoreticular MOFs and their application in methane storage. *Science (80-.).*, 295(5554):469–472, jan 2002.

[89] Peter P Edwards, Vladimir L Kuznetsov, Simon R Johnson, Matthew T J Lodge, and Martin Owen Jones. Sustainable hydrogen energy. *Inorg. Chem.*, (Cambridge University Press), 2006.

[90] Industrial efficiency technology database. Industrial Efficiency Technology & Measures, 2011.

[91] Chikashi Egawa, Tetsuya Nishida, Shuichi Naito, and Kenzi Tamaru. Ammonia decomposition on (1 1 10) and (0 0 1) surfaces of ruthenium. *J. Chem. Soc. Faraday Trans. 1 Phys. Chem. Condens. Phases*, 80(6):1595–1604, jan 1984.

[92] Electrek. Tesla confirms Gigafactory 1 battery production at '~20 GWh' – more than all other carmakers combined, 2018.

[93] Theo Elmer, Mark Worall, Shenyi Wu, and Saffa B. Riffat. Fuel cell technology for domestic built environment applications: State of-the-art review. *Renew. Sustain. Energy Rev.*, 42:913–931, feb 2015.

[94] Key World Energy. IEA, Key World Energy Statistics. *OECD Publ.*, Paris:pp. 6., 2013.

[95] Jan Willem Erisman, Mark A. Sutton, James Galloway, Zbigniew Klimont, and Wilfried Winiwarter. How a century of ammonia synthesis changed the world. *Nat. Geosci.*, 1(10):636–639, oct 2008.

[96] G. Ertl and M. Huber. Mechanism and kinetics of ammonia decomposition on iron. *J. Catal.*, 61(2):537–539, feb 1980.

[97] Vincent Favre-Nicolin and Radovan Černý. FOX, 'free objects for crystallography': A modular approach to ab initio structure determination from powder diffraction. *J. Appl. Crystallogr.*, 35(6):734–743, 2002.

[98] Vincent Favre-Nicolin and Radovan Černý. A better FOX: Using flexible modelling and maximum likelihood to improve direct-space ab initio structure determination from powder diffraction. *Zeitschrift fur Krist.*, 219(12):847–856, jan 2004.

[99] Prepared For. COMPARATIVE QUANTITATIVE RISK ANALYSIS OF MOTOR GASOLINE , LPG , AND QUEST COMPARATIVE QUANTITATIVE RISK ANALYSIS OF MOTOR GASOLINE , LPG , AND Table of Contents. Technical report, 2009.

[100] Richard A. Forman. Order–Disorder Transition in Lithium Imide, Li2NH. *J. Chem. Phys.*, 55(4):1987–1988, aug 1971.

[101] Edward C. Franklin. Potassium ammonosodiate, potassium ammonolithiate, rubidium ammonosodiate and rubidium ammonolithiate. *J. Phys. Chem.*, 23(1):36–53, jan 1919.

[102] A. Fuerte, R. X. Valenzuela, M. J. Escudero, and L. Daza. Ammonia as efficient fuel for SOFC. *J. Power Sources*, 192(1):170–174, jul 2009.

[103] J. C. Ganley, F. S. Thomas, E. G. Seebauer, and R. I. Masel. A priori catalytic activity correlations: The difficult case of hydrogen production from ammonia. *Catal. Letters*, 96(3-4):117–122, jul 2004.

[104] S. Giddey, S. P S Badwal, and A. Kulkarni. Review of electrochemical ammonia production technologies and materials. *Int. J. Hydrogen Energy*, 38(34):14576–14594, nov 2013.

[105] S. Giddey, S. P. S. Badwal, A. Kulkarni, and C. Munnings. *Progress in energy and combustion science*, volume 14. Elsevier, 1988.

[106] S. Giddey, S. P.S. Badwal, C. Munnings, and M. Dolan. Ammonia as a Renewable Energy Transportation Media. *ACS Sustain. Chem. Eng.*, 5(11):10231–10239, nov 2017.

[107] H. N. Gilbert, N. D. Scott, W. F. Zimmerli, and V. L. Hansley. Sodium. *Ind. Eng. Chem.*, 25(7):735–741, jul 1933.

[108] Giles Parkinson. Solar fuels could be Australia's biggest energy export, 2015.

[109] Kiyotaka Goshome, Hiroki Miyaoka, Hikaru Yamamoto, Takayuki Ichikawa, and Yoshitsugu Kojima. Hydrogen Ab/desorption of LiH-KH composite and ammonia system. *Mater. Trans.*, 57(7):1215–1219, 2016.

[110] GOV.UK. Fuel Consumption (ENV01) - GOV.UK, 2017.

[111] Shawn M. Grannell, Dennis N. Assanis, Stanislav V. Bohac, and Donald E. Gillespie. The fuel mix limits and efficiency of a stoichiometric, ammonia, and gasoline dual fueled spark ignition engine. In *J. Eng. Gas Turbines Power*, volume 130, page 042802. ASME, 2008.

[112] Christopher Graves, Sune D. Ebbesen, Mogens Mogensen, and Klaus S. Lackner. Sustainable hydrocarbon fuels by recycling CO 2 and H 2 O with renewable or nuclear energy. *Renew. Sustain. Energy Rev.*, 15(1):1–23, jan 2011.

[113] L. Green. An ammonia energy vector for the hydrogen economy. *Int. J. Hydrogen Energy*, 7(4):355–359, jan 1982.

[114] Wojciech Grochala and Peter P. Edwards. Thermal decomposition of the non-interstitial hydrides for the storage and production of hydrogen. *Chem. Rev.*, 104(3):1283–1315, 2004.

[115] Oliver Gröger, Hubert A. Gasteiger, and Jens Peter Suchsland. Review-Electromobility: Batteries or fuel cells? *J. Electrochem. Soc.*, 162(14):A2605–A2622, jan 2015.

[116] Jianping Guo, Peikun Wang, Guotao Wu, Anan Wu, Daqiang Hu, Zhitao Xiong, Junhu Wang, Pei Yu, Fei Chang, Zheng Chen, and Ping Chen. Lithium imide synergy with 3d transition-metal nitrides leading to unprecedented catalytic activities for ammonia decomposition. *Angew. Chemie - Int. Ed.*, 54(10):2950–2954, mar 2015.

[117] Alex C. Hannon. Results on disordered materials from the GEneral Materials diffractometer, GEM, at ISIS. In *Nucl. Instruments Methods Phys. Res. Sect. A Accel. Spectrometers, Detect. Assoc. Equip.*, volume 551, pages 88–107, 2005.

[118] Danielle A. Hansgen, Dionisios G. Vlachos, and Jingguang G. Chen. Using first principles to predict bimetallic catalysts for the ammonia decomposition reaction. *Nat. Chem.*, 2(6):484–489, jun 2010.

[119] Jian Hao, Yinwei Li, Qiang Zhou, Dan Liu, Min Li, Fangfei Li, Weiwei Lei, Xiaohui Chen, Yanming Ma, Qiliang Cui, Guangtian Zou, Jing Liu, and Xiaodong Li. Structural Phase Transformations of Mg 3 N 2 at High Pressure: Experimental and Theoretical Studies.

[120] Kevin Harrison, Todd Ramsden, Genevieve Saur, Chris Ainscough, Doe Manager, and Eric Miller. Renewable Electrolysis Integrated System Development and Testing - DOE Hydrogen and Fuel Cells Program FY 2011 Annual Progress Report. Technical report, 2003.

[121] Keiji Hashimoto and Naoji Toukai. Decomposition of ammonia over a catalyst consisting of rutheniurn metal and cerium oxides supported on Y-form zeolite. *J. Mol. Catal. A Chem.*, 161(1-2):171–178, nov 2000.

[122] E. Hazrati, G. Brocks, B. Buurman, R. A. De Groot, and G. A. De Wijs. Intrinsic defects and dopants in LiNH2: A first-principles study. *Phys. Chem. Chem. Phys.*, 13(13):6043–6052, 2011.

[123] T. Hejze, J. O. Besenhard, K. Kordesch, M. Cifrain, and R. R. Aronsson. Current status of combined systems using alkaline fuel cells and ammonia as a hydrogen carrier. *J. Power Sources*, 176(2):490–493, feb 2008.

[124] Jeffrey A. Herron, Jiyong Kim, Aniruddha A. Upadhye, George W. Huber, and Christos T. Maravelias. A general framework for the assessment of solar fuel technologies. *Energy Environ. Sci.*, 8(1):126–157, dec 2015.

[125] Alfred K. Hill and Laura Torrente-Murciano. In-situ H2 production via low temperature decomposition of ammonia: Insights into the role of cesium as a promoter. *Int. J. Hydrogen Energy*, 39(15):7646–7654, may 2014.

[126] Satoshi Hino, Takayuki Ichikawa, and Yoshitsugu Kojima. Thermodynamic properties of metal amides determined by ammonia pressure-composition isotherms. *J. Chem. Thermodyn.*, 42(1):140–143, jan 2010.

[127] F. L. Hirshfeld. Can X[U+2010]ray data distinguish bonding effects from vibrational smearing? *Acta Crystallogr. Sect. A*, 32(2):239–244, mar 1976.

[128] Jeremy Hodges. Electric Buses Are Hurting the Oil Industry - Bloomberg, 2018.

[129] Don Hofstrand. Ammonia as a Transportation Fuel — Agricultural Marketing Resource Center, 2009.

[130] John H Holbrook and William C Leighty. Renewable Fuels: Manufacturing Ammonia from Hydropower, 2009.

[131] J. D. Holladay, J. Hu, D. L. King, and Y. Wang. An overview of hydrogen production technologies. *Catal. Today*, 139(4):244–260, jan 2009.

[132] Tricia L. Humphreys, Lee Ann Baldridge, Steven D. Billings, James J. Campbell, and Stanley M. Spinola. Trafficking pathways and characterization of CD4 and CD8 cells recruited to the skin of humans experimentally infected with Haemophilus ducreyi. *Infect. Immun.*, 73(7):3896–3902, jul 2005.

[133] Hazel M.A. Hunter, Joshua W. Makepeace, Thomas J. Wood, O. Simon Mylius, Mark G. Kibble, Jamie B. Nutter, Martin O. Jones, and William I.F. David. Demonstrating hydrogen production from ammonia using lithium imide – Powering a small proton exchange membrane fuel cell. *J. Power Sources*, 329:138–147, oct 2016.

[134] Takayuki Ichikawa, Nobuko Hanada, Shigehito Isobe, Haiyan Leng, and Hironobu Fujii. Mechanism of novel reaction from LiNH2 and LiH to Li 2NH and H2 as a promising hydrogen storage system. *J. Phys. Chem. B*, 108(23):7887–7892, 2004.

[135] Takayuki Ichikawa, Shigehito Isobe, Nobuko Hanada, and Hironobu Fujii. Lithium nitride for reversible hydrogen storage. *J. Alloys Compd.*, 365(1-2):271–276, feb 2004.

[136] Raphael O. Idem and Narendra N. Bakhshi. Production of Hydrogen from Methanol. 1. Catalyst Characterization Studies. *Ind. Eng. Chem. Res.*, 33(9):2047–2055, sep 1994.

[137] IEA. *Energy Technology Perspectives 2012: Pathways to a Clean Energy System (Paris: OECD/IEA, 2012)*. 2012.

[138] IEA. CO2 EMISSIONS FROM FUEL COMBUSTION Highlights. *Iea*, S/V(IEA - STATISTICS):1–139, 2015.

[139] IFA. Energy Efficiency and CO2 Emissions in Ammonia Production. Technical Report September, 2009.

[140] Nobuyuki Imanishi and Osamu Yamamoto. Rechargeable lithium-air batteries: Characteristics and prospects. *Mater. Today*, 17(1):24–30, jan 2014.

[141] The Fuel Cell Industry. Review. *E4tech*.

[142] Institute for Sustainable Process Technology. Institute for Sustainable Process Technology Power to Ammonia. Technical report, Institute for Sustainable Process, 2017.

[143] International Energy Agency. Presentation on World Energy Outlook 2013. *Int. Energy Agency*, page 551 pp., 2013.

[144] International Energy Agency. Electric power transmission and distribution losses, 2014.

[145] Shigehito Isobe, Somei Ohnuki, William I.F. David, Matthias Gutmann, Martin O. Jones, Peter P. Edwards, Takayuki Ichikawa, and Yoshitsugu Kojima. Variable temperature neutron diffraction studies of single crystals of LiND 2. *Int. J. Hydrogen Energy*, 36(13):7909–7913, jul 2011.

[146] J. E Philpott. The On-Site Production of Hydrogen. *Platin. Met. Rev.*, 20(4):110, 1976.

[147] H. Jacobs and B. Harbrecht. Über ein trilithiumnatriumamid, Li3Na(NH2)4, eine verbindung mit lithiumamidverwandter struktur. *J. Less-Common Met.*, 85(C):87–95, may 1982.

[148] H. Jacobs and B. Harbrecht. Schichtenweise Substitution von Kationen im Lithiumamid: Kaliumtrilithiumamid, KLi3(NH2)4 und Kaliumheptalithiumamid, KLi7(NH2)8. *ZAAC [U+2010] J. Inorg. Gen. Chem.*, 518(11):87–100, nov 1984.

[149] H. Jacobs, A. Schardey, and B. Harbrecht. Neue ternäre Alkalimetallhydroxide, MLi2(OH)3mit M [U+2259] K, Rb, Cs sowie ein Caesiumdilithiumamid, CsLi2(NH2)3 – Strukturverwandtschaft zum BaNiO3[U+2010]Typ und zu LiOH. *ZAAC [U+2010] J. Inorg. Gen. Chem.*, 555(12):43–56, dec 1987.

[150] H. Jacobs and E. Von Osten. Die Kristallstruktur einer neuen Modifikation des Kalitunanuids, KNH2. Technical Report 3, 1976.

[151] Herbert Jacobs, Patrick Bohger, and Winfried Kockelmann. RbLi(NH 2) 2, a rubidium amido lithiate investigated by X-ray and neutron diffraction. *Zeitschrift fur Anorg. und Allg. Chemie*, 628(8):1794–1798, aug 2002.

[152] C. J.H. Jacobsen, S. Dahl, B. G.S. Clausen, S. Bahn, A. Logadottir, and J. K. Nørskov. Catalyst design by interpolation in the periodic table: Bimetallic ammonia synthesis catalysts [2]. *J. Am. Chem. Soc.*, 123(34):8404–8405, 2001.

[153] Anna Jedynak, Zbigniew Kowalczyk, Dariusz Szmigiel, Wioletta Raróg, and Jerzy Zieliński. Ammonia decomposition over the carbon-based iron catalyst promoted with potassium. *Appl. Catal. A Gen.*, 237(1-2):223–226, nov 2002.

[154] Lars H. Jepsen, Peikun Wang, Guotao Wu, Zhitao Xiong, Flemming Besenbacher, Ping Chen, and Torben R. Jensen. Synthesis and decomposition of Li3Na(NH2)4and investigations of Li-Na-N-H based systems for hydrogen storage. *Phys. Chem. Chem. Phys.*, 18(3):1735–1742, jan 2016.

[155] Lars H. Jepsen, Peikun Wang, Guotao Wu, Zhitao Xiong, Flemming Besenbacher, Ping Chen, and Torben R. Jensen. Thermal decomposition of sodium amide, NaNH2,

and sodium amide hydroxide composites, NaNH2-NaOH. *Phys. Chem. Chem. Phys.*, 18(36):25257–25264, sep 2016.

[156] Hai Long Jiang and Qiang Xu. Catalytic hydrolysis of ammonia borane for chemical hydrogen storage. *Catal. Today*, 170(1):56–63, jul 2011.

[157] Cai Jianguo, Liu Yangqing, Ma Ruijun, Feng Jian, and Zhou Ya. Nonrigidly foldability analysis of kresling cylindrical origami. Technical Report 4, 2017.

[158] Terry A. Johnson, Scott W. Jorgensen, and Daniel E. Dedrick. Performance of a full-scale hydrogen-storage tank based on complex hydrides. *Faraday Discuss.*, 151(0):327–352, aug 2011.

[159] R. Juza. Amides of the Alkali and the Alkaline Earth Metals. *Angew. Chemie Int. Ed. English*, 3(7):471–481, jul 1964.

[160] X. D. Kang, P. Wang, X. P. Song, X. D. Yao, G. Q. Lu, and H. M. Cheng. Catalytic effect of Al3Ti on the reversible dehydrogenation of NaAlH4. *J. Alloys Compd.*, 424(1-2):365–369, nov 2006.

[161] Asbjørn Klerke, Claus Hviid Christensen, Jens K. Nørskov, and Tejs Vegge. Ammonia for hydrogen storage: Challenges and opportunities. *J. Mater. Chem.*, 18(20):2304–2310, may 2008.

[162] Asbjørn Klerke, Søren Kegnæs Klitgaard, and Rasmus Fehrmann. Catalytic ammonia decomposition over ruthenium nanoparticles supported on nano-titanates. *Catal. Letters*, 130(3-4):541–546, 2009.

[163] Ute. Kolb. *Uniting electron crystallography and powder diffraction : [proceedings of the NATO Advanced Study Institute on Uniting Electron Crystallography and Powder Diffraction : an essential contribution to the fight against terrorism, Erice, Italy, 2-12 June, 201.* Springer, 2012.

[164] Fatih Köleli and Didem Balun Kayan. Low overpotential reduction of dinitrogen to ammonia in aqueous media. *J. Electroanal. Chem.*, 638(1):119–122, jan 2010.

[165] Karl Kordesch, Viktor Hacker, Josef Gsellmann, Martin Cifrain, Gottfried Faleschini, Peter Enzinger, Robert Fankhauser, Markus Ortner, Michael Muhr, and Robert R. Aronson. Alkaline fuel cells applications. *J. Power Sources*, 86(1):162–165, mar 2000.

[166] Z. Kowalczyk, J. Sentek, S. Jodzis, M. Muhler, and O. Hinrichsen. Effect of potassium on the kinetics of ammonia synthesis and decomposition over fused iron catalyst at atmospheric pressure. *J. Catal.*, 169(2):407–414, jul 1997.

[167] Zbigniew Kowalczyk, Sławomir Jodzis, Wioletta Raróg, Jerzy Zieliński, and Jerzy Pielaszek. Effect of potassium and barium on the stability of a carbon-supported ruthenium catalyst for the synthesis of ammonia. *Appl. Catal. A Gen.*, 173(2):153–160, oct 1998.

[168] Florian Kraus and Nikolaus Korber. K2Li(NH2)3 and K2Na(NH 2)3 - Synthesis and crystal structure of two crystal-chemically isotypic mixed-cationic amides. *J. Solid State Chem.*, 178(4):1241–1246, apr 2005.

[169] Rong Lan, John T S Irvine, and Shanwen Tao. Ammonia and related chemicals as potential indirect hydrogen storage materials. *Int. J. Hydrogen Energy*, 37(2):1482–1494, jan 2012.

[170] Rong Lan, John T.S. Irvine, and Shanwen Tao. Synthesis of ammonia directly from air and water at ambient temperature and pressure. *Sci. Rep.*, 3(1):1145, dec 2013.

[171] Rong Lan, John T.S. Irvine, and Shanwen Tao. Synthesis of ammonia directly from air and water at ambient temperature and pressure. *Sci. Rep.*, 3(1):1145, dec 2013.

[172] Rong Lan and Shanwen Tao. Direct ammonia alkaline anion-exchange membrane fuel cells. *Electrochem. Solid-State Lett.*, 13(8):B83, aug 2010.

[173] Rong Lan and Shanwen Tao. Ammonia as a suitable fuel for fuel cells. *Front. Energy Res.*, 2(AUG):35, aug 2014.

[174] Philip J. Landrigan, Richard Fuller, Nereus J.R. Acosta, Olusoji Adeyi, Robert Arnold, Niladri (Nil) Basu, Abdoulaye Bibi Baldé, Roberto Bertollini, Stephan Bose-O'Reilly, Jo Ivey Boufford, Patrick N. Breysse, Thomas Chiles, Chulabhorn Mahidol,

Awa M. Coll-Seck, Maureen L. Cropper, Julius Fobil, Valentin Fuster, Michael Greenstone, Andy Haines, David Hanrahan, David Hunter, Mukesh Khare, Alan Krupnick, Bruce Lanphear, Bindu Lohani, Keith Martin, Karen V. Mathiasen, Maureen A. McTeer, Christopher J.L. Murray, Johanita D. Ndahimananjara, Frederica Perera, Janez Potočnik, Alexander S. Preker, Jairam Ramesh, Johan Rockström, Carlos Salinas, Leona D. Samson, Karti Sandilya, Peter D. Sly, Kirk R. Smith, Achim Steiner, Richard B. Stewart, William A. Suk, Onno C.P. van Schayck, Gautam N. Yadama, Kandeh Yumkella, and Ma Zhong. The Lancet Commission on pollution and health. *Lancet*, 391(10119):462–512, feb 2018.

[175] I. A. Larson, J. M. Ordovas, Z. Sun, J. R. Barnard, J. Lohrmann, G. Feussner, S. Lamon-Fava, and Ernst J. Schaefer. Effects of apolipoprotein A-IV genotype on glucose and plasma lipoprotein levels. *Clin. Genet.*, 61(6):430–436, 2002.

[176] Gil Jae Lee, Jae Hyeok Shim, Young Whan Cho, and Kyung Sub Lee. Reversible hydrogen storage in NaAlH4 catalyzed with lanthanide oxides. *Int. J. Hydrogen Energy*, 32(12):1911–1915, aug 2007.

[177] Nathan S. Lewis. Toward cost-effective solar energy use. *Science (80-.).*, 315(5813):798–801, feb 2007.

[178] Chao Li, Changlong Li, Meiqiang Fan, Haichao Chen, Kangying Shu, Yu Zhang, Mingxia Gao, Yongfeng Liu, and Hongge Pan. Synthesis of a ternary amide LixKy(NH2)x+y and a novel Li3K(NH2)4–xMgH2 combination system for hydrogen storage. *J. Energy Chem.*, 35:37–43, aug 2019.

[179] Gang Li, Masakoto Kanezashi, Tomohisa Yoshioka, and Toshinori Tsuru. Ammonia decomposition in catalytic membrane reactors: Simulation and experimental studies. *AIChE J.*, 59(1):168–179, jan 2013.

[180] Hai Wen Li, Yigang Yan, Shin Ichi Orimo, Andreas Züttel, and Craig M. Jensen. Recent progress in metal borohydrides for hydrogen storage. *Energies*, 4(1):185–214, jan 2011.

[181] Stuart Licht, Baochen Cui, Baohui Wang, Fang Fang Li, Jason Lau, and Shuzhi Liu. Ammonia synthesis by N2and steam electrolysis in molten hydroxide suspensions of nanoscale Fe2O3. *Science (80-.).*, 345(6197):637–640, aug 2014.

[182] Arthur D Little. Guidance for Transportation Technologies : Fuel Choice for Fuel Cell Vehicles. *Fuel*, 2002.

[183] Junguo Liu, Kun Ma, Philippe Ciais, and Stephen Polasky. Reducing human nitrogen use for food production. *Sci. Rep.*, 6:30104, 2016.

[184] Yi Liu, Andrew Z. Fire, Scott Boyd, and Richard A. Olshen. Estimating Clonality. *Chem. Rev.*, 112(2):782–835, feb 2014.

[185] Yongfeng Liu, Yaxiong Yang, Xin Zhang, You Li, Mingxia Gao, and Hongge Pan. Insights into the dehydrogenation reaction process of a K-containing Mg(NH2)2-2LiH system. *Dalt. Trans.*, 44(41):18012–18018, oct 2015.

[186] S. R. Logan, R. L. Moss, and C. Kemball. The catalytic decomposition of ammonia on evaporated iron films. *Trans. Faraday Soc.*, 54(0):922–930, jan 1958.

[187] M. V. Lototskyy, V. A. Yartys, B. G. Pollet, and R. C. Bowman. Metal hydride hydrogen compressors: A review. *Int. J. Hydrogen Energy*, 39(11):5818–5851, apr 2014.

[188] Rebecca Lowton. Thesis.

[189] Rebecca L. Lowton, Martin O. Jones, William I.F. David, Simon R. Johnson, Marco Sommariva, and Peter P. Edwards. The synthesis and structural investigation of mixed lithium/sodium amides. *J. Mater. Chem.*, 18(20):2355–2360, may 2008.

[190] Sean Thomas B. Lundin, Taichiro Yamaguchi, Colin A. Wolden, S. Ted Oyama, and J. Douglas Way. The role (or lack thereof) of nitrogen or ammonia adsorption-induced hydrogen flux inhibition on palladium membrane performance. *J. Memb. Sci.*, 514:65–72, sep 2016.

[191] Andrew E. Lutz, Richard S. Larson, and Jay O. Keller. Thermodynamic comparison of fuel cells to the Carnot cycle. *Int. J. Hydrogen Energy*, 27(10):1103–1111, oct 2002.

[192] Qianli Ma, Jianjun Ma, Sa Zhou, Ruiqiang Yan, Jianfeng Gao, and Guangyao Meng. A high-performance ammonia-fueled SOFC based on a YSZ thin-film electrolyte. *J. Power Sources*, 164(1):86–89, jan 2007.

[193] M. H. Macdonald and R. D. Hill. The products of electrolysis of sodium amide-potassium amide eutectic mixture. Technical Report 1-2, 1960.

[194] Joshua W. Makepeace and William I.F. David. Structural Insights into the Lithium Amide-Imide Solid Solution. *J. Phys. Chem. C*, 121(22):12010–12017, 2017.

[195] Joshua W. Makepeace, Teng He, Claudia Weidenthaler, Torben R. Jensen, Fei Chang, Tejs Vegge, Peter Ngene, Yoshitsugu Kojima, Petra E. de Jongh, Ping Chen, and William I.F. David. Reversible ammonia-based and liquid organic hydrogen carriers for high-density hydrogen storage: Recent progress. *Int. J. Hydrogen Energy*, 44(15):7746–7767, feb 2019.

[196] Joshua W. Makepeace, Hazel M.A. Hunter, Thomas J. Wood, Ronald I. Smith, Claire A. Murray, and William I.F. David. Ammonia decomposition catalysis using lithium-calcium imide. *Faraday Discuss.*, 188(7):525–544, jun 2016.

[197] Joshua W. Makepeace, Martin O. Jones, Samantha K. Callear, Peter P. Edwards, and William I.F. David. In situ X-ray powder diffraction studies of hydrogen storage and release in the Li-N-H system. *Phys. Chem. Chem. Phys.*, 16(9):4061–4070, feb 2014.

[198] Joshua W. Makepeace, Thomas J. Wood, Hazel M.A. Hunter, Martin O. Jones, and William I.F. David. Ammonia decomposition catalysis using non-stoichiometric lithium imide. *Chem. Sci.*, 6(7):3805–3815, jun 2015.

[199] Joshua W. Makepeace, Thomas J. Wood, Phillip L. Marks, Ronald I. Smith, Claire A. Murray, and William I.F. David. Bulk phase behavior of lithium imide-metal nitride ammonia decomposition catalysts. *Phys. Chem. Chem. Phys.*, 20(35):22689–22697, sep 2018.

[200] M. Mamatha, C. Weidenthaler, A. Pommerin, M. Felderhoff, and F. Schüth. Comparative studies of the decomposition of alanates followed by in situ XRD and DSC methods. *J. Alloys Compd.*, 416(1-2):303–314, jun 2006.

[201] Donald W. Marquardt. An Algorithm for Least-Squares Estimation of Nonlinear Parameters. *J. Soc. Ind. Appl. Math.*, 11(2):431–441, jun 1963.

[202] Paul McLaughlin. Climate change, adaptation, and vulnerability: Reconceptualizing societal-environment interaction within a socially constructed adaptive landscape. Technical Report 3, 2011.

[203] M Melaina and M Penev Nrel. Hydrogen Station Cost Estimates Comparing Hydrogen Station Cost Estimates Hydrogen Station Cost Estimates Comparing Hydrogen Station Cost Estimates. *Natl. Renew. Energy Lab.*, (September), 2013.

[204] Guangyao Meng, Cairong Jiang, Jianjun Ma, Qianli Ma, and Xingqin Liu. Comparative study on the performance of a SDC-based SOFC fueled by ammonia and hydrogen. *J. Power Sources*, 173(1):189–193, nov 2007.

[205] R. Metkemeijer and P. Achard. Ammonia as a feedstock for a hydrogen fuel cell; reformer and fuel cell behaviour. *J. Power Sources*, 49(1-3):271–282, apr 1994.

[206] Giacomo Miceli, Clotilde S. Cucinotta, Marco Bernasconi, and Michele Parrinello. First principles study of the LiNH2/Li2NH transformation. *J. Phys. Chem. C*, 114(35):15174–15183, sep 2010.

[207] Joseph H. Montoya, Charlie Tsai, Aleksandra Vojvodic, and Jens K. Nørskov. The challenge of electrochemical ammonia synthesis: A new perspective on the role of nitrogen scaling relations. *ChemSusChem*, 8(13):2180–2186, jul 2015.

[208] C. S. Mørch, A. Bjerre, M. P. Gøttrup, S. C. Sorenson, and J. Schramm. Ammonia/hydrogen mixtures in an SI-engine: Engine performance and analysis of a proposed fuel system. *Fuel*, 90(2):854–864, feb 2011.

[209] Babak Motesharezadeh, Hassan Etesami, Sepideh Bagheri-Novair, and Hormoz Amirmokri. Fertilizer consumption trend in developing countries vs. developed countries. *Environ. Monit. Assess.*, 189(3):103, mar 2017.

[210] Shreya Mukherjee, Surya V. Devaguptapu, Anna Sviripa, Carl R.F. Lund, and Gang Wu. Low-temperature ammonia decomposition catalysts for hydrogen generation. *Appl. Catal. B Environ.*, 226(1):162–181, jun 2018.

[211] M. Müller, J. Senker, B. Asmussen, W. Press, H. Jacobs, W. Kockelmann, H. M. Mayer, and R. M. Ibberson. Orientational order and rotational dynamics of the amide ions in potassium amide. I. Neutron diffraction. *J. Chem. Phys.*, 107(7):2363–2373, 1997.

[212] Tsuyoshi Murakami, Tokujiro Nishikiori, Toshiyuki Nohira, and Yasuhiko Ito. Electrolytic synthesis of ammonia in molten salts under atmospheric pressure. *J. Am. Chem. Soc.*, 125(2):334–335, 2003.

[213] Yuko Nakamori and Shin ichi Orimo. Destabilization of Li-based complex hydrides. *J. Alloys Compd.*, 370(1-2):271–275, may 2004.

[214] Emilio Napolitano, Francesco Dolci, Renato Campesi, Claudio Pistidda, Markus Hoelzel, Pietro Moretto, and Stefano Enzo. Crystal structure solution of KMg(ND)(ND2): An ordered mixed amide/imide compound. *Int. J. Hydrogen Energy*, 39(2):868–876, jan 2014.

[215] Renewable Energy Network. *Global Status Report, Renewable 2017*, volume 72. 2017.

[216] Gerard Novell-Leruth, Ana Valcárcel, Javier Pérez-Ramírez, and Josep M. Ricart. Ammonia dehydrogenation over platinum-group metal surfaces. Structure, stability, and reactivity of adsorbed NHx species. *J. Phys. Chem. C*, 111(2):860–868, 2007.

[217] Office Of and Energy Efficiency. Technical Targets for Onboard Hydrogen Storage for Light-Duty Vehicles. Technical Report 333, 2016.

[218] Kaname Okura, Takeou Okanishi, Hiroki Muroyama, Toshiaki Matsui, and Koichi Eguchi. Ammonia Decomposition over Nickel Catalysts Supported on Rare-Earth Oxides for the On-Site Generation of Hydrogen. *ChemCatChem*, 8(18):2988–2995, sep 2016.

[219] S. Orimo, Y. Nakamori, G. Kitahara, K. Miwa, N. Ohba, T. Noritake, and S. Towata. Destabilization and enhanced dehydriding reaction of LiNH2: An electronic structure viewpoint. *Appl. Phys. A Mater. Sci. Process.*, 79(7):1765–1767, nov 2004.

[220] Shin-ichi Orimo, Yuko Nakamori, Jennifer R Eliseo, Andreas Zttel, Craig M Jensen, and Andreas Zu. Complex Hydrides for Hydrogen Storage Complex Hydrides for Hydrogen Storage. *Mater. Res.*, 107(September):4111–4132, 2007.

[221] William Osborn, Tippawan Markmaitree, and Leon L. Shaw. The long-term hydriding and dehydriding stability of the nanoscale LiNH2+LiH hydrogen storage system. *Nanotechnology*, 20(20):204028, may 2009.

[222] Nick A. Owen, Oliver R. Inderwildi, and David A. King. The status of conventional world oil reserves-Hype or cause for concern? *Energy Policy*, 38(8):4743–4749, aug 2010.

[223] Full Paper, Corresponding Author Secondary, Corresponding Author, Olivier Dupont, Roberto Mazzini, Laurent Schmitt, and Didier Cretenot. Climate change 2001: impacts, adaptation, and vulnerability. Technical Report 06, 2002.

[224] Beatriz S. Parajón-Costa, Claudia C. Wagner, and Enrique J. Baran. Voltammetric and spectroscopic study of chromium(III)/picolinate complexes. *Zeitschrift fur Anorg. und Allg. Chemie*, 629(6):1085–1090, 2003.

[225] John W. Patrick. *Handbook of fuel cells. Fundamentals technology and applications*, volume 83. John Wiley & Sons, Ltd, Chichester, Chichester, England ;, volume 3 edition, 2004.

[226] G. S. Pawley. Unit-cell refinement from powder diffraction scans. *J. Appl. Crystallogr.*, 14(6):357–361, dec 1981.

[227] Lynn F. Pearson and Lynn F. Pearson. The Department of Energy. Technical report, 1981.

[228] J. Perl, J. Shin, J. Schümann, B. Faddegon, and H. Paganetti. TOPAS: An innovative proton Monte Carlo platform for research and clinical applications. *Med. Phys.*, 39(11):6818–6837, oct 2012.

[229] J. Perl, J. Shin, J. Schümann, B. Faddegon, and H. Paganetti. TOPAS: An innovative proton Monte Carlo platform for research and clinical applications. *Med. Phys.*, 39(11):6818–6837, oct 2012.

[230] Dale Perry. *Handbook of Inorganic Compounds, Second Edition*. Taylor & Francis, 2011.

[231] Jean Fabien Petit, Philippe Miele, and Umit B. Demirci. Ammonia borane H3N[sbnd]BH3 for solid-state chemical hydrogen storage: Different samples with different thermal behaviors. *Int. J. Hydrogen Energy*, 41(34):15462–15470, sep 2016.

[232] Giovanni Pireddu, Antonio Valentoni, Christian Bonatto Minella, Claudio Pistidda, Chiara Milanese, Stefano Enzo, Gabriele Mulas, and Sebastiano Garroni. Comparison of the thermochemical and mechanochemical transformations in the 2NaNH2-MgH2 system. *Int. J. Hydrogen Energy*, 40(4):1829–1835, jan 2015.

[233] D. Pukazhselvan, M. Sterlin Leo Hudson, Bipin Kumar Gupta, M. A. Shaz, and O. N. Srivastava. Investigations on the desorption kinetics of Mm-doped NaAlH4. *J. Alloys Compd.*, 439(1-2):243–248, jul 2007.

[234] Darryl S. Pyle, E. Mac A. Gray, and C. J. Webb. Hydrogen storage in carbon nanostructures via spillover. *Int. J. Hydrogen Energy*, 41(42):19098–19113, feb 2016.

[235] Antonio Jesús Ramos-Morcillo, María Ruzafa-Martínez, Serafín Fernández-Salazar, Rafael Del-Pino-Casado, and David Armero Barranco. Actitudes de médicos y enfermeras ante las actividades preventivas y de promoción en atención primaria, 2014.

[236] Wioletta Raróg, Zbigniew Kowalczyk, Jan Sentek, Dominik Składanowski, and Jerzy Zieliński. Effect of K, Cs and Ba on the kinetics of NH 3 synthesis over carbon-based ruthenium catalysts. *Catal. Letters*, 68(3-4):163–168, 2000.

[237] Wioletta Raróg-Pilecka, Dariusz Szmigiel, Zbigniew Kowalczyk, Sławomir Jodzis, and Jerzy Zielinski. Ammonia decomposition over the carbon-based ruthenium catalyst promoted with barium or cesium. *J. Catal.*, 218(2):465–469, sep 2003.

[238] Alexandra Reis. A portfolio of power-trains for Europe : a fact-based analysis. Technical report, 2010.

[239] Aaron J. Reiter and Song Charng Kong. Combustion and emissions characteristics of compression-ignition engine using dual ammonia-diesel fuel. *Fuel*, 90(1):87–97, jan 2011.

[240] H. M. Rietveld. A profile refinement method for nuclear and magnetic structures. *J. Appl. Crystallogr.*, 2(2):65–71, jun 1969.

[241] Job Rijssenbeek, Yan Gao, Jonathan Hanson, Qingzhen Huang, Camille Jones, and Brian Toby. Crystal structure determination and reaction pathway of amide-hydride mixtures. *J. Alloys Compd.*, 454(1-2):233–244, apr 2008.

[242] Jonathan Rittle and Jonas C. Peters. An Fe-N2 Complex That Generates Hydrazine and Ammonia via Fe=NNH2: Demonstrating a Hybrid Distal-to-Alternating Pathway for N2 Reduction. *J. Am. Chem. Soc.*, 138(12):4243–4248, mar 2016.

[243] Emanuele Rizzuto, Pietro Palange, and Zaccaria Del Prete. Characterization of an ammonia decomposition process by means of a multifunctional catalytic membrane reactor. *Int. J. Hydrogen Energy*, 39(22):11403–11410, jul 2014.

[244] Rimma I. Samoilova, Derrick Kolling, Taketoshi Uzawa, Toshio Iwasaki, Antony R. Crofts, and Sergei A. Dikanov. The interaction of the Rieske iron-sulfur protein with occupants of the Q o -site of the bc 1 complex, probed by electron spin echo envelope modulation. Technical Report 7, 2002.

[245] A. Santoru, S. Garroni, C. Pistidda, C. Milanese, A. Girella, A. Marini, E. Masolo, A. Valentoni, N. Bergemann, T. T. Le, H. Cao, D. Haase, O. Balmes, K. Taube, G. Mulas, S. Enzo, T. Klassen, and M. Dornheim. A new potassium-based intermediate and its role in the desorption properties of the K-Mg-N-H system. *Phys. Chem. Chem. Phys.*, 18(5):3910–3920, jan 2016.

[246] Antonio Santoru, Claudio Pistidda, Magnus H. Sørby, Michele R. Chierotti, Sebastiano Garroni, Eugenio Pinatel, Fahim Karimi, Hujun Cao, Nils Bergemann, Thi T. Le, Julián Puszkiel, Roberto Gobetto, Marcello Baricco, Bjørn C. Hauback, Thomas Klassen, and Martin Dornheim. KNH2-KH: A metal amide-hydride solid solution. *Chem. Commun.*, 52(79):11760–11763, 2016.

[247] Sunita Satyapal, John Petrovic, Carole Read, George Thomas, and Grace Ordaz. The U.S. Department of Energy's National Hydrogen Storage Project: Progress towards meeting hydrogen-powered vehicle requirements. *Catal. Today*, 120(3-4 SPEC. ISS.):246–256, feb 2007.

[248] Louis Schlapbach and Andreas Züttel. Hydrogen in intermetallic compounds : surface and dynamic properties. *Nature*, 414(6861):353–358, nov 2014.

[249] Maurice Schlichtenmayer and Michael Hirscher. The usable capacity of porous materials for hydrogen storage. *Appl. Phys. A Mater. Sci. Process.*, 122(4):379, apr 2016.

[250] Richard R. Schrock. Catalytic Reduction of Dinitrogen to Ammonia by Molybdenum. *Catal. without Precious Met.*, pages 25–50, 2010.

[251] F. Schüth, R. Palkovits, R. Schlögl, and D. S. Su. Ammonia as a possible element in an energy infrastructure: Catalysts for ammonia decomposition. *Energy Environ. Sci.*, 5(4):6278–6289, mar 2012.

[252] Julian Sculley, Daqiang Yuan, and Hong Cai Zhou. The current status of hydrogen storage in metal-organic frameworks - Updated. *Energy Environ. Sci.*, 4(8):2721–2735, aug 2011.

[253] Justine Sears, David Roberts, and Karen Glitman. A comparison of electric vehicle Level 1 and Level 2 charging efficiency. In *2014 IEEE Conf. Technol. Sustain. SusTech 2014*, pages 255–258. IEEE, jul 2014.

[254] Robert F. Service. Liquid sunshine. *Science (80-.).*, 361(6398):120–123, 2018.

[255] Godwin Severa, Ewa Rönnebro, and Craig M. Jensen. Direct hydrogenation of magnesium boride to magnesium borohydride: Demonstration of >11 weight percent reversible hydrogen storage. *Chem. Commun.*, 46(3):421–423, dec 2010.

[256] M. Sevilla, A. B. Fuertes, and R. Mokaya. High density hydrogen storage in superactivated carbons from hydrothermally carbonized renewable organic materials. *Energy Environ. Sci.*, 4(4):1400–1410, mar 2011.

[257] Marta Sevilla, Nurul Alam, and Robert Mokaya. Enhancement of hydrogen storage capacity of zeolite-templated carbons by chemical activation. *J. Phys. Chem. C*, 114(25):11314–11319, jul 2010.

[258] Yi Shen and Aik Chong Lua. Synthesis of Ni and Ni-Cu supported on carbon nanotubes for hydrogen and carbon production by catalytic decomposition of methane. Technical Report 3, 2015.

[259] Hai Sheng Zeng, Koji Inazu, and Ken Ichi Aika. The working state of the barium promoter in ammonia synthesis over an active-carbon-supported ruthenium catalyst using barium nitrate as the promoter precursor. *J. Catal.*, 211(1):33–41, oct 2002.

[260] Drew A. Sheppard, Mark Paskevicius, and Craig E. Buckley. Hydrogen desorption from the NaNH2-MgH2 system. *J. Phys. Chem. C*, 115(16):8407–8413, apr 2011.

[261] L. M. Siperko and W. J. Landis. Atomic force microscopy imaging of hydroxyapatite. Technical Report 14, Centre for European Policy Studies, 1993.

[262] V. Smil. Detonator of the population explosion. *Nature*, 400(6743):415, jul 1999.

[263] R. I. Smith, S. Hull, and A. R. Armstrong. Polaris powder diffractometer at ISIS. *Mater. Sci. Forum*, 166-169(pt 1):251–256, jun 1994.

[264] Rasmus Zink Sørensen, Lærke J.E. Nielsen, Søren Jensen, Ole Hansen, Tue Johannessen, Ulrich Quaade, and Claus Hviid Christensen. Catalytic ammonia decomposition: Miniaturized production of COx-free hydrogen for fuel cells. *Catal. Commun.*, 6(3):229–232, mar 2005.

[265] Sesha S. Srinivasan, Hendrik W. Brinks, Bjorn C. Hauback, Dalin Sun, and Craig M. Jensen. Long term cycling behavior of titanium doped NaAlH4 prepared through solvent mediated milling of NaH and Al with titanium dopant precursors. *J. Alloys Compd.*, 377(1-2):283–289, sep 2004.

[266] John Staniforth and R. Mark Ormerod. Clean destruction of waste ammonia with consummate production of electrical power within a solid oxide fuel cell system. *Green Chem.*, 5(5):606–609, oct 2003.

[267] R. Ströbel, M. Oszcipok, M. Fasil, B. Rohland, L. Jörissen, and J. Garche. The compression of hydrogen in an electrochemical cell based on a PE fuel cell design. *J. Power Sources*, 105(2):208–215, mar 2002.

[268] S. P. Szu, M. Greenblatt, and L. C. Klein. The effect of precursors on the ionic conductivity in lithium silicate gels. Technical Report 3-4, 1991.

[269] Jiliang Tang, Yi Chang, Charu Aggarwal, and Huan Liu. A survey of signed network mining in social media. Technical Report 3, 2016.

[270] Yun Lei Teng, Takayuki Ichikawa, Hiroki Miyaoka, and Yoshitsugu Kojima. Improvement of hydrogen desorption kinetics in the LiH-NH3 system by addition of KH. *Chem. Commun.*, 47(44):12227–12229, nov 2011.

[271] The International Council of Clean Transportation. The International Council on Clean Transportation, 2016.

[272] The World Bank. Electric power consumption, 2015.

[273] George Thomas and George Parks. Potential Roles of Ammonia in a Hydrogen Economy: Public Opinion and Input. Technical report, 2006.

[274] K. Mark Thomas. Adsorption and desorption of hydrogen on metal–organic framework materials for storage applications: Comparison with other nanoporous materials. *J. Chem. Soc. Dalt. Trans.*, 0(9):1487–1505, feb 2009.

[275] W. C. Thomlinson, J. F. Kelly, and R. C. Richardson. The spectral density function J1(ω) in solid 3He. Technical Report 7, 1972.

[276] Arthur W. Titherley. XLV. - Sodium, potassium, and lithium amides. *J. Chem. Soc. Trans.*, 65(0):504–522, jan 1894.

[277] Kazuhiko Tokoyoda, Satoshi Hino, Takayuki Ichikawa, Keisuke Okamoto, and Hironobu Fujii. Hydrogen desorption/absorption properties of Li-Ca-N-H system. *J. Alloys Compd.*, 439(1-2):337–341, jul 2007.

[278] S. Tretsiakova-McNally. LECTURE – Introduction to FCH applications and hydrogen safety. Technical Report 1-2, 2015.

[279] W. Tsai and W. H. Weinberg. Steady-state decomposition of ammonia on the Ru(001) surface. *J. Phys. Chem.*, 91(20):5302–5307, sep 1987.

[280] Kostiantyn Turcheniuk, Dmitry Bondarev, Vinod Singhal, and Gleb Yushin. Ten years left to redesign lithium-ion batteries. *Nature*, 559(7715):467–470, jul 2018.

[281] John A. Turner. A realizable renewable energy future. *Science (80-.).*, 285(5428):687–689, jul 1999.

[282] Mehraj ud din Naik, Sami ullah Rather, Renju Zacharia, Chang Su So, Sang Woon Hwang, Ae Rhan Kim, and Kee Suk Nahm. Comparative study of dehydrogenation of sodium aluminum hydride wet-doped with ScCl3, TiCl3, VCl3, and MnCl2. *J. Alloys Compd.*, 471(1-2):L16–L22, mar 2009.

[283] United Nations. World population projected to reach 9.8 billion in 2050, and 11.2 billion in 2100 — UN DESA — United Nations Department of Economic and Social Affairs, 2017.

[284] Francisco A. Uribe, Shimshon Gottesfeld, and Thomas A. Zawodzinski. Effect of ammonia as potential fuel impurity on proton exchange membrane fuel cell performance. *J. Electrochem. Soc.*, 149(3):A293, mar 2002.

[285] U.S. Energy Information Administration. How much gasoline does the United States consume? - FAQ - U.S. Energy Information Administration (EIA), 2018.

[286] Bart A Van Hassel, J M Pasini, and J R Karra. Advancement of Systems Designs and Key Engineering Technologies for Materials Based Hydrogen Storage. Technical report, 2015.

[287] Greg Vezina, Yusuf Bicer, Ibrahim Dincer, Calin Zamfirescu, and Frank Raso. Key Life Cycle Assessment Numbers for NH3 , Green and Brown Energy. Technical report, 2016.

[288] Vivid Economics. Accelerating the EV transition Part 2: electricity system impacts. Technical Report June, WWF, 2018.

[289] Jian Feng Wang, Chiu Sing Choy, Tak Lon Chao, Ko Chun Kit, Kong Pang Pun, Wan Li Ouyang, and Xiao Gang Wang. Simplifying HOG arithmetic for speedy hardware realization. *IEEE Asia-Pacific Conf. Circuits Syst. Proceedings, APCCAS*, 2015-Febru(February):61–64, sep 2015.

[290] Jianhui Wang, Tao Liu, Guotao Wu, Wen Li, Yongfeng Liu, C. Moysés Araújo, Ralph H. Scheicher, Andreas Blomqvist, Rajeev Ahuja, Zhitao Xiong, Ping Yang, Mingxia Gao, Hongge Pan, and Ping Chen. Potassium-modified Mg(NH2)2/2LiH system for hydrogen storage. *Angew. Chemie - Int. Ed.*, 48(32):5828–5832, jul 2009.

[291] Jianhui Wang, Guotao Wu, Yong Shen Chua, Jianping Guo, Zhitao Xiong, Yao Zhang, Mingxia Gao, Hongge Pan, and Ping Chen. Hydrogen sorption from the Mg(NH 2) 2 -KH system and synthesis of an amide-imide complex of KMg(NH)(NH 2). *ChemSusChem*, 4(11):1622–1628, nov 2011.

[292] Li Wang, Yue Zhao, Chunyang Liu, Weimin Gong, and Hongchen Guo. Plasma driven ammonia decomposition on a Fe-catalyst: Eliminating surface nitrogen poisoning. *Chem. Commun.*, 49(36):3787–3789, apr 2013.

[293] S. J. Wang, S. F. Yin, L. Li, B. Q. Xu, C. F. Ng, and C. T. Au. Investigation on modification of Ru/CNTs catalyst for the generation of COx-free hydrogen from ammonia. *Appl. Catal. B Environ.*, 52(4):287–299, oct 2004.

[294] J. J. Weber. Josh Thesis. 2014.

[295] Thomas J. Wood and Joshua W. Makepeace. Assessing Potential Supports for Lithium Amide-imide Ammonia Decomposition Catalysts. *ACS Appl. Energy Mater.*, 1(6):2657–2663, jun 2018.

[296] Thomas J. Wood, Joshua W. Makepeace, and William I.F. David. Isotopic studies of the ammonia decomposition reaction using lithium imide catalyst. *Phys. Chem. Chem. Phys.*, 19(6):4719–4724, feb 2017.

[297] Thomas J. Wood, Joshua W. Makepeace, and William I.F. David. Neutron diffraction and gravimetric study of the manganese nitriding reaction under ammonia decomposition conditions. *Phys. Chem. Chem. Phys.*, 20(13):8547–8553, oct 2018.

[298] Thomas J. Wood, Joshua W. Makepeace, and William I.F. David. Neutron diffraction and gravimetric study of the manganese nitriding reaction under ammonia decomposition conditions. *Phys. Chem. Chem. Phys.*, 20(13):8547–8553, oct 2018.

[299] Thomas J. Wood, Joshua W. Makepeace, Hazel M.A. Hunter, Martin O. Jones, and William I.F. David. Isotopic studies of the ammonia decomposition reaction mediated by sodium amide. *Phys. Chem. Chem. Phys.*, 17(35):22999–23006, aug 2015.

[300] Guanglin Xia, Dan Li, Xiaowei Chen, Yingbin Tan, Ziwei Tang, Zaiping Guo, Huakun Liu, Zongwen Liu, and Xuebin Yu. Carbon-coated Li 3 N nanofibers for advanced hydrogen storage. *Adv. Mater.*, 25(43):6238–6244, nov 2013.

[301] Zhitao Xiong, Jianjiang Hu, Guotao Wu, and Ping Chen. Hydrogen absorption and desorption in Mg-Na-N-H system. *J. Alloys Compd.*, 395(1-2):209–212, may 2005.

[302] H. Yamane, T. H. Okabe, O. Ishiyama, Y. Waseda, and M. Shimada. Ternary nitrides prepared in the Li3N-Mg3N2 system at 900-1000 K. *J. Alloys Compd.*, 319(1-2):124–130, apr 2001.

[303] Qiong Yang, Quan Ping Su, Gui Yun Wang, De Zhong Wen, Yan Hui Zhang, Hui Zheng Bao, and Li Wang. Production of hybrid phage displaying secreted aspartyl proteinase epitope of Candida albicans and its application for the diagnosis of disseminated candidiasis. Technical Report 3, 2007.

[304] Zhuxian Yang, Yongde Xia, and Robert Mokaya. Enhanced hydrogen storage capacity of high surface area zeolite-like carbon materials. *J. Am. Chem. Soc.*, 129(6):1673–1679, 2007.

[305] S. F. Yin, B. Q. Xu, X. P. Zhou, and C. T. Au. A mini-review on ammonia decomposition catalysts for on-site generation of hydrogen for fuel cell applications. *Appl. Catal. A Gen.*, 277(1-2):1–9, dec 2004.

[306] Shuang Feng Yin, Bo Qing Xu, Shui Ju Wang, and Chak Tong Au. Nanosized Ru on high-surface-area superbasic ZrO2-KOH for efficient generation of hydrogen via ammonia decomposition. *Appl. Catal. A Gen.*, 301(2):202–210, feb 2006.

[307] Shuang Feng Yin, Qin Hui Zhang, Bo Qing Xu, Wen Xia Zhu, Ching Fai Ng, and Chak Tong Au. Investigation on the catalysis of CO x -free hydrogen generation from ammonia. *J. Catal.*, 224(2):384–396, jun 2004.

[308] Akihiro Yoshida, Hana Yoshimura, Tomoyuki Terada, Yasuyuki Nakayama, Hiroki Kuno, Toshihiro Miyao, and Shuichi Naito. Preparation of graphite supported Li-N-H hydrogen storage material from Li-graphite intercalation compound and their unique hydrogen release property. *Int. J. Hydrogen Energy*, 36(11):6751–6755, jun 2011.

[309] Pei Yu, Jianping Guo, Lin Liu, Peikun Wang, Fei Chang, Han Wang, Xiaohua Ju, and Ping Chen. Effects of Alkaline Earth Metal Amides on Ru in Catalytic Ammonia Decomposition. *J. Phys. Chem. C*, 120(5):2822–2828, feb 2016.

[310] Armando Zambrano Leal. Sociedad de control y profesión docente. Las imposturas de un discurso y la exigencia de una nueva realidad, 2012.

[311] C. Zamfirescu and I. Dincer. Using ammonia as a sustainable fuel. *J. Power Sources*, 185(1):459–465, oct 2008.

[312] C. Zamfirescu and I. Dincer. Ammonia as a green fuel and hydrogen source for vehicular applications. *Fuel Process. Technol.*, 90(5):729–737, may 2009.

[313] Changjun Zhang and Ali Alavi. A first-principles investigation of LiNH2 as a hydrogen-storage material: Effects of substitutions of K and Mg for Li. *J. Phys. Chem. B*, 110(14):7139–7143, 2006.

[314] Jian Zhang, Jens Oliver Müller, Weiqing Zheng, Di Wang, Dangsheng Su, and Robert Schlögl. Individual Fe-Co alloy nanoparticles on carbon nanotubes: Structural and catalytic properties. *Nano Lett.*, 8(9):2738–2743, sep 2008.

[315] Jian Zhang, Hengyong Xu, Qingjie Ge, and Wenzhao Li. Highly efficient Ru/MgO catalysts for NH3 decomposition: Synthesis, characterization and promoter effect. *Catal. Commun.*, 7(3):148–152, mar 2006.

[316] Junqing Zhang and Yun Hang Hu. Decomposition of lithium amide and lithium imide with and without anion promoter. *Ind. Eng. Chem. Res.*, 50(13):8058–8064, jul 2011.

[317] Junqing Zhang and Yun Hang Hu. Intermediate species and kinetics of lithium imide decomposition. *Int. J. Hydrogen Energy*, 37(13):10467–10472, jul 2012.

[318] Yan Zhong, Huai Ying Zhou, Chao Hao Hu, Dian Hui Wang, and Artem R. Oganov. Theoretical studies of high-pressure phases, electronic structure, and vibrational properties of NaNH 2. *J. Phys. Chem. C*, 116(15):8387–8393, apr 2012.

[319] Di Zhu, Linghong Zhang, Rose E. Ruther, and Robert J. Hamers. Photo-illuminated diamond as a solid-state source of solvated electrons in water for nitrogen reduction. *Nat. Mater.*, 12(9):836–841, sep 2013.

[320] Guijun Zhuang, Youmin Xi, and Alex S.L. Tsang. *Power, conflict, and cooperation: The impact of guanxi in Chinese marketing channels*, volume 39. 2010.